Identifying the mechanism behind mitochondrial changes in the cholinergic neurons of the pedunculopontine nucleus in patients with Parkinson's disease

Huiwen Amelia Lu

MSc

This thesis is submitted for the degree of Doctor of Philosophy at Newcastle University

Mitochondria Research Group

Newcastle University Bioscience Institute

December 2024

Author Declaration

This thesis is submitted for the degree of Doctor of Philosophy at Newcastle University. The research was conducted in the Mitochondria Research Gorup, Newcastle University Bioscience Institute, Newcastle university under the supervision of Dr. Joanna L Elson, Dr. Angela Pyle, Dr. Ilse S Pienaar, Dr. Conor Lawless and Professor Grainne Gorman.

I certify the none of the material presented in this thesis has been previously submitted by me for a degree or qualification at this or any other university.

Abstract

In Parkinson's disease (PD), patients often exhibit higher levels of somatic mitochondrial DNA (mtDNA) damage, particularly large-scale deletions, in their brains. This damage is associated with neuronal loss and has been seen in multiple neuronal types including nigral dopaminergic of the substantia nigra (SN) and cholinergic neurons in the Pedunculopontine Nucleus (PPN). Unlike dopaminergic neurons, PPN cholinergic neurons tend to maintain wild-type mtDNA levels by increasing mtDNA copy number (mtCN) in response to mtDNA deletions.

This study employed ultra-deep sequencing to analyse single cholinergic neurons isolated in an unbiased fashion from postmortem PPN tissue of PD and controls, examining both the mtDNA deletions, and point mutations across various parameters. Comparative analysis of mtDNA deletions was also conducted with nigral dopaminergic neurons to elucidate compensatory response to mtDNA damage. Additionally, single-neuron qRT-PCR was used to quantify the expression of three nuclear genes involved in mitochondria biogenesis, maintenance and mitophagy.

Our findings confirm significantly higher levels of large mtDNA deletions in PD patients compared to aged controls, with deletions ranging from 5-140bp (small) to >1,400bp (large). The distribution of large deletions suggests that replication errors are the primary mechanism underlying their generation, aligning with patterns observed in POLG patients and aged controls. Conversely, the low prevalence of small deletions suggests that oxidative damage is not a major contributor of mtDNA damage in these neurons. Point mutation levels did not differ significantly between groups across various parameters assessed. At the transcriptional level, *PINK1* expression was upregulated in PD neurons, whereas no significant changes were observed in *TFAM* or *PGC1α* expression. These findings suggest that the mitophagy pathway plays a prominent role in regulatory response to mitochondrial changes in PD.

Acknowledgements

To begin with, I want to express my deepest gratitude to my family—my mum, dad, and grandparents. They have always been incredibly supportive of my studies and have generously provided the financial support that enabled me to complete my degree. In particular, I want to acknowledge my grandmother, who was diagnosed with Parkinson's disease when I was a toddler. It was my passion to find a cure for her that inspired me to embark on this research journey.

I am deeply thankful to my friends for their companionship and encouragement throughout the years. A special thanks goes to Effy and Chen, both of whom have been my best friends in Newcastle. We developed a strong and lasting friendship during my time here, and their support has been invaluable. I will always cherish the experiences we shared together. I truly could not have completed this thesis without their unwavering encouragement. I also want to extend my gratitude to Stephanie, Alison, and Caroline for their support and kindness, which have meant so much to me.

I am profoundly grateful to everyone in the mitochondria research group. Throughout my degree, I have felt deeply supported and respected, and whenever I faced challenges, someone from the group was always there to lift my spirits. I want to extend particular thanks to Shivam, Yasmine, Ale, Krutik, Ersong, Omar, and Chen once again, for their kindness and encouragement.

My supervisors have been instrumental in my research journey. My heartfelt thanks go to my primary supervisor, Jo. I would not have been able to complete my studies without her tireless efforts to secure funding for my research and her genuine care for my well-being. Her passion for my project has been a constant source of inspiration. I also want to thank Angela, who continued to offer guidance and encouragement even after leaving the research group. Ilse who's funding provided the sequencing data analyses in this thesis as well as guidance on the PPN and the cholinergic system. I am equally grateful to Annette, Amy, Grainne, and Conor. Your collective support and dedication have been pivotal, and I deeply appreciate everything you have done for me.

I am also incredibly thankful for the vibrant community I found in Newcastle. I want to extend special thanks to Su, Eugene, Alex, Rachel, Chris, Desmond, and Teresa for

making my experience so enriching. The Newcastle University Symphony Orchestra, Music Society, Jesmond Parish Church, Newcastle Chinese Christian Fellowship, and Trinity Gosforth Church have all played a significant role in making my life colourful and meaningful during my studies. I feel truly blessed to have been part of these communities and the activities they offered.

I also acknowledge the use of Grammarly to identify improvements in writing style, and the use of Biorender to generate illustrations.

Above all, all glory belongs to God. I am profoundly grateful for the path You have designed for me and for guiding me throughout this research journey. I will continue to walk confidently in the path You have chosen for me, with faith and gratitude.

Courses and conferences attended

Jumping Rivers Introduction to R – Virtual training course (2021)

Jumping Rivers Statistical modelling with R – Virtual training course (2021)

International society for molecular neurodegeneration (ISMND) 2022 Glial and vascular contributions to neurodegenerative diseases -audit, Athens, Greece (2022)

Northeast postgraduate conference (NEPG) 2022- Poster presentation, Newcastle upon tyne, UK (2022)

The international British neuroscience association (BNA) 2023 festival of neuroscience - Poster presentation, Brighton, UK (2023)

International society for molecular neurodegeneration (ISMND) NextGen 2023 – Virtual conference, Poster presentation (2023)

Federation of European neuroscience societies (FENS) Forum 2024- Poster presentation, Vienna, Austria (2024)

Abbreviations

ATP	Adenosine Triphosphate
8-oxo-dG	8-Dihydro-2′-Deoxyguanosine
A	Adenine
AAC	Amino Acid Changes
ADP	Adenosine Diphosphate
ALAS	5-Aminolevulinate Synthase
AMPK	5′-Adenosine Monophosphate-Activated Protein Kinase
APAF1	Apoptosis Protease Activating Factor 1
ARPD	Akinetic-Rigid PD
ATP6	ATP Synthase Membrane Subunit 6
Bcl-2	B-cell Lymphoma 2
BRP	RNA-Binding Protein
C	Cytosine
CACT	Acylcarnitine Translocase
CB	Conditioning Buffer
CEOP	Chronic External Ophthalmoplegia Plus Syndrome
ChAT	Choline Acetyltransferase
CLIPX	Caseinolytic mitochondrial Matrix Peptidase Chaperone Subunit X
CO	Cytochrome C Oxidase Subunit
CoA	Coenzyme A
COX	Cytochrome C Oxidase
CPEO	Chronic Progressive External Ophthalmoplegia
CPgenIII	Uroporphyrinogen III
CSB	Conserved Sequence Blocks
CSF	Cerebrospinal Fluid
CT	Cycle Threshold
CTD	C-Terminal Domain
CYB	Cytochrome b
DAB	3,3’-Diaminobenzidine
DBS	Double Strand Break
DBS	Deep Brain Stimulation
DIABLO	Direct Inhibitor of Apoptosis Binding Protein with Low Pl
DL	Deletion Load
DLB	Dementia with Lewy Bodies
DNM2	Dynamin-2
DRP1	GTPase dynamin related protein 1
EFGM	Elongation Factor G Mitochondria
EFTs	Elongation Factor Thermo Stable
EFTu	Elongation Factor Thermo Unstable
ERRα	Estrogen-Related Receptor Alpha

ETC	Electron Transport Chain
FADH2	Reduced Flavin Adenine Dinucleotide
FAM	6-Carboxyfluorescein
FASTK	Fas-Activated Serine/Threonine Kinase
FASTKD2	FAS-Activated Serine/Threonine Kinase Domine 2
Fe-S	Iron-Sulphur
FIS1	Mitochondrial Fusion Protein 1
FMN	Flavin Mononucleotide
G	Guanine
G4	G-quadruplex
GP	Globus Palludus
HRP	Horseradish Peroxidase
HSP	Heavy Strand Promoter
HSP1	Heavy-Strand Promoter 1
HSV	Hypervariable Segment
HtrA2/Omi	High-Temperature Requirement Protein A2
IAP	Caspase-Inhibitory Protein
IHC	Immunohistochemistry Imaging Technique
IMC	Image Mass Cytometry
IMM	Inner Mitochondrial Membrane
KSS	Kearns-Sayre Syndrome
LB	Lewy Body
LC	Locus Coeruleus
LC3II	LC3-Phosphatidylethanolamine Conjugate
LCM	Laser Capture Microdissection
LHON	Leber Hereditary Optic Neuropathy
LONP1	ATP-Dependent Lon Protease
L-OPA1	Long Optic Atrophy 1
LPC	Laser Pressure Catapulting
LRRK2	Leucine-Rich Repeat Kinase 2
LSP	Light Strand Promoter
MAPL	Mitochondria-Associated Protein Ligase
MCIA	Mitochondrial Complex I Assembly
MDS	Movement Disorder Society
MDS-UPDRS	the Unified Parkinson's Disease Rating Scale sponsored by the Movement Disorder Society
MDVs	Mitochondrial-Derived Vesicles
MEGE1	Mitochondrial Elongation Factor G1
MELAS	Mitochondrial Encephalomyopathy, Lactic Acidosis, and Stroke-Like Episodes
MFF	Mitochondrial Fusion Factor

MFN	Mitofusin
MGB	Minor Groove Binder
MIDD	Maternally Inherited Diabetes and Deafness
Miro	Rho GTPase
MLR	Mesencephalic Locomotor Region
MMLV	Moloney Murine Leukaemia Virus
MPP	Mitochondrial Processing Protease
MPTP	1-Methyl-4-Phenyl-1,2,3,6-TetrahydroPyridine
MRI	Magnetic Resonance Imaging
MRM1	Mitochondrial rRNA Methyltransferase 1
mRNA	Messenger Ribonucleic Acid
MRPs	Mitochondrial Ribosomal Proteins
mtCN	MtDNA Copy Number
mtDNA	Mitochondrial Deoxyribonucleic Acid
mTERF1	Mitochondrial Termination Factor 1
mtIF	Mitochondrial Initiation Factor
mtLSU	Mitochondrial Large 39S Subunit
mtPAP	Mitochondrial Poly (A) Polymerase
MTS	Mitochondrial Targeting Signal
MTS	Mitochondrial Targeting Sequence
mtSSB	Mitochondrial Single-Stranded DNA-Binding Protein
mtSSU	Mitochondrial Small 28S Subunit
N Model	Electron Input Module
N Site	Negative Side of the Membrane
nAChRs	Nicotinic Acetylcholine Receptors
NADH	Reduced Nicotinamide-Adenine Dinucleotide
NCR	Non-Coding Region
ND	Ubiquinone Oxidoreductase Core Subunit
NDUFS1	NADH Dehydrogenase Iron-Sulphur Protein 1
NDUFV1	Dehydrogenase Flavoprotein 1
NDUFV2	Dehydrogenase Flavoprotein 2
NEF	Nuclear Respiratory Factors
NGS	Next Generation Sequencing
NT	Regulatory Domain
OAA	Oxaloacetate
OMM	Outer Mitochondrial Membrane
OPA1	Optic Atrophy 1
OPTN	Optineurin
OriH	Origin of the Heavy Strand Replication
OriL	Origin of the Light Strand Replication
OXPHOS	Oxidative Phosphorylation
P Model	Proton Translocation Module

P Site	Positive Side of the Membrane
P62	Sequestosome 1
PARL	Presenilin-Associated Rhomboid-Like
PD	Parkinson's Disease
PDD	PD Dementia
PDH	Pyruvate Dehydrogenase
PGC1α	Peroxisome Proliferator-Activated Receptor Gamma Coactivator 1-Alpha
PIGD	Postural Instability and Gait Difficulty
PINK1	Phosphatase and Tensin Homolog Induced Putative Kinase 1
PITRM1	Pitrilysin Metallopeptidase 1
PMD	Postmortem Delay
POLRMT	Mitochondrial DNA RNA Polymerase
POLγ	Polymerase γ
PPARγ	Peroxisome Proliferator-Activated Receptor Gamma
PPN	Pedunculopontine Nucleus
PPNc	PPN pars compacta
PPNd	PPN pars dissipatus
PreP	Presequence Protease
PS	Pearson's Syndrome
PSP	Progressive Supranuclear Palsy
Q	Ubiquinone
Q Model	Electron Output Module
QC	Quality Control
QH2	Ubiquinol
Q_n^-	Ubisemiquinone Anion
RAS	Reticular Activating System
RBR	RING-Between-Ring
RITOLS	Ribonucleotide Incorporation Throughout the Lagging Strand Model
RNase Z	Ribonuclease Z
RNR	Ribosomal RNA
ROS	Reactive Oxygen Species
rRNA	Ribosomal RNA
rRNA	Ribosomal Ribonucleic Acid
RT-PCR	Real-Time Polymerase Chain Reaction
SAA	Seed Amplification Assay
SC	Superior Colliculus
SDH	Succinate Dehydrogenase Complex Flavoprotein Subunit
SDHAF1	Succinate Dehydrogenase Complex Assembly Factor 1
SDM	Strand-Displacement Model
SIRT1	Sirtuin 1

SLSMDs	Single Large-Scale Mitochondrial DNA Deletions
Smac	The Second Mitochondria-Derived Activator of Caspase
SNCA	Alpha-Synuclein
SNpc	Substantia Nigra Pars Compacta
S-OPA2	Soluble Optic Atrophy 1
SSIV	SuperScript IV
STN	Subthalamic Nucleus
T	Thymine
TAC	Tricarboxylic Acid Cycle
TAS	Termination-Associated Sequence
TBST	Tris Buffered Saline with Tween 20
TDPD	Tremor-Dominant PD
TEFM	Transcription Elongation Factor
TFAM	Mitochondrial transcription factor A
TGB1M	Mitochondrial Transcriptional Factor B1
TK	Thymidine Kinase
TL1	tRNA Leucine 1
TM	Transmembrane Domain
TMB	3,3’,5’5’-Tetramethylbenzidine
TMEM126B	T*ransmembrane Protein 126B*
TOM	Translocase of the Outer Membrane
TOMM20	Translocase of Outer Mitochondrial Membrane 20
TOP3A	Topoisomerase 3A
tRNA	Transfer Ribonucleic Acid
Ts/Tv	Transition/ Transversion
Ubl	Ubiquitin-Like Domain
VDAC1	Voltage-Dependent Anion-Selective Channel 1
VIC	Variant of Hexachlorofluorescein
VTA	Ventral Tegmental Area
XIAP	X-linked Inhibitor of Apoptosis
XPNPEP1	X-Prolyl Aminopeptidase 1

Table of Contents

List of Figures

List of Tables

Chapter 1. Introduction

1.1. *Mitochondria origins*

Mitochondria, present in nearly every eukaryotic cell, play a vital role in generating adenosine triphosphate (ATP) to fuel cellular functions. The prevailing belief is that these organelles originated through an endosymbiotic relationship, as postulated by Sagan (Sagan, 1967). Two main theories elucidate the genesis of eukaryotes: one posits a divergence of nucleated *Archeazoa* from prokaryotes, with *Archeazoa* serving as the host for the mitochondrial endosymbiont, as supported by phylogenetic analysis of small subunit ribosomal ribonucleic acid (rRNA) (Cavalier-Smith, 1987; Moreira and Lopez-Garcia, 1998). Recent discoveries, such as *Lokirchaeota*, an *Archaebacterium* with cellular and genomic complexity akin to modern eukaryotic cells, bolster the notion of an archaebacterial progenitor for the eukaryotic nucleus (Spang *et al.*, 2015). The alternative theory, Hydrogen theory, suggests that the endosymbiotic event predates the divergence of eukaryotes from prokaryotes, with subsequent nuclear development forming the eukaryotic cell (Martin and Müller, 1998).This hypothesis gains traction due to the closer genetic relation of eukaryotic nuclear genes to eubacteria compared to archaebacterial homologues. While debate persists regarding the host cell, the endosymbiont, believed to be an a-proteobacteria, is phylogenetically traceable through similarities in present-day mitochondrial deoxyribonucleic acid (mtDNA) and specific genes encoded by the α-*proteobacteria* genome (Esser *et al.*, 2004). This endosymbiotic event between an archaebacterial host and α -*proteobacterial* symbiont (mitochondria) or cyanobacterial symbiont (chloroplast) is estimated to have occurred roughly 1-2 billion years ago (Embley and Martin, 2006). Both theories concur on the transfer of genetic material from the mitochondrial endosymbiont to the nucleus of the Archaebacterium. The evolutionary predecessor of mitochondria, identified as a-*proteobacteria Rickettsia prowazekii*, is supported by phylogenetic similarities in gene coding capacity for the tricarboxylic acid cycle (TCA) and electron transport chain (ETC) enzymes (Andersson and Kurland, 1998; Andersson *et al.*, 1998). This endosymbiotic event stands as a pivotal factor in explaining the independent genome and specific double membrane structure of mitochondria and chloroplasts.

1.2. *Mitochondrial structure*

Mitochondria are abundant rod-like organelles within cells and are primarily responsible for energy production. They exhibit dynamic behaviour, constantly undergoing processes of fission and fusion. Mitochondria consist of two membranes: the outer mitochondrial membrane (OMM) and the inner mitochondrial membrane (IMM) (Mårtensson, Doan and Becker, 2017). The region enclosed by the IMM is known as the mitochondrial matrix, while the space between the IMM and OMM is referred to as the mitochondrial intermembrane space. The OMM acts as a barrier, separating the mitochondria from the surrounding cytosol, and plays a role in regulating mitochondrial dynamics (Anderson *et al.*, 1981). Ensuring the normal function of mitochondria requires the importation of proteins encoded by the nucleus. In this process, key proteins such as the translocase of the outer membrane (TOM), which is embedded in the OMM, play a pivotal role in facilitating protein importation (Araiso, Imai and Endo, 2022)

The IMM houses the ETC and ATP synthesis processes. A proton gradient is established through a series of reactions, which is then utilized as an electrochemical gradient to drive energy production (Nolfi-Donegan, Braganza and Shiva, 2020).

The mitochondrial matrix is where the majority of protein and genomic reactions occur. Inside the matrix, near the IMM, resides mtDNA. This genetic material is distinct from the nuclear genome, operating with essential processes for shape, maintenance, and replication of mitochondria. There are mitochondrial ribosomes, encoded by the mtDNA, which play a crucial role in facilitating the translation of essential proteins of mitochondrial metabolism (Habbane *et al.*, 2021).

1.3. *Glycolysis and TCA cycle*

Food containing glucose ($C_6H_{12}O_6$) is taken up through glucose receptors located on different cells. Following a series of reactions such as glucose-6-phosphate and fructose-6-phosphate, one molecule of glucose is converted into two molecules of pyruvate ($C_3H_4O_3$) and two molecules of nicotinamide-adenine dinucleotide (NADH) (Equation 1.3-1) (Chandel, 2021). NADH serves as a hydrogen storage unit, facilitating the transport of both protons and electrons. After the glycolysis process, the main

product, pyruvate, is transported into the mitochondria matrix. The pyruvate dehydrogenase (PDH), located in the matrix of the mitochondria, then converts pyruvate into a two-carbon structure known as acetyl-CoA, which subsequently enters the tricarboxylic acid or Krebs cycle.

$$\text{Glucose} + 2[NAD^+] + 2[ADP] + 2[Pi] \rightarrow 2\,[\text{Pyruvate}] + 2[NADH] + 2[H^+] + 2[ATP] + 2[H20]$$

Equation 1.3-1 Glucose to pyruvate

Acetyl-CoA enters the TCA cycle by combining with a four-carbon molecule, oxaloacetate (OAA), forming a six-carbon citrate. Subsequently, through a series of reactions involving the loss of several carbons and assisted by various dehydrogenation and synthetase processes, citrate is converted back to oxaloacetate. This transformation results in the generation of 6 molecules of NADH, 2 molecules of reduced flavin adenine dinucleotide ($FADH_2$), and 2 molecules of ATP (Equation 1.3-2) (Martínez-Reyes and Chandel, 2020).

$$\text{Acetyl-CoA} + 3[NAD] + 1[FAD] + GDP + Pi + 2[H_2O] \rightarrow \text{CoA-SH} + 3[NADH] + FADH_2 + 3[H^+] + GTP + 2\,[CO_2]$$

Equation 1.3-2 TCA cycle

Both glycolysis and the TCA cycle contribute to the accumulation of high concentrations of NADH, $FADH_2$, and protons inside the mitochondrial matrix. These processes ensure the necessary preparation stages for entering the oxidative phosphorylation (OXPHOS) reactions located at the inner membrane of the mitochondria.

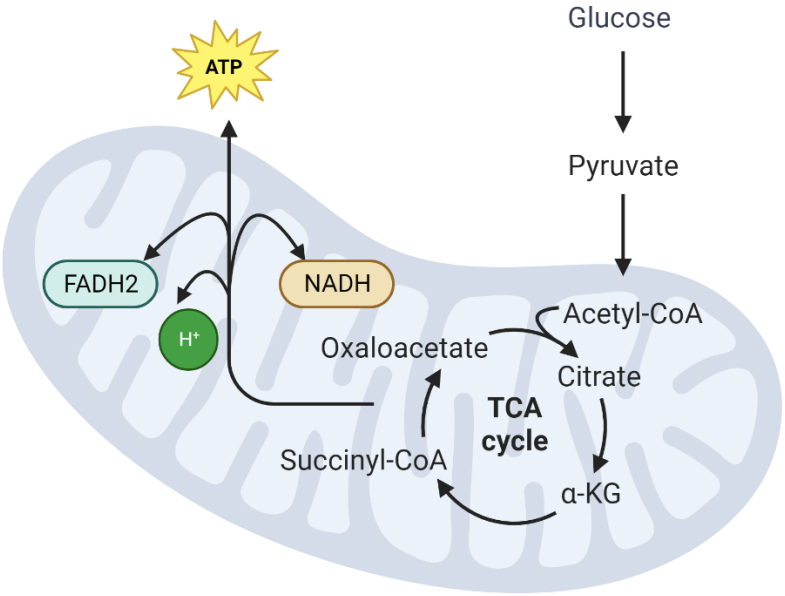

Figure 1.3-1 An illustration of glycolysis and TCA cycle

Glucose taken up by cells is first converted to pyruvate before being transported into the mitochondrial matrix. Within the matrix, pyruvate is converted into the two-carbon molecule Acetyl-CoA, which then enters the tricarboxylic acid cycle (TCA) by forming citrate. Through a series of reactions, citrate is eventually converted back to oxaloacetate, and it reacts with additional Acetyl-CoA to complete the cycle. Meanwhile, this process generates hydrogen carriers such as NADH and FADH, protons, and ATP.

1.4. *OXPHOS and synthesis of ATP*

Mitochondria are double-membraned organelles that play an essential role in maintaining normal cell signalling and homeostasis. The primary function of mitochondria is OXPHOS, a series of reactions carried out by the ETC complexes and complex V located in the inner membrane of mitochondria to generate energy in the form of ATP (*Figure 1.4-1*).

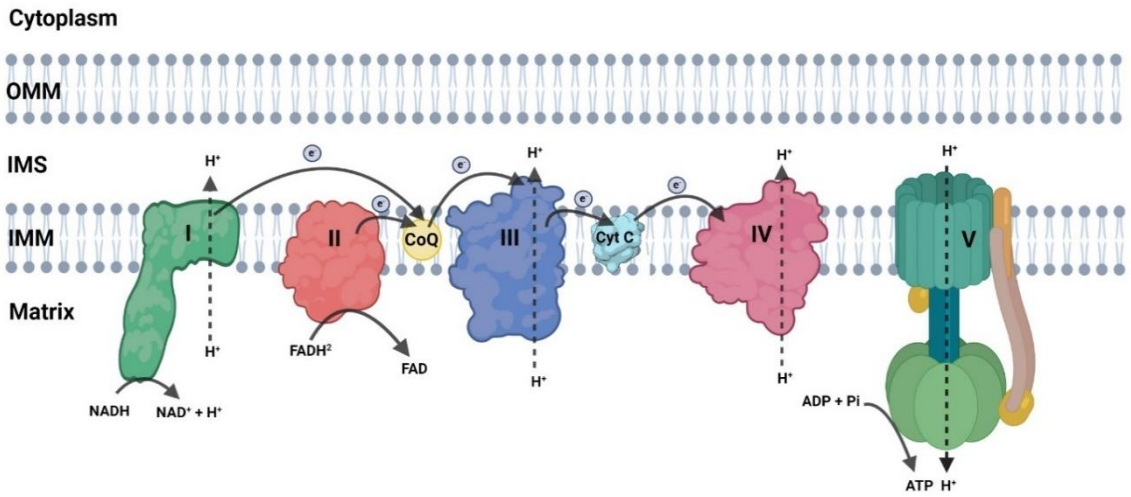

Figure 1.4-1 A schematic representation of OXPHOS reactions complexes

OXPHOS is composed of 5 complexes, Complex I: NADH ubiquinone oxidoreductase; Complex II: succinate dehydrogenase; Complex III: cytochrome bc1 complex; Complex IV: cytochrome c oxidase; Complex V: ATP Synthase, and they transfer electrons from donors to the acceptors while transfer the cross membrane of proton to generate ATP. OMM (outer mitochondrial membrane); IMS (intermembrane space); IMM (inner mitochondrial membrane); CoQ (Coenzyme Q10); Cyt C (cytochrome C).

Complex I is the largest component of the ETC, composed of 45 subunits, 14 of which are core subunits which have been highly conserved across species (Friedrich *et al.*, 1993; Sazanov *et al.*, 2000; Carroll *et al.*, 2006). The molecular weight is around 980 kDa and it was first isolated in 1962 (Hatefi, Haavik and Griffiths, 1962). These core subunits are partly encoded by the nucleus and partly by mtDNA. The structure of Complex I is L-shaped, with three modules: the electron input module (N module), the electron output module (Q module), and the proton translocation module (P module). (Figure 1.4-2)

The N module is composed of NADH dehydrogenase flavoprotein 1 (NDUFV1), NADH dehydrogenase flavoprotein 2 (NDUFV2), and NADH dehydrogenase iron-sulphur protein 1 (NDUFS1). It oxidizes NADH, with the hydrogen being taken by the co-effect

of flavin mononucleotide (FMN). After the oxidation is complete, the electrons are transferred to NDUFV2, which then transfers the electrons to the Q module of Complex I (Zickermann *et al.*, 2003).

Iron-Sulphur (Fe-S) clusters associated with a series of proteins receive the electrons from NDUFV2, initiating a series of redox reactions. Eventually, the electrons are transported to the hydrophobic electron carrier ubiquinone (coenzyme Q), converted to ubiquinol (QH2), and transported inside the membrane to Complex III for further use (Maio and Rouault, 2020; Read *et al.*, 2021).

All the subunits so far are encoded by the nucleus, and the mtDNA-encoded subunits are part of the P module embedded in the inner mitochondrial membrane. Ubiquinone oxidoreductase core subunit 1(ND1) is close to the Q module, forming an interface between the two modules, followed by three small E channel subunits: ND3, ND6, and ND4L. At the distal part of the Q module, there are three homologous antiporter-like subunits: ND2, ND4, and ND5. The expulsion of protons is driven by the conformational change of the ND1 subunit caused by the release of QH2 (Berrisford and Sazanov, 2009), and the entire reaction can be summarised by Equation 1.3-1 Glucose to pyruvate Equation 1.4-1 (Sazanov, 2015).

$$NADH + H^+ + Q + 4H^+_{in} \rightarrow NAD^+ + QH_2 + 4H^+_{out}$$

Equation 1.4-1 Complex I reaction

The assembly of Complex I in *Homo Sapiens* requires multiple assembly factors, transport pathways for importing nucleus-encoded proteins into the mitochondria, and the translation of mtDNA. By combining mitochondrial translation inhibitors or key gene knockouts, such as *transmembrane protein 126B* (*TMEM126B)*, in cell lines with high-resolution complex profiling, the assembly of Complex I appears to be a stepwise process (Fuhrmann, Wittig and Brüne, 2019). In the early stages, some small complexes gradually form, including the 293 kDa mitochondrial complex I assembly (MCIA) complex (Heide et al., 2012) and a 283 kDa complex composed of Q-module subunits, ND1 subunit, and the ND1 adjacent P-module (Q/Pp-a) (Zhu, Vinothkumar and Hirst, 2016). Subsequently, these small complexes start to attract more subunits

and increase in size gradually. The assembly of the N module seems to be the final step in completion (Mimaki et al., 2012).

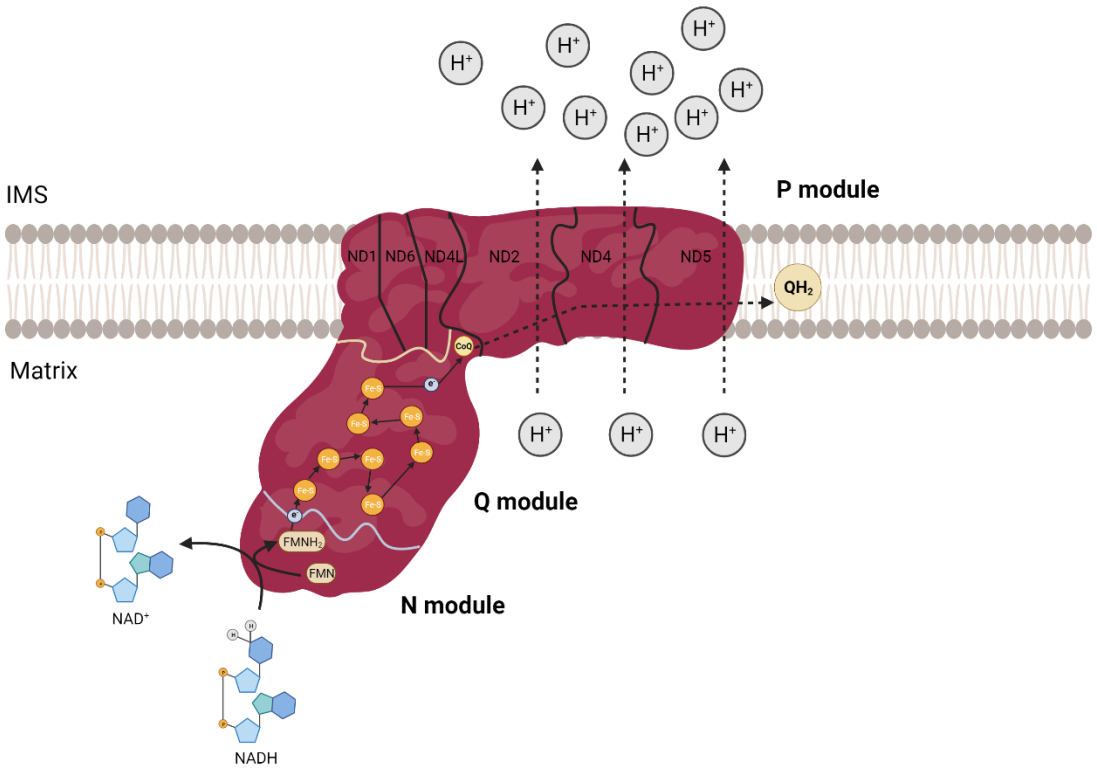

Figure 1.4-2 An illustration of the complex I reactions

FMN facilitates the dehydrogenation of NADH, resulting in the formation of NAD+ and the extraction of hydrogen from it at the N module of complex I. Passing through the hydrogen from the Fe-S cluster (a fundamental association part of several Q module composition proteins like NDUFS2, NDUFS3, NDUFS8) located in the Q module of complex I, the hydrogen is eventually transported to coenzyme Q. The conversion of coenzyme Q to QH2 leads to a conformational change in the nearby P module, driving proton expulsion in the distal part of the P module.

Complex II is the smallest complex in the entire ETC, with a size of only around 140 kDa. It consists of heterotetrametric subunits: succinate dehydrogenase complex flavoprotein subunit A (SDHA), succinate dehydrogenase complex flavoprotein subunit B (SDHB), succinate dehydrogenase complex flavoprotein subunit C (SDHC), and succinate dehydrogenase complex flavoprotein subunit D (SDHD). These subunits are

all encoded and controlled by the same nuclear genes (Bezawork-Geleta *et al.*, 2017). After being transported into the mitochondria through the TIM/TOM import system, subunits are assembled (Rutter, Winge and Schiffman, 2010). The assembly process requires coordination of abundant assembly factors and still require further investigation. Succinate dehydrogenase complex assembly factor 1 (SDHAF1) is an assembly factor which involved in the SDHB recruiting process of Fe-S via LYR motifs, and its mutations has been detected in various patients with complex II deficiency (Ghezzi *et al.*, 2009; Maio *et al.*, 2016). SDHA and SDHB form the hydrophilic head of Complex II, while SDHC and SDHD, embedded within the inner membrane as a membrane anchor, constitute the hydrophobic part of the complex. SDHC and SDHD are linked together by a heme b moiety, providing axial His ligands on each side. The ubiquinone site is located on the surface where SHDB, SHDC, and SHCD meet (Figure 1.4-3).

Despite the small size, complex II is the only subunit which involved in both the TCA cycle and the OXPHOS function of the cell. Plus, it is the only ETC complex which does not involve in any proton pumping. Succinate binds to the binding site of SHDA, where it undergoes oxidation to form fumarate while simultaneously reducing FAD to $FADH_2$, releasing 2 electrons which are transported alongside the three Fe-S clusters worked alongside the SDHB, eventually lead to ubiquinone oxidation (Equation 1.4-2) (Gnaiger, 2023).

$$\text{Succinate} + \text{FAD} + 2[H^+] + Q \rightarrow \text{Fumarate} + FADH_2 + Q \rightarrow \text{Fumarate} + \text{FAD} + QH_2$$

Equation 1.4-2 Complex II reaction

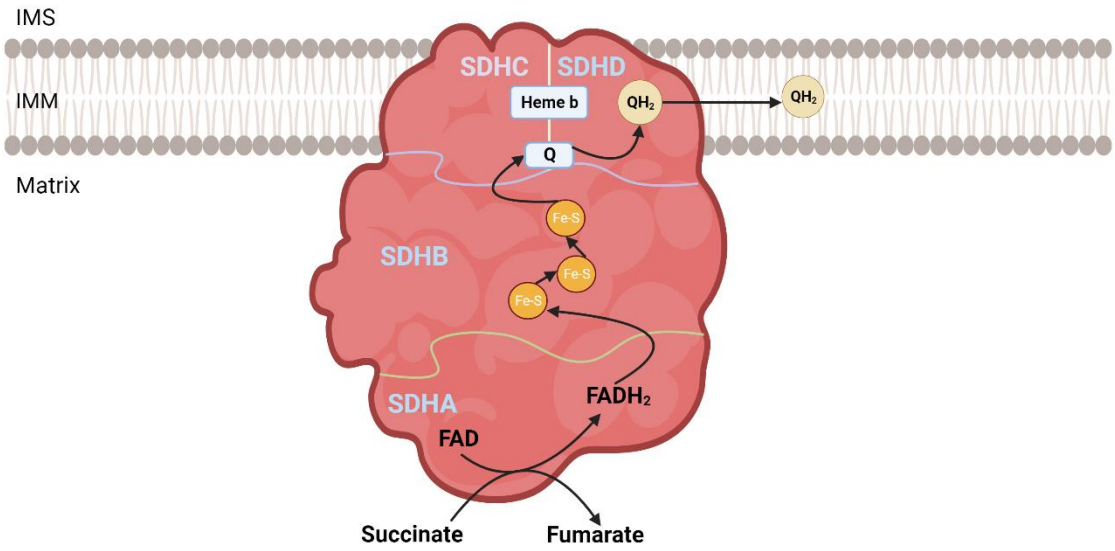

Figure 1.4-3 Complex II structure and reactions

The complex consists of four subunits: SDHA and SDHB form the hydrophilic part of the complex located in the matrix of the mitochondria, while SDHC and SDHD constitute the hydrophobic part within the inner membrane. SDHC and SDHD are connected by a Heme b moiety. Succinate binds to SDHA and undergoes dehydrogenation to fumarate, concurrently reducing FAD to FADH2. The electrons carried by FADH2 undergo a series of redox reactions in Fe-S clusters in SDHB before finally reaching the ubiquinone site in the hydrophobic part of the complex. The reduced form of ubiquinone (Q), ubiquinol (QH2), then transfers electrons within the membrane.

Complex III in humans is a dimer composed of 11 subunits and can be divided into three regions: the intermembrane part, the membrane part, and the matrix part. The function of this complex is to receive electrons and hydrogen from the membrane carrier ubiquinol, producing 2 free cytochrome C and pumping protons into the intermembrane space of the mitochondria. Cytochrome b is a transmembrane protein with 2 heme groups that form an electrical circuit across the membrane. The 2 heme groups are b-560 and b-566, with the low potential heme near the positive side of the membrane (P site) and the high potential heme near the negative side of the membrane (N site) (Matsuno-Yagi and Hatefi, 2001; Trumpower, 2002). The Rieske protein (Iron-sulfur

protein) is anchored to cytochrome b by the amino terminus and contains two Fe-S clusters located near the electropositive surface of the membrane (Xia *et al.,* 2013). The third component, cytochrome c1, is linked to cytochrome b in the C terminus by a hydrophobic helix and contains a heme located on the positive side of the membrane surface, where it reacts with cytochrome C. The Q cycle reaction can mainly be divided into 2 steps and the overall reaction is listed in (Equation 1.4-3) (Brandt and Trumpower, 1994).

In the first step, one molecule of ubiquinol generated from the first two complexes is oxidized in the centre P of the complex, generating 2 free protons and 2 electrons. One electron is passed to the iron-sulfur cluster and then passed to the heme group located at cytochrome C, where it reduces cytochrome c. Another electron is passed to b-566 of cytochrome b, then to b-560, where ubiquinone is reduced to ubisemiquinone anion (Q_n^-) at the center N of the complex (Equation 1.4-4). In the second step of the Q cycle, identical steps occur, as in step one. However, at center N, instead of ubiquinone reduction, the second step uses ubisemiquinone as an ingredient, resulting in the reduction of ubisemiquinone to ubiquinol (Equation 1.4-5) (Yang and Trumpower, 1988; Trumpower, 1990) (Figure 1.4-4).

Complex III: $QH_2 + 2\ cyt\ c^{3+} + 2H^+_{\ in} \longrightarrow Q + 2\ cyt\ c^{2+} + 4H^+_{\ out}$

Equation 1.4-3 Overall complex III reaction

Complex III step 1: $QH_2 + cyt\ c^{3+} \longrightarrow Q_n^- + cyt\ c^{2+} + 2H^+_{\ out}$

Equation 1.4-4 Step 1 reaction of complex III

Complex III step 2: $QH_2 + cyt\ c^{3+} + 2H^+_{\ in} + Q_n^- \longrightarrow Q + cyt\ c^{2+} + 2H^+_{\ out}$

Equation 1.4-5 Step 2 reaction of complex III

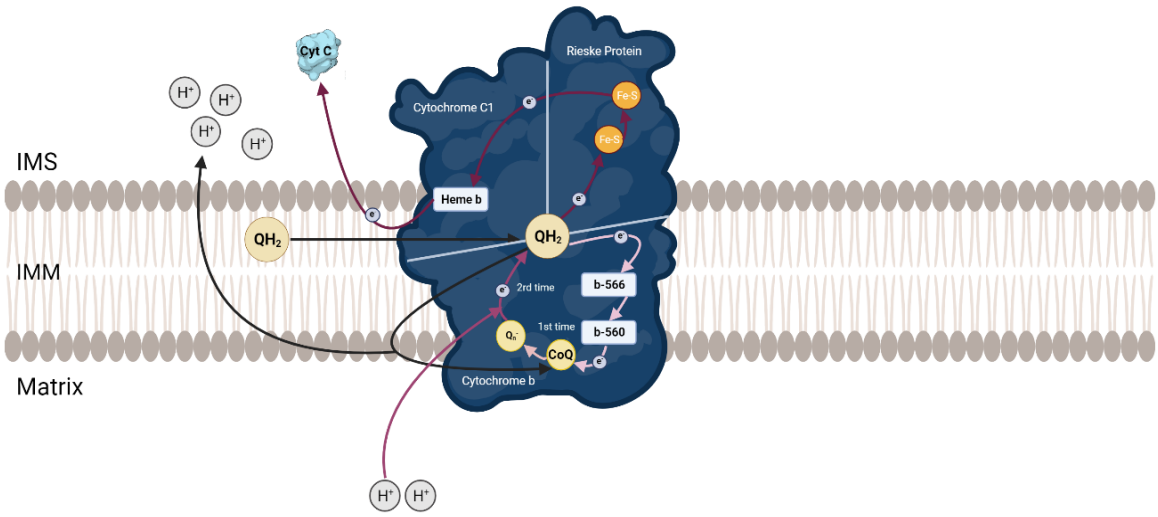

Figure 1.4-4 Complex III reactions in details

The graph illustrates the complete Q cycle reactions, accompanied by a schematic representation of the structure of Complex III. Complex III consists of three essential proteins crucial for ensuring the normal function of cytochrome c reduction. In the first step of the Q cycle, ubiquinol generated from Complexes I and II undergoes oxidation at Complex III, producing 2 molecules of protons and 2 molecules of electrons (depicted by black arrows). One electron is accepted by the heme group b-566 within cytochrome b, then transferred to b-560, ultimately contributing to the reduction of ubiquinone (indicated by light pink arrows). Simultaneously, another electron is taken up by the Fe-S cluster within the Rieske protein and subsequently transferred to the heme b group of cytochrome c1, facilitating the reduction of cytochrome C (depicted by dark red arrows). In the second step of the Q cycle, similar steps occur as in the first step. However, instead of ubiquinone reduction, the second step involves the utilization of ubisemiquinone as an ingredient, resulting in the reduction of ubisemiquinone to ubiquinol (depicted by plum arrows).

Complex IV, also known as cytochrome c oxidase (COX), is the terminal enzyme complex of the OXPHOS chain in mitochondria. This multi-subunit protein complex resides in the inner mitochondrial membrane and catalyses the transfer of electrons from reduced cytochrome c to molecular oxygen, facilitating the formation of water (Equation 1.4-6).

The reaction takes place at the catalytic core, which comprises two heme groups (heme a and heme a3) and a binuclear copper centre (CuA and CuB) that serve as redox-active cofactors. Electrons sequentially reduce these cofactors, ultimately reducing oxygen at the binuclear centre formed by heme a3 and CuB (Rahman *et al.*, 1999; Kadenbach, 2021). This process is tightly coupled to proton translocation across the membrane, thereby contributing to the electrochemical gradient required for ATP synthesis.

The activity of COX is regulated by the ATP/ADP (ADP: adenosine diphosphate) ratio. When the ATP/ADP ratio is high, COX adopts a relaxed state, where its activity is inhibited through conformational changes. Conversely, when the ATP/ADP ratio is low and increased ATP production is required, COX transitions to an active state, generating elevated electrochemical gradients (Kadenbach *et al.*, 2010).

Complex IV: O2 + 4 cyt c2+ + 8H+ in ⟶ 2 H2O + 4 cyt c3+ + 4H+ out

Equation 1.4-6 Complex IV reaction

Complex V, also known as ATP synthase, is a pivotal enzyme within the OXPHOS pathway, responsible for synthesising ATP from ADP and inorganic phosphate. Situated in the inner mitochondrial membrane, ATP synthase utilises the electrochemical gradient generated by the electron transport chain to drive ATP production (Equation 1.4-7). The enzyme consists of two principal components: the membrane-embedded F_0 sector, which functions as a proton channel, and the F_1 sector, a soluble catalytic domain that extends into the mitochondrial matrix. Proton translocation through the F_0 sector induces rotational motion of the central stalk and γ-subunit, resulting in conformational changes within the catalytic sites of the F_1 sector. These changes facilitate the highly efficient phosphorylation of ADP to ATP (Jonckheere, Smeitink and Rodenburg, 2012).

$ADP + P_i + 2H^+out \rightleftharpoons ATP + H_2O + 2H^+in$

Equation 1.4-7 Complex V reaction

1.5. *Other functions of mitochondria*

Additionally, mitochondria play a critical part in a variety of non-OXPHOS functions, including beta-oxidation of fatty acids, cell apoptosis, and calcium ion homeostasis, Iron-sulphur clusters (Giorgi, Marchi and Pinton, 2018; Bock and Tait, 2020). The regulation and maintenance of mitochondrial function depend on the coordination between the nuclear genome and mtDNA.

1.5.1. *Beta oxidation of fatty acids*

Fatty acids are a major source of energy production and play a crucial role in maintaining the energy homeostasis of the human body. Under normal circumstances, fatty acids serve as the primary energy source for the heart, skeletal muscles, and the kidneys. However, when glucose levels are limited, such as during fasting, fatty acid beta-oxidation becomes the primary mechanism for energy production (Houten *et al.,* 2016). Before undergoing beta-oxidation, fatty acids need to be activated to acyl-coenzyme by acyl-CoA synthetases, serving as a preparatory step. The assistance of the mitochondrial transmembrane protein acylcarnitine translocase (CACT), embedded on the IMM, is essential. This protein facilitates the transfer of acylcarnitine, an intermediate product of acyl-CoA, into the mitochondrial matrix, where various acyl-CoA dehydrogenases are located (Tonazzi *et al.*, 2021). The subsequent steps of beta-oxidation occur within the matrix, leading to the production of FADH2, NADH, and acetyl-CoA. These products play a crucial role in fuelling the TCA cycle and OXPHOS reactions.

1.5.2. *Heme biosynthesis*

Heme is one of the components of haemoglobin, containing an iron atom at the centre of its structure, and is essential for various redox reactions, including oxygen transport, detoxification, and gene expression regulation (Swenson *et al.*, 2020). The biosynthesis of heme is a complex and highly conserved process involving multiple enzymes located

in both the cytosol and mitochondria. Glycine is transported into the mitochondrial matrix, where it is catalysed by 5-aminolevulinate synthase (ALAS) and caseinolytic mitochondrial matrix peptidase chapernone subunit X (CLPX) to convert both glycine and succinyl-CoA into 5-aminolevulinate (ALA) (Brown *et al.*, 2018). ALA is then transported back to the cytosol, where it undergoes a series of reactions, ultimately leading to the formation of uroporphyrinogen III (CPgenIII), which is then transported back to the intermembrane space of the mitochondria (Hamza and Dailey, 2012). Following a series of reactions at the mitochondrial inner membrane and the incorporation of iron from the matrix, it matures into heme and is subsequently transported back to the cytosol.

1.5.3. *Apoptosis*

Apoptosis is a process of programmed cell death that helps remove infected or damaged cells beyond repair. The term was first introduced in 1972 (Kerr, Wyllie and Currie, 1972). The B-cell lymphoma 2 (Bcl-2) family of proteins is considered a key regulator of apoptosis. Initially, it was believed that apoptosis was controlled at the nuclear level, as no cytoplasmic changes were observed. However, this assumption was discarded when the link between apoptosis and mitochondria was discovered. In 1990, the Hockebery group found that Bcl-2 family proteins localize to the mitochondrial membrane using immunolocalization techniques (Hockenbery *et al.*, 1990). Furthermore, a reduction in mitochondrial transmembrane potential and the release of cytochrome c was observed prior to the onset of apoptotic signs (Liu *et al.*, 1996; Zamzami *et al.*, 1996).

Despite years of research, the exact link between mitochondrial permeability, mediated by Bcl-2 family proteins, the release of cytochrome c, and the activation of caspases is not yet fully understood. However, some key steps have been identified. When a cell experiences irreversible damage, Bax, a proapoptotic protein from the Bcl-2 family that normally resides in the cytosol, translocate to the OMM once the damage reaches a critical level. This triggers a series of conformational changes, leading to the oligomerization of Bax and another proapoptotic Bcl-2 family protein, Bak. The aggregation of Bax and Bal forms pores in the OMM, allowing the release of cytochrome

c and other proteins from the mitochondrial intermembrane space (Hsu, Wolter and Youle, 1997; Peña-Blanco and García-Sáez, 2018). Once cytochrome c enters the cytosol, it activates the apoptosis protease activating factor 1 (APAF1) through beta-oligomerization in the presence of ATP. This process is crucial for the maturation and activation of caspase-9 and caspase-3, key players in the apoptotic pathway (Belmokhtar *et al.*, 2003).

The release of other soluble proteins from the intermembrane space also enhances cytochrome c mediated apoptosis by suppressing the function of caspase-inhibitory proteins (IAPs). The second mitochondria-derived activator of caspase (Smac), also known as direct inhibitor of apoptosis binding protein with low pl (DIABLO), contains an IAP-binding N-terminus, which allows it to bind to the X-linked inhibitor of apoptosis (XIAP) and reduce the inhibitory effects of IAPs on caspases (Xu *et al.*, 2016). A similar neutralizing function is seen in high-temperature requirement protein A2 (HtrA2), also known as Omi (Li *et al.*, 2010).

Alterations in mitochondria/apoptosis-related proteins and genes have been linked to various diseases. Increased expression of Bcl-2 proteins has been reported in the brains of Parkinson's disease (PD) patients (Mogi *et al.*, 1996). Additionally, a loss of function heterozygous substitution in *HtrA2/Omi (G3395S)* was detected in four sporadic German PD patients (Strauss *et al.*, 2005), though other studies have not found a clear association between *HtrA2/Omi* mutations and PD (Ross *et al.*, 2008). Despite this, a clear link exists between *HtrA2/Omi* and PD, as its phosphorylation depends on phosphatase and PINK1. Mutations in *PINK1* are known to cause early-onset PD (Plun-Favreau *et al.*, 2007).

1.6. *Mitochondrial genetics*

1.6.1. *Mitochondrial genome*

MtDNA is circular and double-stranded DNA, with a heavy strand and a light strand. The heavy strand is guanine-rich, while the light strand is cytosine-rich. It has a bacterial origin, is maternally inherited (Pyle *et al.*, 2015), and constitutes around 0.0006% of the

entire human genome. MtDNA encodes 37 genes, including 13 proteins, 22 transfer ribonucleic acid (tRNA)s, and 2 rRNAs (Anderson *et al.*, 1981) (Figure 1.6-1). All the genes encoded by mtDNA are essential to the OXPHOS reaction. The specific OXPHOS complexes to which these 13 proteins contribute are detailed in (Figure 1.6-2).

Complex I relies on seven mtDNA-encoded proteins: ND1, ND2, ND3, ND4, ND4L, ND5, and ND6. Complex III requires one mtDNA-encoded protein, cytochrome b (CYB). Complex IV utilizes three mtDNA-encoded proteins: cytochrome C1 (CO1), CO2, and CO3. Finally, Complex V requires two mtDNA-encoded proteins: ATP synthase membrane subunit 6 (ATP6) and ATP8. Any alterations in these coding regions can lead to serious conditions, such as Leigh syndrome (LS; associated with the m.8993T>G mutation in the *ATP6* gene) (Na and Lee, 2022), or Leber's hereditary optic neuropathy (LHON; associated with the m.3460G>A mutation the *ND1* gene or the m.11778G>A mutation in the *ND4* gene) (Yu-Wai-Man, Griffiths and Chinnery, 2011; Xu *et al.*, 2016). Due to the critical role of mtDNA-encoded proteins in maintaining proper OXPHOS function, these proteins are often used as markers for assessing mitochondrial OXPHOS functionality. COX, complex IV of the ETC, is essential for ATP production and is commonly targeted during staining processes to distinguish cells with dysfunctional mitochondria (Robinson, 2000).

The mtDNA also encodes 22 tRNAs and 2 rRNAs, which are essential for the translation of OXPHOS proteins. Any damage to or loss of these tRNAs or rRNAs can result in severe conditions. Examples include myoclonic epilepsy and ragged-red fibres (MERRF; associated with the m.8344A>G mutation in the *MT-tRNA-Lys* (*MT-TK)* gene (Shoffner *et al.*, 1990), aminoglycoside-associated nonsyndromic deafness and speech disorder (associated with the m.A1555G mutation in the *ribosomal RNA 1* (*RNR1)* gene, (Ou *et al.*, 2018)), and stroke-like episodes (associated with the m.3243A>G mutation in the *tRNA leucine 1* (*TL1)* gene (Tzen *et al.*, 2003).

The remaining mitochondrial functions depend on proteins encoded by nuclear DNA. Many proteins required for OXPHOS and other mitochondrial processes are translated and assembled in the cytoplasm before being transported to the mitochondrial matrix or inner membrane, like mitochondrial transcription factor A (TFAM), peroxisome proliferator-activated receptor gamma coactivator 1-alpha (PGC1α) (Kitada *et al.*, 1998; Alam *et al.*, 2003; Halling and Pilegaard, 2020).

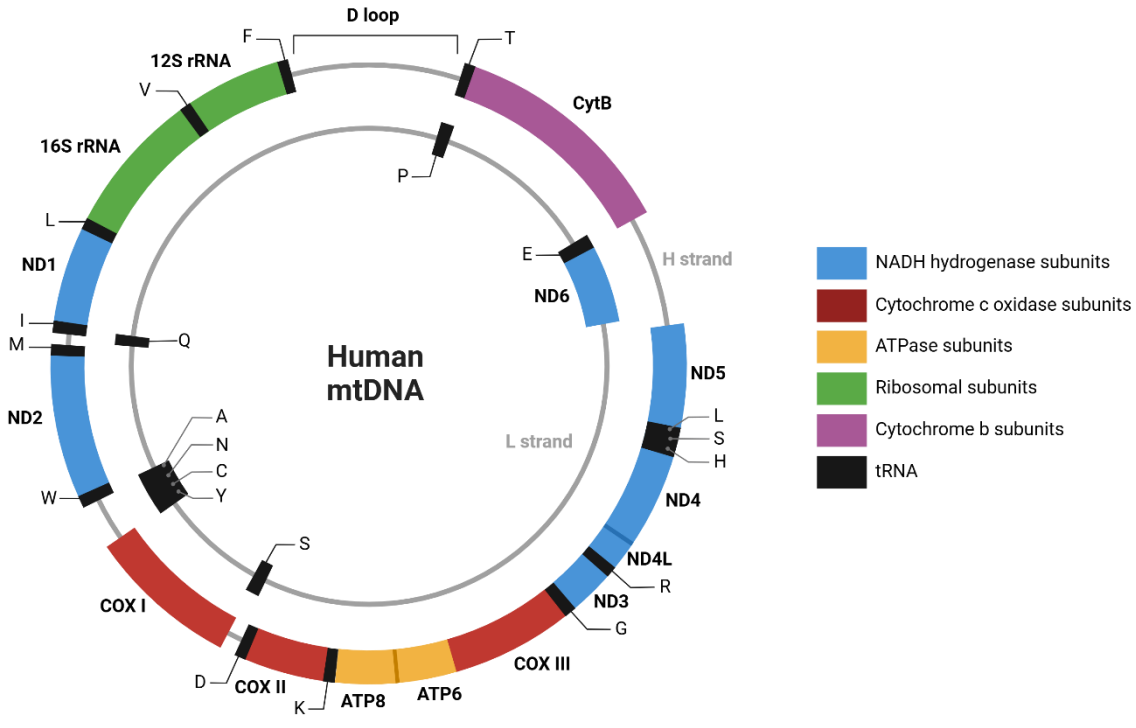

Figure 1.6-1 Human mtDNA genome

This figure shows the human mtDNA sequence map, with different colours representing various coding regions. Blue indicates the coding regions for complex I (NADH dehydrogenase) subunits, red represents the coding regions for complex IV (cytochrome c oxidase) subunits, yellow denotes the coding regions for complex V (ATPase subunits), green represents the ribosomal subunit coding regions, purple indicates the coding regions for complex III (cytochrome b) subunits, and black represents the tRNA regions.

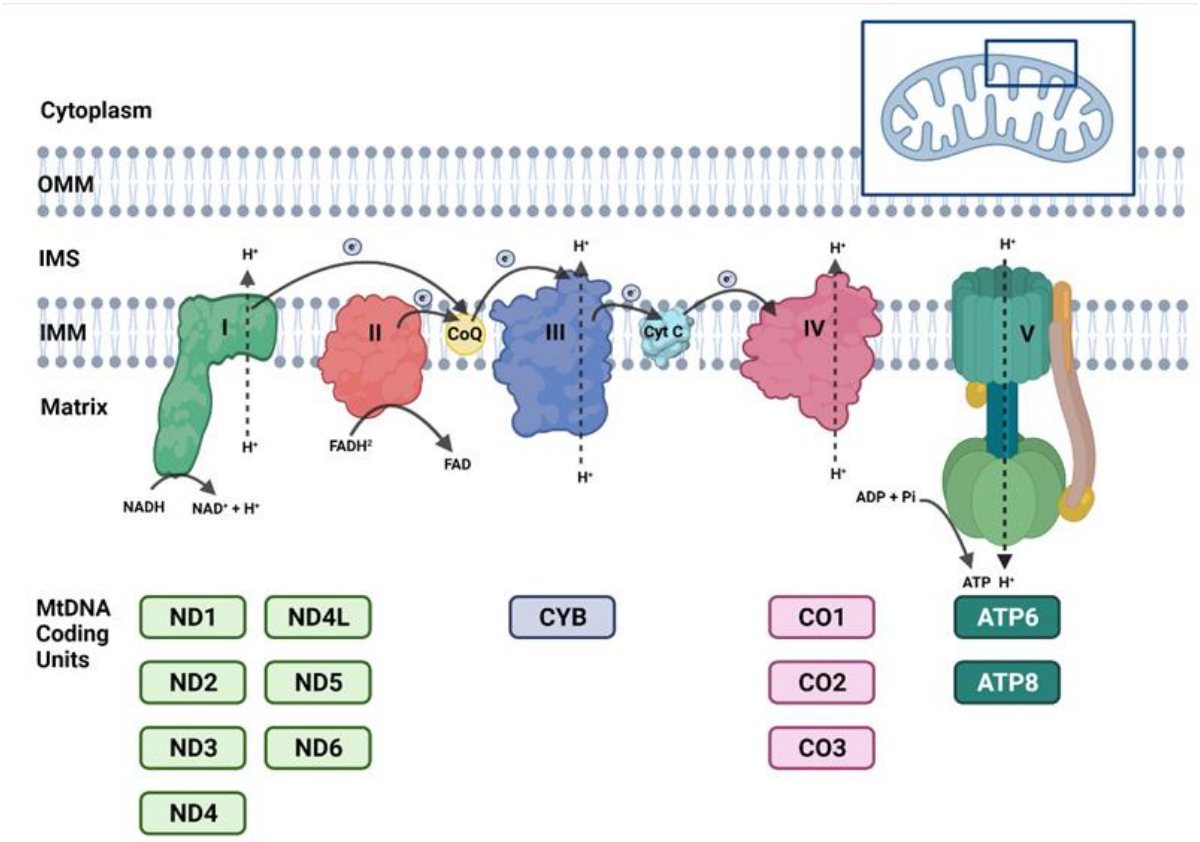

Figure 1.6-2 mtDNA -encoded components of the OXPHOS pathway

This figure illustrates the mitochondrial DNA (mtDNA) and the OXPHOS complexes it encodes. Complex II is the only complex that does not require any mtDNA-encoded proteins. In contrast, Complex I rely on seven mtDNA-encoded proteins: ND1, ND2, ND3, ND4, ND4L, ND5, and ND6. Complex III requires one mtDNA-encoded protein, CYB. Complex IV utilises three mtDNA-encoded proteins: CO1, CO2, and CO3. Finally, Complex V requires two mtDNA-encoded proteins: ATP6 and ATP8. ND, NADH dehydrogenase subunit; CYB, cytochrome b; CO, cytochrome c oxidase; ATP, ATP synthase.

1.6.2. *mtDNA haplogroups*

mtDNA haplogroups represent distinct evolutionary lineages of the mitochondrial genome, defined by specific combinations of genetic variants inherited maternally. These haplogroups have been extensively studied to reconstruct human migration patterns, as they provide a direct link to maternal ancestry due to the non-recombining nature of mtDNA (Giles *et al.*, 1980; Birky, 1995). The development of mtDNA

haplogroups is driven by mutations accumulating over generations, with major branches of the mtDNA phylogenetic tree reflecting ancient population splits. Haplogroups are often geographically structured, with certain lineages predominating in specific population (Figure 1.6-3). Beyond their anthropological significance, variants associated with specific haplogroups can influence mitochondrial function, such as energy production and reactive oxygen species management (Kenney *et al.*, 2013; Vázquez-Coto *et al.*, 2022), thereby modulating susceptibility to diseases. MtDNA haplogroups have been implicated in various diseases and traits, including neurodegenerative disorders, metabolic conditions, and cancer (van der Walt *et al.*, 2004; Hulgan *et al.*, 2011; Terrazzino *et al.*, 2016; Ma *et al.*, 2018). For instance, there was a reduced risk of PD with haplogroups J, K and T and super-haplogroup JT (Hudson *et al.*, 2013).

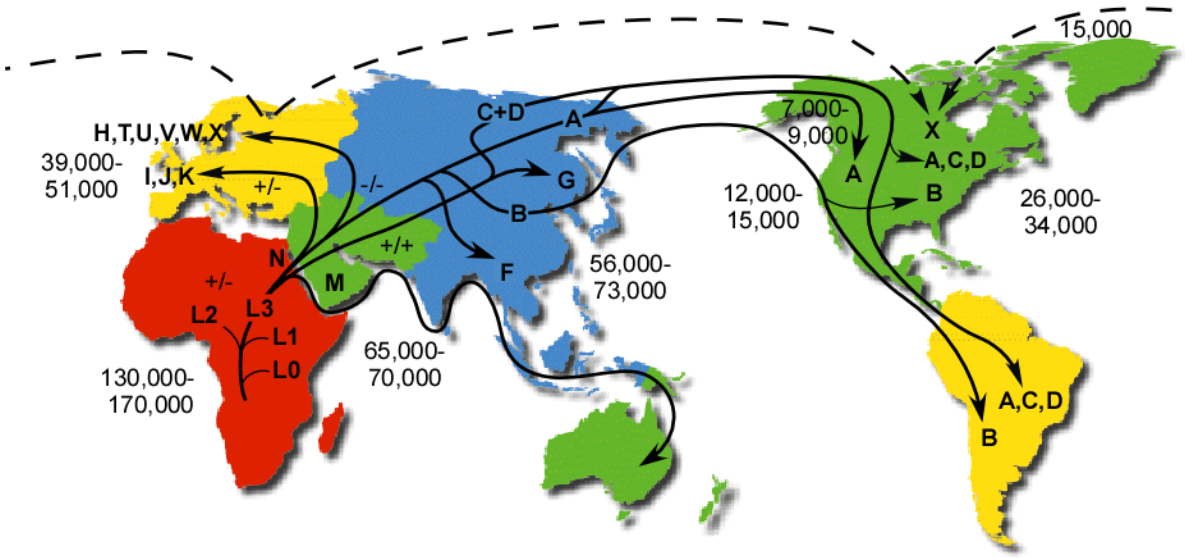

Figure 1.6-3 Map of continent specific mitochondrial haplogroups

This figure illustrates the migration patterns of mitochondrial DNA (mtDNA) haplogroups across the globe. Haplogroups are denoted by letters, and the presence or absence of specific restriction sites is indicated by "+/−". Estimated migration times, shown in years before present, are provided alongside the routes. This figure has been taken from the MITOMAP website (http://www.mitomap.org/WorldMigrations.pdf).

1.6.3. *Mitochondrial DNA transcription and maturation*

The transcription of mtDNA does not involve polymerases similar to those in the nucleus. The process begins when TFAM binds to the upstream region of the light strand promoter (LSP) and twists its sequence, facilitating the recruitment of mitochondrial DNA RNA polymerase (POLRMT) to the LSP at nucleotide position 407, where the transcription of a short RNA, called 7S RNA, is initiated (Ngo, Kaiser and Chan, 2011; Shutt, Bestwick and Shadel, 2011; Morozov *et al.*, 2014, 2015; Yakubovskaya *et al.*, 2014). Upstream of the LSP are three conserved sequence blocks (CSBs), with CSB2 being a guanine-rich sequence. As the newly synthesized RNA passes CSB2, it forms a G-quadruplex structure (G4s), causing transcription to stall (Figure 1.6-4, Figure 1.6-4) (Wanrooij *et al.*, 2010, 2012). At this point, RNase H1 degrades the RNA molecules hybridized to the single-stranded DNA, ensuring origin-specific initiation of mtDNA synthesis (Lockhart *et al.*, 2019).

For the elongation of the light strand transcription, RNA synthesis must continue past CSB2 without forming a G4s. This process is assisted by transcription elongation factor (TEFM), allowing the transcription of the entire mtDNA light strand (Falkenberg *et al.*, 2002). Once transcription reaches the end of the light strand, at the region where tRNA Leu (UUR) is located, mitochondrial termination factor 1 (mTERF1) binds to a 28-base pair region within the tRNA. This binding helps bend the messenger ribonucleic acid (mRNA), connecting it to the heavy strand promoter 1 (HSP1) and facilitating the termination of transcription (Shi *et al.*, 2016).

Research suggests that the termination of light strand transcription is coupled with the elongation of heavy strand transcription. For the initiation of heavy strand transcription, there are two starting sites: HSP1 at position 561, 16bp upstream of the tRNA Phe gene, and heavy strand promoter 2 (HSP2 at nucleotide 646). Transcription initiation from HSP1 tends to be short, terminating before the 3' end of the 16S rRNA, while transcription from HSP2 generally covers the entire mtDNA heavy strand. In vitro study shows that the presence of the termination site allows mTERF to stimulate transcription initiation from HSP1, suggesting a dual role for mTERF in both light strand transcription termination and heavy strand transcription initiation (Martin *et al.*, 2005). This

mechanism could explain observations published in the 1980s, where the rate of rRNA synthesis was found to be 15 to 60 times higher than that of mRNA (Montoya *et al.*, 1982; Montoya, Gaines and Attardi, 1983). However, this theory was challenged by findings from mTERF1 knockout mice, which showed no effect on rRNA levels, suggesting that mTERF1 may instead act to block transcription on the opposite strand of mtDNA (Terzioglu *et al.*, 2013). The precise function of mTERF1 remains an area for further exploration.

Transcript maturation follows full transcription. Most mRNAs and rRNAs are separated by MT-tRNAs and the excision of these tRNA leads to the separation of both mRNAs and rRNAs. This process is known as the tRNA punctuation model, where tRNAs are endonucleolytically excised from both the 5' and 3' ends. Mitochondrial ribonuclease P (RNase P) processes the 5' end, while mitochondrial ribonuclease Z (RNase Z) processes the 3' end (Lopez Sanchez *et al.*, 2011; Bhatta *et al.*, 2021). Both RNase P and RNase Z are proteaceous heterotrimeric endonucleases. Not all RNAs are flanked by tRNAs. In these cases, Fas-activated serine/threonine kinase (FASTK) helps stabilize the RNA, ensuring that RNase P and RNase Z can properly process the RNA molecules. FASTK also plays a role in protecting mRNAs from premature degradation (Ohkubo *et al.*, 2021).

The stability of transcribed RNA is another crucial step after transcription. Mitochondria also contain RNA-binding proteins (RBPs) that bin to specific sequences to prevent degradation, such as FAS-activated serine/threonine kinase domine 2 (FASTKD2), which binds to MT-ND6 (Hasan *et al.*, 2014; Popow *et al.*, 2015). Polyadenylation plays a significant role in RNA stability as well. Almost all mitochondrial mRNAs undergo polyadenylation by mitochondrial poly (A) polymerase (mtPAP), with the exception of MT-ND6. The post-transcriptional modification, by adding poly (A) tails to the mRNA, not only helps stabilize the mRNA but also assists the mitoribosome in identifying transcription stop sites and termination translation (Guydosh and Green, 2017). PNase P cleaved mRNA will either have a U or UA at their 3' end and polyadenylation of it will help in creation of UAA termination codons in those mRNAs (Anderson *et al.*, 1981). This is particularly important for the 8 out of 13 mitochondrial mRNAs that lack stop codons (UAA or UAG) to complete their open reading frame, including C01, CO3, CYB, ND1, ND2, ND3, ND4, ND6 (Temperley *et al.*, 2010).

The regulation of the mtDNA transcription is regulated through the expression of *nuclear respiratory factors 1 and 2 (NEF1 and NRF2).* They can bind to the promoter areas of genes which involved in the transcription like *TFAM* (Virbasius and Scarpulla, 1994), and *mitochondrial transcriptional factor B1* (*TGB1M)* (Gleyzer, Vercauteren and Scarpulla, 2005).

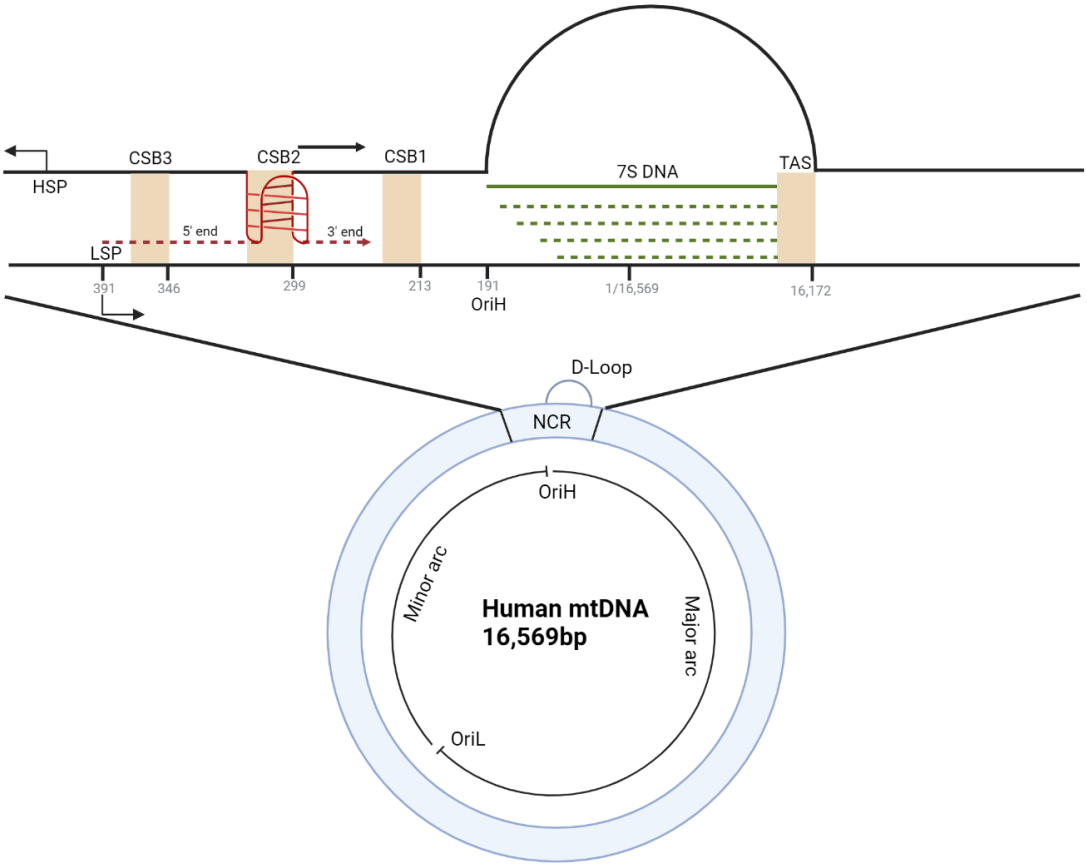

Figure 1.6-4 The initiation of the mtDNA transcription

The initiation of light strand mtDNA transcription begins at the LSP. As transcription progresses and reaches the CSB2, the guanine-rich sequence induces the formation of a G4s structure of the newly synthesised RNA, causing a stall in transcription. LSP: light strand promoter; CSB: conserved sequence block.

1.6.4. *mtDNA replication and separation*

The replication of mtDNA happens not only in dividing cells but also in non-dividing cells, following a process called relaxed replication (Chinnery and Samuels, 1999). The indication of the mtDNA replication requires the help of a couple of factors. After recruiting helicase TWINKLE and DNA polymerase γ (POLγ), a heterotrimer containing one catalytic subunit (POLγA) and two accessory subunits (POLγB). In over 95% of cases, when DNA synthesis reaches the termination-associated sequence (TAS), replication starts from the 3' end of the short RNA sequence known as *OriH* (origin of the heavy strand replication) carried by TWINKLE and POLγ stops after 650 nucleotides (Bogenhagen and Clayton, 1978). Interestingly, the location of OriH is over a hundred base pairs away from the CSB2 sequence; a possible nuclease activity may be responsible for this. Only when replication passes the TAS does the full replication of the H strand commence. The mechanism by which TAS is involved in the termination of replication remains unknown, but it might be linked to the binding of certain proteins. DNA sequences that don't pass the TAS are called 7S DNAs, leading to the D-loop structure of the non-coding region (NCR) of mtDNA (Figure 1.6-5) (Madsen, Ghivizzani and Hauswirth, 1993). The turnover of 7S DNA is quite rapid, with a half-life ranging from 45 to 90 minutes. Loss of function of the mitochondrial elongation factor G1 (*MEGE1)* gene has been observed to be linked with a significant accumulation of 7S DNA in patients' cells (Kornblum *et al.*, 2013).

In other instances, replicated DNA passes the TAS and begins to replicate the full H-strand. There are three main hypothesized models: the strand-displacement model (SDM) (Clayton, 1982; Brown *et al.*, 2005), ribonucleotide incorporation throughout the lagging strand model (RITOLS) (Holt and Reyes, 2012), and the strand-coupled model (Jõers and Jacobs, 2013; Ciesielski, Oliveira and Kaguni, 2016) (Figure 1.6-6). DNA replication is unidirectional in SDM and RITOLS, and the light strand won't start until the replication of the H strand passes the OriL. While the L-strand serves as the template, unwinding and freeing the H-strand are bound and protected by mitochondrial single-stranded DNA-binding protein (mtSSB) in SDM and by RNAs in RITOLS. Chip-C data has shown that the level of mtSSB is the highest in the OriH and decreases alongside the

sequence until it reaches OriL (Polikanov *et al.*, 2015; Lopez Sanchez *et al.*, 2020). Besides, the possibility of the existence of a large number of free RNAs with the presence of RNase H1 is quite low, making the SDM seen as the most plausible model in the field. When replication of the H strand reaches the OriL and TWINKLE unwinds it, a hairpin/loop structure is formed, having a stretch of dT-residues that recruit POLγ to the site and initiate the replication of the OriL (Fusté *et al.*, 2010).

In the strand-coupled model, though, the replication of both H and L strands happens at the same time, just like the way it happens in the nucleus. This model is based on the detection of replication forks as replication intermediates (Holt, Lorimer and Jacobs, 2000; Bezawork-Geleta *et al.*, 2017). However, this model does not meet other observations, like deletions happening mostly in the major arc.

When replication returns to the origin, POLγ continues to replicate and results in a flap by flapping the already primed sequence for initiating replication. The flap can be recognized and cleaved by RNase H1 and MGME1 (Uhler *et al.*, 2016). The cleaned sequence can then be ligated with the beginning of the replicated sequence, forming a complete sequence. The newly synthesized two daughter strands need to be separated and distributed, requiring the help of topoisomerase 3A (TOP3A) (Nicholls *et al.*, 2018).

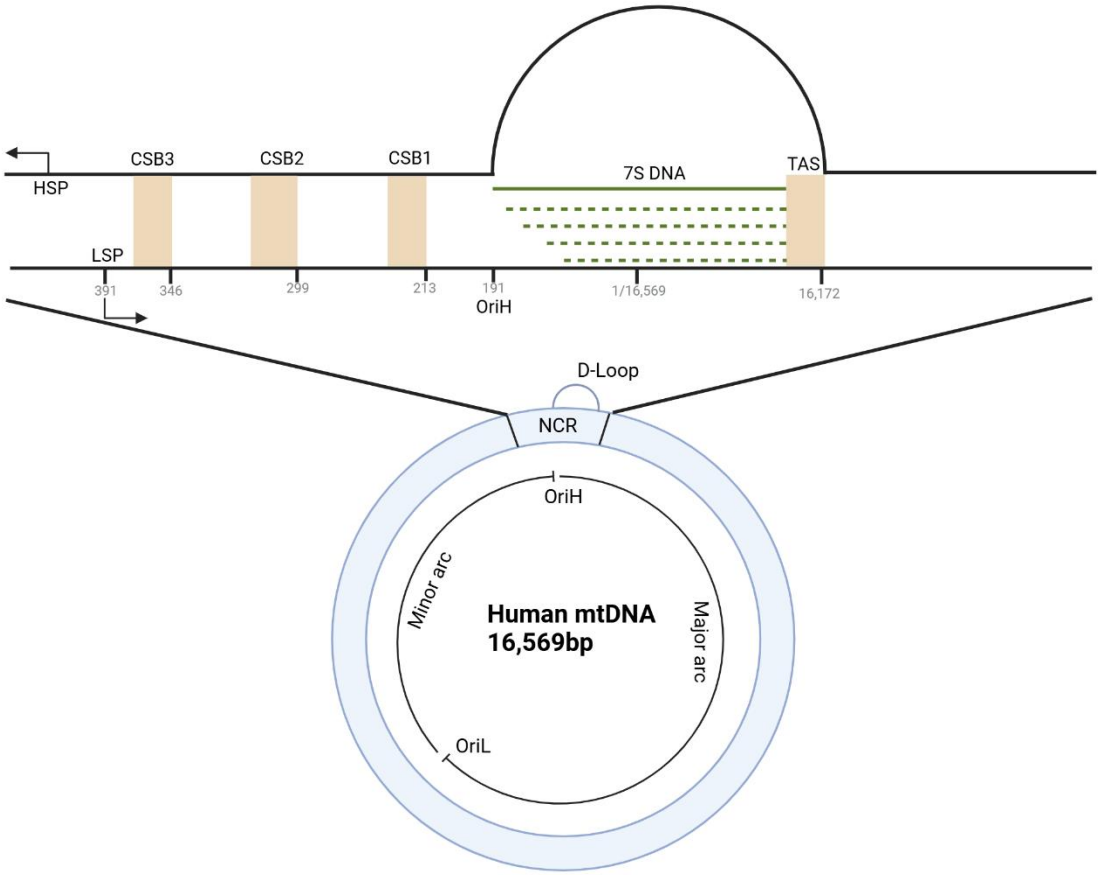

Figure 1.6-5 The initiation of mtDNA replication and 7s DNA

This figure illustrates the replication process of the heavy strand of mtDNA, which initiates at the OriH, located upstream of the CSBs. Replication proceeds until it reaches the TAS, where it terminates. Multiple replication intermediates accumulate near the TAS region, forming the D-loop structure. OriH: origin of heavy strand, CBS: conserved sequence block. TAS: termination-associated sequence.

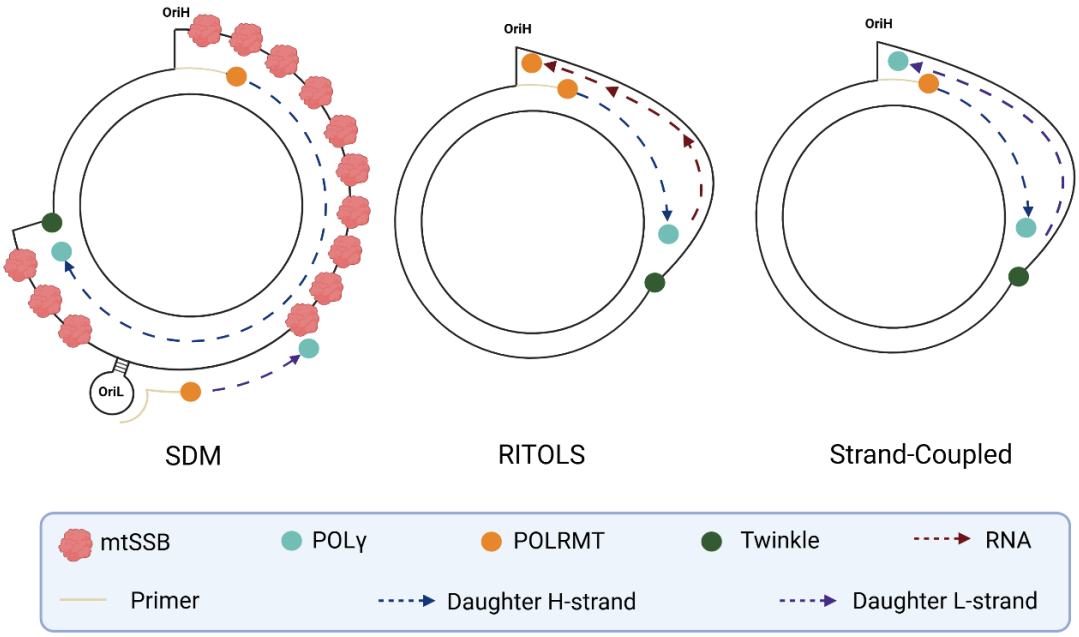

Figure 1.6-6 Three models of replications

This figure illustrates three models of mtDNA replication. In the first model, the SDM, the helicase TWINKLE unwinds the double-stranded mtDNA, and POLRMT synthesises the primer required for initiation at the OriH, facilitating heavy strand replication by POLγ. Replication of the light strand does not begin until heavy strand replication reaches the OriL. During this process, the displaced light strand is protected by mtSSB. Once heavy strand replication passes OriL, a hairpin structure forms, initiating primer synthesis by POLRMT, and the remaining light strand replication is carried out by POLγ. In the RITOLS model, replication is also unidirectional, with light strand replication delayed until heavy strand replication passes OriL. However, in this model, the displaced light strand is protected by synthesised short RNAs instead of mtSSB. In the strand-coupled model, replication of both the heavy and light strands occurs simultaneously. SDM: Strand displacement model; RITOLS: ribonucleotide incorporation throughout the lagging strand model; mtSSB: mitochondrial single-stranded DNA binding protein; POLγ: DNA polymerase γ; POLRMT: RNA polymerase mitochondrial; OriH: Origin of the heavy strand; OriL: Origin of the light strand.

1.6.5. *Translation*

The translation of mtDNA requires a fully mature mitoribosome, which depends on catalytic rRNA that undergoes various modifications, including nucleic base methylation, 2'-O methylation and pseudouridylation. It has been shown that the methylation of highly conserved nucleotides of the rRNA, including Gm2251 and Um2552, by mitochondrial rRNA methyltransferase 1 (MRM1) and MRM2 respectively, can help to modify ribosomal active sites and help to maintain the stability of rRNA scaffold (Polikanov *et al.*, 2015; Lopez Sanchez *et al.*, 2020). Additionally, 80 nuclear-encoded mitochondrial ribosomal proteins (MRPs) are required for this process. The mature mitoribosome consists of two parts: the mitochondrial large 39S subunit (mtLSU) and the mitochondrial small 28S subunit (mtSSU). Mutation of the MRPs has been associated with human disease like, and recent mouse embryos has found that loss of function of 21 *MRPs genes*, including *Mrpl3*, *Mrpl22*, will cause lead to failure of gastrulation initiation (Cheong *et al.*, 2020).

There are differences in codon sequences when comparing the mitochondrial genome to the nuclear genome. In the mitochondrial genome, UGA, which function as a stop codon in the nuclear genome, is translated as tryptophan (Inagaki *et al.*, 1998). Conversely, AGA and AGG, which encode arginine in the nuclear genome, act as stop codons in the mitochondrial context (Sengupta, Yang and Higgs, 2007).

The initiation of the mRNA translation is regulated by mitochondrial initiation factor 2 and 3 (mtIF2 and mtIF3). mtIF3 positions the AUG or AUA initiation codons of the mRNA at the peptidyl (P) site in the mtSSU, stabilizing the binding of the mRNA to the mtSSU (Khawaja *et al.*, 2020). After the binding of mRNA to the mitoribosome, similar to other protein synthesis systems, the translation must be initiated by methionine residues (Lim, Kim and Levine, 2019). However, unlike other systems, mitochondria can only use one type of tRNA, tRNA Met (Haque, Grasso and Spremulli, 2008; Bilbille *et al.*, 2011). Post -translational modification of the first aminoacyl-tRNA through formylation to form fMet-tRNA Met enhanced its affinity for mtIF2. mtIF2 then induces a conformational change in the rRNA, guiding the initiation of translation (Spencer and Spremulli, 2004).

The elongation of the translation is mediated by three mitochondrial elongation factors: elongation factor thermo unstable (EFTu); elongation factor thermo stable (EFTs),

elongation factor G mitochondria (EFGM) (Rosenthal and Bodley, 1987; Spremulli *et al.*, 2004; Atkinson and Baldauf, 2011). In the first step of elongation, EFTu forms a complex with both aminoacyl-tRNA and GTP, guiding the tRNA to the acceptor (A) site of the mitoribosome. EFTu then releases the aminoacyl-tRNA into the A site, a process fuelled by GTP hydrolysis. Afterward, the EFTu-GDP complex dissociates from the mitoribosome, allowing EFTs to bind to the inactive EFTu-GDP complex and promote the regeneration of the active EFTu-GTP complex by releasing GDP (Cai *et al.*, 2000). The next step involves the release of the deacetylated tRNA from the P site. Through GTP hydrolysis, EFGM facilitates the translocation of the peptidyl-tRNA from the A site to the P site and from the P site to the exit (E) site, while simultaneously shifting the mRNA by one codon. Once a stop codon appears at the A site, at least four nucleus-encoded proteins are involved in terminating translation (Zavialov, Buckingham and Ehrenberg, 2001; Uemura *et al.*, 2010; Chen *et al.*, 2012).

1.6.6. *Heteroplasmy and threshold effect*

The presence of multiple copies of mitochondrial DNA within a cell allows for a condition known as heteroplasmy, which refers to the coexistence of more than one mitochondrial genotype within a single cell. Initially, it was assumed that heteroplasmy levels within the same tissue type would be uniform and lead to consistent effects (Holt, Harding and Morgan-Hughes, 1988). To quantify mutation load across different tissues, the concept of heteroplasmy level was introduced.

In the 1990s, the threshold effect was identified, leading to the realization that not all mutations result in functional consequences. Researchers began using heteroplasmy levels to measure the accumulation of variants or deletions within a tissue. This concept is considered significant in understanding the high tolerance of mitochondria to the elevated mutation rate in mtDNA (Sale, 2013; Rong *et al.*, 2021) (Figure 1.6-7). Unlike diploid nuclear genome, multiple copies of mtDNA exist within a single mitochondrion, and each cell contains multiple mitochondria. Dysfunction occurs only when damaged mitochondria reach a critical level, and individual mitochondria remain functional until mutated mtDNA exceeds a high heteroplasmy threshold. This phenomenon, known as the threshold effect, means that biological effects of mtDNA mutations, including

deletions and point mutations, manifest only when they surpass a specific heteroplasmy level (Rossignol *et al.*, 2003). It was further recognized that the heteroplasmy threshold required for an effect varies between tissue types (Holt, Harding and Morgan-Hughes, 1988).

By the 2000s, studies demonstrated that mutant mtDNA could undergo clonal expansion within tissues, resulting in a mosaic distribution of heteroplasmy (Khrapko, 2011). Additionally, mtDNA segregation during cell division was shown to occur randomly, leading to significant variations in heteroplasmy levels between daughter cells, even within the same tissue (Wallace, 1986; Lightowlers *et al.*, 1997; Howell *et al.*, 2000). The threshold level was found to vary among cell types (e.g., mitotic versus post-mitotic cells), tissue types, and mtDNA Copy Numbers (mtCN) (Stewart and Chinnery, 2015).

Despite these advancements, the mechanisms underlying clonal expansion remain unclear, and it is uncertain whether any selective advantage drives the accumulation of mutant mtDNA. Several hypotheses have been proposed. The random genetic drift hypothesis suggests that mutations are selected for replication without a selective advantage, leading to stochastic accumulation (Brown *et al.*, 2001; Elson *et al.*, 2001). Other theories propose selective advantages. For example, the replication advantage theory suggests that deleted mtDNA replicates more quickly due to its shorter sequence compared to wild-type mtDNA (Wallace, 1989). The negative feedback loop theory posits that mtDNA deletions lead to a reduction in mtDNA-encoded proteins (e.g., ND4, ND5, ND6), stimulating compensatory replication of these mitochondria (Kowald and Kirkwood, 2014). Additional theories include the survival of the sickest hypothesis (Yoneda *et al.*, 1992) and the perinuclear niche hypothesis in human skeletal muscle (Vincent *et al.*, 2018). However, no single theory fully explains all observations.

With advancements in sequencing technologies, deep sequencing methods have enabled the detection and monitoring of low levels of heteroplasmy changes, even at the single-cell level. These developments have revealed the dynamic nature of heteroplasmy across tissues and cells during various stages of development and disease progression.

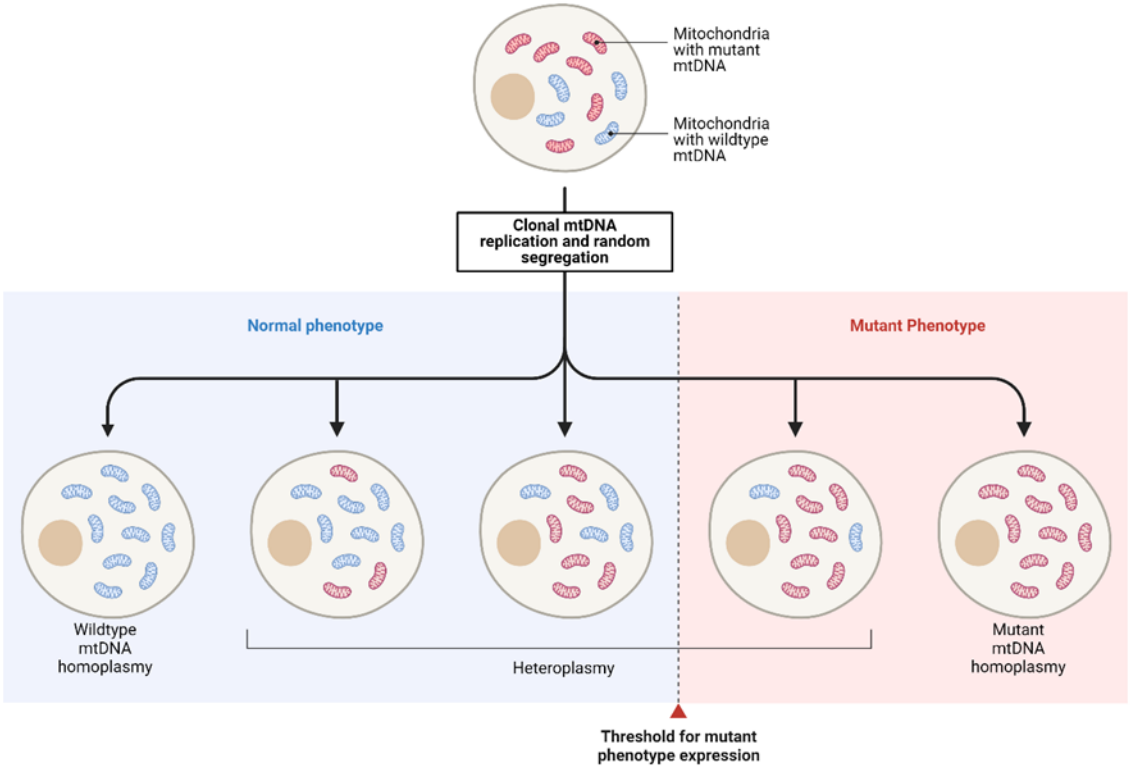

Figure 1.6-7 Heteroplasmy level and threshold effect

When a mitochondrion contains only wide-type mtDNA, it is referred to as homoplasmy. Once mutations are introduced, the mitochondrial genome becomes heteroplasmic. The level of mutation within the mitochondria is described by the degree of heteroplasmy. Through clonal expansion, the heteroplasmy level of a mutation can reach a threshold, at which point it begins to impair mitochondrial function. When the proportion of dysfunctional mitochondria surpasses a critical threshold, it can lead to cellular dysfunction and potentially contribute to degeneration.

1.6.7. *Maternal inheritance and the mitochondrial bottleneck*

In almost all eukaryotes, mitochondrial genome inheritance is typically characterized by maternal transmission, wherein mtDNA is exclusively passed down through the female lineage. However, exceptions to this rule have been documented, with reports of biparental inheritance in select families, albeit such occurrences are rare (Luo *et al.*, 2018; Rius *et al.*, 2019). The underlying mechanism behind maternal inheritance

remains elusive. It is widely hypothesized that post-fertilization mechanisms exist to eliminate mitochondria introduced via sperm. Some studies suggest this may occur through the ubiquitination of sperm (Sutovsky *et al.*, 2000), while others propose the activation of an autophagy pathway following fertilization (Sato and Sato, 2011). A recent study has revealed that sperm harbour intact mtDNA but exhibit altered splicing of the *TFAM* mRNA, compromising their ability to maintain genome stability and potentially leading to diminished or loss of genomic integrity over time (Lee *et al.*, 2023).

The bottleneck effect also plays a significant role in mtDNA transmission across generations. This phenomenon, first observed in Holstein cows, involves a rapid shift in heteroplasmy levels (Ashley, Laipis and Hauswirth, 1989). When a female carries mutated mtDNA, the bottleneck effect may be observed in her offspring. During germline development, mtDNA undergoes a reduction, and any mutated copies are subjected to heightened negative selection pressure. As a result, mature germ cells can exhibit significant variation in allele frequencies, leading to offspring inheriting either a higher proportion of mutated mtDNA or predominantly wild-type alleles (Zhang, Burr and Chinnery, 2018).

Several types of primary mitochondrial disease are caused by maternally inherited mtDNA point mutations. For example, the m.3271T>C mutation has been reported in patients with mitochondrial encephalomyopathy, lactic acidosis, and stroke-like episodes (MELAS) and can also be detected in the blood leukocytes of the patients' mothers (Stenqvist *et al.*, 2005). Similarly, the m.11778G>A mutation has been identified in patients with Leber hereditary optic neuropathy (LHON) and in their mothers (Chinnery *et al.*, 2001).

1.6.8. *mtDNA deletion*

MtDNA mutations can also occur somatically, with somatic mutations such as mtDNA deletions and point mutations being associated with various conditions. Deletions in mtDNA are almost never inherited. Instead, single large-scale mitochondrial DNA deletions (SLSMDs) are typically generated either in the mother’s oocytes during germline development or in the embryo during embryogenesis (Goldstein and Falk,

1993). However, there is one reported case of a 28-year-old man with a 2bp mtDNA deletion in the ND2 gene that may have paternal origins (Schwartz and Vissing, 2002). These deletions can then undergo clonal expansion to reach critical levels, subsequently affecting mitochondrial function and being linked to early-onset diseases. For example, patients with Pearson's syndrome (PS) and Kearns-Sayre syndrome (KSS) harbour high levels of large deletions that are generated early in life. In PS patients, a single mtDNA deletion can lead to the development of anaemia between birth and 31 months of age (Yoshimi *et al.*, 2021, 2022). KSS patients typically exhibit symptoms of mitochondria dysfunction before the age of 20 (Zeviani *et al.*, 1988; Johnson, Bindoff and Turnbull, 1993).

Somatic mtDNA deletions can be generated throughout life. The accumulation of multiple somatic mtDNA deletions is associated with diseases. For example, high level of somatic mtDNA deletion were substantia nigra pars compacta (SNpc) dopaminergic neurons and might be contributed to the neuronal loss observed in that neuron in PD conditions (Bender *et al.*, 2006). There are also papers suggesting that somatic mtDNA deletions as a potential cause of ageing (Larsson, 2010; Sanchez-Contreras and Kennedy, 2022).

The effect of mtDNA deletion seems to be higher in postmitotic tissues in both aging and disease. Unlike mitotic tissues, postmitotic cells such as neurons and muscle fibres do not divide, allowing mtDNA deletions to clonally expand over time without being diluted by cell turnover, also those tissue often requires high energy demands, relying heavily on mitochondrial function (Krishnan *et al.*, 2008). Interestingly, studies have shown that the profiles of mtDNA deletions are remarkably similar across different postmitotic tissues like muscles and the brain. The majority of deletions identified in muscle fibres were large-scale and located within the major arc of the mtDNA, which is consistent with deletions observed in brain tissues, suggesting common mechanisms of formation and expansion. (Reeve *et al.*, 2008; Bris *et al.*, 2021). However, differences emerge at the stage of clonal expansion. In muscle fibres, deletions tend to originate in the perinuclear region, where mitochondrial biogenesis is active. These deletions undergo focal expansion, driven by local replication and retrograde signalling that promotes further biogenesis and the spread of dysfunctional mitochondria (Vincent *et al.*, 2018). In contrast, neurons exhibit a more dispersed and heterogeneous distribution of mtDNA

deletions, with less evidence of focal proliferation, likely reflecting their unique cellular architecture and mitochondrial dynamics (Lawless *et al.*, 2020).

The mechanism underlying mtDNA deletions remains a subject of debate. Three main models have been proposed to explain their formation (Figure 1.6-8). The first model, introduced in the 1980s, was based on the identification of common repeats in KSS and chronic external ophthalmoplegia plus syndrome (CEOP). This model observed two direct repeats at the deletion boundaries, with 5' repeat being preferentially retained (Shoffner *et al.*, 1989). It suggests that during unidirectional replication from OriH to OriL, the mtDNA's replication machinery may cause misalignment of the repeats with downstream sequences. This strand slippage can result in the loss of a portion of genome during replication. Research has also indicated that mtDNA degradation is regulated by replication machinery proteins (Peeva *et al.*, 2018). Additionally, secondary structures formed near the breakpoints may contribute to deletions. Analysis of deletion breakpoints has revealed that they preferentially occur at sequence motifs predicted to form G4s. A recent model replicates the conditions under which mtDNA-specific replication stalling enhances G4 formation, particularly in the major arc, leading to mtDNA loss (Doimo *et al.*, 2023).

The second model suggests that deletions are formed after the repair of the double strand break (DBS). This hypothesis is based on that free radical oxygen is the by-product of the mitochondrial OHPHOS reaction, and mtDNA which is located inside the mitochondria matrix must be under relatively higher level of reactive oxygen species (ROS) stress and therefore more frequently be damaged lead to DSB and there are three repair mechanism has been identified (Haber, 2000; Bowmaker *et al.*, 2003). ROS can induce strand breaks in mtDNA, and subsequent repair processes may result in the loss of genomic segments (Shokolenko *et al.*, 2009). This has also been observed in in vitro models. Exposure to oxidative agents such as hydrogen peroxide or rotenone has been shown to increase the frequency of mtDNA deletions (Ballinger *et al.*, 1999; Heo *et al.*, 2022). In additional, ROS can cause oxidative base modifications, which compromise the fidelity of mtDNA replication and may lead to replication fork stalling. This can result in deletions through the first mechanism described above. Oxidized bases can interfere with the binding and function of DNA POLG, further disrupting mitochondrial genome maintenance (Shokolenko *et al.*, 2009). It is still under debate whether the repair

mechanism is present in mitochondria due to highly efficient functioning damaged mtDNA degradation system formed by the replication proteins.

The third model, copy choice recombination, was suggested back to 2019 by analysing deep sequencing data (Persson *et al.*, 2019), which is a mechanism observed in *E.coli* (Albertini *et al.*, 1982). In this model, during L-strand synthesis, secondary structure is formed like a loop or hairpin, which leads to the dissociation of the DNA polymerase and the 3' end of the nascent strand from the template. There is a chance that the 3' end of the strand will anneal to the downstream of the template then carrying out the replication, which leads to deleted mtDNA generated.

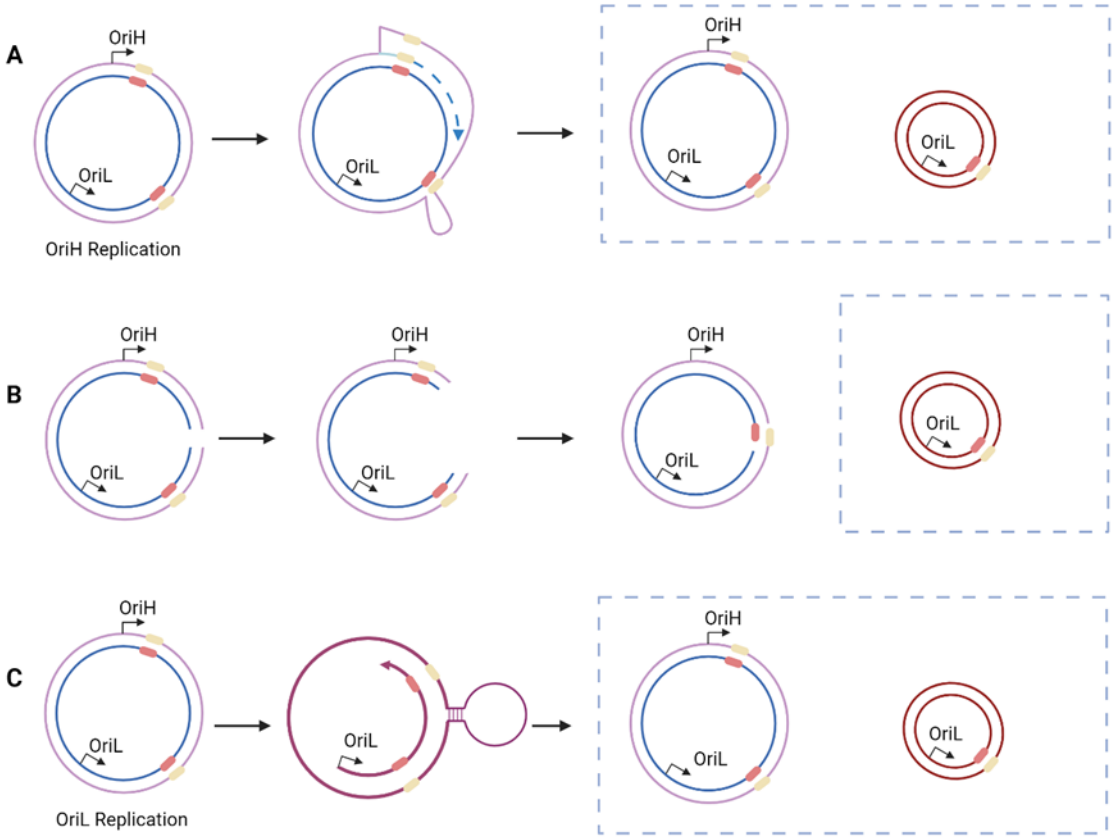

Figure 1.6-8 Three models of mtDNA deletion

This figure illustrates three models of mtDNA deletion formation. In the first model, during replication from OriH to OriL, misalignment of direct repeats can occur, causing strand slippage. This misalignment leads to the omission of a genomic segment during replication. In the second model, deletions arise from the incorrect repair of double-strand breaks induced by ROS or other types of DNA damage. The third model proposes that during replication of the light strand, secondary structures such as loops or hairpins form, causing dissociation of the DNA polymerase and the 3' end of the nascent strand from the template. The 3' end may re-anneal downstream on the template, resuming replication and generating mtDNA with a deletion. OriH: Origin of the heavy strand; OriL: Origin of the light strand.

1.6.9. *mtDNA point mutations*

Point mutations, commonly detected in the mtDNA genome, can be either maternally inherited or somatic mutations that arise throughout an individual's lifetime. Till 2021, around 265 mtDNA pathogenic mtDNA mutations have been identified from 483,626 individuals from United Kingdom (UK) biobank (Yonova-Doing *et al.*, 2021).

Maternally inherited point mutations are passed through the germline and are often associated with mutations within the MT-tRNA genes. These mutations typically impair mitochondrial translation by reducing the availability of functional MT-tRNAs. For example, the m.3243 A>G *tRNA (Leu)(UUR)* mutation, a well-characterised germline alternation, has been linked to severe conditions such as mitochondrial encephalomyopathy, lactic acidosis, and MELAS (Goto, Nonaka and Horai, 1990), maternally inherited diabetes and deafness (MIDD), and chronic progressive external ophthalmoplegia (CPEO).

In contrast, somatic mtDNA point mutations are alterations in the nucleotide sequence of mtDNA that occur post-zygotically and accumulate throughout an individual's lifetime. These mutations can arise due to errors in mtDNA replication by the mtDNA polymerase, POLG (Kujoth *et al.*, 2005). Errors include primary misincorporation events, where the polymerase incorporates the wrong nucleotide during DNA synthesis (eg: inserting adenine opposite a cytosine instead of guanine) (Fromme *et al.*, 2004), and mispairing due to a damaged site, where DNA damage, such as thermal denaturation, leads to chemical modifications. For instance, deamination of cytosine to uracil can result in the polymerase incorrectly inserting adenine opposite uracil (Zheng *et al.*, 2006).

Somatic mtDNA mutations can also result from oxidative damage, given mitochondria's critical role in energy production and their proximity to ROS (Wang, Kreutzer and Essigmann, 1998). ROS-induced DNA damage includes base modification, cause damage to the sugar backbone of the DNA, strand breaks, loss of bases (abasic sites), and the formation of covalent bonds between DNA and proteins. Mutations such as G:C to A:T transitions and G:C to T:A transversions are commonly observed as a result of oxidative damage (Wang, Kreutzer and Essigmann, 1998). Particularly, lesions like thymine glycols and 8-dihydro-2′-deoxyguanosine (8-oxo-dG) are highly mutagenic. For

example, 8-oxo-dG can cause POLG to mis incorporate an adenine opposite the oxidised guanine, resulting in a G:C to T:A transversion (Bohr, 2002; Suzuki and Kamiya, 2017).

Unlike germline mutations, somatic mutations are not inherited but are instead confined to individual's cells, leading to a mosaic pattern of heteroplasmy across tissues. The frequency and spectrum of somatic point mutations are influenced by factors such as age, environmental exposures, and cellular stress. Somatic mtDNA mutations are particularly significant due to their association with aging, neurodegenerative disease, and mitochondrial disorders. These mutations may impair mitochondrial function by disrupting oxidative phosphorylation or inducing apoptosis (Lawless *et al.*, 2020). For example, clonal expansions of somatic mtDNA mutations have been identified in buccal epithelial cells and heart muscle cells (Nekhaeva *et al.*, 2002). Similarly, elevated levels of mtDNA point mutations have been observed in ageing human colonic crypts, often associated with defects in multiple OXPHOS complexes (Greaves *et al.*, 2010).

1.7. *Mitochondrial turnover*

The homeostasis of the mitochondria requires generating and importing new mitochondria or mitochondrial proteins, and the breakdown of misfolded proteins, compartments or even breakdown of the mitochondria.

1.7.1. *Mitochondrial biogenesis*

Mitochondrial biogenesis is the process by which cells increase their mitochondrial mass and number to meet energy demands or adapt to environmental changes. This tightly regulated process involves the coordinated transcription and replication of mtDNA, the synthesis of mitochondrial proteins, and the import of nuclear-encoded proteins into the mitochondria. A central regulator of mitochondrial biogenesis is PGC1α, a highly dynamic transcriptional coactivator with distinct molecular characteristics (Finck and Kelly, 2006). PGC1α is a 91 kDa protein that contains a transcriptional activation domain at its N-terminus, allowing interaction with nuclear

transcription factors such as Peroxisome proliferator-activated receptor gamma (PPARγ) (Puigserver *et al.*, 1998; Handschin and Spiegelman, 2006), as well as other transcription factors including NRF1 and NRF2 (Wu *et al.*, 1999; Gleyzer, Vercauteren and Scarpulla, 2005).These interactions drive the transcription of genes required for mtDNA replication, transcription, and the assembly of mitochondrial protein import machinery (Ventura-Clapier, Garnier and Veksler, 2008).

PGC1α is regulated at multiple levels, including transcriptionally, post-transcriptionally, and post-translationally. It is modulated by upstream signalling pathways such as 5′-adenosine monophosphate-activated protein kinase (AMPK) and Sirtuin 1 (SIRT1), which phosphorylate or deacetylate PGC1α, respectively, to enhance its activity in response to energy stress or metabolic cues (Rodgers *et al.*, 2005). Additionally, PGC1α plays a critical role in regulating the expression of *TFAM* and components of the mitochondrial protein import system through regulating *NRF1* and *NRF2*, ensuring that nuclear-encoded mitochondrial proteins are properly synthesized, transported, and integrated into the mitochondria (Virbasius and Scarpulla, 1994; Scarpulla, 2002). By linking nuclear and mitochondrial genomes, PGC1α ensures the proper expansion and functional integration of mitochondria into cellular metabolic networks. Responsive to stimuli such as exercise, caloric restriction, and oxidative stress, PGC1α integrates mitochondrial biogenesis with cellular energy demands, making it indispensable for maintaining metabolic homeostasis and cellular adaptation (Wu *et al.*, 1999; St-Pierre *et al.*, 2003).

1.7.2. *Mitochondrial protein breakdown*

Proteolytic degradation of substrates by mitochondrial proteases is essential for mitochondrial biogenesis. Multiple proteases in the mitochondrial matrix are involved in this process. Mitochondrial processing protease (MPP) is one such protease essential for cleaving off the presequence of proteins, specifically the mitochondrial targeting signal (MTS), which is crucial for mitochondrial protein importation and recognition by the TOM complex (Richter and Lamppa, 1998; Kunová *et al.*, 2022). Presequence protease (PreP) is responsible for degrading the free presequence accumulated from MPP cleavage and other protein degradation processes (Johnson *et al.*, 2006). Mutations

or dysregulation of these essential proteases can lead to serious effects. Mutations in *PMBPCB,* the gene encoding the catalytic subunit of MPP, have been identified as linked to neurodegeneration and cerebellar atrophy in early childhood (Vögtle *et al.*, 2018). Pitrilysin metallopeptidase 1 (PITRM1) is associated with the accumulation of amyloid-beta peptides in mitochondria, and PITRM1 knockout cells as well as human cerebral organoids have exhibited tau pathology and increased cell death (Pérez *et al.*, 2021).

Mitochondrial proteases also play a role in regulating other mitochondrial functions, such as the quality control process. The cleavage of PINK1 by presenilin-associated rhomboid-like (PARL) in the inner membrane helps maintain relatively low levels of PINK1 to inhibit mitophagy (McQuibban, Saurya and Freeman, 2003; Sík *et al.*, 2004). ATP-dependent Lon protease (LONP1), located in the mitochondrial matrix, is a type of serine protease responsible for degrading misfolded or oxidatively damaged proteins (Matsushima and Kaguni, 2012; Goard and Schimmer, 2014; Matsushima *et al.*, 2021).

1.7.3. *Mitochondrial-derived vesicles*

Vesicular transport is an ancient and highly conserved mechanism of intracellular communication, found in various organisms, including mammals, plants, and yeast (Heyn, Heuschkel and Goettsch, 2023). Among these, mitochondrial-derived vesicles (MDVs) are one of the most abundant vesicle types, primarily responsible for delivering cargo to lysosomes or peroxisomes for degradation (König and McBride, 2024). MDVs were first described in 2008 and have been the subject of extensive research since then (Neuspiel *et al.*, 2008). They have been observed in both single- and double-membrane structures, with diameters ranging from 70 to 150 nm (Popov, 2022).

Several types of MDVs can be identified using specific protein markers. Single-membrane MDVs originate from the outer mitochondrial membrane, and their cargo typically consists of mitochondrial membrane proteins. These vesicles are often positive for translocase of outer mitochondrial membrane 20 (TOMM20), mitochondria-associated protein ligase (MAPL), or both. Evidence suggests the presence of a selective sorting mechanism that determines the cargo composition within MDVs (Heyn, Heuschkel and Goettsch, 2023). Notably, over 107 high-confidence MDV cargo types,

including misfolded proteins and assembled complexes, have been identified in TOMM20-positive MDVs. These vesicles are directed towards the lysosome for degradation (König *et al.*, 2021).

Studies have shown that MDVs are independent of GTPase dynamin related protein (DRP1) expression in cellular models, suggesting that MDVs are not part of the mitochondrial fission process (Ji *et al.*, 2017). Instead, MDVs are triggered under conditions of mitochondrial stress that impair respiratory function, although this stress does not typically lead to mitochondrial depolarisation. The initiation of MDV formation appears to be linked to PINK1 and Parkin, which have also been implicated in PD (Matheoud *et al.*, 2016; Wang *et al.*, 2017). Interestingly, when cells are treated with antimycin A, a mitochondrial complex III inhibitor that induces mitophagy, mitophagy is only observed after 12 to 24 hours, whereas peak MDV formation occurs within 1 to 3 hours (Chan *et al.*, 2011; McLelland *et al.*, 2014). Research has shown that MDVs colocalise with Parkin in a PINK1-dependent manner, and these vesicles, which contain oxidised proteins, are targeted to the lysosome for degradation (Soubannier *et al.*, 2012, 2012). Furthermore, in neurons experiencing mild oxidative damage, MDVs have been observed to release syntaphilin, a protein involved in mitochondrial motility. This release affects mitochondrial transport, preventing their movement back to the soma and protecting them from further degeneration (Lin *et al.*, 2017).

1.7.4. *Mitophagy*

The autophagy process regulates the breakdown of certain cellular components or organelles. Mitophagy, as part of autophagy, is a specific process that focuses on the breakdown of dysfunctional mitochondria. There are three major ways in which mitophagy can be triggered. The PINK1 and PARKIN pathway is one such mechanism that has been investigated, with mutations in these two genes identified in autosomal recessive juvenile parkinsonism.

PINK1 is a mitochondrial serine/threonine-protein kinase encoded by the PINK1 gene located on chromosome 1 at position 1p36.12. It contains an N-terminal mitochondrial targeting sequence (MTS), a transmembrane domain (TM), an N-terminal regulatory

domain (NT), a conserved N-lobe protein kinase domain (N-lobe), a conserved C-lobe protein kinase domain, and a C-terminal domain (CTD). The *PINK1* gene has 8 exons encoding a 581 amino acid protein. Different variants have been identified across various tissue types (Manning *et al.*, 2002). Parkin is an E3 ubiquitin ligase belonging to the RING-between-Ring (RBR) family, containing 5 domains: an N-terminal ubiquitin-like domain (UbI), a C-terminal R0 domain, an R1 domain, an In-between RING domain, and an N-terminal R2 domain. Full-length Parkin forms an auto-inhibited conformation mediated by multiple domain-domain interactions, with the core catalytic residues occluded inside. The activation of Parkin requires interaction with phosphorylated ubiquitin or the phosphorylated UbI domain, which aids in structural remodelling to expose the core residues of Parkin (Chaugule *et al.*, 2011; Riley *et al.*, 2013).

Under normal circumstances, PINK1 is imported into the matrix of the mitochondria, where its part of the MTS and TM domain are cleaved by the MPP, or imported to the intermembrane space, where it is cleaved by the PARL protease. The cleaved PINK1 residues (52 kDa) are then transported back to the cytosol to be degraded by the ubiquitin-proteasome system through the N-end rule pathway and act as an inhibitor of mitophagy (Yamano and Youle, 2013).

Under disease or stressed conditions, the membrane potential of the OMM is disrupted (Narendra *et al.*, 2008), and a high volume of PINK1 becomes stuck to the OMM, forming a homodimer. After autophosphorylation of the dimer at T257, S228, and S402, Parkin is phosphorylated at Ser65 in the UbI domain. The E3 ligase, Parkin, starts to be attracted to the OMM. Unlike other E3 ubiquitin ligases, which have a high affinity toward their substrates, Parkin can ubiquitinate multiple OMM proteins, including Mitofusin 1 and 2 (MFN1 and MFN2), voltage-dependent anion-selective channel 1 (VDAC1), and the translocase of the TOM proteins 20, 40, and 70 (Geisler *et al.*, 2010; Tanaka *et al.*, 2010; Chan *et al.*, 2011). The high number of ubiquitinated proteins then attracts specific autophagy factors like Optineurin (OPTN) and Sequestosome 1 (p62) to trigger engulfment by LC3-phosphatidylethanolamine conjugate (LC3II) autophagosomes (Lee *et al.*, 2010; Heo *et al.*, 2015).

1.7.5. *Fission and fusion*

Fission and fusion are a part of the mitochondria dynamic regulation, and the equilibrium between two processes are vital for determining and maintaining the morphology of mitochondrial while deal with stress at the same time. Fission indicates the separation of one mitochondrion into two, while fusion means multiple mitochondria fuse into one. Fission and fusion process has been shown to be dependent on cell types as the different type of metabolism. In neurons, fission and fusion has been shown to be involved in the formation of synapses and dendritic spins and help with cleaning the damaged mtDNA (Figure 1.7-1). Mitochondrial fission and fusion also influence mtDNA heteroplasmy levels. Fusion facilitates the mixing of mtDNA populations by allowing mitochondrial contents to merge, promoting homogeneity and potentially diluting the effects of deleterious mutations. In contrast, fission enables the segregation of mtDNA variants by dividing mitochondria (Lewis, Uchiyama and Nunnari, 2016; Sabouny and Shutt, 2021). When fission and fusion are inhibited, this can lead to an increased accumulation of mtDNA mutations (Tam *et al.*, 2013). Furthermore, research has shown that the presence of α-synuclein can affect mitochondrial fission and fusion dynamics (Nakamura *et al.*, 2011). Additionally, studies have demonstrated that *Drp1* deletion in mice leads to dopaminergic neuronal death in the striatum (Berthet *et al.*, 2014). These findings suggest that mitochondrial fission and fusion are intricately linked to the pathology of PD (Perlmutter, Braun and Sachs, 2009; Pozo Devoto and Falzone, 2017).

The main tigger of fission or the regulator of fission is the cytosolic soluble DRP1. There are multiple DRP1 regulation receptors and recruitment factors on the OMM, including mitochondrial fusion protein 1 (FIS1), Mitochondrial fusion factor (MFF) as well as in endoplasmic structures (Yoon *et al.*, 2003; Stojanovski *et al.*, 2004; Ji *et al.*, 2017; Di Nottia *et al.*, 2021). After the activation of recruitment factors or the receptors, DRP1 accumulates in the OMM and been activated through the GTP binding and hydrolysis (Praefcke and McMahon, 2004; Sundborger *et al.*, 2014). Then DRP1 start to form dotted structures and to constrict the mitochondrial tubule to mediate membrane fission. The appearance of DRP1 is essential but it cannot lead to fission process alone. The presence of other proteins has been proven to be fundamental as well like the dynamin-

2 (DNM2) and Optic atrophy 1 (OPA1) (Cipolat *et al.*, 2004; Kamerkar *et al.*, 2018). Research have shown that the regulation of fission pathway is influenced by some metabolism levels like the glucose and leptin level are relate to relative DRP1 expression (Santoro *et al.*, 2017; Jong *et al.*, 2019; Zheng, Luo and Liu, 2021).

Fusion is regulated through a couple of proteins and pathways to form a more elongated mitochondria and to maintain low level of metabolism stress. Research have shown that biogenesis pathway related proteins can trigger the fusion pathway like PGC1α, PGC1b, estrogen-related receptor alpha (ERRα) as key regulators in the fusion pathways (Mootha *et al.*, 2003; Schreiber *et al.*, 2004; Cartoni *et al.*, 2005).

MFN1, MFN2 are located in the OMM. MFN1 and MFN2 can fuse together either homo or heterotypic interaction and start the first step of connecting two mitochondria which is regulated in both transcriptional and post translational stage (Ishihara, Eura and Mihara, 2004; Chan, 2006). OPA1, a protein located in the IMM, plays a crucial role in regulating mitochondrial inner membrane fusion. The regulation of OPA1 occurs primarily at the transcriptional level through alternative splicing, as well as via post-translational modifications (Olichon *et al.*, 2007). In humans, there are eight isoforms of OPA1. The long isoform (L-OPA1), located in the IMM, can be cleaved into a short, soluble isoform (S-OPA1). Sufficient levels of L-OPA1 facilitate IMM fusion, whereas the accumulation of S-OPA1 supports the function of DRP1 in mitochondrial fission (Del Dotto *et al.*, 2018).

Mitochondrial fission and fusion are closely linked to mitophagy. Both DRP1 and OPA1 have been shown to play key roles in the regulation of this process (Liao *et al.*, 2017; Tong, Zablocki and Sadoshima, 2020). Studies have demonstrated that the triple ablation of MFN1, MFN2, and DRP1 leads to a significant accumulation of dysfunctional mitochondria (Song *et al.*, 2017).

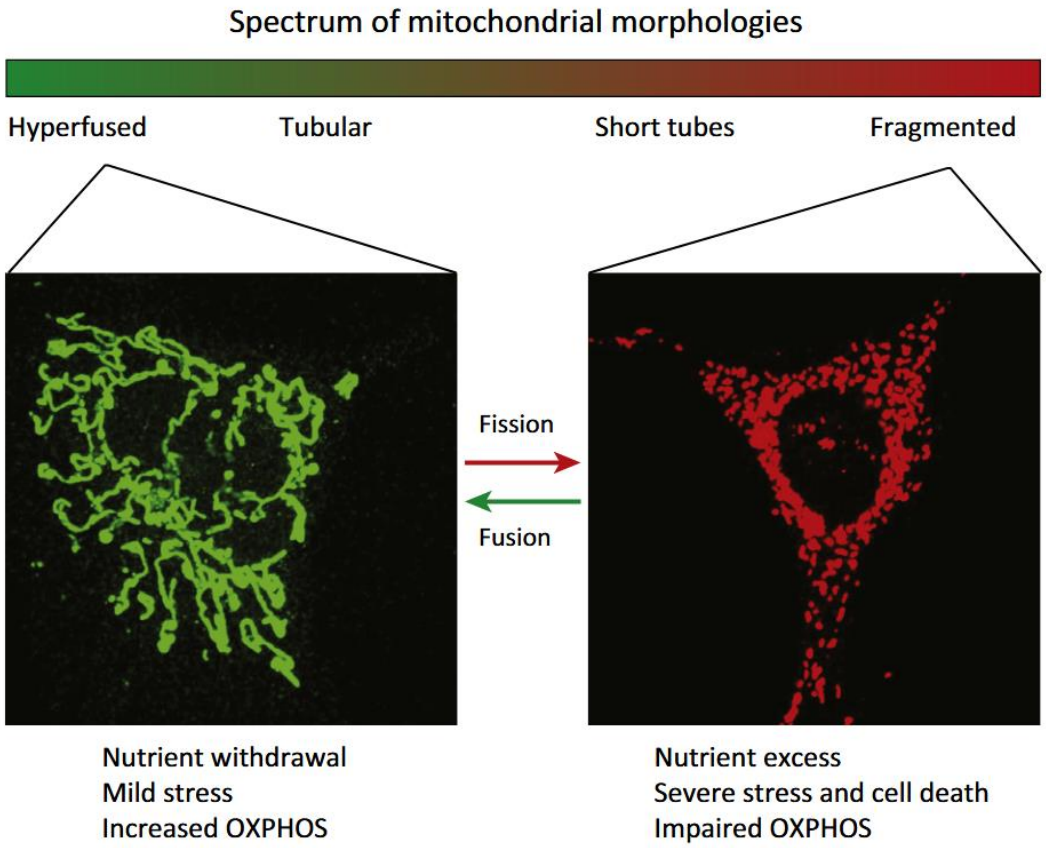

Figure 1.7-1 Fission and fusion

This figure illustrates mitochondrial dynamics. Green staining represents the hyperfused state of mitochondria (following fusion), which is typically observed during nutrient withdrawal, mild stress, or increased OXPHOS activity. Red staining indicates fragmented mitochondria (following fission), commonly observed under conditions of nutrient excess, severe stress, cell death, or impaired OXPHOS. This figure is adapted from (Wai and Langer, 2016).

1.7.6. *MtCN regulations.*

MtCN is tightly regulated and varies across different tissues and cell types (Filograna *et al.*, 2021). Decreases in mtCN are often associated with pathological conditions. For example, reduced mtCN has been reported in the dopaminergic neurons of PD patients (Dölle *et al.*, 2016; Grünewald *et al.*, 2016) and in individuals with breast cancer (Yu *et al.*, 2007). Aging is also associated with reduced mtCN in various cell types, including

lymphocytes (Ding *et al.*, 2015), blood (van Leeuwen *et al.*, 2014; Knez *et al.*, 2016), and skeletal muscle (Wachsmuth *et al.*, 2016). Conversely, an increased mtCN can occur as a compensatory response to mtDNA deletions, driven by over-replication to maintain mitochondrial function, the maintenance of the wild-type hypothesis (Elson *et al.*, 2001; Bai and Wong, 2005).

The regulation of mtCN involves a complex interplay of pathways, including mitochondrial biogenesis, mtDNA maintenance, mitophagy, and mitochondrial fission and fusion. TFAM, a protein that binds to mtDNA in a non-sequence-specific manner, plays a critical role by stabilizing the mtDNA molecule. Insufficient TFAM levels can lead to mtDNA depletion, while overexpression may interfere with mtDNA replication and biogenesis. It has been hypothesized that TFAM regulates protein binding within a 500-base-pair region encompassing the D-loop and the two promoter regions (Ghivizzani *et al.*, 1994).

PGC1α is another key factor in mtDNA replication, as it regulates the expression of *NRF1* and *NRF2*, which drive the transcription of *TFAM* and *POLγ*. These proteins are essential for initiating and sustaining mtDNA replication. The levels of PGC1α are modulated by cellular energy demands (Lin *et al.*, 2004), stress signals (Miller, Clark and Anderson, 2019), and post-translational modifications (Luo *et al.*, 2019).

The PINK1/Parkin pathway is also crucial for mtCN regulation by mediating the selective removal of dysfunctional mitochondria through mitophagy. This process prevents the accumulation of damaged mtDNA that could compromise mitochondrial function. By facilitating the turnover of defective mitochondria, PINK1 indirectly maintains a healthy mitochondrial population with functional mtDNA, thereby contributing to the regulation of mtCN. Additionally, mitophagy clearance mediated by PINK1 ensures that cells adapt to bioenergetic demands by promoting the replication of healthy mitochondria to replenish the mitochondrial pool (Abramov *et al.*, 2011).

Mitochondrial fission and fusion create a dynamic equilibrium that ensures the proper replication and distribution of mtDNA across the mitochondrial network. Disruptions in this balance can lead to uneven mtDNA segregation or the accumulation of defective mitochondria, ultimately impairing mtCN regulation (Twig *et al.*, 2008).

1.8. *PD*

1.8.1. *PD stages and developments.*

PD is the second most common neurodegenerative disease worldwide. It is a progressive neurodegenerative disorder characterized by a wide range of motor symptoms, including resting tremor, bradykinesia, and rigidity, as well as non-motor symptoms such as cognitive impairments and sleep disorders. The four cardinal features of PD are commonly summarised by acronyms TRAP: Tremor at rest, Rigidity, Akinesia (Bradykinesia), and Postural instability. The progression of the disease can be found in (Figure 1.8-1) (Frank, Pari and Rossiter, 2006).

Before the onset of visible symptoms, the underlying mechanisms of PD, including neurodegeneration, are already well underway. At this prodromal stage, approximately 50-60% of dopaminergic neurons in the SNpc have already been lost (Fearnley and Lees, 1991; Mahlknecht, Seppi and Poewe, 2015). The prodromal stage of PD is marked by substantial pathological changes and diverse research efforts aimed at understanding these early processes. Advances in biomarkers, imaging techniques, and genetic analyses offer hope for earlier detection and the possibility of slowing or preventing disease progression (Yilmaz *et al.*, 2019).

The International Parkinson and Movement Disorder Society (MDS) has proposed research criteria that outline several factors associated with an increased probability of developing PD (Berg *et al.*, 2015). For instance, men have a 1.5-fold higher risk of developing PD compared to women, and individuals with a first-degree relative who experienced PD with onset after age 50 have an approximately 10% risk of developing the disease. Other prodromal symptoms include hyposmia, constipation, and depression, which further underscore the importance of early identification.

Significant progress has been made in biomarker development over recent years. For example, magnetic resonance imaging (MRI) has demonstrated its utility in detecting non-clinical changes in brain areas. Diffusivity measures at field strengths of at least 1.5 T have revealed significant alterations in the substantia nigra, olfactory tract, and cortex during the prodromal stage (Ibarretxe-Bilbao *et al.*, 2010; Rolheiser *et al.*, 2011;

Mahlknecht, Seppi and Poewe, 2015). Genetic studies, particularly genome-wide association studies (GWAS), have identified mutations linked to PD, including on chromosome 4 encoding *alpha-synuclein (SNCA)* and on chromosome 12 encoding the GTPase enzyme *leucine-rich repeat kinase 2 (LRRK2)*. These genes are associated with mitochondrial function and the regulation of mitophagy (Nalls *et al.*, 2019; Kim *et al.*, 2024).

In addition to imaging and genetic markers, molecular biomarkers are emerging as potentially easier and more accessible tools for early detection. For example, the analysis of circular RNA in whole blood has shown promise (Beric *et al.*, 2024; Whittle *et al.*, 2024). Furthermore, the seed amplification assay (SAA), originally developed for detecting prion protein isoforms, has been adapted to detect alpha-synuclein seeds in cerebrospinal fluid (CSF). This method has demonstrated potential for distinguishing individuals with PD from healthy controls in several studies (Russo *et al.*, 2021).

When clinical symptoms do start to appear, the diagnosis of PD can normally be performed in three steps, as outlined by the UK Parkinson's Disease Brain Bank clinical criteria for the diagnosis of probable PD. Step 1 is that patients have bradykinesia. Step 2 is that other cases of parkinsonism must be excluded, such as exposure to 1-methyl-4-phenyl-1,2,3,6-tetrahydropyridine (MPTP) or other secondary cases. Step 3 is the patients must meet at least three supportive positive criteria, such as the presence of rest tremor, a significant response to levodopa therapy lasting five years or more, or persistent asymmetry with symptoms more severe on the side of onset (Clarke *et al.*, 2016).

Monitoring disease progression poses a significant challenge due to the lack of a definitive diagnostic test for PD and the broad spectrum of motor and non-motor symptoms involved. Several scales have been developed to track motor impairment progression, including the Hoehn and Yahr scale (Hoehn and Yahr, 1998), the Unified Parkinson's Disease Rating Scale (UPDRS) (Disease, 2003), and the updated version of the UPDRS, sponsored by the Movement Disorder Society, known as the MDS-UPDRS (Goetz *et al.*, 2008).

Given the diverse clinical profiles observed in PD (Table 1.8-1), providing effective treatment requires grouping symptoms into distinct categories and identifying the

underlying pathogenic mechanisms that link them (Prime *et al.*, 2020). Apart from the divided symptoms, genomic analysis could also provide an insight to the treatments. For example, for patients with loss of function in *PINK1* gene can respond well to small molecule activators of mitophagy (Miller and Muqit, 2019). This approach enables more personalised and targeted therapeutic strategies for individual patients.

It is important to note that parkinsonism is not synonymous with PD as several other conditions can also result in parkinsonism. For instance, patients with Multiple System Atrophy (MSA) may experience difficulties with breathing or swallowing due to a loss of muscle control (Wenning *et al.*, 2022). Progressive supranuclear palsy (PSP) can lead to weakness or paralysis of the muscles around the eyes (Rowe, Holland and Rittman, 2021), while patients with dementia with Lewy bodies (DLB) often exhibit stiff limbs and slowed movements (Capouch, Farlow and Brosch, 2018). The use of certain medications may also induce parkinsonism, a condition referred to as drug-induced parkinsonism (DIP). Dopaminergic antagonists that target the D2 dopamine receptor such as metoclopramide and levosulpiride, which are commonly used to treat upper gastrointestinal motility disorders (Shin and Chung, 2012), as well as haloperidol, a typical antipsychotic, can all lead to DIP (Rafiq *et al.*, 2022) .

In the light of the advancements in understanding PD and the development of accurate in vivo detection method for alpha-synuclein, alongside the recognised heterogeneity of the condition, novel classification and staging systems have been proposed. The SynNeurGe framework classifies PD based on three components: the presence of pathological alpha-synuclein aggregations (Syn), evidence of neurodegeneration through neuroimaging (Neur), and the existence of pathogenic genetic variants (Ge) (Höglinger *et al.*, 2024). Complementing this, the Neural Alpha-Synuclein Disease Integrated Staging System (NSD-ISS) offers a biologically anchored staging model, delineating disease progression from preclinical stages to advanced functional impairment by integrating molecular pathology, dopaminergic dysfunction, and clinical symptomatology (Simuni *et al.*, 2024). These systems represent a paradigm shift towards a more nuanced and biologically informed understanding of PD. But at current stage, these advanced approaches remain confined to research settings due to ethical concerns. Nonetheless, both hold potential for future clinical application.

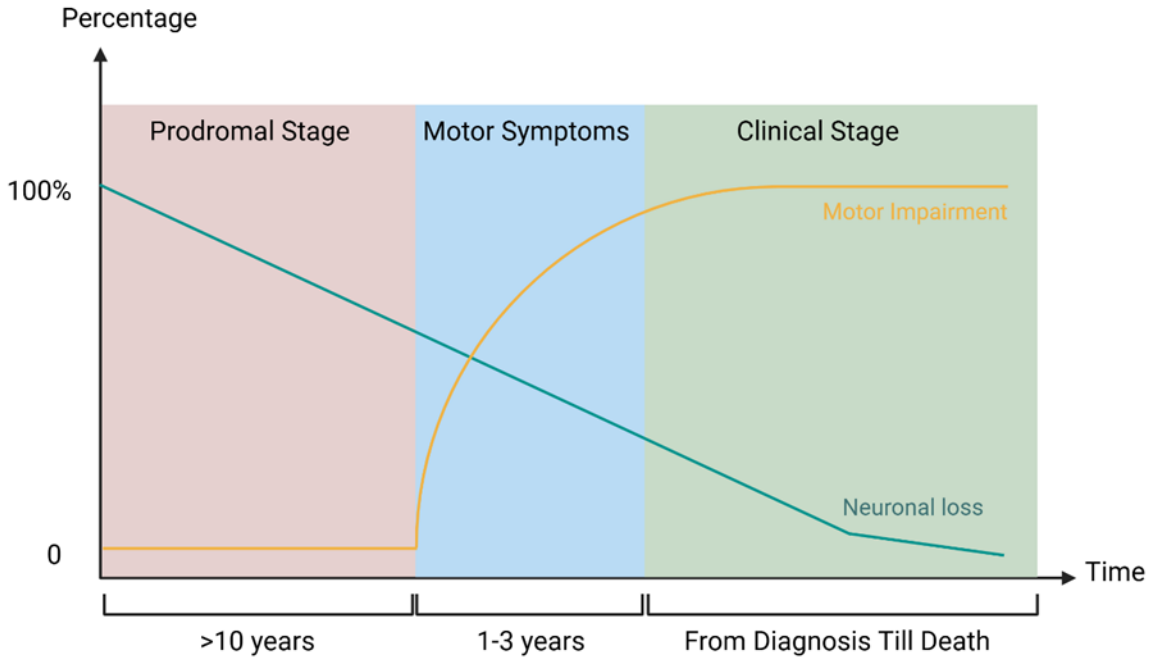

Figure 1.8-1 PD progression and stages

This plot illustrates the progression of motor impairment and neuronal loss over time, divided into three stages of PD. During the prodromal stage (typically lasting around 10 years before the onset of motor symptoms, shown in pink), neuronal loss has already begun, but no observable motor impairment occurs. However, some non-motor symptoms, such as sleep disturbances and constipation, may be detectable during this stage. The disease then progresses into the motor symptoms period, typically lasting 1–3 years (depicted in blue). During this stage, neuronal loss continues to worsen, and mild motor impairment begins to emerge. However, the motor symptoms remain subtle, and a diagnosis is usually not made at this point. As motor impairment becomes more pronounced, a diagnosis is made during the clinical phase (shown in green). By this stage, neuronal loss has reached a severe level, and treatment options are limited. In the graph, neuronal loss is represented in green, while motor impairments are indicated in yellow.

Types	Symptoms	Course	Treatments
Tremor-Dominant (TD) PD (Prime *et al.*, 2020)	Predominantly motor related symptoms Characterized by tremor at rest. Patients may also experience bradykinesia and rigidity.	Generally slower progression of symptoms and better response to dopaminergic therapies	Tremor is the primary target, responses well to levodopa and thalamus focus DBS
Postural instability and gait difficulty (PIGD) PD (Prime *et al.*, 2020)	Predominantly motor related symptoms Characteristics include freezing of gait, difficulty walking and postural instability.	More rapid progression, have more severely functional impairment and be less responsive to L-Dopa therapy than TDPD patients.	Gait and balance symptoms dominate but response less reliably to both pharmacological and surgical intervention
Akinetic-Rigid (AR) PD	Prominent bradykinesia and rigidity. Tremor is either absent or less severe	Increased risk pf dementia comparing to tremor subtype. Often associated with a more rapid progression and greater disability over time	Focus is on rigidity and akinesia, with strong responses to levodopa and DBS
Mixed PD	Exhibits a combination of resting tremor, bradykinesia and rigidity without a single predominant feature	Variable progression	Requires a balanced approach
PD Dementia (PDD) (Aarsland *et al.*, 2021)	Patients with PD motor symptoms typically exhibit at least two of four cognitive impairments: executive function, attention, visuospatial abilities, and memory.	Approximately 24-31% of PD patients develop dementia. Typically, PDD manifests years after the onset of motor symptoms	Begin with medications to treat motor symptoms (dopaminergic enhancers) and gradually introduce medications to support cognition, keeping in mind their potential strong side effects

Table 1.8-1 PD subtypes

1.8.2. *PD neuropathology changes*

The neuropathological changes in the brains of PD patients are predominantly found in the SNpc. Degeneration of dopaminergic neurons in SNpc, leading to reduced dopamine production in the midbrain, is one of the hallmarks of PD (Poewe *et al.*, 2017).

In addition to neuronal atrophy in SNpc, Lewy body (LB) pathology plays a central role in the pathogenesis of PD although the exact mechanisms remain unclear. Eosinophilic protein or Lewy bodies are composed of abnormally aggregated alpha-synuclein, a small protein encoded by the *SNCA* gene. Alpha-synuclein is abundantly expressed in the presynaptic terminals of neurons in the central nervous system and plays a role in neurotransmitter release. Under normal conditions, alpha-synuclein's synthesis, folding, and degradation are tightly regulated, maintaining a dynamic equilibrium (Kramer and Schulz-Schaeffer, 2007; Bridi *et al.*, 2021). In PD, this equilibrium is disrupted, leading to the aggregation of alpha-synuclein into insoluble forms, which eventually accumulate within neuronal cytoplasm as Lewy bodies (Figure 1.8-2).

The progression of Lewy body pathology in PD has been described using Braak Lewy body staging, proposed by Heiko Braak in 2003 (Braak *et al.*, 2003). Braak's hypothesis suggests that the spread of Lewy bodies correlates with the progression of PD neuropathology (Figure 1.8-3). In the early stages (Braak Lewy body stages I and II), Lewy body lesions are predominantly found in the gut, or in the olfactory systems, then move to the dorsal motor nucleus of the vagus, intermediate reticular zone, and coeruleus/subcoeruleus complex. During these stages, patients typically exhibit non-motor symptoms such as constipation or sleep disorders, corresponding to the prodromal phase of PD.

From Braak Lewy body stages III and IV, Lewy body pathology progresses to the SNpc, leading to dopaminergic neuron loss and the onset of motor symptoms such as bradykinesia, rigidity, and tremor. Lesions also appear in the temporal limbic cortex and LC, indicating the spread of pathology both upward to the cortex and downward to the spinal cord. During these stages, patients develop classical Parkinsonism. In Braak Lewy body stages V and VI, Lewy body pathology extends to the neocortex, premotor areas, and primary motor cortex, resulting in widespread neurodegeneration. At this

stage, patients experience severe motor dysfunction and profound non-motor impairments, including dementia and other cognitive deficits.

With advances in understanding LB and the application of immunostaining techniques, other brain regions have begun to attract attention. Researchers have recognized that neuronal degeneration can also occur in additional areas of the brain. Commonly affected regions include the locus coeruleus (LC) in the brainstem and the ventral tegmental area (VTA), both of which are subcortical nuclei containing dopaminergic and noradrenergic neuron populations (Sharma *et al.*, 2010; Faget *et al.*, 2016). More recently, other nuclei, such as the pedunculopontine nucleus (PPN) in the brainstem, have also been identified as undergoing pathological changes during the progression of PD.

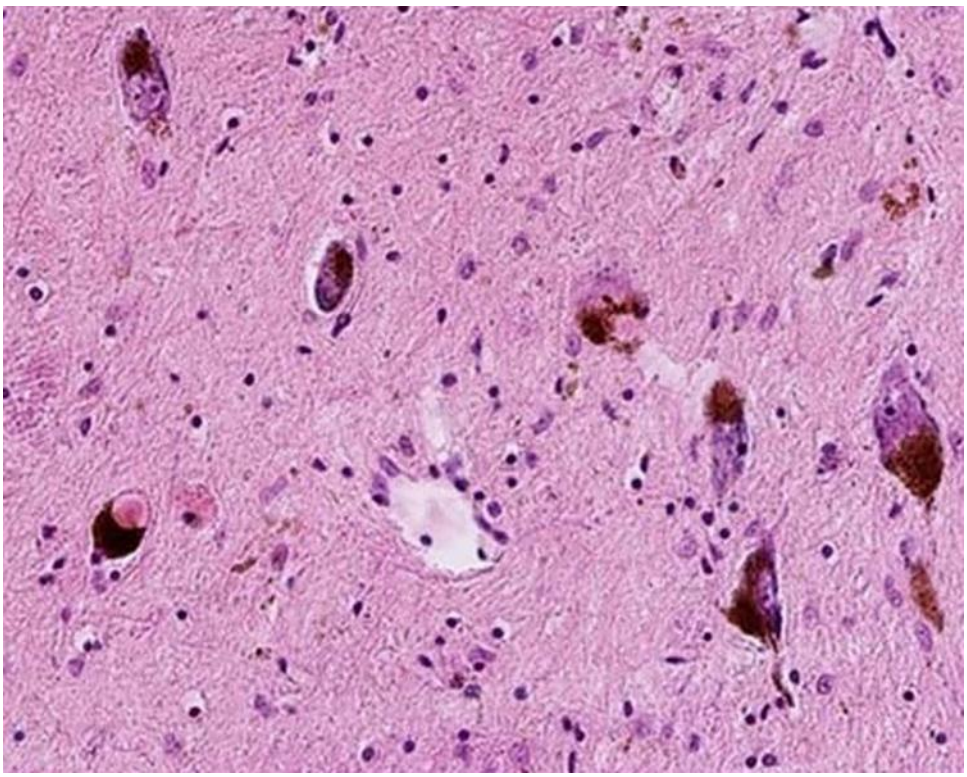

Figure 1.8-2 Lewy body pathology

This figure illustrates the appearance of common Lewy body (LB) pathology in a haematoxylin and eosin (H&E) stained histological section. LBs appear as intracytoplasmic, eosinophilic inclusions within neuronal cells. The periphery of the LBs is densely stained, creating a halo-like appearance. Image adapted from (Menšíková *et al.*, 2022).

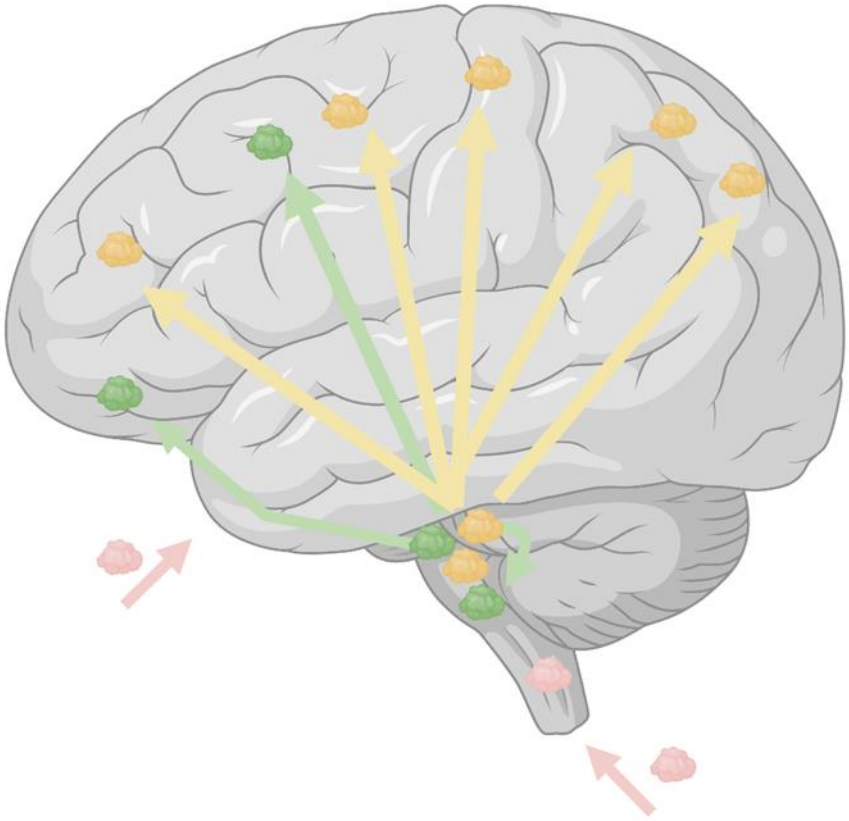

Figure 1.8-3 Lewy body pathology progression at different Braak stages

This figure illustrates the progression of Lewy body (LB) pathology across different Braak stages. Pink represents Braak stages I and II, during which LB lesions are predominantly found in the dorsal motor nucleus of the vagus, the intermediate reticular zone, and the coeruleus-subcoeruleus complex. At these stages, patients typically do not exhibit motor symptoms. Green represents Braak stages III and IV, where LB pathology begins to appear in the upper midbrain, primarily affecting the substantia nigra pars compacta (SNpc) and starts to emerge in the cortex. Yellow represents Braak stages V and VI, during which LB pathology is detected in widespread regions of the brain, including the neocortex, premotor areas, and primary motor cortex.

1.8.3. *PPN*

PPN is located within the mesencephalic locomotor region (MLR) in the upper brainstem and forms part of the reticular activating system (RAS). It plays a crucial role in the initiation and regulation of locomotor movements, as well as in modulating gait and posture by activating reticulospinal pathways. The PPN is anatomically divided into two subnuclei: the pars compacta (PPNc) and the pars dissipatus (PPNd) (Mesulam *et al.*, 1983; Lavoie and Parent, 1994). The PPNc contains densely packed neurons, which are typically larger in size and include cholinergic and glutamatergic neurons (Mesulam *et al.*, 1989; Steriade, 2004). In contrast, the PPNd is characterised by a more dispersed distribution of neurons, predominantly composed of small to medium-sized GABAergic neurons (Vincent and Kimura, 1992; Lavoie and Parent, 1994) (Figure 1.8-4).

The projections of the PPN are diffuse and vary according to neuronal type. Cholinergic neurons of the PPN typically extend their innervations to more distant regions and have longer projections compared to other neuronal types. These include ascending pathways targeting the thalamus, basal ganglia, and dopaminergic neurons in the VTA (Beninato and Spencer, 1987; Bolam, Francis and Henderson, 1991) (Figure 1.8-5). In contrast, GABAergic and glutamatergic neurons predominantly project to nearby areas within the midbrain and brainstem (Futami, Takakusaki and Kitai, 1995; Charara, Smith and Parent, 1996). Moreover, PPN projections are topographically organised. Neurons in the caudal PPN, particularly cholinergic neurons, primarily project to limbic structures, while neurons in the rostral PPN mainly send projections to motor-related structures, such as the SNpc, with glutamatergic neurons playing a significant role.

The connection between the PPN and PD can be traced to the interaction between excitatory synapses on dopaminergic neurons in the SNpc. The PPN is a well-established source of excitatory inputs to these neurons. In vivo studies have demonstrated that PPN activation increases the spike rate of SNpc neurons (Galtieri *et al.*, 2017). Additionally, SNpc dopaminergic neurons express some of the highest levels of nicotinic acetylcholine receptors (nAChRs) in the brain and are strongly

excited by nicotine (Nashmi *et al.*, 2007). One hallmark of PD is the loss of dopaminergic neurons in the SNpc. The research linking PPN activation with the excitation of dopaminergic neurons has prompted further investigation into the relationship between the PPN and PD.

In recent years, PPN-deep brain stimulation (DBS) has garnered attention for its potential therapeutic effects (Mazzone *et al.*, 2005). For PD patients with gait or locomotion impairments, low-frequency PPN-DBS has resulted in symptom improvement in some cases (Moro *et al.*, 2010; Thevathasan *et al.*, 2011; Welter *et al.*, 2015), although the outcomes remain inconsistent (Ferraye *et al.*, 2010; Dayal *et al.*, 2021). The inconsistency may arise because the PPN is a small, unpigmented region within the midbrain that is difficult to target, and it also contains a complex mix of neuronal types (Hamani *et al.*, 2016). Despite the growing interest in this midbrain structure, key questions remine: in such a heterogeneous region, which specific subregions are most relevant to PD pathogenesis or progression, or is the entire PPN crucial?

Early investigations revealed that in late-stage PD, nearly half of PPN cholinergic neurons are lost (Hirsch *et al.*, 1987; Shinotoh *et al.*, 1999). Furthermore, there is a correlation between the prevalence of falls in PD patients and reduced acetylcholine (ACh) release in the thalamus, attributed to the loss of PPN cholinergic neurons (Bohnen *et al.*, 2009). Not all PD-related symptoms are associated with cholinergic loss. For example, the transmission from the PPN to the ventral medulla and spinal cord—key pathways for locomotor activation—is predominantly mediated by glutamatergic neurons rather than cholinergic ones. A hypothesis proposed by Pahapill and Lozano suggests that both PPN glutamatergic and cholinergic neurons play essential roles in the regulation of gait and locomotion (Pahapill and Lozano, 2000). PPN glutamatergic neurons, which provide the primary output from the PPN to the spinal cord and ventral medulla, are critical for initiating programmed movements and gait. In contrast, PPN cholinergic neurons are more closely connected to the basal ganglia and thalamus, contributing to the maintenance of gait. This dual role of glutamatergic and cholinergic neurons in gait regulation is further supported by evidence from recent studies (Roseberry *et al.*, 2016; Caggiano *et al.*, 2018).

Although cholinergic neurons constitute only 25-30% (approximately 3,000 in rat brain) of the neuronal population within the PPN (Wang and Morales, 2009), their large soma size (20–40 μm in diameter) and functional importance mean that their dysfunction can still cause substantial disruption to the areas connectively (Honda and Semba, 1995; Ichinohe, Teng and Kitai, 2000). In contrast, dopaminergic neurons in the SNpc, which are smaller (10-14 μm in diameter) are more numerous (around 25,000 in rat brain) (Nair-Roberts *et al.*, 2008; Vidyadhara *et al.*, 2021), can also produce significant consequences when damaged. A similar relationship in relative neuronal size and abundance is observed in the human nervous system. The human PPN contains approximately 17,400 cholinergic neurons, each with an average diameter of around 40 μm, and extends approximately 10 mm in the rostro caudal direction (Manaye *et al.*, 1999; Sharma *et al.*, 2025). In comparison, each side of the human SNpc contains approximately 300,000 to 550,000 dopaminergic neurons, with a mean soma diameter of around 25 μm (Hardman *et al.*, 2002).

In exploring why these distinct neuronal types exhibit different vulnerability in PD, mitochondrial dysfunction has emerged as a key molecular. Evidence from human postmortem staining has shown that the expression of OXPHOS complexes in cholinergic neurons differs significantly from other neuronal types (Pienaar *et al.*, 2013). Specifically, when examining cholinergic neurons in isolation, both mtDNA deletions and copy number variations were found to be elevated compared to aged controls. As a neuronal type highly vulnerable to cell death in PD patients, this suggests that mtDNA changes may play a role in their degeneration (Bury *et al.*, 2017).

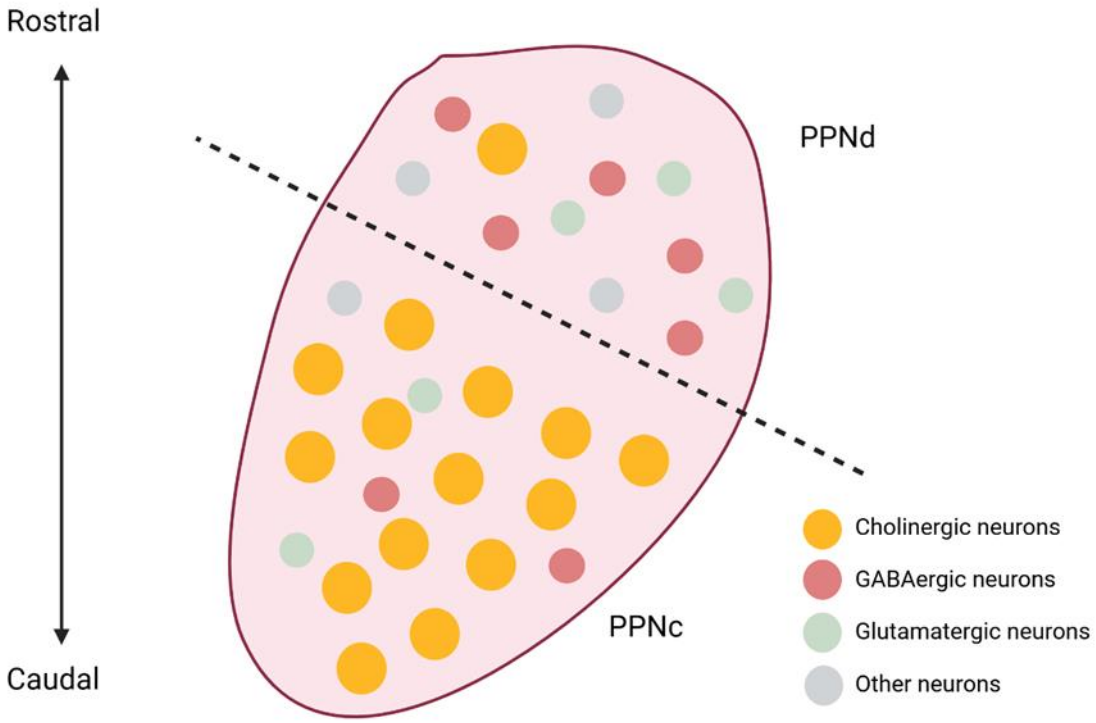

Figure 1.8-4 The structure of PPN and its neuronal composition

This illustration shows the two subdivisions of the PPN structure. The rostral part of the PPN is called the PPN pars dissipatus (PPNd), while the caudal part is referred to as the PPN pars compacta (PPNc). The neuronal composition of each part is distinct. PPNc is characterized by compact clusters of large neurons and a high population of cholinergic neurons, while PPNd contains small to medium-sized neurons, including GABAergic, glutamatergic, and other types, which are more widely distributed compared to those in PPNc.

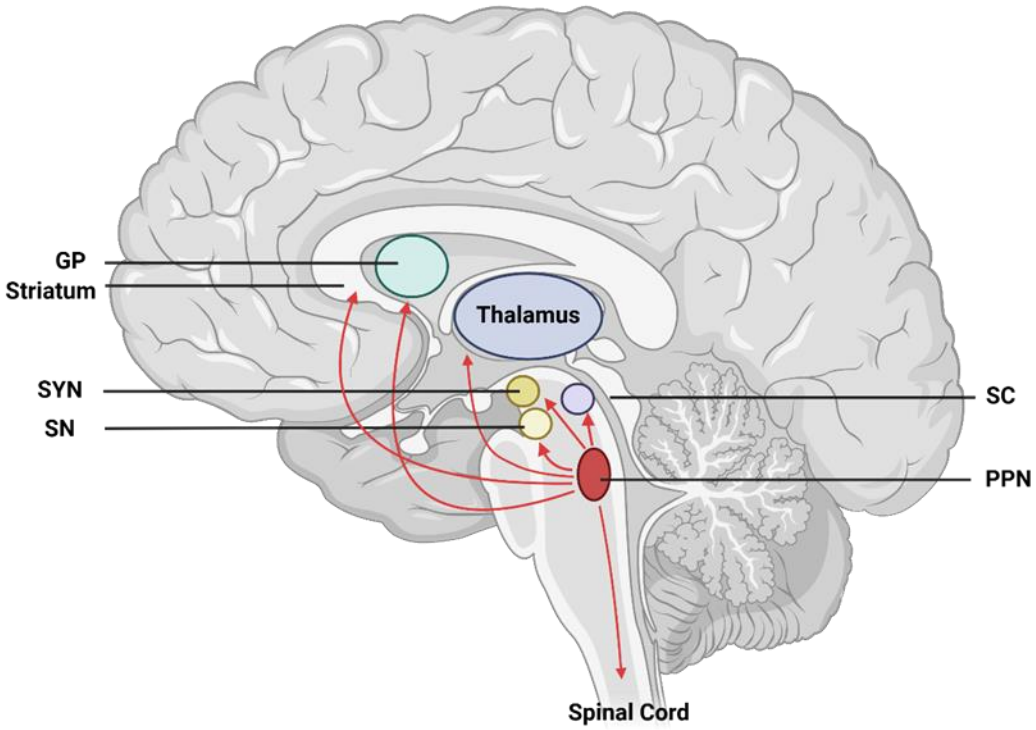

Figure 1.8-5 Cholinergic connection between PPN to other neuronal structures

This figure illustrates the cholinergic projections from PPN to various neuronal structures including GP, striatum, SYN, SN, SC, thalamus and spinal cord. These projections are critically involved in a range of functions, including movement initiation and coordination (SN), motor planning and execution (GP), sensory integration and arousal (SC and thalamus), and the modulation of spinal motor circuits (spinal cord). GP: Globus Palludus; STN: Subthalamic Nucleus; SN: Substantia nigra; SC: Superior colliculus

1.8.4. *Molecular mechanisms contributing to PD.*

Various pathways contribute to the pathogenesis of PD, with mitochondrial dysfunction being a major focus of research in recent years. The link between PD and mitochondrial dysfunction was first identified in the 1980s when a group of drug users inadvertently consumed synthesis drugs contaminated with MPTP. This compound is rapidly converted to MPP^+, which inhibits complex I of the mitochondrial OXPHOS chain

(Langston *et al.*, 1984). These individuals developed parkinsonism, underscoring the critical role of mitochondrial impairment in PD pathogenesis (Langston *et al.*, 1983). Since its discovery, MPTP has been widely used to generate PD models in rodents and primates, enabling significant advancements in understanding neurodegeneration and motor system developments. Furthermore, targeted disruption of complex I in mice has been shown to induce dopaminergic degeneration and parkinsonian symptoms, providing additional support for the role of mitochondrial dysfunction in PD (González-Rodríguez *et al.*, 2021).

Beyond toxicological models, studies on idiopathic PD have further elucidated the connection between mitochondrial dysfunction and PD. Mutations in genes *PARK6* (encoding PINK1) and *PARK2* (encoding Parkin) are among the most frequent cases of autosomal recessive early-onset PD. Both genes are integral to the mitochondrial quality control process known as mitophagy, regulating the clearance of dysfunction mitochondria as well as mitochondrial fission and fusion. These processes are critical for maintaining mitochondrial homeostasis.

Changes in the mitochondrial genome are also implicated in PD. Multiple studies have reported that dopaminergic neurons in the SNpc of PD patients harbour high levels of mtDNA deletions compared to the aged-matched controls (Reeve *et al.*, 2008; Nido *et al.*, 2018). However, it remains unclear whether mitochondrial dysfunction arises as a consequence of PD progression, leading to the generation or accumulation of mtDNA deletions (Buneeva *et al.*, 2020; Henrich *et al.*, 2023), or whether a high burden of mtDNA deletions acts as a causative factor in PD pathogenesis (Tresse *et al.*, 2023). Evidence exists to support both scenarios. For example, Rho0 cells with identical nuclear DNA, fused with mtDNA-containing platelets from either PD or control cases, exhibit PD-like alternations, including increased α -synuclein oligomerization, reduced ATP levels (Ghosh *et al.*, 1999; Esteves *et al.*, 2008).

Further investigation into mtDNA changes has revealed significant findings in specific brain regions. A study on human postmortem tissue using real-time PCR (ND1/ND4 method) demonstrated that cholinergic neurons in the PPN of PD patients harbour significantly high levels of mtDNA deletions and increased mtCN compared to age-matched controls (Bury *et al.*, 2017). Interestingly, the elevation of mtCN appears to be a compensatory mechanism specific to PPN cholinergic neurons, as SNpc

dopaminergic neurons more commonly exhibit a decrease in mtCN despite similarly high levels of mtDNA deletions (Bender *et al.*, 2006; Dölle *et al.*, 2016; Pyle *et al.*, 2016). mtDNA point mutations have also been linked to PD, with studies reporting elevated somatic mtDNA point mutations in early-onset PD patients (Lin *et al.*, 2012). However, this observation has not been consistently replicated in other PD subtypes, as demonstrated in human postmortem studies (Reeve *et al.*, 2009).

Mitochondria-related therapeutic approaches are an active area of research. Although no clinical trials have been conducted to date, mitochondrial Rho GTPase (Miro)-targeting therapies have shown promise in preclinical studies. Miro, an OMM protein, plays a critical role in maintaining mitochondrial dynamics and mitochondria axonal transport. Miro disfunction, characterised by its prolonged retention on the OMM and disruption of mitophagy, can be mitigated through Miro reduction. In human fibroblast, Miro reduction has been shown to restore mitophagy (Panchal and Tiwari, 2021). Similarly, in Drosophila models, Miro reduction not only restored mitophagy but also rescued locomotor deficits and reduced dopaminergic neurodegeneration (Hsieh *et al.*, 2016, 2019; Shaltouki *et al.*, 2018).

Other key mechanisms implicated in PD pathogenesis include alpha-synuclein aggregation, neuroinflammation, and oxidative stress. Mitochondria are central to cellular energy production and ROS regulation, and their dysfunction can lead to oxidative stress and neuronal damage. Meanwhile, lysosomes are responsible for degradation and recycling of cellular waste, including misfolded proteins. Impairment of lysosomal function disrupts this clearance process, promoting the accumulation of pathological alpha-synuclein (Navarro-Romero, Montpeyó and Martinez-Vicente, 2020). In turn, aggregated alpha-synuclein can interfere with both mitochondrial dynamics and lysosomal integrity, creating a vicious cycle. Also, all these processes are closely linked to metabolic disruptions and alterations, such as impaired mitochondrial function, disrupted energy production, and altered redox balance (Calabresi *et al.*, 2023). Growing evidence suggests that these metabolic dysregulations play a central role in the disease, leading to the emerging hypothesis that PD may, in part, be considered a metabolic disorder (Anandhan *et al.*, 2017). This crosstalk suggests that disturbances in one system can amplify dysfunctions in the others, ultimately driving the neurodegenerative process observed in PD.

1.9. *Overall aims and objectives.*

The overall aim of this project was to investigate mitochondrial changes in cholinergic neurons of the PPN in PD cases compared to aged controls. Specifically, the study sought to understand why PD PPN cholinergic neurons exhibit an increased mtCN, a phenomenon not observed in dopaminergic neurons of the SNpc. To achieve this, the project focus on the following objectives:

1) To investigate mtDNA deletion accumulation and its characteristics in cholinergic neurons of the PPN in both PD and aged control cases using next generation sequencing (NGS) deep sequencing data.
2) To investigate mtDNA point mutations accumulation and its characteristics in cholinergic neurons of the PPN in both PD and aged control cases using NGS deep sequencing data.
3) To explore potential changes in transcriptional levels across three key pathways, including biogenesis, maintenance, and mitophagy, involved in the regulation of mtCN.

Chapter 2. Methodology

2.1. *Reagents, equipment, solution and consumables*

2.1.1. *Equipment and software*

Equipment or Software	Supplier
TubeCollector 2x200 CM II	Zeiss
PALM RoboSoftware 4.6	Zeiss
Inverted Zeiss microscope (Axiovert 200M)	Zeiss
Eppendorf Thermomixer	Eppendorf
ABI Step one software	Applied Biosystem
ABI Step-one Plus Real Time PCR system	Applied Biosystem
Autoclave	Prior Clave
R v4.2.1	R
R studio v2023.06.0+421	R Studio
UV hood	Bioair
ZEN blue	Zeiss
Microcentrifuge 5418R	Eppendorf
Combi-Spin PVC 2044 Centrifuge	Grant-bio
LSE Vortex Mixer	Corning
Research Plus 200µl Pipette	Eppendorf
Research Plus 1000µl Pipette	Eppendorf
Research Plus 2.5µl Pipette	Eppendorf
Research Plus 20µl Pipette	Eppendorf
Staining box	Pyramid

ThermoMixer C	Eppendorf
Veriti 96-Well Fast Thermal Cycler	Applied Biosystem
Retriever 2100	Aptum
NanoDrop One	Thermo Scientific
PH Meter 3150	Fisher Scientific
3ml Graduated Pasteur Pipette	Star Lab
Micro (Flea) Magnetic Stirring Bars	Fisher Scientific
Magnetic Stirrers	Fisher Scientific
QuantStudio 7 Real-Time PCR system	ThermoFisher Scientific
QuqntStudio 7 software 1.0.3	ThermoFisher Scientific
Design and Analysis Software 2.6.0	ThermoFisher Scientific
Purelab Flez 2 Water Purification Unit	Elga
Zeiss Axioscan7 scanner	Zeiss

Table 2.1-1 Equipment and software table

2.1.2. *Molecular genetic reagents*

Reagent	**Supplier**
Nuclease free water	Qiagen
Taqman Assays (Hs00273372_s1) VIC-MGB	ThermoFisher Scientific
Taqman Assays (Hs00173304_m1) FAM-MGB	ThermoFisher Scientific
Taqman Assays (Hs00260868_m1) FAM-MGB	ThermoFisher Scientific
Taqman Assays (Hs00958021_m1) ABY	ThermoFisher Scientific

Taqman Assays (Hs01073348_g1) FAM-MGB	ThermoFisher Scientific
Customized Taqman Assays	ThermoFisher Scientific
RNaseZAP (AM9780)	Invitrogen
Super PAP Pen (008899)	Life Technologies
PicoPure RNA Isolation Kit (KIT0204)	Applied Biosystem
PureLink DNase (12185010)	Invitrogen
Anti-Choline Acetyltransferase Antibody (AB144P)	Sigma-Aldrich
Horse Anti-Goat IgG Antibody, Peroxidase (PI-9500-1)	Vector Laboratories
NovaRED Substrate Kit, Peroxidase (SK-4800)	Vector Laboratories
SuperScript IV VILO Master Mix (11756050)	ThermoFisher Scientific
PowerTrack SYBR Green Master Mix	Applied Biosystem
Tetro cDNA Synthesis Kit (BIO65043)	Meridian Bioscience
Taqman Universal PCR Master Mix (4304437)	ThermoFisher Scientific
Taqman Fast Advanced Master Mix (4444557)	ThermoFisher Scientific
TaqPath 1xStep RT-qPCR MasterMix (A15299)	ThermoFisher Scientific
TaqMan PreAmp MasterMix Kit (4384267)	ThermoFisher Scientific

Table 2.1-2 Molecular genetic reagents

2.1.3. *Chemical reagents*

Chemical	**Supplier**
PBS tablet (P4417)	Sigma-Aldrich
Potassium chloride (P3911)	Sigma-Aldrich
Sodium chloride (S9888)	Sigma-Aldrich
Ethanol (10048291)	Fisher Scientific

Buffer Solution PH 4 (10741614)	Fisher Scientific
Buffer Solution PH 7 (10287063)	Fisher Scientific
Buffer Solution PH10 (10414795)	Fisher Scientific
Electrode Storage Solution (10758891)	Fisher Scientific
Tween 20 (P1379)	Sigma-Aldrich
Trizma Base (T1503)	Sigma-Aldrich
TE Buffer (v6231)	Promega

Table 2.1-3 Chemical reagents

2.1.4. *Consumables*

Consumables	**Supplier**
0.2ml Thin-walled PCR tubes	Star Lab
0.5ml Thin-walled PCR tubes	Star Lab
1.5ml Eppendorf	Eppendorf
Disposable Scalpel	Swann-Morton
PCR-Cooler	Eppendorf
15ml Conical Centrifuge Tubes (339650)	ThermoFisher
50ml Screw Cap Tubes (62.559.001)	Sarstedt
MicroAmp Optical 384-well Reaction Plate with Barcode	Applied Biosystem
MicroAmp Optical Adhesive Film	Applied Biosystem
10µl graduated TipOne Filter Tips	Star Lab
10/20µl graduated TipOne Filter Tips	Star Lab

Table 2.1-4 Consumables

2.1.5. *Solutions*

Immunohistochemistry solutions	**Recipe**
1x Tris-buffered saline with Tween (TBST) (PH 7.4) 1L	8.8g NaCl 0.2g Kcl 3g Tris Base 50µl Tween-20 1L Nanopure water
1x PBS	1 PBS tablet in 200ml Nanopure water
10% blocking serum	100µl horse blocking serum 900µl TBST
1x Primary ChAT antibody	1µl Primary ChAT antibody (goat anti-ChAT) 150µl TBST
1x secondary antibody	1µl HRP horse anti-goat 120 PBS
1x NovaRED	5ml distilled water 3 drops Reagent 1 2 drops Reagent 2 2 drops Reagent 3 3 drops Reagent 4

qPCR solutions	**Recipe**
2x DNase I reaction buffer	20µl 10x DNase I reaction buffer

	80µl distilled water
1x DNase mixture	10µl DNase 40µl 2x DNase I reaction buffer
RT Reaction mixture	4µl superscript IV VILO mastermix Template RNA (1pg to 2.5ug) Nucleus-free water to 20µl
qPCR 10µl reaction	5µl mastermix 0.5µl each Taqman assay cDNA (1 to 100ng) water to 10µl

Table 2.1-5 Buffers and recipes

2.2. *Patient cohorts*

This study included six age-matched control, and seven individuals diagnosed with PD. Due to the limited availability of post-mortem brain tissue, it was not feasible to apply strict inclusion criteria based on specific clinical phenotype, as this would have significantly reduced the number of eligible cases. Therefore, broader criteria were adopted. All PD cases included has received a clinical diagnosis based on characteristic symptoms and supportive neuroimaging findings, and each diagnosis was subsequently confirmed through neuropathological examination at autopsy. Control cases were selected based on the absence of any reported motor impairments during life and the lack of neuropathological evidence of PD following post-mortem analysis.

Case	Sex	PD duration (y)	Clinical history	Medications	Haplogroup	Age at death (y)	PMI (h)	Braak LB stage	Braak Tau stage	Number of neurons analysed
Control1	M	/	Mild cognitive impairment; COPD; pneumonia; Chronic kidney disease; congestive heart failure	Paracetamol; Zopiclone; Pregabalin	U5b2a1a1	82	20	NA	2	5
Control2	M	/	Pneumonia; temporal lobe epilepsy; mild generalised atrophy	Unknown	H3b1b1	85	30	NA	2	5
Control3	M	/	Depressive episode; Malignant neoplasm of prostate	Unknown	H24a	89	72	NA	2	5
Control4	F	/	Sarcoma of the chest	Unknown	H3b	55	48	NA	1	5

Control5	M	/	MI; End-stage renal failure; Hereditary fibrinogen amyloidosis	Thyroxine; Simvastatin	V	69	34	NA	3	6
Control6	M	/	Metastatic colorectal cancer; Cerebral amyloid angiopathy	Cyclizine; Haloperidol; Metoclopramide	K2b1a1a	73	55	NA	2	6
	5:1					77.83 ± 8.6	43.2 ± 18.9			
PD1	M	20	PD, Dementia	Rotigotine; Lorazepam; Sertraline; Olanzapine; Sinemet; Entacapone	X2c1a	83	7	3	2	7
PD2	F	8	Advanced PD; Aspiration pneumonia	Madopar; Stalevo; Citalopram	W1	65	46	3	1	5

PD3	F	10	Idiopathic PD with dementia; Aspiration pneumonia	Sinemet; Clonazepam; Rivastigmine; Quetiapine	J1b1a1a	82	24	6	2	4
PD4	M	7	PD with dementia	Madopar	R6b	74	43	5	3	5
PD5	M	8	Idiopathic PD with dementia;	Madopar; Sinemet, Ropinirole; Rasagiline; Stalevo; Rotigotine; Clonazepam;	H1g1	77	36	6	4	5
PD6	F	15	Idiopathic PD	Entacapone; Madopar; Stalevo; Pramipexole;	H1af1b	86	19	4	3	2
PD7	M	24	PD	Sinemet; Rivastigmine	J1b1a1a	80	24	6	1	5
	4:3	13.2 ± 6.7				78.1 ± 7	28.4 ± 14			

Table 2.2-1 Demographics of patients included in this study

2.3. *Bioinformatics analysis*

2.3.1. *Illumina deep sequencing on single neurons*

Illumina deep sequencing of single cholinergic neurons was performed by Rafiqul Hussain at the Newcastle University Genomics Core Facility, under the direction of Dr Jonathan Coxhead. Special thanks are extended to Dr Alex Bury for conducting the PCR preparation work (Bury *et al.*, 2021). Detailed steps of the preparation and sequencing workflow are shown in (Figure 2.3-1). Single neurons were lysed as template for PCR to generate three overlapping amplicons spanning the entire mitochondrial genome (Figure 2.3-2). In use of these three overlapping fragments enhances the likelihood of obtaining complete mtDNA coverage by enabling the amplification of smaller and more manageable regions.

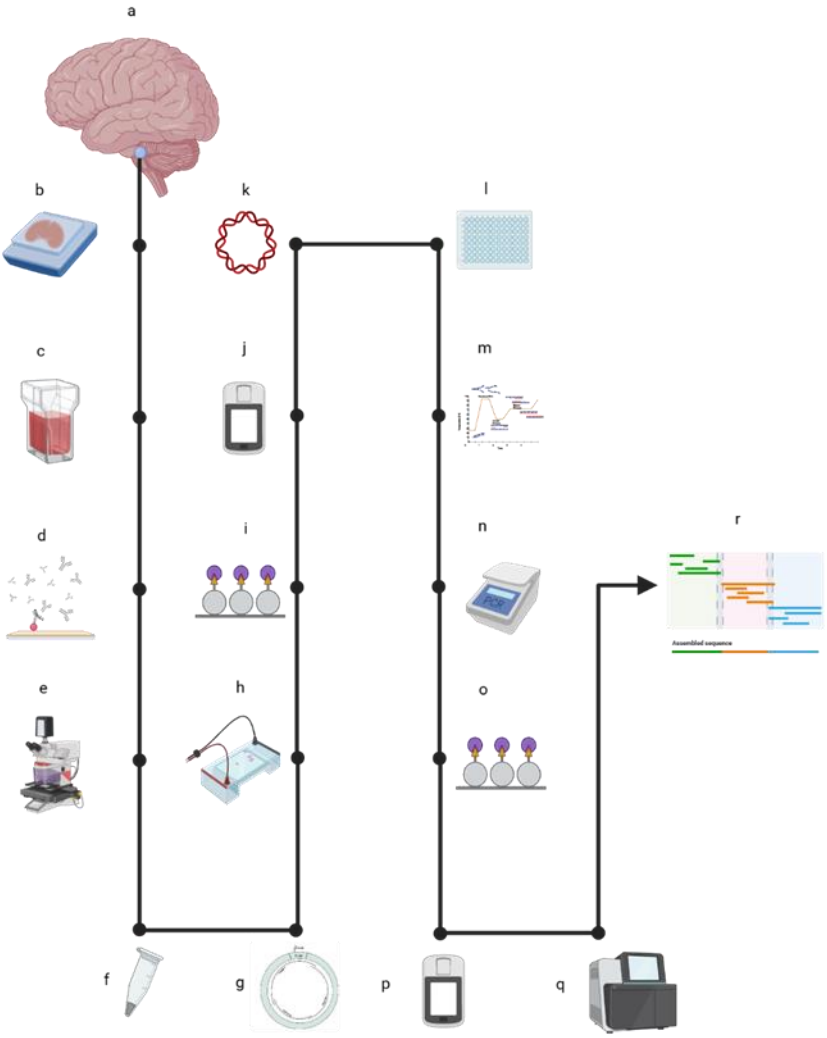

Figure 2.3-1 Flow graph of sample processing steps for NGS

a: Patients brain block obtained from the brain tissue bank; b: 5µm serial sections cut from each control and PD case, c: the first and last sections from each control and PD case are stained for Luxol Fast blue and Hematoxylin/Eosin to conform the presence of PPN; d: Sections stained using an anti-ChAT antibody to identify cholinergic neurons in PPN; e: individual PPN cholinergic neurons are extracted by LCM (laser capture microdissection); f: collected neuron was lysed overnight; g: Lysate used as template for PCR to generate 3 overlapping amplicons spanning the entire mitochondrial genome; h: PCR amplicon size confirmed by agarose electrophoresis; i: Samples cleaned up using AMPure beads to remove unwanted components like small DNA fragments, buffer salts; j: Sample mtDNA concentrations measured and diluted

in nuclease-free water to normalise to 1ng/µl using Qubit Broad Range &High Sensitivity kits; k: all 3 overlapping amplicons pooled to generate amplicons covering entire mtDNA genome in individual cells; l: Prepare the library using DNA segments from 10-49 ng of DNA samples; m: Pooled sample volumes & concentrations measured to determine number of entire mtDNA genome in individual neurons; n: PCR amplification; o: PCR products cleaned with purification beads; p: Bead cleaned-up library was validated and quantified using HSD5000 ScreenTape assay and Qubit; q: Sequencing with Illumina NextSeq 500; r: Illumina sequencing BAM files.

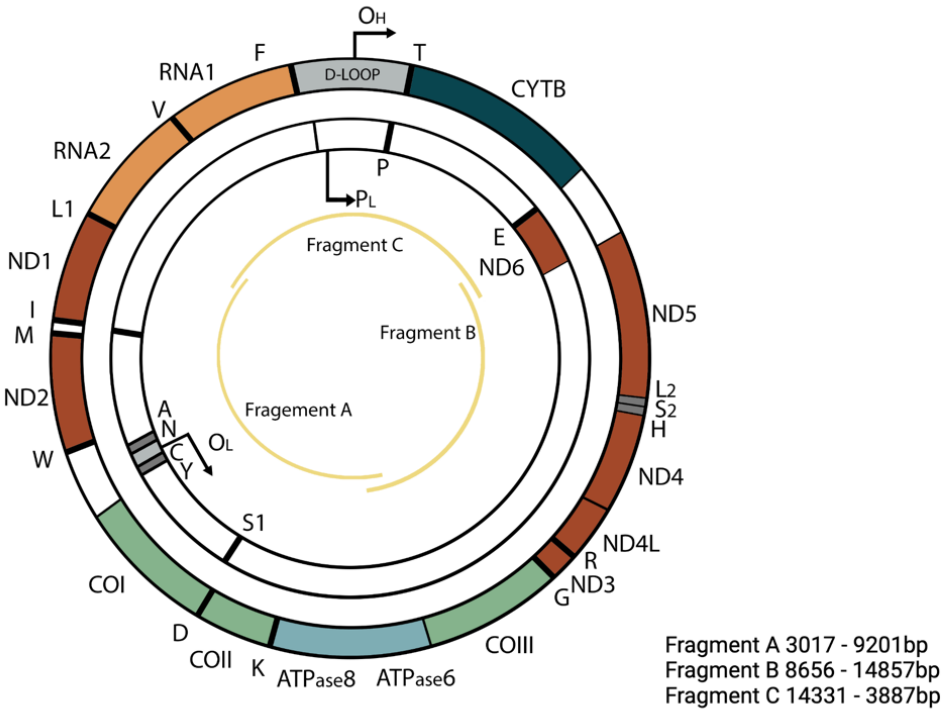

Figure 2.3-2 A schematic showing of the three fragments used for whole mtDNA sequencing

Three overlapping fragments that were sequenced to cover the entire mtDNA genome. Fragment A (3017 – 9201bp); B (8656 – 14857) and C (14331 – 3887bp).

2.3.2. *Identifying deletions using eKLIPse and quality control*

eKLIPSe is a novel pipeline which was designed to detect mtDNA deletions from next generation sequencing data (Goudenège *et al.,* 2019). To suit our Illumina reads sequence with a low error rate, BLAST setting '-gapopen = 5' and '-gapext = 2' were used as described in the manual. Deletion position shift = 5 (breakpoint sliding-window size); Mapped part length = 10 (upstream perfect matched mapping length) to suit the needs of short read data; Soft-clip min length = 15 (the minimum length of the following the perfect matched sequence which is partly aligned to the reference sequence); Blast %id threshold (the threshold of BLAST percentage identity). Down sampling was disabled to run through all the samples. To suit our research interest, the minimum size was set as 5bp. Quality score was set to equal 60 (Figure 2.3-3). The quality control steps were done in RStudio Version 1.4. 42 deletions were survived from five QC steps.

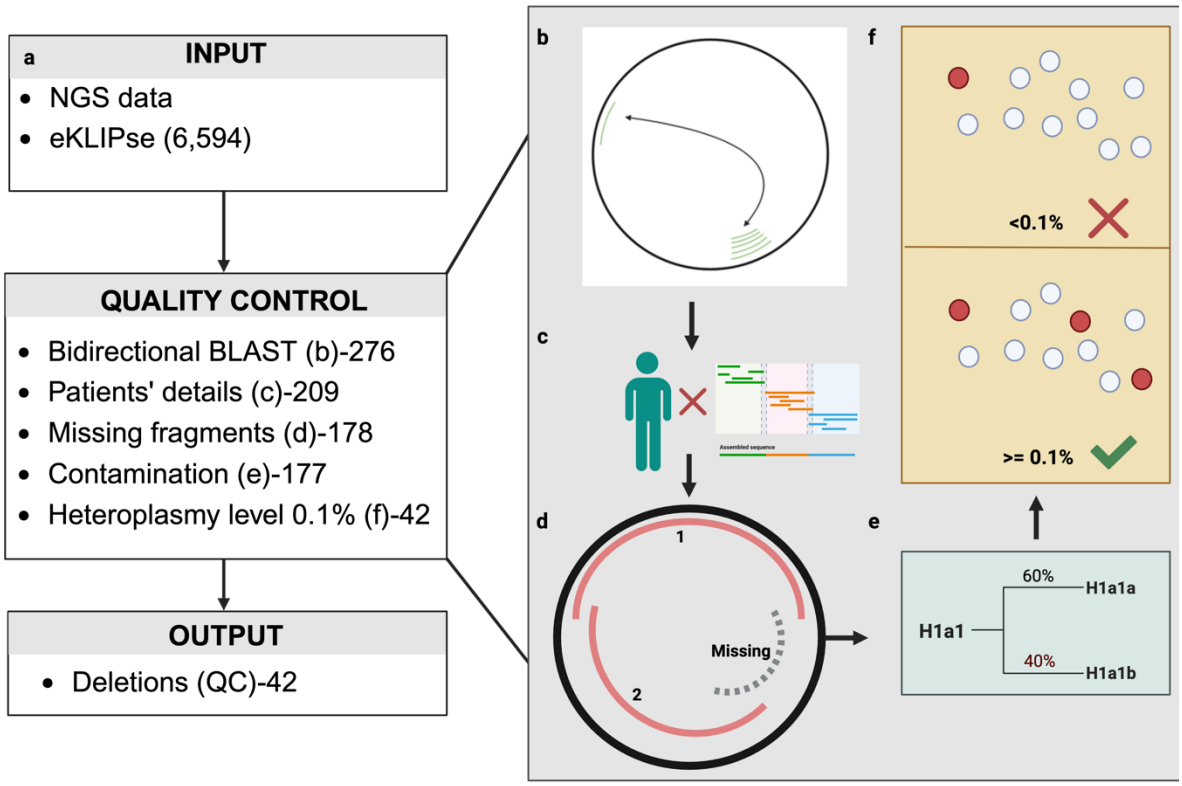

Figure 2.3-3 Quality control steps for reporting mtDNA deletion

(A) 6954 deletions were detected by eKLIPse and after five QC steps only 42 deletions remained. (B) The ends of each end of the deletions were compared to the reference gene using BLAST. It was counted as a true deletion when each end of the BLAST result scored above three. (C) Any point mutation that could not linked with a specific patient was filtered out. (D) Three slightly overlapping fragments were used to sequence the entire mtDNA. Looking at the circo plot, some neurons with missing fragments were filtered out during analysis. (E) Output from mtDNA-server include the contamination level of the neurons. Neurons with high haplogroup contamination level were filtered out. (F) Red circles are mtDNA harbouring deletions. White circles are wild type mtDNA. The lowest heteroplasmy level of the deletion was set as 0.1% according to the average sequencing coverage (PD: 80,233 ± 16229; Control 75,623 ± 9752 reads).

2.3.3. *Identifying mtDNA point mutations using mtDNA server and quality control.*

MtDNA-Server was used to detect point mutations using deep sequence NGS data (BAM file) from single cholinergic neurons (Weissensteiner *et al.*, 2016, https://mitoverse.readthedocs.io/mtdna-server/mtdna-server/). The output of the mtDNA-Server includes coverage, mutation, substitution, Maplocus, AAC (amino acid changes), MutPred_score (Pejaver *et al.,* 2020). 20,488 point mutations were detected by the mtDNA-Servers analysis. After a series of QC steps, including checks for strand bias checking, contaminations checking, somatic checking, 2,245 point mutations were used for further analysis (Figure 2.3-4).

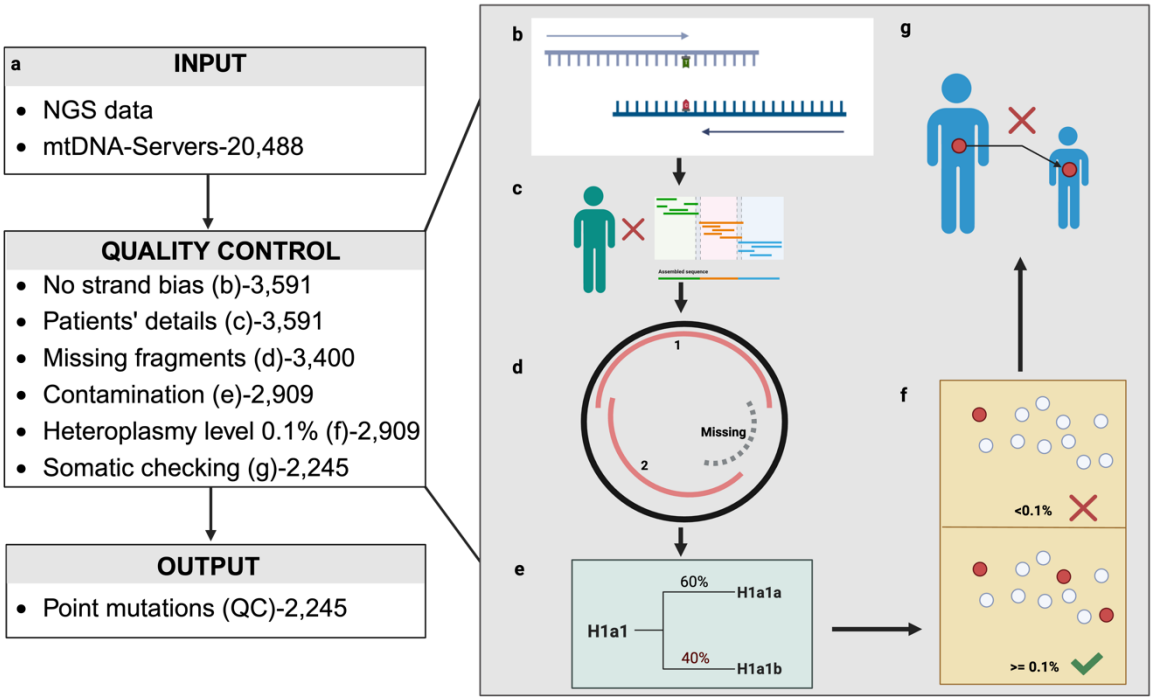

Figure 2.3-4 mtDNA point mutations quality control

(A) After running the dataset through mtDNA-Servers, 20,488 point mutations were detected. Quality controls (QC) consisted of 6 steps. (B) filter out any point mutations that did not pass the strand bias test. Strand bias test ensures that information presented by the forward and reverse strand agree with each other. (C) Any point mutation that was not linked with a specific patient has been filtered out. This is due to labels missing during the experiments. (D) Any point mutation that does not have whole mtDNA sequence data were filtered out. (E) Any point mutation that has a high haplogroup contamination level were filtered out. (F) The lowest heteroplasmy level of a point mutation was set as 0.1% according to the average sequencing coverage (PD: 80,233 ± 16229; Control 75,623 ± 9752 reads). (G) We have sequenced multiple neurons from each patient. If a single point mutation occurred in multiple neurons of one patent, instead of forming inside the patient, this variant may be inherited from his or her mother. The current work only focuses on somatic mutations, hence inherited variants were filtered out.

2.3.4. *Deletion breakpoint classification*

The breakpoints have been sorted into three types, type I, type II, and type III. I set definition of the type I deletion as at least 3 identical nucleotides in the breakpoint. For type II deletion, it can be problematic to define it as there are various definitions. In this research, we used the definition of type II deletions previously published (Reeve *et al.,* 2008) as an example and set 2 rules for defining the imperfect repeats: 1) Similar patterns found in the breakpoint of the deletion. 2) For short repeats (less than 5 nucleotides), only 1 mismatched based was identified; for long repeats, only 2 mismatched based were identified, and each change could affect 2 nucleotides at most (Figure 2.3-5).

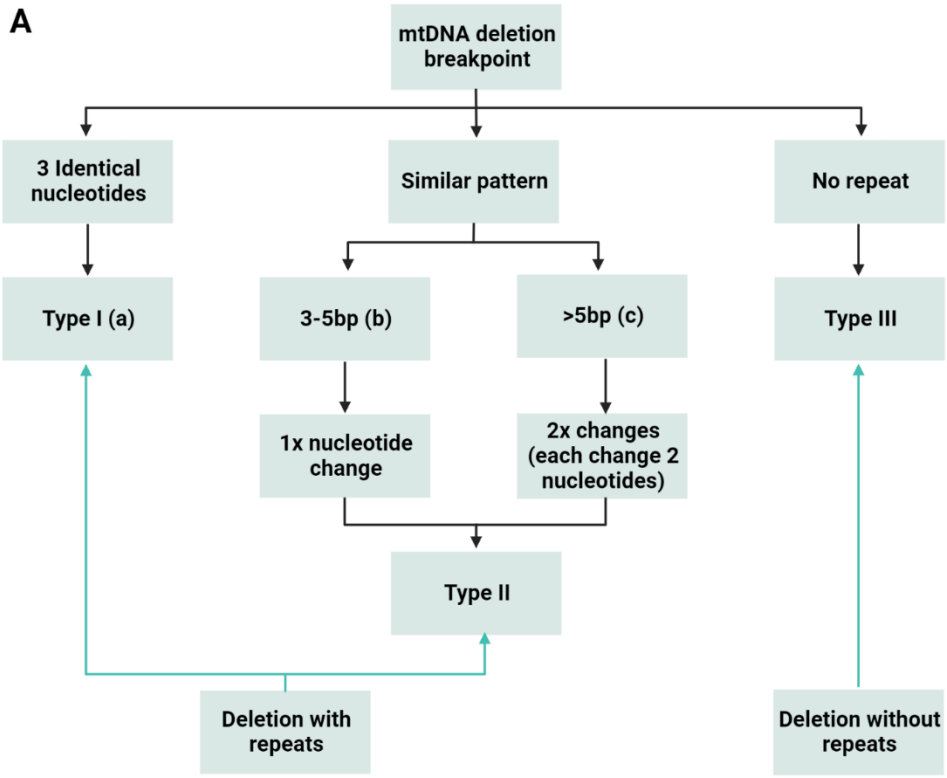

B

	5' sequence	3' sequence
a	*CCCAATCCACATCA(AAACCC)*	*(AAACCC)CCCCTCCCCCGCTT*
b	*CCTCCCCCGCTTCTGG(CCAC)*	*(CCCC)GCCCATCCTACCCAGC*
c	*AACCCAATCC(ACATCACAAC)*	*(ACATCACCCC)ATAAACAAAT*

Figure 2.3-5 Definition of different breakpoint types

mtDNA deletions can be sorted into 3 categories according to the characteristics of the breakpoints. There is no universal definition to breakpoints, and the definition we adapted in this research is based on the deletions published in (Reeve *et al.*, 2008). *For Type I deletion, it requires a perfect repeat in the breakpoints and the repeat sequence needs to be at least 3 base pairs (B.a). Type II deletion contains similar sequence at the breakpoints. If the similar sequence is between 3 to 5 base pair, only one nucleotide change could be seen in the sequence (B.b). If the similar sequence is*

above 5 base pair, two changes could be in the sequence, and each change could alter 2 nucleotides at most (b.c). For other deletions, which does not contain any sequence share similarity, are defined as Type III deletions.

2.3.5. *Free energy calculation and secondary structure prediction.*

The free energy calculation was carried out by two pipelines, one was mentioned by previous researcher, UNAFold, and another more productive in handling our dataset, Seqfold, will be mentioned in Chapter. 3. The calculation of free energy and prediction of secondary structure were performed using the 'Two State Melting Hybridization' application of the DINAMelt web server which is a part of the UNAFold. To obtain the sequence for running calculation and prediction, 25, 50 and 100 base pairs of the sequence centred on the breakpoint were selected for each mtDNA deletion (Figure 2.3-6) and the sequences were located using the alignment function (rCRS to sequence FASTA), which utilizes the MUSCLE algorithm within the MEGA11 software. After retrieving the sequences, they were inputted into the DINAMelt (Nido *et al.,* 2018; http://www.unafold.org) for running the prediction process. Detailed application of our data using Seqfold can be found in detail on GitHub (https://github.com/lwlss/mtDNAFreeEnergy).

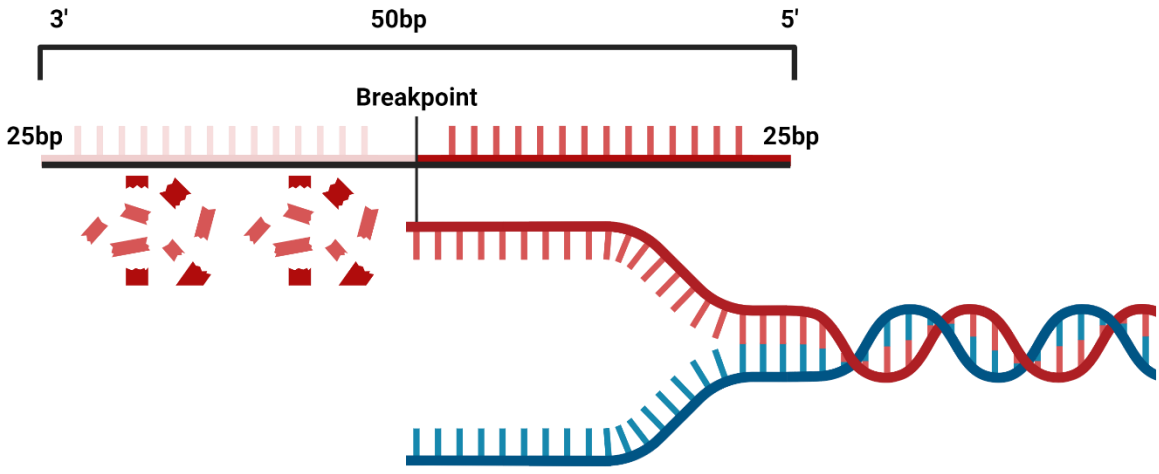

Figure 2.3-6 A scheme showing the sequences used for free energy calculation

This graph illustrates the selection process for conducting the 50 bp free energy analysis. Each breakpoint was positioned at the centre of the sequence. Similar procedures were followed when conducting the 25 bp (13 + 12 bp) and 100 bp (50 bp in each direction) analyses to obtain the respective sequences.

2.3.6. *Point mutation recurrent point mutations probability calculation*

A recurrent point mutations is defined as a single point mutation detected at least three times in neurons within the same condition (PD or control). The probability of this occurrence was calculated using the two steps. The first step was to the average mutation per site (λ). This is obtained by dividing the total number of mutations by the number of affected sites. The second step was to calculate the probability using the Poisson distribution ($P[X = x] = \frac{\lambda^x e^{-\lambda}}{x!}$), where x is a discrete random variable representing the number of occurrences. The total number of mutations and affected sites for each condition is provided in (Table 2.3-1).

	Total mutation	**Affected sites**
PD	1312	1209
Control	933	769
PD (DL<1%)	570	556
Control (DL < 1%)	708	685

Table 2.3-1 Total mutation count and number of affected sites.

2.4. *Multiplex qPCR from single neuron*

2.4.1. *Cholinergic staining*

Cholinergic neurons staining was performed using immunohistochemistry imaging technique (IHC). Choline acetyltransferase (ChAT), the enzyme catalysing the

biosynthesis of acetylcholine, is highly expressed in cholinergic neurons and serves as a common marker for specific cholinergic neurons staining. 30mm fresh frozen human post-mortem slides were taken out at room temperature for 30 minutes. Then a hydrophobic pen was used to trace around each section, ensuring some space was left to add solutions (Figure 2.4-1), and a solid barrier was in place to contain all the liquid. Allow a couple of minutes for it to dry. Subsequently, TBST was used to wash the slides three times for 2 minutes each. Apply pre-vortexed 10% blocking serum (horse; Vector laboratories, Cambridge, UK, S-2000) in TBST and incubate 30 minutes at room temperature. Remove excess blocking serum before adding primary goat anti-ChAT (diluted in TBST at a 1:150 ratio) (Polyconal goat anti-ChAT, AB144P, Milipore, MA, USA) and incubating 2 hours at room temperature. Rinse the tissue twice before adding the secondary antibody at 1:120 ratio (Horse radish peroxidase horse anti-goat in TBST, Vector laboratories, Cambridge, UK, PI-9500) and incubate for 1 hour at room temperature. Rinse sections in PBS for 3 minutes, repeating this process three times. Tissues need to be treated with choose peroxidase substrate, in this case is NovaRED (Vector NovaRED substrate Kit, Peroxidase, Cambridge, UK, SK-4800) to visualize the targeted proteins. After 8 minutes of the incubation with NovaRED working solution, rinse tissues briefly with water for 3 times.

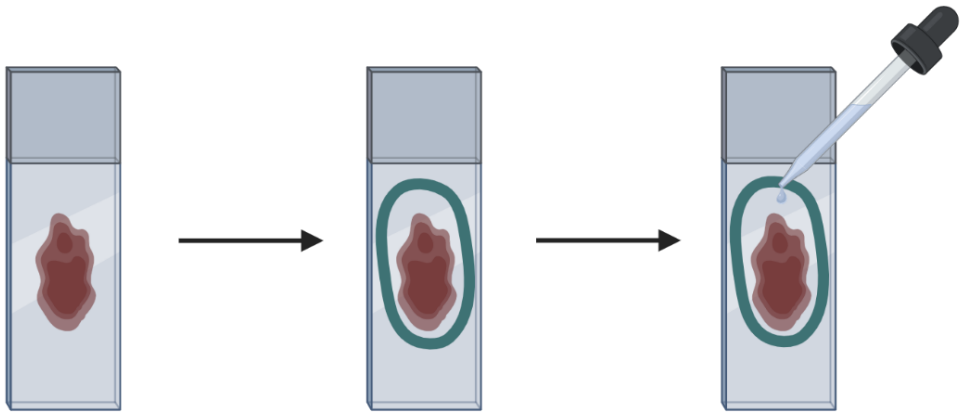

Figure 2.4-1 Illustration of the staining process.

The tissue slide was in left position. Then a close circle was drawn using hydrophobic pen near the section. Solutions was applied adjacent to but not directly onto the tissues.

2.4.2. *PPN identification*

All tissue slides were cut in series, with the first and last slides from each brain block stained using standard protocols (haematoxylin and eosin, and Luxol fast blue) for mapping purposes. Mapping slides were scanned using a Zeiss Axioscan7 scanner. Nearby anatomical tracts include the Lateral Lemniscus (LL), Medial Lemniscus (ML), and Superior Cerebellar Decussation (SCD), with the PPN triangulated between these three structures (Figure 2.4-2).

The PPN typically appears as a slightly curved, “boomerang”-shaped cluster of cholinergic neurons. Its orientation may vary, appearing more vertical in some sections and more horizontal in others. The PPN can also be identified based on its proximity to the LC, as the dopaminergic neurons in this region are visible without staining due to the presence of neuromelanin, the black pigment they secrete (Figure 2.4-3).

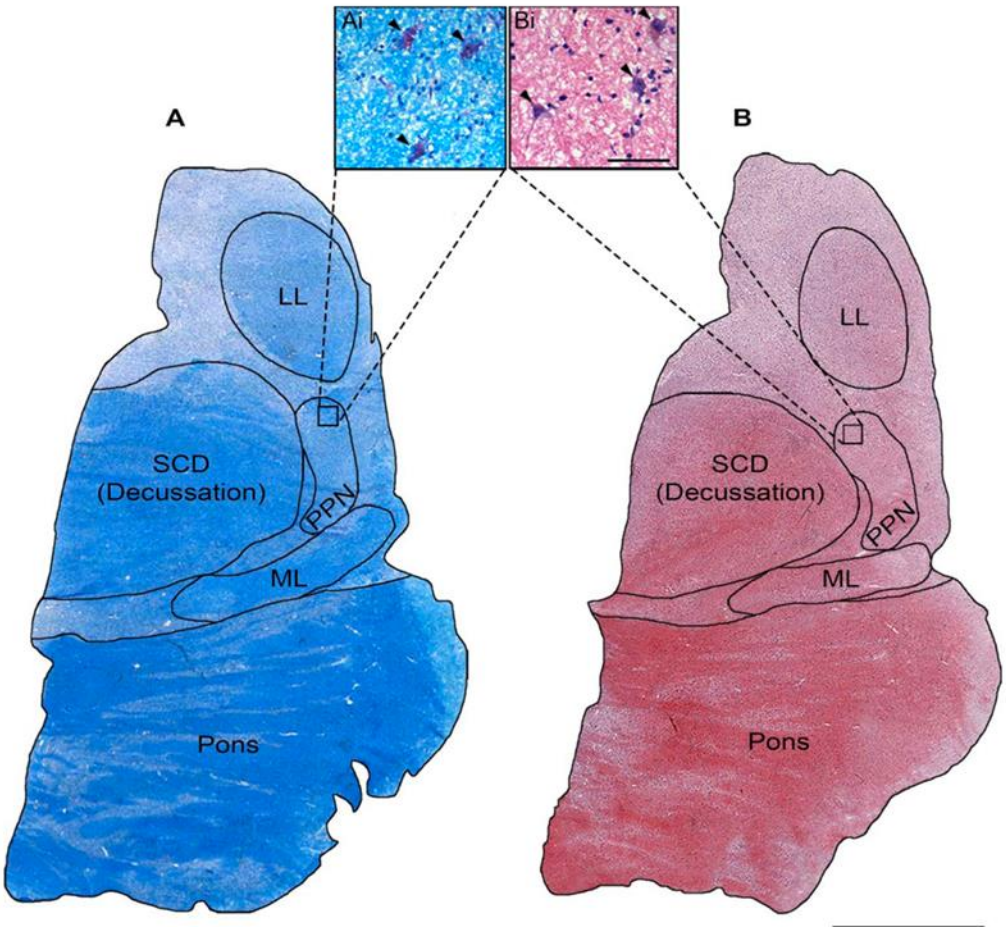

Figure 2.4-2 PPN and nearby structures

In section A, the most rostral, and section B, immediately adjacent along the rostrocaudal axis where the cryostat was collected, mapped outlines delineate the anatomical location of the PPN in relation to significant neighbouring structures, such as the lateral lemniscus (LL), medial lemniscus (ML), and superior cerebellar decussation (SCD).

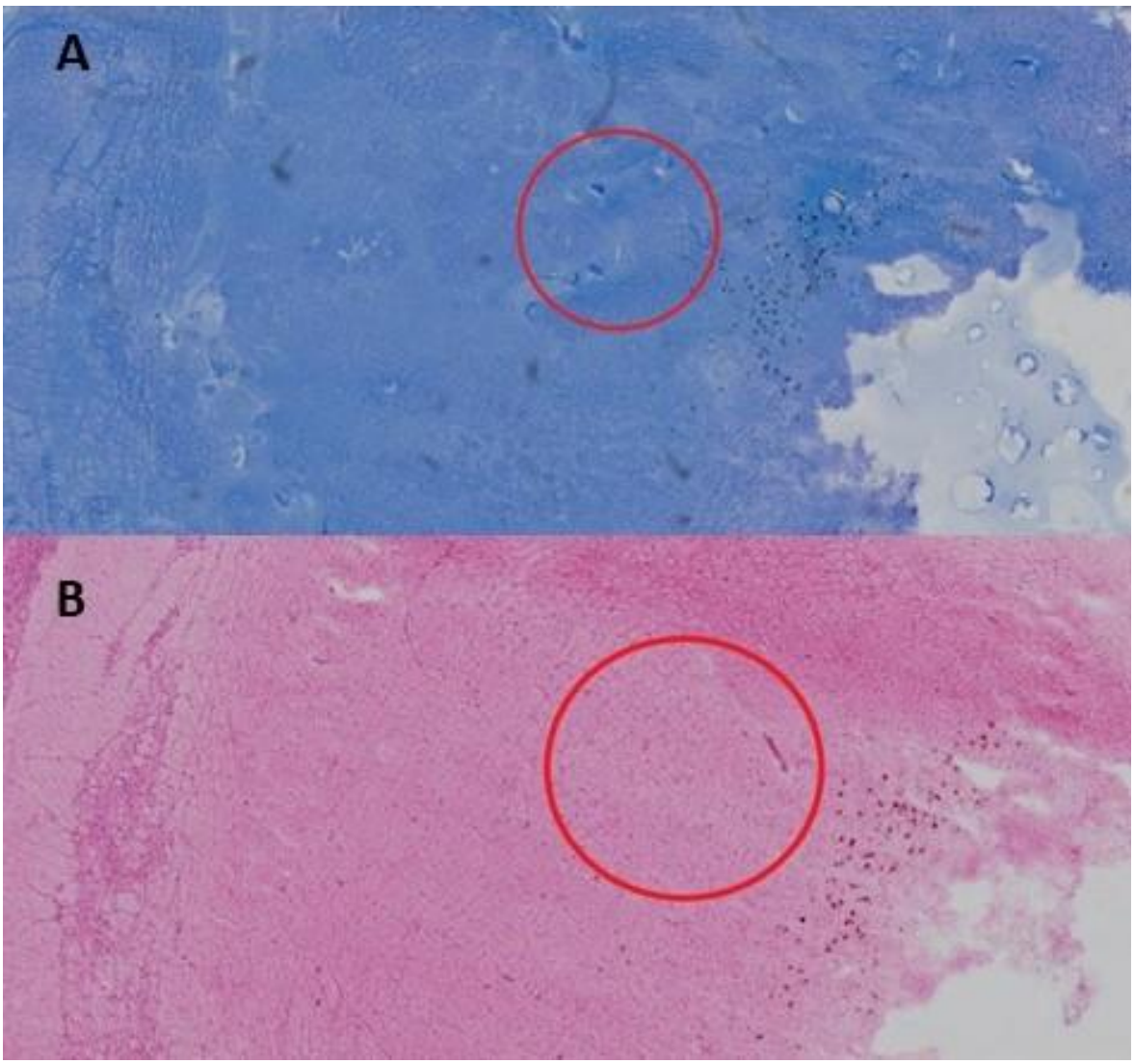

Figure 2.4-3 PPN mapping slides

A was stained using Luxol fast blue, while B was stained by haematoxylin and eosin (HE). For each mapping slide, the PPN was identified by a histologist and a circle was drawn on the slide to highlight it. During the experimental process, those mapping slides were used to locate the PPN on the adjacent slide.

2.4.3. *Laser capture microdissection (LCM)*

Before LCM, all tissues need to be treated with a series of ethanol concentrations (50%, 75%, 95%, 100%) for 30 seconds each for dehydration. After dehydration, tissues need to be air dry before proceeding to the microscope. Individual PPN cholinergic neurons were isolated using P.A.L.M MicroBeam Laser-Capture Microdissection system 4.6

coupled to an inverted Zeiss microscope (Axiovert 200M; Carl Zeiss, Oberkochen, Germany). They were then placed individually into the 0.2ml Thin-walled PCR tubes (Star Lab, UK) attached to the tubecollector (2x200 CMII, Zeiss, Germany) containing lysis buffer from the PicoPure RNA Isolation Kit (KIT0204, Applies biosystem, USA). After collection, the tube is then placed under the microscope, and neuron debris must be seen unless it cannot be used for downstream application.

2.4.4. *RNA extraction and reverse transcription*

RNA extraction was carried out using the PicoPure RNA Isolation Kit (KIT0204, Applied Biosystem, USA). After LCM, each neuron was in 12µl of lysis buffer from the isolation kit. After vortex and centrifuge the tubes, samples were incubated in 42 degree for 30 minutes. Precondition the RNA purification column (10 minutes left from the incubation process): pipette 250µl of conditioning buffer (CB) onto the purification column filter membrane. Incubate the RNA purification column with conditioning buffer for 5 minutes at room temperature. Centrifuge the purification column in the provided collection tube at 16,000 x g for 1 minute. Pipette 12µl (the same amount of extraction buffer) of 70% ethanol into the neuron lysis from the first part. Mix well by pipetting up and down; do not centrifuge. Pipette the cell extract and ethanol mixture into the preconditioned purification column. To bind RNA to the column, centrifuge for 2 minutes at 100 x g, immediately followed by a centrifugation at 16,000 x g for 30 seconds to remove flowthrough. Pipette 100µl of wash buffer (W1) into the purification column and centrifuge for 1 minute at 8,000 x g, then discard the liquid in the collection tube. Add 50µl of DNase to the column and incubate at room temperature for 20 minutes. Add 40µl of Wash Buffer 1 to the column, centrifuge at 8,000 x g for 15 seconds, then discard the liquid in the collection tube. Add 100µl of Wash Buffer 2 to the column, centrifuge at 8,000 x g for 1 minute, then discard the liquid. Repeat the wash step with 100µl of Wash Buffer 2, and then centrifuge again at 16,000 x g for 2 minutes (if there is residual wash buffer in the column, centrifuge again at 16,000 x g for 1 minute). Transfer the column to a 0.5ml microcentrifuge tube. Add 10µl of Elution Buffer directly onto the column membrane by gently touching the membrane surface with the pipette tip. Incubate at room temperature for 5 minutes. Centrifuge at 1,000 x g for 1 minute to distribute the

elution buffer within the column, then centrifuge again at 16,000 x g for 1 minute to elute RNA. Pure RNA was used for reverse transcription using SuperScript IV VILO master mix (11756050, Invitrogen, USA). Detailed reaction recipe can be found in (Table 2.1-5).

2.4.5. *Primers and assays for RT-PCR*

Off shelf Taqman assays were purchased for amplification of different targets using Real-Time polymerase chain reaction (RT-PCR). TFAM (Hs00273372_s1, VIC, ThermoFischer, USA), PINK1 (Hs00260868_m1, FAM, ThermoFissher, USA). Customized assay was designed for PGC1 α as there are multiple mRNA variants and the off-shelf ones does not have a good amplification rate. The detailed information of these 3 assays is listed in (Table 2.4-1).

Assays	Primers/Probes	Sequence	Exons Boundary	Location	Size (bp)
TFAM (Hs00260868_m1, VIC)	Pre-designed assay	n/a	1	410-503	93
PINK1 (Hs00260868_m1, FAM)	Pre-designed assay	n/a	1-2	431-535	104
PGC1a	Forward primer	TGTGGATGAAGACGGATTGC	3	1010-1029	63
	Reverse primer	TTGTCAGTGGTCACGTCTCCAT		1072-1029	
	Probe	CTCATTTGATGCGCTGAC_FAM		1031-1048	

Table 2.4-1 The detail information of Taqman assays used in experiments

The forward (F) and reverse (R) primer sequences used for amplifying the various genes of interest for qRT-PCR analysis and the probe (P) sequences, utilising either a FAM or VIC fluorescent dye attachment for detecting and analysing the P-labelled PCR product, combined with nonfluorescent quencher (NFQ) and minor groove binder (MGB) at the 3' end. Custom standard templates were generated using the given sequences to produce a standard curve. Expected product sizes are shown in base pairs (bp). Abbreviations used: Base-pairs, bp; Not available, n/a; Probe, P; R; Reverse; S, Standard. TFAM reference sequence was based on the homo sapiens transcription factor A transcript variant 1, mRNA (NM_003201.2). PGC1a reference sequence was based on the homo sapiens PPARG coactivator 1, transcript variant 1, mRNA (NM_001330751.2). PINK1 reference sequence was based on the homo sapiens PTEN induced kinase 1 (PINK1), mRNA (NM_032409.2).

2.4.6. *Standard curve and qRT-PCR*

The starting material for constructing the standard curve consisted of designed gene sequences (GeneArt sequence, Invitrogen) to cover the entire amplified sequences from each Taqman assay. The DNA fragments for each assay were listed in (Table 2.4-2). The MasterMix utilized was Taqman fast advanced master mix for qPCR (5ml, 4444557, Applied Biosystems).

cDNA generated from reverse transcription was utilized as the template of the qRT-PCR. 10ul of reaction volume was employed for each run. The formula used in each reaction is detailed in (Table 2.1-5). The Taqman assay selected for each gene are as follow: TFAM. After dispending the reaction mixture into each well. The entire plate placed into QuantStudio 7 instrument. The running program is outlined in (Figure 2.4-4).

	Single plex	**Duplex**
Fast Advanced MasterMix (2x)	5 µL	5 µL
FAM dye Taqman assay 1 (20x)	1 µL	0.5 µL
VIC dye Taqman assay 2 (20x)	n/a	0.5 µL
1-10 ng cDNA	4 µL	4 µL
Total	10 µL	10 µL

Table 2.4-2 Single and duplex PCR reaction mixture

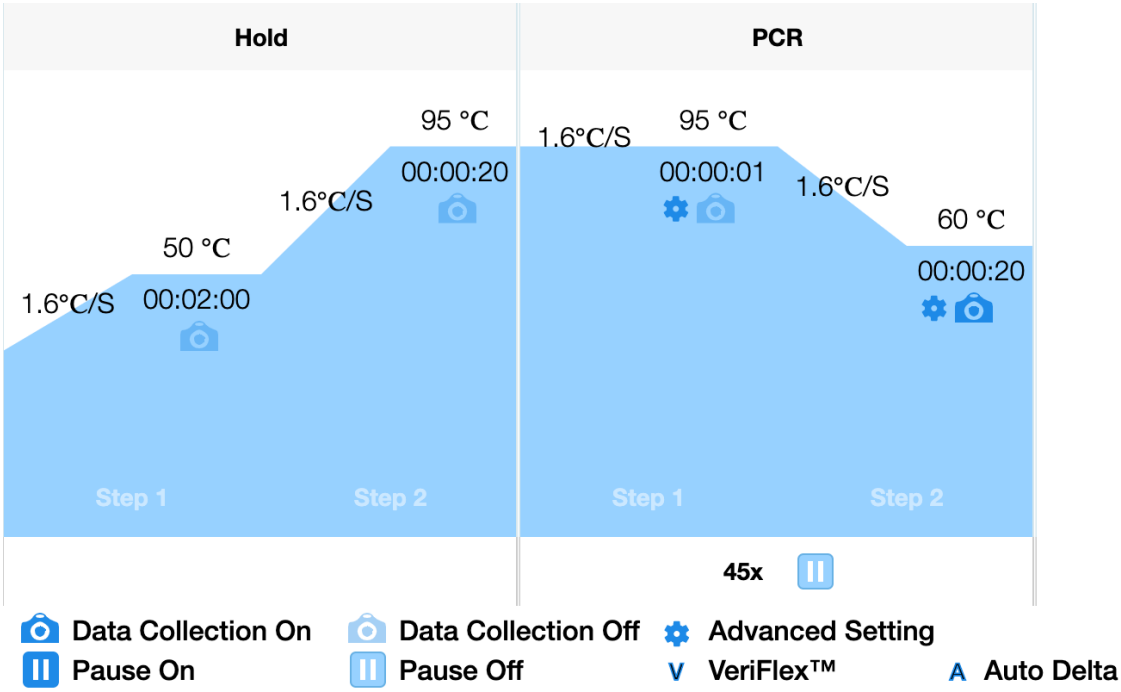

Figure 2.4-4 PCR cycles

The temperature, duration, and cycle settings used in the qPCR reaction were as follows: During the hold stage, samples were held at 50°C for 2 minutes, followed by 95°C for 20 seconds. In the PCR stage, each cycle involved heating the samples to 95°C for 1 second, followed by cooling to 60°C for 20 seconds before proceeding to the next cycle. The PCR stage consisted of a total of 45 cycles.

2.4.7. *Copy number calculation*

After the qRT-PCR runs, both the CT values from the standard curves and unknown samples are obtained. The amount of DNA in each standard curve is known. By comparing each unknown samples with the standard curve, the relative CT value is determined. The CN was calculated through this formula. $CN = (X * 6.0221 * 10^{23})/(N * 607.4\frac{g}{mol} * 1 * \frac{10^9 ng}{g})$. Where: X represents the amount of amplicon (ng); 6.0221*10^23 is Avogadro's constant; N denotes the length of the amplicon (bp); 607.4 g/mol signifies the average weight of each base pair in the double stranded DNA amplicon. The length of amplicon of chosen assays are listed in (Table 2.4-3).

Target Name	Strings Sequence	Length (bp)
TFAM	1 GGAGGCTCTC CGAGATTGGG GTCGGGTCAC TGCCTCATCC ACCGGAGCGA TGGCGTTTCT 61 CCGAAGCATG TGGGGCGTGC TGAGTGCCCT GGGAAGGTCT GGAGCAGAGC TGTGCACCGG 121 CTGTGGAAGT CGACTGCGCT CCCCCTTCAG TTTTGTGTAT TTACCGAGGT GGTTTTCATC 181 TGTCTTGGCA AGTTGTCCAA AGAAACCTGT AAGTTCTTAC CTTCGATTTT CTAAAGAACA 241 ACTACCCATA TTTAAAGCTC AGAACCCAGA TGCAAAAACT ACAGAACTAA TTA	293
PGC1a	1 CTTCCTCTGA CCCCAGAGTC ACCAAATGAC CCCAAGGGTT CCCCATTTGA GAACAAGACT 61 ATTGAACGCA CCTTAAGTGT GGAACTCTCT GGAACTGCAG GCCTAACTCC ACCCACCACT 121 CCTCCTCATA AAGCCAACCA AGATAACCCT TTTAGGGCTT CTCCAAAGCT GAAGTCCTCT 181 TGCAAGACTG TGGTGCCACC ACCATCAAAG AAGCCCAGGT ACAGTGAGTC TTCTGGTACA 241 CAAGGCAATA ACTCCACCAA GAAAGGGCCG GAGCAATCCG AGTT	284
PINK1	1 GCGCGGTTGC AGCGGCAGTT CGTGGTGCGG GCCTGGGGCT GCGCGGGCCC TTGCGGCCGG 61 GCAGTCTTTC TGGCCTTCGG GCTAGGGCTG GGCCTCATCG AGGAAAAACA GGCGGAGAGC 121 CGGCGGGCGG TCTCGGCCTG TCAGGAGATC CAGGCAATTT TTACCCAGAA AAGCAAGCCG 181 GGGCCTGACC CGTTGGACAC GAGACGCTTG CAGGGCTTTC GGCTGGAGGA GTATCTGATA 241 GGGCAGTCCA TTGGTAAGGG CTGCAGTGCT GCTGTGTATG AAGCCACCAT GCCTACATTG 301 CCCAGAAC	305

Table 2.4-3 DNA strings used for standard curv

2.4.8. *Quality control of data points*

Quality control steps were implemented to address potential noise introduced by the 45 cycles of amplification. Quality control for the data involved three key steps. First, the amplification status was required to be conclusive, meaning the instrument compared the ΔRn of each well to an automatically set threshold. If the amplification status was inconclusive, the instrument still generated a Ct value, but it could not confirm whether amplification had occurred. Reactions with inconclusive amplification status were excluded from further analysis. The second step involved manually reviewing the amplification plot and melting curve for each data point. This review ensured a steady increase in targeted fluorescence after each cycle, while the ROX background fluorescence signal remained consistent. An example of good amplification plots can be seen in (Figure 2.4-5). Data points that did not meet these criteria were excluded. Finally, the minimum detectable copy number was set to at least 4 to ensure reliable quantification. This threshold was chosen based on the 45 amplification cycles, as exponential amplification starting with a single cDNA copy generates at least 4 copies after 2 cycles, providing a sufficient signal for accurate detection.

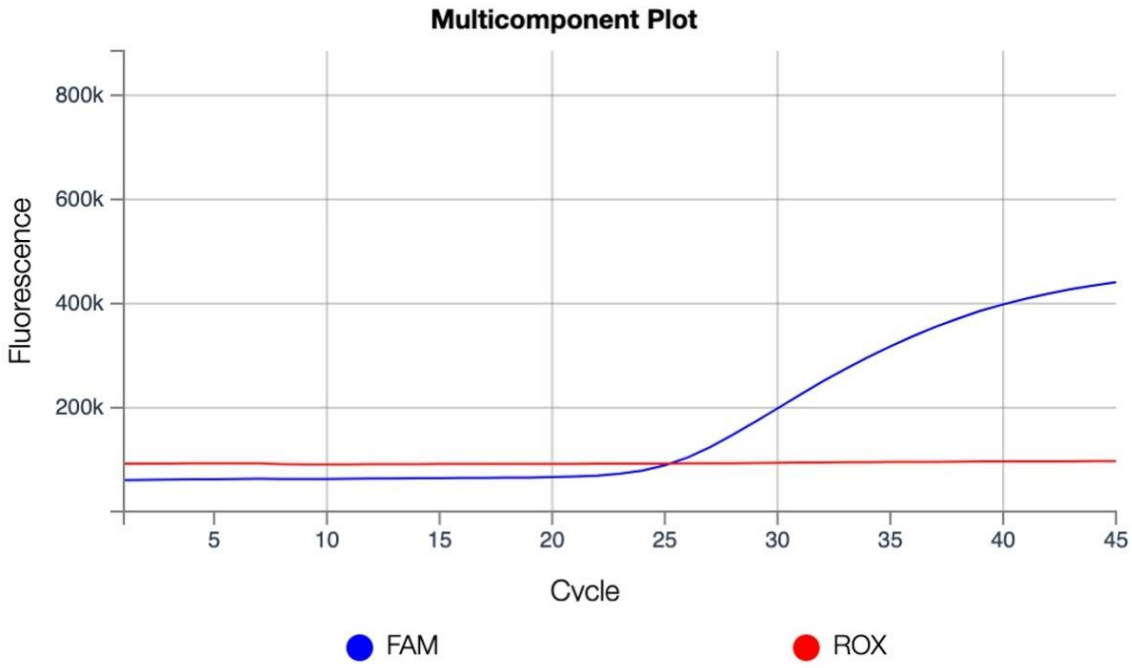

Figure 2.4-5 An example of good amplification plots

The x-axis represents the number of cycles, and the y-axis indicates the level of fluorescence. FAM is the target dye, while ROX serves as the background fluorescence. To include a data point, a manual check must be performed to ensure a steady increase in fluorescence after each cycle, while the ROX background fluorescence signal remains constant. Blue represents the FAM dye, and red represents the ROX reference dye.

Chapter 3. mtDNA deletions

3.1. *Aims*

The integrity of mtDNA is crucial for maintaining mitochondrial function, and mtDNA deletions can disrupt this integrity, potentially leading to mitochondrial dysfunction. Previous studies have reported elevated levels of mtDNA deletions in dopaminergic neurons within the SNpc and cholinergic neurons in PPD of patients with PD. Using alternative methodologies, next-generation sequencing (NGS), carried out on PD and aged match control sample from PPN cholinergic neurons, could help confirm these findings and provide further insights into the characteristics of mtDNA deletions, particularly in comparing PD and control. This chapter examines the somatic mtDNA deletions in individual cholinergic neurons from the PPN of patients with PD and age-matched controls. Following rigorous quality control steps, deletions were analysed across five dimensions: the overall characterization of mtDNA deletions, deletion size and heteroplasmy levels, deletion locations, breakpoint types and associated free energy changes, and the correlation between individual cases and the number of deletions.

3.2. *Results*

3.2.1. *Quality control of deletion data*

The quality control steps for the eKLIPse analysis were primarily based on the QC steps of the eKLIPse pipeline and an in-house QC pipeline. The QC steps of the eKLIPse pipeline involved in putting all QC parameters into the software interface. These QC parameters were determined based on the characteristics of mtDNA deletions and in accordance with the software developer's guidelines for reporting short read high quality sequence data. After mtDNA deletions were reported and reviewed, sequencing depth was first analysed for each neuron to ensure no bias between the PD and the aged control groups (Figure 3.2-1). The mean sequencing depth was 80,223 ± 16229 reads for control neurons and 75,623 ± 9752 reads for PD neurons. The average depth of

sequence for each neuron is listed in (Table 3.2-1). Additional manual quality control steps were then implemented to verify that the detected deletions were not artifacts and reliable. A literature review was conducted to identify the best parameters for running eKLIPse (Table 3.2-2). Till 2021, eleven papers have cited eKLIPse, but only one recorded the parameter settings used, and those were set to default values. Consequently, the manual and the original eKLIPse paper were consulted and several trial runs were conducted to determine the optimal parameters suited to our data.

For the eKLIPse QC steps, downsampling was set to 0 to include all potential deletions. The number of threads was set to 4, which is the default setting. Given the Illumina sequencing technique used in this research, the minimum read quality was set to 60, which is 40 points higher than the default settings. A range of minimum read qualities, from 20 to 60, was tested, and no significant differences were observed, indicating that the high quality of the sequencing data. For the soft-clipping settings of the eKLIPse QC steps, the soft-clipping length was reduced to 15, and the upstream mapping length was reduced to 10, following the recommended settings for short-read data. The breakpoint sliding window was set to 5, as per the default setting. eKLIPse BLAST settings were configured with gap open cost set at 5 and the gap extension cost at 2, in line with reduced error rates and stricter gap associated with Illumina sequencing technology. Both the BLAST identical percentage threshold and BLAST coverage percentage threshold were kept at their default values of 80% and 70% respectively.

After obtaining all detected deletions (6,594 in total) using the sequence data via eKLIPse, several in-house quality control filters were applied. To increase the reliability of the detected deletions, a bidirectional BLAST was performed. In this step, breakpoints from both directions of a deletion needed to be detected more than three times, which reduced the number of deletions to 276. Deletions were then further filtered out if they could not be assigned to a specific patient, due to missing ID tags during the handling of materials, leaving 209 deletions. Subsequently, only sequences containing all three fragments were included. The PCR technique used in this study amplified the entire mtDNA genome in three overlapping fragments, and the absence of one fragment could lead to data discrepancies, reducing the count to 178 deletions. A contamination check was then performed to ensure that the haplogroup of all neurons from the same patient was consistent, resulting in 177 deletions remaining. The final step of quality control

filtration ensured that the heteroplasmy level was not below 0.1%, resulting in a total of 42 retained deletions. This threshold was determined based on the sequencing depth, with an average sequencing coverage of 80,223 ± 16,229 reads for control neurons and 75,623 ± 9,752 reads for PD neurons. A heteroplasmy level of 0.1% corresponds to a copy number in the tens, depending on the total mtCN in the sample, which is considered a reasonable threshold for samples processed with PCR amplification. Moreover, a 0.1% threshold is widely accepted and has been employed in several published studies (Just, Irwin and Parson, 2015; Dölle *et al.*, 2016). Deletions after all the QC steps were listed in (Table 3.2-3). Following QC steps, deletions reported by eKLIPse were validated using the MitoSAlt pipeline (Basu *et al.*, 2020), another well-established tool for detecting mtDNA rearrangements, to confirm their reliability.

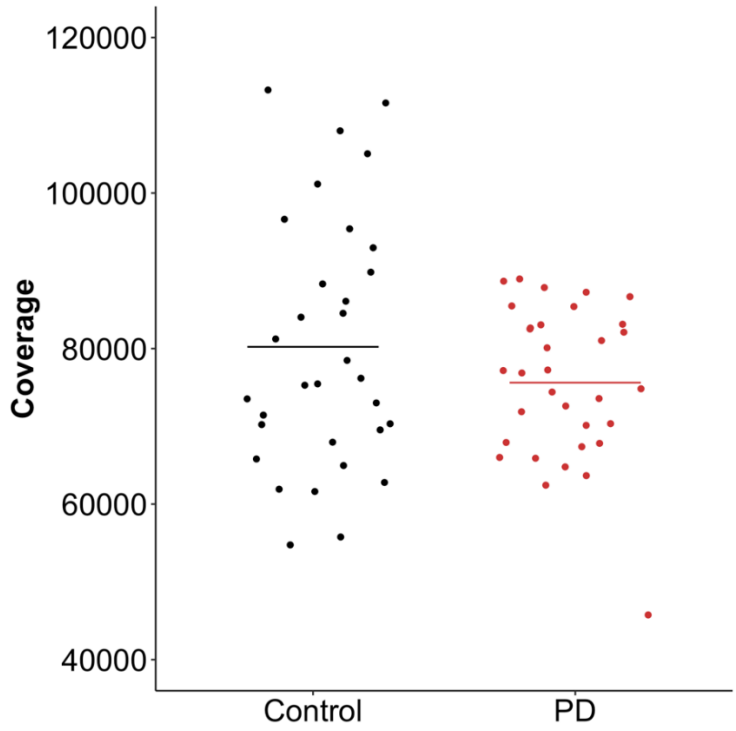

Figure 3.2-1 Depth of coverage in different cases

The graph represents a comparison of Illumina sequencing coverage between two conditions. The average coverage for control neurons was 80,223 ± 16229 reads, compared to 75,623 ± 9752 reads for PD cases. Although the control cases showed higher average coverage than the PD cases ($p = 0.17$, t-test), the difference was not statistically significant. This confirms the reliability of subsequent tests conducted between the two groups. Control neurons are represented in black, while red indicates PD neurons.

Sample	Case	Mean depth (Reads)	Sample	Case	Mean depth (Reads)
6	Control1	67964	17	PD1	67928
10	Control1	96626	18	PD1	67381
11	Control1	65800	19	PD1	67811
39	Control1	101157	32	PD1	80099
45	Control1	81233	48	PD1	70344
3	Control2	69543	49	PD1	63665
4	Control2	61915	52	PD1	87848
42	Control2	73529	20	PD2	65894
43	Control2	64961	21	PD2	74412
61	Control2	95400	22	PD2	76863
12	Control3	55770	50	PD2	81030
24	Control3	54753	59	PD2	62432
41	Control3	113253	14	PD3	88951
55	Control3	89825	16	PD3	82103
56	Control3	108004	40	PD3	83129
1	Control4	76179	46	PD3	64788
2	Control4	61620	23	PD4	73573
7	Control4	73013	25	PD4	77247
8	Control4	78481	26	PD4	85403
57	Control4	84538	27	PD4	72614
5	Control5	62784	51	PD4	87243
9	Control5	70331	29	PD5	77173
36	Control5	86088	30	PD5	88688
62	Control5	105056	31	PD5	82647
63	Control5	88315	53	PD5	66000
64	Control5	92965	60	PD5	45750
15	Control6	71446	28	PD6	82523
34	Control6	75462	33	PD6	86675
35	Control6	70226	13	PD7	71878
54	Control6	84035	44	PD7	74833

65	Control6	75289	47	PD7	70127
66	Control6	111585	58	PD7	85481
			68	PD7	83055
80223 ± 16229			**75623 ± 9752**		

Table 3.2-1 Average depth of coverage in sequenced neuron

This table lists the depth of coverage for each sequenced neuron grouped by patient case. The average sequencing depth for both control and PD groups was calculated and is displayed in the bottom row of the table. The average coverage for the control group was 80,223 ± 16229 reads, while for the PD group it was 75,623 ± 9752 reads.

Paper	Use it or not	Data type	Genome	Parameters	Deletion detected	Single cell	deletion size	Main finding
Genomic Landscape of the Mitochondrial Genome in the United Arab Emirates Native Population (Aljasmi *et al.*, 2020)	Yes	2 overlapping fragments PCR, Ion Torrent short fragments	mtDNA	NM	No	No	NM	used for long-range structural variation
Mitochondrial DNA alterations may influence the cisplatin responsiveness of oral squamous cell carcinoma (Aminuddin *et al.*, 2020)	Yes	2 overlapping fragments PCR, Nanopore mtDNA sequencing	mtDNA	NM	No	No	NM	No deletion found in oral squamous cell carcinoma
Accurate mapping of mitochondrial DNA deletions and duplications using	Yes	stimulated sequencing reads	mtDNA	NM	Yes	No	Yes	eKLIPse only identified around 50% of stimulated mtDNA deletion in low heteroplasmic level

deep sequencing (Basu *et al.*, 2020)								
Mitochondrial DNA deletion mutations increase exponentially with age in human skeletal muscle (Herbst *et al.*, 2020)	Yes	Droplet digital amplification products, Illumina sequencing	mtDNA	Default	Yes	No	Large size deletion (>1000bp)	use eKLIPse as reference to new developed droplet digital PCR assay for quantitates human mtDNA deletion frequency, and eKLIPse has detected multiple large deletions
Dominant mutations in mtDNA maintenance gene SSBP1 cause optic atrophy and foveopathy (Piro-Megy *et al.*, 2020)	Yes	2 overlapping 8.5kb fragments, Ion Torrent sequencing	mtDNA	NM	Yes	No	NM	Use eKLIPse to search frequency difference of mtDNA deletion in blood and urine of SSBP1 patient, and there was no significant difference
Mitochondrial genome variation in male LHON patients with the m.11778G > A mutation	Yes	Long range PCR, Illumina sequencing	mtDNA	NM	Yes	No	Large size deletion (>1000bp)	No large deletion (>1000bp) was detected

(Piotrowska-Nowak *et al.*, 2020)								
First characterization of LHON pedigrees in North Africa (Bouzidi *et al.*, 2020)	Yes	Sanger sequencing	mtDNA	NM	No	No	NM	No deletion detected
To Be a Champion of the 24-h Ultramarathon Race. If Not the Heart … Mosaic Theory? (Gajda *et al.*, 2021)	Yes	Single primer pair PCR, Paired-end read Illumina sequencing	mtDNA	NM	No	No	NM	No deletion detected
Mitochondrial Diseases: A Diagnostic Revolution (Schon *et al.*, 2020)	No							Mentioned eKLIPse could use to detect mtDNA deletion
Mutation m.3395A > G in MT-ND1 leads to variable pathologic	No							Use the sequence method mentioned in eKLIPse paper

manifestations (Cortes *et al.*, 2020)		
Splice-Break: exploiting an RNA-seq splice junction algorithm to discover mitochondrial DNA deletion breakpoints and analyses of psychiatric disorders (Hjelm *et al.*, 2019)	No	Mentioned want to use eKLIPse in the future
Thinking outside the nucleus: Mitochondrial DNA copy number in health and disease (Castellani *et al.*, 2020)	No	Mentioned eKLIPse as a novel pipeline could be used to detect mtDNA deletion

Table 3.2-2 eKLIPse citation till 2021

Case	Sample	5'BP	3'BP	Heteroplasmy (%)	Repetition	ID	Size	Type	Repeats	Maj/Min
PD1	13	8896	13948	15.59982465	8897-CCCTA-8901 <> 13948-CCCTA-13952	PD1041	5052	I	5	Major arc
PD1	44	9504	14772	0.589603374	9504-CCT-9508 <> 14772-CCT-14776	PD1041	5268	I	3	Major arc
PD1	47	460	2489	6.936847611	461-CCC-463 <> 2489-CCC-2491	PD1041	2029	I	3	Minor arc
PD2	19	9639	11325	4.314026037	9640-CCTGAGC-9646 <> 11325-CCTGAGC-11331	PD1046	1686	I	7	Major arc
PD2	32	8714	13052	0.425507797	None	PD1046	4338	III	NG	Major arc
PD3	21	6190	8346	0.270156146	None	PD1048	2156	III	NG	Major arc
PD3	21	8804	13295	0.336132162	8805-ACCAACCAC-8813 <> 13295-ACCAACCAC-13303	PD1048	4491	I	9	Major arc
PD3	21	8859	14243	0.448698494	8857-GC(A)C-8862 <> 14242-GCC(C)-14243	PD1048	5384	II	4	Major arc
PD3	21	8993	13710	1.244380523	None	PD1048	4717	II	5	Major arc
PD3	21	9487	13723	0.935409124	9486-TCGCAGGATT-9497 <> 13723-TCGCAGGATT-13734	PD1048	4236	I	10	Major arc
PD3	21	9506	14243	0.396500594	9502-AGCC-9507<>14241-AGCC-14246	PD1048	4737	I	4	Major arc
PD3	21	10183	13070	0.3121336	10184-CCCTA-10188 <> 13070-CCCTA-13074	PD1048	2887	I	5	Major arc

PD3	22	8793	14792	1.760559694	8794-CACTCATT-8801 <> 14792-CACTCATT-14799	PD1048	5999	I	8	Major arc
PD3	22	9436	13956	14.29915799	9437-AGGCCTTC-9444 <> 13956-AGGCCTTC-13963	PD1048	4520	I	8	Major arc
PD3	50	5822	8268	3.332164184	5823-AGC-5825 <> 8268-AGC-8270	PD1048	2446	I	3	Major arc
PD4	14	9077	14525	14.4545028	9078-TAACCT-9083 <> 14525-TAACCT-14530	PD1053	5448	I	6	Major arc
PD4	14	9293	12300	0.426494577	9294-GGCC-9297 <> 12300-GGCC-12303	PD1053	3007	I	4	Major arc
PD4	14	9313	13122	0.592483799	9314-CTTCCAC-9320 <> 13122-CTTCCAC-13128	PD1053	3809	I	7	Major arc
PD4	14	9503	11861	0.488324438	9504-GCCTT-9508 <> 11861-GCCTT-11865	PD1053	2358	I	5	Major arc
PD4	16	430	566	0.235764677	431-CACCCCCCA-439 <> 566-CACCCCCCA-574	PD1053	136	I	9	Minor arc
PD4	16	3566	5023	0.629240113	3565-CCC(C)C-3571 <> 5022-CCC(A)C-5028	PD1053	1457	II	5	Minor arc
PD4	16	9504	14156	6.794256077	None	PD1053	4652	III	NG	Major arc
PD4	16	10278	13763	0.493445085	10277-CCCC-10282 <> 13761-CCCC-13767	PD1053	3485	I	4	Major arc
PD4	16	12430	14417	0.153369106	12431-ACCCC-12435 <> 14417-ACCCC-14421	PD1053	1987	I	5	Major arc
PD4	40	9026	14288	15.32272494	None	PD1053	5262	III	NG	Major arc

PD4	46	8915	14370	31.83740945	None	PD1053	5455	III	NG	Major arc
PD4	46	10996	13836	3.518227136	10997-AGCC-11000 <> 13836-AGCC-13839	PD1053	2840	I	4	Major arc
PD5	25	10304	13975	1.392286925	10305-AACCTGCC-10312 <> 13975-AACCTGCC-13982	PD1055	3671	I	8	Major arc
PD6	29	9430	14073	3.783082346	9431-CCAAAAAGGC-9440 <> 14073-CCAAAAAGGC-14082	PD1063	4643	I	10	Major arc
PD6	30	9643	14242	3.662901676	9644-AGC-9646 <> 14242-AGC-14244	PD1063	4599	I	3	Major arc
PD6	31	8930	14417	6.5637285	8931-ACCCCT-8936 <> 14417-ACCCCT-14422	PD1063	5487	I	6	Major arc
PD6	60	9347	13855	1.623489158	9348-CTAACCAACA-9357 <> 13855-CTAACCAACA-13864	PD1063	4508	I	10	Major arc
PD7	33	15331	15379	1.77243342	15332-CACCTCC-15338 <> 15379-CACCTCC-15385	NP14087	48	I	7	Major arc
Control1	11	9487	13723	0.6113092	9486-TCGCAGGATT-9497 <> 13723-TCGCAGGATT-13734	PDC126	4236	I	10	Major arc
Control1	39	9167	12981	6.5331792	None	PDC126	3814	III	NG	Major arc
Control2	57	9859	14112	5.852480559	9860-CTTC-9863 <> 14112-CTTC-14115	NP09136	4253	I	4	Major arc
Control2	57	11621	14440	4.791310311	11620-TACTC-11626 <> 14440-TACTC-14440	NP09136	2819	I	5	Major arc
Control3	9	9777	14243	1.433245174	None	NP10011	4466	III	NG	Major arc

Control3	36	8648	8668	0.160383918	8648-GACTAATCA-8656 <> 8669-GACTAATCA-8677	NP10011	20	I	9	Major arc
Control4	65	10748	14124	2.626047931	10747-AA(A)CCTA-10754 <>14126-AA(C)CCTA-14133	NP13107	3376	II	7	Major arc
Control5	43	297	348	4.872779189	298-CCAAACCCC-306 <> 348-CCAAACCCC-356	NP13109	51	I	9	Minor arc
Control6	45	195	239	0.409566085	195-TA(C)TAA-202<> 235-TA(A)TAA-242	NP13161	44	II	6	Minor arc

Table 3.2-3 Deletion after all the QC steps

Deletions that passed all QC steps are listed in this table. The 'Case' refers to the identifier used for analysis in this research, while the 'Sample' refers to the unique identifier for each neuron. '5'BP' and '3'BP' indicate the 5' and 3' breakpoint of each deletion. 'Repetition' indicates whether any repetition was found near each breakpoint. 'ID' is the reference number for the brain bank. 'Size' specifies the size of the deletion, and 'Type' indicates whether the deletion has a perfect (I), imperfect (II), or no repeat (III) near the breakpoints. 'Repeats' describes the repeat size for type I or type II deletions.

3.2.2. *Number of deletions detected per neuron and their heteroplasmy levels*

Detailed characterisation of mtDNA deletions has been conducted in SNpc dopaminergic neurons using several methodologies (Reeve *et al.*, 2008; Dölle *et al.*, 2016). This study, for the first time, examines the detailed characteristics of somatic mtDNA deletions found in individual PPN neurons taken from PD cases and aged controls using NGS techniques, as detailed in the methods. Prior studies have considered similar questions in DA neurons of the SNpc using long-range PCR assays that amplified between the regions m.7293 and m.13859 and between m. 6377 and m.019 (Reeve *et al.*, 2008). With NGS methods having also been applied to the same neurons and region more recently (Dölle *et al.*, 2016; Guitton *et al.*, 2022). However, the NGS approach, which is novel to the cholinergic neurons of the PPN, enabled us to detect both large and small deletions and make a detailed study of the nature of the deletions. Using three overlapping primers that cover the entire mtDNA, the complete mtDNA sequence was analysed, allowing for the detection of every deletion across the mtDNA genome. This investigation was important as unlike the DA neurons of SNpc in PD (Guitton *et al.*, 2022) the remaining cholinergic neurons of the of the PPN in patients seems able to maintain wild type mtDNA in PD as well as wild type neurons (Bury *et al.*, 2017).

The size range of deletions observed in the dataset exhibits an interesting pattern, with deletions falling into two distinct clusters: one ranging from 5 to 140 bp and another above 1,400 bp. (Figure 3.2-2) illustrates this size division with approximately 88% of detected deletions classified as large deletions. Previous studies utilizing long-range PCR have also detected deletions of mtDNA, ranging from 1,763 bp to 9,445 bp, again primarily within the major arc (Reeve *et al.*, 2008) as well as studies using ND1 (minor arc) and ND4 (major arc) deletion method, a higher number of deletions in ND4 were detected in PD neurons comparing to aged control (Dölle *et al.*, 2016).

With 42 mtDNA deletions identified with heteroplasmy levels above 0.1% from 63 neurons extracted from the PPN of seven PD patients and six age-matched controls, and the circle plots of each neuron can be found in (Figure 3.2-3). Higher incidence of

neurons containing at least one deletion species in PD cases vs aged controls (p = 0.029*, X^2 = 4.742, Chi-square test). Neurons from PD3 exhibited the highest average incidence of mtDNA deletions, with an average of 2.75 deletions per neuron. Notably a single neuron from PD2 had the highest individual number, with a total of 7 (Figure 3.2-4).

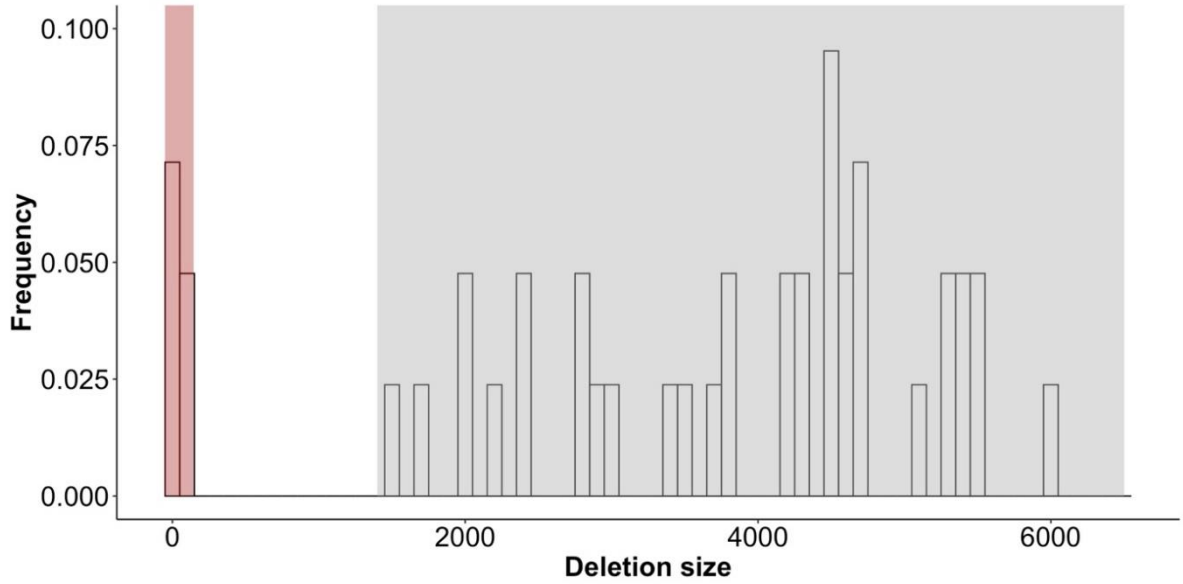

Figure 3.2-2 Two clusters of deletion sizes

Deletions identified in PPN cholinergic neurons exhibit two distinct size categories. These deletions are classified as either small, spanning from 5 to 140 base pairs (referred to as small deletions), or exceeding 1,400 base pairs (referred to as large deletions). Large deletions constitute 88% (n=37) of the deletions observed, with the remaining 11% (n=5) categorized as small deletions. The x-axis denotes the size of deletions, while the y-axis represents the frequency (count/all deletions) of deletions.

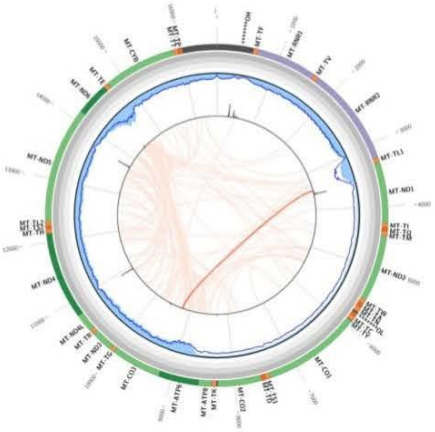

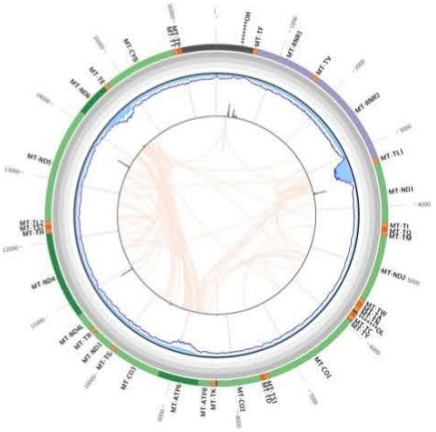

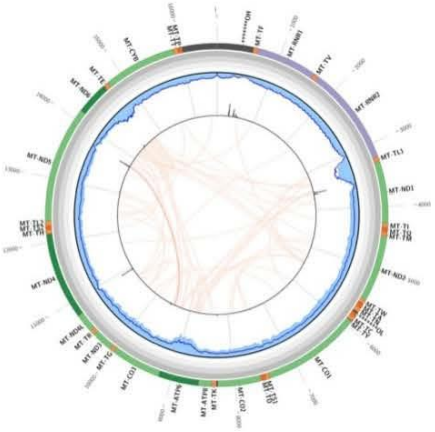

[9487, 13723]: 0.611%

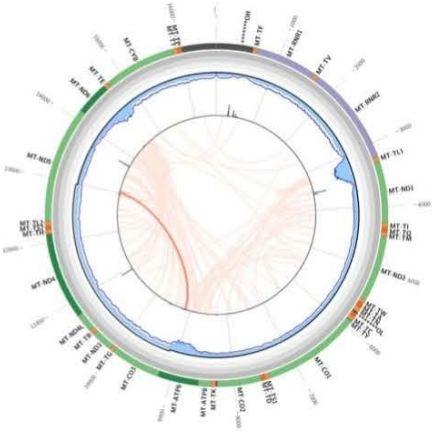

[9167,12981]: 6.53%

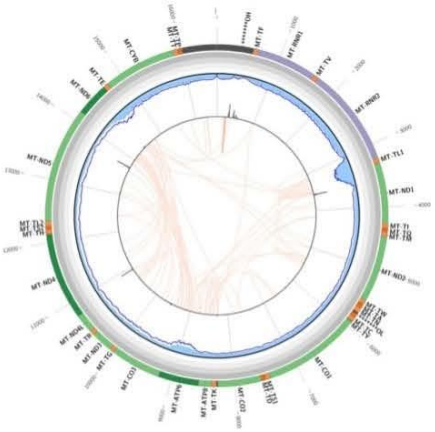

[195, 239]: 0.41%

Control1

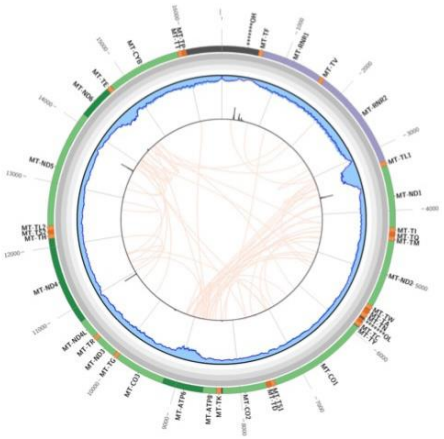

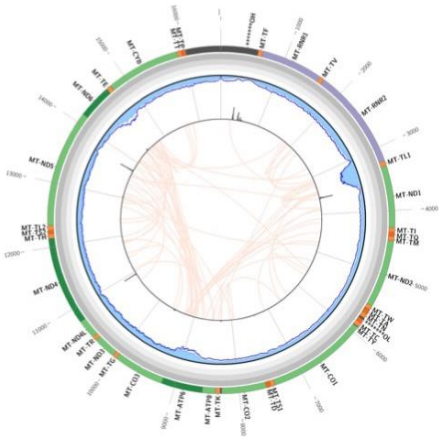

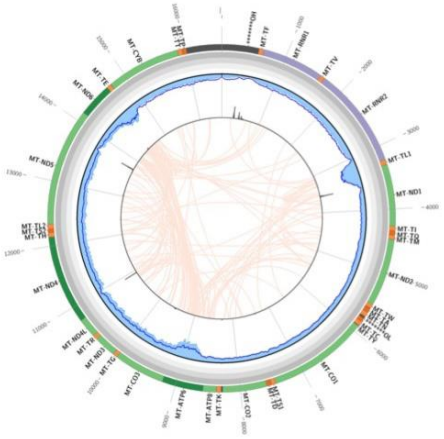

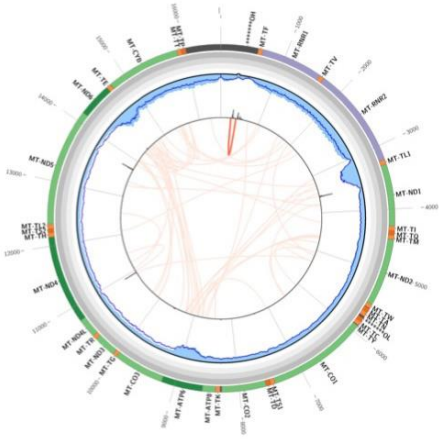

[297,348]: 4.87%

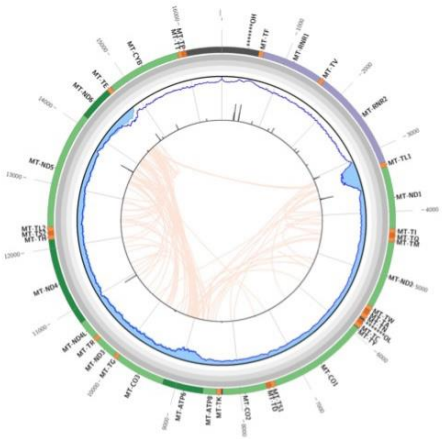

Control2

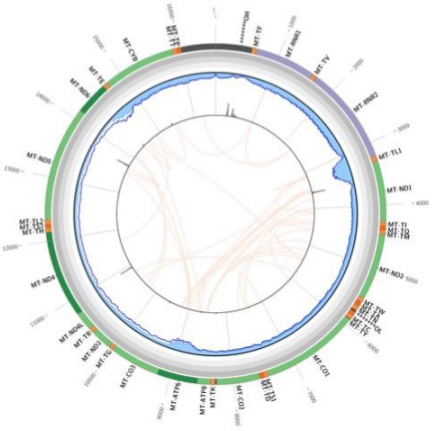

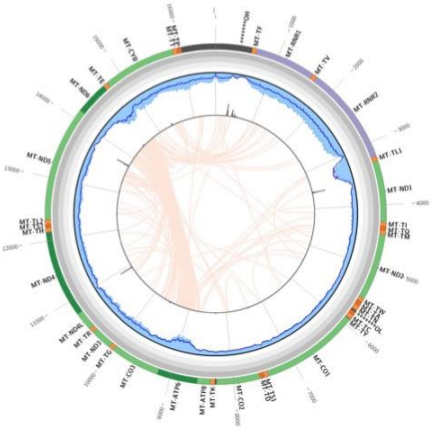

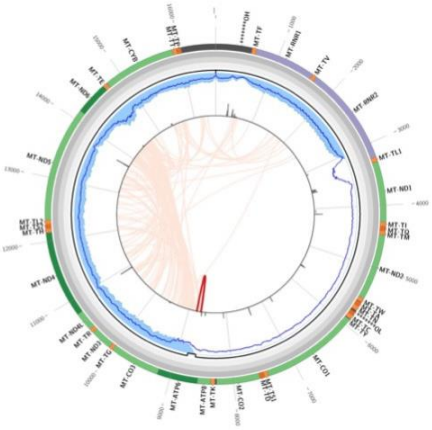

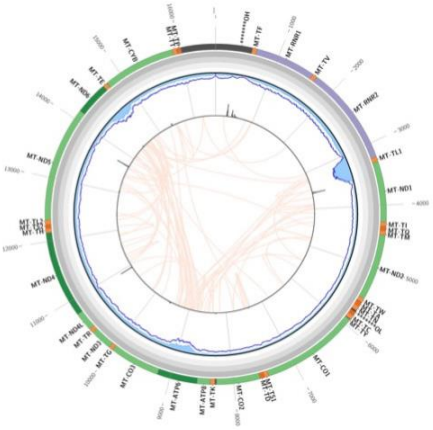

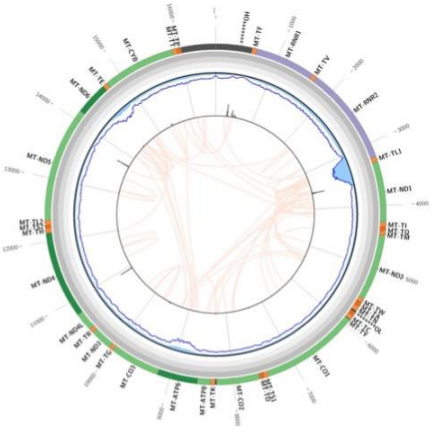

Control3

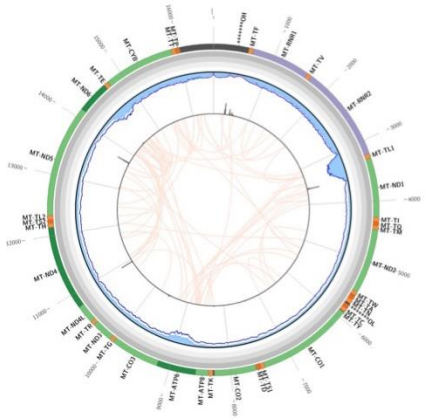

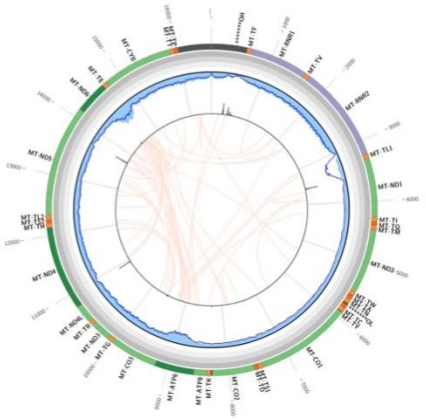

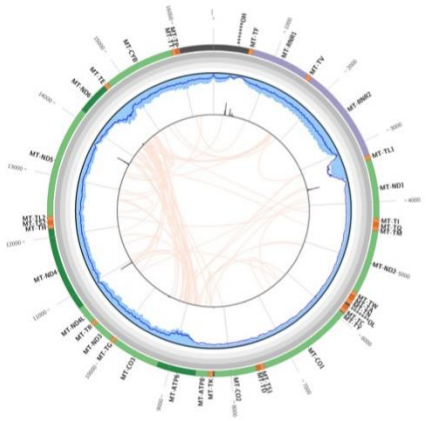

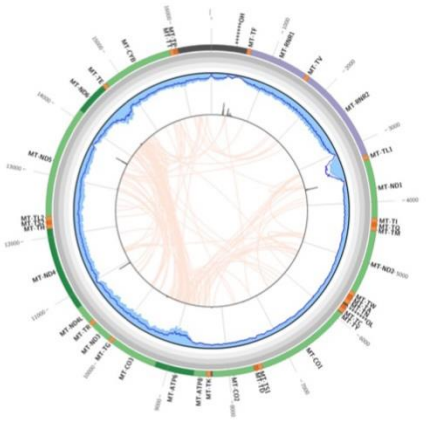

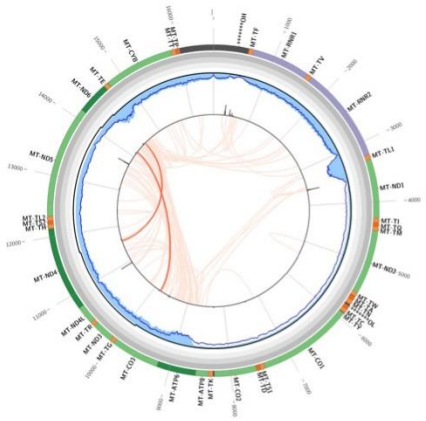

[9859, 14112]: 5.85%

[11621,14440]: 4.79%

Control4

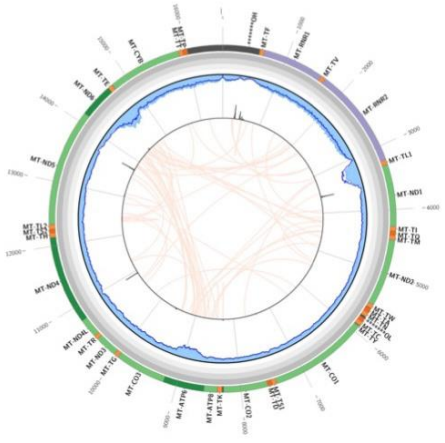

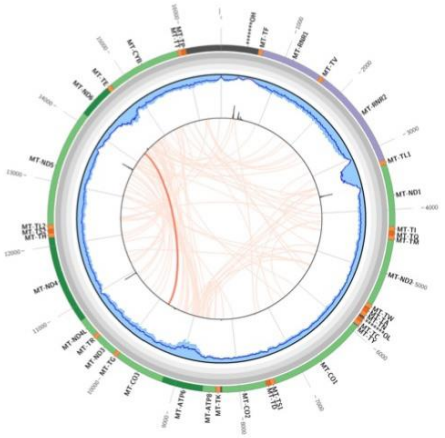

[9777,14243]: 1.43%

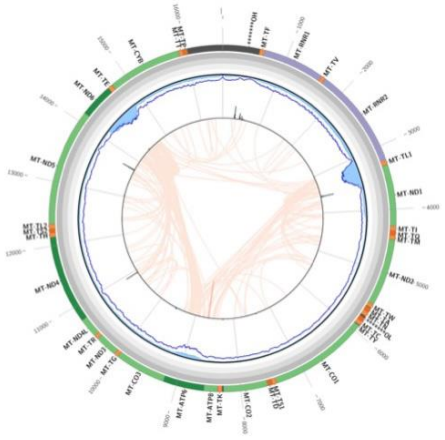

[8668,8648]: 0.16%

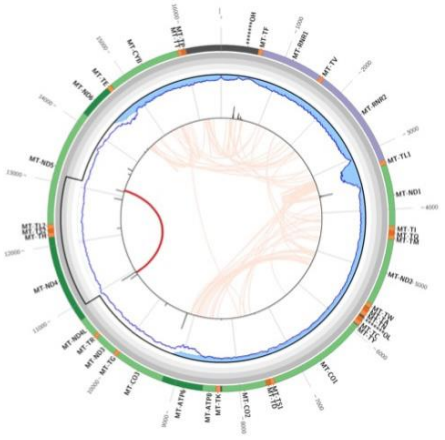

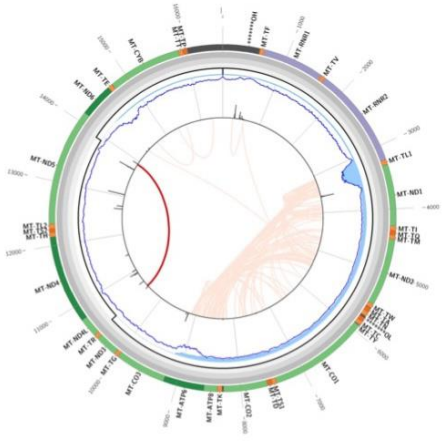

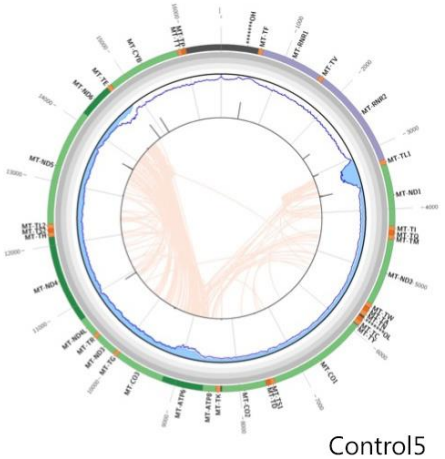

Control5

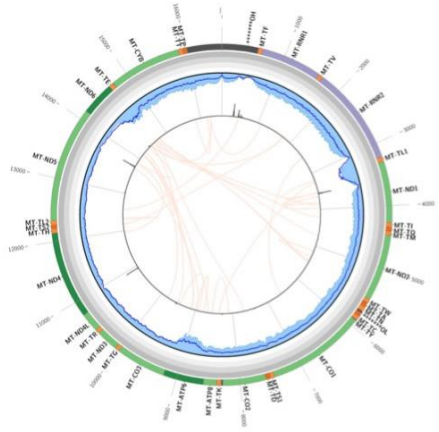

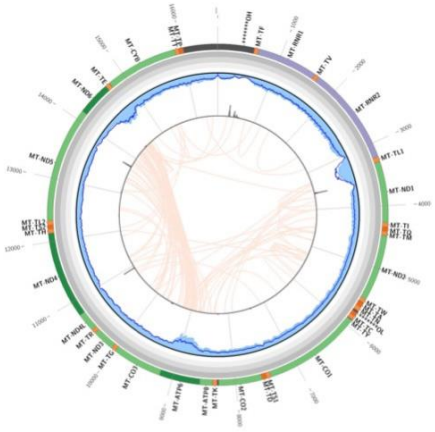

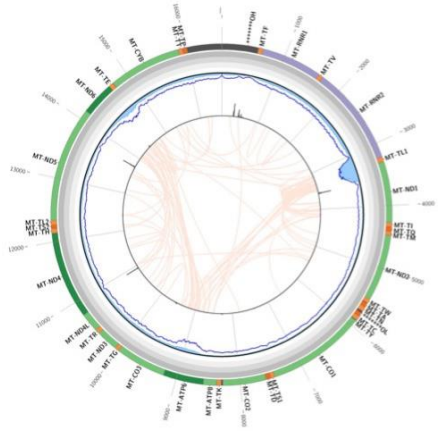

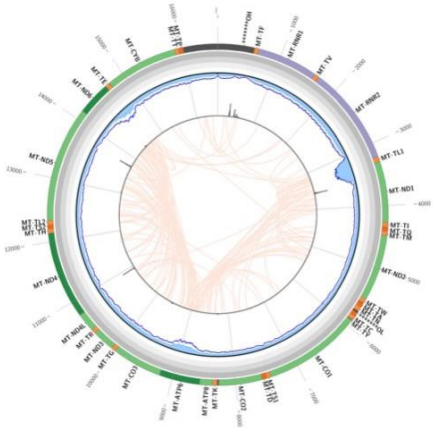

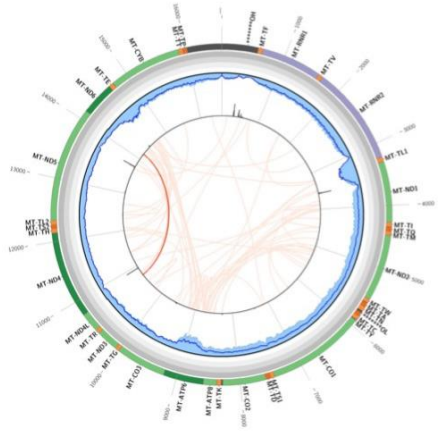

[10748,14124]: 2.63%

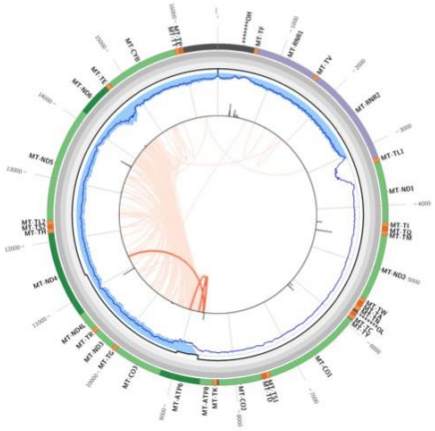

Control6

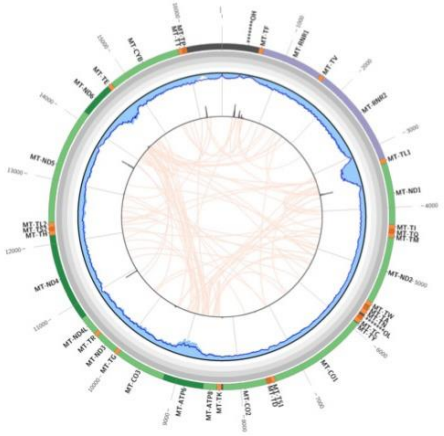

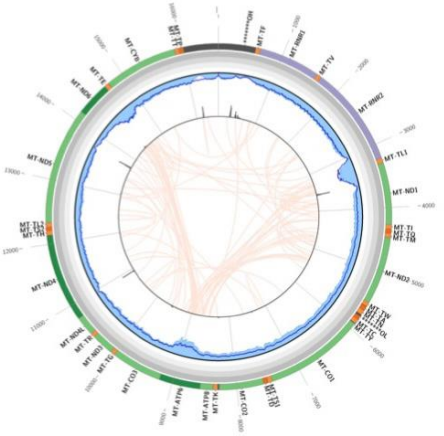

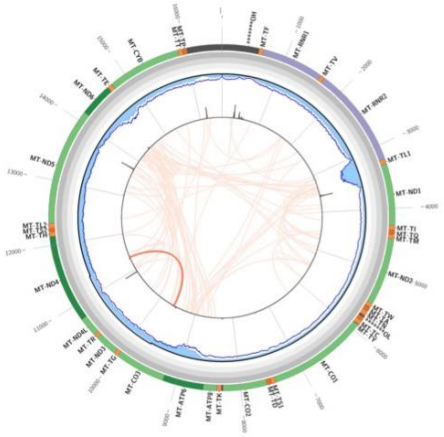

[9639,11325]: 4.31%

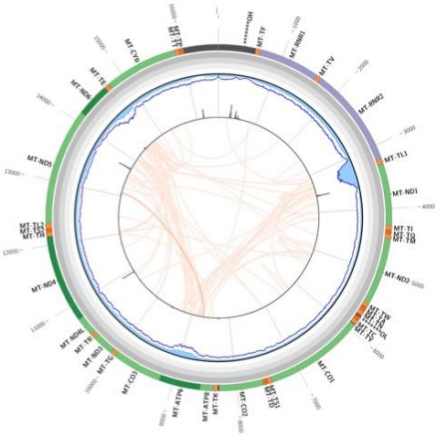

[6190,8346]: 0.270%

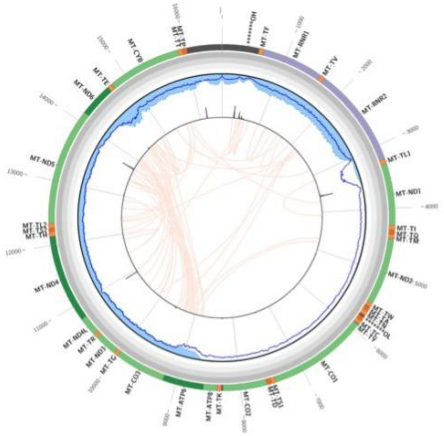

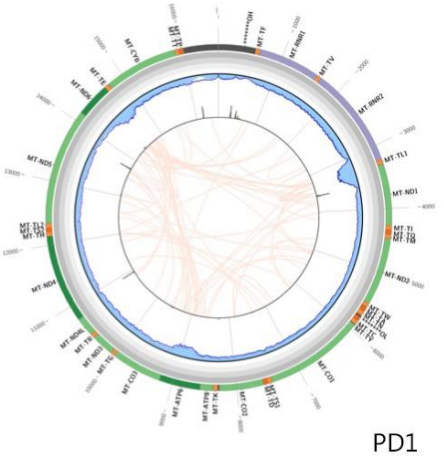

PD1

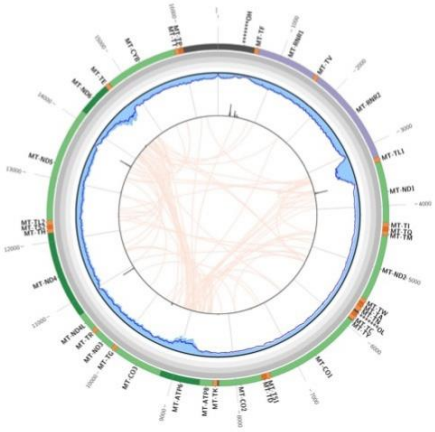

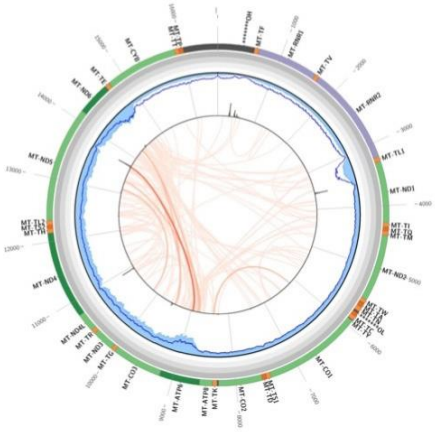

[6190,8346]: 0.27%

[8801;13295]: 0.336%

[8859,14243]: 0.449%

[8993,13710]: 1.24%

[9487,13723]: 0.935%

[9506,14243]: 0.397%

[10183,13070]: 0.312%

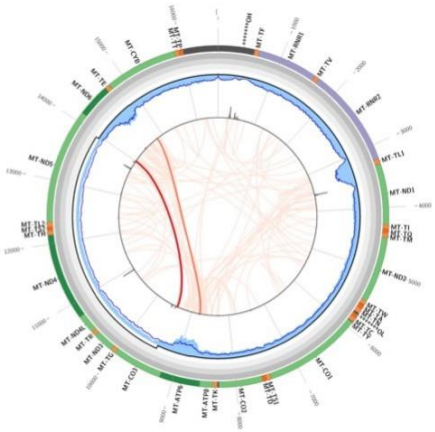

[8793,14792]: 1.76%

[9436,13956]: 14.30%

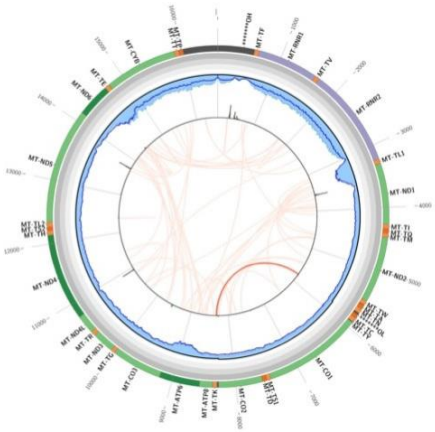

[5822,8268]: 3.33%

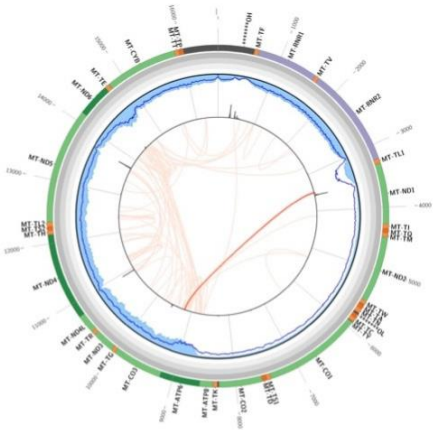

PD2

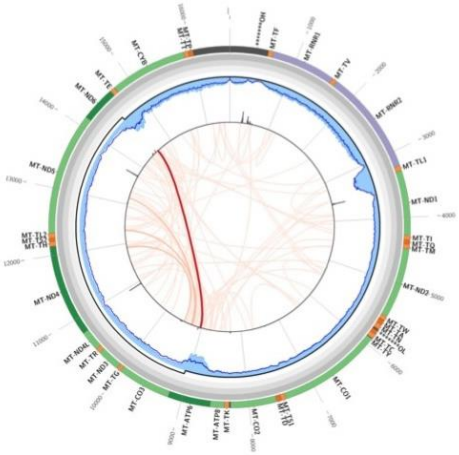

[9077,14525]: 14.45%

[9293,12300]: 0.426%

[9313,13122]: 0.592%

[9503,11861]: 0.488%

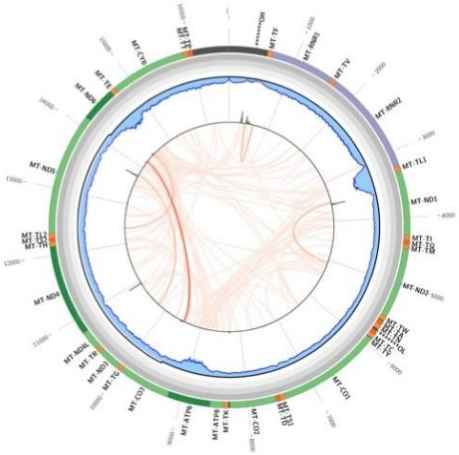

[430,566]: 0.236%

[3566,5023]: 0.630%

[9504,14156]: 6.79%

[10278,13763]: 0.493%

[12430,14417]: 0.153%

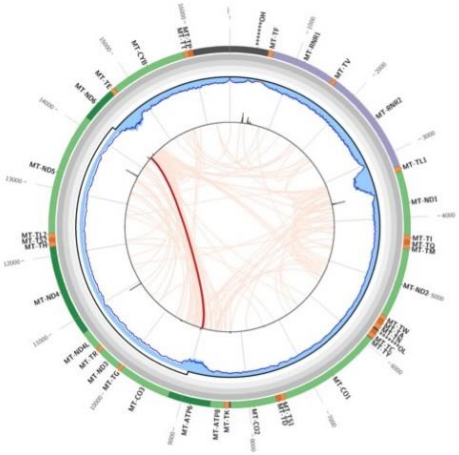

[9026,14288]: 15.32%

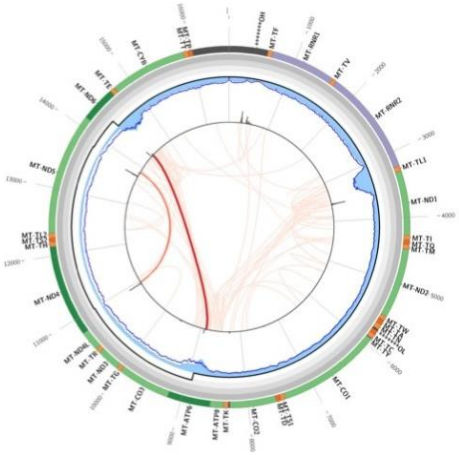

[10996,13836]: 3.52%

PD3

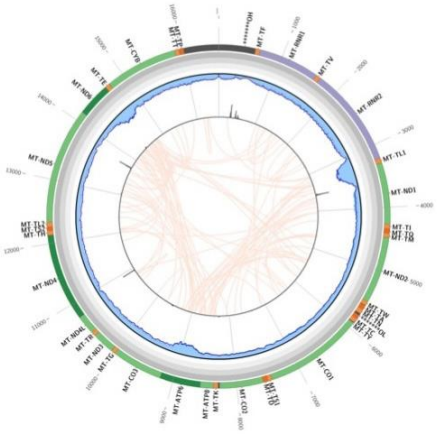

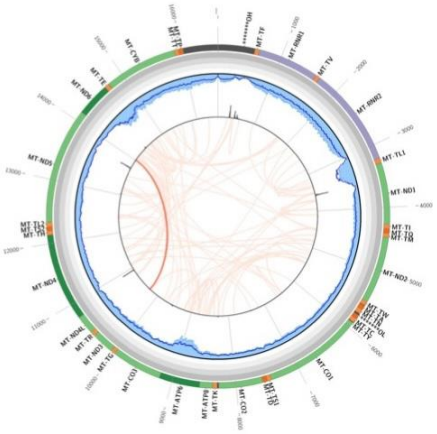

[10304,13975]: 1.39%

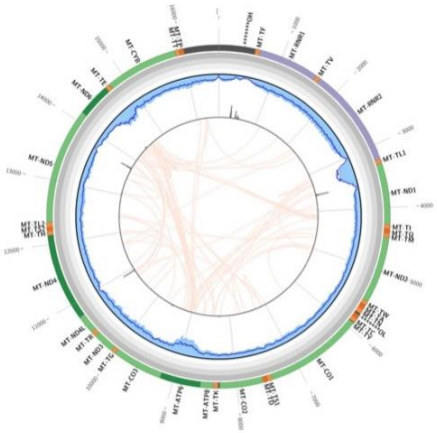

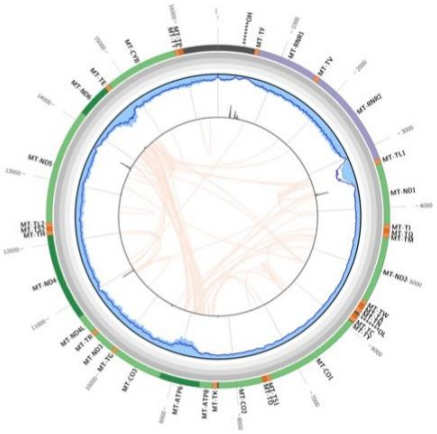

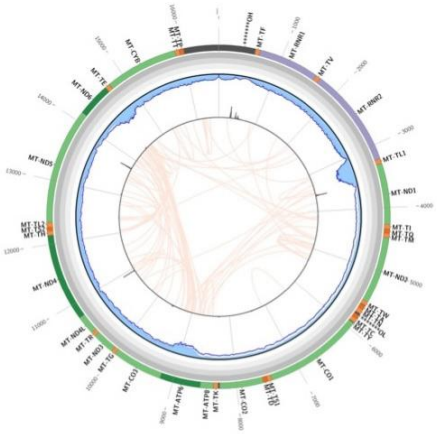

PD4

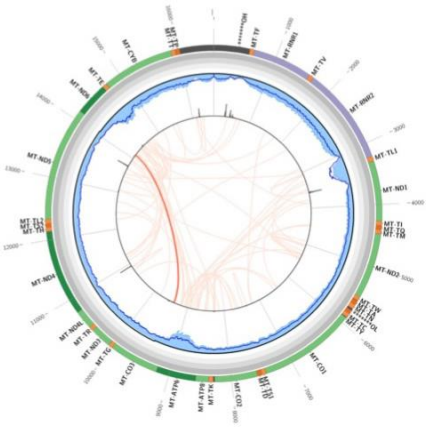

[9430,14073]: 3.78%

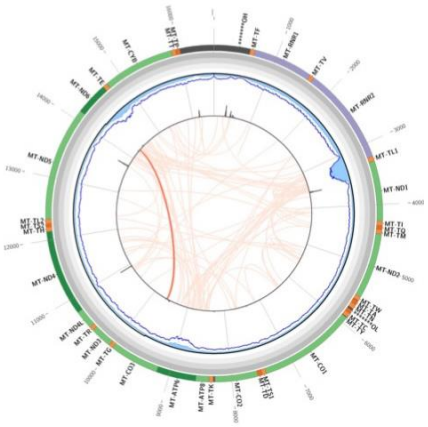

[8930,14242]: 3.66%

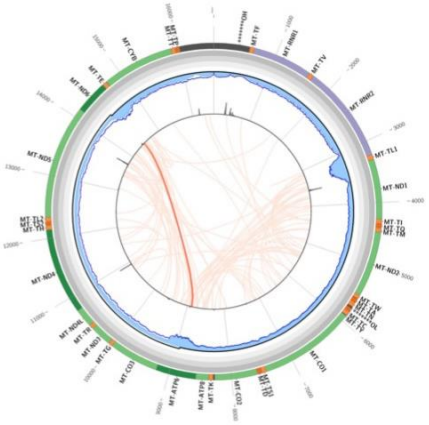

[8930, 14417]: 6.56%

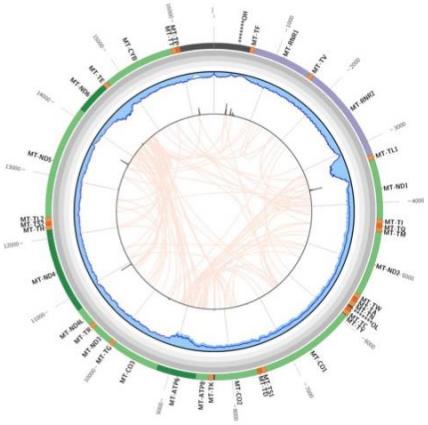

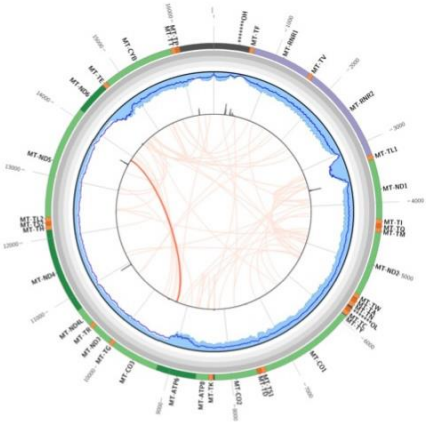

[9347,13855]: 1.62%

PD5

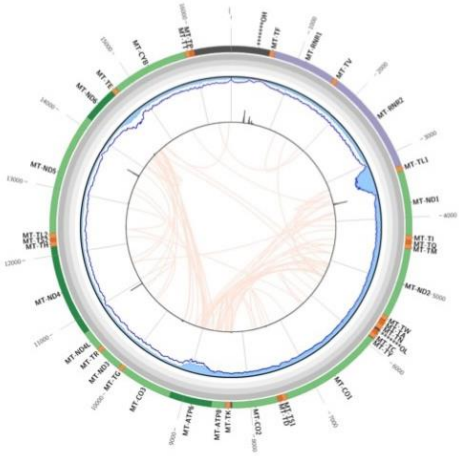

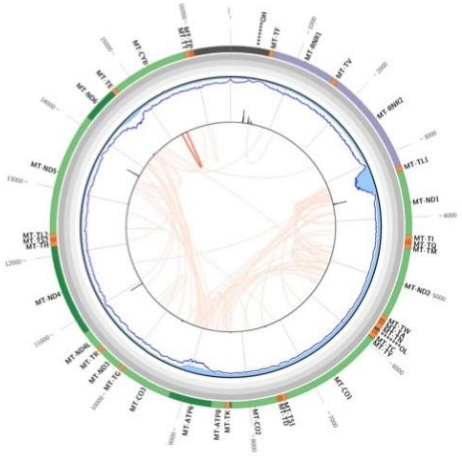

[15331,15379]: 1.77%

PD6

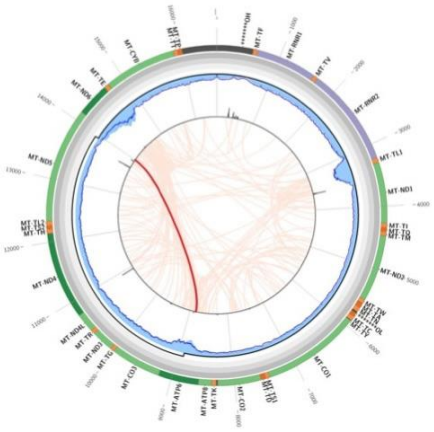

[8896,13948]: 15.60%

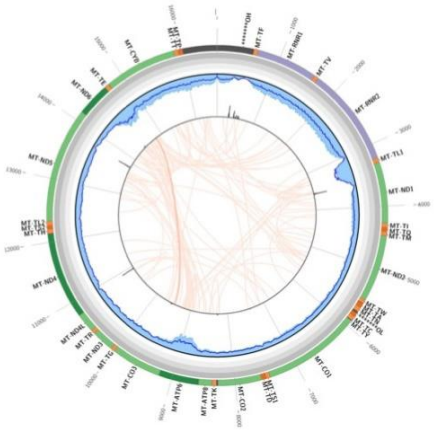

[9504,14772]: 0.59%

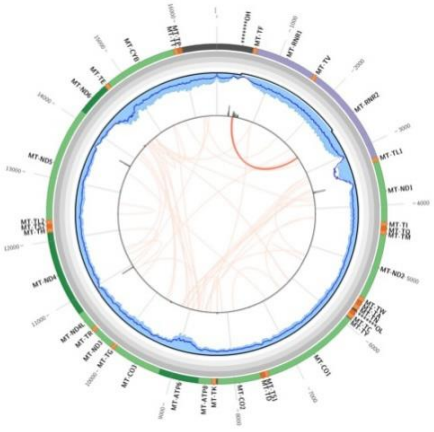

[460,2489]: 6.94%

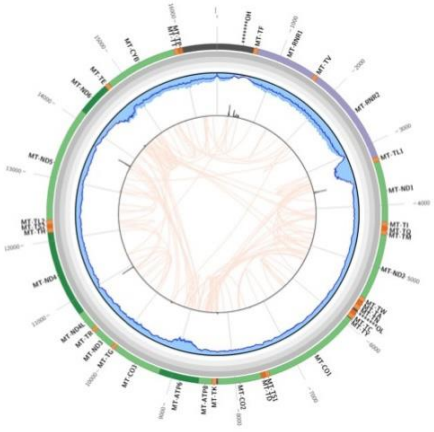

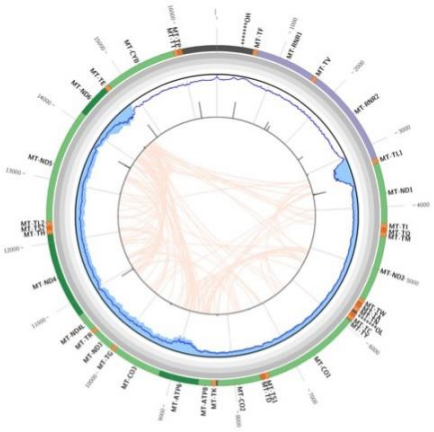

PD7

Figure 3.2-3 Circos plots of all the sequenced neurons

The Circos plots generated from several single neurons from each patient are displayed, with the case number indicated in the bottom right corner of each page. Each plot represents the mtDNA of a single neuron. The outer circle depicts the mitochondrial genome, with gene names clearly labelled. Red arcs within the plot highlight the deletions detected through the eKLIPse pipeline, where the shade of the lines correspond to the heteroplasmic levels. Dark red indicates that the heteroplasmy level is above 10%, lighter red indicates heteroplasmy level between 1 and 10%, while lightest red indicates heteroplasmy level below 1%. Black vertical spikes represent soft-clipping peaks, which mark potential breakpoints for deletions. The blue-shaded area in the middle reflects the sequencing coverage depth across the genome, showing the coverage of each region in the individual sample. The ladder-like black line within the plot represents the cumulative percentage of deletions in specific regions of the mtDNA. Below each Circos plot, deletions that passed the in-house quality control are listed, along with their corresponding heteroplasmic levels. Neurons from PD3 exhibited the highest incidence of mtDNA deletions, with an average of 2.75 deletions per neuron. In contrast, no deletions were detected in any of the five neurons captured from Control3.

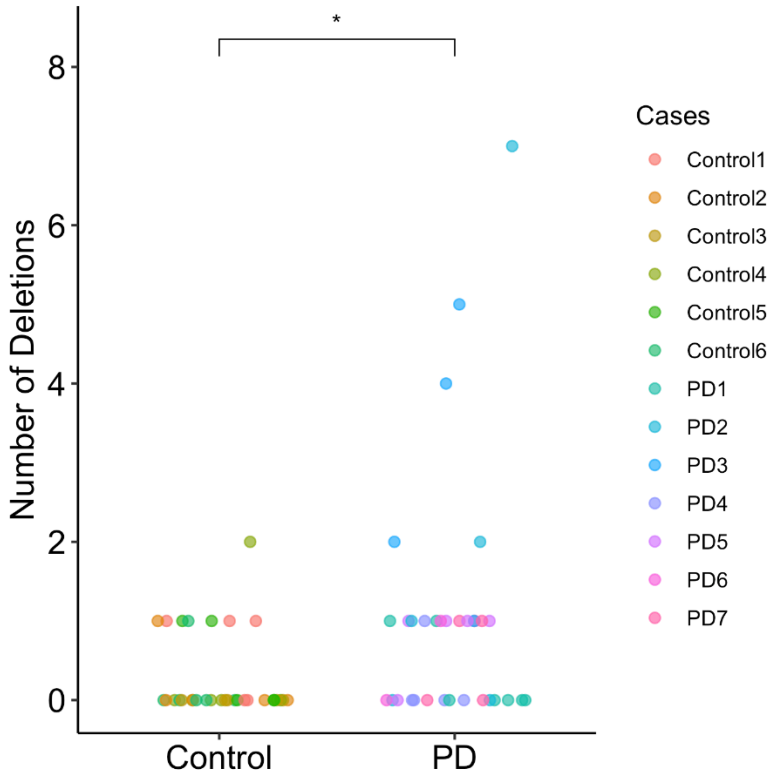

Figure 3.2-4 High incidence of deletions in PD cases

This figure shows the number of deletions per neuron. Neurons collected from PD cases were more likely to accumulate mtDNA deletions compared to the aged controls (p = 0.029, X2 = 4.742 Chi-square test). Different colours represent neurons collected from different patients.*

In the dataset, each neuron harboured a unique mtDNA deletion, supporting the notion that these deletions arise somatically and subsequently undergo clonal expansion. The identification of two distinct size clusters in our dataset, as depicted in (Figure 3.2-2) prompted the classification of deletions into large and small categories for further analysis.

(Bender *et al.*, 2006) first detected mitochondrial dysfunction in dopaminergic neurons of the SNpc in both the PD and control cases in association with high levels of mtDNA deletion, using sequential histochemical staining for the activities of COX and SDH. The work by Bender et al was followed by a study that defined the properties of the deletions

in the SNpc, particularly the location and nature of the breakpoints (Reeve *et al.*, 2008). With neurons being selected using COX/SDH staining. In contrast, the neurons here were collected in an unbiased fashion (Bury *et al.*, 2017), with staining for neuronal type only, with the subsequent deep NGS sequencing in mean sequence depth is 80,223 ± 16229 reads and 75,623 ± 9752 reads for control and PD neurons respectively. The use of an unbiased method limited the ability to link deletions with mitochondrial function, but it provided a comprehensive overview of mtDNA deletions. This approach is better suited to the aims of this project, which primarily focuses on deletions present at very low heteroplasmy levels, as such levels are unlikely to cause harm to neurons.

Using NGS, we were able to detect both large and small deletions from a total of 32 and 33 neurons from control and PD respectively. The deletions were categorised as follows: PD large (31), PD small (2), control large (6) and control small (3). In line with previous studies, our work showed that there were more deletions in each neuron present in individuals with PD as compared to aged controls (Figure 3.2-5. A), Notably higher number of deletions were detected in the group containing deletion sizes >1400 bp, in the PD cases n = 0.94± 1.5, and in the control cases n = 0.19 ± 0.47 (p = 0.002**, Wilcox). Neurons with a high number of deletions originate from a diverse range of cases, including PD3 and PD4, which ensures that these neurons are not an artifact of a single individual's pathology. No significant difference was observed in small deletions when compared between PD (0.061 ± 0.24) and the controls (0.094 ± 0.30), p = 0.63, Wilcox test. Our data also support there being greater levels of clonal expansion of deleted mtDNA in PD cases (4.3 ± 7.6%) vs controls (0.68 ± 2.2%) (Figure 3.2-5. B), with a significant difference in the large deletion load (p = 0.012*, t-test). Neurons with a high deletion load originate from a diverse range of cases, including PD2 and PD3. However, no such difference (p = 0.5, t-test) was seen when the small deletions were considered in PD (0.061 ± 0.31%), and control (0.17 ± 0.86%).

The heteroplasmy level of a deletion can indicate its stage of clonal expansion. A deletion with low heteroplasmy level may have only recently entered the clonal expansion process, while a deletion with high heteroplasmy level likely indicates that it has already undergone significant clonal expansion. In this study, deletions were grouped into three heteroplasmic categories: 0.1-1% (low), 1-10% (middle), and above

10% (high). A higher incidence of deletions was detected in all three heteroplasmic groups in PD cases compared to aged controls. In the low heteroplasmic range, 15 deletions were detected in PD neurons, while only 3 were observed in aged control neurons. In the middle heteroplasmic range, 13 deletions were found in PD cases compared to 6 in the aged control group. In the high heteroplasmic range, only 4 deletions were detected, all of which were in PD cases. However, these differences were not statistically significant (chi-square test, $p = 0.294$) (Figure 3.2-6). This observation suggests that the process of generating or seeding new deletions may be slightly altered under PD conditions, potentially leading to a higher chance of clonal expansion at later stages.

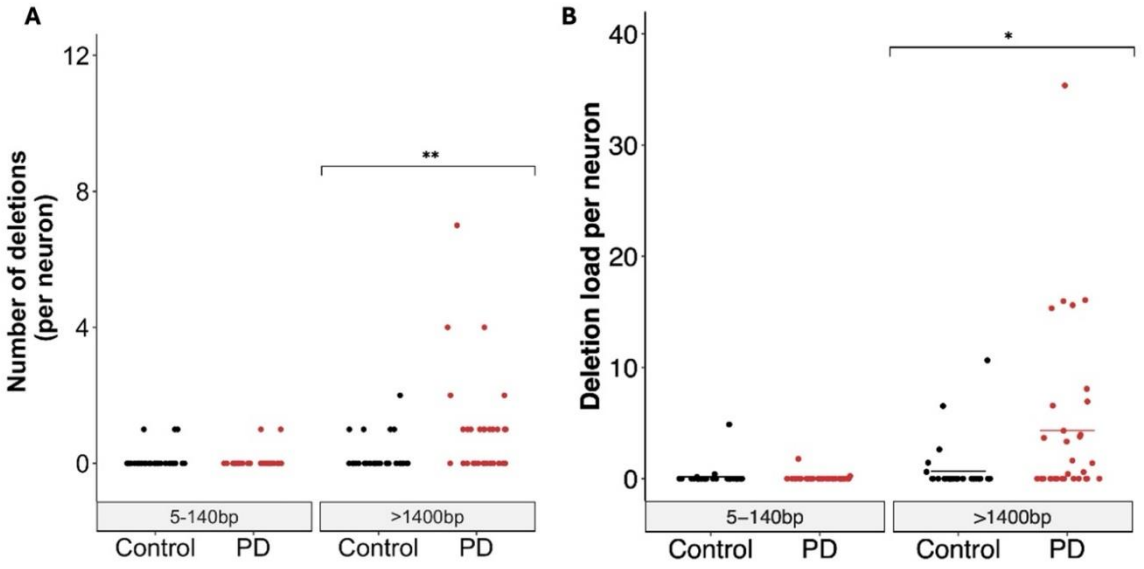

Figure 3.2-5 Number of deletions and deletion load in each neuron

Graph A: Shows the number of deletions (above 0.1% heteroplasmic level) per neuron. There was an increased number of deletions in the large deletion category (exceeding 1400 base pairs) in the PD cases (n = 0.55 ± 1.0) compared to the control (n = 0.16 ± 0.44) (p = 0.013, Wilcox). No significant difference was observed in small deletions that range from 5 to 140 base pairs (p = 0.65, Wilcox), PD (0.06 ± 0.24) and control (0.086 ± 0.28) (p =0.65, Wilcox). Graph B: Shows the deletion load (the total deletion heteroplasmic level, above 0.1%) in each neuro. The total deletion load was calculated by summing deleted molecules with a heteroplasmy level > 0.1 by neuron. An increase in the deletion load was observed when considering the large deletions above 1400bp, in the PD cases (4.3 ± 7.6%) versus the control cases (0.68 ± 2.2%) (p = 0.012*, t-test). No significant difference was detected between this in small deletions size between 5 and 140bp, in the PD cases (0.061 ± 0.31%) versus the control cases (0.17 ± 0.86%) (p = 0.5, t-test). Control neurons are represented in black, while red indicates PD neurons.*

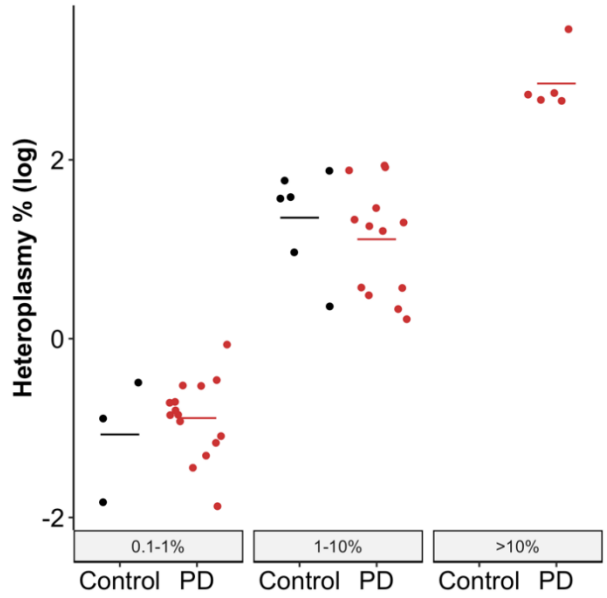

Figure 3.2-6 Deletions in different heteroplasmy level

This figure illustrates the number of deletion incidents across different heteroplasmy levels in captured cholinergic neurons. In the low heteroplasmic range (0.1 to 1%), more deletions were detected in PD PPN cholinergic neurons (15) compared to the aged control group (3). Similarly, in the middle heteroplasmic range (1-10%), PD neurons showed more deletions (13) compared to the aged control (6). For deletions in high heteroplasmic level (above 10%), PD neurons exhibited 4 deletions, while none were observed in the aged control group. However, these differences were not statistically significant (chi-square test, p = 0.294).

3.2.3. *Location of the deletions on the mitochondrial chromosome*

We examined the spatial distribution of the deletions. After aligning all deletions with the reference sequence, it was clear as in prior studies they predominantly reside (He *et al.*, 2002; Bua *et al.*, 2006) within the major arc of mtDNA, with 88% of all detected deletions falling within this region.

Among the 31 large deletions observed in PD cases, the most frequent genomic location of the 5' end of a deletion was *MT-CO3* (38.7%), followed by *MT-ATP6*

(32.3%). The most frequent genomic location for the 3' end of the deletion was *MT-ND5* (42%), with *MT-ND6* being the second most common (29%). In the 6 large deletions observed in the aged control group, the most frequent genomic location for the 5' end of the deletion was also *MT-CO3* (50%). For the 3' end, *MT-ND5* was also the most common (67%), followed by *MT-ND6* (33%) (Figure 3.2-7).

Small deletions are distributed across the mitochondrial genome. Among the two small deletions observed in PD cases, one 48 bp deletion was located within *MT-CYB* gene, while the 3' end breakpoint of another deletion from a different PD case was located at the *mitochondrial heavy-strand promoter* (MT-*HSP1)* m.566. In the aged control group, three small deletions were observed. One was located within the *MT-ATP6* gene in the major arc, while the remaining two were found in the non-coding region, with the 5' breakpoint located within the *hypervariable segment 2 (HSV2)*. This distribution may suggest that these deletions result from stochastic events rather than sequence-dependent mechanisms, potentially influenced by reactive oxygen species or random DNA repair errors.

A total of 84 breakpoints were identified from 42 deletions detected in this project. Of these, 11 breakpoints were reported at least twice, with one 3' breakpoint (14243) appearing three times. When comparing these breakpoints to those reported in the MitoBreak database, none of the exact deletions matched. Furthermore, 71.4% of the breakpoints, from both 5' and 3' ends, were not previously reported in MitoBreak. Among the breakpoints that were reported in MitoBreak, 20.2% appeared once, 6.0% appeared twice, and 2.4% appeared four times. Similarly, this paper (Nido *et al.*, 2018), which also used Illumina deep sequencing, reported that only 31 out of 373 unique deletions (8.3%) were present in the MitoBreak database. The uniqueness of the deletion breakpoints observed in this study suggests that different methods may identify different breakpoints. NGS techniques have only recently been applied to the identification of mtDNA deletions in the past few years, and deletions detected using previous methods like long range PCR, may differ slightly from those detected with newer techniques. Long-range PCR selectively amplifies specific regions of mtDNA, often targeting large amplicons that span regions of particular interest. In contrast, NGS offers a high-throughput, unbiased approach, enabling the detection of

deletions across the entire mitochondrial genome, regardless of their location. This also underscores the limitations of the MitoBreak database, as not all deletions have been included or reported.

Only 5 out of 42 deletions (12%) were found within the minor arc (3 from PD cases and 2 from the controls), of those, 2 were large deletions, both found in PD cases. The remaining deletions were located within the major arc. This observation aligns with the analysis of deletion reported in MitoBreak. An analysis of MitoBreak deletions revealed that out of 1,369 recorded deletions, only 28 (1.9%) occurred within the minor arc, while 1,128 (82.4%) were located in the major arc. Additionally, 10 deletions (0.73%) removed the full minor arc and part of the major arc, and 201 deletions (14.7%) affected both the minor and major arcs. The percentage of deletions within the minor arc in this research is higher than reported in MitoBreak, likely due to the limitations of some studies in detecting minor arc deletions. Most common methods for detecting deletions amplify large fragments, including *mitochondrial encoded ubiquinone oxidoreductase core subunit 4* (MT-ND4) within the major arc, before proceeding to sequencing.

When comparing the genomic locations of the breakpoints in deletions detected in paper published in (Reeve *et al.*, 2008), all reported deletions were large, with a total of 59 deletions across three conditions (aged control, PD, and POLG). The most frequent genomic location for the 5' end of a deletion was *mitochondria encoded cytochrome C Oxidase I* (*MT-CO1)* (52.5%), followed by *mitochondria encoded cytochrome C Oxidase II (MT-CO2)* (17%). For the 3' end, the most common location was *MT-ND5* (47.5%) followed by *MT-CYB* (25.4%). In this study, the 5' breakpoints are positioned farther from the OriL compared to those found in (Reeve *et al.*, 2008), while the 3' end locations of the deletions reported in this project (*MT-ND5* 40.5% and *MT-ND6* 26.2%) are closer to the OriL, suggesting that relatively smaller deletions were detected in this project. Aside from this difference, similar observations were made, showing no significant variation in the genomic locations of the breakpoints across different conditions and types of neurons. Figure 3.2-8 shows the locations of the deletions detected in the cholinergic neurons of the PPN alongside those detected in the dopaminergic neurons of the SNpc (Reeve *et al.*, 2008) from PD and POLG

patients. These patients exhibit either loss of function or reduced or altered enzyme activity, leading to disrupted mtDNA replication. A similar breakpoint distribution was observed across patients with different conditions.

These results suggest that the mechanism leading to the formation of these deletions in these distinct patient groups and neuronal types across different brain regions is likely similar, despite the differing biochemical profiles of two types of neurons. Additionally, they indicate that the locations of mtDNA deletions are not primarily determined by the efficiency of mtDNA replication and repair, which is regulated by POLG enzyme activity.

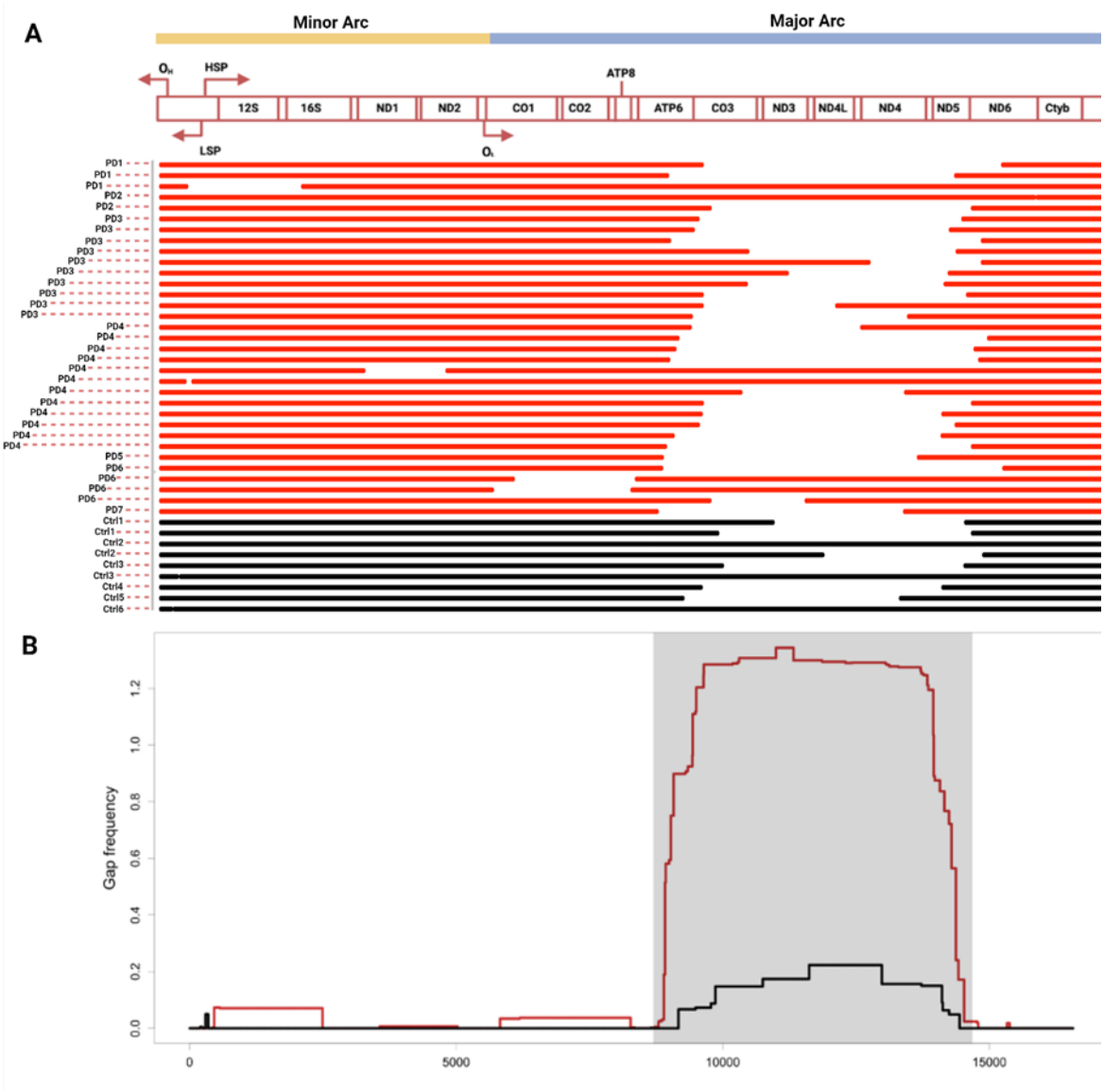

Figure 3.2-7 Distribution of PPN cholinergic neurons deletions

Graph A: Illustrates the distribution of deletions detected in PPN cholinergic neurons. The majority, 88%, of deletion lines are concentrated in the region of the major arc for both PD and control cases. Notably, there are missing coding regions in complex I and IV, ATP synthesis, and certain tRNA sequences. The patients' number of each deletion is labelled on the left-hand side. Graph B: Reveals a prominent peak at ATP6 and ND6 the major arc. The frequency of gaps in PD surpasses that of the aged control group. Control cases are represented in black, while PD cases are denoted in red.

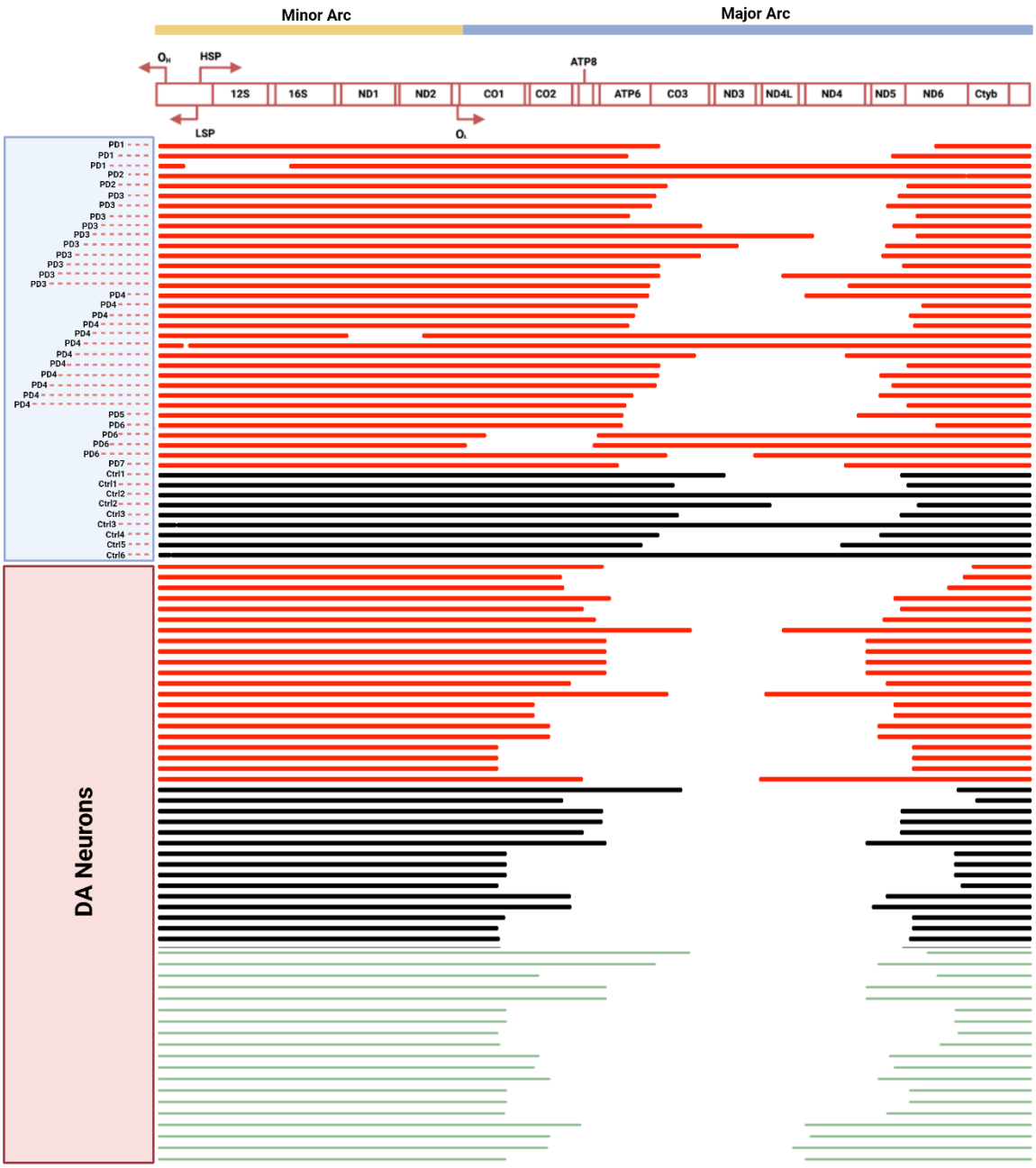

Figure 3.2-8 Distribution of deletions from different types of neurons and conditions

These graphs show all mtDNA deletions detected in different areas and different cases. The blue box on the left-hand side, indicating patient IDs, shows deletions from PPN cholinergic neurons from 12 cases (6 PD, 6 control), and the red box labelled as 'DNA neurons' shows the deletions from SNpc dopaminergic neurons from three different cases (PD, POLG, and control). When aligning these deletions together, a similar hotspot area for accumulating mtDNA deletions was observed, indicating that a similar mechanism might be behind mtDNA deletions in different

areas, different neurons, and different cases. Black represents control, red indicates PD, while green signifies POLG.

3.2.4. *Breakpoint types and free energy*

Many of the identified mtDNA deletions in humans are bordered by short tandem sequence repeats (Samuels, Schon and Chinnery, 2004; Krishnan *et al.*, 2008). To explore whether this pattern is also prevalent across the deletions in our sample, breakpoints were categorized using two categorisation methods of the breakpoints into types I, II and III as well as a simpler classification of repeats and no-repeats (Reeve *et al.*, 2008). Type I deletions contain similar sequence (at least 3 identical nucleotides) at the breakpoint, Type II deletions need to have similar pattern (either with 1 nucleotide change in a 3 to 5 bp sequence, or have 2 changes in sequence longer than 5bp, while there is no repeat can be found in the breakpoints of type III deletions (Figure 2.3-5). This classification originated from (Degoul *et al.*, 1991), where deletions with perfect repeats were defined as type I, as they were the most prevalent. Imperfect deletions, classified as type II, were the second most common. Deletions without any repeats, the least frequently detected, were categorized as type III. This may suggest that different mechanisms are responsible for generating mtDNA deletions, making it important to categorise deletions accordingly (Samuels, Schon and Chinnery, 2004; Reeve *et al.*, 2008). It was found that majority of deletion breakpoints observed in our dataset are flanked by short repeat sequences, 28 out of 33 and 7 out of 9 in PD and control respectively (Figure 3.2-9). When repeats in deletion breakpoints, majority of the repeats are perfect or type I repeats, 26 out of 28 and 5 out of 7 in PD and control respectively.

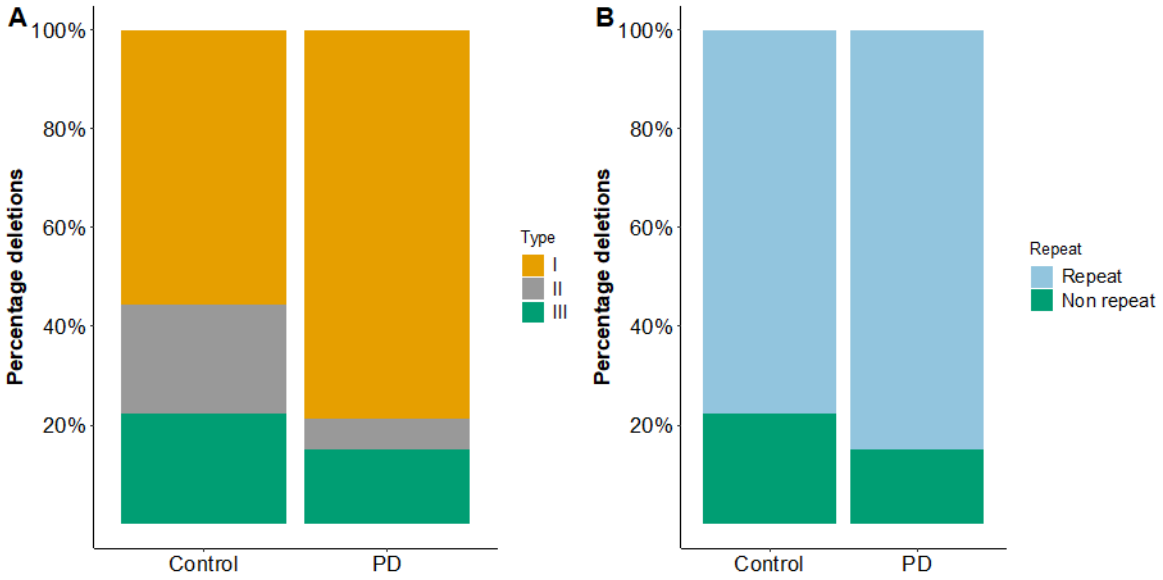

Figure 3.2-9 Cholinergic neurons deletion breakpoint types

Comparison of deletion break points. Classified using two methods. Graph A: The percentages of different types of deletion breakpoints (type I as deletion with identical repeat in breakpoint, type II as deletion with similar pattern in breakpoint, while type III as deletions with no repeat around the breakpoint area) were compared between PD cases and the controls. PD cases showed a higher frequency of type I deletions (PD: n = 26, 78%; Control: n = 5, 55.6%), and a lower frequency of type II and III deletions compared to the control group, although the difference is not significant (p = 0.263, Chi-square test). Type I deletions are depicted in orange, type II in grey, and type III in green. Graph B: The percentages of deletion breakpoints with or without repeats were compared between PD and control groups. Deletions with repeat means similar or identical pattern can be found in sequence near deletion breakpoint. In both group, neurons tended to accumulate more deletions with repeats, PD (84%, n = 28, total deletion of 33), Control (70%, n = 7, total deletion of 9), p = 1, chi-square test. Deletions without repeats are represented in blue, while those with repeats are in green. This analysis involved 25 PPN cholinergic neurons from 6 controls and 32 neurons from 7 PD cases.

Our findings are broadly in line with those from (Reeve *et al.*, 2008) who studied categories of breakpoints in the DA neurons of the SNpc. In both PPN cholinergic and SNpc DA neurons from control cases, the majority of deletions detected involve direct repeat sequences, at 77% and 83% respectively, with type I deletions being the most prevalent at 56% and 50%. Type II deletions accounted for 22% and 33% respectively. A similar pattern was observed in PD cases, where 84% and 86% of PPN cholinergic and SNpc DA neurons' deletions contained repeats. Of these, 78% and 63% were type I deletions, and 7% and 23% were type II deletions. There was a limited presence (16% and 14% in ChAT and DA neurons respectively) of type III deletions in both types of neurons in PD cases (Figure 3.2-10). The distribution of deletion types reported in the MitoBreak database study also resembles our findings (Damas, Carneiro, *et al.*, 2014), and those of Reeve et al, 2008 with approximately 60% perfect repeats, 30% imperfect repeats, and 10% no direct repeat.

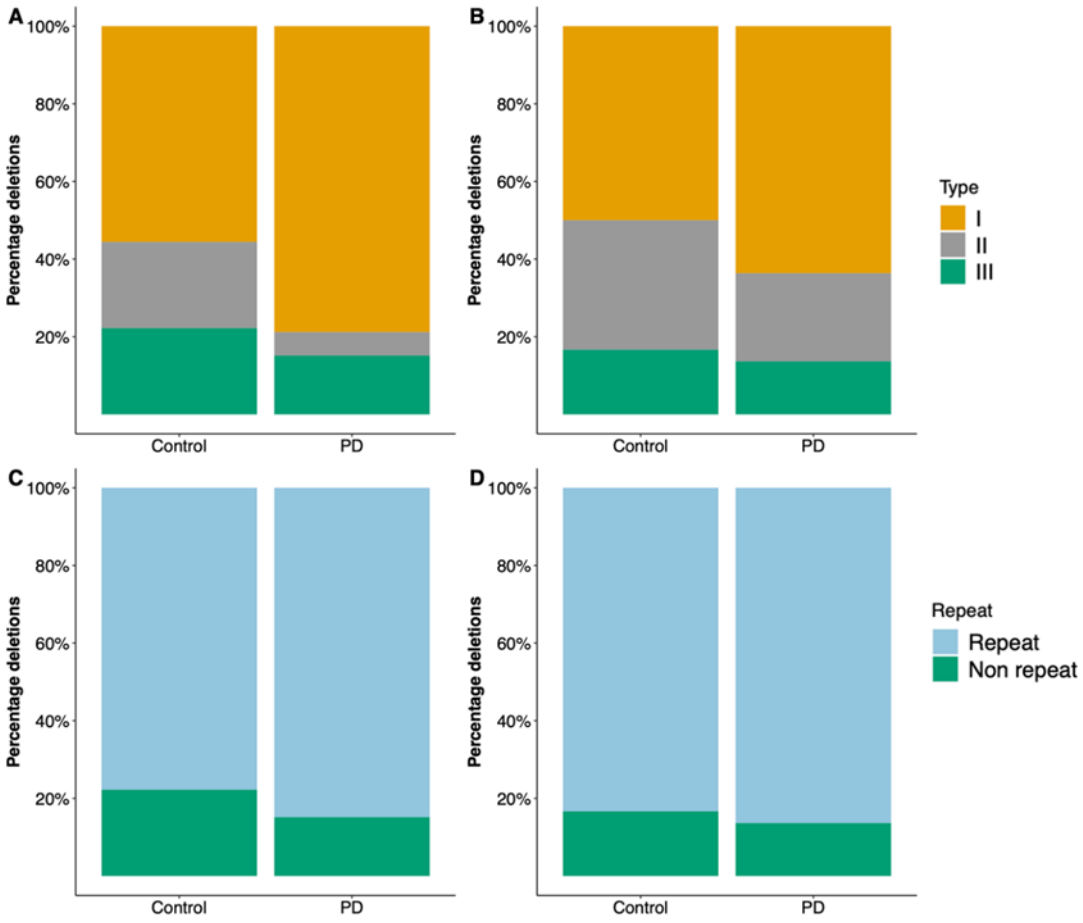

Figure 3.2-10 Comparison of DA and ChAT neuron breakpoints

Graph A and B: Showing the percentages of different types of deletion breakpoints (type I as deletion with identical repeat in breakpoint, type II as deletion with similar pattern in breakpoint, while type III as deletions with no repeat around the breakpoint area) were compared between PD cases and the controls. Graph A shows the results from PPN ChAT neurons, while graph B shows that from the SNpc DA neurons. In both types of neurons, both control and PD neurons deletions shows similar composition. PD cases showed a higher frequency of type I deletions (ChATPD: 78%; DAPD: 63%; ChATConrtol: 56% ; DAControl: 50%), and a lower frequency of type II (ChATPD: 7% ; DAPD: 23%; ChATControl: 22%; DAConrtol: 33%) and III (ChATPD: 16%; DAPD: 14%; ChATConrtol: 22% ; DAControl: 17%) deletions compared to the control group, although the difference is not significant (ChAT: p = 0.263; DA: p = 0.675;Chi-square test). Type I deletions are depicted in orange, type II in grey, and type III in green. Graph C and D: Showing the percentages

of deletion breakpoints with or without repeats were compared between PD and control groups in two types of neurons (left from PPN cholinergic neurons, right from SNpc dopaminergic neurons). Deletions with repeat means similar or identical pattern can be found in sequence near deletion breakpoint. In both group from two types of neurons, neurons tended to accumulate more deletions with repeats, ChATPD (84%, n = 28, total deletion of 33), DAPD (86%, n = 19, total deletion of 22); ChATControl (70%, n = 7, total deletion of 9), DAControl (83%, n = 15, total deletion of 18). No difference was observed between PD and control in both neuronal types (ChAT: p = 1, DA: p = 1, chi-square test). Deletions without repeats are represented in blue, while those with repeats are in green. This analysis involved 9 PPN cholinergic neurons deletions from 6 controls, 33 deletions from 7 PD cases and 22 dopaminergic neurons deletions from 5 controls, and 18 deletions from 5 PD cases.

When examining the breakpoint composition in detail, the comparison between the PD and control groups revealed several notable findings. Sequences around the breakpoints (10bp before and 10bp after) were used to analyse the composition of the breakpoint. For already deleted sequence, the nucleotide information is obtained from other neurons captured and sequenced from the same patients. Firstly, in the context of repeat length comparison, PD deletion breakpoints appear to have similar repeat lengths compared to controls (Control: 7.14 ± 2.27; PD: 5.93 ± 2.34 p = 0.24, t-test, Figure 3.2-11-A). Secondly, regarding the number of C tracts 20bp around the breakpoints, PD exhibits a trend towards accumulating more deletions with C tracts around the breakpoints compared to controls (Control: 0.857 ± 0.9; PD: 1.54 ± 1.26, p = 0.067, t-test, Figure 3.2-11-B). Finally, concerning GC content% around the breakpoints, sequences around deletions detected in PD neurons have higher GC contents than in the aged control group. This difference was statistically significant (Control: 0.43 ± 0.23; PD = 0.51 ± 0.36, p = 0.043*, t-test, Figure 3.2-11-C). These

findings suggest potential differences in the molecular characteristics of deletion breakpoints between PD cases and controls. The higher GC context observed around PD deletion breakpoints, along with the tread of increased associated with C tracts near these breakpoints, suggests that specific molecular mechanisms may underline the increased propensity for mtDNA deletion in the context of PD. This pattern points to the possibility that nucleotide sequences or structural features in the mtDNA could play a role in making certain regions more susceptible to deletion events in PD.

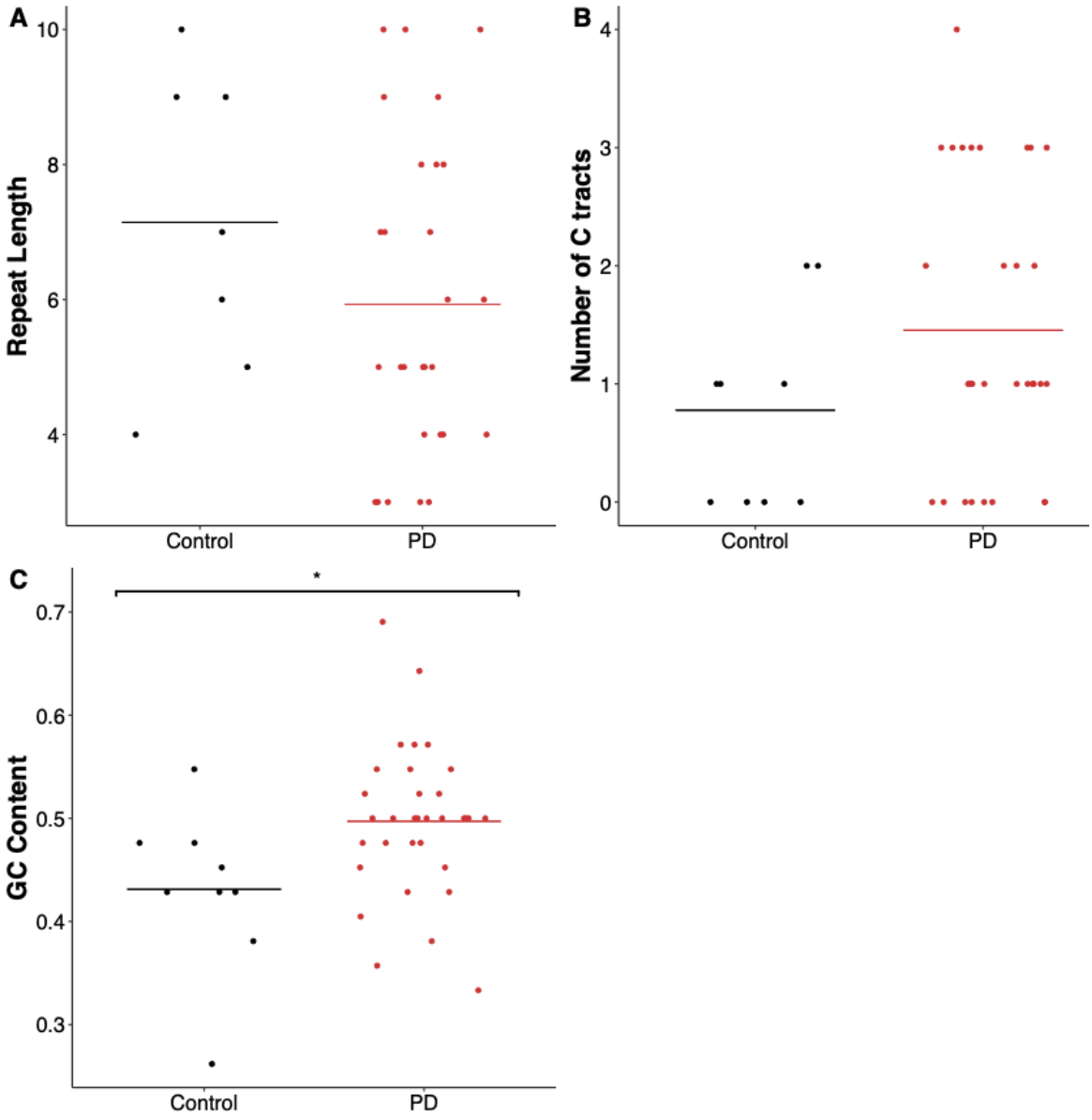

Figure 3.2-11 Breakpoint comparisons in different aspect

The breakpoints of both groups have been compared in different aspects. A: Repeat length comparison. PD deletion breakpoints appear to have smaller repeat lengths, although the p-value is not statistically significant (p = 0.24, t-test). B: Number of C tracts ± 10 bp from the breakpoints. PD seems to exhibit a trend towards accumulating more deletions with C tracts around (p = 0.067, t-test). C: GC content% around the breakpoints (±10 bp). Sequences around deletions detected in PD neurons have higher GC contents than in the aged control (p = 0.043, t-test). Black represents control, while red indicates PD. A total of twenty-five PPN cholinergic neurons were studied, comprising 6 from controls and 32 from PD cases.*

The role of direct repeats in deletion formation, particularly in the context of PD affecting the SNpc region, has been supported in various studies. Nido's group calculated that if the generation of deletions were independent of the underlying repeats, only a small fraction (5.1%) of the breakpoints would randomly occur within tandem repeats (Nido *et al.*, 2018). However, in real-life analyses, the majority of deletions are found to occur with perfect or imperfect repeats. This underscores the significance of direct repeats in facilitating deletion events. The mechanism behind deletion formation implicates miss annealing of homologous sites during replication, a concept proposed by (Clayton, 1982). In this scenario, an asynchronous model of replication is considered, where the 5'- and 3'-repeat ends, situated in the heavy and light strands respectively, become exposed as single strands, allowing for hybridization. Subsequently, the 5'-repeat sequence is degraded, resulting in the retention of only the 3'-repeat sequence in the deleted mitochondrial DNA, as suggested (Figure 3.2-12). This model provides insights into the molecular processes underlying the generation of deletions within mitochondrial DNA associated with PD pathology.

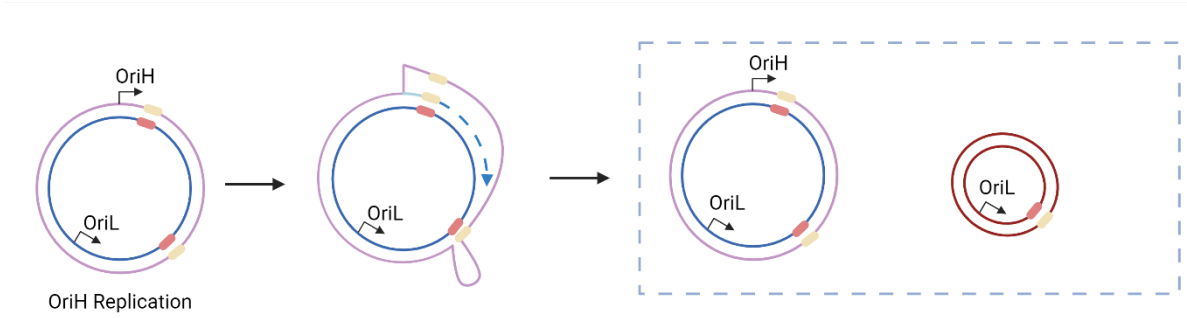

Figure 3.2-12 Generation of deletion Clayton model

This graph illustrated that during the replication of the major arc, the repeat part of the unwound heavy strand misaligns to the similar or same repeat part located in the downstream of the light strand, which will eventually lead to loss of the sequence of the folded area (5' repeat) during the light strand replication after the heavy strand replication passed the OriL.

3.2.5. *Free energy work*

To explore the possible impact of sequence homology in the form of tandem repeats and the formation of deletions, we conducted *in silico* calculations to assess the hybridization stabilities between mtDNA segments along the major arc. Previous studies suggest that duplex stability provides a more reliable predictor of deletion distribution than solely relying on perfect tandem repeats (Guo et al., 2010).

For each deletion, we computed the free energy (ΔG) of the secondary structure formed by the hybridization between the 5 and 100 bp segments centred on each breakpoint, using two pieces of free energy prediction software: UNAFold and SeqfolFigure 3.2-13 depicts the logarithmic display of the free energy plot predicted by UNAFold and Seqfold, demonstrating their predictions of the two pipelines are well correlated (r= 0.71, p=3.1 x 10^{-7}) it is advantageous to use both not only for replication but also to take advantage of the features offered by each.

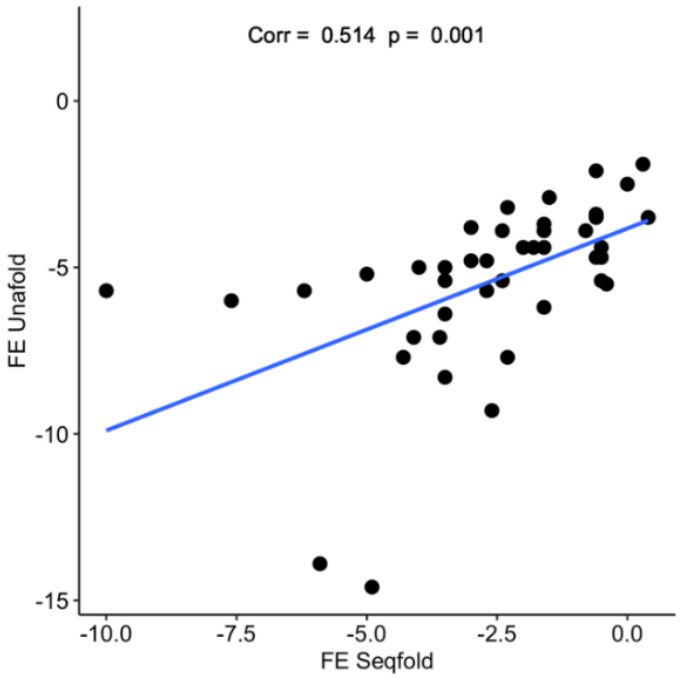

Figure 3.2-13 Correlation between results from Seqfold and UNAFold

This graph shows the linger plot of free energy predicted by UNAfold and Seqfold. X axis is the free energy predicted by Seqfold, while y axis is the free energy predicted by UNAFold. The correlation between the results from 2 pipelines is r=0.514, p = 0.001.

Figure 3.2-14 shows the free energy analysis pipelines as used in this study and how they were applied. Aligning the segments of the mtDNA to the mtDNA reference sequence reveals two segments around these breakpoints. The length of each segment depends on the pre-selected window size, with the sequence around the breakpoint having a length equal to half the window size (HWS). After retaining the sequences, both are input into a secondary structure prediction pipeline, such as UNAFold or Seqfold. UNAFold requires two sequences as input, whereas Seqfold can only handle single sequences needing a strategy to concatenate the two sequences. In this case, we simply concatenate the two sequences in a 5' to 3' order. The pipeline then proceeds with the prediction. For UNAFold, the output includes secondary structures and Gibbs free energy, while for Seqfold, only Gibbs free energy is available.

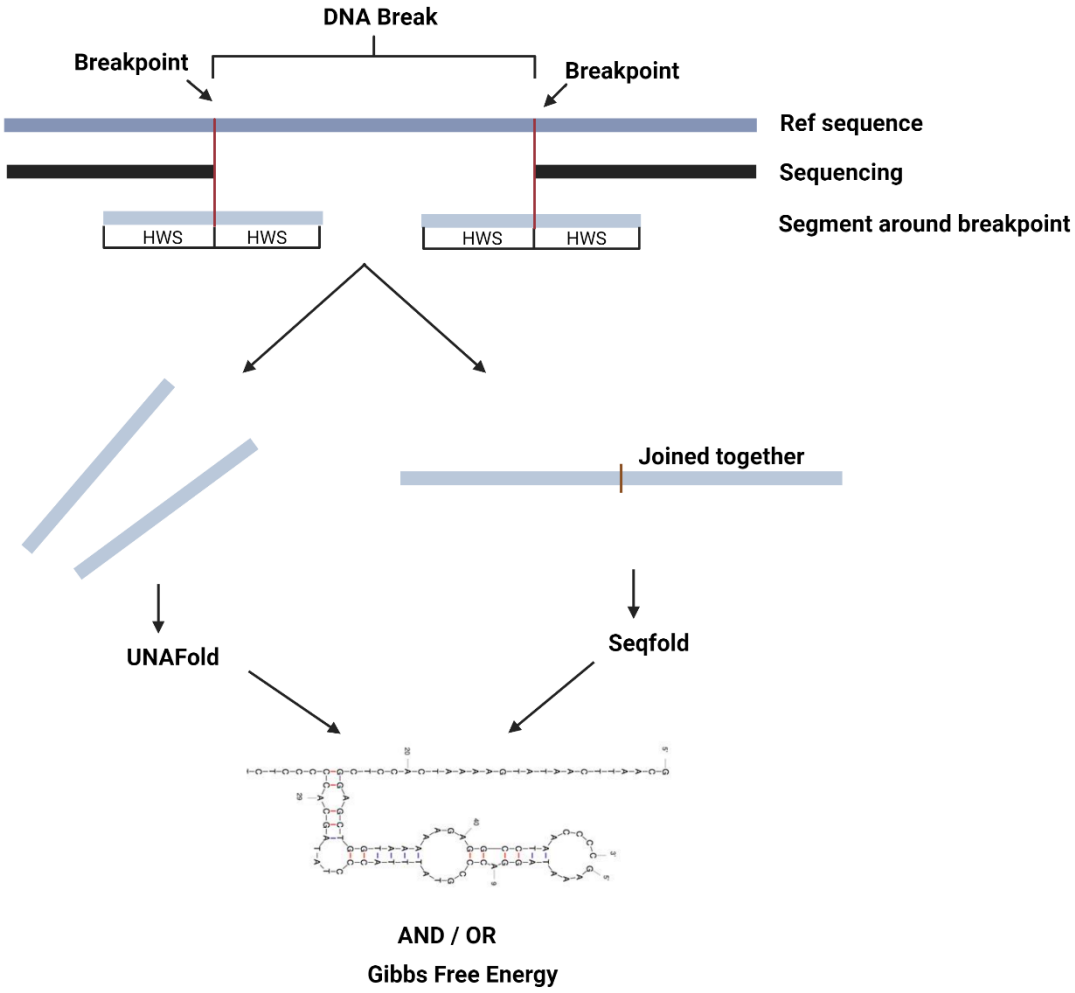

Figure 3.2-14 Free energy analysis pipeline

The upper panel of the illustration reveals that for each deletion, there exist two breakpoints. When aligning the segments of the mtDNA to the mtDNA reference sequence, two sequences around the breakpoints can be identified. The length of each sequence depends on the pre-selected window size, with the sequence around the breakpoint having a length equal to half the window size (HWS). After retaining the sequences, both sequences are inputted into a secondary structure prediction pipeline, such as UNAFold or Seqfold. UNAFold requires two sequences as input, whereas Seqfold can only process one sequence. In this case, we simply concatenate the two sequences in a 5' to 3' order. The pipeline then proceeds with the prediction. For UNAFold, the output includes secondary structures and Gibbs free energy, while for Seqfold, only Gibbs free energy is available.

A range of window sizes, varying from 5 to 49 with a gap of 1bp, and from 50 to 100 with a gap of 5bp, were employed in Seqfold to generate free energy predictions for sequences irrespective of the nature of the break points. We compared the difference in free energy between the PD and control groups by examining the absolute mean of the PD / Control ratio. The impact of the window sizes is shown in (Figure 3.2-15).

Free energies were then computed using the SeqFold pipeline, with three window sizes (25bp, 50bp, and 100bp) chosen for prediction. Overall, no significant difference was observed between PD and control deletions, however, PD deletions tended to have lower free energy when using window sizes of 25 and 50 bp. When grouping deletions based on the presence or absence of repeats, deletions with repeats in PD cases exhibited a significantly lower predicted free energy compared to controls in both the 50bp ($p = 0.012$*, t-test, Figure 3.2-17) and 25bp windows ($p = 0.02$*, t-test, Figure 3.2-18). There was no significant difference between PD and aged controls when using a window size of 100bp ($p = 0.082$, t-test, Figure 3.2-16). The comparison of deletions with repeats across three different window sizes is shown in the summary plot (Figure 3.2-19).

Figure 3.2-20 illustrates the stable secondary structure predicted for one PD deletion breakpoint. The predicted secondary structures of the 50bp sequences surrounding the deletions breakpoints for all mtDNA deletions from all PD cases that passes QC steps are provided at the end of this chapter.

Additionally, free energy prediction was carried out in PD DA SNpc neurons, serving as a disease control, using a window size of 50bp. Surprisingly, the deletion free energy of PD cholinergic PPN neurons was significantly lower than that of PD DA SNpc neurons ($p = 0.032$*, t-test). This may suggest potential differences in the molecular characteristics of deletion breakpoints between different neuronal types, based on their distinct chemistries. No difference was found between PD DA SNpc neurons and control PPN cholinergic neurons (Figure 3.2-21).

Furthermore, when grouping deletions based on the presence or absence of repeats (Figure 3.2-22) the deletion free energy of repeats in PD cholinergic neurons was significantly lower than that of PD DA SNpc neurons (p = 0.0045**, t-test).

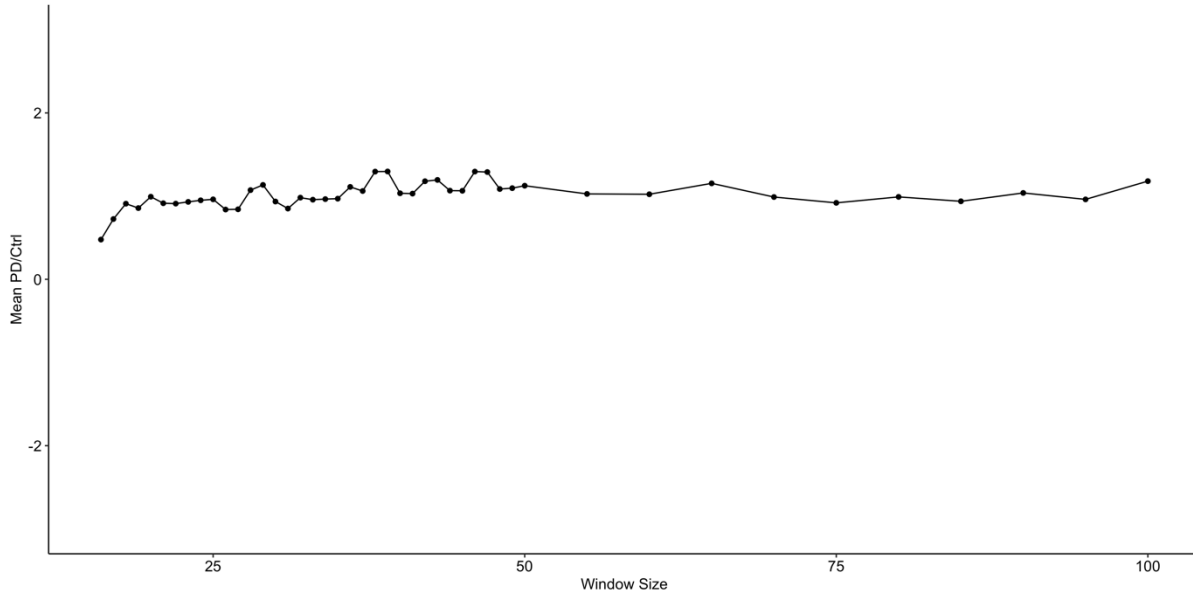

Figure 3.2-15 Window size comparison

Different window sizes were utilized to predict free energy, with the X-axis representing these varying window sizes and the Y-axis denoting the ratio between the absolute mean PD and mean control free energy. Across all window sizes tested, it appears that the choice of window size does not significantly affect the calculation of free energy when comparing between PD and control conditions.

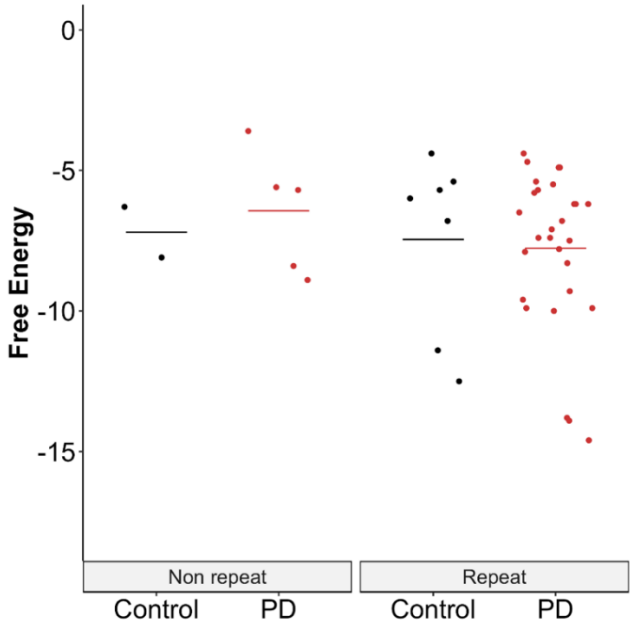

Figure 3.2-16 Free energy analysis in 100bp sequence around the breakpoint

Free energies were calculated using 25bp sequences around the deletion breakpoint. No clear difference has been found in deletions with non-repeat breakpoints (p = 0.6, t-test) and with repeat breakpoint as well (p = 0.82, t-test). Two tests were conducted, and the p-value threshold was adjusted to 0.025 after Bonferroni correction. The study involved 25 PPN cholinergic neurons from 6 control cases and 32 neurons from 7 individuals with PD. Black represents control cases, while red indicates PD cases.

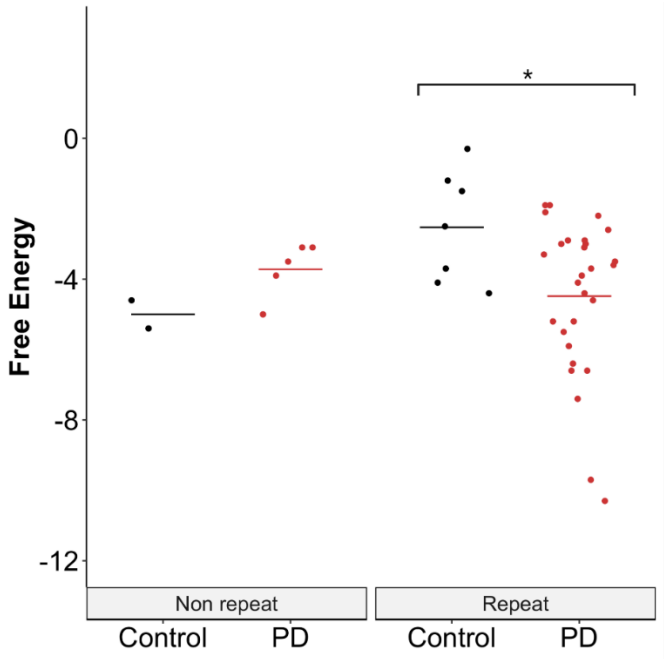

Figure 3.2-17 Free energy analysis in 50bp sequence around the breakpoint

Free energies were calculated using 50bp sequences around the deletion breakpoint. No clear difference has been found in deletions with non-repeat breakpoints. However, a significantly lower free energy was observed in deletion with repeats in the PD group (p = 0.012). Two tests were conducted, and the p-value threshold was adjusted to 0.025 after Bonferroni correction. The study involved 25 PPN cholinergic neurons from 6 control cases and 32 neurons from 7 individuals with PD. Black represents control cases, while red indicates PD cases.*

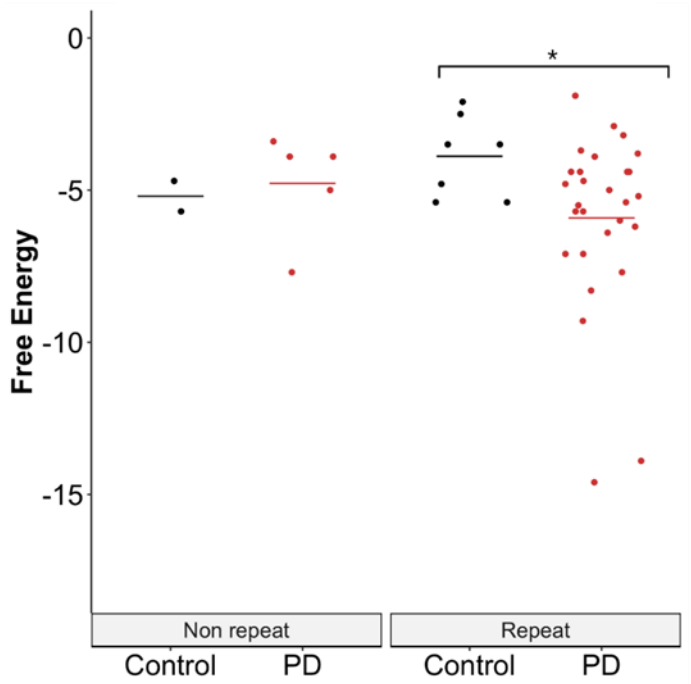

Figure 3.2-18 Free energy analysis in 25bp sequence around the breakpoint

Free energies were calculated using 25bp sequences around the deletion breakpoint. No clear difference has been found in deletions with non-repeat breakpoints. However, a significantly lower free energy was observed in deletion with repeats in the PD group (p = 0.02). Two tests were conducted, and the p-value threshold was adjusted to 0.025 after Bonferroni correction. The study involved 25 PPN cholinergic neurons from 6 control cases and 32 neurons from 7 individuals with PD. Black represents control cases, while red indicates PD cases.*

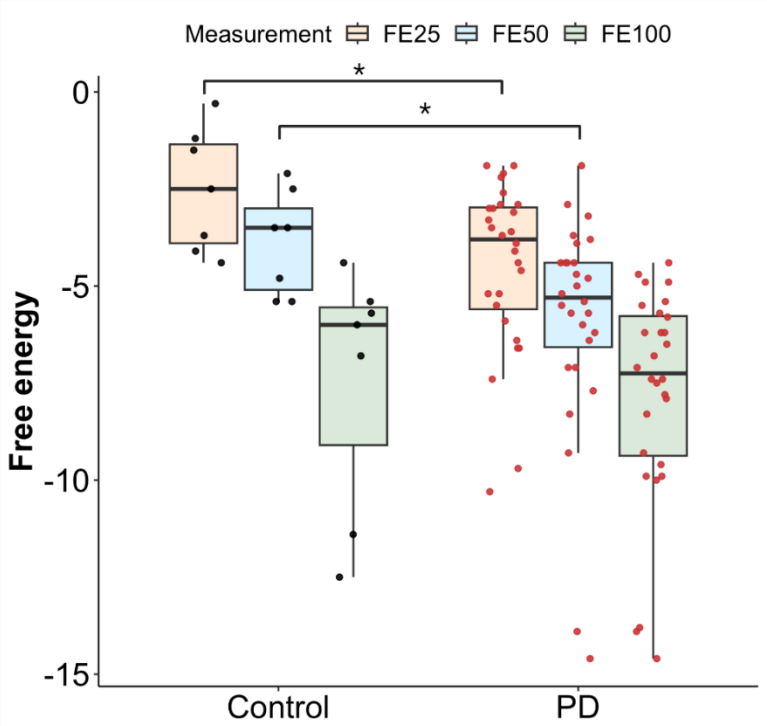

Figure 3.2-19 Free energy analysis of all repeat breakpoints

The free energy of all deletions with repeats is included in this graph. For each breakpoint, three measurements were taken: 25bp, 50bp and 100bp. The uncorrected t-test p value is shown on the graph to illustrate trends. No clear difference has been found in 100bp free energy analysis between the PD and the control groups. However, a significant difference was found in both 25bp (p = 0.02) and 50bp windows (p = 0.012). In both cases, PD neurons have deletion breakpoints with lower free energy compared to the aged control. Three tests were conducted, and the p-value threshold was adjusted to 0.017 after Bonferroni correction. The study involved 25 PPN cholinergic neurons from 6 control cases and 32 neurons from 7 individuals with PD. Black represents control cases, while red indicates PD cases.*

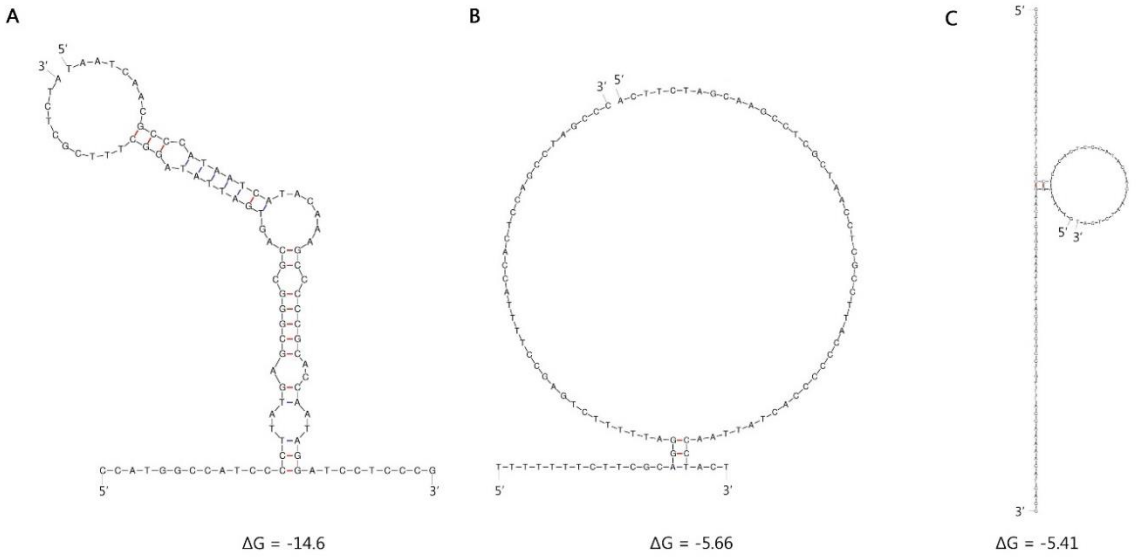

Figure 3.2-20 Free energy example figure panel generated from 50bp sequences around the deletion breakpoints

There are 3 common types of secondary structures (A: Hairpin structure; B: big head structure; C: long tail structure) were predicted by UNAFold pipeline as showed on this graph.

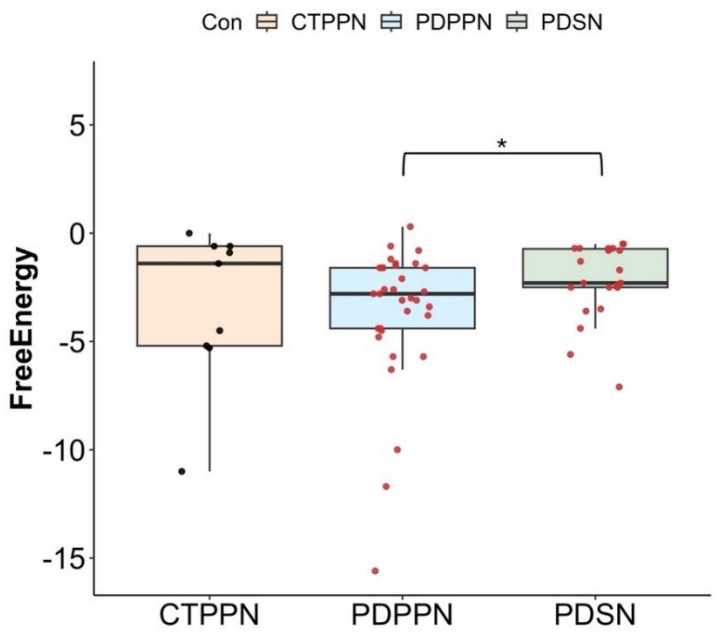

Figure 3.2-21 Free energy comparison among three groups

The graph compares the free energy among three groups: CTPPN, which includes all the deletions from PPN regions in aged controls; PDPPN, which includes all the deletions from PPN regions in PD cases; and PDSN, which includes all the deletions from SNpc regions, as mentioned in this paper. There is no significant difference in free energy between CTPPN and PDPPN groups, nor between the CTPPN and PDSN groups. Interestingly, the free energy in the PDSN group is significantly higher than in the PDPPN group (method = t-test, p = 0.032). Window size as 50bp. Black represents control cases, while red indicates PD cases.*

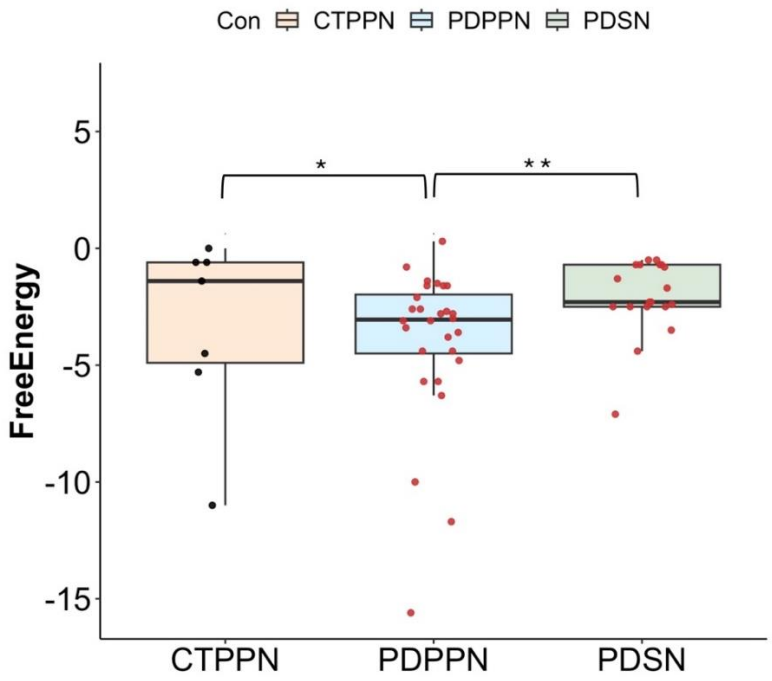

Figure 3.2-22 Comparison of free energy among three groups for deletions containing repeats

The graph compares the free energy of deletion with repeat around the breakpoints among three groups: CTPPN, which includes all the deletions from PPN regions in aged controls; PDPPN, which includes all the deletions from PPN regions in PD cases; and PDSN, which includes all the deletions from SNpc regions, as mentioned in this paper. There is not much difference in free energy between CTPPN and PDPPN groups, nor between the CTPPN and PDSN groups. Interestingly, the free energy in the PDSN group is significantly higher than in the PDPPN group (method = t-test, p = 0.0045). Window size as 50bp. Black represents control cases, while red indicates PD cases.*

3.2.6. *Correlations*

To investigate whether the number of deletions is associated with case parameters, a series of tests were conducted. In PD neurons, there was a trend suggesting that the number of deletions increases with post-mortem delay (PMD), but this correlation was

not statistically significant (R = 0.15, p = 0.38, Pearson's correlation). In control neurons, the trend was reversed, showing a decrease in deletions with increasing PMD, but again, the correlation was not significant (R = -0.29, p = 0.11, Pearson's correlation) (Figure 3.2-23-A). These results suggest that PMD does not strongly or systematically affect the number of deletions, supporting the conclusion that the observed differences in deletion levels in this study are primarily tissue-based.

No significant correlation was observed between age and the number of deletions (PD: R = -0.166, p = 0.357; Control: R = -0.136, p = 0.457, Pearson's correlation) (Figure 3.2-23-B), indicating that aging does not directly affect the number of deletions. This further supports the conclusion that differences in deletions are primarily associated with PD conditions. However, this finding contrasts with previous reports in dopaminergic neurons of SNpc, where the level of deletions was found to be positively correlated with age (Bender *et al.*, 2006; Dölle *et al.*, 2016). This discrepancy could be attributed to the differing chemical characteristics of two neuron types. Additionally, in PD neurons, females accumulated more deletions than males with PD (p = 0.041*, t-test) (Figure 3.2-24), whereas no such difference was observed in control neurons between the sex's (p = 0.75, t-test). This finding does not align with previous studies reporting a higher incidence of PD in males compared to females (Baldereschi *et al.*, 2000; Berg *et al.*, 2015).

When analyzing PD-related parameters, no correlation was found between Braak Lewy body stage and the number of deletions (R = 0.088, p = 0.63, Pearson's correlation), nor between disease duration and the number of deletions per neuron (R = -0.214, p = 0.33, Pearson's correlation) (Figure 3.2-23 -C,D). These results suggest that disease progression does not significantly influence the accumulation of mtDNA deletions. This finding aligns with a similar observation in SN neurons, where a study reported Lewy body positive neurons in PD condition had higher deletion levels comparing to aged control, while that difference was not observed in Lewy body negative neurons (Müller *et al.*, 2013), and this could reflect the multifactorial nature of PD progression. However, these findings should be interpreted with caution due to the limited sample size. Only 42 deletions passed the quality control steps and were analyzed, with data derived from only 13 patients (6 controls and 7 PD cases).

When group all the PD neurons based on PD duration and age at death. Individuals aged 70 years or young were classified as the lower age group, while those older than 70 years were classified as the higher age group. A PD duration of 10 years or less was defined as a short duration, and more than 10 years as long duration. Only one PD case fell within the lower age range (PD2), but this case lacked PD duration data. Therefore, neurons were grouped into two categories: 'HigherAge&Long' and 'HigherAge&Short'. Only four neurons were included in the 'HigherAge&Short' duration group, all originating from the same case, which limits the statistical power of this analysis. Nonetheless, a significantly higher number of deletions was observed in the 'HigherAge&Short' group compared to the 'HigherAge&Long' group ($p = 0.0029^*$, Wilcox test) (Figure 3.2-25)

Regarding the free energy data (Figure 3.2-26, Figure 3.2-27, Figure 3.2-28), no clear correlation was found between the age of the patients and the FE25, FE50, FE100 of deletions with repeats in either PD or control neurons (FE25: PD: $R = 0.3$, $p = 0.12$; Control: $R = -0.13$, $p = 0.79$ / FE50: PD: $R = 0.39$, $p = 0.06$; Control: $R = 0.39$, $p = 0.38$ / FE100: PD: $R = 0.23$, $p = 0.24$; Control: $R = -0.67$, $p = 0.10$, Pearson's correlation). In contrast, a significant positive correlation was observed between Braak Lewy body stage and the FE25/FE50 of deletions with repeats in PD neurons (FE25: $R = 0.44$, $p = 0.019$; FE50: $R = 0.46$, $p = 0.01$, Pearson's correlation). This correlation was not statistical when comparing FE100 ($R = 0.38$, $p = 0.05$, Pearson's correlation). Additionally, a significant negative correlation was observed between disease duration and FE25 ($R = -0.52$, $p = 0.04^*$, Pearson's correlation). Although the correlation between disease duration and FE50 or FE100 remained negative, it was not statistically significant (FE50: $R = -0.44$, $p = 0.085$/ FE100: $R = -0.44$, $p = 0.091$, Pearson's correlation). These results suggest that deletions with higher free energy, may contribute to earlier α-synuclein-specific pathology and as the disease progresses, mtDNA deletions may play an increasingly prominent role in the later stages of the disease.

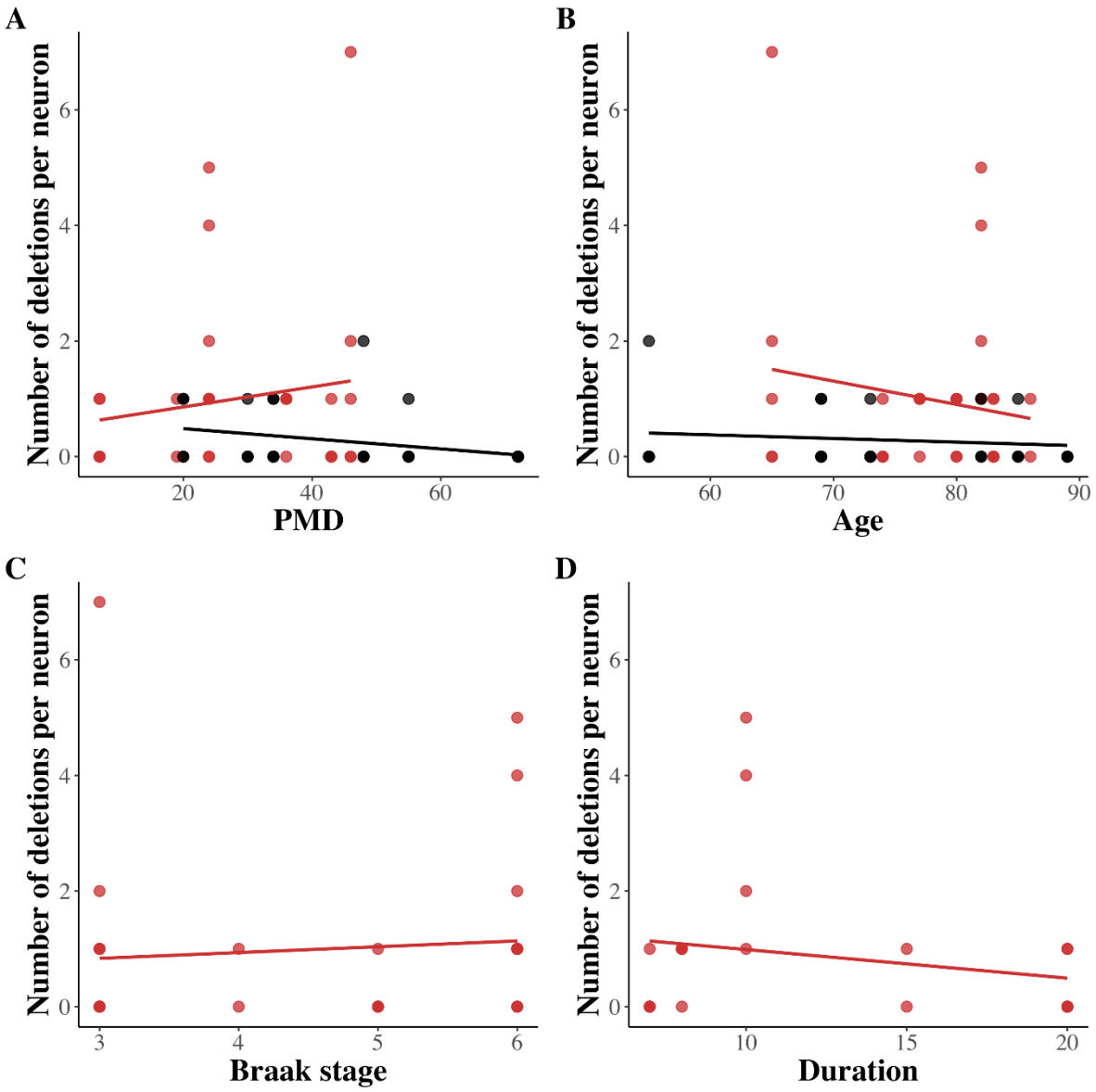

Figure 3.2-23 Correlation between the number of deletions per neuron and case parameters

These plots illustrate the correlation between the number of deletions per neuron and four case parameters: post-mortem delay (PMD), age, Braak stage, and disease duration. No significant correlation was observed between PMD and the number of deletions in either PD or control neurons (PD: R = 0.15, p = 0.38; Control: R = -0.29, p = 0.11, Pearson's correlation). Similarly, no correlation was found between age and the number of deletions (PD: R = -0.166, p = 0.357; Control: R = -0.136, p = 0.457, Pearson's correlation). Analyses of Braak stage and disease duration were conducted only for PD neurons, as these parameters are not applicable to control neurons. No correlation was identified between Braak Lewy body stage and the number of

deletions (R = 0.088, p = 0.63, Pearson's correlation), nor between disease duration and the number of deletions per neuron (R = -0.214, p = 0.33, Pearson's correlation). Red represents PD neurons, while black represents control neurons.

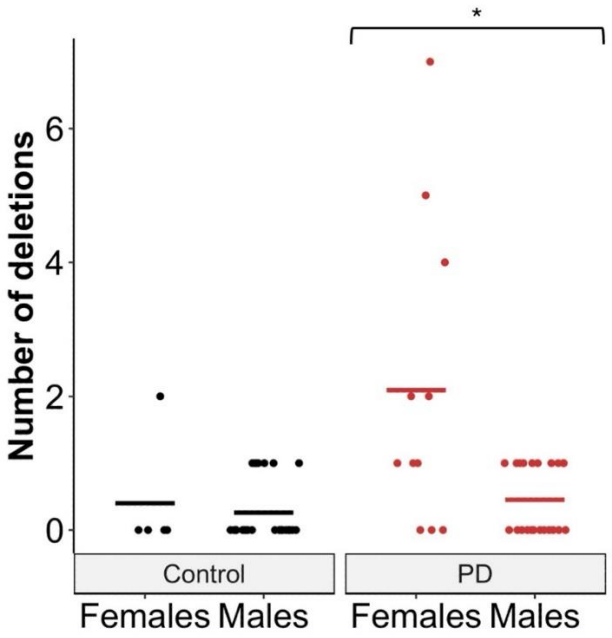

Figure 3.2-24 Number of deletions by sex

This plot shows no significant difference in the number of deletions per neuron between female and male control neurons (p = 0.75, t-test). However, PD female neurons accumulated significantly more deletions per neuron compared to PD male neurons (p = 0.041, t-test). Red represents PD neurons, and black represents control neurons.*

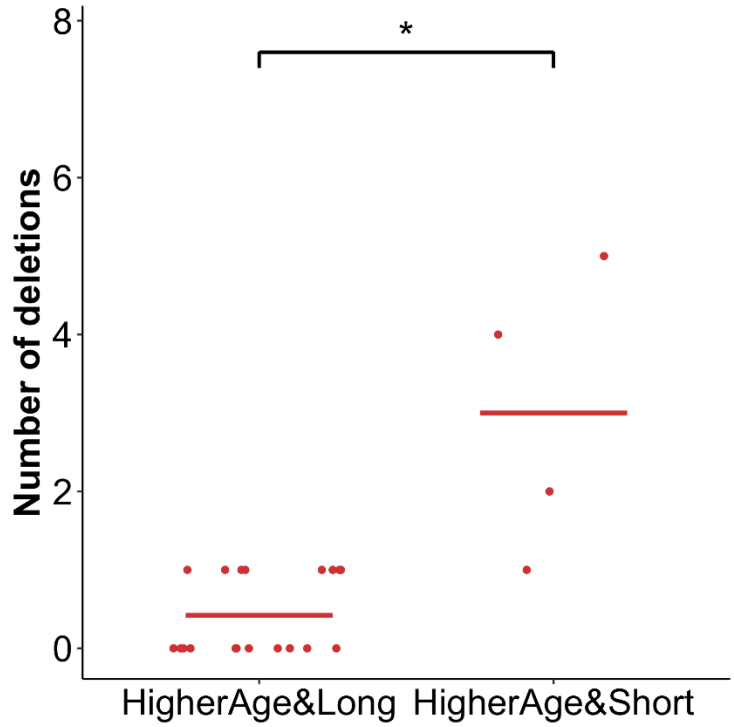

Figure 3.2-25 Number of deletions by PD duration and age at death

All PD neurons were grouped based on PD duration and age at death. Individuals aged 70 years or younger were classified as the lower age group, while those older than 70 years were classified as the higher age group. A PD duration of 10 years or less was defined as short duration, and more than 10 years as long duration. Only one PD case fell within the lower age range, but this case lacked PD duration data. Therefore, neurons were grouped into two categories: 'HigherAge&Long' and 'HigherAge&Short'. Only four neurons were included in the 'HigherAge&Short' group, all originating from the same case, which limited the statistical power of this analysis. Nonetheless, a significant higher number of deletions was observed in the 'HigherAge&Short' group compared to the 'HigherAge&Long' group (p = 0.0029, Wilcox test). The x-axis represents the two groups, and y-axis indicates the number of deletions per neuron.*

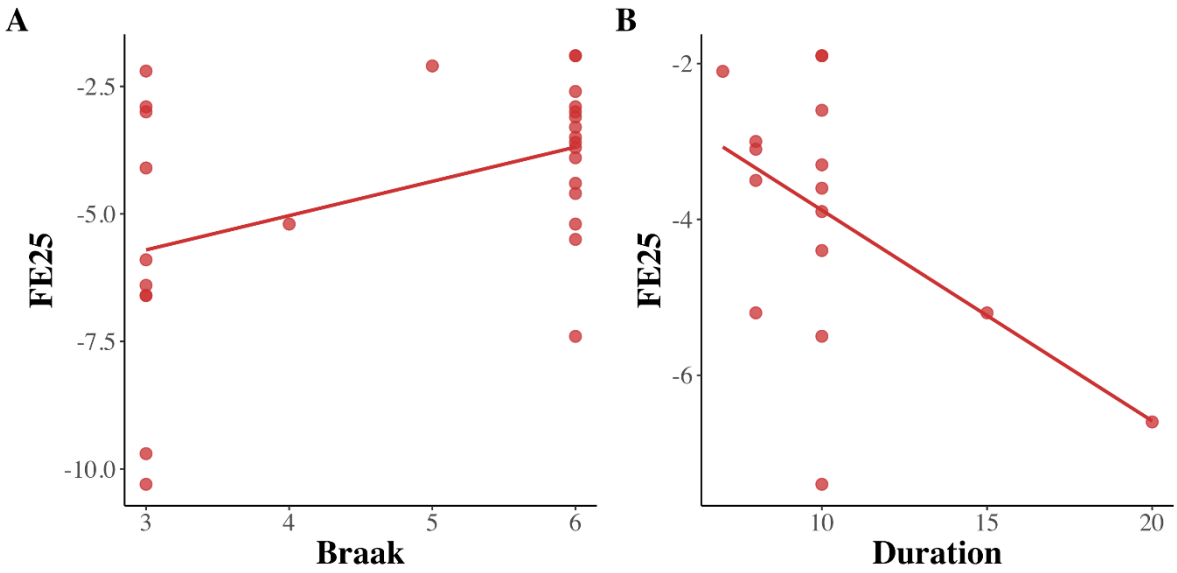

Figure 3.2-26 Correlation between FE25 of deletions with repeats and case parameters

These plots illustrate the correlation between the FE25 of deletions with repeats and two PD case parameters: Braak Lewy body stage and disease duration. A positive correlation was observed between Braak Lewy body stage and FE25 (R = 0.44, p = 0.019, Pearson's correlation), while a negative correlation was observed between disease duration and FE25 (R = -0.52, p = 0.04*, Pearson's correlation). Red represents PD neurons.*

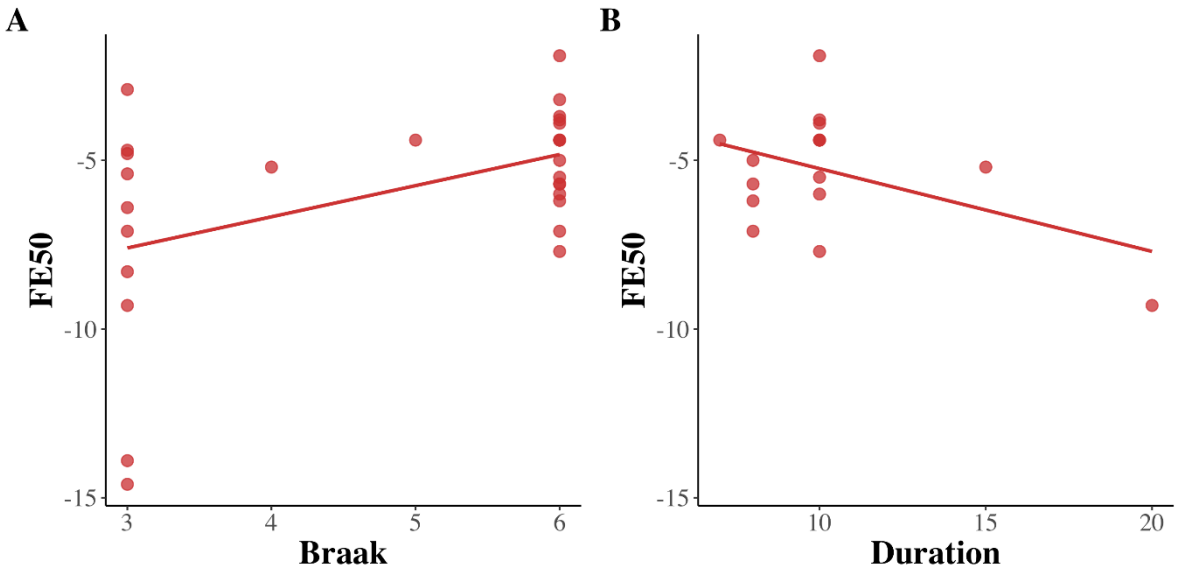

Figure 3.2-27 Correlation between FE50 of deletions with repeats and case parameters

These plots illustrate the correlation between the FE50 of deletions with repeats and two PD case parameters: Braak Lewy body stage and disease duration. A positive correlation was observed between Braak Lewy body stage and FE50 (R = 0.46, p = 0.01, Pearson's correlation). Conversely, a negative correlation was observed between disease duration and FE50; however, this correlation was not statistically significant (R = -0.44, p = 0.085, Pearson's correlation). Red represents PD neurons.*

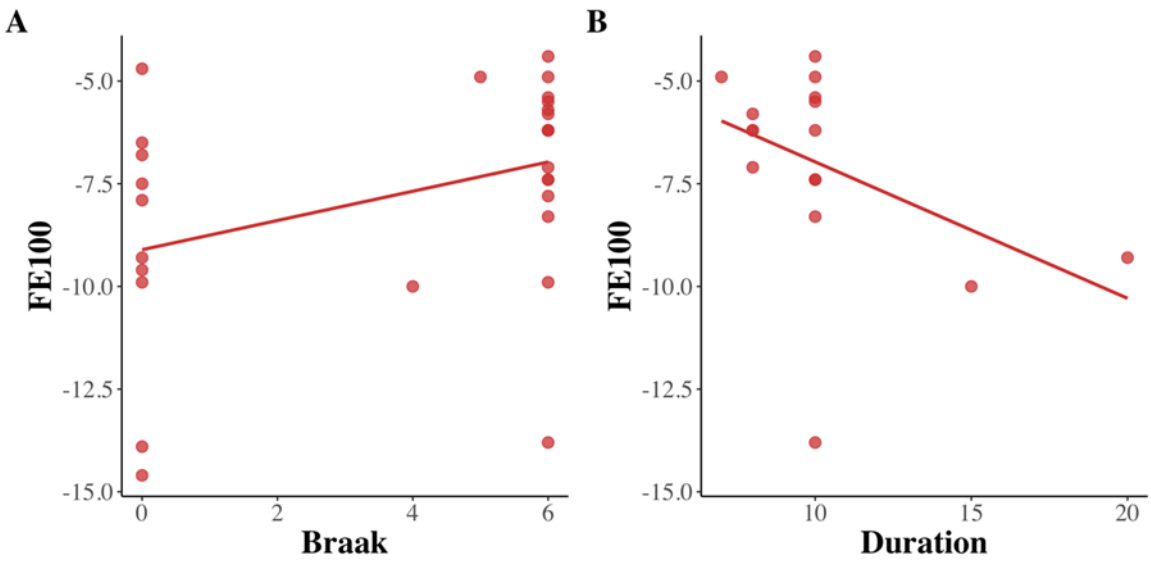

Figure 3.2-28 Correlation between FE100 of deletions with repeats and case parameters

These plots illustrate a weak correlation between the FE100 of deletions with repeats and two PD case parameters: Braak Lewy body stage and disease duration. A positive correlation was observed between Braak Lewy body stage and FE100 (R = 0.38, p = 0.05, Pearson's correlation). Conversely, a negative correlation was observed between disease duration and FE100; however, this correlation was not statistically significant (R = -0.44, p = 0.091, Pearson's correlation). Red represents PD neurons.

3.3. *Discussion*

The majority of mtDNA deletions detected in PPN cholinergic neurons are localized within the same region in both PD and control groups, spanning the major arc. Only a small portion (7.18%) of deletions were found within the minor arc, an observation that aligns with the deletions reported in MitoBreak (1.9%). This observation suggests a potential association between the genesis of these deletions and mtDNA replication errors, possibly stemming from the replication-slippage mechanism. This mechanism posits mis-annealing during the displacement of the H-strand throughout replication, or through copy-choice recombination.

Of particular interest is the observation that deletions in SNpc dopaminergic neurons from aged controls, PD cases, and POLG cases are also concentrated within a similar mtDNA region (within the major arc of mtDNA genome), despite variations in methodology and the distinct biochemical profiles of different neuronal types. Neurons vary in their susceptibility to oxidative stress. Dopaminergic neurons especially those in SNpc, are highly susceptible to oxidative stress due to intrinsic factors such as dopamine metabolism, which generates ROS and quinones, elevated iron levels, and calcium-dependent pacemaking activity that increase mitochondrial workload (Meiser, Weindl and Hiller, 2013; Duda, Pötschke and Liss, 2016). While in contrast, cholinergic neurons produce minimal oxidative by products during neurotransmission and maintain more stable calcium homeostasis and antioxidant defences (Naarala *et al.*, 1997). These results suggest that the mechanism leading to the formation of these deletions in this distinct patient groups and neuronal types across different brain regions is likely similar. Additionally, they indicate that the locations of mtDNA deletions are not primarily determined by the efficiency of mtDNA replication and repair, which is regulated by POLG enzyme activity. However, an observation suggests that the deletions reported in (Reeve *et al.*, 2008) are larger compared to the cholinergic deletions detected in this study. This could indicate a specific mechanism of deletions generation based on the distinct chemistries of neuronal types, or it may simply be due to differences in methodology and primer targeting. In 2008, deletion analysis in SNpc dopaminergic neurons was performed using primers that covered a 10Kb fragment spanning the major arc of the mtDNA, along with long-range PCR and BigDye terminator cycle sequencing. In contrast, this study used three sets of primers covering the entire mitochondrial genome, utilizing Illumina next-generation sequencing. This suggests that, potentially, the underlying mechanism governing mtDNA deletion generation exhibits similarity across different neuron types and conditions. Furthermore, it implies that alternative mechanisms may contribute to the heightened frequency of deletion generation or enhanced accumulation. Although the mechanism behind mtDNA deletion generation appears to be similar, the neuronal response in terms of mtDNA copy number differs, being downregulated in SNpc dopaminergic neurons and upregulated in PPN cholinergic neurons. This discrepancy may reflect differences in

downstream pathways responsible for handling or compensating for mtDNA damage. Chapter 5 will explore this aspect in more detail.

There are only two large deletions located within the minor arc. One spans the entire *MT-12S rRNA* region and part of the *MT-16S* rRNA region in a neuron from PD1, while the other occurs between *MT-ND1* and *MT-ND2* in a neuron from PD4. The *MT-ND1*, *MT-ND2*, and *MT-16S* rRNA sequences share the characteristic of being relatively conserved and lacking significant numbers of direct or tandem repeats, making them less prone to large-scale deletions (He *et al.*, 2002; McFadden *et al.*, 2004; Yang *et al.*, 2014). However, all these regions have the potential to form secondary structures, such as stem-loops and hairpins which are critical for ribosome function.

Of the five small deletions, two are located within the major arc. One was detected in Conrtol3 within the *MT-ATP6* region, and the other in PD7 within the *MT-CYB* region. Neither the *MT-ATP6* or the *MT-CYB* gene sequences are rich in repetitive contents. The remaining three small deletions, found in the minor arc, are all located within the heavy strand replication regions near the D-loop, which is rich in direct and inverted repeats and has been reported as a hotspot for mtDNA deletion breakpoints in numerous studies across various diseases (Wheelhouse *et al.*, 2005; Damas, Samuels, *et al.*, 2014; Fontana and Gahlon, 2020). These repeat sequences may increase the likelihood of replication errors, slippage, and recombination events, potentially leading to deletions. Based on the five small deletions detected, no clear common pattern emerges in the distribution of small deletions, suggesting that their locations may be randomly selected.

As no discernible difference was noted regarding the distribution of mtDNA deletions across various conditions, we opted to inspect the composition of each deletion breakpoint, which is regarded as a pivotal determinant in deletion generation. Subtle distinctions were identified between PD and control groups; PD deletion breakpoints exhibited a higher GC content. Given that GC bonds form three hydrogen bonds, rendering them more stable than AT bonds, which only form two hydrogen bonds, this prompted us to investigate whether PD tendencies lean towards forming more stable structures between the two sequences surrounding the breakpoint area. Stable secondary structure might lead to stalling of mtDNA replication by involving

perturbation in components responsible for replication fork progression and stability. This disruption increases the likelihood of replication slippage or misalignment events, facilitating the formation of large-scale deletions (Wanrooij and Falkenberg, 2010). A prior study briefly touched upon this aspect, and we adopted their methodology, incorporating secondary structure prediction and Gibbs free energy calculations to analyse the stability of deletion breakpoints (Nido *et al.*, 2018). Remarkably, PD deletion breakpoints appeared to form more stable secondary structures, requiring higher energy to disrupt them, particularly when incorporating both 25 and 50 base pairs of sequence around the breakpoint for prediction. No difference was observed when comparing the 100 base pairs of sequence between PD and aged control, suggesting that the secondary structure is confined to a small region near the breakpoint, contributing to the specificity of the deletion breakpoints.

These observations suggest that PD cases may exhibit specific molecular characteristics in their mtDNA sequences that increase the likelihood of forming secondary structures, which could disrupt replication and lead to deletions. This hypothesis is supported by our data, where a higher number of low-level deletions were detected in PD cases compared to the aged control group. Previous studies have reported an association between certain mitochondrial haplogroups (e.g., haplogroup J and super-haplogroup JT) and a reduced risk of developing PD (Gaweda-Walerych *et al.*, 2008; Hudson *et al.*, 2013). This suggests that even small changes in mtDNA may impact PD development, leading further possibility to hypothesis that specific mtDNA molecular characteristics influence the formation of deletions in PD.

SNpc DA neurons in PD cases were included in this comparative analysis. Unexpectedly, SNpc DA neurons exhibited higher free energy levels, indicating less stable secondary structures compared to PPN cholinergic PD neurons. When examining breakpoints with repeats, PPN cholinergic PD neurons showed lower Gibbs free energy levels than both PD SNpc cholinergic aged control neurons and PPN cholinergic control neurons. This may suggest potential differences in the molecular characteristics of deletion breakpoints between different neuronal types, driven by their distinct chemistries. These differences could lead to more stable secondary structures around the breakpoints, potentially promoting the accumulation of deletions.

In PD neurons, a higher number of accumulated deletions and a greater deletion load have been reported comparing to aged control. This finding aligns with previous literature on cholinergic neurons and supports the hypothesis that mtDNA deletions play a significant role in PD pathogenesis. These observations highlight the potential therapeutic relevance of targeting deletion heteroplasmy and the associated threshold effect. One such strategy is mitochondrial transfer. Mitochondria transfer between cells has been demonstrated through mechanisms such as tunnelling nanotubes. In the central nervous system, it has been reported that astrocytes can transfer mitochondria to damaged neurons, and damages neurons can transfer damaged mitochondria to astrocytes as well to help maintaining the function of neurons (Davis *et al.*, 2014; Hayakawa *et al.*, 2016). Promising results have been observed in vivo mice and rat models (Chang *et al.*, 2016; Shi *et al.*, 2017). However, several challenges remain. Identifying suitable mitochondrial donors is difficult, and there are ethical concerns, particularly regarding the alteration of an individual's mtDNA. Additionally, achieving precise targeting of affected neurons during mitochondrial transplantation is a major hurdle. Off-target effects are possible when mitochondria are introduced into tissues, raising further safety concerns. These limitations must be addressed before therapeutic mitochondrial transfer can be considered a viable treatment option.

The correlation analysis between the number of accumulated mtDNA deletions in individual neurons revealed no significant associations with PMD, age, Braak Lewy body stage, or disease duration. Although no clear correlation was found between disease progression and the mtDNA deletion levels, this does not rule out a potential role of mtDNA deletions in PD progression. The complexity and heterogeneity of PD may involve multiple underlying mechanisms, making it difficult to detect consistent patterns. Further studies including patients with more comparable disease stages may help clarify these associations. However, a significant difference was observed between male and female PD neurons, with female PD neurons exhibiting a higher accumulation of deletions. This difference was particularly evident in two female cases, PD2 and PD3, whereas another female case, PD6, did not show an increased number of deletions. This finding is intriguing and contrasts with previous literature reporting a higher incidence of PD in males compared to females (Pavon, Whitson and Okun, 2010;

Moisan *et al.*, 2016). It is possible that the observed differences in mtDNA deletions contribute to the sex-based variations in PD incidence like toxicant exposure or differences in oestrogen levels (Zolkipli-Cunningham and Falk, 2017; Godschalk *et al.*, 2018; Shaw, 2021), warranting further investigation into the role of mtDNA deletions in disease susceptibility. The lower number of mtDNA deletion observed in neurons captured from cases with higher age and long disease duration compared to those from lower age and short disease duration, is an interesting finding. It may suggest that the accumulation of mtDNA deletions contributes to faster disease progression or earlier death. However, as all neurons in the lower age and short duration group came from a single patient, the ability to draw broader conclusion is limited.

An intriguing correlation was observed regarding free energy. Both FE25 and FE50 demonstrated a positive correlation with Braak Lewy body stage, while FE25 showed a negative correlation with disease duration, and FE50 exhibited a trend towards a similar negative correlation. Notably, these correlations weakened when analysed with FE100. These findings further suggest that the relationship between free energy and PD is localised to a small region near the mtDNA deletion breakpoints. Additionally, they imply that as the disease progresses, mtDNA sequences may become increasingly prone to forming secondary structures, although the accumulation of Lewy body pathology may interfere with this process.

There are, however, some limitations to this research. First, only postmortem human brain tissue was used. PPN neurons that underwent severe pathological changes may have already been lost during the progression of the disease, and the remaining neurons may not be fully representative. Also, only a limited number of neurons can be collected, due to the challenge of obtaining high-quality DNA from postmortem tissue and the high costs associated with deep sequencing (Nido *et al.*, 2018). Additionally, PCR was used in the library preparation process before sequencing, which may have affected the accuracy of the heteroplasmy levels of detected deletions and potentially amplified contaminant sequences. However, a strict set of in-house quality control steps was implemented to mitigate these issues. Lastly, deletions detected via Illumina sequencing were compared with those identified using different methodologies. These methodological differences may reduce the reliability of the comparison. However, as

the aim of this research is to analyse the differences between PD and the aged control neurons of the same type and from the same area, despite the aforementioned limitations, a confident comparison can still be made as long as the same methodology was consistently applied.

Chapter 4. mtDNA point mutations

4.1. *Aims*

The aim of this chapter is to analyse point mutation data generated using mtDNA-Server from Illumina deep sequencing. Following a series of rigorous quality control steps, the analysis focuses on several key aspects: the burden of point mutations in single neurons, the regional variation in point mutation burden, the characteristics of detected point mutations, their genomic distribution, their potential impact on neuronal function, and their correlation with specific cases.

4.2. *Results*

4.2.1. *Post-bioinformatic quality control*

The detection of point mutations was conducted using mtDNA-Server (Weissensteiner *et al.*, 2016) https://mitoverse.readthedocs.io/mtdna-server/mtdna-server/), as described in the methodology section (2.3.3 Identifying mtDNA point mutations using mtDNA server and quality control.). The pipeline initially detected a total of 20,488 point, and several quality control steps were implemented to ensure the reliability and relevance of the detected mutations for this research.

The first quality control step ensured that there was no strand bias, meaning that the coverage of point mutations from both the 5' to 3' and the 3' to 5' direction was above 20 reads per base pair. Following this step, the number of point mutations was reduced from 20,488 to 3,591. This significant reduction compared to other quality control stages may reflect the limited sensitivity of the pipeline in detecting true variants or could be attributable to the sequencing methodology employed. Specifically, the Illumina sequencing platform is known to introduce biases, leading to underrepresentation of GC-rich and AT-rich regions in sequencing results (Benjamini and Speed, 2012). Two neurons could not be linked back to original patient data and were therefore excluded from the analysis. 3,491 point mutations. The third step

ensured that all three mtDNA fragments were present without any missing fragments, reducing the number of point mutations to 3,400. The fourth step involved checking for contamination from other mtDNA haplogroups. Ensuring the dataset is free from contamination is critical, as unfiltered contamination can lead to erroneous conclusions (Budowle *et al.*, 2004; Bandelt, van Oven and Salas, 2012). Seven neurons showed varying levels of contamination, with 3 from the control group and from the PD group. Among these, only one neuron exhibited a high contamination level (44.7%) and was subsequently excluded from the analysis. Contamination levels in the remaining neurons were below 5.2%. Point mutations with heteroplasmy levels lower than contamination threshold of each neuron was excluded due to the potential influence of contamination. In contrast, point mutations with heteroplasmy levels exceeding the contamination threshold of each neuron were retained, as the higher levels are unlikely to be impacted by contamination.

The fifth quality control step excluded point mutations with a heteroplasmy level below 0.1%, resulting in a total of 2,909 point mutations. The mean sequencing depth was 80,223 ± 16,229 reads for control neurons and 75,623 ± 9,752 reads for PD neurons (Table 4.2-1). A heteroplasmy level of 0.1% corresponds to a copy number in the tens of copies, depending on the total mtDNA content in the sample, and is considered a reasonable threshold for samples subjected to PCR amplification. This threshold is widely accepted and has been applied in several published studies (Just, Irwin and Parson, 2015; Dölle *et al.*, 2016) and is consistent with the cutoff used in the deletion chapter (Chapter 3.2.1). The final quality control step ensured that point mutations were not inherited by verifying that each mutation was detected only once across neurons from a single individual. This step resulted in a total of 2,245 point mutations retained for analysis.

Of the 65 neurons analysed, 21 (32.3%) exhibited mid and high deletion loads, exceeding 1%. Detailed information on these deletions is provided in the (Chapter 3.2.2). Among these 21 neurons, 5 were from the 32 control neurons, while 16 were from the 33 PD neurons. The presence of neurons with above 1% deletion load of large size deletions may influence the number of point mutations or the point mutation load observed in each neuron. A series of correlation tests were run. No correlation was

observed between the mtDNA deletion load and the number of point mutations per neuron in both control and PD cases (R = 0.30, p = 0.15; R = 0.11, p = 0.58; respectively, Pearson's correlation, Figure 4.2-1). Similar observation was observed when calculating the correlation between mtDNA deletion load and the point mutation load per neuron. No correlation was observed in control and PD cases (R =0.36, p = 0.084; R = 0.167, p = 0.40; respectively, Pearson's correlation, Figure 4.2-2).

Although no clear correlation was observed between either the number of point mutations or the point mutation load and deletion load within a neuron, high deletion load may have some influence on point mutations, as the deleted sequence may also contain some point mutations. To minimise the impact of deletions on point mutations while still including a substantial amount of data, two datasets were used for further analysis: one including all point mutations, and another after filtering out point mutations in neurons with medium or high deletion loads.

Sample	**Case**	**Mean depth (Reads)**	**Sample**	**Case**	**Mean depth (Reads)**
6	Control1	67964	17	PD1	67928
10	Control1	96626	18	PD1	67381
11	Control1	65800	19	PD1	67811
39	Control1	101157	32	PD1	80099
45	Control1	81233	48	PD1	70344
3	Control2	69543	49	PD1	63665
4	Control2	61915	52	PD1	87848
42	Control2	73529	20	PD2	65894
43	Control2	64961	21	PD2	74412
61	Control2	95400	22	PD2	76863
12	Control3	55770	50	PD2	81030
24	Control3	54753	59	PD2	62432
41	Control3	113253	14	PD3	88951

55	Control3	89825	16	PD3	82103
56	Control3	108004	40	PD3	83129
1	Control4	76179	46	PD3	64788
2	Control4	61620	23	PD4	73573
7	Control4	73013	25	PD4	77247
8	Control4	78481	26	PD4	85403
57	Control4	84538	27	PD4	72614
5	Control5	62784	51	PD4	87243
9	Control5	70331	29	PD5	77173
36	Control5	86088	30	PD5	88688
62	Control5	105056	31	PD5	82647
63	Control5	88315	53	PD5	66000
64	Control5	92965	60	PD5	45750
15	Control6	71446	28	PD6	82523
34	Control6	75462	33	PD6	86675
35	Control6	70226	13	PD7	71878
54	Control6	84035	44	PD7	74833
65	Control6	75289	47	PD7	70127
66	Control6	111585	58	PD7	85481
			68	PD7	83055
80,223 ± 16229			**75,623 ± 9752**		

Table 4.2-1 Average depth of coverage in sequenced neuron

This table presents the depth of coverage, as reported by the mtDNA-Server, for each sequenced neuron, grouped by patient case. The average sequencing depth for both control and PD groups was calculated and is displayed in the bottom row of the table. The average coverage for the control group was 80,223 ± 16229, while for the PD group it was 75,623 ± 9752.

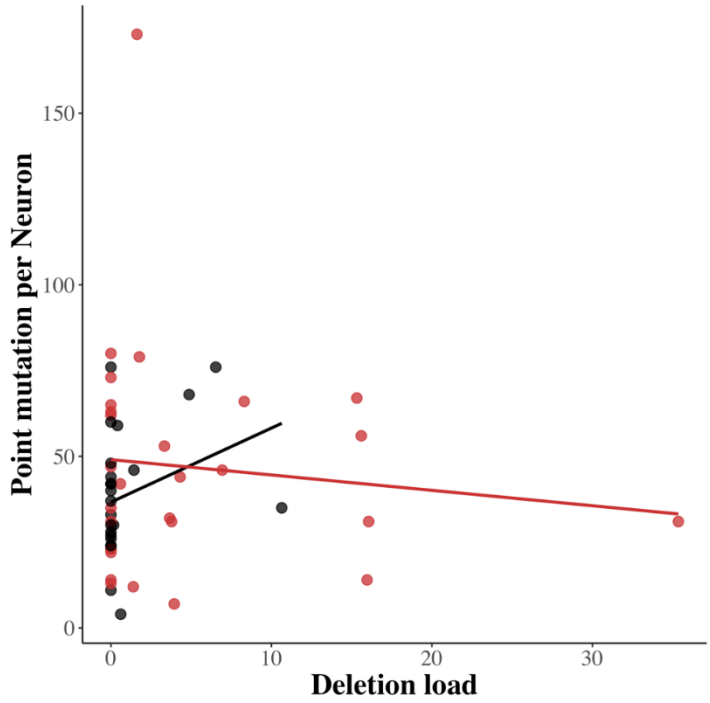

Figure 4.2-1 No correlation between mtDNA deletion load and the number of point mutations

This figure shows no correlation between mtDNA deletion load and the number of point mutations per neuron both in control and in PD (R = 0.30, p = 0.15; R = 0.11, p = 0.58; respectively, Pearson's correlation). Red represents PD neurons, while black represent control neurons.

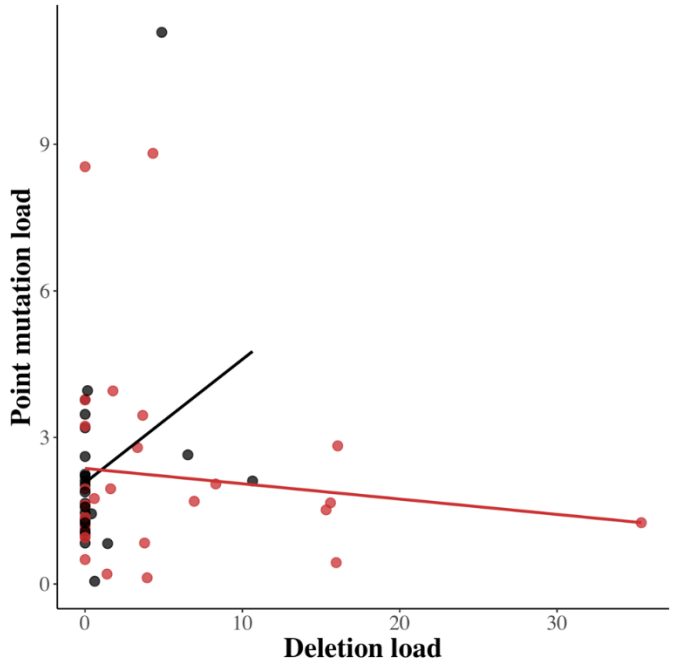

Figure 4.2-2 No correlation between mtDNA deletion load and point mutation load

This plot shows the correlation between mtDNA deletion load and point mutation load. There was no corelation observed between deletion load and point mutation load in both control and PD neurons (R =0.36, p = 0.084; R = 0.167, p = 0.40; respectively, Pearson's correlation). Red represents PD neurons, while black represents control neurons.

4.2.2. *Point mutation burden in single neurons*

Somatic variants are the primary focus of this project, while inherited variants were also analysed to ensure that no potentially pathogenic mutations were overlooked. All inherited variants detected across the cases are listed in Table 4.2-2. These variants are well-distributed across the mitochondrial genome, with no definitively pathogenic mtDNA mutations identified. This is likely due to germline selection, which eliminates strongly deleterious variants before birth.

The analysis of somatic point mutation burden and total mutation load was the initial focus when comparing different conditions. Point mutation burden refers to the total

number of mutations present within a single neuron, whereas total mutation load is calculated as the sum of the heteroplasmy levels of all point mutations. Although the threshold may differ between individual variants and the total mutation load may have limited biological interpretability, it can still provide a general overview of point mutation accumulation. Furthermore, the effect of a single variant can vary depending on the haplogroup context (Queen *et al.*, 2017; Schaefer *et al.*, 2022).

Investigating differences in point mutation burden and total mutation load between individual PPN cholinergic neurons from PD patients and control groups offers valuable insights into the role of mutations in disease pathology. Elevated point mutation burden and total mutation load could indicate an increased susceptibility to mitochondrial dysfunction, as a greater number of mutations may significantly impair mitochondrial function (Goto, Nonaka and Horai, 1990; Taylor *et al.*, 2003; Coxhead *et al.*, 2016).

When including all point mutations without filtering out due to deletion load, no statistically significant difference between two groups was evident, though PD neuron (46.9 ± 32.8) seems to accumulate more point mutations than aged control (38.9 ± 18.6) ($p = 0.28$, t-test, Figure 4.2-3-A). After grouping all point mutations by heteroplasmy level (0.1-1% as low level, 1-10% as middle level, and above 10% as high heteroplasmy level), we found that, on average, control neurons had 1.75 ± 1.75 low heteroplasmy point mutations (0.1-1%), while PD neurons had 4.41 ± 9.57, suggesting that PD neurons may accumulate more low-level point mutations. However, this difference was not statistically significant ($p = 0.28$, t-test). For middle heteroplasmy level point mutations (1-10%), control neurons had an average of 34.1 ± 19.2, compared to 41.6 ± 28.0 in PD neurons. Again, PD neurons showed an increase in middle-level point mutations, though this difference was also not significant ($p = 0.26$, t-test). For high-level point mutations, control neurons had an average of 5 ± 4.03, while PD neurons had 4.06 ± 4.89, with no significant difference observed between the two conditions ($p = 0.52$, t-test, Figure 4.2-4-A). However, an interesting observation has been spotted as the number of middle levels heteroplasmy level point mutations accumulates the most comparing to low and high level heteroplasmy level point mutations.

Regarding the point mutation load per neuron, no significant difference was observed between PD and aged control groups when including all point mutations. PD neurons

had a higher average point mutation load (4.68 ± 2.31) compared to aged controls (4.27 ± 2.17), but this difference was not statistically significant (p = 0.52, t-test). When point mutation load was grouped by patient, no clear outliers were observed, with all patients displaying similar levels of point mutation load (Figure 4.2-5-A).

After excluding all neurons with deletion load above 1%, still no difference was observed between two groups (p = 0.27, t-test; Figure 4.2-3-B) when comparing the number of point mutation per neuron. PD neurons still accumulate a higher number of point mutations (43.8 ± 22.9) than the controls (35.4 ± 16.9). When grouping point mutations by heteroplasmy levels, control neurons had an average of 1.17 ± 0.41 low heteroplasmy point mutations (0.1-1%), compared to 2.75 ± 2.19 in PD neurons. While PD neurons exhibited an increase in low level point mutations, the difference was not statistically significant, with the result approaching but not reaching the 0.05 threshold (p = 0.082, t-test). For middle heteroplasmy level point mutations (1-10%), control neurons had an average of 31.0 ± 18.0, while PD neurons had 39.4 ± 22.7, with no significant difference (p = 0.28, t-test). For high-level point mutations, control neurons had an average of 5 ± 4.05, while PD neurons had 3.6 ± 3.69, while this result was close to the 0.05 threshold there was no significant difference observed between the conditions (p = 0.38, t-test, Figure 4.2-4). As for point mutation load per neuron, PD neurons showed a higher point mutation load (2.17 ± 2.12) than aged controls (1.93 ± 1.01), though the difference remained statistically insignificant (p = 0.71, t-test). In addition, no clear differences were observed among different patients within the same condition (Figure 4.2-5-B).

Case	Haplogroup	Inherited mutations
Control1	U5b2a1a1	1N 73G 150T 263G 750G 896G 1438G 1721T 2706G 3106N 3124Y 3197C 4732G 4769G 7028T 7403N 7768G 8860G 9477A 9545N 9550N 11467G 11719A 12308G 12372A 13057N 13617C 13637G 13681N 14182C 14424N 14766T 15326G 15511C 16192T 16311C
Control2	H3b1b1	153G 263G 750G 1438G 2581G 3106N 3119N 3124Y 4769G 5147A 6776C 7403N 8860G 9545N 9550N 10322C 13057N 13681N 13813A 14424N 15326G 16111T 16129A 16256T 16519C
Control3	H24a	1N 263G 750G 1438G 3106N 3333T 4769G 7403N 8157Y 8860G 15326G 15383C 16362C 16519C
Control4	H3b	263G 750G 1438G 4769G 6776C 8860G 15326G 16129A 7403N 9545N 9550N 16519C
Control5	V	1N 72C 195C 263G 750G 1438G 2706G 3119M 3124Y 4580A 4769G 7028T 8860G 9560N 10490Y 13057N 15326G 15449C 15904T 16153A 16298C

Control6	K2b1a1a	1N 73G 146C 263G 750G 1438G 1811G 2217T 2706G 3106N 3480G 4769G 5231A 6221C 7028T 7403M 8533A 8860G 9055A 9698C 9716C 10550G 11299C 11467G 11719A 11869A 12308G 12372A 13057N 13135A 13681N 14037G 14167T 14766T 14798C 15326G 16187T 16222T 16224C 16270T 16311C 16519C
PD1	X2c1a	1N 73G 153G 195C 225A 227G 263G 750G 1438G 1719A 2706G 3106N 4769G 6221C 6371T 7028T 7403N 8705C 8860G 9545N 9550N 9560N 11719A 12705T 13057N 13681N 13966G 14470C 14766T 15326G 16108T 16182M 16183C 16189C 16223T 16255A 16278T 16519C
PD2	W1	73G 119C 189G 195C 204C 207A 263G 709A 750G 1243C 1438G 2706G 3106N 3119N 3124N 3505G 4769G 5046A 5460A 7028T 7403N 7864T 8251A 8860G 8994A 9254N 9541Y 9630A 11674Y 11719A 11776Y 11947G 12285N 12414N 12705N 13057N 13812N 14198N 14766T 15326G 15884C 16223T 16292T 16320T 16519C
PD3	J1b1a1a	73G 242T 263G 295T 462T 489C 595A 750G 1438G 2158C 2706G 3010A 3106N 3119N 3124Y 4216C 4769G 5460A 5463T 6911C 7028T 7403N 8269A 8545A 8557A 8745G 8860G 9545N 9550N 10398G 11251G 11719A 12007A 12612G 13708A 13879C 14766T 15326G 15452A 16069T 16126C 16145A 16172C 16192T 16222T 16261T 16519C

PD4	R6b	1N 73G 195C 246C 263G 750G 1438G 2706G 3106N 4769G 4991A 7028T 7364G 7403N 7984A 8860G 9254G 9545N 9550N 9560N 11719A 11776C 12285C 13057N 13681N 13812C 14766T 15326G 15431N 15884A 16066G 16126C 16179T 16245T 16266T 16278T 16362C 16519C
PD5	H1g1	1N 72N 263G 750G 1438G 3010A 3119N 3124Y 4769G 8602C 8860G 13057N 14212C 15326G 16189C 16519C
PD6	H1af1b	1N 73G 263G 750G 1438G 3010A 3106N 4769G 7403N 8860G 10437N 13057N 15326G 15646T 16129A 16357C
PD7	J1b1a1a	73G 242T 263G 295T 462T 489C 595A 750G 1438G 2158C 2706G 3010A 3106N 3119N 3124Y 4216C 4769G 5460A 5463T 6911C 7028T 7403N 8269A 8545A 8557A 8745G 8860G 9545N 9550N 10398G 11251G 11719A 12007A 12612G 13708A 13879C 14766T 15326G 15452A 16069T 16126C 16145A 16172C 16192T 16222T 16261T 16519C

Table 4.2-2 Inherited point mutations in each case

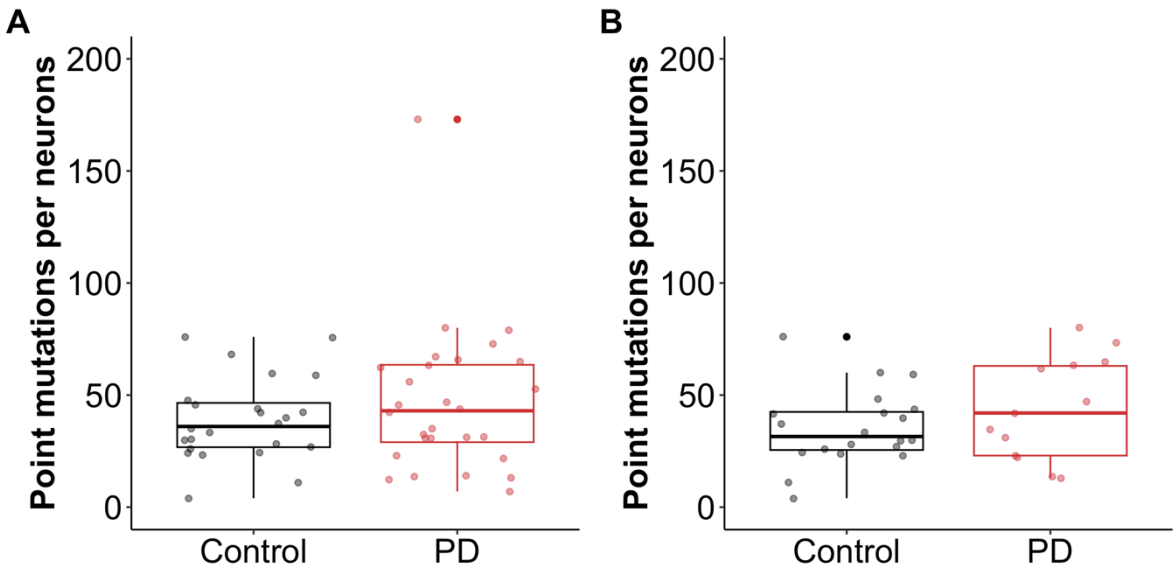

Figure 4.2-3 The number of point mutation per neuron

A: More point mutations were detected in individual neurons from PD cases (46.9 ± 32.8) compared to the aged control (38.9 ± 18.6), though this difference was not statistically significant (p = 0.28, t-test). B: This plot shows only point mutations in neurons with deletion loads below 1% heteroplasmy. Again, more point mutations were detected in single neurons from PD cases (43.8 ± 22.9) than in the aged control (35.4 ± 16.9), but the difference remained statistically insignificant (p = 0.27, t-test). Black represents neurons from control cases, while red represents neurons from PD cases.

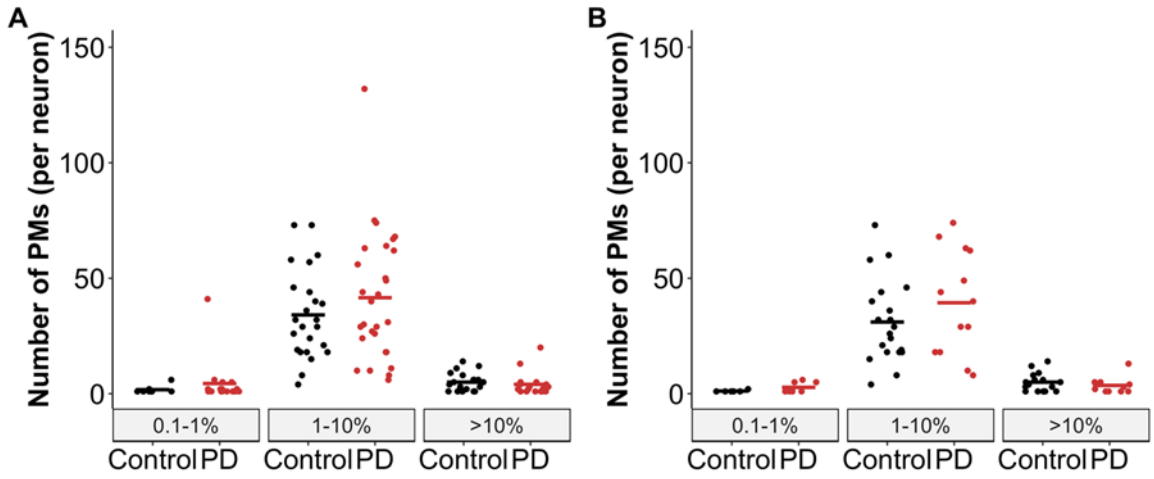

Figure 4.2-4 The number of point mutations in different heteroplasmy levels

These plots compare the number of point mutations in each neuron across different heteroplasmy levels (0.1-1% as low level, 1-10% as middle level, and above 10% as high level). Graph A shows that when including all point mutations, no significant differences were observed in the accumulation of point mutations at any level. PD neurons appeared to accumulate more low- and middle-level point mutations but fewer high-level point mutations; however, none of these comparisons were statistically significant (p = 0.28, 0.26, 0.52; t-test, respectively). Graph B shows similar results after excluding neurons with a deletion load above 1%. PD neurons displayed more point mutations at both low and middle heteroplasmy levels (p = 0.082, p = 0.28; t-test), while fewer high-level point mutations were observed in PD neurons compared to aged controls (p = 0.38, t-test). Black represents neurons from control cases, while red represents neurons from PD cases.

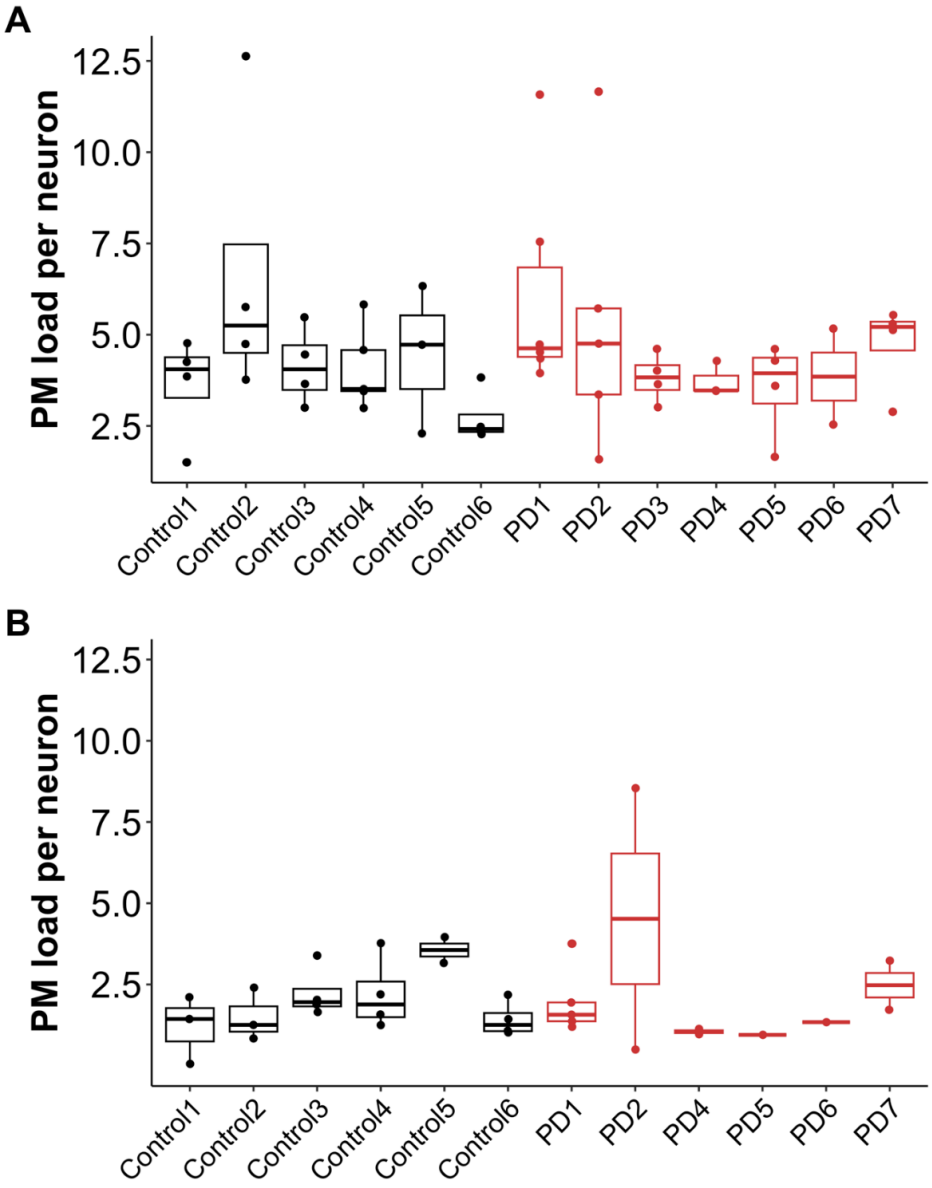

Figure 4.2-5 Point mutation load of each neuron

This plot illustrates the point mutation load per neuron across different cases. Graph A, which included all point mutations, shows that the average point mutation load in control cases was 4.27 ± 2.17, while in PD cases it was higher at 4.68 ± 2.31. However, no significant difference was observed between PD and control cases (p = 0.52, t-test). Graph B, which only shows point mutations detected in neurons with a deletion load below 1%, indicates that the average point mutation load in control cases was 1.93 ± 1.01, while in PD cases it was higher at 2.17 ± 2.12. Again, no significant difference was observed (p = 0.71, t-test). Neurons from control cases are represented in black, while neurons from PD cases are shown in red.

4.2.3. *Point mutation burden in different regions*

MtDNA point mutations in coding regions for each OXPHOS complex were analysed separately. When including all point mutations, more mutations were observed in complex I (10.4 ± 10.7) and complex IV (4.16 ± 2.82) in PD cases compared to the aged controls (I: 7.58 ± 4.21; IV: 4.13 ± 2.51), though no significant differences were observed ($p = 0.42$ and 0.88, respectively; t-test). Conversely, control cases exhibited more point mutations in complex III (2.14 ± 1.35) and complex V (2.31 ± 1.08) compared to PD neurons (III: 2.04 ± 1.19; V: 2.11 ± 1.05), but again, these differences were not significant ($p = 0.89$ and 0.57, respectively; t-test) (Figure 4.2-6-A).

The higher point mutation counts in complex I may not necessarily reflect a greater tendency for mutation accumulation or vulnerability; rather, it could simply be due to the larger coding region of complex I compared to the other complexes. To account for this, the number of point mutations was normalised by the length of each complex. After normalisation, similar results were observed, with more point mutations in complex I (0.0019 ± 0.00195) and complex IV in PD cases (0.00188 ± 0.00127) compared to aged controls (I: 0.00138 ± 0.00076; IV: 0.00186 ± 0.00113), though the differences were not significant ($p = 0.2$ and 0.92, respectively; t-test). Similarly, more point mutations were detected in complex III (0.00188 ± 0.00118) and complex V (0.00249 ± 0.00116) in the aged control group compared to PD cases (III: 0.00179 ± 0.00104; V: 0.00227 ± 0.00113), but no significant differences were found ($p = 0.82$ and 0.59, respectively; t-test). There was also no longer any significant difference in the number of point mutations in complex I compared to the other complexes (Figure 4.2-7-A).

When grouping the data normalised by gene length in individual cases, no clear patterns emerged. However, a relatively high accumulation of complex III point mutations was observed in PD1, while complex I point mutations were elevated in PD5 (Figure 4.2-8-A).

In the rRNA and tRNA regions, PD neurons (rRNA: 6.16 ± 3.33; tRNA: 3.96 ± 3.08) exhibited a higher average accumulation of point mutations compared to aged control neurons (rRNA: 4.46 ± 3.54; tRNA: 2.95 ± 1.53). However, these differences were not

statistically significant (p = 0.14 and 0.16, respectively; t-test) (Figure 4.2-9-A; Figure 4.2-10-A).

All point mutations were then categorized as synonymous or non-synonymous. Synonymous point mutations do not lead to amino acid changes, while non-synonymous mutations do result in amino acid changes. PD neurons accumulated more synonymous (17.3 ± 13.8) and non-synonymous (29.1 ± 20.4) point mutations than aged controls (14.4 ± 6.65 for synonymous; 24.1 ± 13.5 for non-synonymous), but these differences were not significant (p = 0.33 and 0.3, respectively; t-test). In both PD and control cases, the number of non-synonymous point mutations (26.8 ± 17.6) was higher than that of synonymous mutations (15.9 ± 11.1), with this difference being highly significant (p = 0.00029***) (Figure 4.2-11-A).

This observation is expected, as a single nucleotide change often alters the encoded amino acid, particularly in codons where changes in the first or second position frequently result in amino acid substitution (Bofkin and Goldman, 2007).

When excluding all point mutations detected in neurons with a deletion load above 1%, more point mutations were observed in complex I (9.92 ± 6.44), complex III (2.45 ± 1.37), and complex V (2.3 ± 1.16) in PD neurons compared to the aged controls (I: 7 ± 3.91; III: 1.92 ± 1.12; V: 2.23 ± 1.17), although these differences were not statistically significant (p = 0.34, 0.36, and 0.88, respectively; t-test). More point mutations were detected in complex IV in aged control neurons (4.11 ± 2.71) compared to PD cases (3.75 ± 2.86), but this difference was also not statistically significant (p = 0.58, t-test) (Figure 4.2-6-B). After normalisation, similar results were observed. More point mutations were detected in complex I (0.00181 ± 0.00117), complex III (0.00215 ± 0.0012), and complex V (0.00248 ± 0.00125) in PD neurons compared to aged controls (I: 0.00128 ± 0.000712; III: 0.00169 ± 0.000978; V: 0.00241 ± 0.00126), though the differences remained non-significant (p = 0.16, 0.32, and 0.89, respectively; t-test). Similarly, more point mutations were observed in complex IV in aged control neurons (0.00185 ± 0.00122) compared to PD cases (0.00169 ± 0.00129), but this difference was not statistically significant either (p = 0.73; t-test) (Figure 4.2-7-B). When the normalised data were grouped by individual cases, no

clear patterns emerged. A relatively high accumulation of complex III point mutations was still observed in PD1, but no high accumulation was observed in any complexes for PD5 (Figure 4.2-8-B).

In the rRNA and tRNA regions, PD neurons accumulated more point mutations in both rRNA (5.25 ± 3.49) and tRNA (3.38 ± 1.33) regions compared to aged controls (rRNA: 4.56 ± 3.55; tRNA: 2.89 ± 1.49), though these differences were not statistically significant ($p = 0.6$ and 0.34, respectively; t-test) (Figure 4.2-9-B; Figure 4.2-10-B).

When grouping mutations as synonymous or non-synonymous, PD neurons accumulated more of both synonymous (17.2 ± 10.3) and non-synonymous (26.1 ± 12.8) point mutations than aged controls (13.6 ± 6.24 for synonymous; 21.4 ± 11.9 for non-synonymous), but these differences were also not statistically significant ($p = 0.27$; t-test). In both PD and control cases, the number of non-synonymous mutations (23.2 ± 12.3) was higher than synonymous mutations (15.0 ± 8.11), with this difference being statistically significant ($p = 0.0022$**; t-test) (Figure 4.2-11-B).

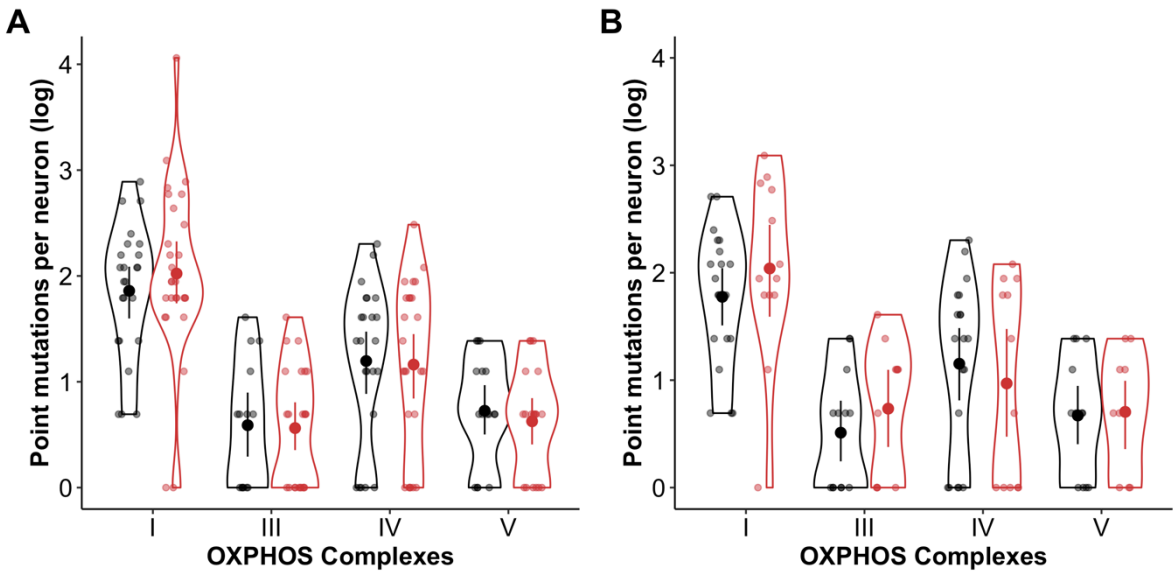

Figure 4.2-6 Point mutations in OXPHOS complexes per neuron

Graph A shows no significant difference in point mutations within the mtDNA coding regions of the OXPHOS complexes (I, III, IV, and V) between PD and control cases (p = 0.42, 0.89, 0.88, and 0.57, respectively; t-test) when including all point mutations. Both PD and control neurons exhibited a higher number of point mutations in complex I compared to complexes III, IV, and V. Neurons from control cases are represented in black, while red indicates PD cases. Graph B presents the data after excluding point mutations detected in neurons with a deletion load above 1%. Similar to the results with all point mutations included, no significant difference was found in the accumulation of point mutations within the OXPHOS complex coding regions (I, III, IV, and V) between PD and control cases (p = 0.34, 0.36, 0.58, and 0.88, respectively; t-test). Both PD and control neurons continued to show a higher number of point mutations in complex I compared to complexes III, IV, and V. Neurons from control cases are represented in black, while neurons from PD cases are shown in red.

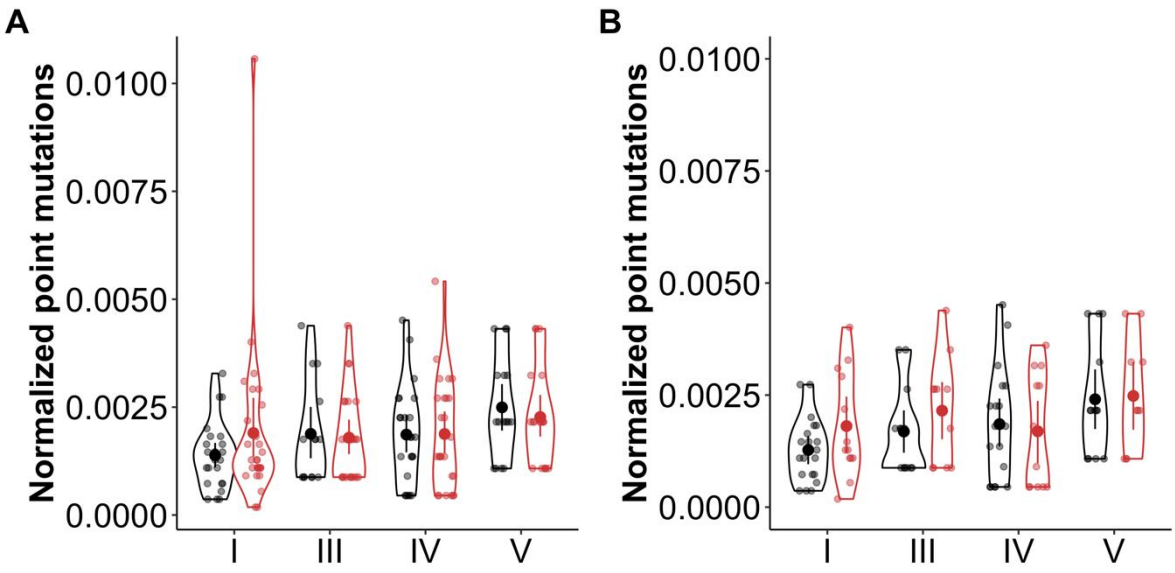

Figure 4.2-7 Point mutation in OXPHOS complexes per neuron after normalisation

Plot A illustrates the normalised point mutations per neuron across different OXPHOS complexes. No significant differences were observed between control and PD groups across all four complexes (p = 0.2, 0.82, 0.92, and 0.59 for complexes I, III, IV, and V, respectively; t-test). Similarly, after normalisation, no significant differences were found in the distribution of point mutations across the complexes. Plot B shows the results after excluding point mutations detected in neurons with a deletion load above 1%, with no significant differences observed between control and PD groups across all four complexes (p = 0.16, 0.32, 0.73, and 0.89, respectively; t-test). Neurons from control cases are represented in black, while red represents PD cases.

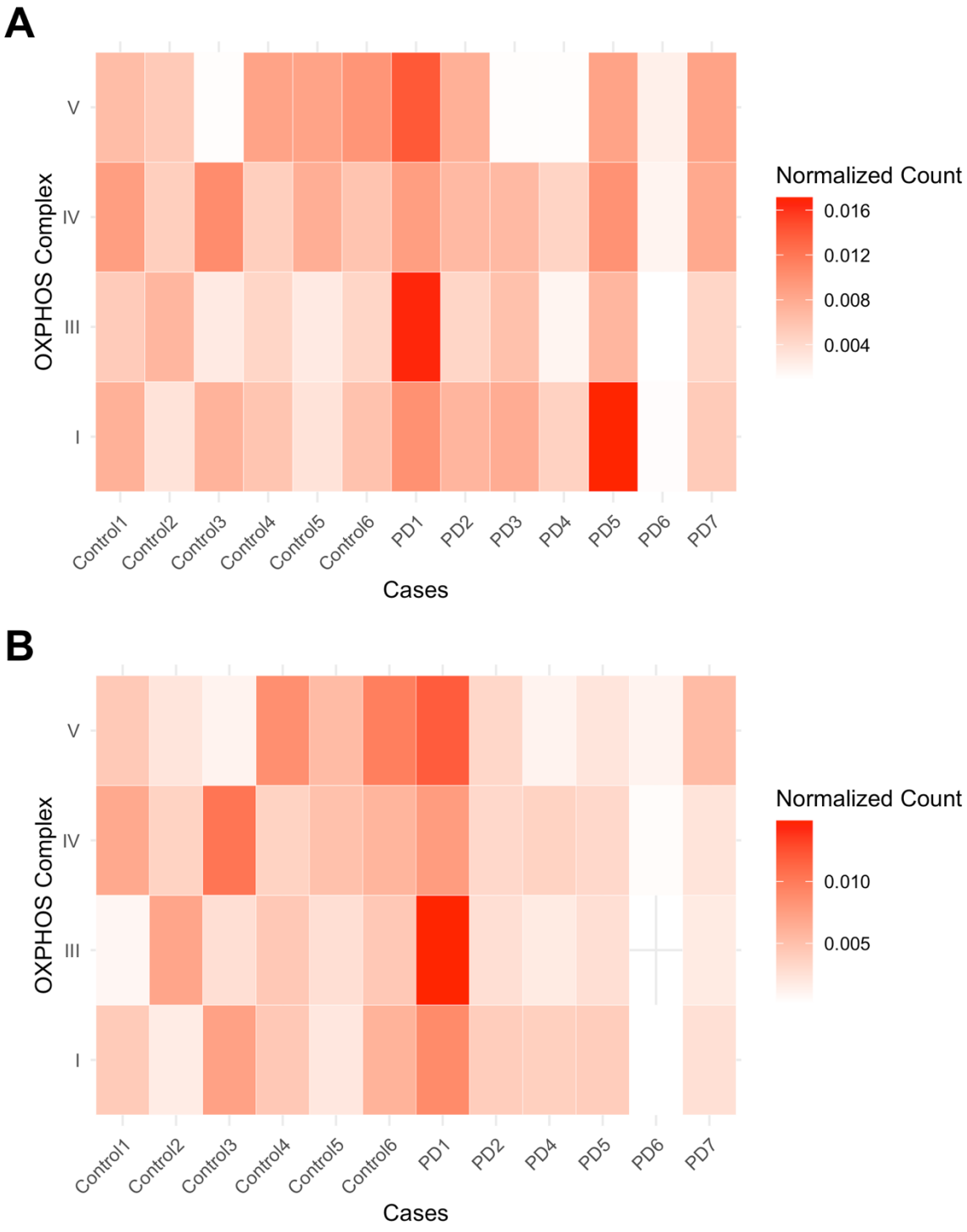

Figure 4.2-8 Point mutation burden in different cases across OXPHOS complex regions

Heatmap showing the frequency of point mutations detected in the mtDNA coding sequences of the four OXPHOS complexes, normalised by the gene length. Graph A reveals no clear pattern in the distribution of point mutations across different cases,

except that PD1 shows higher accumulation of point mutations in complex III, and PD5 shows higher accumulation in complex I. Graph B shows the results after filtering out point mutations in neurons with a deletion load above 1%; again, no distinct pattern is observed across cases. PD1 still exhibits a higher accumulation of point mutations in complex III, but no noticeable differences are seen in PD5 across any complexes.

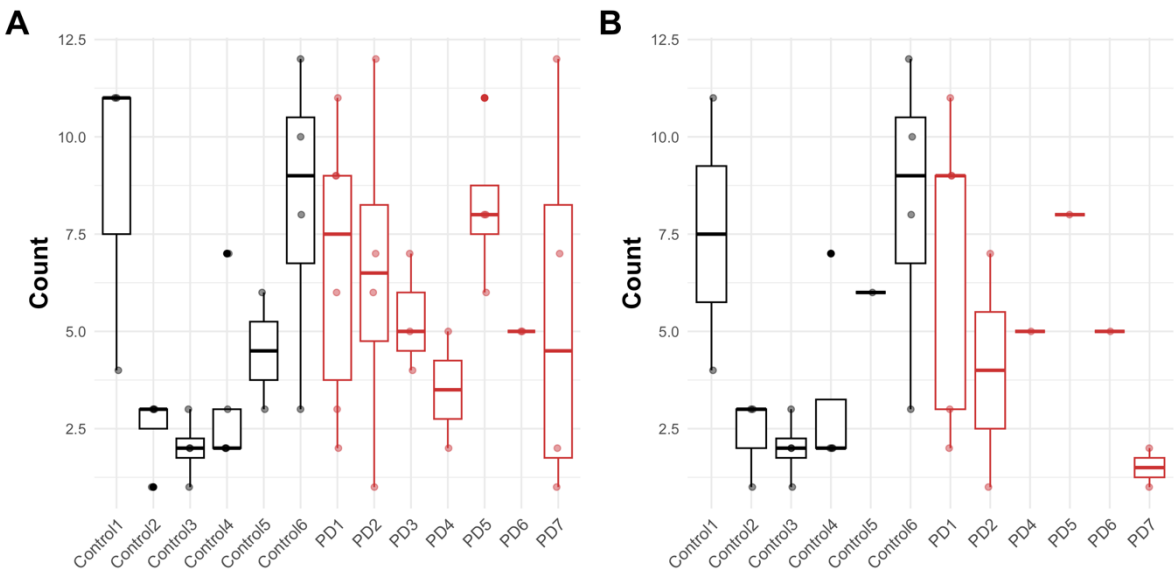

Figure 4.2-9 Number of point mutations in rRNA areas per neuron

Graph A shows that when including all point mutations, PD cases (6.16 ± 3.33) accumulated more point mutations in rRNA regions compared to aged controls (4.46 ± 3.54), though the difference was not statistically significant (p = 0.14; t-test). Graph B shows that after filtering out neurons with a deletion load above 1%, PD neurons (5.25 ± 3.49) still accumulated more point mutations in rRNA regions compared to control neurons (4.56 ± 3.55), but this difference was also not significant (p = 0.6; t-test). Neurons from control cases are represented in black, while red represents PD cases.

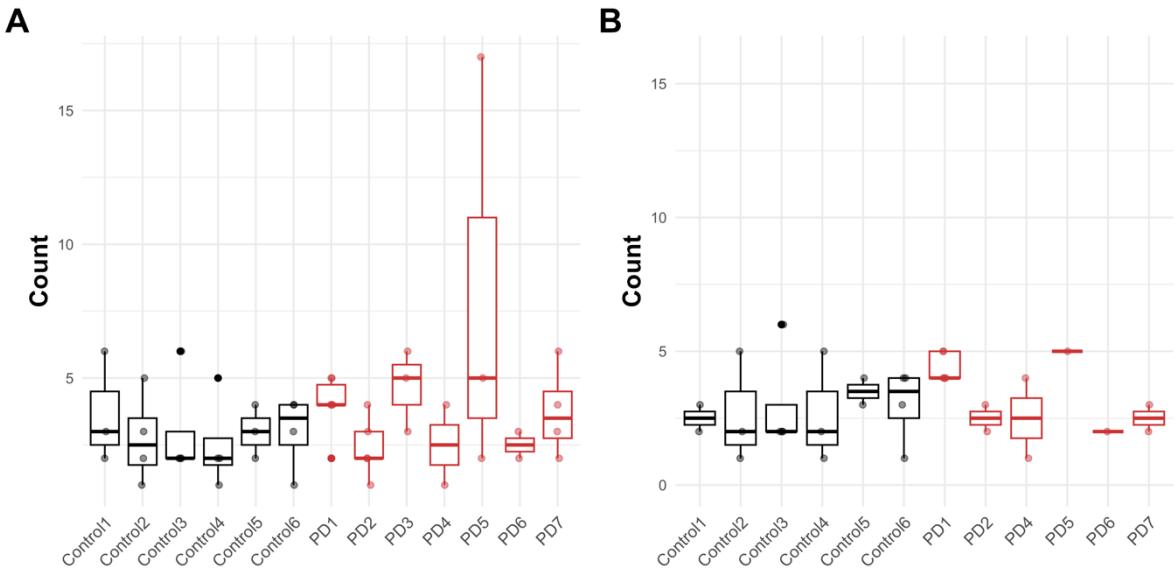

Figure 4.2-10 Number of point mutations in tRNA areas per neuron

Graph A shows that when including all point mutations, PD cases (3.96 ± 3.08) accumulated more point mutations in tRNA regions compared to aged controls (2.95 ± 1.53), though the difference was not statistically significant (p = 0.16; t-test). Graph B shows that after filtering out neurons with a deletion load above 1%, PD neurons (3.38 ± 1.33) still accumulated more point mutations in tRNA regions compared to control neurons (2.89 ± 1.49), but this difference remained non-significant (p = 0.34; t-test). Neurons from control cases are represented in black, while red represents PD cases.

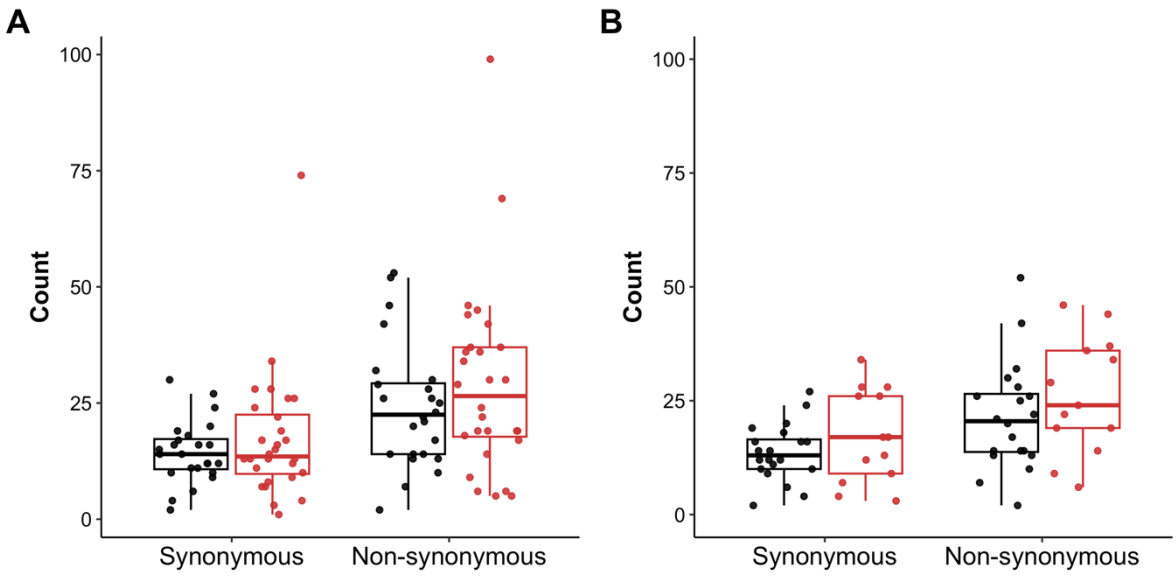

Figure 4.2-11 Number of synonymous and non-synonymous point mutations per neuron

*Graph A shows that when including all point mutations, PD cases accumulated more synonymous (17.3 ± 13.8) and non-synonymous (29.1 ± 20.4) point mutations compared to aged controls (14.4 ± 6.65 for synonymous; 24.1 ± 13.5 for non-synonymous), though these differences were not statistically significant (p = 0.33 and 0.3, respectively; t-test). In both PD and control cases, the number of non-synonymous mutations (26.8 ± 17.6) was higher than synonymous mutations (15.9 ± 11.1), with this difference being highly significant (p = 0.00029***; t-test). Graph B shows similar observations after filtering out point mutations in neurons with a deletion load above 1%. PD cases still accumulated more synonymous (17.2 ± 10.3) and non-synonymous (26.1 ± 12.8) point mutations compared to aged controls (13.6 ± 6.24 for synonymous; 21.4 ± 11.9 for non-synonymous), but these differences remained not significant (p = 0.27; t-test). Neurons from control cases are represented in black, while red represents PD cases.*

4.2.4. *Traits of point mutations detected*

The transition/ transversion (Ts/Tv) ratio provides insights into mutational processes within a genome, potentially indicating selective pressures (Dagan, Talmor and Graur, 2002; Lyons and Lauring, 2017) and underlying mutational mechanisms (Zhang and Gerstein, 2003; Pauly, Procario and Lauring, 2017). Transitions involve changes between two purines (adenine (A) and guanine (G)) or two pyrimidines (cytosine (C) and thymine (T)), while transversions occur between a purine and a pyrimidine, like changing from adenine to cytosine or thymine to guanine (Figure 4.2-12). The proportion of G:C to T:A is also an important indicator of the mechanism driving point mutations and is typically associated with levels of oxidative DNA damage within the cell. To examine the characteristics of point mutations detected in PPN cholinergic neurons, these two indicators were calculated.

When including all point mutations, neurons from control cases had a higher Ts/Tv ratio (4.27 ± 2.40) compared to PD neurons (3.28 ± 1.48), though this difference was not statistically significant ($p = 0.088$, t-test, Figure 4.2-13-A). As for the proportion of G:C to T:A transversions, it was also similar between PD (0.549 ± 0.262) and aged control neurons (0.535 ± 0.278), with no significant difference ($p = 0.8$, t-test, Figure 4.2-14-A).

After excluding point mutations detected in neurons with a deletion load above 1%, the Ts/Tv ratio in control neurons (4.22 ± 2.59) remained higher in PD neurons (4.04 ± 1.27), though the difference was still not significant ($p = 0.79$, t-test, Figure 4.2-13-B). Similarly, no significant difference was observed in the proportion of G:C to T:A transversions between PD (0.565 ± 0.265) and aged control (0.543 ± 0.284) ($p = 0.73$, t-test, Figure 4.2-14-B).

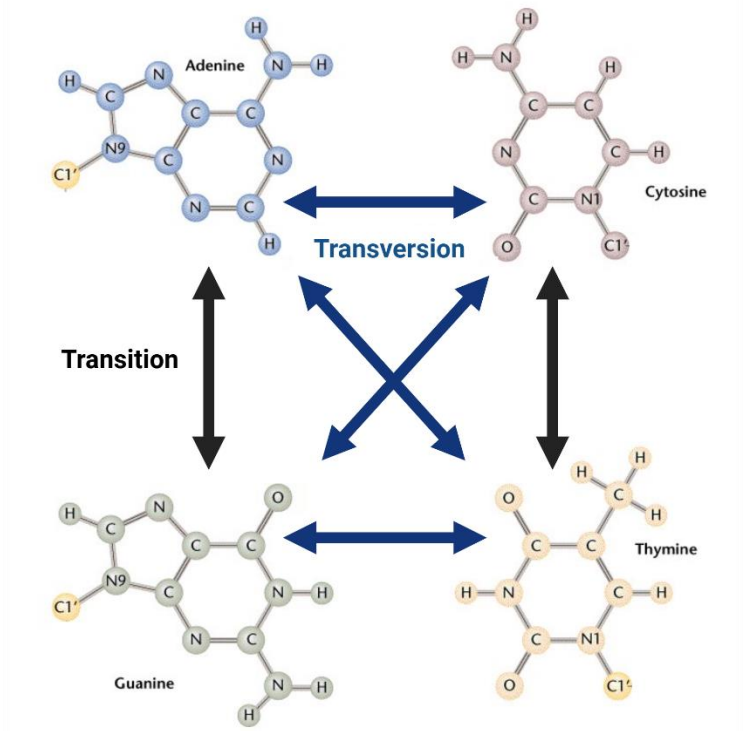

Figure 4.2-12 Point mutation transition and transversion

This graph illustrates the two types of nucleotide changes caused by point mutations. The first type, transition, occurs between two purines (adenine and guanine) or two pyrimidines (cytosine and thymine), which have similar structures. The second type, transversion, involved changes between nucleotides with different molecular structures. This includes changes from adenine to cytosine or thymine, cytosine to guanine or adenine, thymine to guanine or cytosine, and guanine to adenine or thymine.

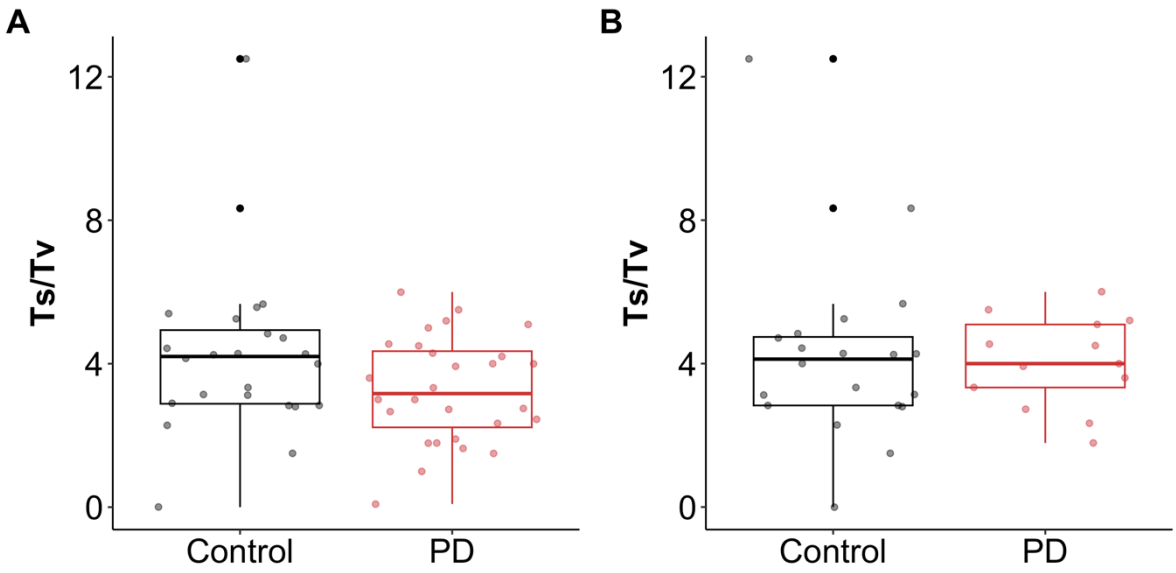

Figure 4.2-13 Ts/Tv ratio comparisons

Graph A shows the Ts/Tv ratio when including all point mutations. Neurons from control cases had a higher ratio (4.27 ± 2.40) than neurons from PD cases (3.28 ± 1.48), though this difference was not statistically significant (p = 0.088, t-test). After excluding point mutations detected in neurons with a deletion load above 1%, as shown in Graph B, the Ts/Tv ratio in control neurons (4.22 ± 2.59) remained higher than that in PD neurons (4.04 ± 1.27), but the difference was still not significant (p = 0.79, t-test). Neurons from control cases are represented in black, while red represents PD cases. Ts/Tv ratio = Transition/Transversion ratio.

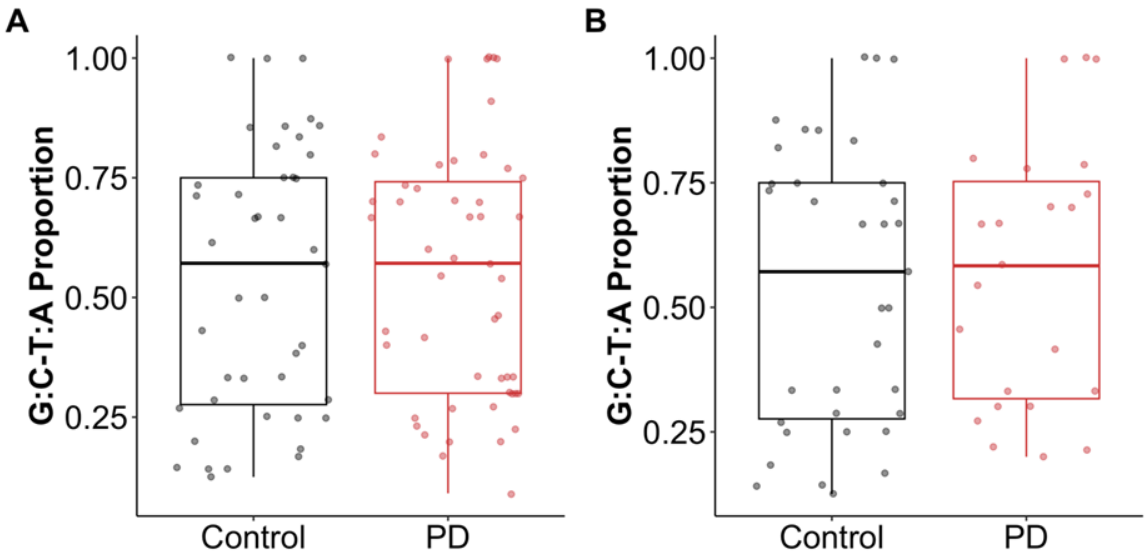

Figure 4.2-14 The number of G:C to T:A transversions in single neuron

Figure A shows that when including all point mutations, the proportion of G:C to T:A transversions in control neurons (0.535 ± 0.278) was similar to that in PD neurons (0.549 ± 0.262), with no significant difference observed (p = 0.8; t-test). After excluding point mutations detected in neurons with a deletion load above 1%, as shown in Figure B, the proportion of G:C to T:A transversions remained similar between control (0.543 ± 0.284) and PD neurons (0.565 ± 0.265) (p = 0.73, test). Neurons from control cases are represented in black, while red represents PD cases.

4.2.5. *Distribution of point mutations*

The distribution of point mutations can provide insights into the generation or accumulation patterns of these mutations. When including all point mutations, they were plotted across the entire mtDNA genome, both in a circular linear format (Figure 4.2-15) and a linear format (Figure 4.2-16). No distinct pattern in point mutation distribution was observed, nor was there a significant difference between PD cases and aged controls. However, in both PD and control cases, a higher accumulation of high-level point mutations was detected in the D-loop region. Outside the D-loop region, no other notable distribution patterns were observed.

The majority of cases in both PD and control groups exhibited similar levels of accumulation. Notably, PD1 and PD2 harboured more high-level point mutations than other cases, and these high-level mutations were primarily concentrated within single neurons (Neuron 10 from PD1 and Neuron 20 from PD2) when plotted by individual neuron (Figure 4.2-17). All control neurons across different cases showed similar levels of accumulation (Figure 4.2-18).

When excluding neurons with deletion load higher than 1%. Fewer point mutations were detected in both conditions, while PD2 still harboured a high level of point mutations (Figure 4.2-19; Figure 4.2-20). All high-level mutations in PD2 were located within the major arc and were detected exclusively in Neuron 20 (Figure 4.2-21). The remaining high-level point mutations in PD cases were confined to the control region. In contrast, high-level point mutations in control cases were distributed across the entire mtDNA genome and were found in different neurons from various control cases (Figure 4.2-22).

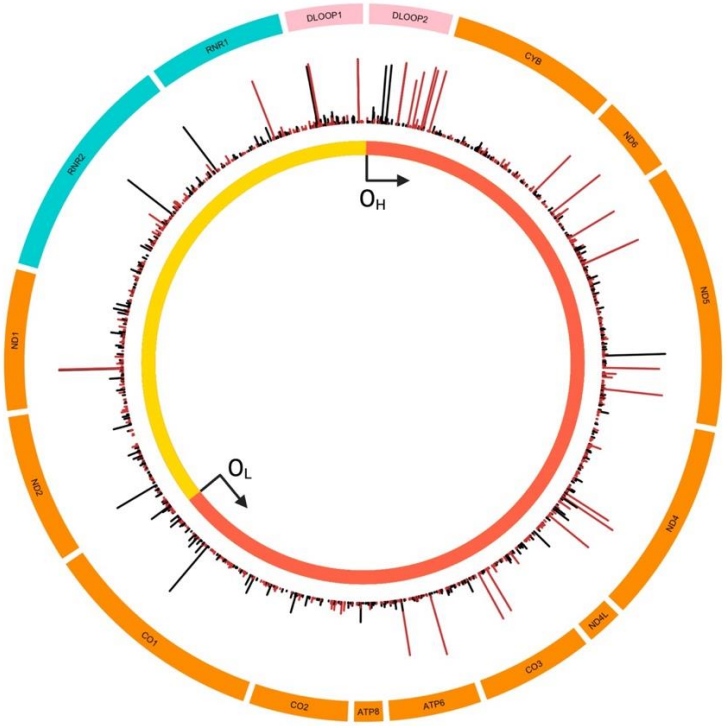

Figure 4.2-15 Circle plot showing point mutation distribution

In this circular plot, the outer circle displays the names of genomic regions, with orange indicating protein-coding regions, blue representing RNA-coding regions, and pink marking the D-loop or control regions. The middle circle illustrates the heteroplasmy levels of point mutations, with taller spikes indicating higher heteroplasmic levels. The inner circle shows the major and minor arcs, along with the origins of the heavy and light strands, where red represents the heavy strand and light yellow indicates the light strand. As shown in the middle circle, point mutations are distributed across the entire mtDNA genome, with certain regions accumulating higher levels of point mutations. For both PD and control cases, the D-loop region shows a higher accumulation of point mutations. In general, PD cases tend to accumulate more high-level heteroplasmic point mutations. Red spikes indicate point mutations in PD cases, while black spikes represent mutations in control cases.

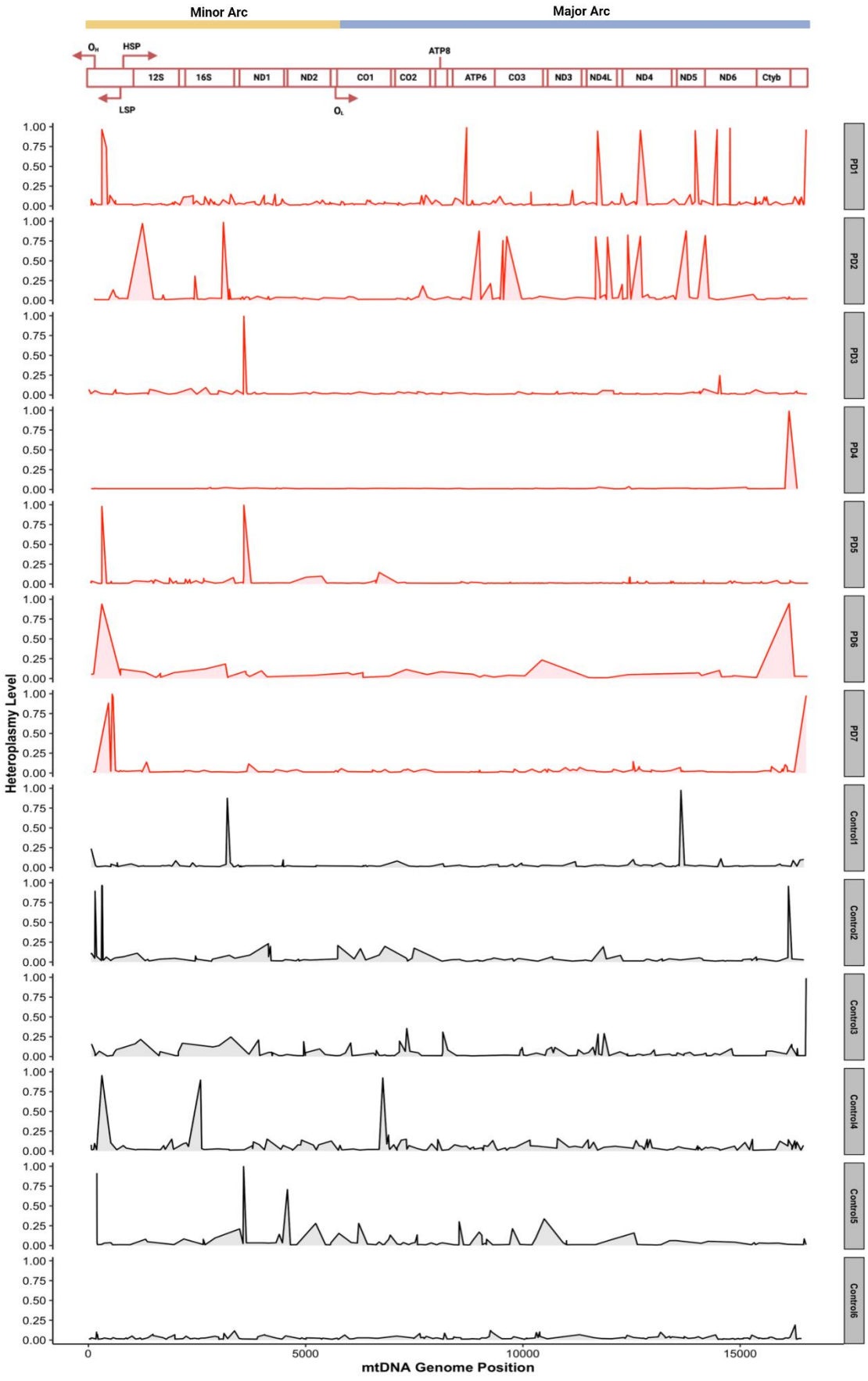
Minor Arc
Major Arc
O_H
HSP
ATP8
12S
16S
ND1
ND2
CO1
CO2
ATP6
CO3
ND3
ND4L
ND4
ND5
ND6
Ctyb
LSP
O_L
Heteroplasmy Level
1.00
0.75
0.50
0.25
0.00
PD1
PD2
PD3
PD4
PD5
PD6
PD7
Control1
Control2
Control3
Control4
Control5
Control6
0
5000
10000
15000
mtDNA Genome Position

Figure 4.2-16 Point mutation distribution of all neurons

This figure illustrates the heteroplasmy levels of point mutations detected across the entire linearized mtDNA genome for different cases. PD1 and PD2 accumulate more high-level point mutations than any other PD cases, most of which are located within the major arc of the mtDNA genome. For the remaining PD cases, the frequency of high-level point mutations is much lower. In control cases, all show similar profiles, with several high-level point mutations detected in all cases except Control6. The major (in blue) and minor arc (in yellow) indicators, along with gene regions, are displayed above the case plots.

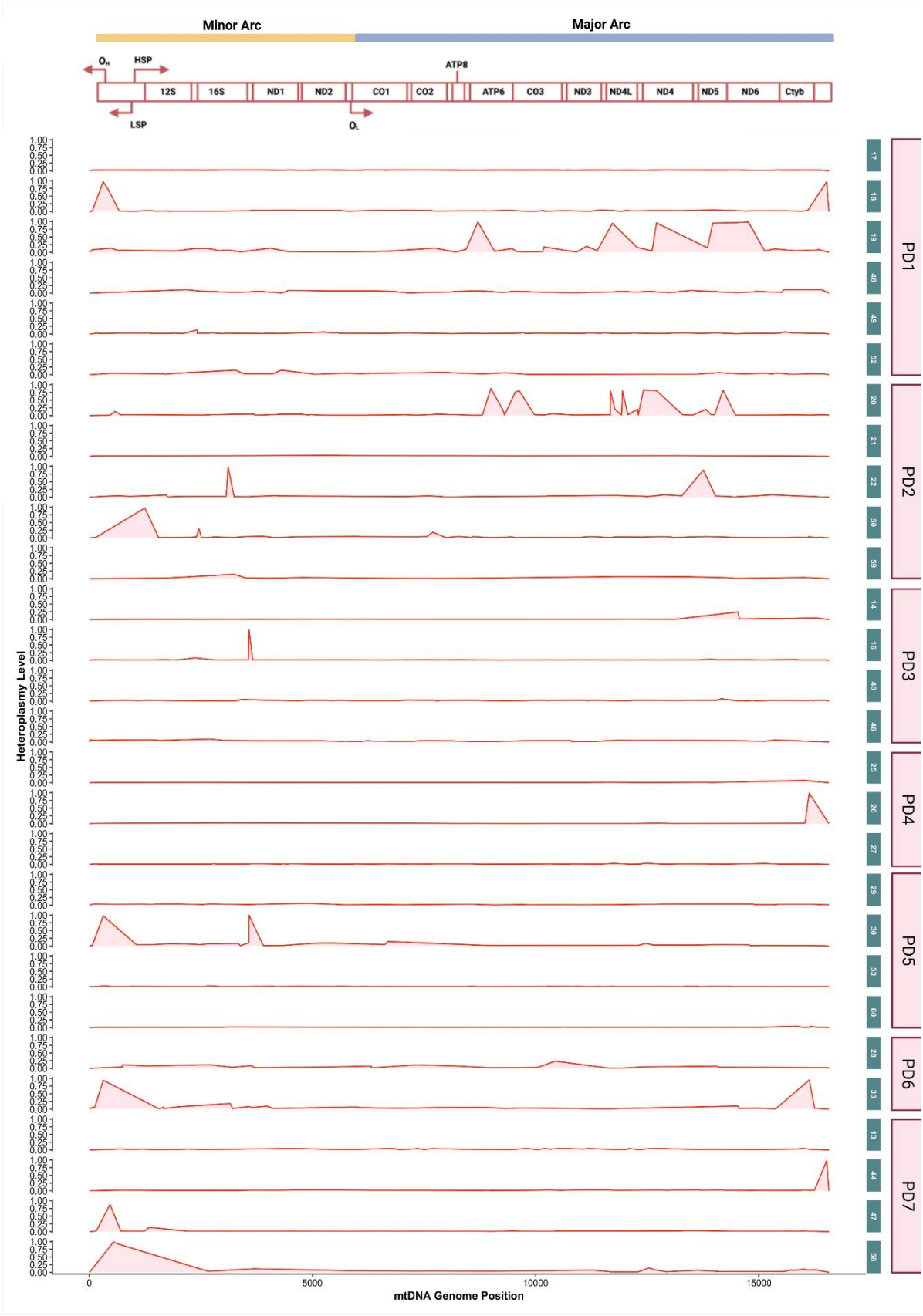

Figure 4.2-17 Point mutation distribution in PD neurons

This figure shows the distribution of point mutations in individual neurons from PD cases. As previously noted, PD1 and PD2 harbour more high-level point mutations, and when mutations are grouped by individual neuron, the majority of high-level point mutations are concentrated within a single neuron. Neuron 10 from PD1 and neuron 20 from PD2 each account for a large proportion of the high-level point mutations detected in these cases. In the remaining neurons from all PD cases, point mutations are primarily located in the minor arc, control regions, or near the control regions. The major (blue) and minor arc (yellow) indicators, along with gene regions, are displayed above the case plots.

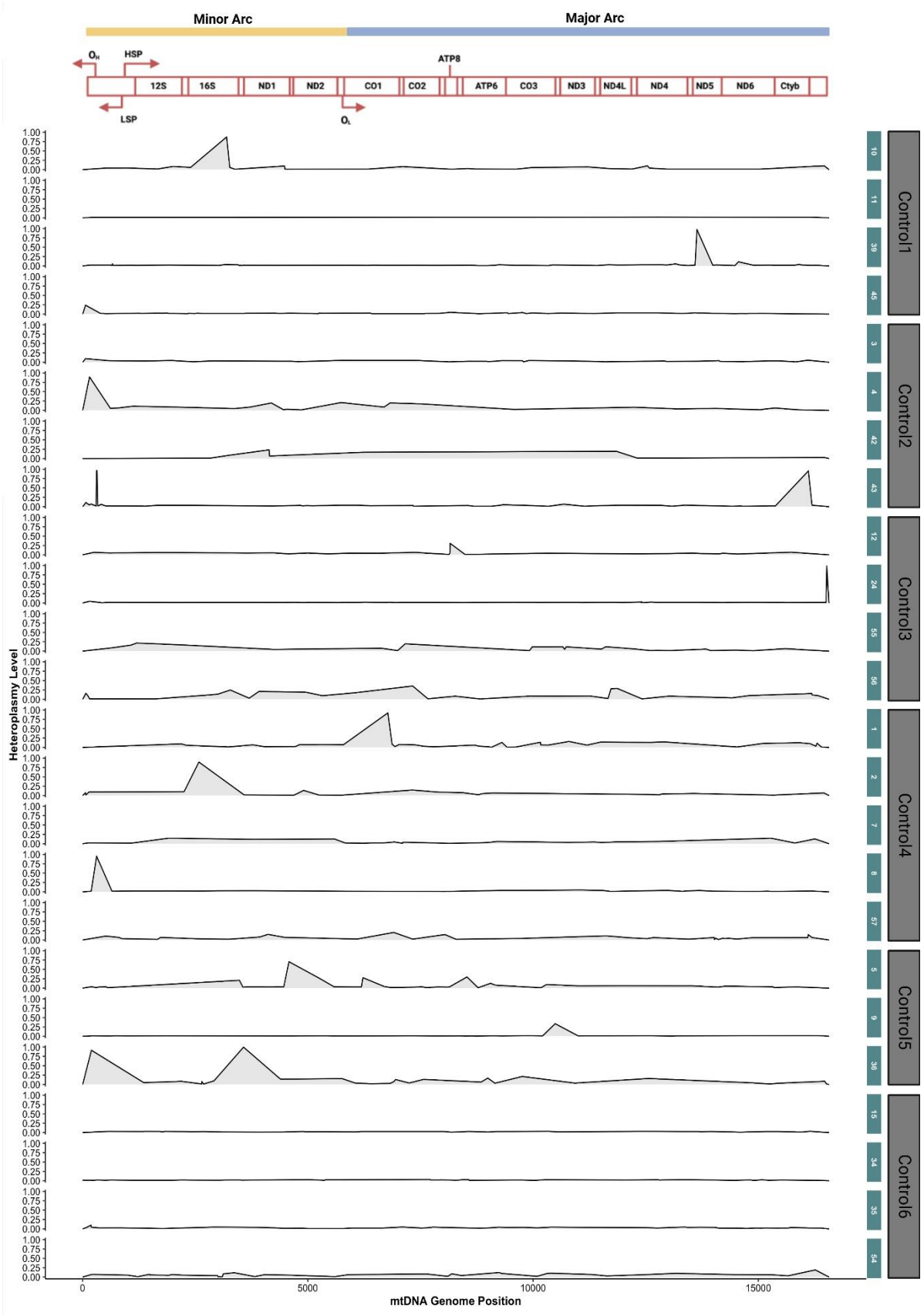

Figure 4.2-18 Point mutation distribution in control neurons

This plot illustrates the distribution of point mutations across the entire genome in individual neurons. Point mutations are not confined to specific neurons but are distributed across all neurons within each case. The locations of point mutations span the entire mtDNA genome. The major (blue) and minor arc (yellow) indicators, along with gene regions, are displayed above the case plots.

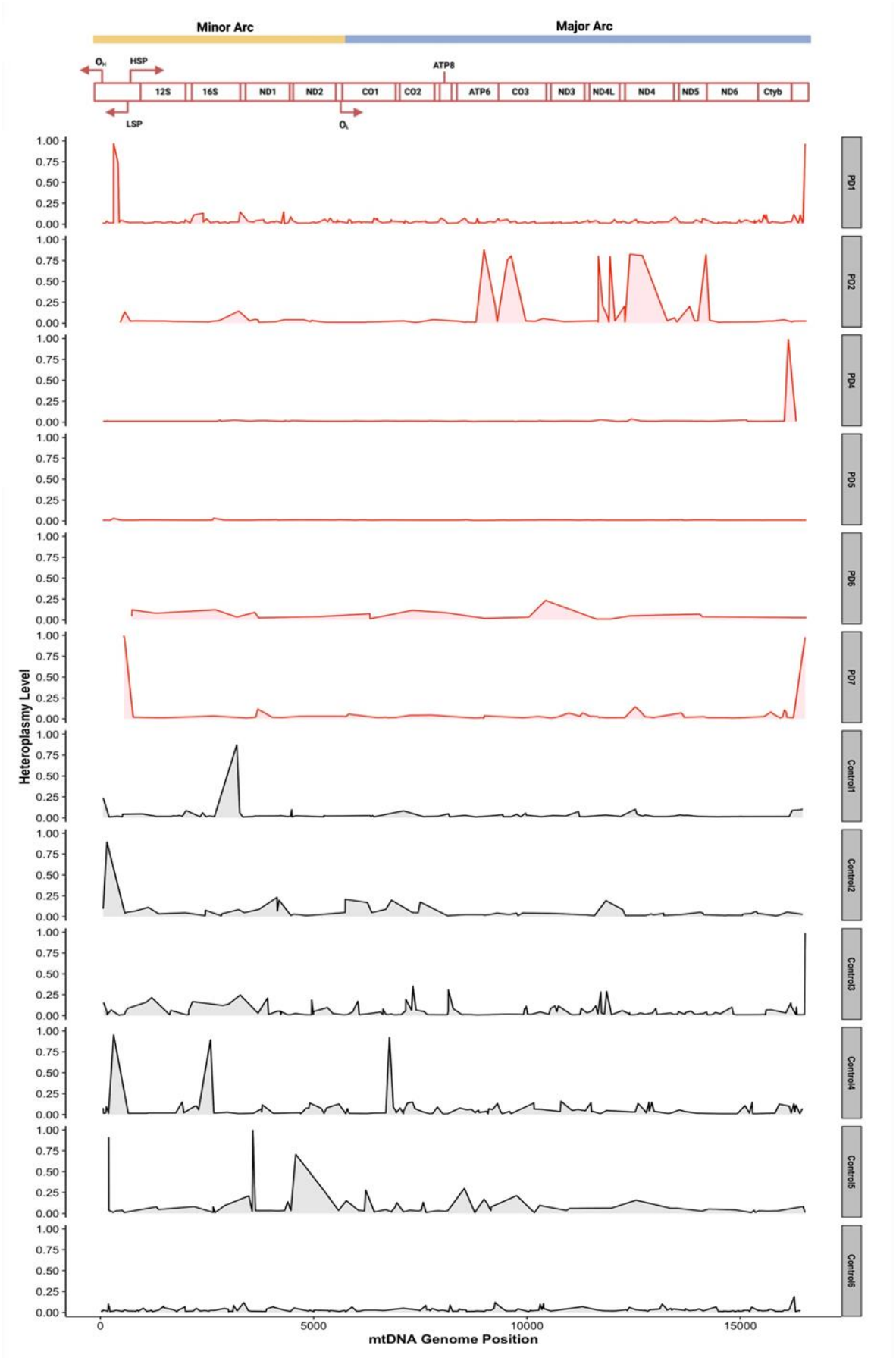
Minor Arc
Major Arc
O_H
HSP
ATP8
12S
16S
ND1
ND2
CO1
CO2
ATP6
CO3
ND3
ND4L
ND4
ND5
ND6
Ctyb
LSP
O_L
Heteroplasmy Level
1.00
0.75
0.50
0.25
0.00
PD1
PD2
PD4
PD5
PD6
PD7
Control1
Control2
Control3
Control4
Control5
Control6
0
5000
10000
15000
mtDNA Genome Position

Figure 4.2-19 The distribution of point mutations from neurons below 1% DL

After filtering out neurons with a deletion load above 1%, fewer high- and low-level point mutations were detected in PD neurons, although PD2 still showed an accumulation of high-level point mutations. In control cases, point mutations remained distributed across the entire genome. For both conditions, the D-loop region persisted as a hotspot for accumulation. Red indicates PD cases, while black represents control cases. The major (blue) and minor arc (yellow) indicators, along with gene regions, are displayed above the case plots.

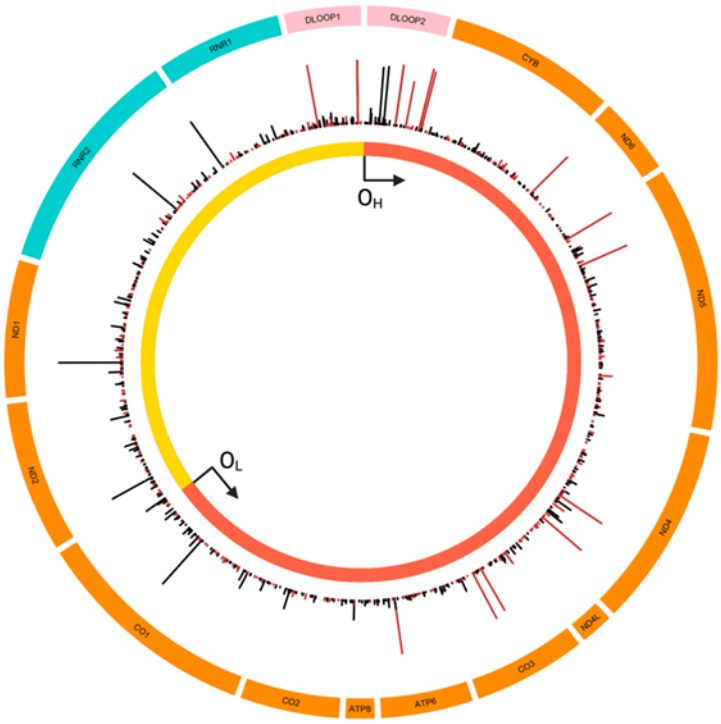

Figure 4.2-20 Circle plots show point mutations from neurons below 1% DL

In this circular plot, the outer circle displays the names of genomic regions, with orange indicating protein-coding regions, blue representing RNA-coding regions, and pink marking the D-loop or control regions. The middle circle illustrates the heteroplasmy levels of point mutations, with taller spikes indicating higher heteroplasmic levels. The inner circle shows the major and minor arcs, along with the origins of the heavy and light strands, where red represents the heavy strand and light yellow indicates the light strand. After excluding all the neurons with deletion load higher than 1%, there were still point mutations accumulate across the entire mtDNA genome, with D loop as a hotspot still in both conditions. For point mutations outside the D-Loop region, majority of the control high level control point mutations were accumulated in the minor arc, while all PD high level point mutations are within the major arc.

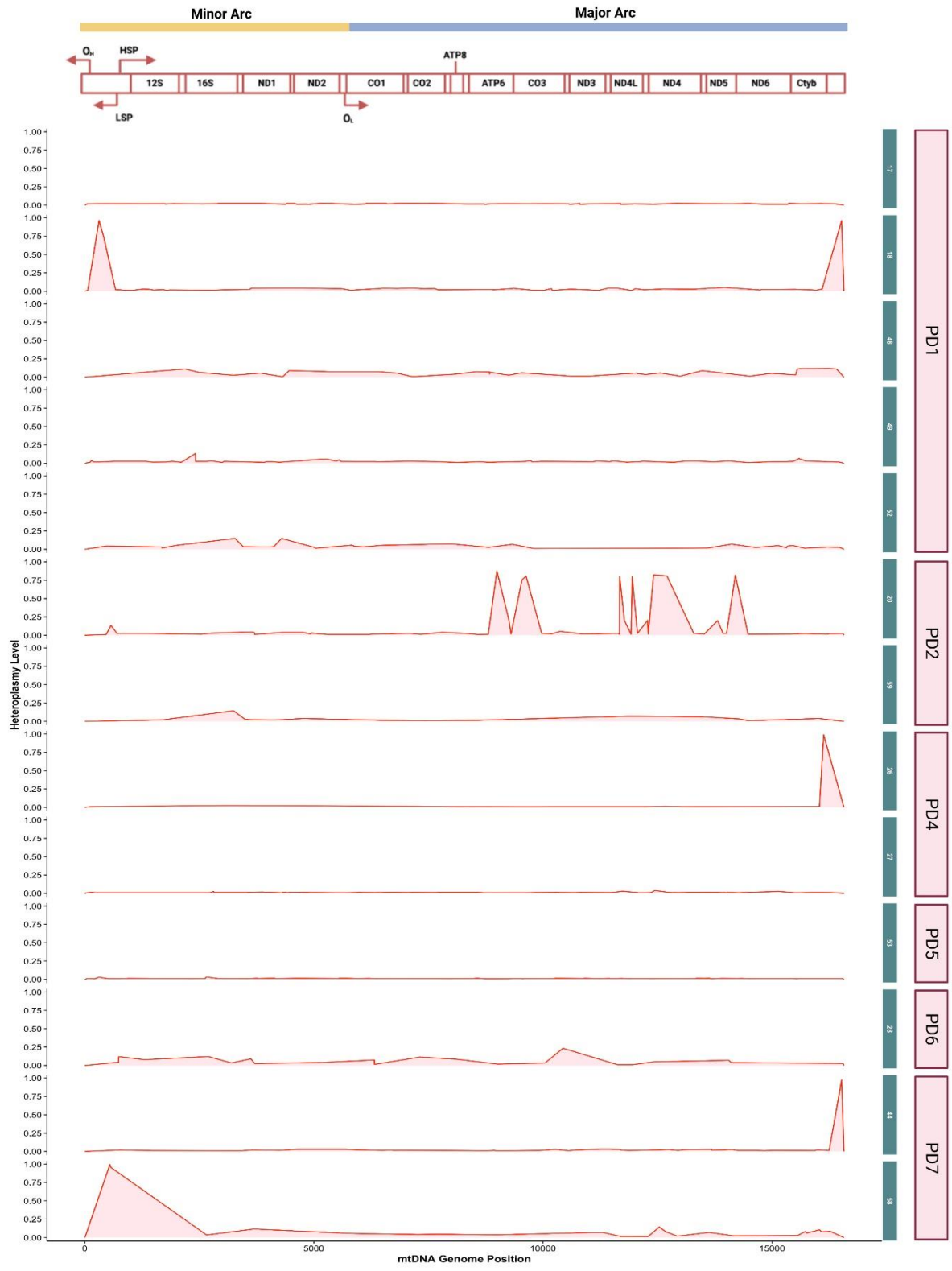

Figure 4.2-21 PD neurons point mutation distribution where DL is below 1%

After filtering out neurons with a deletion load above 1%, fewer point mutations were included in PD cases. PD2 still harbours more high-level point mutations than other

cases, with the majority of these high-level mutations located in neuron 20. Apart from neuron 20, no other neurons from PD2 or other PD cases showed a notable accumulation of high-level point mutations. The major (blue) and minor arc (yellow) indicators, along with gene regions, are displayed above the case plots.

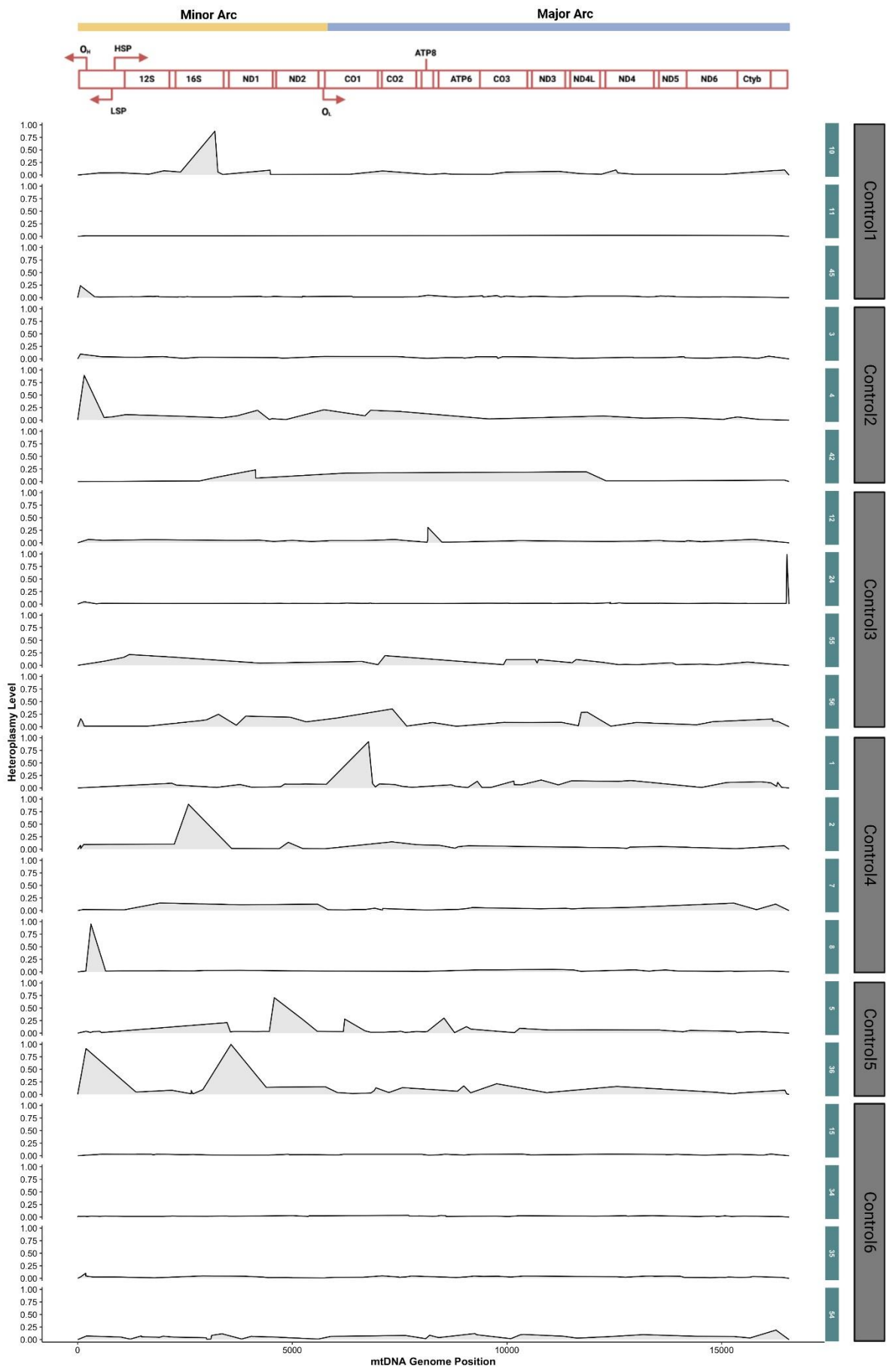
Minor Arc
Major Arc
O_H
HSP
ATP8
12S
16S
ND1
ND2
CO1
CO2
ATP6
CO3
ND3
ND4L
ND4
ND5
ND6
Ctyb
LSP
O_L
Heteroplasmy Level
mtDNA Genome Position
0
5000
10000
15000
Control1
Control2
Control3
Control4
Control5
Control6

Figure 4.2-22 Control neurons point mutation distribution where DL is below 1%.

This plot illustrates the distribution of point mutations across the entire genome in individual neurons after filtering neurons with deletion load higher than 1%. Point mutations are not confined to specific neurons but are distributed across all neurons within each case. The locations of point mutations span the entire mtDNA genome. The major (blue) and minor arc (yellow) indicators, along with gene regions, are displayed above the case plots

A point mutation was classified as a hotspot if it appeared at least ten times at the same location across all neurons within the same condition (either control or PD). No hotspot was detected, however any point mutation that recurred at least three times was classified as a recurrent point mutation. Based on a Poisson distribution, the probability of a point mutation occurring at the same location three times is approximately 7.2% in PD cases and 8.8% in control cases. A total of 14 recurrent point mutations were detected across all neurons, with 8 out of 14 found in PD neurons and 6 out of 14 in aged controls. The majority (57.1%) of these recurrent point mutations were located within the D-loop or control region, with approximately 50% of PD recurrent point mutations and 67% of control recurrent point mutations falling in this area. The remaining recurrent point mutations were distributed throughout the mtDNA genome, with one recurrent point mutation detected in each of the following regions: ND1, CO1, CO2, ATP6, ND4, and ND5 (Figure 4.2-23-A, Table 4.2-3). No clear difference was shown between the PD and control recurrent point mutations distributions.

When excluding neurons with deletion load higher than 1%, only four were identified, defined as the same mutation appearing at least three times. The probability of a point mutation occurring at the same location three times is approximately 6.4% in PD cases and 6.5% in control cases (Poisson distribution). Of these, three recurrent point mutations were detected in controls, while only one was found in PD cases. The control recurrent point mutations were located in the CO1, CO2, and HV1 regions, while the single PD recurrent point mutation was found in the ND4 region (Figure 4.2-23-B, Table 4.2-4).

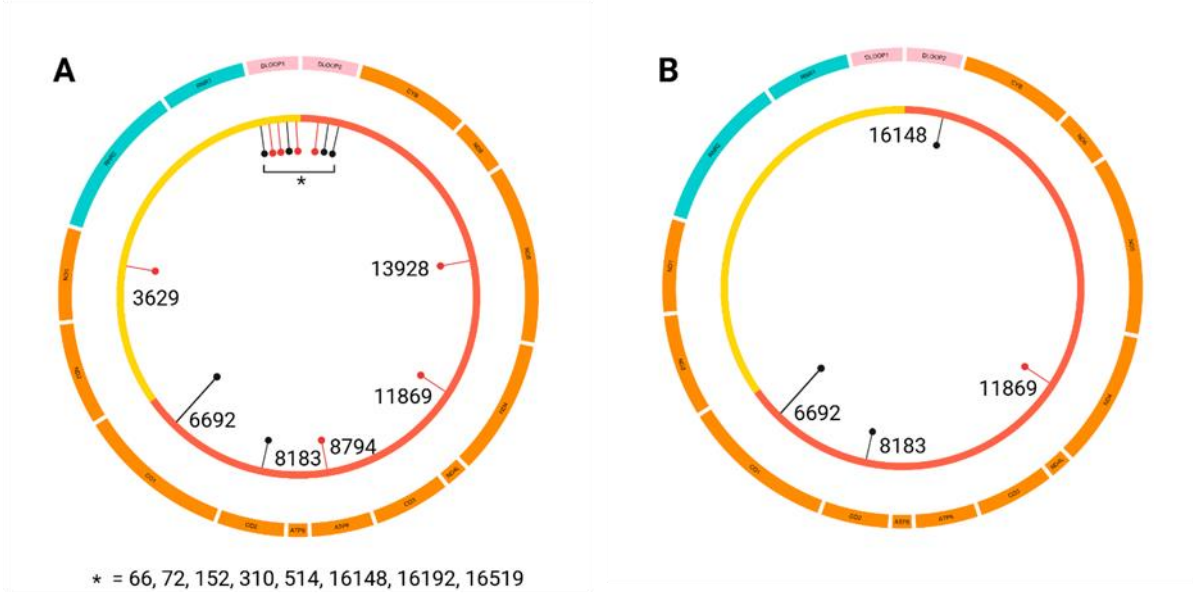

Figure 4.2-23 Recurrence of point mutations across the mtDNA genome

These two plots display the distribution of recurrent point mutations across the mtDNA genome. Plot A shows all recurrent point mutations, with multiple point mutations located in the control region, present in both control and PD cases. There were 14 recurrent point mutations detected in total and 8 of them were from PD neurons, while 6 from the aged control neurons. A large proportion of the recurrent point mutations were located inside the D-Loop regions, 50% for PD mutations, and 67% for control mutations. Plot B displays the recurrent point mutations after excluding neurons with a deletion load greater than 1%. In this filtered dataset, only 4 recurrent point mutations were detected, with just one recurrent point mutation located within the control region. The inner circle of each plot indicates the count of point mutations, with black representing recurrent point mutations detected in control neurons and red indicating PD neurons. The inner circle also distinguishes the major and minor arcs of the mtDNA, with orange representing the major arc and yellow the minor arc. The outer circle illustrates different genomic regions: orange for protein-coding regions, blue for RNA regions, and pink for the D-loop or control region.

Position	Nucleotide change	Condition	Area	Count
66	G-del	PD	*HV2*	3
72	T-C	Control	*HV2*	3
152	T-C	PD	*HV2*, OriH	3
310	T-C	PD	*HV2*, OriH, *CSB2*	3
514	C-del	Control	Noncoding	3
3629	C-T	PD	*ND1*	3
6692	A-D	Control	*CO1*	4
8138	A-C	Control	*CO2*	3
8794	C-A	PD	*ATP6*	3
11869	C-T	PD	*ND4*	3
13928	G-A	PD	*ND5*	3
16148	C-T	Control	*NV1*	3
16192	C-T	Control	*HV1*	3
16519	T-C	PD	Noncoding	3

Table 4.2-3 Point mutation recurrent point mutations from all neurons

A total of 14 recurrent point mutations (defined as identical point mutations appearing at least three times) were detected across the PPN cholinergic neurons, with 8 in PD cases and 6 in controls. The D-loop or control region exhibited a high frequency of recurrent point mutations with 8 out of 14 (58%) located in this area. Particularly, multiple recurrent point mutations were identified within the hypervariable segments, HV1 and HV2. Additionally, two recurrent point mutations were found in the origin of the heavy strand (position 152 and 310) both from PD neurons. The remaining recurrent point mutations *were distributed throughout the mtDNA genome, located in the ND1, CO1, CO2, ATP6, ND4 and ND5 genes. ND1: NADH Dehydrogenase subunit 1; CO1: Cytochrome c oxidase subunit I; CO2: Cytochrome c oxidase subunit II; ATP6: ATP synthase F0 subunit 6; ND4: NADH dehydrogenase subunit 4; ND5: NADH dehydrogenase subunit 5; HV1: Hypervariable segment 1; HV2: Hypervariable segment 2; OriH: origin of the heavy strand; CSB: conserved sequence block.*

Position	Nucleotide change	Condition	Area	Count
6692	A-D	Control	*CO1*	4
8138	A-C	Control	*CO2*	3
11869	C-T	PD	*ND4*	3
16148	C-T	Control	*HV1*	3

Table 4.2-4 Recurrent point mutations from neurons below 1% DL

There were only 4 recurrent point mutations remaining after neurons with a DL above 1% were excluded. Three are detected from the control, while one from the PD. One recurrent point mutation (16148) was within the control region. CO1: Cytochrome c oxidase subunit I; CO2: Cytochrome c oxidase subunit II; ND4: NADH dehydrogenase subunit 4; HV1: Hypervariable segment 1.

4.2.6. *The impact of point mutations on neurons*

MutPred is a reliable computational model which is based upon protein sequence, and which models changes of structural features and function sites between wild-type and mutant sequences. The tool provides reliable predictions and is widely used in the field of genetic variation (Thusberg, Olatubosun and Vihinen, 2011; Wei *et al.*, 2017). Based on these changes, it generates a MutPred score, which suggests the likelihood of a non-synonymous point mutation causing a functional change that may lead to disease in later stages ((Li *et al.*, 2009), http://mutdb.org/mutpred).

When including all point mutations with high MutPred scores (above 0.5), PD cases (0.71 ± 0.099) showed similar MutPred scores to aged controls (0.71 ± 0.107) ($p = 0.93$; t-test) (Figure 4.2-24-A). Regarding the distribution of these point mutations, they were spread across the coding regions of the mtDNA genome, with no specific patterns observed (Figure 4.2-25-A). When grouped by individual neurons, PD neurons accumulated more point mutations (14.8 ± 11.5) with high MutPred scores compared to aged controls (11.8 ± 5.58), but this difference was not statistically significant (Figure 4.2-26-A). Similarly, when grouped by cases and coding regions, no clear patterns were

observed between PD and aged controls or overall, except PD5 harboured more point mutations with high MutPred scores in the major arc coding regions, including ND5, ND4, ND3, and CO3 comparing to other cases (Figure 4.2-27). The normalisation of each coding region was performed by dividing the number of point mutations in each area by the length of the corresponding gene.

After excluding point mutations detected in neurons with a deletion load above 1%, no significant difference was observed between PD (0.703 ± 0.097) and control cases (0.707 ± 0.108) when comparing the point mutations with high MutPred scores ($p = 0.7$; t-test) (Figure 4.2-24-B). Additionally, no clear pattern or difference was observed in the distribution of high MutPred score point mutations between PD and aged controls (Figure 4.2-25-B). When grouped by individual neurons, PD neurons harboured more point mutations with high MutPred scores compared to aged controls, though this difference was not statistically significant (Figure 4.2-26-B). Similarly, when grouped by coding regions and individual cases, no clear pattern emerged, except that Control 6 and PD1 exhibited higher numbers of point mutations with high MutPred scores (Figure 4.2-28). The lack of a significant difference in the mean variant pathogenicity score was not unexpected, as the previous study examining DLB-PD patients and aged controls similarly found no association (Wei *et al.*, 2017).

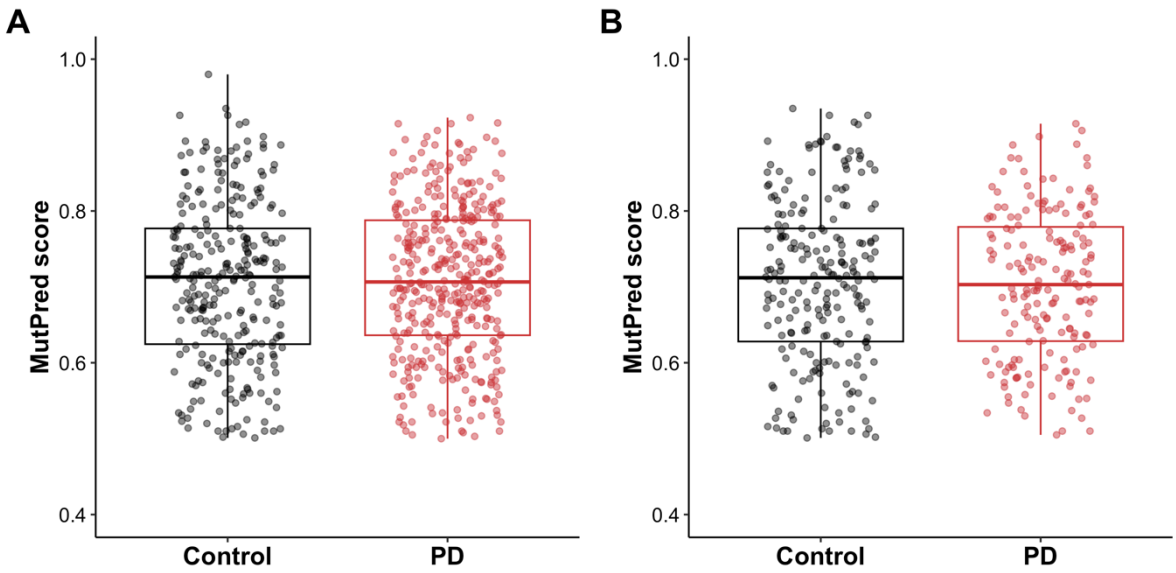

Figure 4.2-24 Point mutation with high MutPred score (⩾ 0.5)

These plots compare the MutPred scores above 0.5 between PD and control groups. Plot A includes all point mutations and shows no significant difference between PD (0.71 ± 0.099) and control (0.71 ± 0.107) MutPred scores (p = 0.93; t-test). Plot B includes only point mutations detected in neurons with a deletion load below 1%, and again, no significant difference was observed between PD (0.703 ± 0.097) and control (0.707 ± 0.108) MutPred scores above 0.5 (p = 0.7; t-test). Point mutations from control cases are represented in black, while red represents PD cases.

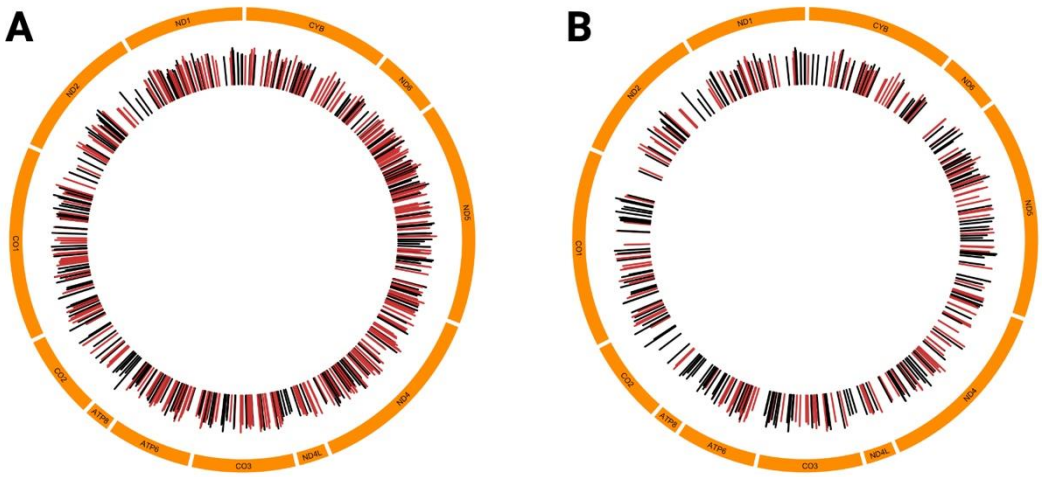

Figure 4.2-25 Distribution of point mutations with MutPred score above 0.5

These plots illustrate the distribution of point mutations with MutPred scores above 0.5 in both PD and control cases. Plot A includes all point mutations, while Plot B excludes point mutations detected in neurons with a deletion load above 1%. In both plots, point mutations are distributed across the entire mtDNA genome coding regions, with fewer point mutations observed in Plot B. Point mutations from control cases are represented by black spikes, while red spikes represent PD cases. The outer orange circle illustrates difference coding regions.

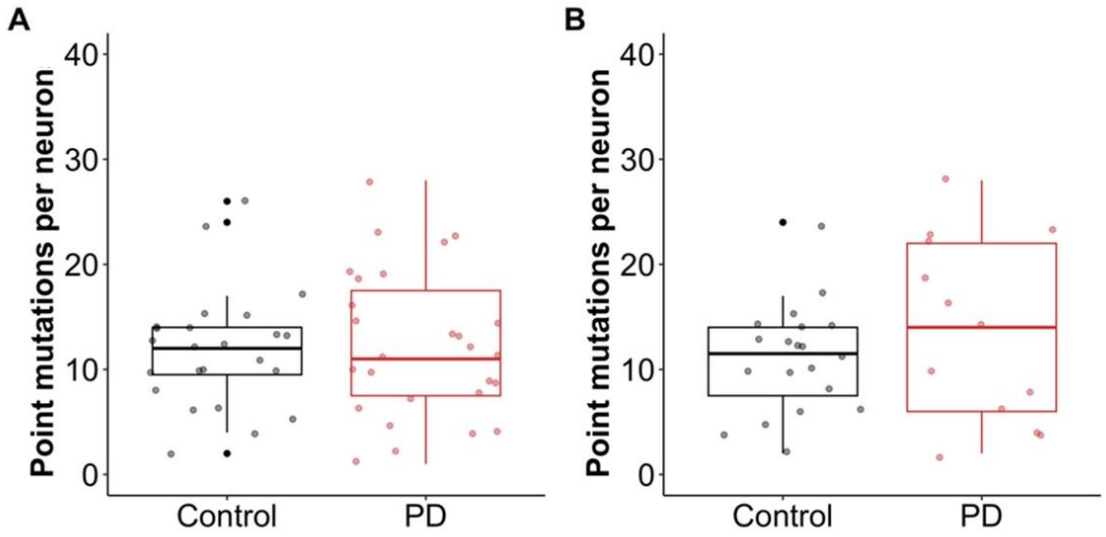

Figure 4.2-26 Number of point mutations with MutPred score above 0.5 per neuron

These plots illustrate the number of point mutations with MutPred scores above 0.5 per neuron. In Plot A, PD neurons harbour more point mutations with MutPred scores above 0.5 (14.8 ± 11.5) compared to neurons from aged controls (11.8 ± 5.58), though the difference was not statistically significant (p = 0.78; t-test). In Plot B, after excluding neurons with a deletion load above 1%, PD neurons (13.8 ± 8.71) still accumulate more MutPred score point mutations compared to aged controls (11 ± 5.06), but again, the difference was not significant (p = 0.31; t-test). Neurons from control cases are represented in black, while red represents PD cases.

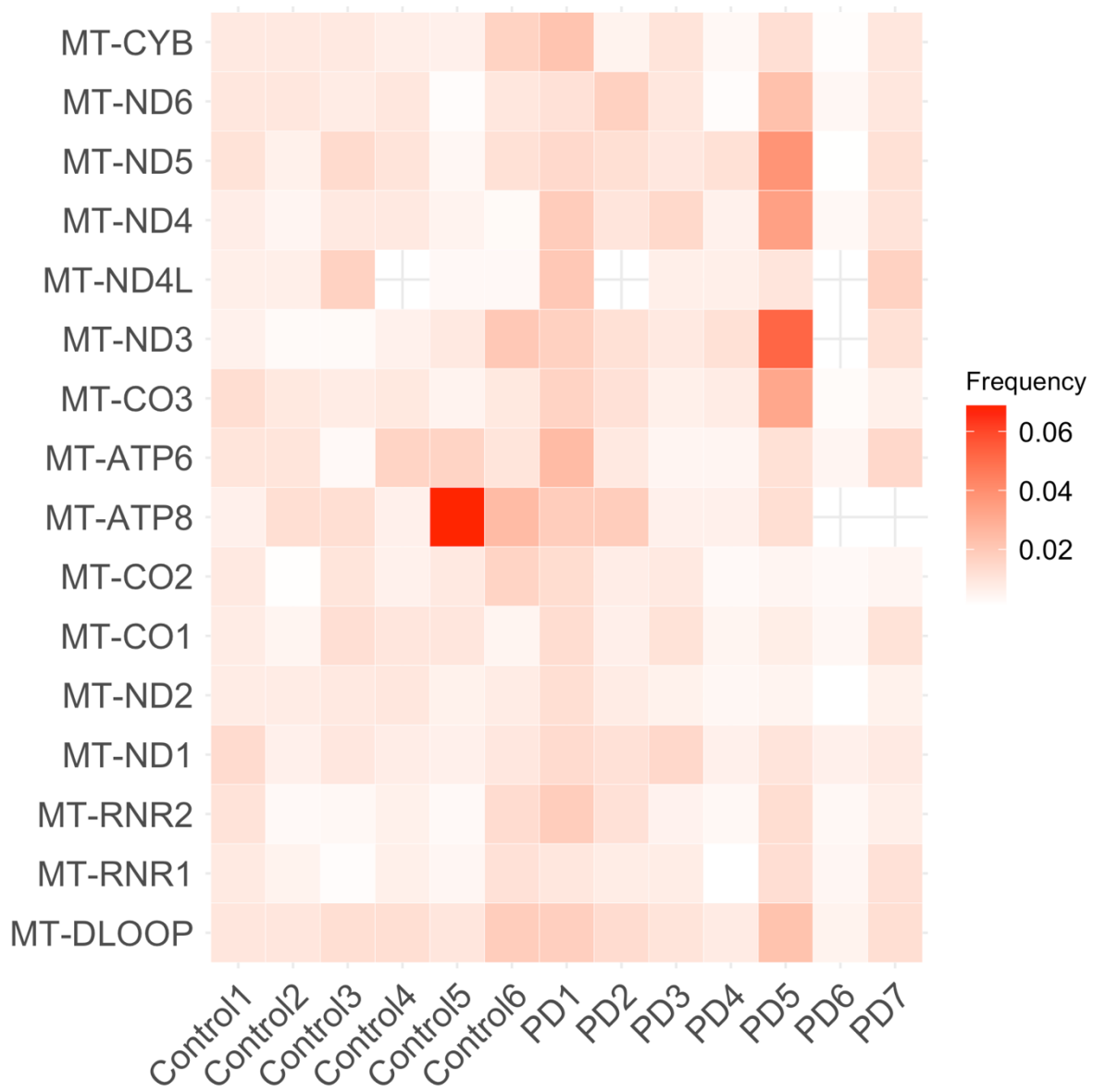

Figure 4.2-27 Normalised frequency of point mutations with high MutPred score in different genomic regions

This heatmap illustrates the normalised frequency of point mutations (by the length of the coding region) with high MutPred scores (≥ 0.5) accumulating in different mtDNA genomic regions. No distinct pattern was observed, except that PD5 harboured more point mutations with high MutPred scores in the major arc coding regions, including ND5, ND4, ND3, and CO3, compared to other cases. Additionally, Control 6 showed a higher frequency of point mutations in the ATP8 region compared to other regions.

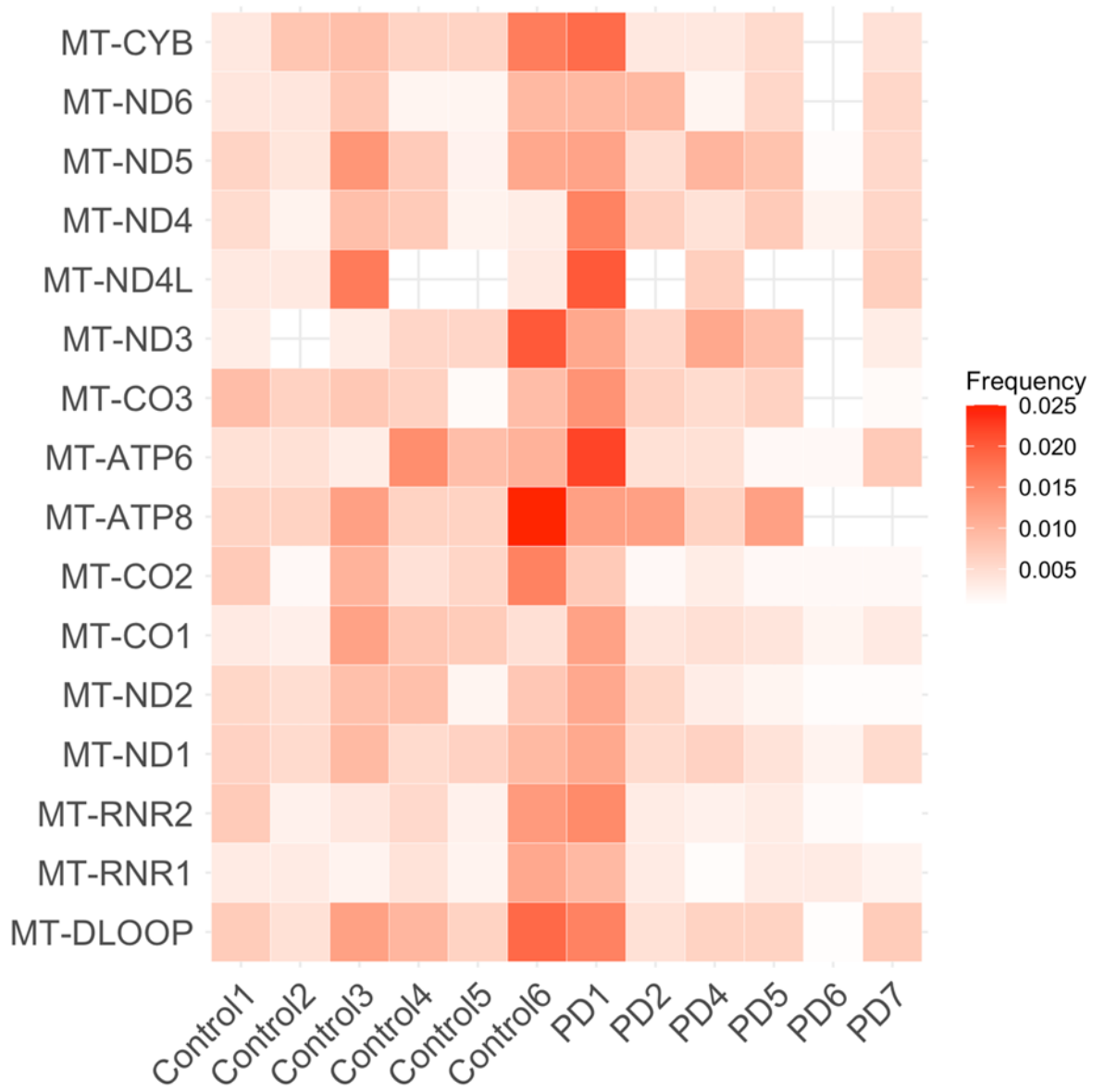

Figure 4.2-28 Normalised frequency of point mutations from neurons with DL less than 1% with high MutPred score in different genomic regions

This heatmap illustrates the normalised frequency of point mutations (by the length of the coding region) with high MutPred scores (≥ 0.5) from neurons with a deletion load no greater than 1%, accumulated in different mtDNA genomic regions. No distinct pattern was observed, except that Control 6 and PD1 harboured higher numbers of point mutations with high MutPred scores.

4.2.7. *Correlations*

A correlation analysis was conducted to investigate potential relationships between the number of point mutations per neuron and postmortem delay (PMD), patient age, Braak stage, and disease duration. When including all neurons, no correlation was observed between the number of point mutations per neuron and PMD (PD: R = 0.0065, p = 0.74; Control: R = 0.045, p = 0.83; Pearson's correlation, Figure 4.2-29-A), suggesting that PMD did not influence the results. Similarly, no correlation was found between the number of point mutations per neuron and patient age (PD: R = 0.15, p = 0.44; Control: R = 0.16, p = 0.44; Pearson's correlation, Figure 4.2-30-A), or Braak stage (PD: R = 0.18, p = 0.35; Pearson's correlation, Figure 4.2-31-A), indicating that neither the aging process nor disease progression is associated with the accumulation of point mutations. No correlation was observed between the number of point mutations per neuron and disease duration (R = -0.088, p = 0.72; Pearson's correlation, Figure 4.2-32-A). Furthermore, no clear difference was observed between different sex in both PD (p = 0.89, t-test) and control neurons (p = 0.085, t-test, Figure 4.2-33-A), supporting the conclusion that these factors are not related to point mutation accumulation.

When neurons with a deletion load above 1% were excluded, no correlation was observed between the number of point mutations per neuron and PMD (PD: R = -0.19, p = 0.95; Control: R = 0.33, p = 0.16; Pearson's correlation, Figure 4.2-29-B), confirming that PMD did not affect the results. Similarly, no correlation was found between the number of point mutations per neuron and patient age (PD: R = 0.004, p = 0.99; Control: R = 0.074, p = 0.76; Pearson's correlation, Figure 4.2-30-B) or Braak stage (PD: R = 0.05, p = 0.87; Pearson's correlation, Figure 4.2-31-B), indicating that neither the aging process nor disease progression is related to point mutation accumulation. No correlation was observed between the number of point mutations per neuron and disease duration (R = -0.13, p = 0.74; Pearson's correlation, Figure 4.2-32-B). Finally, no clear difference was observed between different sex in both PD (p = 0.45, t-test) and control neurons (p = 0.27, t-test) (Figure 4.2-33-B), further supporting the conclusion that these factors are not associated with point mutation accumulation.

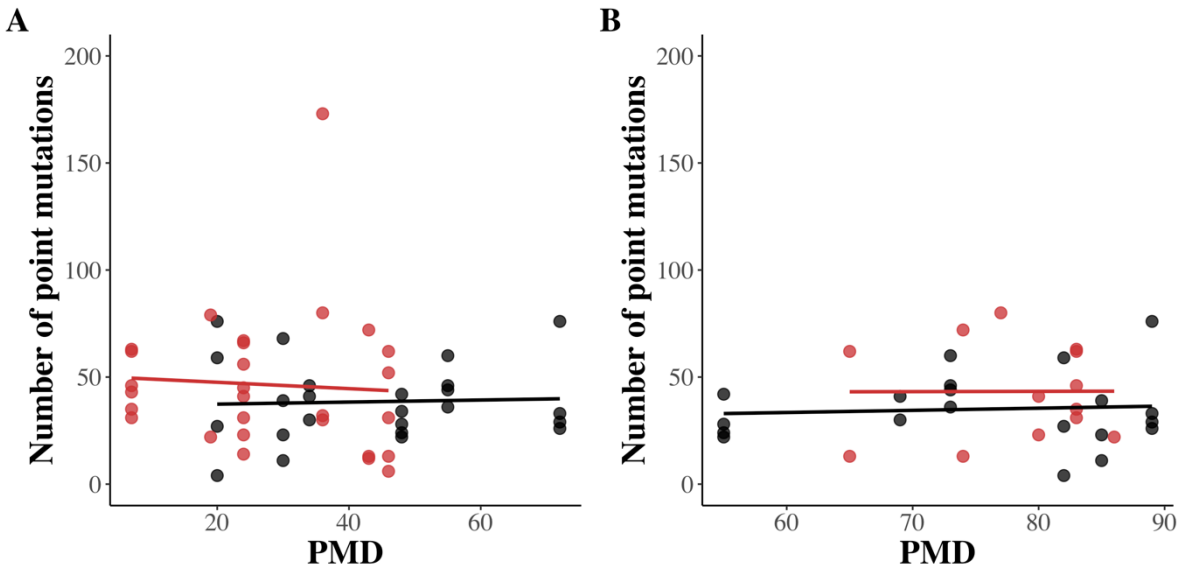

Figure 4.2-29 No correlation between number of point mutations per neuron and postmortem delay

In Plot A, no increase in the number of point mutations was observed with increasing postmortem delay (PMD) in either PD neurons (R = -0.065, p = 0.74; Pearson's correlation) or control neurons (R = 0.045, p = 0.83; Pearson's correlation). In Plot B, after excluding neurons with a deletion load greater than 1%, no increase in the number of point mutations was observed with increasing PMD in either PD neurons (R = -0.19, p = 0.95; Pearson's correlation) or control neurons (R = 0.33, p = 0.16; Pearson's correlation). Black represents control neurons, while red indicates PD neurons.

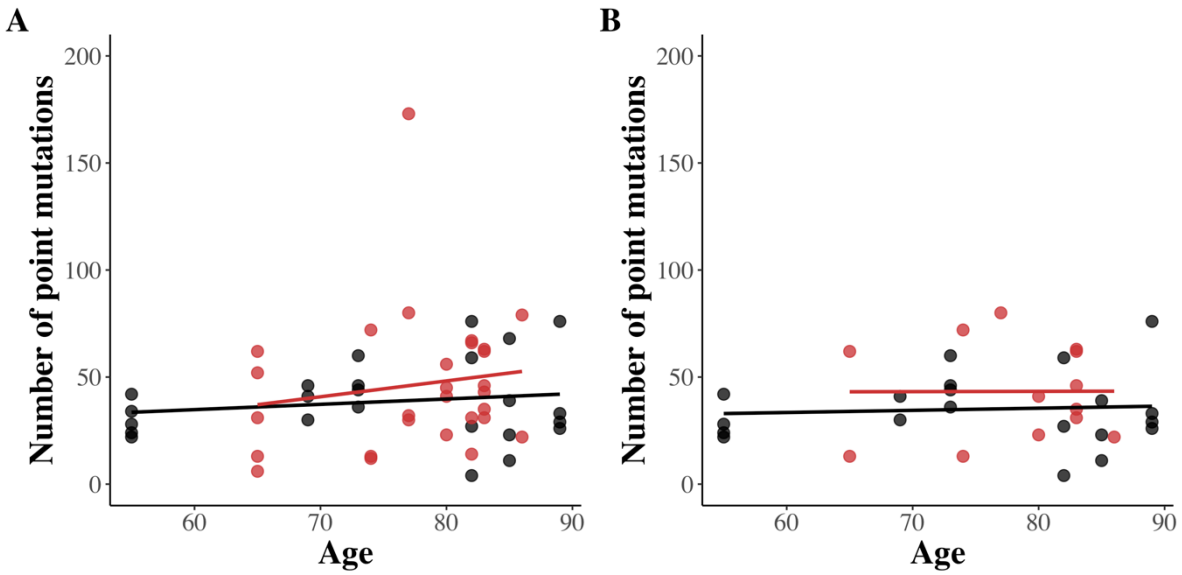

Figure 4.2-30 No correlation between number of point mutations per neuron and age

In Plot A, no clear increase in the number of point mutations per neuron was observed with age in either PD neurons (R = 0.15, p = 0.44; Pearson's correlation) or control neurons (R = 0.16, p = 0.44; Pearson's correlation). In Plot B, after excluding neurons with a deletion load above 1%, the number of point mutations per neuron still showed no clear increase with age in both PD neurons (R = 0.004, p = 0.99; Pearson's correlation) and control neurons (R = 0.074, p = 0.76; Pearson's correlation). Black represents control neurons, while red indicates PD neurons.

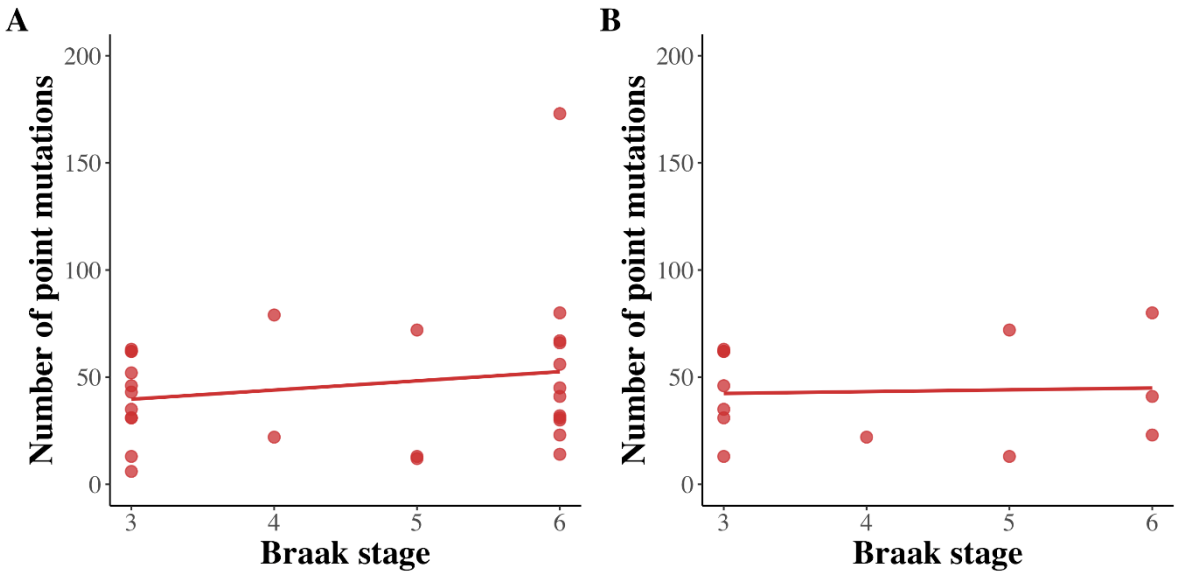

Figure 4.2-31 No correlation between the number of point mutations per neuron and Braak stage

In Plot A, when including all point mutations, no increase in the number of point mutations was observed with increasing Braak stage in PD cases (R = 0.18, p = 0.35; Pearson's correlation). In Plot B, after excluding neurons with a deletion load above 1%, no increase in the number of point mutations was observed with increasing Braak stage in PD cases (R = 0.05, p = 0.87). Black represents control neurons, while red indicates PD neurons.

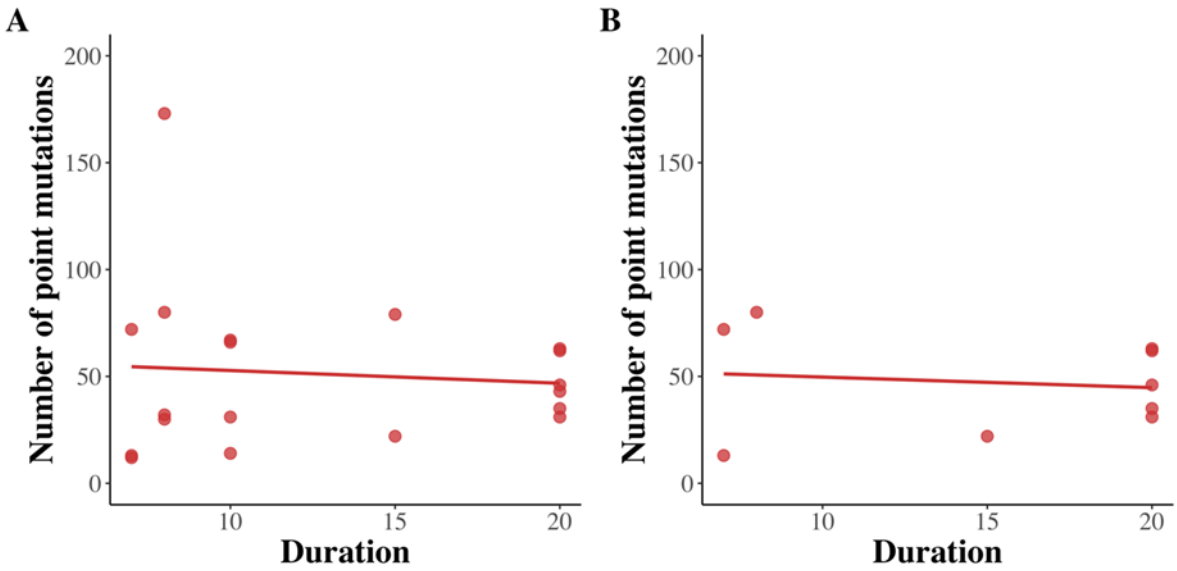

Figure 4.2-32 No correlation between the number of point mutations per neuron and disease duration

In Plot A, when including all point mutations, no increase in the number of point mutations was observed with increasing disease duration in PD cases (R = -0.088, p = 0.72; Pearson's correlation). In Plot B, after excluding neurons with a deletion load above 1%, no increase in the number of point mutations was observed with increasing disease duration in PD cases (R = -0.13, p = 0.74, Pearson's correlation). Black represents control neurons, while red indicates PD neurons.

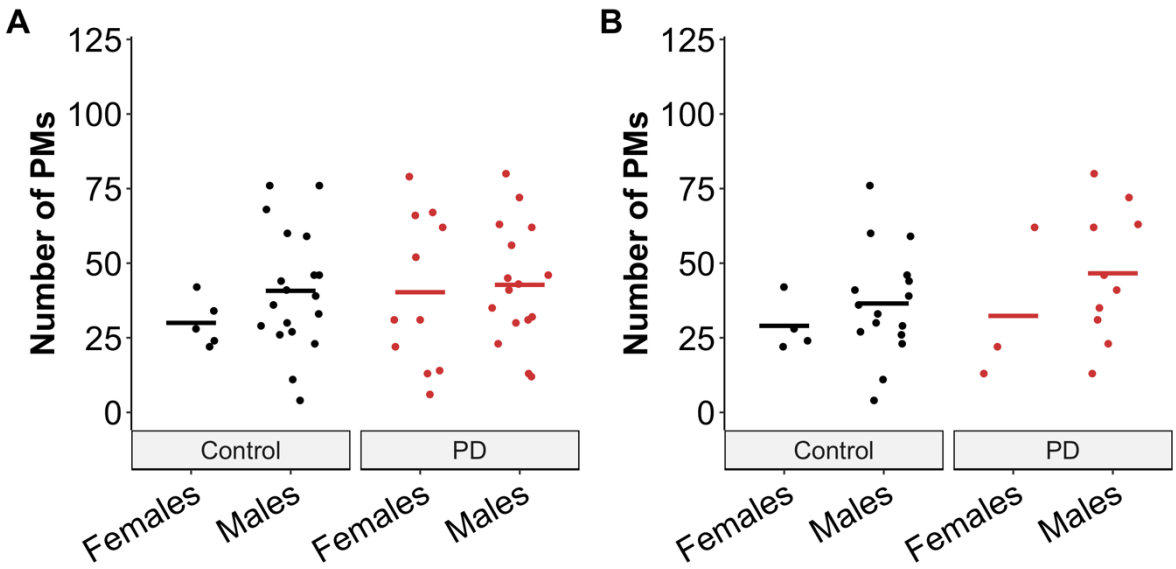

Figure 4.2-33 No difference in the number of point mutations per neuron and sexes

In Plot A, when including all point mutations, males exhibited a higher accumulation of point mutations than females in both PD (p = 0.79, t-test) and control neurons (p = 0.085, t-test), though the differences were not statistically significant. In Plot B: After excluding neurons with a deletion load above 1%, males still accumulated more point mutations than females in both PD (p = 0.45, t-test) and control neurons (p = 0.27, t-test), though these differences remained not significant. PMs= point mutations.

4.3. *Discussion*

To ensure accuracy, all analyses were conducted using point mutations from either all neurons or neurons with a deletion load no greater than 1%. This approach was taken to account for potential interaction between mtDNA deletions and point mutations (Hjelm *et al.*, 2023). Across all analyses, including the number of point mutations per neuron, point mutation load, distribution, and correlation tests, no differing trends were observed between conditions in either cohort. The only notable difference was that analyses excluding neurons with high deletion loads included fewer point mutations. This outcome was expected, as point mutations present in those excluded neurons were omitted from the analysis. The consistency in trends and test results indicates that deletion load has a limited impact on the level of point mutations. This also confirmed

the effectiveness of the in-house quality control steps for point mutations and supports the high quality of the point mutation data detected and analysed in this research.

The accumulation of point mutations and point mutation load in PD neurons was higher than in control neurons, though the difference was not statistically significant. When examining the number of point mutations at different heteroplasmy levels within individual neurons, it is noteworthy that mutations with middle heteroplasmy levels are more frequently observed compared to those with low or high heteroplasmy levels across both conditions. Low heteroplasmy levels likely represent newly arisen mutations that have not yet undergone substantial clonal expansion. This suggests that at a late stage of life, no significant surge in errors or 'seeds' occurs (Linnane *et al.*, 1989), and the damage primarily originates from mutations that occurred earlier and underwent slow clonal expansion (Elson *et al.*, 2001; Greaves *et al.*, 2014). In contrast, high heteroplasmy levels indicate mutations that have completed clonal expansion and now dominate the mitochondrial genome, which aligns with the observation in paper (Reeve *et al.*, 2009). Mutations at middle heteroplasmy levels may reflect an intermediate phase, where clonal expansion has occurred to some degree but has not progressed further. This distribution pattern might suggest the potential involvement of selective mechanisms, possibly mediated through mitophagy pathways, that limit the progression of certain mutations. Previous studies have shown that mtDNA point mutations can induce mitophagy, potentially linked to a loss of mitochondrial membrane potential or oxidative stress (Gilkerson *et al.*, 2012; Lin *et al.*, 2019).

No clear differences in the accumulation of point mutations within the OXPHOS complex coding regions or RNA areas were observed, either within the same cases or between PD and control neurons. The accumulation of point mutations appeared evenly distributed across different regions. Interestingly, the higher incidence observed in tRNA compared to rRNA in primary mitochondrial disease was not observed in this study (Wong *et al.*, 2002). This discrepancy may reflect differences between inherited and somatic mutations. In mtDNA disease, the observed mutational landscape is shaped by what passes through the germline bottleneck (Bergstrom and Pritchard, 1998), whereas in somatic mutations, both population level and cellular selection pressures influence the mutational profile (Schon, DiMauro and Hirano, 2012).

When point mutations were divided by individual cases, no significant differences were observed among cases, suggesting that there were no outliners within the cohort and that the results are representative of all 13 cases. Also, no clear correlation was observed between patients details with any of the analysed did in this research.

The distribution of point mutations was found to be spread across the entire mitochondrial genome, with no distinct patterns observed in most regions except for the control region (m.16024 – m.576). In both PD and control neurons, a higher frequency of point mutations was detected in the control region or the D-loop region. This finding is consistent with the D-loop's critical role as the primary non-coding regulatory region of mtDNA, containing essential elements such as OriH and promoters for transcription initiation. The elevated mutation burden in the D-loop may reflect its increased susceptibility to replication errors and oxidative damage, as its displaced stranded conformation during replication renders it more vulnerable compared to the double-stranded coding regions. Additionally, the D-loop serves as a hotspot for replication and transcription activity, leading to greater exposure to ROS generated by mitochondrial respiration. The lack of coding constraints in this non-coding region may also permit the accumulation of mutations over time, as there is no selective pressure to maintain functional protein sequences.

However, this result contrasts with observations from studies of SNpc and frontal cortex tissue homogenates from PD patients, which reported increased somatic mtDNA variation, particularly in the coding regions *COX1*, *COX2*, and *CYTB* (Coxhead *et al.*, 2016). This discrepancy may arise because the current study focused specifically on cholinergic neurons, whereas brain homogenates consist of multiple cell types, including astrocytes, glia cells, and neurons.

Our analysis revealed no significant differences in the number of synonymous and non-synonymous point mutations, or in the number of mutations with a MutPred score above 0.5, between PD and control neurons. This suggests that the mutational burden, in terms of both quantity and predicted pathogenic potential, is comparable between these groups. Synonymous mutations, which are generally considered neutral, were observed at similar frequencies, indicating that overall mtDNA mutation rates do not differ substantially between PD and control neurons.

No hotspots were detected in these neurons, likely because the recurrence of mutations was too low to distinguish from random variation. Nevertheless, to explore the data further, we examined the recurrent mutations that were observed. Interesting, 6 out of 14 (42.9%) are located in the *HV1* and *HV2* regions. This is not surprising, as the hypervariable regions are prone to exhibiting a high degree of polymorphism due to several factors. Their proximity to the mtDNA replication initiation site increases the likelihood of replication errors, leading to point mutations (Meyer, Weiss and von Haeseler, 1999). Additionally, their noncoding nature makes them less constrained by functional selective pressures (Aquadro and Greenberg, 1983). HV polymorphisms have also been linked to aging; previous research has reported that a point mutation in the *HV2* region (m.189A>G,(Del Bo *et al.*, 2002) is associated with aging skeletal muscle cells. Furthermore, it is noteworthy that all of the recurrence variants detected variants detected in d-loop region in this study have been previously reported in the literature as mutable (Coskun, Beal and Wallace, 2004; Bragoszewski *et al.*, 2008; Greaves *et al.*, 2009; Williams *et al.*, 2013; Reznik *et al.*, 2016).

A search of the MitoMap database (https://www.mitomap.org/allelesearch.html) revealed two previously unreported point mutations: m.3629C>T in the *ND1* coding region, found in PD neurons, and m.8138A>C in the *CO2* coding region, found in control neurons. All other variants had been reported in the MitoMap database. Several of these variants have been frequently reported, with most hotspots located in hypervariable regions or the control region. For example, m.152T>C, located in the *HV2* and *OriH* regions, has been detected in PD patients across various studies (Ozawa *et al.*, 1991; Vives-Bauza *et al.*, 2002; Khusnutdinova *et al.*, 2008), and has been suggested to be associated with hypertension (Kwaśniewski *et al.*, 2023). Additionally, one hotspot located in a complex coding region (m.13928G>A) has been mentioned in multiple studies. This mutation has been associated with Leber's metabolic syndrome (Qian *et al.*, 2005) and is thought to affect mitochondrial matrix pH, influencing intracellular calcium dynamics (Kazuno *et al.*, 2006).

Similarly, the comparable frequencies of non-synonymous mutations and mutations with high MutPred scores suggest that PD-associated neuronal dysfunction may not be driven solely by an increased accumulation of potentially deleterious mtDNA

mutations. This finding may also reflect the unbiased neuron selection method used in this research, as the neurons analysed, from both PD and control groups, may not yet exhibit mitochondrial dysfunction.

The Ts/Tv ratio serves as an indicator of mutation pressure and provides insights into the mechanisms underlying point mutation generation. No significant difference was observed in the Ts/Tv ratio between PD and control groups, with both exhibiting similar values around 4. This consistency suggests that the mutational processes influencing mtDNA in the studied samples are not significantly different between the two conditions. A Ts/Tv ratio around 4 indicates a mutation spectrum dominated by transitions, which are characteristic of mtDNA mutagenesis driven by replication errors and spontaneous deamination, rather than transversions, which are typically associated with oxidative stress-induced damage. This aligns with the strong bias observed from homoplasmic mtDNA point mutations, with transitions occurring approximately 15 times more frequently than transversions (Belle *et al.*, 2005).

The G:C to T:A transversion base changes are associated with 8-oxo-dG levels, a well-established marker of oxidative DNA damage, and can serve as an indicator for extent of oxidative DNA damage (De Bont and van Larebeke, 2004; Kino *et al.*, 2017; Suzuki and Kamiya, 2017). There is no notable variation in the level of the G:C to T:A base changes between the PD and control groups, with values of approximately 0.55 in both groups. However, this value is higher than the 0.3 reported in SNpc dopaminergic neurons (Dölle *et al.*, 2016), which could suggest higher oxidative stress in cholinergic neurons or reflect differences in the methodologies used.

These findings further support the notion that oxidative stress while a hallmark of PD pathology (Henchcliffe and Beal, 2008; Puspita, Chung and Shim, 2017), may not be the primary driver of the observed mtDNA point mutations profiles in this study.

Chapter 5. Transcriptional changes

5.1. *Aims*

Both PPN cholinergic neurons and SNpc dopaminergic neurons are severely affected in PD and are considered key targets for therapeutic rescue, yet they exhibit very different responses in terms of mtCN ((Jankovic, 2008; French and Muthusamy, 2018). A previous study by Bury and colleagues made an observation (Bury *et al.*, 2017), that the mtCN of cholinergic neurons within the PPN area are increased in PD cases (mean = 10,706 ± 1441) compared to the aged controls (mean = 7,017 ± 825) ($p = 0.029$*, 2-way Anova). This finding contrasts with results from dopaminergic neurons in the SNpc of PD patients (Reeve *et al.*, 2008; Grünewald *et al.*, 2016). The regulation of mtCN is a complex process involving multiple pathways. In this research, we used single-neuron multiplex RT-PCR to measure the transcriptional levels of selected genes in individual neurons, aiming to better understand the mtCN response. Three pathways were mainly focused on in this research and are likely involved in this alternation: biogenesis pathway, maintenance pathway, and the mitophagy pathway. A detailed description of these three pathways can be found here (Chapter 1 sections 1.6.4, 1.7.1, 1.7.4, 1.7.6).

PGC1α was chosen as the key target for the biogenesis pathway due to its ability to regulate key factors involved in mtDNA transcription and replication, such as coactivation of NRFs (St-Pierre *et al.*, 2003; Finck and Kelly, 2006). *TFAM* was selected as a crucial target for the mtDNA maintenance pathway, as it ensures packaging and organization of mtDNA within the mitochondrion, protecting it from oxidative damage and degradation (Alam *et al.*, 2003). For the mitophagy pathway, *PINK1* was selected for its role in detecting damaged mitochondria, phosphorylating ubiquitin and the E3 ubiquitin ligase Parkin, and initiating the recruitment of mitophagosomes to degrade the damaged mitochondria (Okatsu *et al.*, 2012; Matsuda, Kitagishi and Kobayashi, 2013).

The aim of this chapter is to measure the transcriptional levels of essential genes regulating the copy number of mtDNA in single PPN cholinergic neurons and determine whether there are any discernible differences between PD and control neurons. Single neuron analysis was chosen because brain tissue comprises a heterogeneous mixture

of cell types, and bulk measurements from homogenised samples can be confounded by background noise and cell-type heterogeneity. Moreover, individual neurons may exhibit distinct transcriptional profiles, rendering pooled neuronal analyses less informative. This study also aims to provide a deeper understanding of the variability in transcriptional responses across different neuronal subtypes. The patterns identified here will serve as a basis for comparison with dopaminergic neurons from SNpc.

To achieve this, multiplex RT-PCR is employed to quantify the expression levels of three key target genes, each representing critical pathways of interest: *PGC1α* for mitochondrial biogenesis, *TFAM* for mitochondrial maintenance, and *PINK1* for mitophagy, using single cholinergic neurons laser captured from PPN.

5.2. *Optimisation*

To measure RNA levels in single cholinergic neurons from the PPN, a series of preparatory steps were required. The entire experimental process is outlined in the (Figure 5.2-1). To ensure reliable results, multiple steps required optimization, including the staining method, the LCM procedure, the reverse transcriptional protocol, and the RT-PCR techniques.

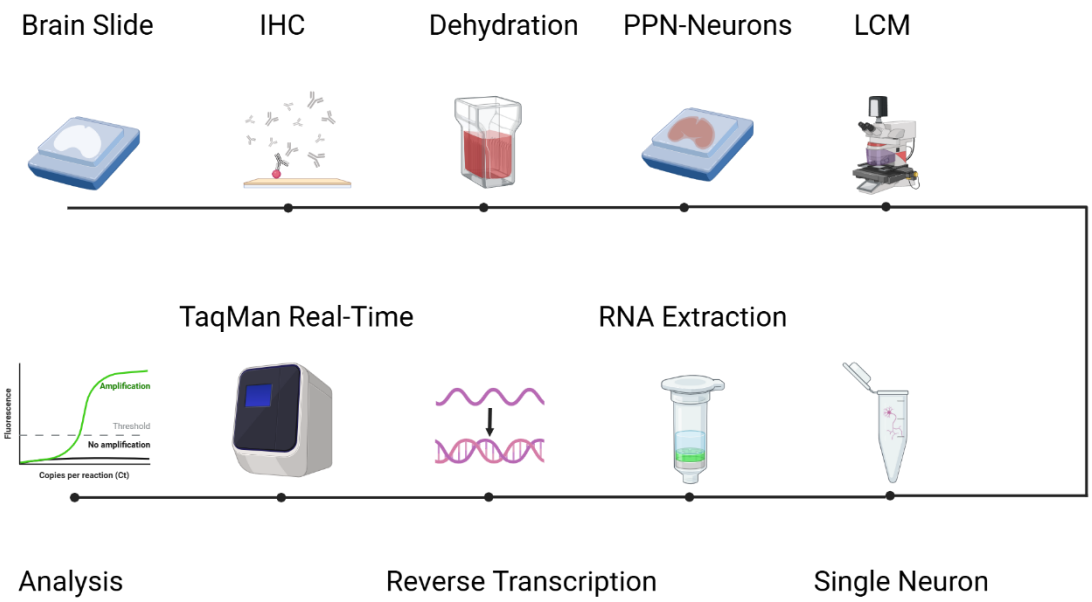

Figure 5.2-1 Flowchart of the transcriptional level protocol

This flowchart outlines the experimental workflow from brain blocks to RT-PCR analysis of target genes. The process begins with preparing brain slides containing the targeted area obtained from the brain bank. Using ChAT IHC, cholinergic neurons are stained. Following dehydration, the PPN and cholinergic neurons within the targeted region are identified using ChAT staining and mapping slides. LCM is the performed to isolate single cholinergic neurons. RNA is extracted, followed by reverse transcription into cDNA. The final steps involve conducing RT-PCR on target genes using TaqMan assay system and performing amplification analysis to determine the copy number of the genes of interest. ChAT: Choline Acetyltransferase; IHC: Immunohistochemistry; LCM: Laser capture microdissection.

5.2.1. *Staining optimisation*

To measure RNA levels in single cholinergic neurons from the PPN, a series of preparatory steps were required. The entire experimental process is outlined in the Figure 5.2-2.

Identifying the PPN area is very challenging. As a non-pigmented region, its boundaries are not clearly defined. However, with the help of mapping slides (on which the PPN was identified by a neurologist using serial brain sections from the same block as the target slice) and its location relative to the LC (a pigmented area near the PPN), the identification process became feasible.

After identifying the PPN, the next step was to visualize the cholinergic neurons within this region, as these neurons lack natural pigmentation. As described in the methodology chapter (Chapter. 2), ChAT, the enzyme responsible for catalysing the biosynthesis of acetylcholine, is highly expressed in cholinergic neurons and is commonly used as a specific marker for these neurons. Although a protocol for labelling cholinergic neurons using ChAT IHC method has already available within the research group, adjustments were necessary. The previous methodology did not include a dehydration step, which is essential for the downstream application of LCM. As LCM requires dehydrated slides, optimization of the protocol was undertaken to ensure compatibility with this experimental requirement.

For human postmortem tissue cholinergic IHC staining, 3,3’,5’5’-Tetramethylbenzidine (TMB) was used as the substrate. Unfortunately, due to the TMB’s solubility in ethanol, all slides stained using TMB-IHC experienced blurriness, making it difficult to distinguish both the PPN area and cholinergic neurons from their neighbouring areas and cells. To address this issue, we optimised the final step of the IHC staining by replacing horseradish peroxidase (HRP) substrate from TMB to NovaRED, which is insoluble in ethanol and does not pose a risk of damaging RNA structures, unlike the commonly used ethanol-insoluble HRP substrate 3,3’-diaminobenzidine (DAB).

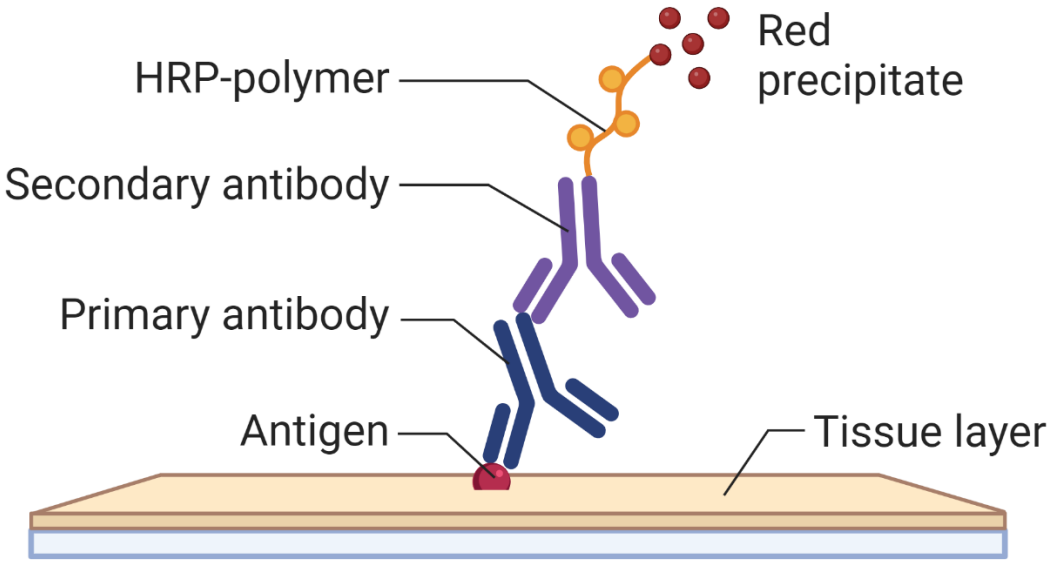

Figure 5.2-2 HRP-IHC reaction illustration

This illustration shows the reactions that occur during IHC staining. First, the primary antibody binds to the antigen of the target protein. Next, the secondary antibody, conjugated to an HRP polymer, binds to the primary antibody. Finally, the HRP reacts with NovaRED, resulting in a red precipitate. There is a wide range of HRP substrates that can react with HRP, each with different advantages. Therefore, HRP substrates can be optimised based on specific requirements.

A comparison was made between TMB and NovaRED as HRP substrates. Slides from one patient were stained using identical ChAT staining protocol described in the method chapter (2.4.1), with the only variation being the HRP substrate used in the final step. In this step, either TMB or NovaRED was applied for the same duration on each slide. After staining, both slides were dehydrated using the same method, involving treatment with a series of ethanol concentrations (50%, 75%, 95%, 100%) for 30 seconds each. Following dehydration, both slides were observed under an inverted Zeiss microscope (Axiovert 200M; Carl Zeiss, Oberkochen, Germany). Staining results can be seen in (Figure 5.2-3, Figure 5.2-4).

After selecting NovaRED as the HRP substrate, the reaction time was optimized. A series of slides were stained using the identical ChAT staining protocol mentioned previously, with the only variation being the reaction time of NovaRED, ranging from 5 to 15 seconds with 1-second intervals. Upon comparison, the image obtained at 8 seconds provided the clearest identification of the target area and has been adopted for future staining. Although the staining background is occasionally unclear due to the shortened incubation time to prevent RNA degradation, careful observation is necessary when identifying neurons.

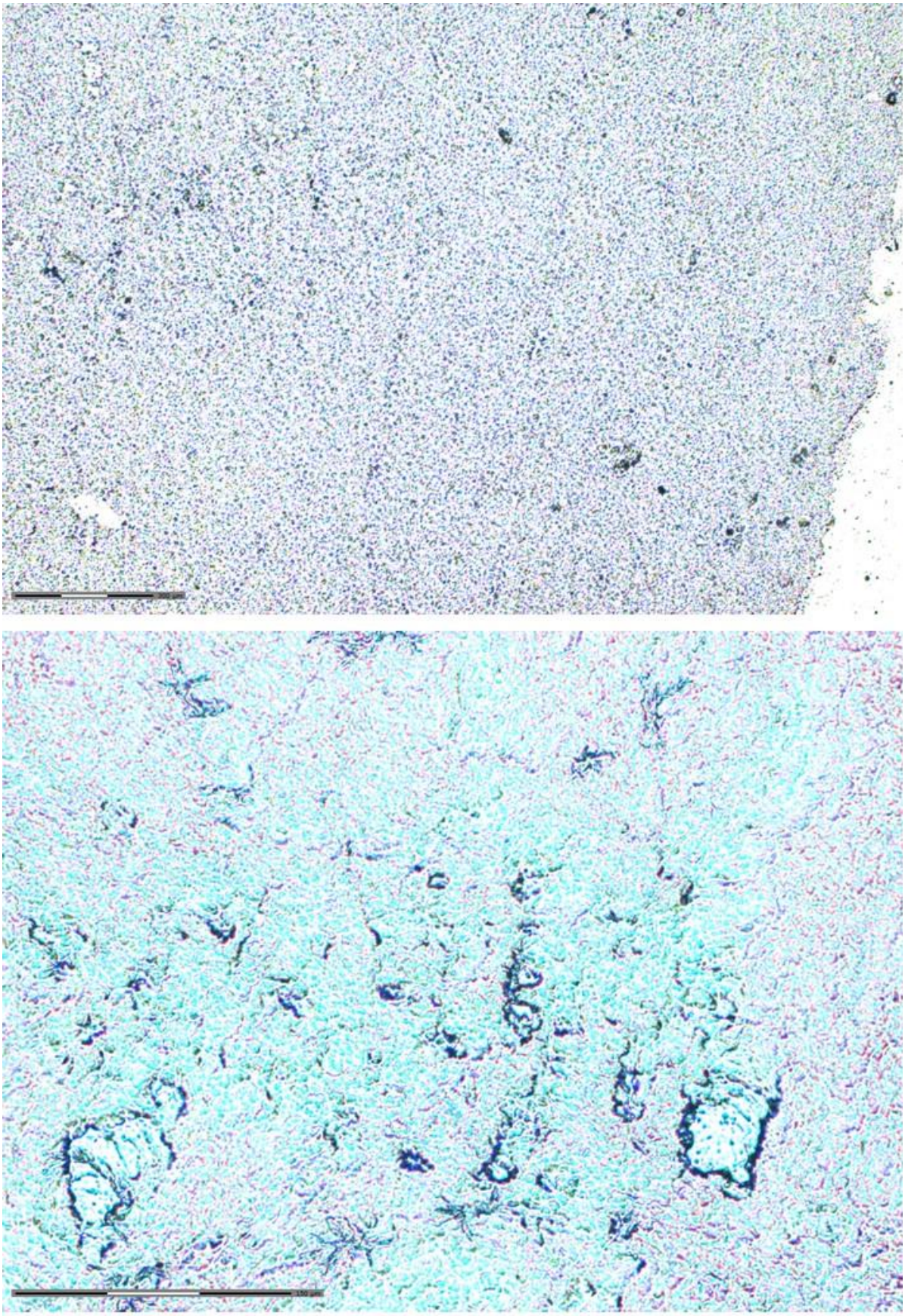

Figure 5.2-3 PPN after TMB as HRP substrate

After ethanol dehydration, the entire image appears blurry at both magnifications due to the dissolution of TMB blue precipitate in ethanol. Neither the clear edges of the PPN nor the cholinergic neurons are easily observable. The upper panel was captured at 5x magnification, while the lower panel was captured at 20x magnification using an inverted Zeiss microscope.

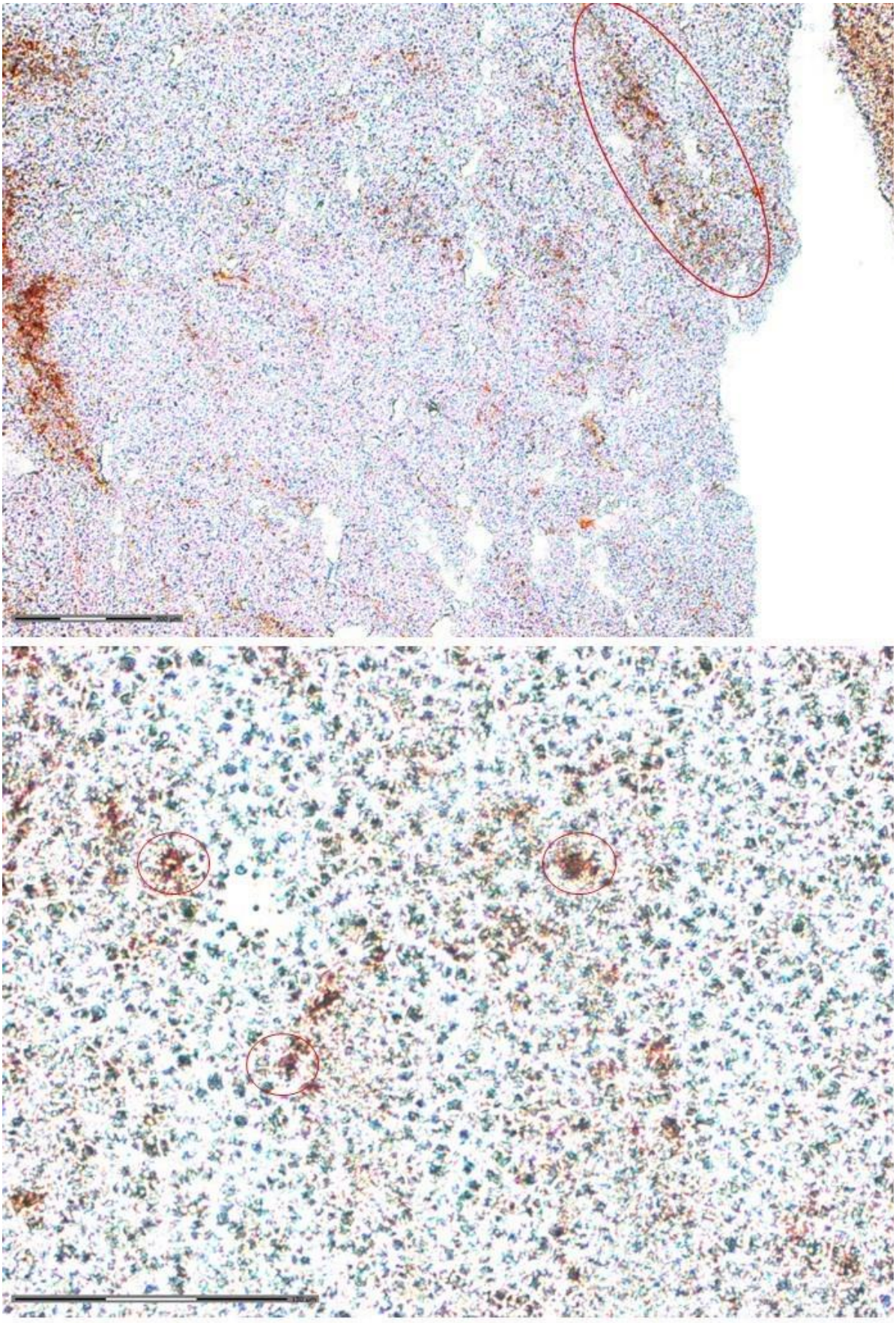

Figure 5.2-4 PPN after NovaRed as HRP substrate

After ethanol dehydration, the clean edge of the PPN, circled in red, is still visible in the upper panel of the image, as well as the clear edge of the cholinergic neurons, also circled in red. The upper panel was captured at 5x magnification, while the lower panel was captured at 20x magnification using an inverted Zeiss microscope.

5.2.2. *Optimization of the LCM and the RNA extraction*

The entire LCM process follows the protocol optimized and described in a previous study (Bury *et al.*, 2017) and is detailed in the (Chapter 2.4.3). The laser cutting energy and angle vary across individual slides and are optimized for each slide using the Calibration Wizard function of the P.A.L.M MicroBeam Laser-Capture Microdissection system (version 4.6).

The next step requiring optimization was determining the number of neurons to include in each sample. Different quantities of neurons were tested, and RNA was extracted from each sample and assessed for both quality and quantity using a NanoDrop™ One Microvolume UV-Vis spectrophotometer (ThermoFisher, USA). RNA concentration and purity were evaluated by examining the 260/280 and 260/230 ratios. Nucleic acids typically absorb light at 260 nm, while proteins, phenol, and other contaminants absorb at 280 nm. Absorbance at approximately 230 nm indicates the presence of salts and other chemicals. For pure RNA, a 260/280 ratio close to 1.8 is expected, and the 260/230 ratio typically ranges between 2.0 and 2.2, often higher than the 260/280 ratio. According to these standards, RNA quality and quantity were measured for samples containing varying numbers of neurons. In over 20 single-neuron samples, none produced usable NanoDrop results. Both the 260/230 and 260/280 ratios were far outside the acceptable range or were undetectable. As a result, multiple neurons were pooled for further testing. Pooled samples containing two, four, six, and eight neurons were prepared using LCM, and RNA was extracted from each. However, the ratios of RNA samples from pooled neurons also fell outside the acceptable range (Table 5.2-1-Before optimization).

Due to the poor quality of RNA extraction, even from pooled neurons, further optimization of the LCM technique and settings was undertaken to improve RNA quality.

During the LCM process, it is crucial to keep the energy used for both margin cutting and laser pressure catapulting (LPC) as low as possible, as excessively high laser energy can reduce the quantity of extracted RNA. Additionally, tissue handling time must be limited to four hours, as prolonged handling has been shown to decrease RNA quality and weaken RT-PCR signals. Given that ChAT IHC staining takes approximately three and a half hours after removing tissue from -80 °C storage, the remaining time for laser capture is limited to 30 minutes. To maximize efficiency, multiple slides from the same patient were processed within a single day. Optimization of the laser energy and cutting angle was performed on the first slide of the series, with the same settings applied to subsequent slides from the same patient.

Following the optimization of LCM, the RNA extraction protocol was refined to further enhance RNA quality (2.4.4 RNA extraction and reverse transcription). The standard PicoPure RNA extraction protocol recommended by ThermoFisher was modified by incorporating a 15-minute incubation on ice during the ethanol precipitation step to improve RNA concentration and desalting. Additionally, a 5-minute incubation at room temperature was added after applying the elution solution onto the extraction membrane to facilitate RNA dissolution into the elution buffer. This elution step was repeated to ensure thorough RNA recovery. Despite these adjustments, the quality of RNA extracted from pooled neurons improved only slightly and remained suboptimal (Table 5.2-1-After optimization).

Ensuring the reliability of NanoDrop measurements is challenging when RNA quantities are low, even though the RNA can still be successfully transcribed into cDNA and reliably detected through RT-PCR (Figure 5.2-5). Consequently, RNA extracted from tissue samples was not measured using NanoDrop prior to reverse transcription. Instead, negative controls were incorporated into both the reverse transcription and RT-PCR steps to ensure the biological validity of all collected data points. Despite the high dropout rate (up to 95% in some cases), single neurons consistently generated repeatable Ct values, demonstrating their suitability as starting material for RT-PCR analysis. Given the importance of studying changes at the single-neuron level, subsequent experiments utilized single neurons as the starting material.

	Before optimization			After optimization		
Neuron(s)	ng/µl	260/280	260/230	ng/ µl	260/280	260/230
2	1.30	1.05	1.53	1.50	1.72	1.62
4	1.00	1.69	0.68	1.20	1.86	2.01
6	1.41	1.41	0.97	2.10	1.21	1.72
8	13.9	1.50	0.56	4.30	1.65	1.92

Table 5.2-1 RNA quality of pooled neurons

The NanoDrop results of pooled neurons (two, four, six and eight) are shown in this table. Before optimizing the RNA extraction step, the RNA quality and both ratios were low and unreliable. After optimization, there was a slight increase in both quality and quantity of the extracted RNA across all pooled neurons samples.

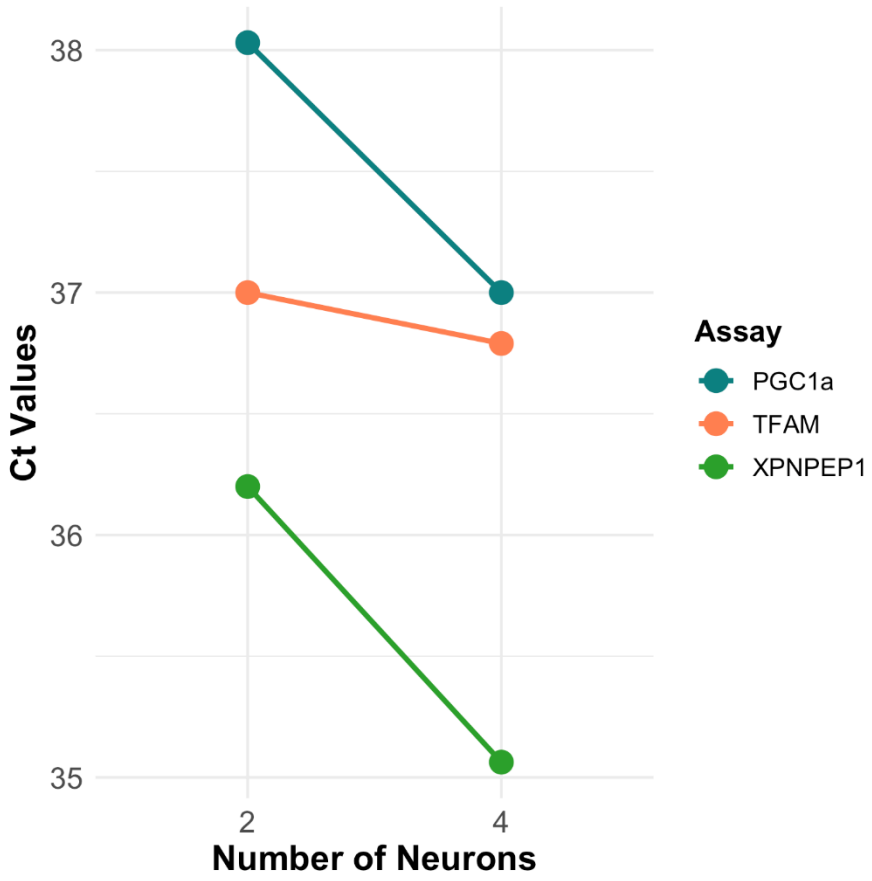

Figure 5.2-5 Neuron number and decreased Ct value

This figure illustrates that as the cell number increased, the Ct values for all targets decreased, indicating a higher amount of targeted mRNA in the original material. This suggests the capability of RT-PCR to effectively detect mRNA. Cycle threshold (Ct). Blue represents the assay for PGC1α orange for TFAM, and green for (X-Prolyl Aminopeptidase 1) XPNPEP1.

5.2.3. *Reverse transcriptional systems.*

There are multiple approaches to performing RT-PCR. It can be conducted directly from RNA as one-step RT-PCR or as a two-step process where RNA is first reverse transcribed into cDNA before proceeding with PCR. The two-step method allows for the storage of reverse-transcribed cDNA, while the one-step method saves time and minimises RNA degradation by reducing sample handling.

Two types of reverse transcriptase kit were purchased and compared: the Tetro cDNA synthesis kit containing moloney murine leukaemia virus (MMLV) reverse transcriptase (BIO65043, Meridian Bioscience, USA), and the SuperScript IV VILO MasterMix (11756050, ThermoFisher, USA) containing SuperScript IV (SSIV) Reverse transcriptase. The Tetro MMLV cDNA synthesis kit contains both oligo and random DNA primers and hexamers (RPs). Oligo primers containing a segment of repeating deoxythymidines (dT), which targets the RNA with polyA tail, while RPs are beneficial/target RNA without polyA tail and can randomly align to RNA, initiating reverse transcription. Different PCR settings are required when adding different primers. During the incubation stage, MMLV oligo primers requires incubation at 45°C for 30 minutes. In contrast, MMLV RPs require an additional 10-minute incubation at 25 °C before the 45°C incubation for 30 minutes (Table 5.2-2).

To identify the optimal method for using the Tetro cDNA synthesis kit, a series of tests were conducted to evaluate the performance of various primers and settings combinations using *TFAM* TaqMan assay (Hs00273372_s1, ThermoFisher, USA), TaqMan universal MasterMix (4304437, ThermoFisher, USA), and RNA extracted from homogenized human midbrain postmortem tissues. RNA extraction was performed with the PicoPure RNA isolation kit (KIT0204, ThermoFisher, USA) following the protocol detailed in the methodology chapter (Chapter 2.3.4). This comparison demonstrates that adding oligo primers or both oligo primers and RPs under the oligo reaction settings resulted in lower Ct values compared to other combinations (mean = 33.18 ± 0.53 and 32.96 ± 0.43 respectively) (Table 5.2-3, Figure 5.2-6). For future comparisons, only oligo primers and the combination of oligo plus RPs under the oligo reaction settings will be used when employing MMLV reverse transcriptase.

	Preparation	Reverse Transcription	Termination
MMLV Oligos	n/a	45 °C for 30 minutes	85°C for 5 minutes
MMLV RPs	25°C for 10 minutes	45°C for 30 minutes	85°C for 5 minutes
SuperScript IV	25 °C for 10 minutes	50°C for 10 minutes	85°C for 5 minutes

Table 5.2-2 Reverse transcription thermal cycling conditions for different systems

This table summarises the PCR settings for different stages when using different reverse transcriptional system.

Assays	Reverse transcription	Settings	Ct mean
TFAM **(Hs00273372_s1)**	MMLV+Oligos	Oligo	33.18 ± 0.53
TFAM **(Hs00273372_s1)**	MMLV+RPs	Oligo	35.48 ± 0.13
TFAM **(Hs00273372_s1)**	MMLV +Oligos +RPs	Oligo	32.96 ± 0.43
TFAM **(Hs00273372_s1)**	MMLV+Oligos	RPs	33.46 ± 0.17
TFAM **(Hs00273372_s1)**	MMLV+RPs	RPs	35.67 ± 1.15
TFAM **(Hs00273372_s1)**	MMLV +Oligos +RPs	RPs	33.91 ± 0.32

Table 5.2-3 Optimization of MMLV primers and settings

This table shows the RT-PCR results of using various primer and settings combinations in same material and TaqMan assays. No clear different was observed among all the runs, but when adding oligo primers or both oligo primers and RPs under the oligo reaction settings resulted in lower Ct values compared to other combinations (mean = 33.18 ± 0.53 and 32.96 ± 0.43 respectively).

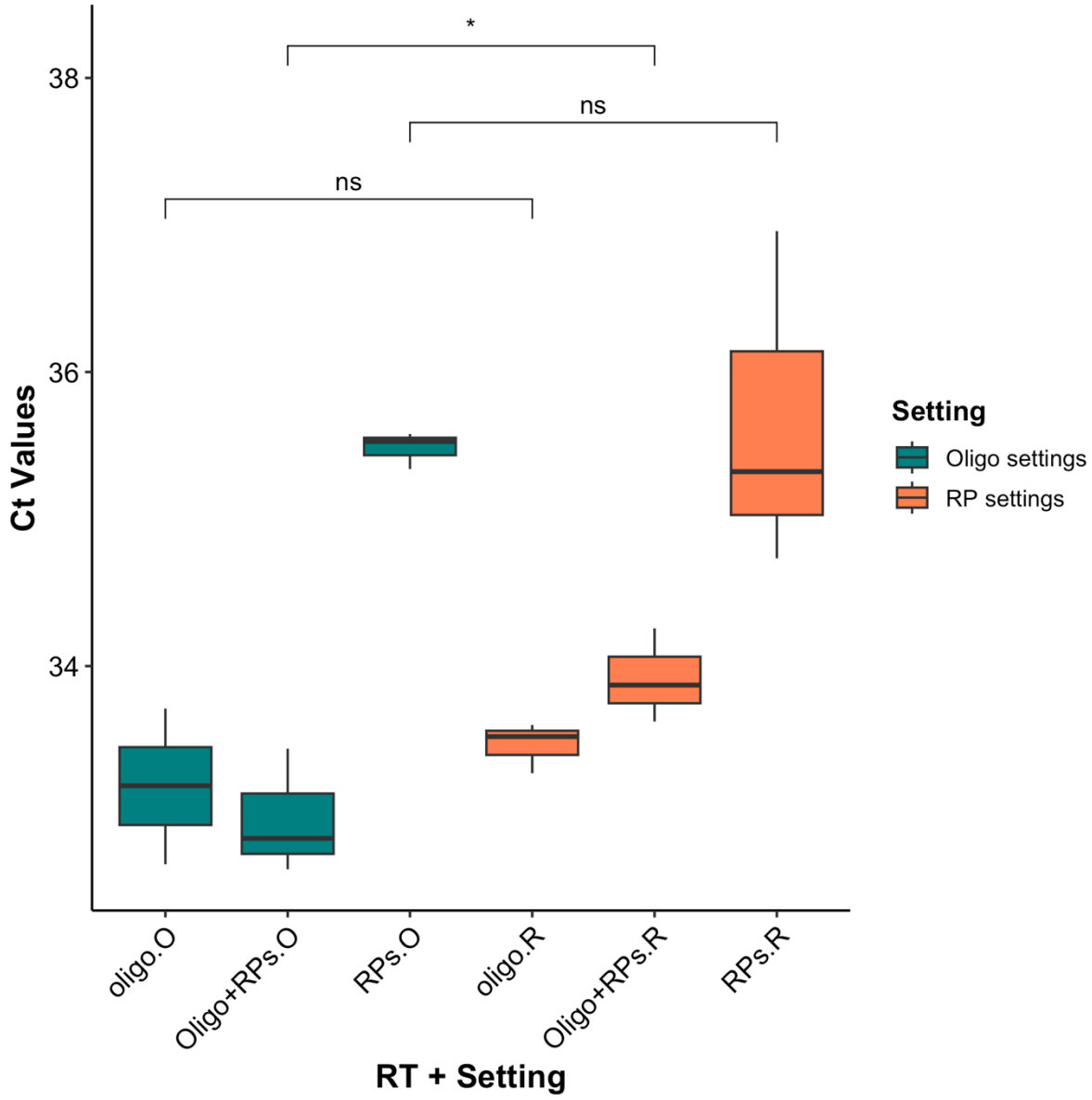

Figure 5.2-6 Optimization of MMLV primers and settings

This plot shows the Ct values of different reaction conditions when either or both Oligo and RPs were added. The Ct value was lower when Oligo and RPs were included in the reverse transcription reaction mix using the Oligo settings (mean = 32.96 ± 0.43). When using the Oligo in combination with RP settings, the Ct value was the lowest compared to the other groups (mean = 33.47 ± 0.17), but it was still higher than the Ct value obtained when both Oligo and RPs were added using the Oligo settings. Additionally, when both Oligo and RPs were added, the reaction using Oligo settings produced a lower Ct value compared to the RP settings (p = 0.036, t-test). Cycle threshold (Ct). Blue represents the oligo settings, and orange for EP settings.*

Further comparisons were made to determine the best method for performing reverse transcription using MMLV kit when detecting three different targets. The cDNA used for these assays was generated through two different MMLV reserve transcription methods, either using only Oligo primers or using both Oligos and RPs. Taqman Universal MasterMix was used for all reactions. Details of the results can be found in (Table 5.2-4, Figure 5.2-7). Results from a single assay are unlikely to fully demonstrate its capability, as different assays target distinct sequences, potentially yielding varying results. Additionally, testing multiple assays can help enhance suitability and reliability in multiplex assay applications. Three assays were used to test, in all three assays tested (*TFAM* (Hs00273372_s1, ThermoFisher, USA), *PGC1α* (Customized assay 1, ThermoFisher, USA), *X-prolyl aminopeptidase 1* (*XPNPEP1)* (Hs00958021_m1, ThermoFisher, USA)), adding both the Oligo and RPs resulted in a significantly lower Ct value. The difference between *TFAM* were ($p = 0.0009 < 0.001$, t-test), between *PGC1α* were ($p = 0.005 < 0.01$, t-test), and between *XPNPEP1* were ($p = 0.003 < 0.01$, t-test). Based on these results, the combination of oligo primers and RPs under the oligo reaction settings will be used for future comparisons when employing MMLV reverse transcriptase.

Assays	**Reverse transcription**	**Ct mean**
***TFAM* (Hs00273372_s1)**	MMLV+Oligos	36.88 ± 0.10
***TFAM* (Hs00273372_s1)**	MMLV +Oligos +RPs	35.13 ± 0.20
***PGC1α* (Customized assay 1)**	MMLV+Oligos	37.57 ± 1.0
***PGC1α* (Customized assay 1)**	MMLV +Oligos +RPs	31.13 ± 0.29
***XPNPEP1* (Hs00958021_m1)**	MMLV+Oligos	36.39 ± 0.61
***XPNPEP1* (Hs00958021_m1)**	MMLV +Oligos +RPs	33.12 ± 0.36

Table 5.2-4 MMLV RT optimization using three targets

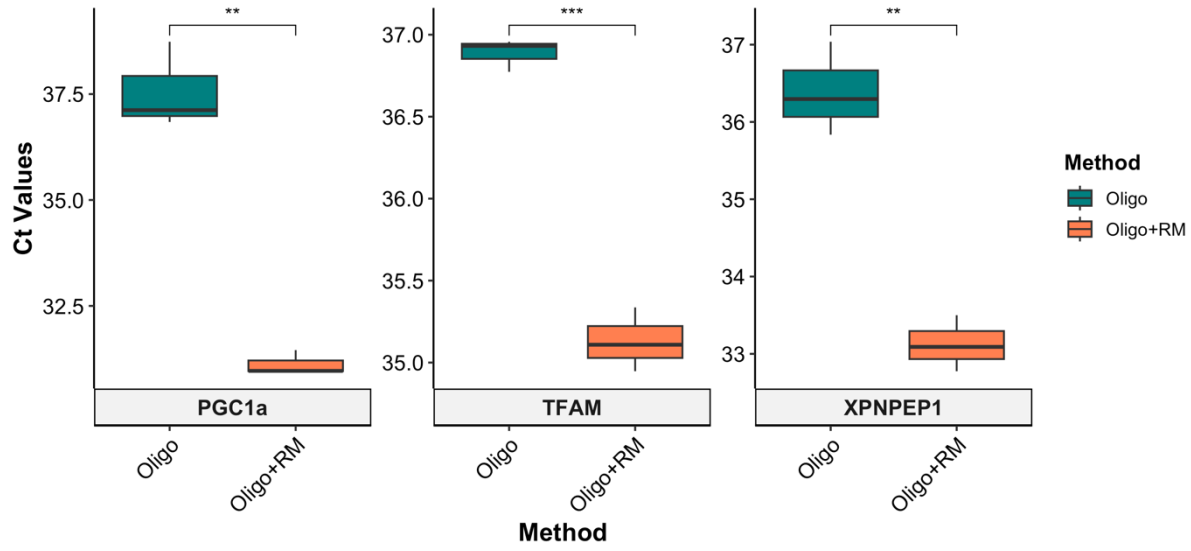

Figure 5.2-7 MMLV RT optimization using three targets

In all three assays tested (TFAM (Hs00273372_s1), PGC1α (Customized assay 1), XPNPEP1 (Hs00958021_m1)), adding both the Oligo and RPs resulted in a significantly lower Ct value. The difference between TFAM were ($p = 0.0009 < 0.001$, t-test), between PGC1α were ($p = 0.005 < 0.01$, t-test), and between XPNPEP1 were ($p = 0.003 < 0.01$, t-test). Cycle threshold (Ct). Blue represents the oligo settings, and orange for EP settings.

The use of another reverse transcriptase (SSIV) is relatively straightforward and does not require optimization, as all components are pre-mixed in the MasterMix. Therefore, SSIV is used for further comparisons without any additional optimization. The incubation times and temperatures for the various stages are summarised in the table (Table 5.2-2). Initially, the reaction mixture is incubated at 25 °C for 10 minutes to allow primer annealing. Reverse transcription then occurs at 50 °C for 10 minutes. Finally, just like MMLV kit, the reverse transcriptase is inactivated at 85 °C for 5 minutes.

5.2.4. *RT-PCR MasterMix optimizations*

Various MasterMixes for RT-PCR are available (including both one-step and two-step options), and three alternatives were tested in this research. For the one-step MasterMix (TaqPath 1xStep RT-qPCR MasterMix A15299, ThermoFisher, USA), prior reverse transcription is not required, as the reagents included in the MasterMix reverse transcribe RNA to cDNA before proceeding with RT-PCR. In contrast, for the two-step MasterMixes (TaqMan Fast Advanced MasterMix 4444557, ThermoFisher, USA and TaqMan universal MasterMix), previously optimized MMLV and SSIV systems were tested for compatibility with the RT-PCR MasterMix during further optimization. For all three types of MasterMix, ROX is included as a passive reference dye to normalise signal variations. It provides consistent background fluorescence, allowing for more accurate quantification of target amplification by correcting for well-to-well differences, such as pipetting inconsistencies or instrument-related fluctuations. The optimal temperatures, incubation times and the reaction mix formulas are provided in (Table 5.2-5, Table 5.2-6 respectively). To determine the optimal MasterMix and reverse transcription system for this research, five sample-handling protocols were designed and tested using three different gene assays. These included: 1) Fast advanced MasterMix with MMLV, oligo primers and RPS; 2) Universal MasterMix with MMLV, oligo primers and RPs; 3) Fast advanced MasterMix with SSIV; 4) Universal MasterMix with SSIV and 5) TaqPath 1-step RT-qPCR MasterMix alone. For these optimization tests, RNA was extracted from human brain tissue homogenate as previously described in this chapter.

The results of the tests can be found listed in (Table 5.2-7 and Figure 5.2-8). There was a significant difference when using different reagents. The p-values are as follows: for *PGC1α*, $p < 0.0001$****; for *TFAM*, $p < 0.0001$****; for *XPNPEP1*, $p < 0.0001$****. For both the *PGC1α* and *XPNPEP1* assays, the lowest Ct values were observed when using One-step RT-PCR with TaqPath 1 step MasterMix, although this was not the case for *TFAM* detection. Reverse transcription using MMLV resulted in lower Ct values compared to SSIV. When considering all assays, the combination of SSIV with the Universal MasterMix produced the best overall results (mean Ct for all assays = 31.06 ± 0.49), followed by the Fast Advanced MM (mean Ct for all assays = 32.5 ± 0.10). Based on these results, both combinations are suitable for further optimization steps. However,

the unique properties of each MasterMix make them more appropriate for specific applications. The TaqMan Universal MasterMix is optimized for single plex reactions, while the TaqMan Fast Advanced MasterMix is designed to support assays across multiple channels. Although the TaqMan Universal MasterMix exhibited superior performance in single plex tests, the TaqMan Fast Advanced MasterMix is better suited for experiments requiring a multiplex detection system, making it the preferred option in such scenarios.

MM	UNG Incubation	RT	Polymerase activation	PCR cycles (40)	
	Hold	Hold	Hold	Denature	Anneal
TaqPath 1xStep MasterMix	25 °C for 2m	50 °C for 15m	95°C for 2m	95°C for 3s	60°C for 30s
TaqMan Fast Advanced MasterMix	50 °C for 2m	n/a	95°C for 20s	95°C for 1s	60°C for 20s
TaqMan Universal MasterMix	50 °C for 2m	n/a	95°C for 10s	95°C for 15s	60°C for 1m

Table 5.2-5 MasterMix settings

The reaction time and temperature of each stage for different MasterMix are listed in this table. Minutes (m); Second (s); MasterMix (MM); Uracil-N-glycosylase (UNG)

	Fast advanced MasterMix (2x)	Universal MasterMix (2x)	TaqPath 1-step (4x)
MasterMix	5.0 µL	5.0 µL	2.5 µL
Taqman assay (20x)	0.5 µL	0.5 µL	0.5 µL
RNA or cDNA	1 pg to 100 ng in nuclease-free water	1ng to 100 ng of nuclease-free water	Use as much RNA sample as needed up to the maximum allowed by the reaction volume
Add nuclease-free water to	10 µL	10 µL	10 µL

Table 5.2-6 PCR reaction mix for different MasterMix

The volume of each reagent required for different MasterMix to prepare the reaction mix is listed in this table.

Assays	Steps	Reverse transcription	RT PCR	Ct mean
TFAM **(Hs00273372_s1)**	Two	MMLV	TaqMan Fast Advanced MasterMix	33.99 ± 0.86
TFAM **(Hs00273372_s1)**	Two	MMLV	TaqMan Universal MasterMix	36.33 ± 0.61
TFAM **(Hs00273372_s1)**	Two	SuperScript IV VILO MasterMix	TaqMan Fast Advanced MasterMix	33.48 ± 0.36
TFAM **(Hs00273372_s1)**	Two	SuperScript IV VILO MasterMix	TaqMan University MasterMix	32.00 ± 0.14

***TFAM* (Hs00273372_s1)**	One	n/a	TaqPath 1xStep RT-qPCR MasterMix	34.27 ± 0.23
***PGC1α* (Customized assay 1)**	Two	MMLV	TaqMan Fast Advanced MasterMix	35.66 ± 0.25
***PGC1α* (Customized assay 1)**	Two	MMLV	TaqMan Universal MasterMix	36.08 ± 0.77
***PGC1α* (Customized assay 1)**	Two	SuperScript IV VILO MasterMix	TaqMan Fast Advanced MasterMix	32.81 ± 0.15
***PGC1α* (Customized assay 1)**	Two	SuperScript IV VILO MasterMix	TaqMan University MasterMix	31.95 ± 0.052
***PGC1α* (Customized assay 1)**	One	n/a	TaqPath 1xStep RT-qPCR MasterMix	30.96 ± 0.047
***XPNPEP1* (Hs00958021_m1)**	Two	MMLV	TaqMan Fast Advanced MasterMix	35.37 ± 0.23
***XPNPEP1* (Hs00958021_m1)**	Two	MMLV	TaqMan Universal MasterMix	36.23 ± 0.56
***XPNPEP1* (Hs00958021_m1)**	Two	SuperScript IV VILO MasterMix	TaqMan Fast Advanced MasterMix	31.28 ± 0.53
***XPNPEP1* (Hs00958021_m1)**	Two	SuperScript IV VILO MasterMix	TaqMan University MasterMix	31.00 ± 0.23
***XPNPEP1* (Hs00958021_m1)**	One	n/a	TaqPath 1xStep RT-qPCR MasterMix	30.87 ± 0.11

Table 5.2-7 Reverse transcription and RT-PCR MasterMix optimization

Different combinations of reverse transcriptase and RT-PCR MasterMix have been listed in in table. Three assays were used to test, including TFAM, PGC1α, and XPNPEP1. The RT-PCR results are listed in the table. Moloney Murine Leukaemia Virus (MMLV)

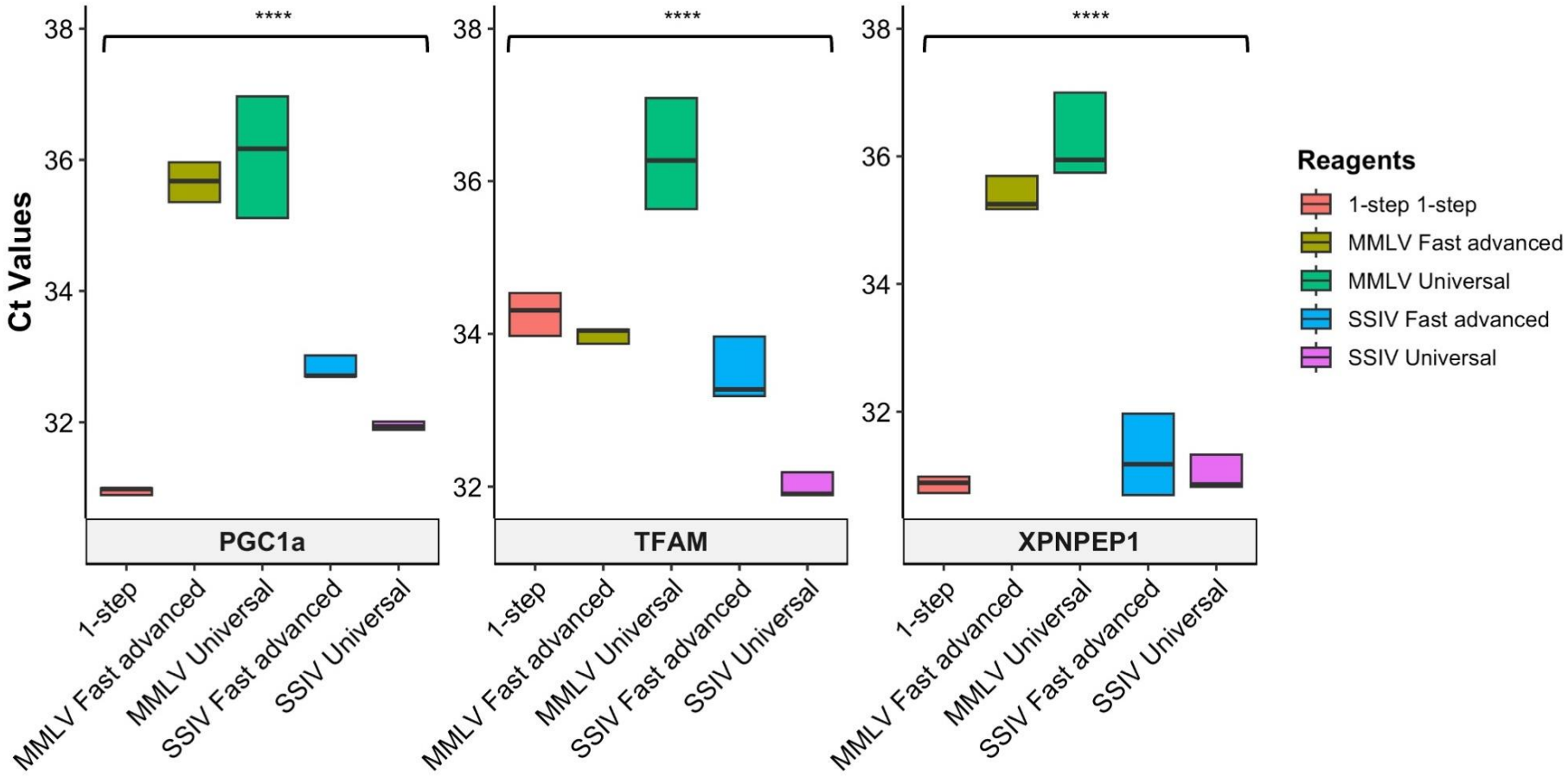

Figure 5.2-8 Reverse transcription and RT-PCR MasterMix optimization

*This figure shows the Ct difference when using different reverse transcriptase and TaqMan MM For all three assays, there was a significant difference when using different reagents. The p-value are as follows: for PGC1α, p < 0.0001****; for TFAM, p < 0.0001****; for*

*XPNPEP1, p < 0.0001****. For both the PGC1α and XPNPEP1 assays, the lowest Ct values were observed when using One-step RT-PCR PCR with TaqPath 1 step MasterMix, although this was not the case for TFAM detection. Reverse transcription using MMLV resulted in lower Ct values compared to SSIV. When considering all assays, the combination of SSIV with the Universal MasterMix produced the best overall results (mean Ct for all assays = 31.06 ± 0.49), followed by the Fast Advanced MasterMix (mean Ct for all assays = 32.5 ± 0.10). SuperScript IV VILO MasterMix (SSIV); Moloney Murine Leukaemia Virus (MMLV); Cycle threshold (Ct). Red represents using 1 step MasterMix, yellow for MMLV with fast advanced MasterMix, green for MMLV with universal MasterMix, blue for SSIV with fast advanced MasterMix, while purple for SSIV with universal MasterMix.*

5.2.5. *RT-PCR assay optimization*

Off-the-shelf TaqMan assays were purchased for the amplification of various targets. Several targets were selected to test their compatibility with human postmortem midbrain tissue in this study, including *TFAM* in the mtDNA maintenance pathway, *PGC1α* in the mtDNA biogenesis pathway, *PINK1* and *LC3B* in the mitophagy pathway, and a housekeeping gene, *XPNPEP1*. *XPNPEP1* is a member of an aminopeptidase family, which degrades bradykinin, a blood pressure-regulating peptide, and has not been associated with neurodegenerative conditions in the central nervous system of humans (Durrenberger *et al.*, 2012).

Taqman assays were tested/optimised using RNA extracted from homogenized human midbrain postmortem tissues like mentioned earlier in the chapter. Reverse transcription of the extracted RNA was carried out according to the protocol described in the methodology chapter (Chapter 2.4.4 RNA extraction and reverse transcription), using the SSIV MasterMix based on the reverse transcription results from (Chapter 5.2.4).

Before purchasing the assays, a literature search was conducted to identify any previously published TaqMan assays that demonstrated a good detection rate with human CNS postmortem tissue or neuronal cells. A list of publications using these assays can be found in (Table 5.2-8). No Taqman assay was used to test human brain tissues or neuronal cells of both *TFAM* and *LC3B*. Based on the result of this literature search, a list of TaqMan assays were ordered in and tested (Table 5.2-9).

Based on the RT-PCR results, most assays previously used to amplify neuronal cell or tissue RNA in publications successfully generated robust amplification with RNA extracted from human midbrain tissue homogenates in this research. For example, assays targeting *XPNPEP1*(Hs00958021_m1) and *PINK1* (Hs00260868_m1) produced reliable results. However, unexpectedly, the assay for *PGC1α* (Hs00173304_m1), which has been successfully used to detect transcriptional levels in the prefrontal cortex (Asghar *et al.*, 2022), failed to amplify *PGC1α* cDNA in midbrain tissue homogenate. This discrepancy may be attributed to the presence of multiple transcriptional variants of

PGC1α, which could result in differential expression across brain regions or alternative splicing events that are not targeted by the selected assay (Soyal *et al.*, 2019).

For target assays that had not previously been used in human brain tissue or neurons, assays were picked to cover different transcript variants. Two assays for *TFAM* and one assay for *LC3B* were purchased and tested. Based on their amplification performance in midbrain tissue homogenates, the *TFAM* TaqMan assay (Hs00273372_s1) and *LC3B* TaqMan assay (Hs00797944_S1) were selected for future work. Details of the tested assays, including the targeted transcript variants, amplification performance, can be found in (Table 5.2-9).

Target	Assay ID	Sample	Reference
PGC1α	Hs00173304_m1	Prefrontal cortex postmortem brain homogenate	(Asghar *et al.*, 2022)
XPNPEP1	Hs00958021_m1	iPCS-derived spinal neuron (iPSN)	(Zaepfel *et al.*, 2021)
PINK1	Hs00260868_m1	SH-SY5Y cells and cortical neurons	(Liu *et al.*, 2020)

Table 5.2-8 Literature search of Taqman assays used in neuronal cells or tissues

After conducting a literature search, no TaqMan assays for TFAM and LC3B were found to have been used in human brain tissues or neurons in published studies. However, TaqMan assays for PGC1α, XPNPEP1, and PINK1 were identified that has been used in target type of tissues or neurons.

Gene	Assay	Target transcripts	Good amplification
TFAM	Hs01073348_g1	NM_001270782.1 NM_003201.2 XM_011540120.2 XM_011540121.2	No
	Hs00273372_s1	NM_001270782.1 NM_003201.2 NR_073073.1 XM_011540120.2 XM_011540121.2	Yes
XPNPEP1	Hs00958021_m1	NM_001167604.1 NM_001324128.1 NM_001324131.1 NM_001324132.1 NM_001324133.1 NM_001324134.1 NM_001324135.1 NM_001324136.1 NM_020383.3 XM_011540134.1 XM_017016613.1 XM_017016614.1 XM_017016615.1	Yes
PINK1	Hs00260868_m1	NM_032409.2	Yes
LC3B	Hs00797944_S1	NM_022818.4	Yes
PGC1α	Hs00173304_m1	NM_013261.3 XM_005248131.4 XM_005248132.1 XM_005248134.4 XM_011513765.2 XM_011513766.1 XM_011513767.2 XM_011513768.1 XM_011513769.2 XM_011513770.2 XM_011513771.1 XM_017007664.1	No
	Hs01016722_m1	NM_013261.3	No

Table 5.2-9 Tested Taqman assays

All TaqMan assays showed consistent amplification results during repetition, except for *PGC1α*. To address this, four new customised primer sets targeting different *PGC1α* transcript variants and areas were designed and optimised using PowerTrack SYBR Green MasterMix (A46012, ThermoFisher, USA). Both the reaction mixture (Table 5.2-10) and thermos cycling conditions (Table 5.2-11) are listed below. Detailed information for each primer set can be found in (Table 5.2-12). Different target areas in same transcript variants for all four primer sets can be found in (Figure 5.2-10). The use of SYBR green for optimization was chosen due to its time and cost efficiency. Unlike TaqMan detection, SYBR Green does not require the design of a specific probe sequence for each set of primers, allowing for quick selection of primers with good coverage of the transcript variants in the target tissue. For primers demonstrating strong amplification, probes were subsequently designed and used for further optimization like other TaqMan assays. RNA extracted from brain tissue homogenate was used to evaluate the performance of each primer set in reporting transcriptional levels (Figure 5.2-9). Primer set 1 demonstrated the best amplification of the target material, with the lowest Ct value of 33.4 ± 0.61, and primer set 2 showed a relatively moderate ability to detect *PGC1α* mRNA level, with a Ct value of 37.7 ± 1.78. In contrast, primer set 3 only amplified in 4 out of 10 samples, with an average Ct value of 41.6 ± 1.78, while primer set 4 failed to amplify at all. Based on these results, both primer set 1 and primer set 2 were further developed with customized TaqMan FAM probes and tested for efficiency alongside other TaqMan probes.

Components	Volume for 1 reaction (µL)
PowerTrack SYBR Green MasterMix	10
Forward and reverse primers	1
Nuclease-free water	6.5
DNA (1-10 ng) with yellow sample buffer	2.5
Total PCR volume	20

Table 5.2-10 Reaction mixture for SYBR Green MasterMix

DNA wase mixed with yellow sample buffer, available with the PowerTrack SYBR Green MasterMix kit, before added to the reaction mixture. 2ul of 1 to 10ng DNA needed to be mixed with 0.5 µL yellow sample buffer, forward and reverse primers needed to be mixed before adding to MasterMix.

Steps	Temperature	Duration	Cycles
Enzyme activation	95 °C	2m	1
Denature	95 °C	15s	40
Anneal/extend	60 °C	60s	

Table 5.2-11 Thermal cycling conditions for SYBR Green MasterMix

The reaction time and temperature of each stage for SYBR Green MasterMix are listed in this table. Minutes (m); Second (s)

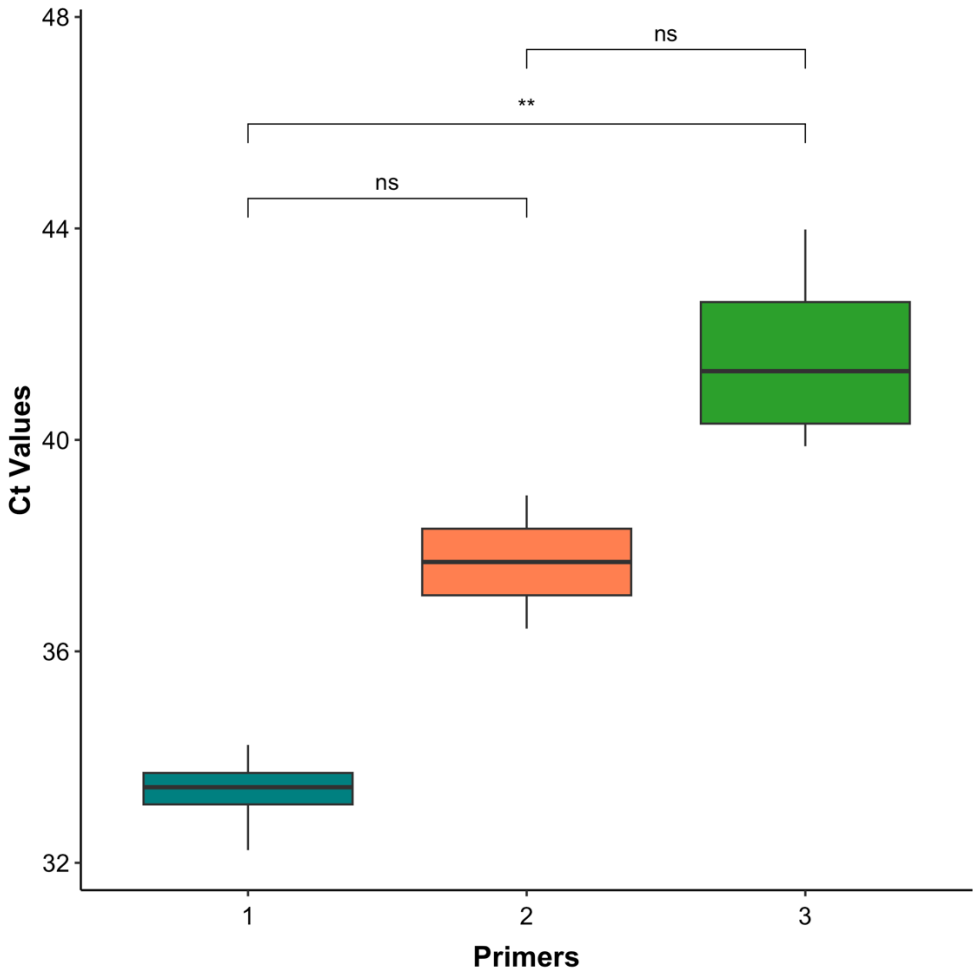

Figure 5.2-9 PGC1α primer testing results

*Four sets of primers were designed to amplify PGC1α, targeting different regions or transcript variants. The first primer set showed the best amplification, with the lowest Ct value of 33.4 ± 0.61. Primer set 2 produced the second-best result, with a Ct value of 37.7 ± 1.78. Primer set 3 performed less effectively, with an average Ct value of 41.6 ± 1.78, while primer set 4 failed to produce any amplification. There was a significant difference in performance between primer set 1 and primer set 3 (p = 0.0023**, t-test).*

Primer sets	Primer sequences	Product size	Probes	Target transcripts
1 Forward	TGTGGATGAAGACGGATTGC	63	CTCATTTGATGCGCTGAC-FAM-MGB	NM_013261.5 NM_001330751.2 NM_001330752.2 NM_001330753.2 NM_001354825.2 NM_001354826.2 NM_001354827.2
1 Reverse	TTGTCAGTGGTCACGTCTCCAT			
2 Forward	AGAGAACAGAAACAGCAGCAGAGA	63	AAATGCACCTCCAAAAA-FAM-MGB	NM_013261.5 NM_001330751.2 NM_001330752.2 NM_001330753.2 NM_001354825.2 NM_001354826.2 NM_001354827.2
2 Reverse	TGCGACTGTGTGTGGGACTT			
3 Forward	CCGAGCCGAGCTGAACA	57	n/a	NM_013261.5 NM_001330751.2 NM_001330752.2 NM_001354825.2 NM_001354826.2
3 Reverse	TCGTCGTCAAAAACAGCTTGA			

				NM_001354827.2
4 Forward	CACCGAAATTCTCCCTTGTATGT	61	n/a	NM_013261.5 NM_001330751.2 NM_001330752.2 NM_001330753.2 NM_001354825.2 NM_001354826.2 NM_001354827.2
4 Reverse	TGGGCCGACGGCTGTA			

Table 5.2-12 Primer sets tested for PGC1α

Each primer set consists of both forward and reverse primers. The probe for primer sets 1 and 2 are labelled with FAM-MGB. 6-carboxyfluorescein (FAM), a fluorescent reporter dye, is attached to the 5' end of the probes, while the minor groove binder (MGB), functioning as a quencher, is attached to the 3' end.

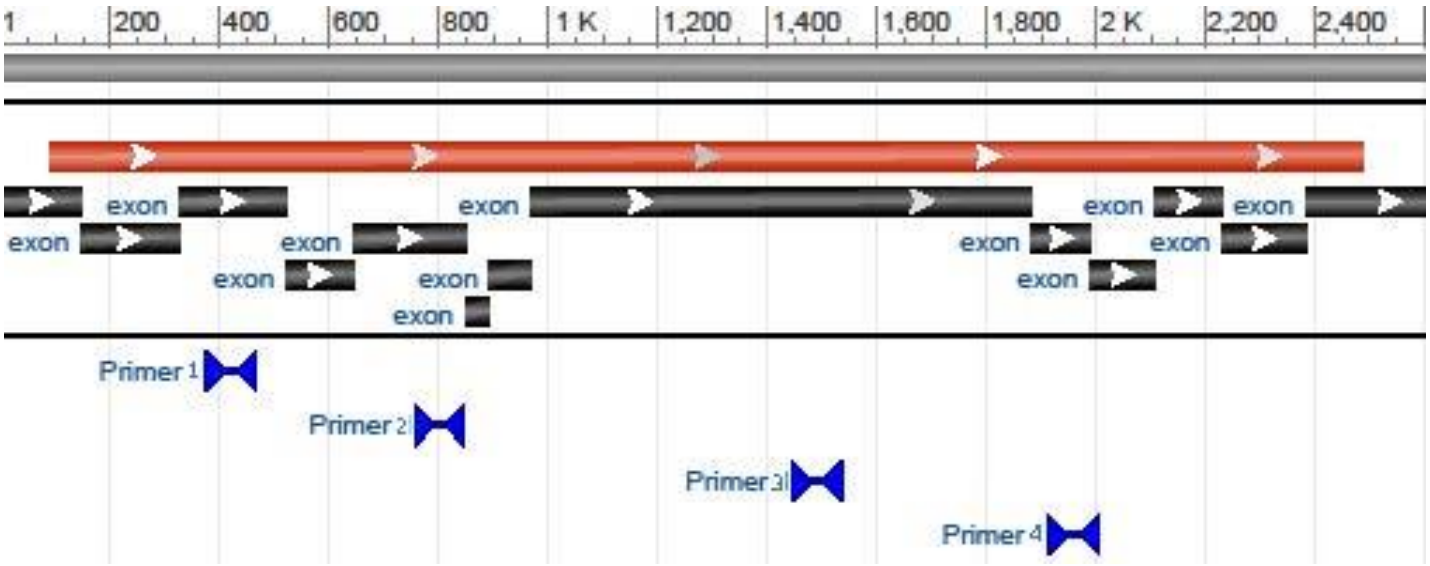

Figure 5.2-10 Primer positions in PPARGC1A gene

This figure shows the different area the primers are targeting in the homo sapiens PPARG coactivator 1 alpha (PPARGC1A), transcript variant 2, mRNA. Primer set 1 target within exon 3, primer set 2 spans exons 5 and 6, primer set 3 targets exon 8, and primer set 4 spans exons 9 and 10. The gene is labelled in red, primers in black, and primers in blue.

5.2.6. *Assay efficiencies*

As the limited quantity of RNA remaining in human postmortem tissue, makes it difficult to produce a serial dilution to generate a reliable standard curve. Therefore, DNA strings, specific for the target region, were purchased to test the efficiency of the assay once it has been confirmed that has the capability of detecting transcript variants in sample tissues (Figure 5.2-11). Details of the DNA strings have been listed in (Table 5.2-13), and the standard curve of all the assays are displayed in (Figure 5.2-12). All DNA strings were designed based on the target sequence and serially diluted at 1:10 ratio, starting with a concentration of 0.00002ng/ µL. The majority of assays demonstrated good efficiency, with values falling within the range of 90% to 110%. One assay (*PGC1α*-c2) slightly exceeded the optimal efficiency range at 111.22%, but it was still considered acceptable. The R^2 values for standard curve were above 0.99 for all assays, except for PINK, which had an R^2 of 0.922 but remained within an acceptable threshold.

Target	Assay ID	Strings Sequence	Length (bp)	Standard Curve Efficiency (%)
TFAM	Hs00273372_s1	1 GGAGGCTCTC CGAGATTGGG GTCGGGTCAC TGCCTCATCC ACCGGAGCGA TGGCGTTTCT 61 CCGAAGCATG TGGGGCGTGC TGAGTGCCCT GGGAAGGTCT GGAGCAGAGC TGTGCACCGG 121 CTGTGGAAGT CGACTGCGCT CCCCCTTCAG TTTTGTGTAT TTACCGAGGT GGTTTTCATC 181 TGTCTTGGCA AGTTGTCCAA AGAAACCTGT AAGTTCTTAC CTTCGATTTT CTAAAGAACA 241 ACTACCCATA TTTAAAGCTC AGAACCCAGA TGCAAAAACT ACAGAACTAA TTA	293	104.42
PGC1α	Customed assay 1	1 CTTCCTCTGA CCCCAGAGTC ACCAAATGAC CCCAAGGGTT CCCCATTTGA GAACAAGACT 61 ATTGAACGCA CCTTAAGTGT GGAACTCTCT GGAACTGCAG GCCTAACTCC ACCCACCACT 121 CCTCCTCATA AAGCCAACCA AGATAACCCT TTTAGGGCTT CTCCAAAGCT GAAGTCCTCT 181 TGCAAGACTG TGGTGCCACC ACCATCAAAG AAGCCCAGGT ACAGTGAGTC TTCTGGTACA 241 CAAGGCAATA ACTCCACCAA GAAAGGGCCG GAGCAATCCG AGTT	284	108.50
PGC1α	Customed assay 2	1 CTCAAATATC TGACCACAAA CGATGACCCT CCTCACACCA AACCCACAGA GAACAGAAAC 61 AGCAGCAGAG ACAAATGCAC CTCCAAAAAG AAGTCCCACA CACAGTCGCA GTCACAACAC 121 TTACAAGCCA AACCAACAAC TTTATCTCTT CCTCTGACCC CAGAGTCACC AAATGACCCC 241 AAGGGTTCCC CATTTGAGAA CAAGACTATT GAACGCACCT TAAGTGTGGA ACTCTCTGGA	300	111.22
PGC1α	Hs00173304_m1	1 CAACACTTAC AAGCCAAACC AACAACTTTA TCTCTTCCTC TGACCCCAGA GTCACCAAAT 61 GACCCCAAGG GTTCCCCATT TGAGAACAAG ACTATTGAAC GCACCTTAAG TGTGGAACTC 121 TCTGGAACTG CAGGCCTAAC TCCACCCACC ACTCCTCCTC ATAAAGCCAA CCAAGATAAC 181 CCTTTTAGGG CTTCTCCAAA GCTGAAGTCC TCTTGCAAGA CTGTGGTGCC ACCACCATCA 241 AAGAAGCCCA GGTACAGTGA GTCTTCT	267	110.44

PINK1	Hs00260868_m1	1 GCGCGGTTGC AGCGGCAGTT CGTGGTGCGG GCCTGGGGCT GCGCGGGCCC TTGCGGCCGG 61 GCAGTCTTTC TGGCCTTCGG GCTAGGGCTG GGCCTCATCG AGGAAAAACA GGCGGAGAGC 121 CGGCGGGCGG TCTCGGCCTG TCAGGAGATC CAGGCAATTT TTACCCAGAA AAGCAAGCCG 181 GGGCCTGACC CGTTGGACAC GAGACGCTTG CAGGGCTTTC GGCTGGAGGA GTATCTGATA 241 GGGCAGTCCA TTGGTAAGGG CTGCAGTGCT GCTGTGTATG AAGCCACCAT GCCTACATTG 301 CCCAGAAC	308	98.32
XPNPEP1	Hs00958021_m1	1 CCCAACAATT TCCAGTACGG GACCCAACGG CGCCATCATT CACTACGCGG ATGGCACCAC 61 AGATGTGACG CGGACAATGC ATTTTGGGAC CCCTACAGCC TACGAGAAGG AATGCTTCAC 121 ATATGTCCTC AAGGGCCACA TAGCTGTGAG TGCAGCCGTT TTCCCGACTG GAACCAAAGG 181 TCACCTTCTT GACTCCTTTG CCCGTTCAGC TTTATGGGAT TCAGGCCTAG ATTACTTGCA 241 CGGGACTGGA CATGGTGTTG GGTCTTTTTT G	261	106.20

Table 5.2-13 DNA string sequences used to test assay efficiency

The details of each DNA string designed for standard curve generation in each assay are listed in this table, including the assay ID (catalogue number from ThermoFisher), the DNA sequence, the length of the strands, and the assay efficiency calculated using the designed DNA strings.

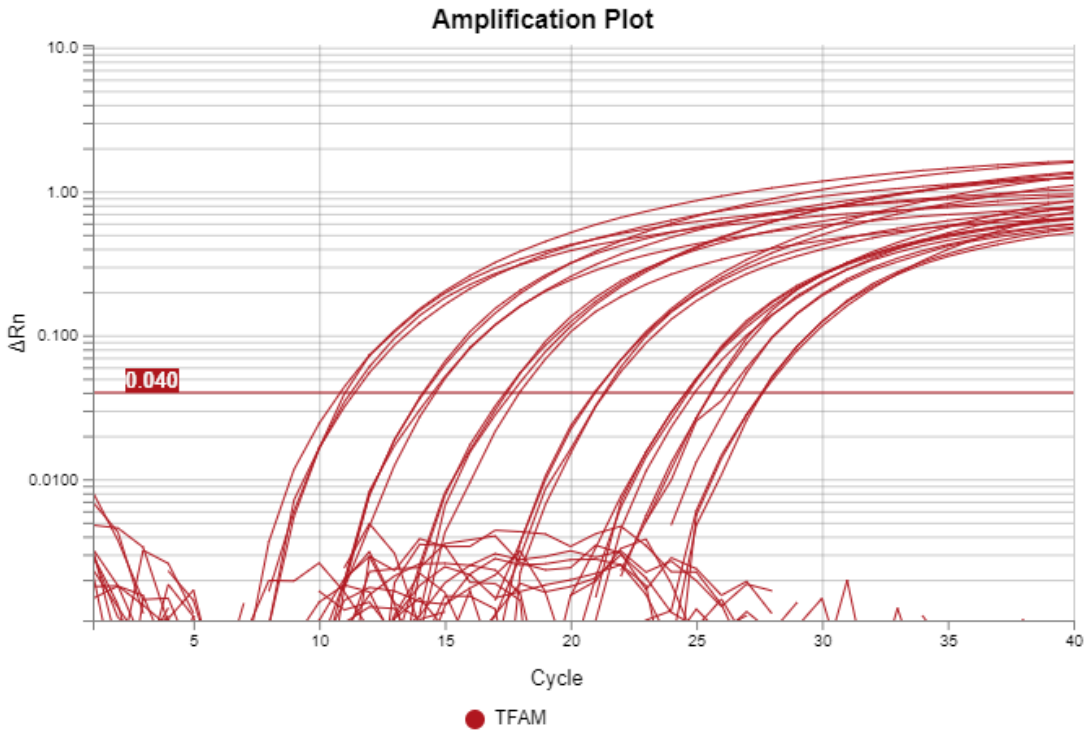

Figure 5.2-11 Example good amplification generated using targeted DNA strings

This figure shows the amplification plot of a serially diluted TFAM DNA string. The x-axis represents the cycle number of the amplification, while the y-axis displays the change in fluorescence emission intensity (ΔRn), demonstrating good reliability and resulting in a robust standard curve. The reporting cycle for each concentration shows a consistent gap of approximately 3.4, with assay standard curve efficiency around 100%.

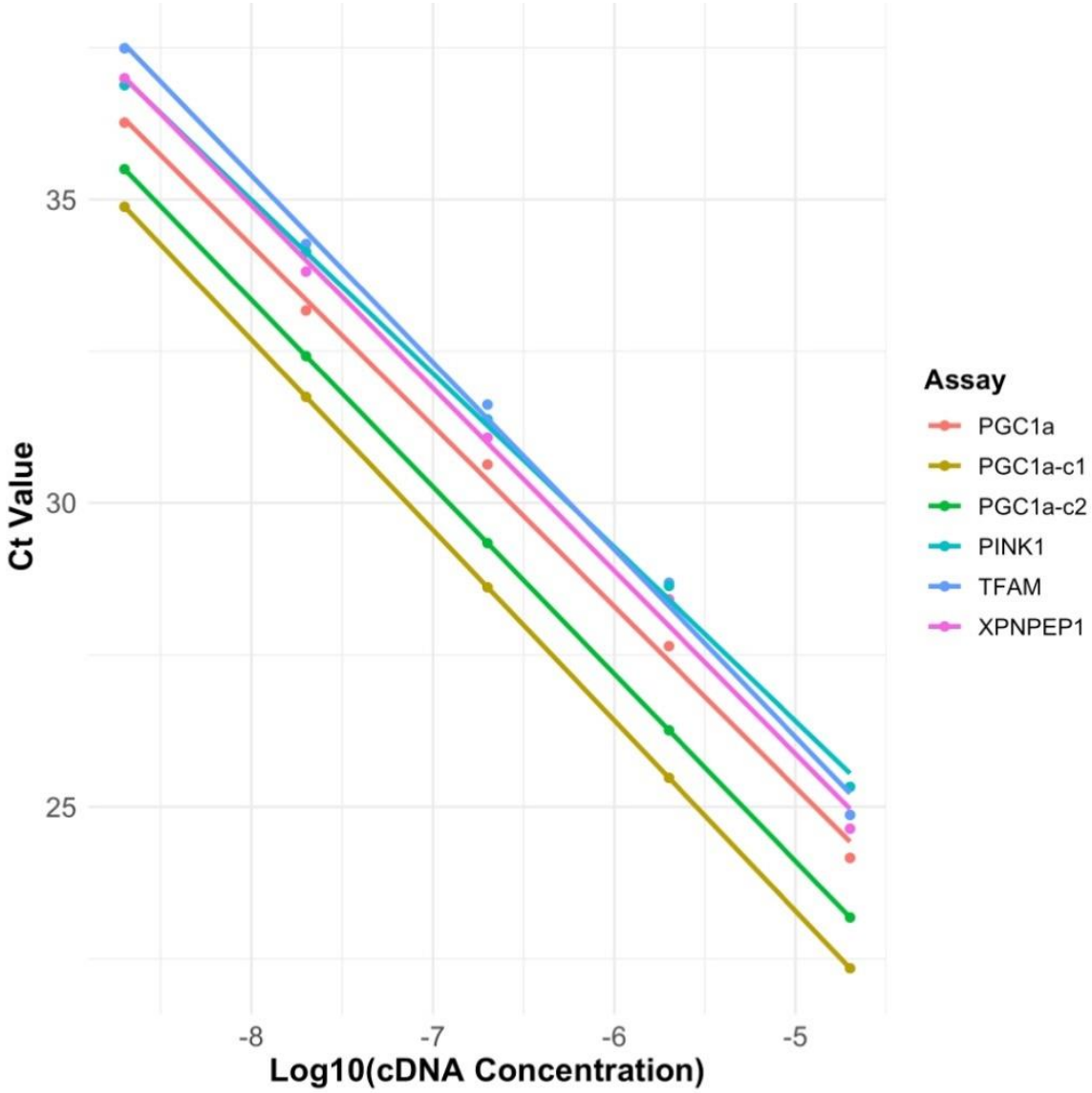

Figure 5.2-12 Standard cruve assay efficiency of all the assays tested

This graph displays the standard curves and efficiency of the assays tested. X-axis, on a log10 scale, represents the cDNA concentration, while the y-axis displays the corresponding mean Ct values obtained from triplex replication. All DNA strands were designed based on the target sequence and serially diluted at 1:10 ratio, starting with a concentration of 0.00002 ng/ µL. Most assays demonstrated good standard curve efficiency, with values ranging between 90% and 110%. One assay (PGC1α -c2)

slightly exceeded optimal efficiency at 111,22% but remained within the acceptable range. The R^2 values for standard curve were above 0.99 for all assays, except for PINK, which had an R^2 of 0.922 but remained within an acceptable threshold.

5.2.7. *Multiplexing the RT-PCR reactions*

Due to the limited starting material and the need to detect multiple targets from the same sample, a single plex approach may not yield all the necessary results. Consequently, multiplexing has emerged as a valuable technique, enabling the detection of multiple targets using a limited amount of RNA. The maximum capacity of an RT-PCR system is five targets, as the real-time instrument can detect signals within a specific wavelength range, and there are five TaqMan dyes (6-Carboxyfluorescein (FAM), Variant of Hexachlorofluorescein (VIC), ABY, JUN, and Mustang purple.) with fluorescence emission spectra that do not overlap within that range (Figure 5.2-13). In this research, a triplex RT-PCR system was initially designed and tested. This approach was chosen because the available RNA quantity was sufficient to support the use of a triplex RT-PCR system, and developing the triplex system did not require extensive optimization. For the triplex system, three channels were selected with corresponding fluorescent reporters: FAM (517 nm), VIC (551 nm), and ABY (580 nm).

A number of TaqMan assays were tested using neuron samples to compare assay efficiencies, with the goal of selecting the best assay and assigning the optimal dye for each. Three targets, *TFAM, PGC1α,* and *XPNPEP1*, were initially selected for designing a triplex method. *TFAM* is used to assess the maintenance level of mtDNA, *PGC1α* to evaluate the biogenesis level of mtDNA, and *XPNPEP1* serves as a housekeeping gene to normalise the data when using pooled neurons.

According to the test result, the efficiencies of *TFAM* and *XPNPEP1* were higher than that of *PGC1α*. Since FAM is the most sensitive assay and is associated with the brightest dye available, it needed to be assigned to the least efficient target to balance the overall efficiency of the assays. Therefore, FAM was assigned to *PGC1α*, VIC to *TFAM*, and ABY

dye to *XPNPEP1*, with all assays probes having a minor groove binder (MGB) attached to the 3' end as a quencher.

A comparison of assay efficiency was conducted between single plex and multiplex formats. Ideally, the use of multiplex should not affect the assay efficiency observed in single plex tests. Standard curves were generated for each assay under both single plex and multiplex conditions.

The reaction formula of both single plex and multiplex setups using Fast Advanced MasterMix can be found in (Table 5.2-14). The results of *TFAM*, *XPNPEP1*, and *PGC1α* are showing in (Figure 5.2-14). The efficiency is: *PGC1α* single plex (101.05%, $R^2 = 0.981$), triplex (101.845%, $R^2 = 0.980$); *TFAM* single plex (104.423%, $R^2 = 0.995$), triplex (105.792%, $R^2 = 0.984$); *XPNPEP1* single plex (105.217%, $R^2 = 0.983$), triplex (98.852%, $R^2 = 0.956$). The assay efficiencies remained within a reasonable range compared to those of the single plex, confirming that triplex reaction established does not adversely affect the PCR results. However, despite this well-optimized system, when the triplex reaction was applied to cDNA samples reverse transcribed from RNA extracted from human PPN cholinergic neurons, no *PGC1α* amplification was detected after testing 50 samples. This may be due to the low expression level of *PGC1α* mRNA. To address this issue, a duplex assay (*TFAM*-VIC-MGB and *XPNPEP1*-ABY-MGB) and a single plex assay (*PGC1α* -FAM-MGB) was performed on the same sample. This approach reduces competition between assays, making it easier to detect *PGC1α* mRNA.

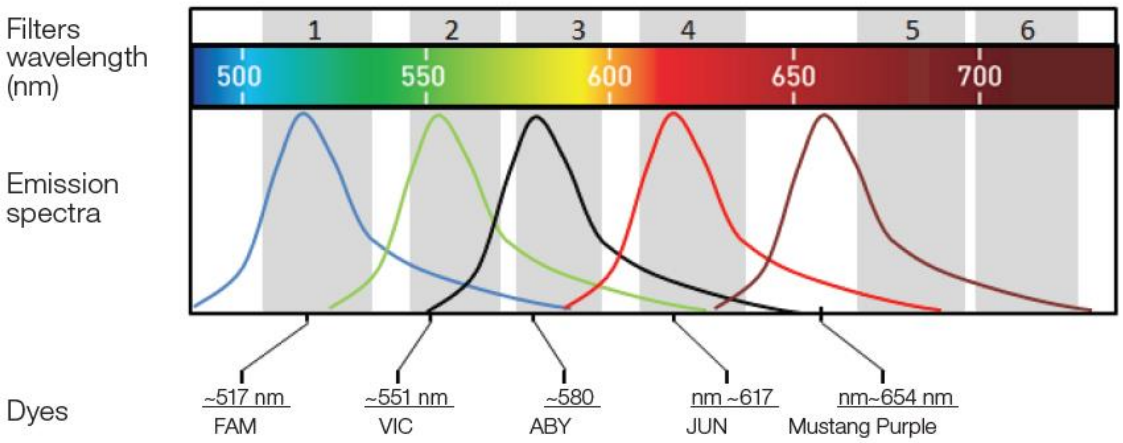

Figure 5.2-13 Fluorescence emission spectra of different TaqMan dyes

This figure illustrates the different fluorescence emission wavelengths of five dyes: 6-Carboxyfluorescein (FAM), Variant of Hexachlorofluorescein (VIC), ABY, JUN, and Mustang purple. These dyes allow each calibrated instrument to detect five targets in a single reaction. The grey zones represent the filters available on QS7 RT-PCR system. Graph adapted from Applied Biosystem (Product bulletin for TaqMan multiplex RT-PCR).

	Single plex	**Duplex**	**Triplex**
Fast Advanced MasterMix (2x)	5 µL	5 µL	5 µL
FAM dye Taqman assay 1 (20x)	0.5 µL	0.5 µL	0.5 µL
VIC dye Taqman assay 2 (20x)	n/a	0.5 µL	0.5 µL
ABBY dye Taqman assay 3 (20x)	n/a	n/a	0.5 µL
cDNA/ DNA strings	1-10 ng	1 – 10 ng	1-10 ng
Add nuclease-free water to	10 µL	10 µL	10 µL

Table 5.2-14 Multiple PCR reaction mixture

When using DNA strings as the starting material, only 1 µL of it was added into the reaction, while for cDNA, reverse transcribed from RNA would add up to 4.5 µL.

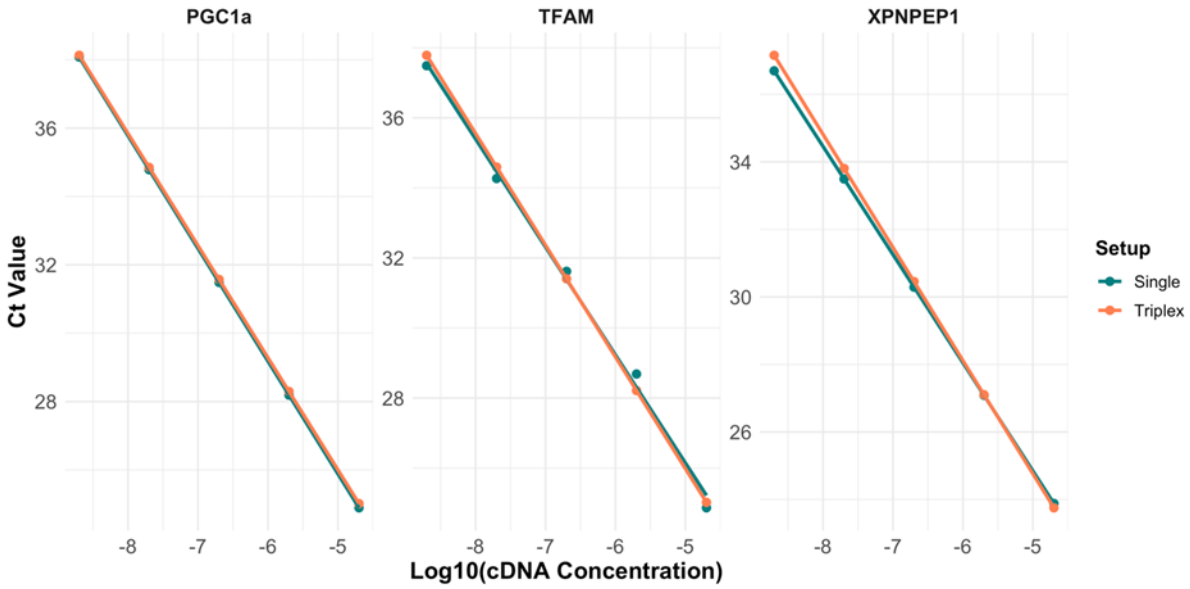

Figure 5.2-14 Assay efficiency comparison single plex and triplex

This graph displays the standard curves and efficiency of the assays tested either in single plex or in triplex. X-axis, on a log10 scale, represents the cDNA concentration, while the y-axis displays the corresponding mean Ct values obtained from triplicate measurements. There is no clear difference between when using the assay either single plex or triplex. The efficiency is: PGC1α single plex (101.05%, R2 = 0.981), triplex (101.845%, R2 = 0.980); TFAM single plex (104.423%, R2 = 0.995), triplex (105.792%, R2 = 0.984); XPNPEP1 single plex (105.217%, R2 = 0.983), triplex (98.852%, R2 = 0.956). Green represents single plex result, and orange for triplex.

After optimizing RNA extraction at the single-neuron level, the inclusion of the housekeeping gene *XPNPEP1* was deemed unnecessary. Concurrently, the mitophagy pathway plays a crucial role in regulating mtCN, making it valuable to assess the transcriptional levels of this pathway. *PINK1* or *LC3B* were incorporated into the detection process, leading to the exclusion of *XPNPEP1* as a target. The original FAM channel assigned to *XPNPEP1* was reassigned to both *PINK1* and *LC3B*. Both assays with FAM had a good amplification of LCM single-neuron samples. Upon comparing the compatibility of the *PINK1* and *LC3B* assays in a triplex format, it was observed that the transcriptional expression level of *LC3B* (Mean Ct = 32.5 ± 0.18) was generally lower than that of *TFAM* in VIC channel (Mean *TFAM* Ct = 35.35 ± 0.63), which could introduce some bias in detection. Therefore, *PINK1* (Mean Ct = 33.75 ± 0.45), whose transcriptional level was similar to *TFAM*-VIC, was selected as the mitophagy pathway.

The standard curves showing the assay efficiencies for single plex, and duplex assays are shown in (Figure 5.2-15). No significant change in assay efficiency (*PINK1* = 98.32%; *TFAM* = 101.48%) was observed when performing the duplex reaction (*PINK1* = 97.59%; *TFAM* = 93.48%), so this single-duplex method was used in all subsequent experiments.

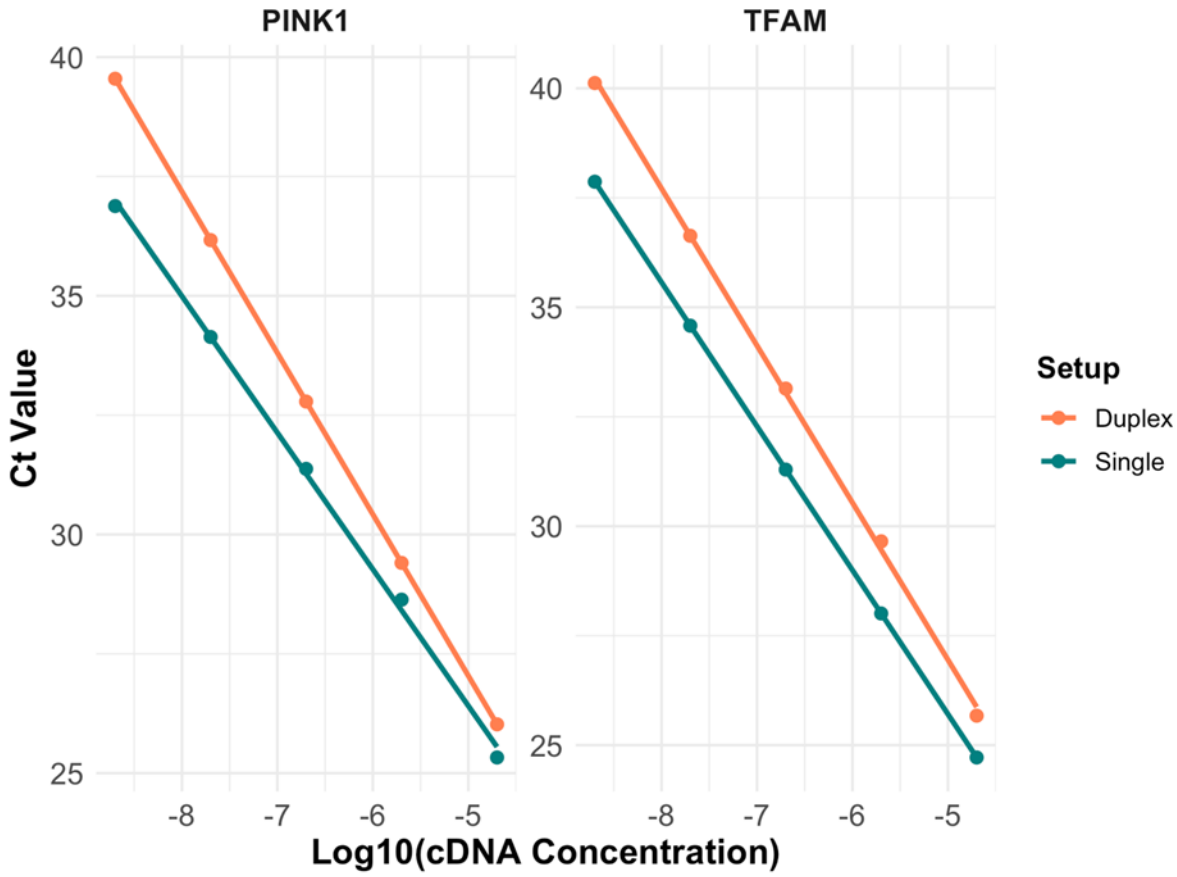

Figure 5.2-15 Comparison of efficiency between single and duplex PCR

This graph presents the standard curves and efficiencies of the assays tested in either single plex or duplex formats. The x-axis, shown on a log10 scale, represents the cDNA concentration, while the y-axis displays the corresponding mean Ct values obtained from triplicate measurements. There is no significant difference between using the assay in either single plex or duplex form. For PINK1, the single plex efficiency is 98.32% with R2 of 0.922, while the duplex efficiency is 98.59% with an R2 of 0.992. For TFAM, the single plex efficiency is 101.48% with an R2 of 0.981, and the duplex efficiency is 93.48% with an R2 of 0.995. Green represents the single plex result, and orange the duplex result.

5.2.8. *Pre-amplification before the RT-PCR*

Due to consistently low Ct values reported in RT runs, a pre-amplification step was considered before RT-PCR. The TaqMan PreAmp MasterMix Kit (4384267, ThermoFisher, USA) was utilized following the guidelines outlined in the TaqMan PreAmp user guide. This method enables pre-amplification of the cDNA to enhance assay sensitivity and efficiency.

For this optimisation experiment, an assay pool was generated by combining three 20X TaqMan assays. The pooled TaqMan assay was the diluted using 1X TE buffer to achieve a final concentration of 0.2X for each assay. The reaction mixture, as detailed in (Table 5.2-15) was then prepared, and cDNA was pre-amplified under the thermal cycling conditions outlined in (Table 5.2-16).

A comparison between samples with and without the pre-amplification step is shown in (Figure 5.2-16). While a noticeable improvement in Ct values was observed in samples that underwent the pre-amplification step, this improvement was neither reliable nor consistent across different genes within the same tissue samples. Without the preamplification step, the mean Ct values of all the reactions (36.7 ± 1.27), was higher than those with preamplification (28.9 ± 6.66) ($p < 0.0001$****, t-test). A decrease in Ct values was observed when additional neurons were used without reamplification: *TFAM* dropped from 37.59 ± 0.77 to 36.04 ± 0.24 to 35.99 ± 0.48; *PGC1α* dropped from 38.60 ±0.53 to 37.75 ±0.37 (no signal detected with a single neuron); *XPNPEP1* dropped from 36.94 ± 0.96 to 34.96 ± 0.27 (For both *PGC1α* and *XPNPEP1* assay, no signal was detected when using single neuron). However, with preamplification step, the drop in Ct values was not consistent across all assays as the number of neurons increased. *TFAM* Ct increased from 21.5 ± 0.67 for a single neuron to 31.2 ± 1.08 for two neurons, then to 29.0 ± 2.33 for four neurons. *PGC1α* drop from 33 ± 0.05 for a single neuron to 29.6 ± 0.65 for four neurons, but no signal was detected when using two neurons. As a result, the pre-amplification step was excluded from future experiments.

	Volume per reaction	Final concentration
TaqMan PreAmp MasterMix (2x)	25 µL	1x
Pooled TaqMan assays (0.2x each assay)	12.5 µL	0.05x each assay
1-250 ng cDNA samples	12.5 µL	0.02-5 ng/µL
Total	50 µL	n/a

Table 5.2-15 Preamplification reaction mixture

Step	Temperature	Time	Cycles
Enzyme Activation	95 °C	10 minutes	Hold
Denature	95 °C	15 seconds	10
Anneal/Extend	60 °C	4 minutes	
Enzyme inactivation	99 °C	10 minutes	Hold
Final	4 °C	forever	Hold

Table 5.2-16 Thermal cycling for preamplification

Products on ice for immediate use, or in aliquots at -20 °C for up to 7 days.

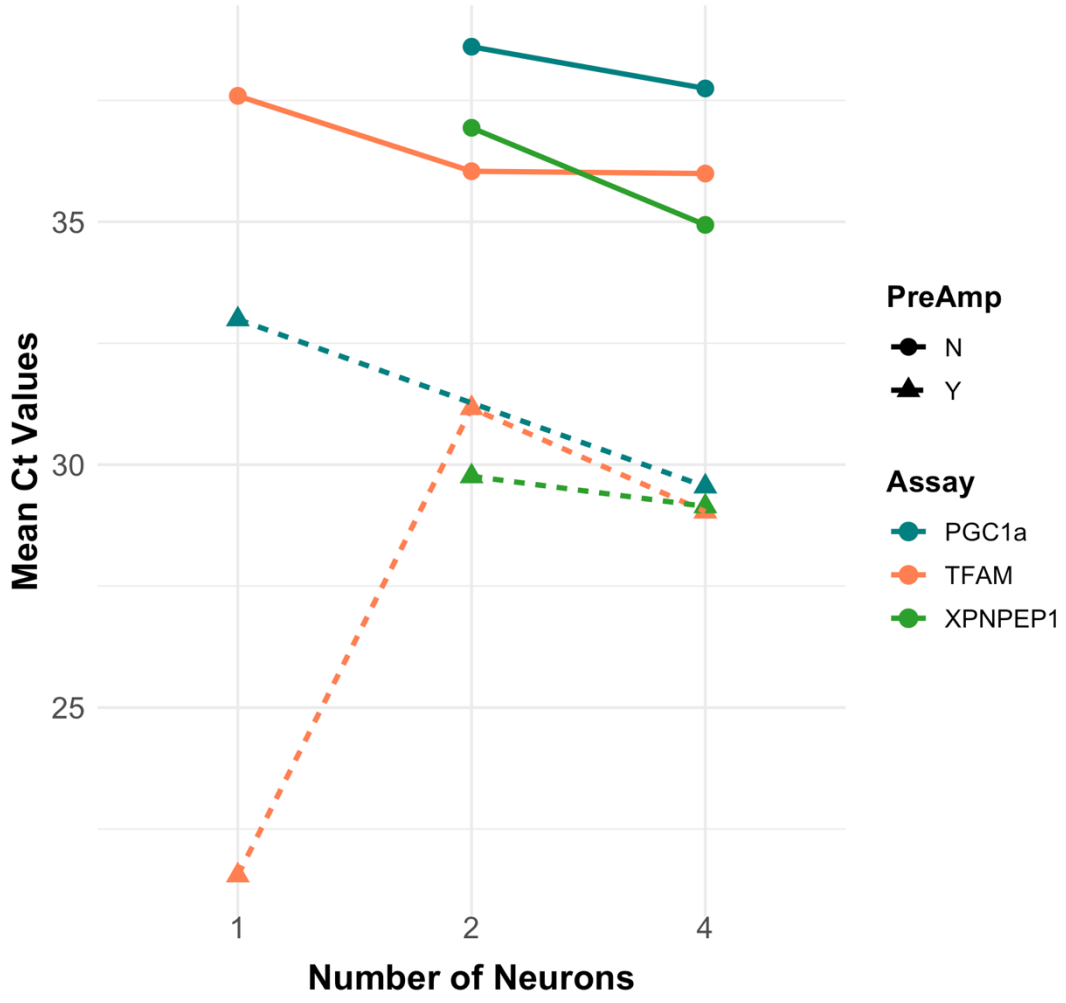

Figure 5.2-16 Results before and after preamplification

*This plot shows the mean Ct values when using different number of neurons as starting material. The x-axis represents the number of neurons used, and the y-axis shows the mean Ct values obtained from triplicate measurements. Without preamplification step, the mean Ct values of all the reactions (36.7 ± 1.27), was higher than those with preamplification (28.9 ± 6.66) ($p < 0.0001$****, t-test). A decrease in Ct values was observed when additional neurons were used without reamplification: TFAM dropped from 37.59 ± 0.77 to 36.04 ± 0.24 to 35.99 ± 0.48; PGC1α dropped from 38.60 ±0.53 to 37.75 ±0.37 (no signal detected with a single neuron); XPNPEP1 dropped from 36.94 ± 0.96 to 34.96 ± 0.27 (For both PGC1α and XPNPEP1 assay, no signal was detected when using single neuron). However, with the preamplification*

step, the drop in Ct values was not consistent across all assays as the number of neurons increased. TFAM Ct increased from 21.5 ± 0.67 for a single neuron to 31.2 ± 1.08 for two neurons, then to 29.0 ± 2.33 for four neurons. PGC1α drop from 33 ± 0.05 for a single neuron to 29.6 ± 0.65 for four neurons, but no signal was detected when using two neurons. In the plot, triangle dots represent reactions with preamplification, while circle dots represent reactions without preamplification. Blue indicates PGC1α, orange represents TFAM, and green represents XPNPEP1.

5.3. *Results*

5.3.1. *Data point inclusion*

At least six tissue slides from each PD patient and control were subjected to the series of methods outlined in methodology chapter (Chapter 2.4) and the RNA transcriptional levels of three target genes were recorded.

Due to the low RNA levels in postmortem single neurons, only a limited number of neurons tested in this experiment yielded successful results. To ensure the integrity and clarity of negative controls, all data points used for analysis underwent three steps of quality control to confirm they were not the result of artifacts or contamination. The full description of quality control steps can be found in methodology chapter (Chapter 2.4.8). The quality control process involved three key steps. The first step is to ensure amplification status value was required to be conclusive. The second step involves reviewing the amplification plot and melting curve for each data point. To include a data point, a manual check must be performed to confirm a steady increase in targeted fluorescence after each cycle, while the ROX background fluorescence signal remains constant. In the final step, data points with a copy number below 4 in each reaction, deemed inconsistent with PCR methodology, are excluded after calculating the copy number.

For each patient, the goal was to include at least five reliable data point for each target gene. However, due to high dropout date of RT-PCR data points and limited research funding and time, the threshold was lowered to three. Despite this adjustment, it remained challenging to achieve this target for both *PGC1α* and *TFAM*. Fortunately, one

gene, *PINK1*, did meet the criteria, with at least three data points obtained for each case (Table 5.3-1).

Six PD cases and six age matched control were included in the transcriptional data analysis. A total of 552 reactions were performed on *PINK1* level in control cases (92 reactions per case), while 414 of that was performed on *PINK1* level in PD cases (69 reactions per case). A total of 694 reactions were performed on *PGC1α* levels in control cases (115.7 reactions per case), while 511 of that was performed on *PGC1α* level in PD cases (85.16 reactions per case). A total of 722 reactions were performed on *TFAM* level in control cases (120.3 reactions per case), while 596 of that was performed on *TFAM* level in PD cases (99.3 reactions per case). After three quality control steps, all remaining data points were validated. 68 data points (Drop-off rate = 87.7%) were collected in all controls for *PINK1*, and 85 data points for PD cases (Drop-off rate = 79.5%). 22 *PGC1α* results were collected for controls (96.8%), while 68 for PD (86.7%). 35 *TFAM* results was collected for controls (95.2%), while 55 for PD (90.8%).

	PINK1		*PGC1α*		*TFAM*	
	Performed	**Passed**	**Performed**	**Passed**	**Performed**	**Passed**
Control1	114	13	114	3	114	6
Control2	126	3	66	0	126	2
Control3	102	15	274	4	102	11
Control4	32	7	72	1	136	1
Control5	52	27	52	12	52	13
Control6	126	3	116	2	192	2
PD1	108	10	108	28	108	14
PD2	26	12	105	5	90	7
PD3	98	5	82	1	182	3
PD4	80	18	114	5	114	8
PD5	36	9	36	16	36	7
PD6	66	31	66	13	66	16

Table 5.3-1 The number of reactions performed and successfully passing quality control for each target in each patient

Numbers highlighted in grey indicate insufficient data for completing the collection.

While data collection for PINK1 was successfully completed for all PD cases and controls, the collection for PGC1α and TFAM was incomplete due to a high drop-off rate.

5.3.2. *Upregulation of PINK1*

After the data exclusion based on the strategies mentioned previously, the remaining data points for all targets were analysed through R. *PINK1* RNA was significantly upregulated (p <0.00001****, t-test) in PPN cholinergic neurons in PD cases (1349 ± 1509) comparing to the controls (385 ± 774), while there was no clear change of both the *PGC1α* (Control = 29.5 ± 23.3; PD = 47.1 ± 56.6; p= 0.119 , t.test) and *TFAM* RNA expression (Control = 90.5 ± 223; PD = 33.8 ± 26.7; p = 0.419 , t-test) between the PD cases and the controls (Figure 5.3-1).

When grouping the collected *PINK1* CN data by case, several PD cases (PD1, PD6 and PD7) exhibited higher *PINK1* copy number, as did one control case (Control5) (p < 2.2e-16, ANOVA). Another control case also showed a higher mean PINK1 CN, however, due to a high standard deviation (712.64), it was still considered within the normal range for controls. This suggests that certain traits in these patients may have contributed to the observed upregulation of *PINK1* (Figure 5.3-2). The detection of high *PINK1* CN in control5 is not unexpected, as mitophagy is a tightly regulated pathway even under normal ageing conditions (Picca *et al.*, 2023).

After correlation analysis, age at death was the only trait shown to correlate significantly with *PINK1* copy number (r = 0.26, p = 0.007*, Pearson's correlation), with higher PINK1 copy number level in patients with greater age at death (Figure 5.3-3). For other parameters, the correlations were as follows: PD duration & *PINK1* CN (r = 0.16, p = 0.11, Pearson's correlation); PMI (r = -0.15, p = 0.092, Pearson's correlation); and Braak LB stage (r = 0.061, p = 0.57, Pearson's correlation).

It would be interesting to see if there is any correlation between the *PINK1* copy number and mtDNA deletion (number of deletions per neurons or deletion heteroplasmy level). Although no direct comparison can be made as they are from different neurons, mean value of these parameters for each case was calculated. One correlation was found after the comparisons. A strong negative correlation was found between the *PINK1* copy number and the number of mtDNA deletion per neuron in PD cases (r = -0.637, p = 0.01*, Pearson's correlation), while this was not detected in control cases (r = 0.297, p = 0.18, Pearson's correlation) (Figure 5.3-4).

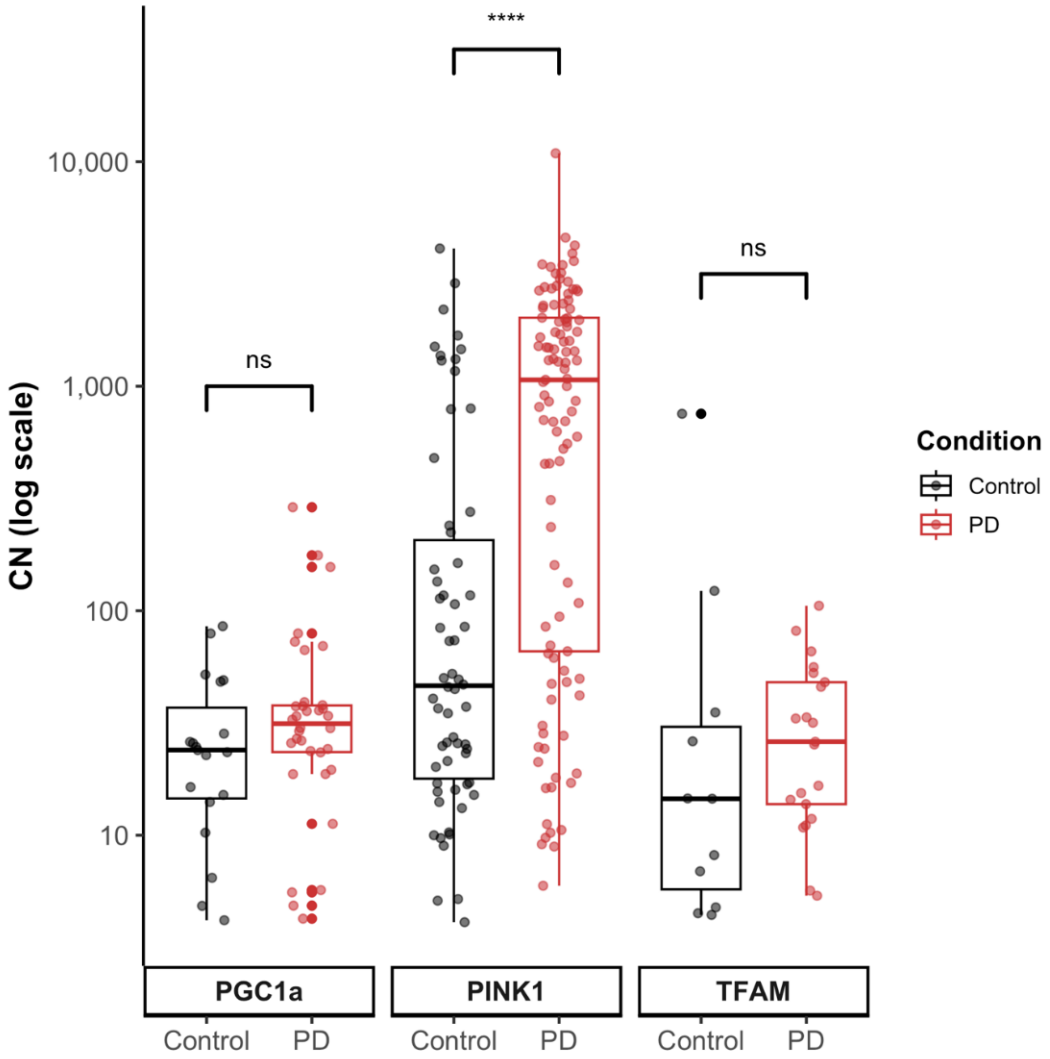

Figure 5.3-1 Three targets transcriptional comparison between PD and controls

The x-axis displays the tested assays, and the y-axis (in log display) displays the copy number of each gene. Each data point represents the copy number of the target gene in one single neuron. For both PGC1α and TFAM, there was no clear difference between the PD (PGC1α: 47.1 ± 56.6; TFAM: 33.8 ± 26.7) and controls (PGC1α: 29.5 ± 23.3; TFAM: 90.5 ± 223). However, a significant difference was observed in the copy number of PINK1. A significant upregulation of PINK1 was noted in PD patients (PD: 1349 ± 1509; Control: 385 ± 774). Black represents control cases, while red represents PD cases.

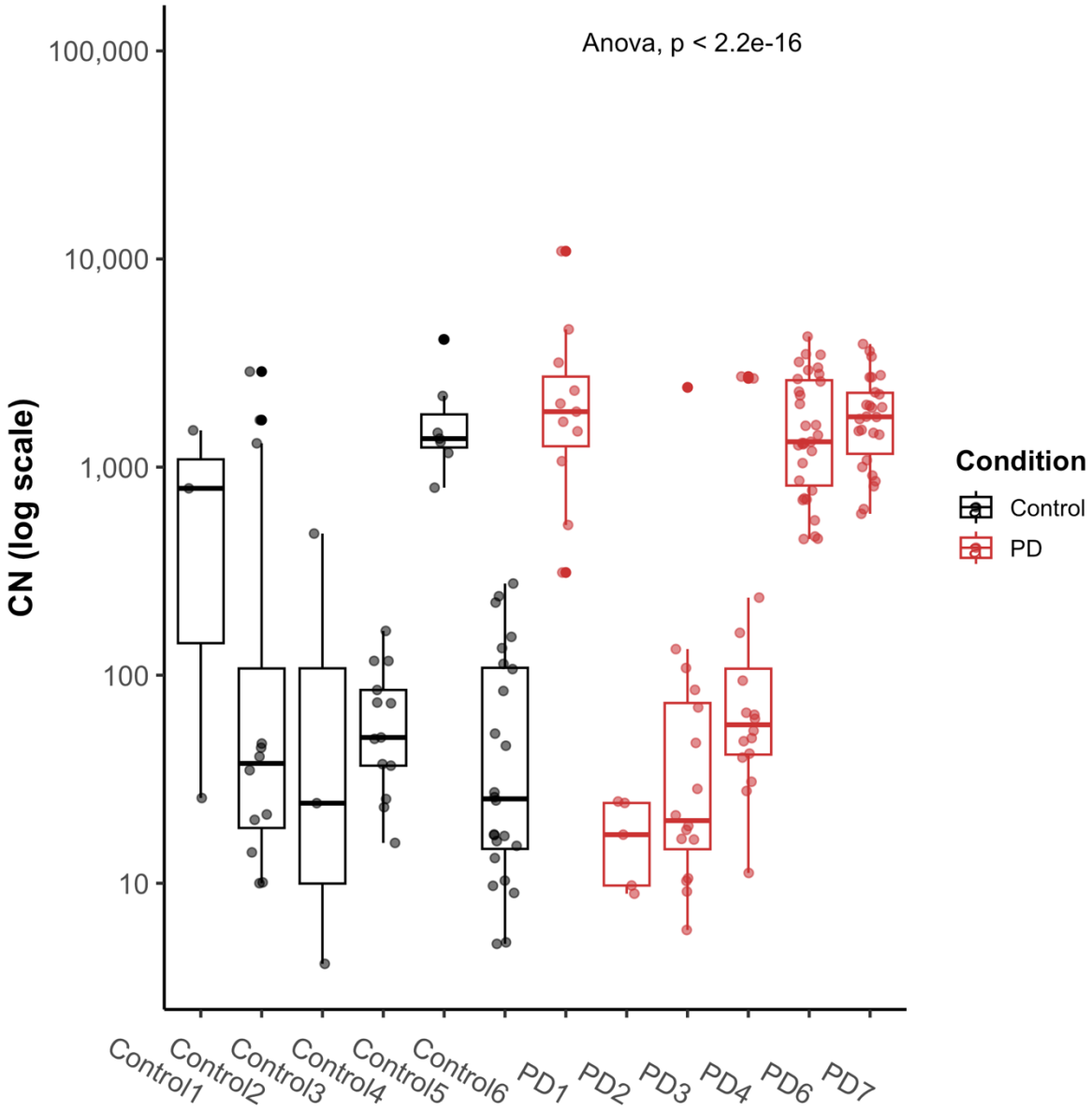

Figure 5.3-2 PINK1 transcription level in different cases

The x-axis displays the different cases, and the y-axis shows the PINK1 copy number on a logarithmic scale. When grouping the collected data by case, several PD cases (PD1, PD6 and PD7) exhibited higher PINK1 copy number, as did one control case (Control5). A significant difference in PINK1 copy number was observed among individual cases (p < 2.2e-16, ANOVA). This suggests that specific traits in these patients may have contributed to the observed upregulation of PINK1. Black represents control cases, while red represents PD cases.

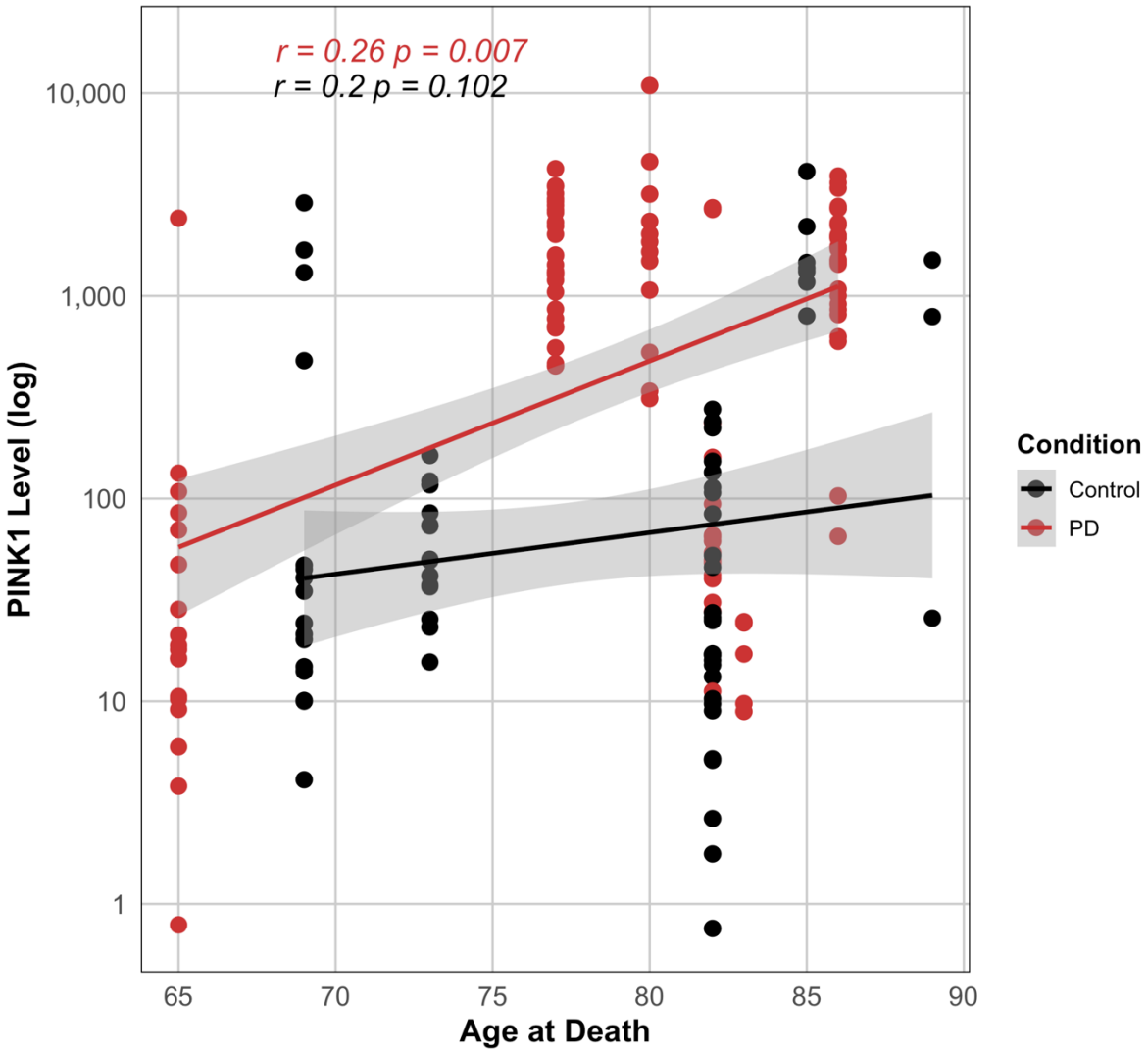

Figure 5.3-3 Correlation between age at death and PINK1 copy number

The x-axis displays the age at death of the patients from whom the neurons were extracted, while the y-axis (in log display) shows the PINK1 copy number. In PD cases, a positive correlation was observed between age at death and PINK1 copy number level (r = 0.26, p = 0.007, Pearson's correlation), with higher PINK1 copy number level in patients with greater age at death. In contrast, no significant correlation was observed in control cases (r = 0.2, p = 0.102, Pearson's correlation). Black represents control cases, while red represents PD cases.*

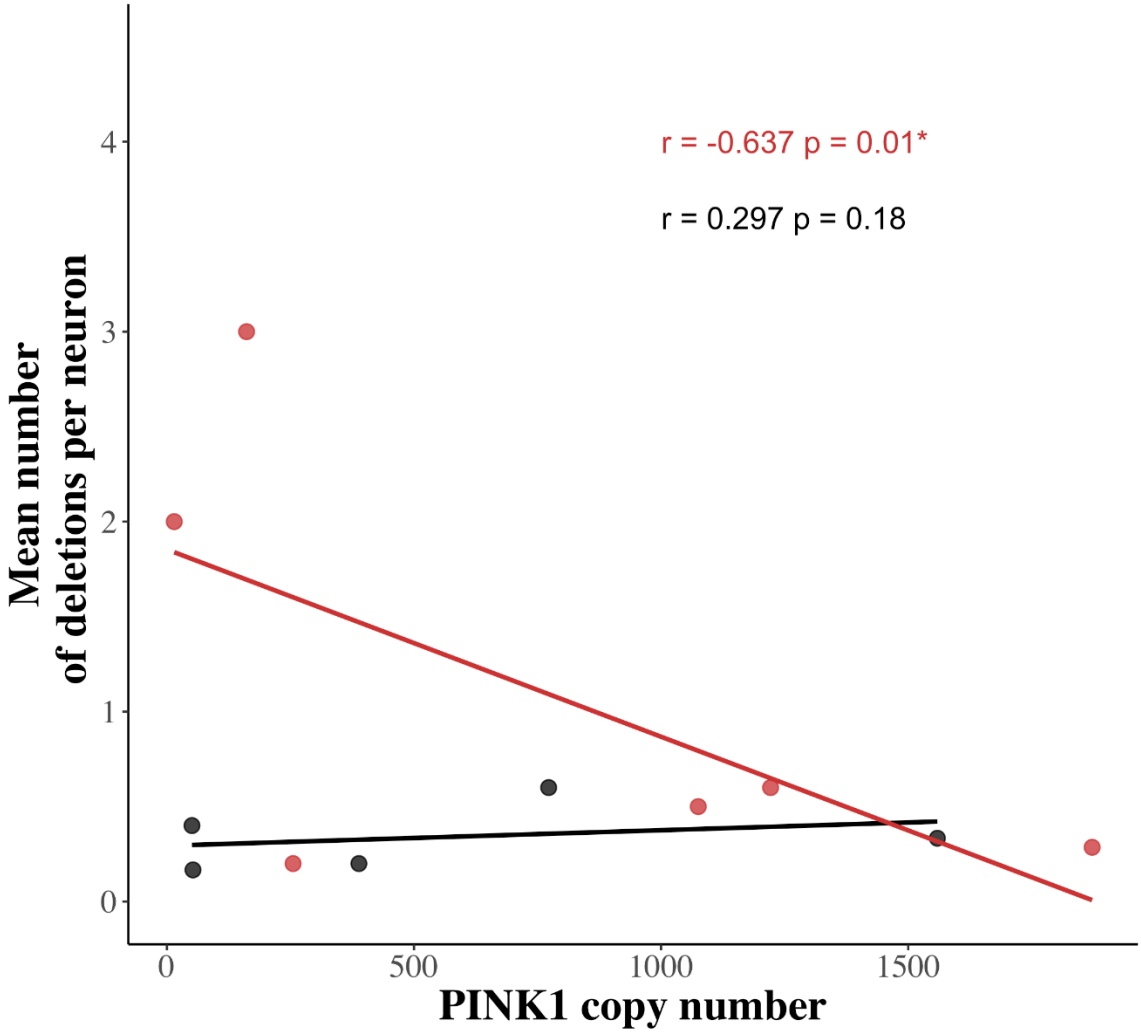

Figure 5.3-4 PINK1 copy number correlation with deletions

The x-axis displays the PINK1 copy number in single neurons, while the y-axis shows the mean number of deletions per neuron. In PD cases, a significant negative correlation was observed between PINK1 copy number and mtDNA deletions (r = -0.629, p = 0.01, Pearson's correlation), with higher PINK1 copy numbers found in neurons exhibiting fewer deletions. In contrast, no significant correlation was observed in control cases (r = 0.297, p = 0.18, Pearson's correlation). Black represents control cases, while red represents PD cases.*

5.4. *Discussion*

PGC1α has multiple isoforms/transcript variants expressed within the brain (Soyal *et al.*, 2012; Souder *et al.*, 2023), which makes it challenging to identify or design the appropriate assay. Neither the TaqMan *PGC1α* assays (Hs00173304_m1 and Hs01016722_m1) nor the customized *PGC1α* primer set 4 were able to amplify the *PGC1α* transcript variants within the cholinergic neurons of the PPN in human. This may be due to the low efficiency of the primers in the RT-PCR reactions or the possibility that these transcript variants are not expressed in this region. In comparison, primer set 1 and 2 demonstrated efficient amplification of the target gene, both targeting a consistent list of transcript variants, including NM_013261.5; NM_001330751.2; NM_001330752.2; NM_001330753.2; NM_001354825.2; NM_001354826.2; NM_001354827.2.

When an assay does not target all these transcript variants, like primer set 3 (which lacks NM_001330753.2), Hs00173304_m1 (lacking NM_001330751.2; NM_001330752.2; NM_001330753.2; NM_001354825.2; NM_001354826.2; NM_001354827.2), and Hs01016722_m1(which excludes all the transcript variants targeted by primer sets1 and 2), amplification is not achieved. Interestingly, despite targeting all eight variants, primer set 4 also failed to yield amplification. This lack of signal may be contributed to partially degraded RNA, the targeted region falling within a degraded sequence, or the absence of *PGC1α expression*.

The upregulation of *PINK1* RNA level is an intriguing observation. This finding suggests that *PINK1* is the only target identified with a differential expression level between PD cases and controls. Although this difference was not observed in all individual cases, possibly due to the complex mechanism underlying PD and the fact that mitophagy is a universal pathway, a higher proportion of PD cases overall exhibited elevated *PINK1* copy number. The observed upregulation of *PINK1*, alongside an increase in mtCN (reported previously in (Bury *et al.*, 2017)), is a compelling indication of mitochondrial stress or damage. PINK1 plays a pivotal role in mitochondrial quality control system, functioning as a sensor of mitochondrial dysfunction and initiating mitophagy to remove damaged mitochondria (1.7.4 Mitophagy). The increase in *PINK1* transcriptional level likely reflects a neuronal response to mitochondrial distress signals, potentially caused

by accumulated deletions reported in (3.2.2 Number of deletions detected per neuron and their heteroplasmy levels) (Newman and Shadel, 2018). The concurrent rise in mtCN may represent a compensatory mechanism aimed at preserving mitochondrial function and maintaining cellular energy homeostasis. However, this increase in mtCN does not necessarily equate to improved mitochondrial functionality (Filograna *et al.*, 2021). Dysfunctional mitochondria may persist, particularly if the newly synthesized mtDNA harbours mutations or deletions (Rahman and Copeland, 2019). Such persistent mitochondrial stress could lead to the sustained upregulation of PINK1, perpetuating the cycle of mitochondrial dysfunction and cellular distress (Park *et al.*, 2006; Du *et al.*, 2017; Quinn *et al.*, 2020).

Due to the unbiased method of neuron selection used in this research, it is possible that some neurons may be COX deficient, though this cannot be confirmed with certainty. Previous studies have reported atrophy of the PPN cholinergic neurons in PD cases, as well as a decreased expression of VDAC1 (Pienaar *et al.*, 2013). VDAC1 is a protein anchored in the outer mitochondrial membrane, critical for transporting small molecules and maintaining membrane potential and is a key substrate of *PINK1/Parkin* pathway. The decreased expression of VDAC1 might drive the transcription of *PINK1* in an attempt to compensate for insufficient mitophagy, which is necessary for removing damaged mitochondria. Additionally, PINK1 indirectly interact with autophagy pathways like (Lazarou *et al.*, 2015). This process is a vital component of cellular homeostasis, influencing functions such as ETC energy production (Liu *et al.*, 2011), reactive oxygen species production (Xiao *et al.*, 2017), and lipid metabolism (Lu *et al.*, 2024). The increased level of *PINK1* might also be associated with observed loss of approximately 50% of PPN cholinergic neurons in PD patients (Pienaar *et al.*, 2013). Furthermore, PINK1 has connections to other pathways, which could serve as potential direction for further research. The elevated levels of *PINK1* may lead to decrease in mitochondrial fusion proteins, such as mitofusion1 and mitofusion2, thereby suppressing fusion and promoting fission (Chen and Dorn, 2013; Ge, Dawson and Dawson, 2020).

No differences were observed in transcriptional level of either *TFAM* or *PGC1α*, suggesting that the increased mtCN is unlikely to result from the overexpression of these two target genes. In the case of *PGC1α*, it is possible that alternative pathways could be activating transcription factors such as NRF1 and NRF2 (Virbasius and Scarpulla, 1994;

Gureev, Shaforostova and Popov, 2019) (details can be found in 1.7.1 and 1.7.6). Additionally, even with unchanged level of *PGC1α* or *TFAM* transcription (King *et al.*, 2018; Luo *et al.*, 2019; Reardon and Mishanina, 2022), their activity could be regulated post-translationally, through a mechanism such as phosphorylation or acetylation, which could enhance their protein activity.

Although, no single-neuron transcriptional changes on any of the target genes were measured in SNpc dopaminergic neurons in the literature, previous research has explored mitochondrial-related protein levels in individual SNpc dopaminergic neurons in PD. Both TFAM and PINK1 expression were found to be decreased in SNpc dopaminergic neurons (Chen *et al.*, 2020, 2023), suggesting that distinct compensatory pathways may be active in different types of neurons. This remains a critical area of research, as various neuronal types respond differently under specific conditions (Zimprich *et al.*, 2004; Liu *et al.*, 2013; Jiao *et al.*, 2022; Rappe *et al.*, 2024).

Age at death correlates with *PINK1* copy number level in PD cases, suggesting that *PINK1* plays a disease-specific role in modulating in the progression and severity of PD. In normal ageing, mitochondrial functional declines gradually and may not necessarily tied to *PINK1* (Harman, 1956; Son and Lee, 2019). Alternatively, this decline could result from diminished capacity new mitochondria with age, partly due to reduced activity of transcription factors such as PGC1*α,* which regulates mitochondrial biogenesis (Gureev, Shaforostova and Popov, 2019). This observation further implies that PD patients who do not exhibit *PINK1* upregulation might experience more severe mitochondrial dysfunction, potentially contributing to earlier mortality.

The RT-PCR method used in this research has some limitations. It is not highly sensitive to detecting RNA that may have undergone slight degradation and can easily generate false positive or negative results, particularly for samples with very low Ct values, as seen in this case. Therefore, it is critical to carefully verify the amplification of each data point and consistently include negative controls. Setting a threshold of 4 copies per reaction for the copy number helps to exclude data points that are not meaningful within the context of PCR analysis, as the presence of target cDNA sequence is unlikely to remain undetected until the final two cycles of amplification. In the future, techniques with higher tolerance for low-integrity RNA, such as RNA scope or RNA-seq, could be considered. Additionally, the use of postmortem tissue in this research introduces a

potential bias in the neuronal population, as neurons with severe damage may have already been lost before the patients' death.

In conclusion, for the detection of *PGC1α* mRNA levels in human postmortem brain tissue, a potential region and prevalent transcription variants have been suggested. Despite technical limitations, comparable results were obtained. Upregulation of the *PINK1* mitophagy pathway was observed at the transcriptional level, which may be linked to previously reported changes, such as the atrophy of cholinergic neurons in this area, loss of the cholinergic population, and a decrease in the membrane protein VDAC1 (Pienaar *et al.*, 2013). These changes are closely associated with the progression of PD. The absence of clear RNA changes in *PGC1α* and *TFAM* suggests that downstream alterations or alternative pathways may be involved in the previously reported upregulation of mtCN (Bury *et al.*, 2017). The changes observed might be specific to cholinergic neurons, given the contradictory results reported in SNpc dopaminergic neurons (Reeve *et al.*, 2008; Grünewald *et al.*, 2016). Further studies are needed to investigate the underlying reasons for this discrepancy.

Chapter 6. General discussion

PPN cholinergic neurons are known to be a mitochondria vulnerable neuronal subtype in PD (Pienaar *et al.*, 2013), and there is significant interest in understanding their response to PD-related conditions. Previous studies have highlighted differences in mtDNA CN changes in PPN cholinergic neurons (Bury *et al.*, 2017) compared to SNpc dopaminergic neurons (Pyle *et al.*, 2016), whose degeneration is a hallmark of PD. These differences raise intriguing questions about how different neuronal types respond to PD in the context of mitochondrial dynamics.

To explore this further, a series of tests were conducted to examine mitochondrial changes at various levels, including mtDNA deletions, mtDNA point mutations, and the transcriptional expression of key genes involved in three pathways regulating mtCN: biogenesis, maintenance, and mitophagy. The key fundings from these analyses are summarised below for discussion.

6.1. *Major findings and limitations*

6.1.1. *The size of the mtDNA deletions was not a continuous distribution*

MtDNA deletion has been widely reported in studies investing single neurons from post-mortem tissue in PD research, and all of the deletions reported are only large deletions (over 1,000bp). No studies to date have identified small deletion in these contexts (Valiente-Pallejà *et al.*, 2022). This discrepancy may arise from methodological limitations and the specific research focus of these studies. Most publications prioritise the analysis of clonally expanded mtDNA deletions, which are more likely to result in mitochondrial dysfunction. For instance, earlier studies (Bender *et al.*, 2006; Reeve *et al.*, 2008) utilised COX-SDH staining to select dopaminergic neurons from the SNpc for analysis, followed by long-range PCR. While effective for detecting large deletions, this method is unsuitable for identifying deletions with low heteroplasmy levels. Similarly, other studies have employed ND1/ND4 qPCR to estimate the overall deletion burden in neurons without focusing on specific deletions (Dölle *et al.*, 2016; Bury *et al.*, 2017).

To date, only one study has employed NGS deep sequencing to investigate deletions in dopaminergic neurons from the SNpc, but no small deletions were identified. This might be attributable to the small cohort size, which included only two patients (Nido *et al.*, 2018). By contrast, studies examining broader contexts—such as post-mortem brain homogenates and blood samples—have detected 127 small deletions ranging from 50 bp to 1,000 bp using NGS techniques (Thivierge, 2008). However, these findings were not derived from single-neuron analyses, and differences in cell types may confound direct comparisons.

The mtDNA deletions reported in Chapter 3 can be categorised as either small (ranging from 5 to 140 bp) or large (exceeding 1,400 bp). Notably, no deletions were observed within the intermediate size range of 140 bp to 1,400 bp, and this deviation from a normal distribution was consistent across both PD patients and aged controls. This finding suggests the involvement of two distinct mechanisms underlying these deletion types. Small deletions are likely generated by oxidative damage, as previous studies have demonstrated that double strand breaks in mtDNA promote the formation of such deletions. In contrast, the occurrence of larger deletions may implicate strand displacement as a mechanism in mtDNA replication. The predominance of large deletions within the major arc further supports this hypothesis.

However, there are limitations to the methodology used in this research. While NGS is a powerful tool for detecting mtDNA deletions, the technique does rely solely on PCR amplification, making it challenging to accurately quantify heteroplasmy levels. Additionally, the use of three targeted primers in some NGS protocols may truncate longer deletions that extend beyond the amplified regions. These limitations underscore the need for more comprehensive and sensitive methodologies to fully characterise the spectrum of mtDNA deletions in different contexts.

6.1.2. *The mtDNA deletions are in the same position in both PD and control cases*

In Chapter 3, it is noteworthy that the distribution of mtDNA deletions predominantly occurs within the same genomic region, particularly for large deletions in both PD and aged control cases. Of the 37 large deletions identified, only 2 were located within the

minor arc, while the remaining deletions were confined to the major arc. Interestingly, when aligned with deletions reported in dopaminergic neurons of the SNpc from both PD and aged control cases in a study (Reeve *et al.*, 2008), a similar regional distribution was observed. Despite differences in methodology, neuronal selection strategies, and neuronal types, the deletions were consistently located within the same regions. Furthermore, a comparable distribution pattern was observed in neurons from patients with *POLG* mutations, suggesting that mtDNA deletions may arise through mechanisms associated with mtDNA replication. This finding aligns with other studies in PD neurons. For instance, single dopaminergic neurons from the SNpc of PD patients, analysed using NGS techniques, also revealed deletions primarily confined to the major arc.

A search of the MitoMap database corroborates these findings, showing that the majority of reported deletions across various conditions are located within the same genomic region. For example, the 4,977 bp common deletion, frequently reported in conditions such as KSS (Zeviani *et al.*, 1988) and various cancers (Tseng *et al.*, 2009; Yusoff *et al.*, 2019), also falls within this region. This consistency in the distribution of mtDNA deletions suggests the involvement of a shared underlying mechanism driving their formation.

Moreover, these observations indicate that differences in the response to maintaining mtCN between PPN cholinergic neurons and SNpc dopaminergic neurons are unlikely to stem from variations in the mechanism of mtDNA deletion formation. Instead, other factors may influence the distinct responses observed in these neuronal types.

6.1.3. *Levels of point mutations remained unchanged*

In Chapter 4, a series of comparisons was conducted to investigate potential differences in somatic point mutations between PD and aged control cholinergic neurons. Despite multiple statistical tests, no significant differences were observed between PD and control neurons. This finding aligns with results reported in SNpc dopaminergic neurons isolated from human post-mortem tissue. In that study, only point mutations with high clonal expansion were analysed due to methodological limitations (Reeve *et al.*, 2009).

However, our data contrast with findings from studies on tissue homogenates from the SNpc and frontal cortex. In those studies, a higher prevalence of somatic point mutations was observed in genes encoding cytochrome c oxidase (complex IV) in PD post-mortem brain tissue compared to aged controls, using NGS techniques (Coxhead *et al.*, 2016). In the present study, only one PD patient exhibited relatively elevated levels of point mutations (after normalisation) in complex III, while another PD patient showed higher normalised levels in complex I. No clear differences were observed in the accumulation of mutations in any area or in complex IV. This discrepancy may stem from the fact that tissue homogenates encompass multiple cell types and extracellular contents, making it impossible to pinpoint changes specific to individual neurons. By contrast, our research focuses on single-cell analyses, which provide a more targeted investigation of cholinergic neurons.

6.1.4. *Middle heteroplasmy point mutations accumulate the most*

Also, in Chapter 4, when comparing the number of point mutations across different heteroplasmy groups, it is notable that fewer point mutations were observed in both low and high heteroplasmy levels compared to those with middle heteroplasmy levels in both conditions. The limited detection of point mutations at low heteroplasmy levels aligns with findings in the literature, which suggest that mutations typically occur early in life and that the mutation rate remains relatively stable throughout the lifespan (Greaves *et al.*, 2014). Our results, which show a similar pattern in both control and PD neurons, indicate that the PD condition does not induce a surge in mtDNA point mutations later in life, which could happen in ageing and under stress condition (Linnane *et al.*, 1989).

The reduced accumulation of point mutations at high heteroplasmy levels, coupled with the higher accumulation at middle heteroplasmy levels, suggests the involvement of mechanisms that limit clonal expansion. These mechanisms might regulate mitochondrial dynamics to segregate highly mutated mtDNA or activate mitophagy pathways to eliminate mitochondria harbouring high-level mutations. Such processes could actively mitigate clonally expanded point mutations, ensuring that only a small proportion reach high heteroplasmy levels. Alternatively, these results could indicate the presence of processes that restrict continuous clonal expansion in neurons. It is

also possible, given the post-mortem nature of this research, that neurons accumulating high levels of point mutations may have already degenerated by the time of sampling. However, previous studies have demonstrated the presence of clonally expanded deletions in various types of neurons under PD conditions, indicating that clonal expansion is a key feature of mtDNA dynamics in PD (Bender *et al.*, 2006; Bury *et al.*, 2017).

6.1.5. *Free energy differences in breakpoint sequence*

In Chapter 4 when examining the deletion composition, a significant difference was found in the free energy (FE) of 25bp and 50bp windows in deletions with repeats, but not in 100bp windows. In neurons from PD cases, both the FE25 and FE50 is significantly lower than the neurons captured in aged controls, which means that in both 25bp and 50 bp windows around deletion breakpoints with repeats they are more likely to generate secondary structures like G4s and those secondary structures would be more stable. This could be interpreted as there are subtle differences within the PD mtDNA sequence, and those subtle difference could lead to the disease prevalence observed in different haplogroup. Publications have shown that people in some haplogroups, are more likely to develop PD and people in some specific haplogroups have less chance of developing PD comparing to others (Pyle *et al.*, 2005; Gaweda-Walerych *et al.*, 2008; Hudson *et al.*, 2013). This difference cannot be seen when analysing the free energy in 100bp size window, which could suggest that this difference is within a small area near the mtDNA breakpoint. A similar finding has been seen in deletion breakpoint analysis of dopaminergic neurons form SNpc in PD patients, where 50bp segments centred on each breakpoint of deletions from PD dopaminergic neurons was calculated and compared those with 50bp long segments extracted randomly using the reference sequence. Results show that the free energy from 50bp segment centred at PD breakpoints is significantly lower than that calculated using random 50bp segments (Nido *et al.*, 2018).

Several other studies support this finding. For instance, (Dong *et al.*, 2014) demonstrated that mtDNA deletion breakpoints are likely to form G4 secondary structures. A more resent in vivo study (Doimo *et al.*, 2023) reported a similar observation, suggesting that in human cells, G4 structures formed near mtDNA

breakpoint may impede the progression of replication forks, ultimately leading to deletions.

It is particularly interesting to observe that the differences in FE25 and FE50 values correlate with Braak stages and disease duration in opposite ways. A positive correlation was identified between FE25 and FE50 values and Braak Lewy body stages, whereas negative correlations were observed between these free energy measures and disease duration. This suggests that as the disease progresses, mtDNA sequences become more prone to forming secondary structures. However, the accumulation of Lewy body pathology may interfere with this process.

This finding contrasts with results from studies on single Lewy body-positive neurons isolated from the SNpc. In those studies, increased mtDNA damage was observed in Lewy body-positive midbrain neurons (Müller *et al.*, 2013). These contrasting results highlight the complex interplay between mtDNA stability, secondary structure formation, and pathological changes during the progression of PD.

6.1.6. *PINK1 transcriptional levels*

Regarding the transcriptional changes recorded in Chapter 5, it is notable that the differences in *PINK1* expression between PD and aged control cholinergic neurons were not uniformly detected across all PD cases. Instead, these differences were observed in neurons from three PD cases and even in one control case. This variability may reflect the heterogeneity of PD, a condition characterised by diverse pathogenic mechanisms. The findings suggest that alterations in *PINK1* transcriptional changes may not influence all PD subtypes. However, no clear associations were identified when comparing diagnostic or medication histories, although a correlation was observed between age at death and *PINK1* transcriptional levels. Notably, no significant changes in mtDNA deletions or point mutations were detected in these cases. Interestingly, a previous study reported downregulation of *PINK1* expression in PD dopaminergic neurons from the SNpc using image mass cytometry (IMC) (Chen *et al.*, 2023). This contrasts with our findings, which could indicate that PPN cholinergic neurons respond differently compared to SNpc dopaminergic neurons. However, these discrepancies may also arise

from differences in the levels being examined—our study focused on transcriptional changes, while the other study assessed protein expression (Gunawardana and Niranjan, 2013). Additionally, the two studies employed distinct methodologies to examine. This result aligns with the observation reported in 2018 (Bury *et al.*, 2017), which found that mtCN was upregulated in PPN cholinergic neurons. The concurrent upregulation of mtCN and *PINK1* transcriptional levels might suggest that these cholinergic neurons are under significant stress, actively attempting to eliminate damaged mitochondrial components while maintaining normal mtDNA content.

No significant changes were observed in the transcriptional levels of *TFAM* and *PGC1α* in PPN cholinergic neurons under PD conditions. Although transcriptional data for these targets is limited in previous studies, protein expression levels could provide further insights. This finding contrasts with existing literature. For example, *PGC1α* knockout in the SNpc of adult mice caused dopaminergic neuron loss, suggesting that decreased expression of *PGC1α* expression contributes to dopaminergic neuronal loss, a hallmark of PD (Jiang *et al.*, 2016). However, studies using human tissues to examine single SNpc dopaminergic neurons have not reported clear transcriptional changes in PGC1α (Chen *et al.*, 2020). Similarly, TFAM has been reported to show decreased expression in various neurodegenerative disease models, including mouse models of Alzheimer's disease (AD), PD, and Huntington's disease (Kim *et al.*, 2010; Grünewald *et al.*, 2016; Petrov *et al.*, 2016; Kang, Chu and Kaufman, 2018). Similar findings have been observed in single SNpc dopaminergic neurons using human postmortem tissue (Chen *et al.*, 2020). The lack of transcriptional changes in PPN cholinergic neurons under PD conditions may indicate a distinct response in this neuronal population.

It is important though to consider the limitations of using post-mortem brain tissue, which is harvested after the patient's death. This approach only provides a snapshot of the brain's state at the late stages of disease progression. Neurons most affected by PD may have already degenerated by the time of analysis, potentially skewing the findings. Additionally, transcriptional data do not necessarily reflect protein expression levels. Future studies should prioritise protein-level comparisons to obtain a more comprehensive understanding of these targets in PD conditions.

6.2. *Final conclusions and future work*

This research identified several changes affecting mitochondria and the mitochondrial genome. Consistent with previous studies, an increase in mtDNA deletions was observed. Notably, this study is the first to report deletions occurring in the minor arc of single midbrain neurons in PD. These deletions were categorised into two distinct size groups, with large deletions being more prevalent. This finding suggests the involvement of mechanisms in PD neurons that may predispose them to generating large deletions, potentially associated with the observed differences in free energy at deletion breakpoints. However, NGS method employed in this study may not comprehensively detect mtDNA deletions, as this technique struggles to reliably distinguish between mtDNA deletions and duplications. Future research could benefit from using nanopore sequencing, which reads unfragmented templates and provides better resolution for analysing long deletions (Lu, Giordano and Ning, 2016).

Due to the inherent limitations of post-mortem research, specific clinical phenotypes were not selected, and information such as ethnicity and environmental exposure was unavailable. These constraints limited the ability to perform detailed correlation analysis. However, as the primary aim of this study was to compare pathological changes between PD and control groups and both cohorts were subject to the same limitations. The comparative analysis remains valid. Nevertheless, future studies incorporating these additional parameters would be valuable for more comprehensively characterising the condition.

Additionally, this work is the first to demonstrate mRNA changes in single PPN cholinergic neurons in both PD and aged control cases. The elevated transcriptional levels of *PINK1* in PD cases suggest a role for mitophagy pathways in the response of cholinergic neurons. While *PINK1* is a critical trigger and sensor within the mitophagy pathway, it also performs additional roles, such as protecting cells from proteasome inhibitor-induced death (Wang *et al.*, 2007) and regulating autophagy (Akabane *et al.*, 2016). These findings highlight the importance of further investigating other targets within the mitophagy pathway to better understand the broader regulatory mechanisms involved.

Chapter 7. Appendices

7.1. *Free energy*

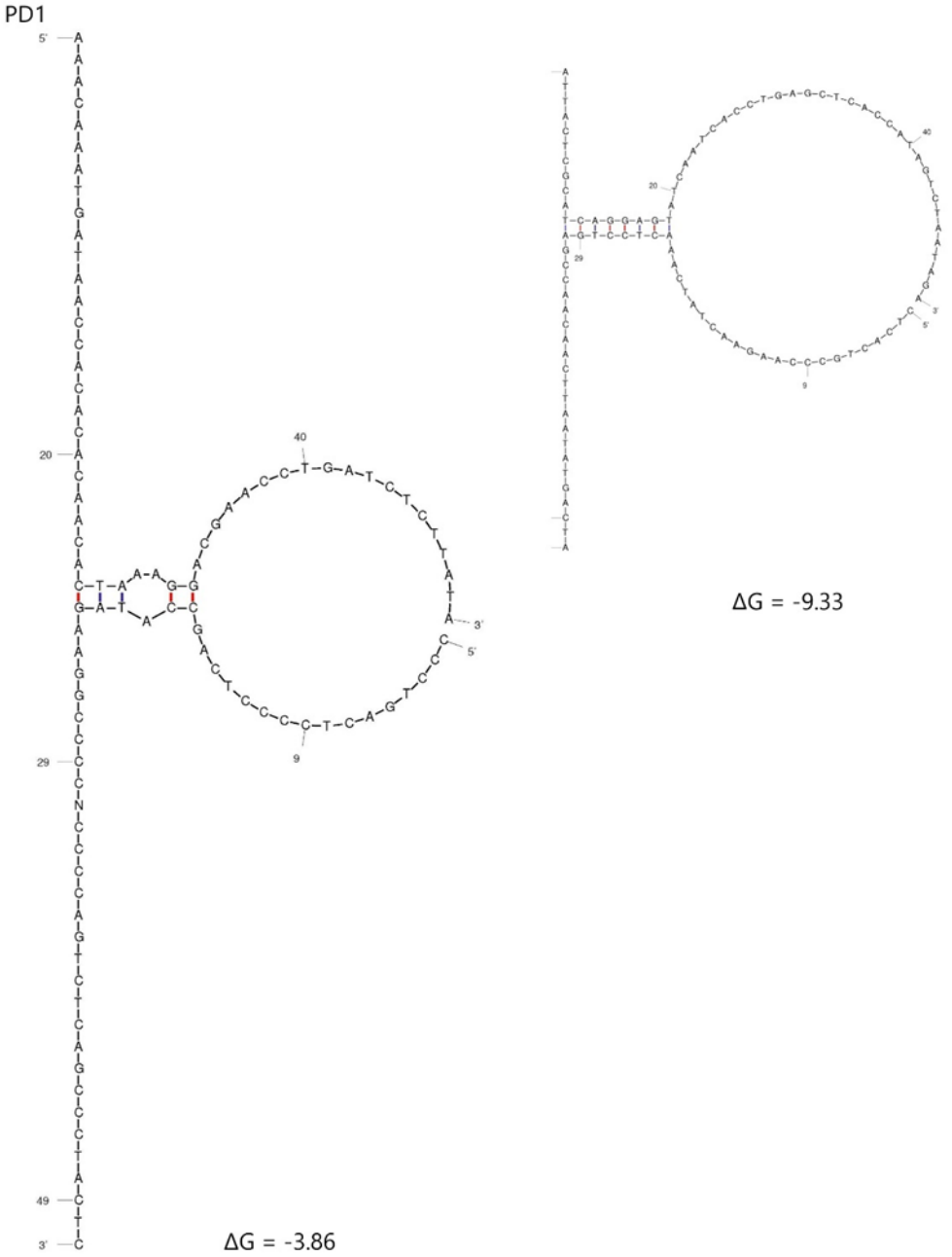

PD2

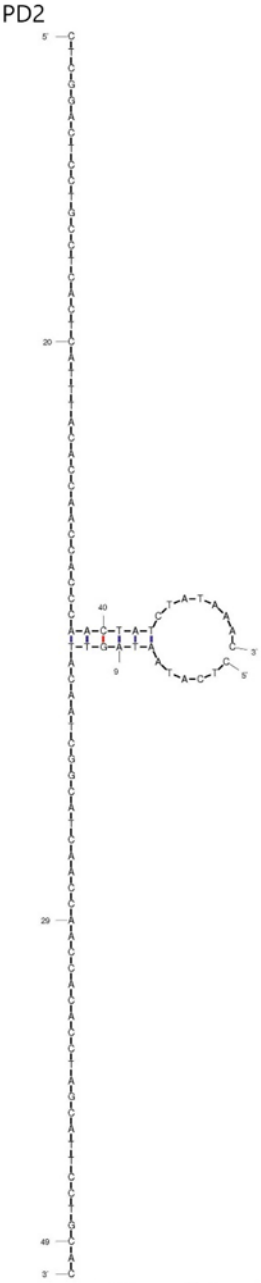

ΔG = -4.72

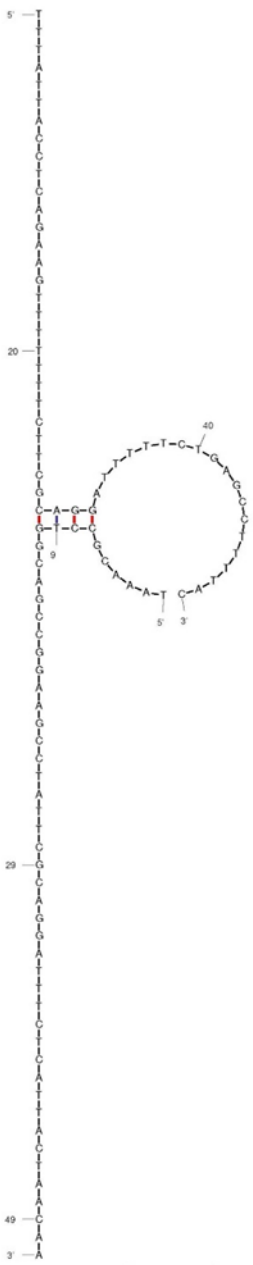

ΔG = -5.41

ΔG = -7.11

PD2

ΔG = -7.66

ΔG = -4.76

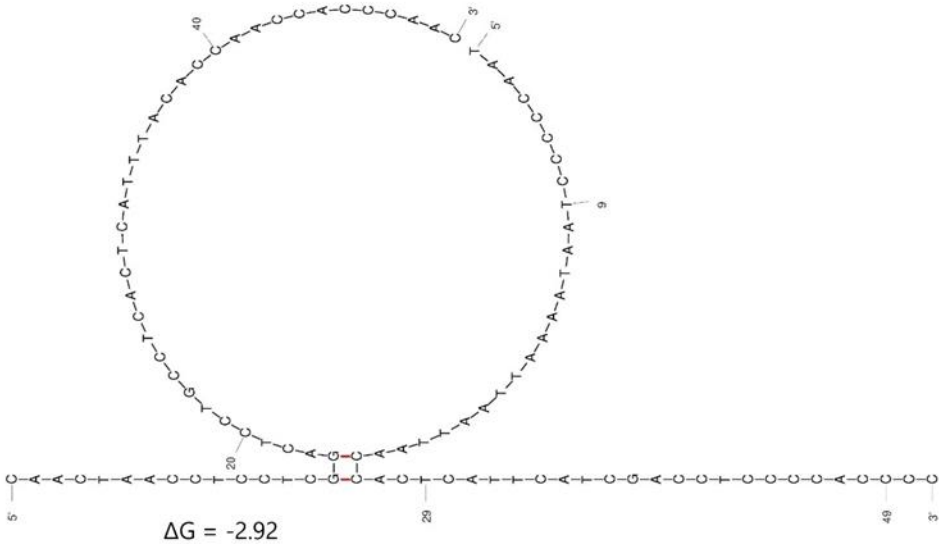

ΔG = -2.92

PD2

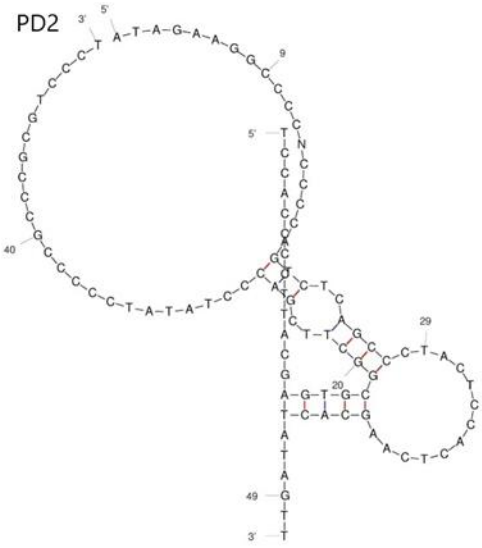

ΔG = -8.29

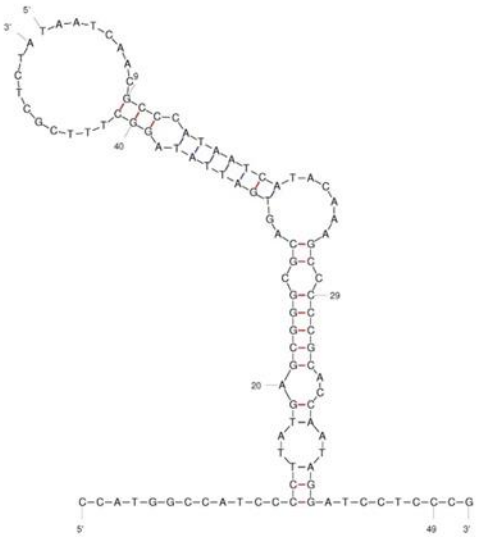

ΔG = -14.61

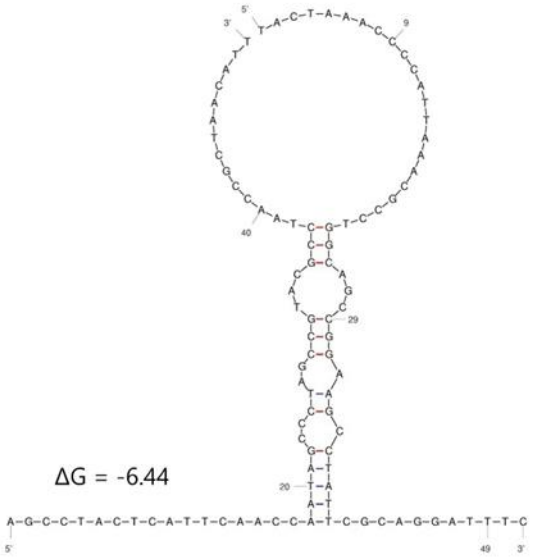

ΔG = -6.44

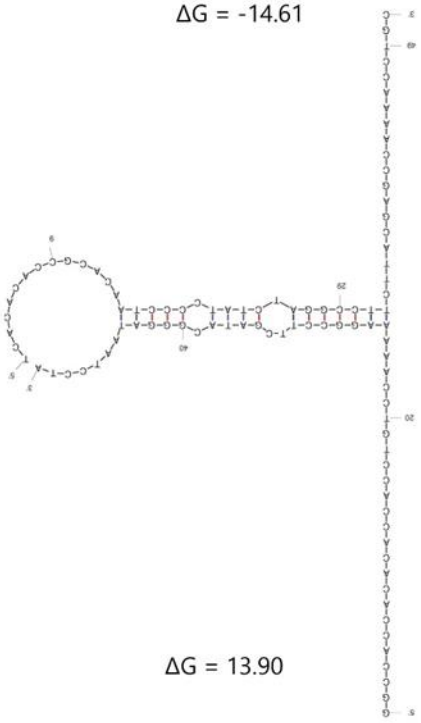

ΔG = 13.90

PD3

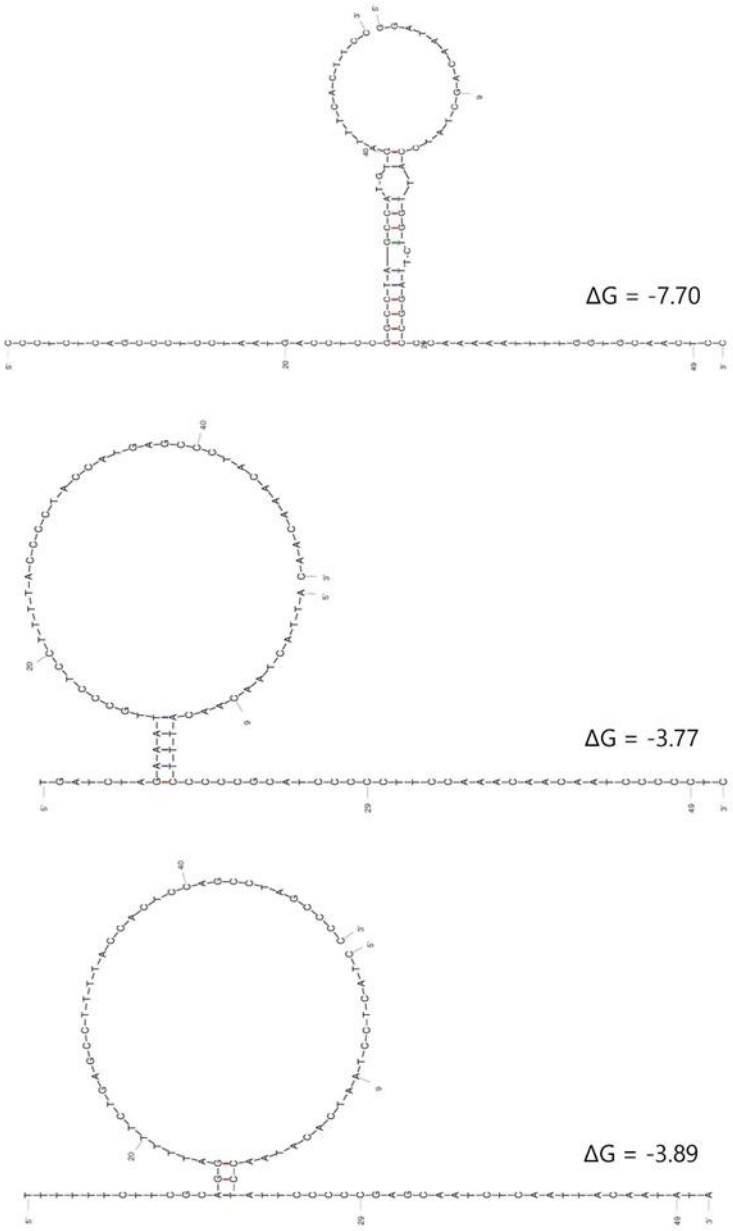

PD3

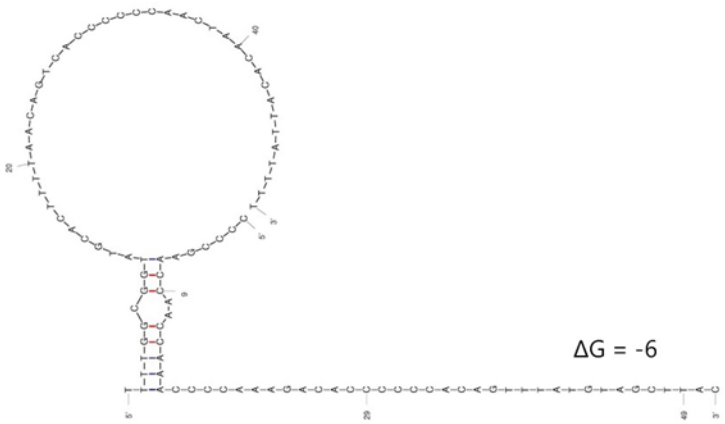

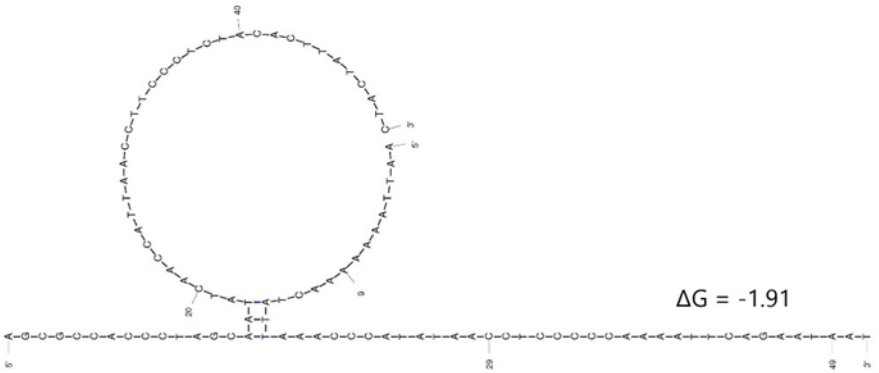

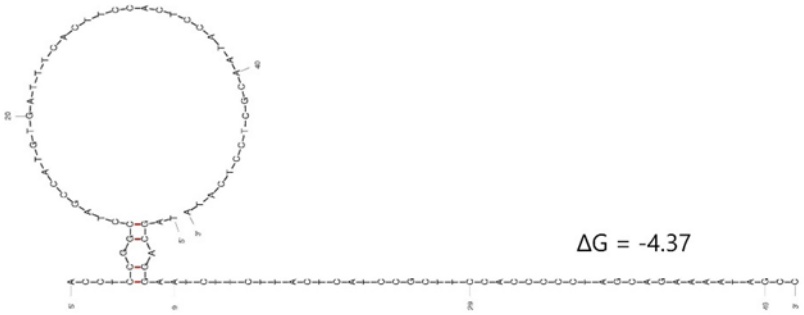

PD3

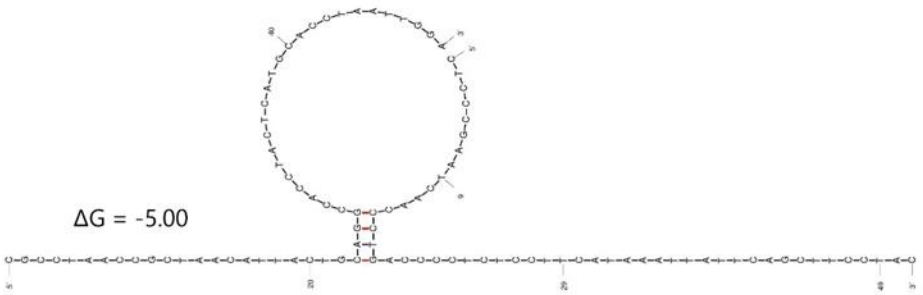

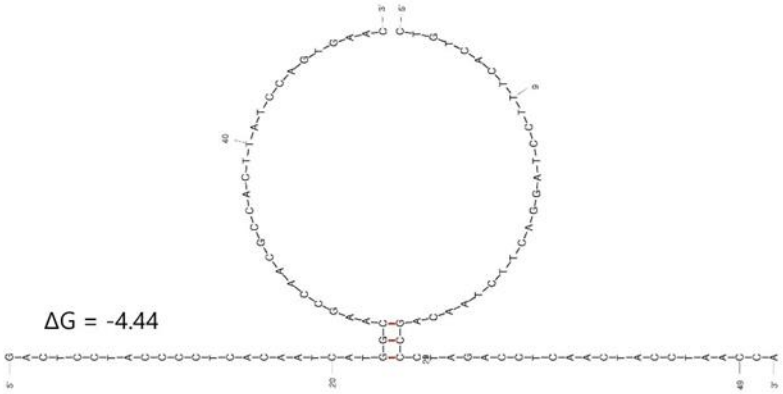

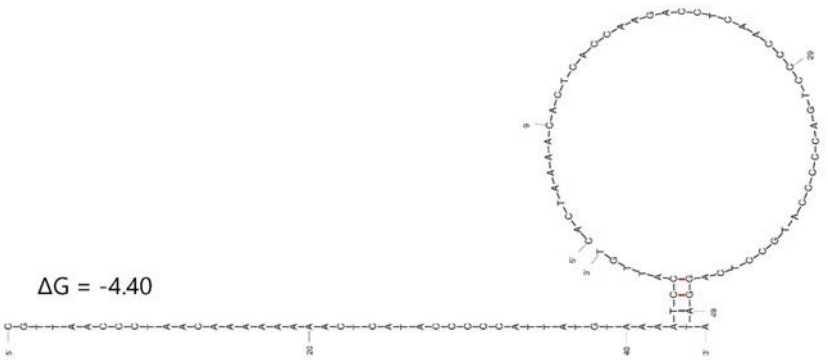

PD3

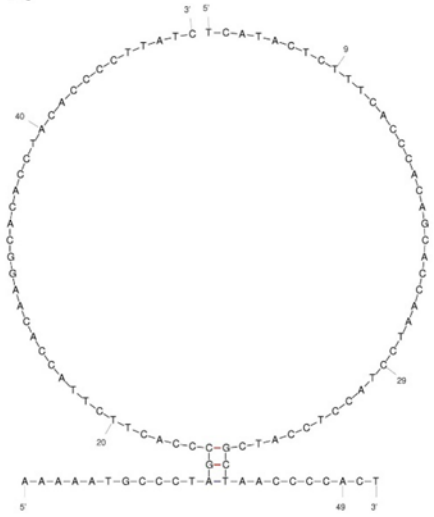

ΔG = -3.35

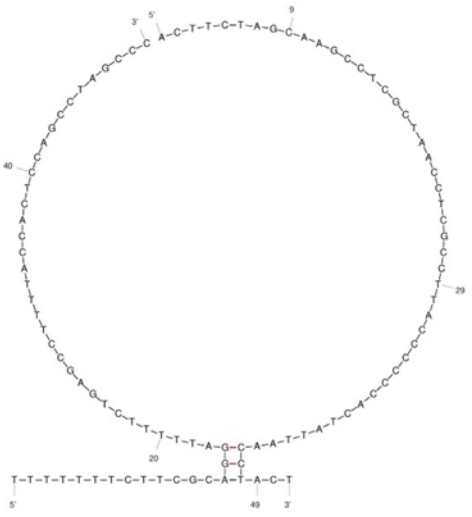

ΔG = -3.89

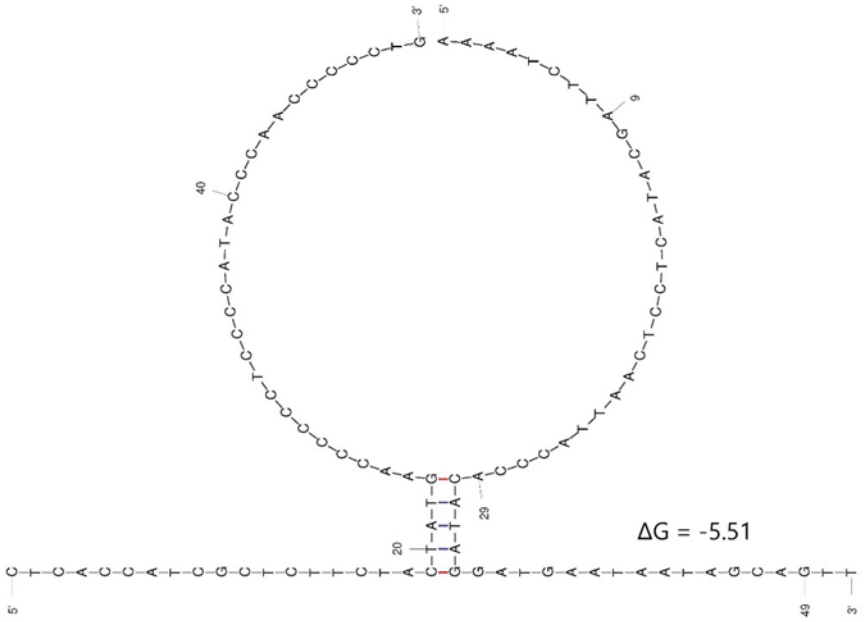

ΔG = -5.51

PD4

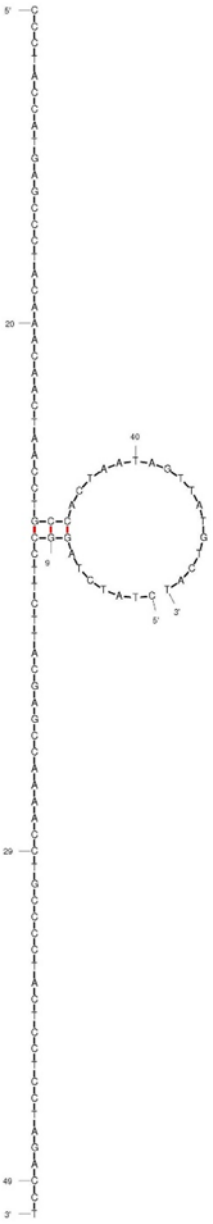

ΔG = -4.44

PD5

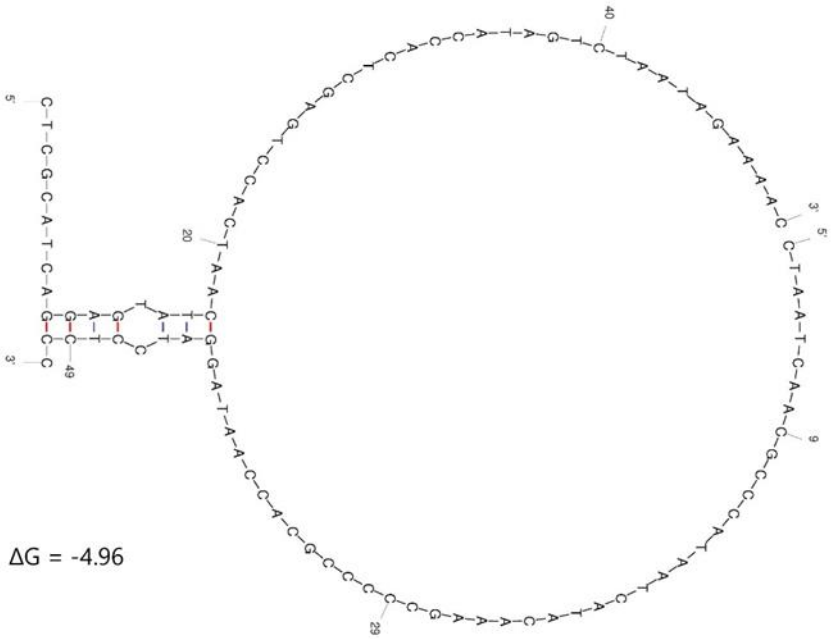

ΔG = -4.96

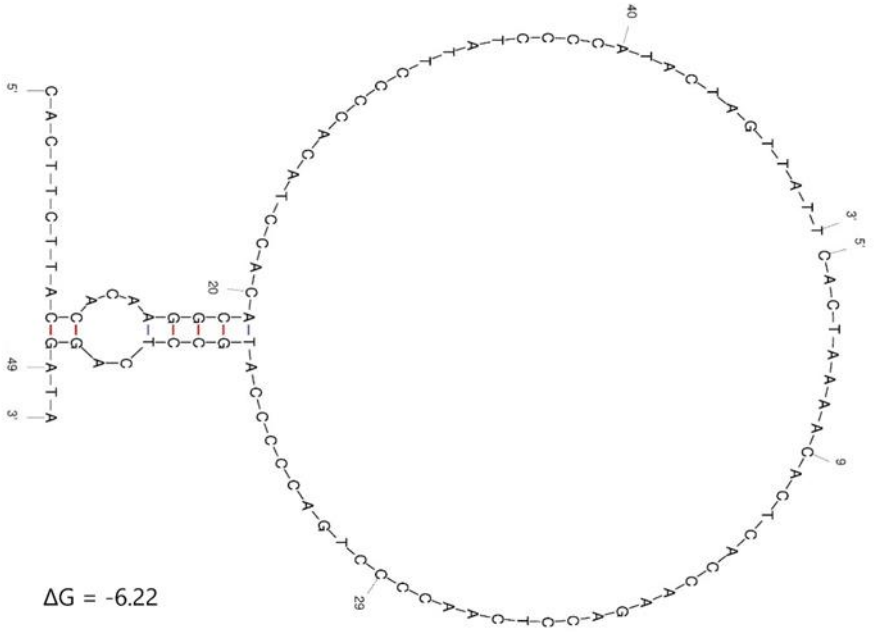

ΔG = -6.22

PD5

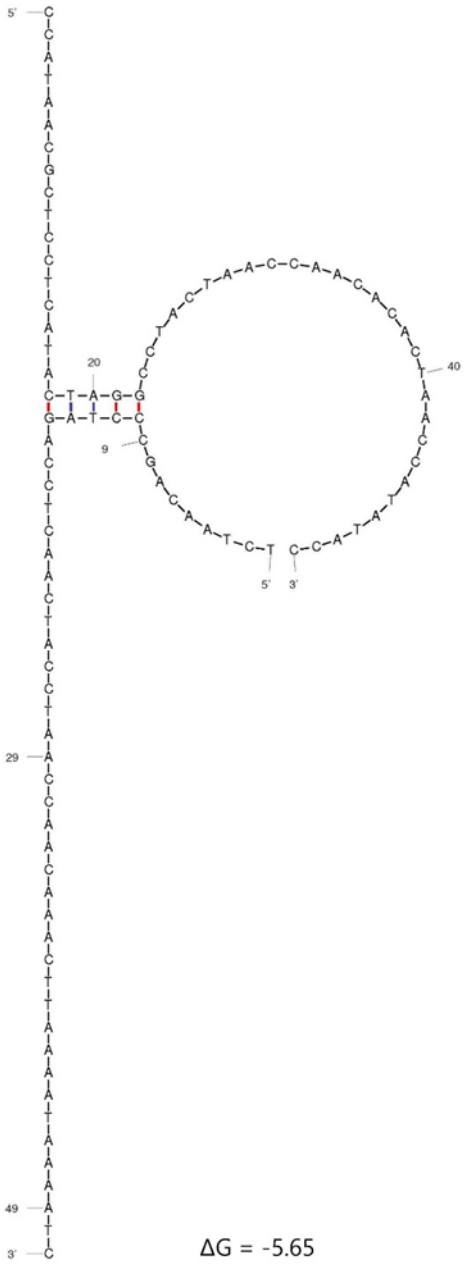

ΔG = -5.65

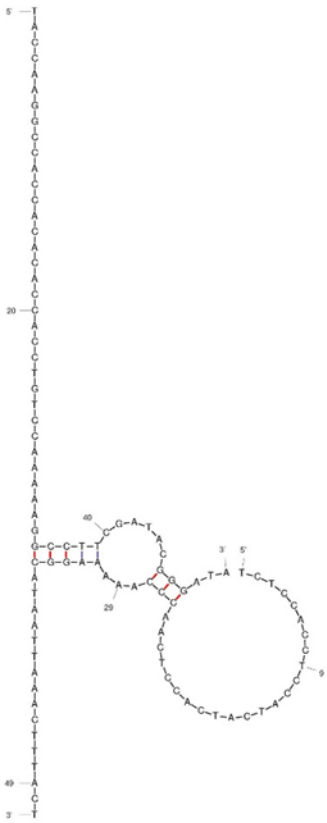

ΔG = -7.14

PD6

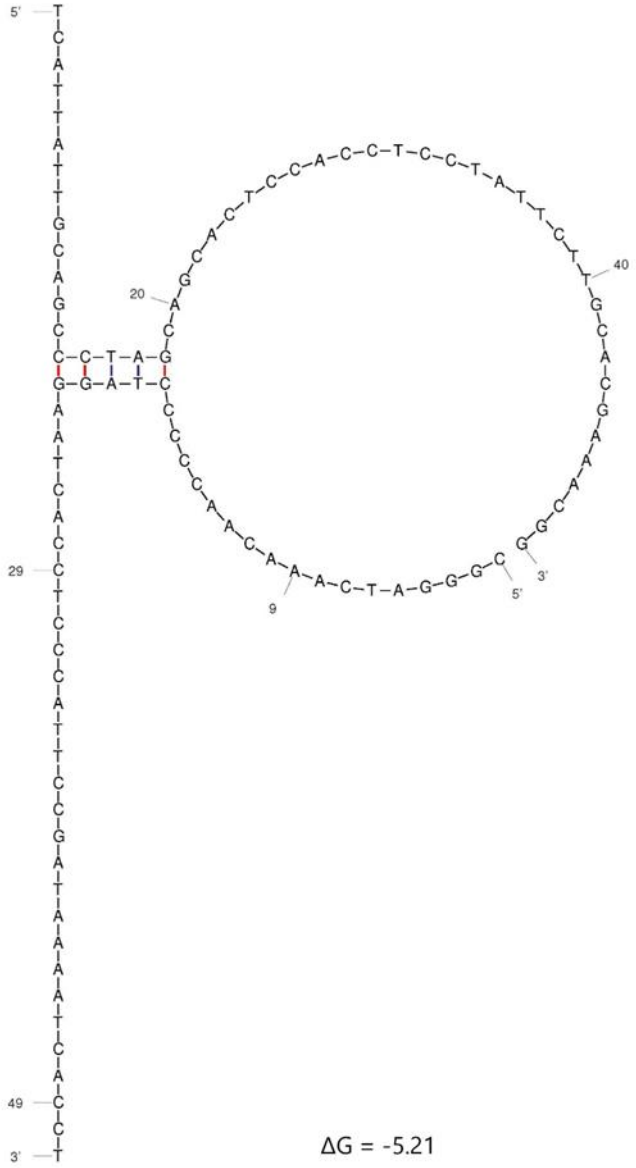

ΔG = -5.21

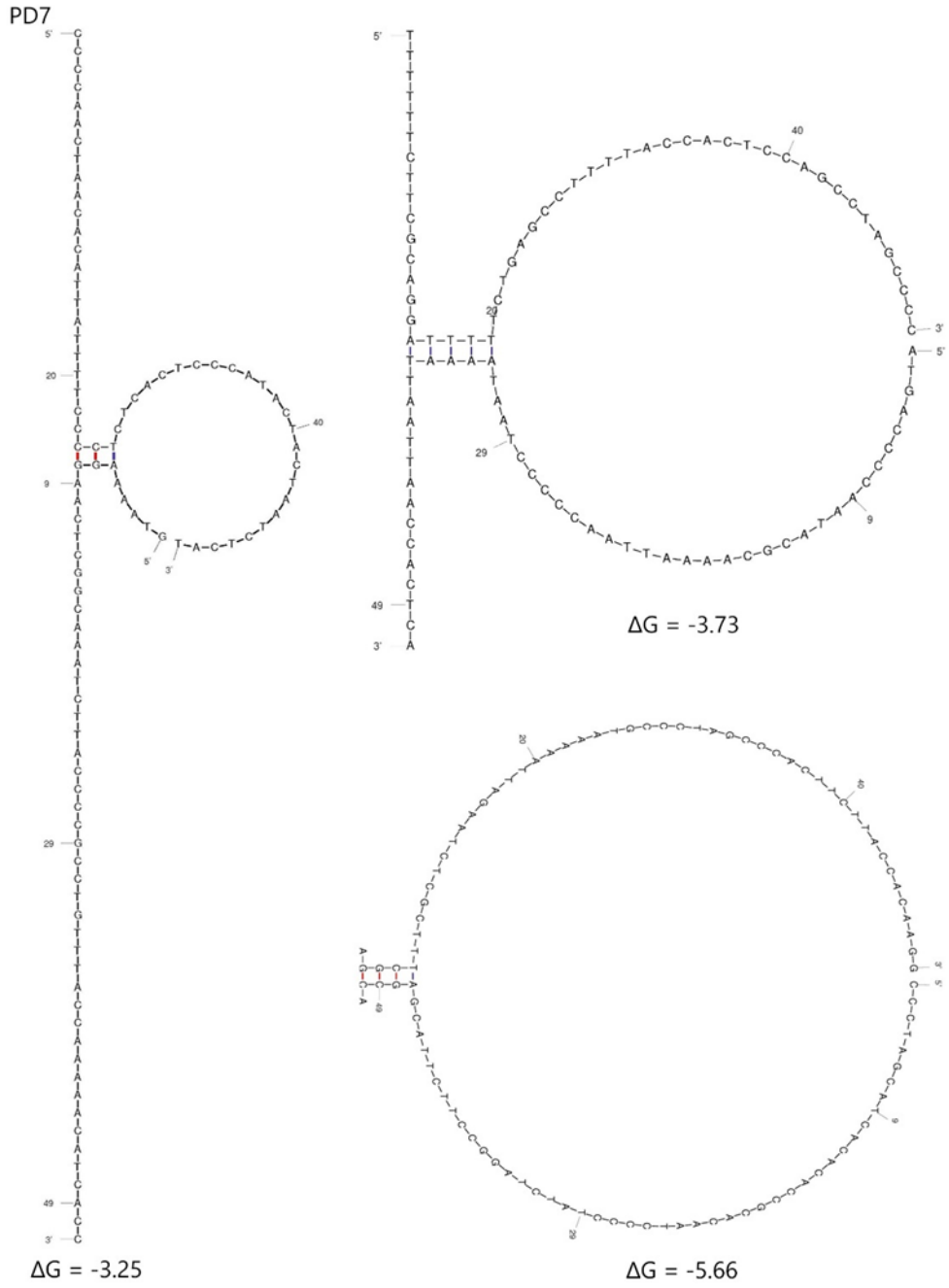

Figure 7.1-1 The secondary structures of PD cases predicted using UNAFold

The case number is labelled at the top-left corner of each page, and the predicted free energy is represented as ΔG.

Chapter 8. References

Aarsland, D. *et al.* (2021) 'Parkinson disease-associated cognitive impairment', *Nature Reviews. Disease Primers*, 7(1), p. 47. Available at: https://doi.org/10.1038/s41572-021-00280-3.

Abramov, A.Y. *et al.* (2011) 'Bioenergetic consequences of PINK1 mutations in Parkinson disease', *PloS One*, 6(10), p. e25622. Available at: https://doi.org/10.1371/journal.pone.0025622.

Akabane, S. *et al.* (2016) 'Constitutive Activation of PINK1 Protein Leads to Proteasome-mediated and Non-apoptotic Cell Death Independently of Mitochondrial Autophagy*', *Journal of Biological Chemistry*, 291(31), pp. 16162–16174. Available at: https://doi.org/10.1074/jbc.M116.714923.

Alam, T.I. *et al.* (2003) 'Human mitochondrial DNA is packaged with TFAM', *Nucleic Acids Research*, 31(6), pp. 1640–1645. Available at: https://doi.org/10.1093/nar/gkg251.

Albertini, A.M. *et al.* (1982) 'On the formation of spontaneous deletions: The importance of short sequence homologies in the generation of large deletions', *Cell*, 29(2), pp. 319–328. Available at: https://doi.org/10.1016/0092-8674(82)90148-9.

Aljasmi, F.A. *et al.* (2020) 'Genomic Landscape of the Mitochondrial Genome in the United Arab Emirates Native Population', *Genes*, 11(8), p. 876. Available at: https://doi.org/10.3390/genes11080876.

Aminuddin, A. *et al.* (2020) 'Mitochondrial DNA alterations may influence the cisplatin responsiveness of oral squamous cell carcinoma', *Scientific Reports*, 10(1), p. 7885. Available at: https://doi.org/10.1038/s41598-020-64664-3.

Anandhan, A. *et al.* (2017) 'Metabolic Disorder Dysfunction in Parkinson's Disease: Bioenergetics, Redox Homeostasis and Central Carbon Metabolism', *Brain research bulletin*, 133, pp. 12–30. Available at: https://doi.org/10.1016/j.brainresbull.2017.03.009.

Anderson, S. *et al.* (1981) 'Sequence and organization of the human mitochondrial genome', *Nature*, 290(5806), pp. 457–465. Available at: https://doi.org/10.1038/290457a0.

Andersson, S.G.E. *et al.* (1998) 'The genome sequence of Rickettsia prowazekii and the origin of mitochondria', *Nature*, 396(6707), pp. 133–140. Available at: https://doi.org/10.1038/24094.

Andersson, S.G.E. and Kurland, C.G. (1998) 'Reductive evolution of resident genomes', *Trends in Microbiology*, 6(7), pp. 263–268. Available at: https://doi.org/10.1016/S0966-842X(98)01312-2.

Aquadro, C.F. and Greenberg, B.D. (1983) 'Human mitochondrial DNA variation and evolution: analysis of nucleotide sequences from seven individuals', *Genetics*, 103(2), pp. 287–312. Available at: https://doi.org/10.1093/genetics/103.2.287.

Araiso, Y., Imai, K. and Endo, T. (2022) 'Role of the TOM Complex in Protein Import into Mitochondria: Structural Views', *Annual Review of Biochemistry*, 91(1), pp. 679–703. Available at: https://doi.org/10.1146/annurev-biochem-032620-104527.

Asghar, M. *et al.* (2022) 'Mitochondrial biogenesis, telomere length and cellular senescence in Parkinson's disease and Lewy body dementia', *Scientific Reports*, 12(1), p. 17578. Available at: https://doi.org/10.1038/s41598-022-22400-z.

Ashley, M.V., Laipis, P.J. and Hauswirth, W.W. (1989) 'Rapid segregation of heteroplasmic bovine mitochondria.', *Nucleic Acids Research*, 17(18), p. 7325. Available at: https://doi.org/10.1093/nar/17.18.7325.

Atkinson, G.C. and Baldauf, S.L. (2011) 'Evolution of elongation factor G and the origins of mitochondrial and chloroplast forms', *Molecular Biology and Evolution*, 28(3), pp. 1281–1292. Available at: https://doi.org/10.1093/molbev/msq316.

Bai, R.-K. and Wong, L.-J.C. (2005) 'Simultaneous detection and quantification of mitochondrial DNA deletion(s), depletion, and over-replication in patients with mitochondrial disease', *The Journal of molecular diagnostics: JMD*, 7(5), pp. 613–622. Available at: https://doi.org/10.1016/S1525-1578(10)60595-8.

Baldereschi, M. *et al.* (2000) 'Parkinson's disease and parkinsonism in a longitudinal study: two-fold higher incidence in men. ILSA Working Group. Italian Longitudinal Study on Aging', *Neurology*, 55(9), pp. 1358–1363. Available at: https://doi.org/10.1212/wnl.55.9.1358.

Ballinger, S.W. *et al.* (1999) 'Hydrogen peroxide causes significant mitochondrial DNA damage in human RPE cells', *Experimental Eye Research*, 68(6), pp. 765–772. Available at: https://doi.org/10.1006/exer.1998.0661.

Bandelt, H.-J., van Oven, M. and Salas, A. (2012) 'Haplogrouping mitochondrial DNA sequences in Legal Medicine/Forensic Genetics', *International Journal of Legal Medicine*, 126(6), pp. 901–916. Available at: https://doi.org/10.1007/s00414-012-0762-y.

Basu, S. *et al.* (2020) 'Accurate mapping of mitochondrial DNA deletions and duplications using deep sequencing', *Plos Genetics*, 16(12), p. e1009242. Available at: https://doi.org/10.1371/journal.pgen.1009242.

Belle, E.M.S. *et al.* (2005) 'An investigation of the variation in the transition bias among various animal mitochondrial DNA', *Gene*, 355, pp. 58–66. Available at: https://doi.org/10.1016/j.gene.2005.05.019.

Belmokhtar, C.A. *et al.* (2003) 'Apoptosome-independent pathway for apoptosis. Biochemical analysis of APAF-1 defects and biological outcomes', *The Journal of Biological Chemistry*, 278(32), pp. 29571–29580. Available at: https://doi.org/10.1074/jbc.M302924200.

Bender, A. *et al.* (2006) 'High levels of mitochondrial DNA deletions in substantia nigra neurons in aging and Parkinson disease', *Nature Genetics*, 38(5), pp. 515–517. Available at: https://doi.org/10.1038/ng1769.

Beninato, M. and Spencer, R.F. (1987) 'A cholinergic projection to the rat substantia nigra from the pedunculopontine tegmental nucleus', *Brain Research*, 412(1), pp. 169–174. Available at: https://doi.org/10.1016/0006-8993(87)91455-7.

Benjamini, Y. and Speed, T.P. (2012) 'Summarizing and correcting the GC content bias in high-throughput sequencing', *Nucleic Acids Research*, 40(10), p. e72. Available at: https://doi.org/10.1093/nar/gks001.

Berg, D. *et al.* (2015) 'MDS research criteria for prodromal Parkinson's disease', *Movement Disorders: Official Journal of the Movement Disorder Society*, 30(12), pp. 1600–1611. Available at: https://doi.org/10.1002/mds.26431.

Bergstrom, C.T. and Pritchard, J. (1998) 'Germline bottlenecks and the evolutionary maintenance of mitochondrial genomes', *Genetics*, 149(4), pp. 2135–2146. Available at: https://doi.org/10.1093/genetics/149.4.2135.

Beric, A. *et al.* (2024) 'Circulating blood circular RNA in Parkinson's Disease; from involvement in pathology to diagnostic tools in at-risk individuals', *NPJ Parkinson's disease*, 10(1), p. 222. Available at: https://doi.org/10.1038/s41531-024-00839-3.

Berrisford, J.M. and Sazanov, L.A. (2009) 'Structural Basis for the Mechanism of Respiratory Complex I', *The Journal of Biological Chemistry*, 284(43), pp. 29773–29783. Available at: https://doi.org/10.1074/jbc.M109.032144.

Berthet, A. *et al.* (2014) 'Loss of mitochondrial fission depletes axonal mitochondria in midbrain dopamine neurons', *The Journal of Neuroscience: The Official Journal of the Society for Neuroscience*, 34(43), pp. 14304–14317. Available at: https://doi.org/10.1523/JNEUROSCI.0930-14.2014.

Bezawork-Geleta, A. *et al.* (2017) 'Mitochondrial Complex II: At the Crossroads', *Trends in Biochemical Sciences*, 42(4), pp. 312–325. Available at: https://doi.org/10.1016/j.tibs.2017.01.003.

Bhatta, A. *et al.* (2021) 'Structural basis of RNA processing by human mitochondrial RNase P', *Nature Structural & Molecular Biology*, 28(9), pp. 713–723. Available at: https://doi.org/10.1038/s41594-021-00637-y.

Bilbille, Y. *et al.* (2011) 'The human mitochondrial tRNAMet: Structure/function relationship of a unique modification in the decoding of unconventional codons', *Journal of molecular biology*, 406(2), pp. 257–274. Available at: https://doi.org/10.1016/j.jmb.2010.11.042.

Birky, C.W. (1995) 'Uniparental inheritance of mitochondrial and chloroplast genes: mechanisms and evolution', *Proceedings of the National Academy of Sciences of the United States of America*, 92(25), pp. 11331–11338. Available at: https://doi.org/10.1073/pnas.92.25.11331.

Bock, F.J. and Tait, S.W.G. (2020) 'Mitochondria as multifaceted regulators of cell death', *Nature Reviews Molecular Cell Biology*, 21(2), pp. 85–100. Available at: https://doi.org/10.1038/s41580-019-0173-8.

Bofkin, L. and Goldman, N. (2007) 'Variation in Evolutionary Processes at Different Codon Positions', *Molecular Biology and Evolution*, 24(2), pp. 513–521. Available at: https://doi.org/10.1093/molbev/msl178.

Bogenhagen, D. and Clayton, D.A. (1978) 'Mechanism of mitochondrial DNA replication in mouse L-cells: introduction of superhelical turns into newly replicated molecules', *Journal of Molecular Biology*, 119(1), pp. 69–81. Available at: https://doi.org/10.1016/0022-2836(78)90270-x.

Bohnen, N.I. *et al.* (2009) 'History of falls in Parkinson disease is associated with reduced cholinergic activity', *Neurology*, 73(20), pp. 1670–1676. Available at: https://doi.org/10.1212/WNL.0b013e3181c1ded6.

Bohr, V.A. (2002) 'Repair of oxidative DNA damage in nuclear and mitochondrial DNA, and some changes with aging in mammalian cells1, 2 1Guest Editor: Miral Dizdaroglu 2This article is part of a series of reviews on "Oxidative DNA Damage and Repair." The full list of papers may be found on the homepage of the journal.', *Free Radical Biology and Medicine*, 32(9), pp. 804–812. Available at: https://doi.org/10.1016/S0891-5849(02)00787-6.

Bolam, J.P., Francis, C.M. and Henderson, Z. (1991) 'Cholinergic input to dopaminergic neurons in the substantia nigra: a double immunocytochemical study', *Neuroscience*, 41(2–3), pp. 483–494. Available at: https://doi.org/10.1016/0306-4522(91)90343-m.

Bouzidi, A. *et al.* (2020) 'First characterization of LHON pedigrees in North Africa', *Eye*, 34(11), pp. 2138–2139. Available at: https://doi.org/10.1038/s41433-019-0755-x.

Bowmaker, M. *et al.* (2003) 'Mammalian Mitochondrial DNA Replicates Bidirectionally from an Initiation Zone*', *Journal of Biological Chemistry*, 278(51), pp. 50961–50969. Available at: https://doi.org/10.1074/jbc.M308028200.

Braak, H. *et al.* (2003) 'Staging of brain pathology related to sporadic Parkinson's disease', *Neurobiology of Aging*, 24(2), pp. 197–211. Available at: https://doi.org/10.1016/S0197-4580(02)00065-9.

Bragoszewski, P. *et al.* (2008) 'Limited clinical relevance of mitochondrial DNA mutation and gene expression analyses in ovarian cancer', *BMC cancer*, 8, p. 292. Available at: https://doi.org/10.1186/1471-2407-8-292.

Brandt, U. and Trumpower, B. (1994) 'The Protonmotive Q Cycle in Mitochondria and Bacteria', *Critical Reviews in Biochemistry and Molecular Biology*, 29(3), pp. 165–197. Available at: https://doi.org/10.3109/10409239409086800.

Bridi, J.C. *et al.* (2021) 'Presynaptic accumulation of α-synuclein causes synaptopathy and progressive neurodegeneration in Drosophila', *Brain Communications*, 3(2), p. fcab049. Available at: https://doi.org/10.1093/braincomms/fcab049.

Bris, C. *et al.* (2021) 'Improved detection of mitochondrial DNA instability in mitochondrial genome maintenance disorders', *Genetics in Medicine: Official Journal of the American College of Medical Genetics*, 23(9), pp. 1769–1778. Available at: https://doi.org/10.1038/s41436-021-01206-w.

Brown, B.L. *et al.* (2018) 'Structure of the Mitochondrial Aminolevulinic Acid Synthase, a Key Heme Biosynthetic Enzyme', *Structure (London, England: 1993)*, 26(4), pp. 580-589.e4. Available at: https://doi.org/10.1016/j.str.2018.02.012.

Brown, D.T. *et al.* (2001) 'Random genetic drift determines the level of mutant mtDNA in human primary oocytes', *American Journal of Human Genetics*, 68(2), pp. 533–536. Available at: https://doi.org/10.1086/318190.

Brown, T.A. *et al.* (2005) 'Replication of mitochondrial DNA occurs by strand displacement with alternative light-strand origins, not via a strand-coupled mechanism', *Genes & Development*, 19(20), pp. 2466–2476. Available at: https://doi.org/10.1101/gad.1352105.

Bua, E. *et al.* (2006) 'Mitochondrial DNA–Deletion Mutations Accumulate Intracellularly to Detrimental Levels in Aged Human Skeletal Muscle Fibers', *The American Journal of Human Genetics*, 79(3), pp. 469–480. Available at: https://doi.org/10.1086/507132.

Budowle, B. *et al.* (2004) 'Addressing the use of phylogenetics for identification of sequences in error in the SWGDAM mitochondrial DNA database', *Journal of Forensic Sciences*, 49(6), pp. 1256–1261.

Buneeva, O. *et al.* (2020) 'Mitochondrial Dysfunction in Parkinson's Disease: Focus on Mitochondrial DNA', *Biomedicines*, 8(12), p. E591. Available at: https://doi.org/10.3390/biomedicines8120591.

Bury, A.G. *et al.* (2017) 'Mitochondrial DNA changes in pedunculopontine cholinergic neurons in Parkinson disease', *Annals of Neurology*, 82(6), pp. 1016–1021. Available at: https://doi.org/10.1002/ana.25099.

Bury, A.G. *et al.* (2021) 'The Isolation and Deep Sequencing of Mitochondrial DNA', in V. Weissig and M. Edeas (eds) *Mitochondrial Medicine: Volume 3: Manipulating Mitochondria and Disease- Specific Approaches*. New York, NY: Springer US, pp. 433–447. Available at: https://doi.org/10.1007/978-1-0716-1270-5_27.

Caggiano, V. *et al.* (2018) 'Midbrain circuits that set locomotor speed and gait selection', *Nature*, 553(7689), pp. 455–460. Available at: https://doi.org/10.1038/nature25448.

Cai, Y.C. *et al.* (2000) 'Interaction of mitochondrial elongation factor Tu with aminoacyl-tRNA and elongation factor Ts', *The Journal of Biological Chemistry*, 275(27), pp. 20308–20314. Available at: https://doi.org/10.1074/jbc.M001899200.

Calabresi, P. *et al.* (2023) 'Alpha-synuclein in Parkinson's disease and other synucleinopathies: from overt neurodegeneration back to early synaptic dysfunction', *Cell Death & Disease*, 14(3), p. 176. Available at: https://doi.org/10.1038/s41419-023-05672-9.

Capouch, S.D., Farlow, M.R. and Brosch, J.R. (2018) 'A Review of Dementia with Lewy Bodies' Impact, Diagnostic Criteria and Treatment', *Neurology and Therapy*, 7(2), pp. 249–263. Available at: https://doi.org/10.1007/s40120-018-0104-1.

Carroll, J. *et al.* (2006) 'Bovine Complex I Is a Complex of 45 Different Subunits*', *Journal of Biological Chemistry*, 281(43), pp. 32724–32727. Available at: https://doi.org/10.1074/jbc.M607135200.

Cartoni, R. *et al.* (2005) 'Mitofusins 1/2 and ERRα expression are increased in human skeletal muscle after physical exercise', *The Journal of Physiology*, 567(Pt 1), pp. 349–358. Available at: https://doi.org/10.1113/jphysiol.2005.092031.

Castellani, C.A. *et al.* (2020) 'Thinking outside the nucleus: Mitochondrial DNA copy number in health and disease', *Mitochondrion*, 53, pp. 214–223. Available at: https://doi.org/10.1016/j.mito.2020.06.004.

Chan, D.C. (2006) 'Mitochondrial fusion and fission in mammals', *Annual Review of Cell and Developmental Biology*, 22, pp. 79–99. Available at: https://doi.org/10.1146/annurev.cellbio.22.010305.104638.

Chan, N.C. *et al.* (2011) 'Broad activation of the ubiquitin-proteasome system by Parkin is critical for mitophagy', *Human Molecular Genetics*, 20(9), pp. 1726–1737. Available at: https://doi.org/10.1093/hmg/ddr048.

Chandel, N.S. (2021) 'Glycolysis', *Cold Spring Harbor Perspectives in Biology*, 13(5), p. a040535. Available at: https://doi.org/10.1101/cshperspect.a040535.

Chang, J.-C. *et al.* (2016) 'Allogeneic/xenogeneic transplantation of peptide-labeled mitochondria in Parkinson's disease: restoration of mitochondria functions and attenuation of 6-hydroxydopamine-induced neurotoxicity', *Translational Research: The Journal of Laboratory and Clinical Medicine*, 170, pp. 40-56.e3. Available at: https://doi.org/10.1016/j.trsl.2015.12.003.

Charara, A., Smith, Y. and Parent, A. (1996) 'Glutamatergic inputs from the pedunculopontine nucleus to midbrain dopaminergic neurons in primates: Phaseolus vulgaris-leucoagglutinin anterograde labeling combined with postembedding glutamate and GABA immunohistochemistry', *The Journal of Comparative Neurology*, 364(2), pp. 254–266. Available at: https://doi.org/10.1002/(SICI)1096-9861(19960108)364:2<254::AID-CNE5>3.0.CO;2-4.

Chaugule, V.K. *et al.* (2011) 'Autoregulation of Parkin activity through its ubiquitin-like domain', *The EMBO journal*, 30(14), pp. 2853–2867. Available at: https://doi.org/10.1038/emboj.2011.204.

Chen, C. *et al.* (2020) 'Investigation of mitochondrial biogenesis defects in single substantia nigra neurons using post-mortem human tissues', *Neurobiology of Disease*, 134, p. 104631. Available at: https://doi.org/10.1016/j.nbd.2019.104631.

Chen, C. *et al.* (2023) 'Parkinson's disease neurons exhibit alterations in mitochondrial quality control proteins', *npj Parkinson's Disease*, 9(1), pp. 1–14. Available at: https://doi.org/10.1038/s41531-023-00564-3.

Chen, J. *et al.* (2012) 'Unraveling the Dynamics of Ribosome Translocation', *Current opinion in structural biology*, 22(6), pp. 804–814. Available at: https://doi.org/10.1016/j.sbi.2012.09.004.

Chen, Y. and Dorn, G.W. (2013) 'PINK1-phosphorylated mitofusin 2 is a Parkin receptor for culling damaged mitochondria', *Science (New York, N.Y.)*, 340(6131), pp. 471–475. Available at: https://doi.org/10.1126/science.1231031.

Cheong, A. *et al.* (2020) 'Nuclear-encoded mitochondrial ribosomal proteins are required to initiate gastrulation', *Development (Cambridge, England)*, 147(10), p. dev188714. Available at: https://doi.org/10.1242/dev.188714.

Chinnery, P.F. *et al.* (2001) 'Leber hereditary optic neuropathy: Does heteroplasmy influence the inheritance and expression of the G11778A mitochondrial DNA mutation?', *American Journal of Medical Genetics*, 98(3), pp. 235–243. Available at: https://doi.org/10.1002/1096-8628(20010122)98:3<235::aid-ajmg1086>3.0.co;2-o.

Ciesielski, G.L., Oliveira, M.T. and Kaguni, L.S. (2016) 'Animal Mitochondrial DNA Replication', *The Enzymes*, 39, pp. 255–292. Available at: https://doi.org/10.1016/bs.enz.2016.03.006.

Cipolat, S. *et al.* (2004) 'OPA1 requires mitofusin 1 to promote mitochondrial fusion', *Proceedings of the National Academy of Sciences of the United States of America*, 101(45), pp. 15927–15932. Available at: https://doi.org/10.1073/pnas.0407043101.

Clarke, C.E. *et al.* (2016) 'Clinical effectiveness and cost-effectiveness of physiotherapy and occupational therapy versus no therapy in mild to moderate Parkinson's disease: a large pragmatic randomised controlled trial (PD REHAB)', *Health Technology Assessment (Winchester, England)*, 20(63), pp. 1–96. Available at: https://doi.org/10.3310/hta20630.

Clayton, D.A. (1982) 'Replication of animal mitochondrial DNA', *Cell*, 28(4), pp. 693–705. Available at: https://doi.org/10.1016/0092-8674(82)90049-6.

Cortes, N.G. *et al.* (2020) 'Mutation m.3395A > G in MT-ND1 leads to variable pathologic manifestations', *Human Molecular Genetics*, 29(6), pp. 980–989. Available at: https://doi.org/10.1093/hmg/ddaa020.

Coskun, P.E., Beal, M.F. and Wallace, D.C. (2004) 'Alzheimer's brains harbor somatic mtDNA control-region mutations that suppress mitochondrial transcription and replication', *Proceedings of the National Academy of Sciences of the United States of America*, 101(29), pp. 10726–10731. Available at: https://doi.org/10.1073/pnas.0403649101.

Coxhead, J. *et al.* (2016) 'Somatic mtDNA variation is an important component of Parkinson's disease', *Neurobiology of Aging*, 38, p. 217.e1-217.e6. Available at: https://doi.org/10.1016/j.neurobiolaging.2015.10.036.

Dagan, T., Talmor, Y. and Graur, D. (2002) 'Ratios of radical to conservative amino acid replacement are affected by mutational and compositional factors and may not be indicative of positive Darwinian selection', *Molecular Biology and Evolution*, 19(7), pp. 1022–1025. Available at: https://doi.org/10.1093/oxfordjournals.molbev.a004161.

Damas, J., Carneiro, J., *et al.* (2014) 'MitoBreak: the mitochondrial DNA breakpoints database', *Nucleic Acids Research*, 42(Database issue), pp. D1261–D1268. Available at: https://doi.org/10.1093/nar/gkt982.

Damas, J., Samuels, D.C., *et al.* (2014) 'Mitochondrial DNA Rearrangements in Health and Disease—A Comprehensive Study', *Human Mutation*, 35(1), pp. 1–14. Available at: https://doi.org/10.1002/humu.22452.

Davis, C.O. *et al.* (2014) 'Transcellular degradation of axonal mitochondria', *Proceedings of the National Academy of Sciences of the United States of America*, 111(26), pp. 9633–9638. Available at: https://doi.org/10.1073/pnas.1404651111.

Dayal, V. *et al.* (2021) 'Pedunculopontine Nucleus Deep Brain Stimulation for Parkinsonian Disorders: A Case Series', *Stereotactic and Functional Neurosurgery*, 99(4), pp. 287–294. Available at: https://doi.org/10.1159/000511978.

De Bont, R. and van Larebeke, N. (2004) 'Endogenous DNA damage in humans: a review of quantitative data', *Mutagenesis*, 19(3), pp. 169–185. Available at: https://doi.org/10.1093/mutage/geh025.

Degoul, F. *et al.* (1991) 'Different mechanisms inferred from sequences of human mitochondrial DNA deletions in ocular myopathies.', *Nucleic Acids Research*, 19(3), pp. 493–496.

Del Bo, R. *et al.* (2002) 'Evidence and age-related distribution of mtDNA D-loop point mutations in skeletal muscle from healthy subjects and mitochondrial patients', *Journal of the Neurological Sciences*, 202(1–2), pp. 85–91. Available at: https://doi.org/10.1016/s0022-510x(02)00247-2.

Del Dotto, V. *et al.* (2018) 'Eight human OPA1 isoforms, long and short: What are they for?', *Biochimica et Biophysica Acta (BBA) - Bioenergetics*, 1859(4), pp. 263–269. Available at: https://doi.org/10.1016/j.bbabio.2018.01.005.

Di Nottia, M. *et al.* (2021) 'Mitochondrial Dynamics: Molecular Mechanisms, Related Primary Mitochondrial Disorders and Therapeutic Approaches', *Genes*, 12(2), p. 247. Available at: https://doi.org/10.3390/genes12020247.

Ding, J. *et al.* (2015) 'Assessing Mitochondrial DNA Variation and Copy Number in Lymphocytes of ~2,000 Sardinians Using Tailored Sequencing Analysis Tools', *PLoS genetics*, 11(7), p. e1005306. Available at: https://doi.org/10.1371/journal.pgen.1005306.

Disease, M.D.S.T.F. on R.S. for P. (2003) 'The Unified Parkinson's Disease Rating Scale (UPDRS): Status and recommendations', *Movement Disorders*, 18(7), pp. 738–750. Available at: https://doi.org/10.1002/mds.10473.

Doimo, M. *et al.* (2023) 'Enhanced mitochondrial G-quadruplex formation impedes replication fork progression leading to mtDNA loss in human cells', *Nucleic Acids Research*, 51(14), pp. 7392–7408. Available at: https://doi.org/10.1093/nar/gkad535.

Dölle, C. *et al.* (2016) 'Defective mitochondrial DNA homeostasis in the substantia nigra in Parkinson disease', *Nature Communications*, 7. Available at: https://doi.org/10.1038/ncomms13548.

Dong, D.W. *et al.* (2014) 'Association of G-quadruplex forming sequences with human mtDNA deletion breakpoints', *BMC Genomics*, 15(1), p. 677. Available at: https://doi.org/10.1186/1471-2164-15-677.

Du, F. *et al.* (2017) 'PINK1 signalling rescues amyloid pathology and mitochondrial dysfunction in Alzheimer's disease', *Brain*, 140(12), pp. 3233–3251. Available at: https://doi.org/10.1093/brain/awx258.

Duda, J., Pötschke, C. and Liss, B. (2016) 'Converging roles of ion channels, calcium, metabolic stress, and activity pattern of Substantia nigra dopaminergic neurons in health and Parkinson's disease', *Journal of Neurochemistry*, 139 Suppl 1(Suppl Suppl 1), pp. 156–178. Available at: https://doi.org/10.1111/jnc.13572.

Durrenberger, P.F. *et al.* (2012) 'Selection of novel reference genes for use in the human central nervous system: a BrainNet Europe Study', *Acta Neuropathologica*, 124(6), pp. 893–903. Available at: https://doi.org/10.1007/s00401-012-1027-z.

Elson, J.L. *et al.* (2001) 'Random Intracellular Drift Explains the Clonal Expansion of Mitochondrial DNA Mutations with Age', *The American Journal of Human Genetics*, 68(3), pp. 802–806. Available at: https://doi.org/10.1086/318801.

Embley, T.M. and Martin, W. (2006) 'Eukaryotic evolution, changes and challenges', *Nature*, 440(7084), pp. 623–630. Available at: https://doi.org/10.1038/nature04546.

Esser, C. *et al.* (2004) 'A Genome Phylogeny for Mitochondria Among α-Proteobacteria and a Predominantly Eubacterial Ancestry of Yeast Nuclear Genes', *Molecular Biology and Evolution*, 21(9), pp. 1643–1660. Available at: https://doi.org/10.1093/molbev/msh160.

Esteves, A.R.F. *et al.* (2008) 'Mitochondrial function in Parkinson's disease cybrids containing an nt2 neuron-like nuclear background', *Mitochondrion*, 8(3), pp. 219–228. Available at: https://doi.org/10.1016/j.mito.2008.03.004.

Faget, L. *et al.* (2016) 'Afferent Inputs to Neurotransmitter-Defined Cell Types in the Ventral Tegmental Area', *Cell Reports*, 15(12), pp. 2796–2808. Available at: https://doi.org/10.1016/j.celrep.2016.05.057.

Falkenberg, M. *et al.* (2002) 'Mitochondrial transcription factors B1 and B2 activate transcription of human mtDNA', *Nature Genetics*, 31(3), pp. 289–294. Available at: https://doi.org/10.1038/ng909.

Fearnley, J.M. and Lees, A.J. (1991) 'Ageing and Parkinson's disease: substantia nigra regional selectivity', *Brain: A Journal of Neurology*, 114 (Pt 5), pp. 2283–2301. Available at: https://doi.org/10.1093/brain/114.5.2283.

Ferraye, M.U. *et al.* (2010) 'Effects of pedunculopontine nucleus area stimulation on gait disorders in Parkinson's disease', *Brain: A Journal of Neurology*, 133(Pt 1), pp. 205–214. Available at: https://doi.org/10.1093/brain/awp229.

Filograna, R. *et al.* (2021) 'Mitochondrial DNA copy number in human disease: the more the better?', *FEBS Letters*, 595(8), pp. 976–1002. Available at: https://doi.org/10.1002/1873-3468.14021.

Finck, B.N. and Kelly, D.P. (2006) 'PGC-1 coactivators: inducible regulators of energy metabolism in health and disease', *The Journal of Clinical Investigation*, 116(3), pp. 615–622. Available at: https://doi.org/10.1172/JCI27794.

Fontana, G.A. and Gahlon, H.L. (2020) 'Mechanisms of replication and repair in mitochondrial DNA deletion formation', *Nucleic Acids Research*, 48(20), pp. 11244–11258. Available at: https://doi.org/10.1093/nar/gkaa804.

Frank, C., Pari, G. and Rossiter, J.P. (2006) 'Approach to diagnosis of Parkinson disease', *Canadian Family Physician*, 52(7), pp. 862–868.

French, I.T. and Muthusamy, K.A. (2018) 'A Review of the Pedunculopontine Nucleus in Parkinson's Disease', *Frontiers in Aging Neuroscience*, 10. Available at: https://doi.org/10.3389/fnagi.2018.00099.

Friedrich, T. *et al.* (1993) 'Attempts to define distinct parts of NADH:ubiquinone oxidoreductase (complex I)', *Journal of Bioenergetics and Biomembranes*, 25(4), pp. 331–337. Available at: https://doi.org/10.1007/BF00762458.

Fromme, J.C. *et al.* (2004) 'Structural basis for removal of adenine mispaired with 8-oxoguanine by MutY adenine DNA glycosylase', *Nature*, 427(6975), pp. 652–656. Available at: https://doi.org/10.1038/nature02306.

Fuhrmann, D.C., Wittig, I. and Brüne, B. (2019) 'TMEM126B deficiency reduces mitochondrial SDH oxidation by LPS, attenuating HIF-1α stabilization and IL-1β expression', *Redox Biology*, 20, pp. 204–216. Available at: https://doi.org/10.1016/j.redox.2018.10.007.

Fusté, J.M. *et al.* (2010) 'Mitochondrial RNA Polymerase Is Needed for Activation of the Origin of Light-Strand DNA Replication', *Molecular Cell*, 37(1), pp. 67–78. Available at: https://doi.org/10.1016/j.molcel.2009.12.021.

Futami, T., Takakusaki, K. and Kitai, S.T. (1995) 'Glutamatergic and cholinergic inputs from the pedunculopontine tegmental nucleus to dopamine neurons in the substantia nigra pars compacta', *Neuroscience Research*, 21(4), pp. 331–342. Available at: https://doi.org/10.1016/0168-0102(94)00869-h.

Gajda, R. *et al.* (2021) 'To Be a Champion of the 24-h Ultramarathon Race. If Not the Heart … Mosaic Theory?', *International Journal of Environmental Research and Public Health*, 18(5), p. 2371. Available at: https://doi.org/10.3390/ijerph18052371.

Galtieri, D.J. *et al.* (2017) 'Pedunculopontine glutamatergic neurons control spike patterning in substantia nigra dopaminergic neurons', *eLife*, 6, p. e30352. Available at: https://doi.org/10.7554/eLife.30352.

Gaweda-Walerych, K. *et al.* (2008) 'Mitochondrial DNA haplogroups and subhaplogroups are associated with Parkinson's disease risk in a Polish PD cohort', *Journal of Neural Transmission (Vienna, Austria: 1996)*, 115(11), pp. 1521–1526. Available at: https://doi.org/10.1007/s00702-008-0121-9.

Ge, P., Dawson, V.L. and Dawson, T.M. (2020) 'PINK1 and Parkin mitochondrial quality control: a source of regional vulnerability in Parkinson's disease', *Molecular Neurodegeneration*, 15(1), p. 20. Available at: https://doi.org/10.1186/s13024-020-00367-7.

Geisler, S. *et al.* (2010) 'PINK1/Parkin-mediated mitophagy is dependent on VDAC1 and p62/SQSTM1', *Nature Cell Biology*, 12(2), pp. 119–131. Available at: https://doi.org/10.1038/ncb2012.

Ghezzi, D. *et al.* (2009) 'SDHAF1, encoding a LYR complex-II specific assembly factor, is mutated in SDH-defective infantile leukoencephalopathy', *Nature Genetics*, 41(6), pp. 654–656. Available at: https://doi.org/10.1038/ng.378.

Ghivizzani, S.C. *et al.* (1994) 'In organello footprint analysis of human mitochondrial DNA: human mitochondrial transcription factor A interactions at the origin of replication', *Molecular and Cellular Biology*, 14(12), pp. 7717–7730. Available at: https://doi.org/10.1128/mcb.14.12.7717-7730.1994.

Ghosh, S.S. *et al.* (1999) 'Use of cytoplasmic hybrid cell lines for elucidating the role of mitochondrial dysfunction in Alzheimer's disease and Parkinson's disease', *Annals of the New York Academy of Sciences*, 893, pp. 176–191. Available at: https://doi.org/10.1111/j.1749-6632.1999.tb07825.x.

Giles, R.E. *et al.* (1980) 'Maternal inheritance of human mitochondrial DNA', *Proceedings of the National Academy of Sciences of the United States of America*, 77(11), pp. 6715–6719. Available at: https://doi.org/10.1073/pnas.77.11.6715.

Gilkerson, R.W. *et al.* (2012) 'Mitochondrial autophagy in cells with mtDNA mutations results from synergistic loss of transmembrane potential and mTORC1 inhibition', *Human Molecular Genetics*, 21(5), pp. 978–990. Available at: https://doi.org/10.1093/hmg/ddr529.

Giorgi, C., Marchi, S. and Pinton, P. (2018) 'The machineries, regulation and cellular functions of mitochondrial calcium', *Nature Reviews Molecular Cell Biology*, 19(11), pp. 713–730. Available at: https://doi.org/10.1038/s41580-018-0052-8.

Gleyzer, N., Vercauteren, K. and Scarpulla, R.C. (2005) 'Control of mitochondrial transcription specificity factors (TFB1M and TFB2M) by nuclear respiratory factors (NRF-1 and NRF-2) and PGC-1 family coactivators', *Molecular and Cellular Biology*, 25(4), pp. 1354–1366. Available at: https://doi.org/10.1128/MCB.25.4.1354-1366.2005.

Gnaiger, E. (2023) ‘Complex II ambiguities—FADH2 in the electron transfer system’, *The Journal of Biological Chemistry*, 300(1), p. 105470. Available at: https://doi.org/10.1016/j.jbc.2023.105470.

Goard, C.A. and Schimmer, A.D. (2014) ‘Mitochondrial matrix proteases as novel therapeutic targets in malignancy’, *Oncogene*, 33(21), pp. 2690–2699. Available at: https://doi.org/10.1038/onc.2013.228.

Godschalk, R. *et al.* (2018) ‘Paternal Exposure to Environmental Chemical Stress Affects Male Offspring’s Hepatic Mitochondria’, *Toxicological Sciences: An Official Journal of the Society of Toxicology*, 162(1), pp. 241–250. Available at: https://doi.org/10.1093/toxsci/kfx246.

Goetz, C.G. *et al.* (2008) ‘Movement Disorder Society-sponsored revision of the Unified Parkinson’s Disease Rating Scale (MDS-UPDRS): Scale presentation and clinimetric testing results’, *Movement Disorders*, 23(15), pp. 2129–2170. Available at: https://doi.org/10.1002/mds.22340.

Goldstein, A. and Falk, M.J. (1993) ‘Single Large-Scale Mitochondrial DNA Deletion Syndromes’, in M.P. Adam et al. (eds) *GeneReviews®*. Seattle (WA): University of Washington, Seattle. Available at: http://www.ncbi.nlm.nih.gov/books/NBK1203/ (Accessed: 18 December 2024).

González-Rodríguez, P. *et al.* (2021) ‘Disruption of mitochondrial complex I induces progressive parkinsonism’, *Nature*, 599(7886), pp. 650–656. Available at: https://doi.org/10.1038/s41586-021-04059-0.

Goto, Y., Nonaka, I. and Horai, S. (1990) ‘A mutation in the tRNA(Leu)(UUR) gene associated with the MELAS subgroup of mitochondrial encephalomyopathies’, *Nature*, 348(6302), pp. 651–653. Available at: https://doi.org/10.1038/348651a0.

Goudenège, D. *et al.* (2019) ‘eKLIPse: a sensitive tool for the detection and quantification of mitochondrial DNA deletions from next-generation sequencing data’, *Genetics in Medicine*, 21(6), pp. 1407–1416. Available at: https://doi.org/10.1038/s41436-018-0350-8.

Greaves, L.C. *et al.* (2009) ‘Quantification of mitochondrial DNA mutation load’, *Aging Cell*, 8(5), pp. 566–572. Available at: https://doi.org/10.1111/j.1474-9726.2009.00505.x.

Greaves, L.C. *et al.* (2010) ‘Defects in multiple complexes of the respiratory chain are present in ageing human colonic crypts’, *Experimental Gerontology*, 45(7–8), pp. 573–579. Available at: https://doi.org/10.1016/j.exger.2010.01.013.

Greaves, L.C. *et al.* (2014) ‘Clonal Expansion of Early to Mid-Life Mitochondrial DNA Point Mutations Drives Mitochondrial Dysfunction during Human Ageing’, *PLOS Genetics*, 10(9), p. e1004620. Available at: https://doi.org/10.1371/journal.pgen.1004620.

Grünewald, A. *et al.* (2016) ‘Mitochondrial DNA Depletion in Respiratory Chain-Deficient Parkinson Disease Neurons’, *Annals of Neurology*, 79(3), pp. 366–378. Available at: https://doi.org/10.1002/ana.24571.

Guitton, R. *et al.* (2022) 'Ultra-deep whole genome bisulfite sequencing reveals a single methylation hotspot in human brain mitochondrial DNA', *Epigenetics*, 17(8), pp. 906–921. Available at: https://doi.org/10.1080/15592294.2022.2045754.

Gunawardana, Y. and Niranjan, M. (2013) 'Bridging the gap between transcriptome and proteome measurements identifies post-translationally regulated genes', *Bioinformatics*, 29(23), pp. 3060–3066. Available at: https://doi.org/10.1093/bioinformatics/btt537.

Gureev, A.P., Shaforostova, E.A. and Popov, V.N. (2019) 'Regulation of Mitochondrial Biogenesis as a Way for Active Longevity: Interaction Between the Nrf2 and PGC-1α Signaling Pathways', *Frontiers in Genetics*, 10. Available at: https://www.frontiersin.org/article/10.3389/fgene.2019.00435 (Accessed: 10 June 2022).

Guydosh, N.R. and Green, R. (2017) 'Translation of poly(A) tails leads to precise mRNA cleavage', *RNA (New York, N.Y.)*, 23(5), pp. 749–761. Available at: https://doi.org/10.1261/rna.060418.116.

Habbane, M. *et al.* (2021) 'Human Mitochondrial DNA: Particularities and Diseases', *Biomedicines*, 9(10), p. 1364. Available at: https://doi.org/10.3390/biomedicines9101364.

Haber, J.E. (2000) 'Partners and pathways: repairing a double-strand break', *Trends in Genetics*, 16(6), pp. 259–264. Available at: https://doi.org/10.1016/S0168-9525(00)02022-9.

Halling, J.F. and Pilegaard, H. (2020) 'PGC-1α-mediated regulation of mitochondrial function and physiological implications', *Applied Physiology, Nutrition, and Metabolism = Physiologie Appliquee, Nutrition Et Metabolisme*, 45(9), pp. 927–936. Available at: https://doi.org/10.1139/apnm-2020-0005.

Hamani, C. *et al.* (2016) 'Pedunculopontine Nucleus Region Deep Brain Stimulation in Parkinson Disease: Surgical Anatomy and Terminology', *Stereotactic and Functional Neurosurgery*, 94(5), pp. 298–306. Available at: https://doi.org/10.1159/000449010.

Hamza, I. and Dailey, H.A. (2012) 'One ring to rule them all: trafficking of heme and heme synthesis intermediates in the metazoans', *Biochimica Et Biophysica Acta*, 1823(9), pp. 1617–1632. Available at: https://doi.org/10.1016/j.bbamcr.2012.04.009.

Handschin, C. and Spiegelman, B.M. (2006) 'Peroxisome Proliferator-Activated Receptor γ Coactivator 1 Coactivators, Energy Homeostasis, and Metabolism', *Endocrine Reviews*, 27(7), pp. 728–735. Available at: https://doi.org/10.1210/er.2006-0037.

Haque, Md.E., Grasso, D. and Spremulli, L.L. (2008) 'The interaction of mammalian mitochondrial translational initiation factor 3 with ribosomes: evolution of terminal extensions in IF3mt', *Nucleic Acids Research*, 36(2), pp. 589–597. Available at: https://doi.org/10.1093/nar/gkm1072.

Hardman, C.D. *et al.* (2002) 'Comparison of the basal ganglia in rats, marmosets, macaques, baboons, and humans: volume and neuronal number for the output, internal

relay, and striatal modulating nuclei', *The Journal of Comparative Neurology*, 445(3), pp. 238–255. Available at: https://doi.org/10.1002/cne.10165.

Harman, D. (1956) 'Aging: a theory based on free radical and radiation chemistry', *Journal of Gerontology*, 11(3), pp. 298–300. Available at: https://doi.org/10.1093/geronj/11.3.298.

Hasan, A. *et al.* (2014) 'Systematic Analysis of the Role of RNA-Binding Proteins in the Regulation of RNA Stability', *PLoS Genetics*, 10(11), p. e1004684. Available at: https://doi.org/10.1371/journal.pgen.1004684.

Hatefi, Y., Haavik, A.G. and Griffiths, D.E. (1962) 'Studies on the Electron Transfer System: XL. PREPARATION AND PROPERTIES OF MITOCHONDRIAL DPNH-COENZYME Q REDUCTASE', *Journal of Biological Chemistry*, 237(5), pp. 1676–1680. Available at: https://doi.org/10.1016/S0021-9258(19)83761-4.

Hayakawa, K. *et al.* (2016) 'Transfer of mitochondria from astrocytes to neurons after stroke', *Nature*, 535(7613), pp. 551–555. Available at: https://doi.org/10.1038/nature18928.

He, L. *et al.* (2002) 'Detection and quantification of mitochondrial DNA deletions in individual cells by real-time PCR', *Nucleic Acids Research*, 30(14), p. e68. Available at: https://doi.org/10.1093/nar/gnf067.

Heide, H. *et al.* (2012) 'Complexome profiling identifies TMEM126B as a component of the mitochondrial complex i assembly complex', *Cell Metabolism*, 16(4), pp. 538–549. Available at: https://doi.org/10.1016/j.cmet.2012.08.009.

Henchcliffe, C. and Beal, M.F. (2008) 'Mitochondrial biology and oxidative stress in Parkinson disease pathogenesis', *Nature Clinical Practice. Neurology*, 4(11), pp. 600–609. Available at: https://doi.org/10.1038/ncpneuro0924.

Henrich, M.T. *et al.* (2023) 'Mitochondrial dysfunction in Parkinson's disease – a key disease hallmark with therapeutic potential', *Molecular Neurodegeneration*, 18(1), p. 83. Available at: https://doi.org/10.1186/s13024-023-00676-7.

Heo, G. *et al.* (2022) 'Rotenone causes mitochondrial dysfunction and prevents maturation in porcine oocytes', *PloS One*, 17(11), p. e0277477. Available at: https://doi.org/10.1371/journal.pone.0277477.

Heo, J.-M. *et al.* (2015) 'The PINK1-PARKIN Mitochondrial Ubiquitylation Pathway Drives a Program of OPTN/NDP52 Recruitment and TBK1 Activation to Promote Mitophagy', *Molecular Cell*, 60(1), pp. 7–20. Available at: https://doi.org/10.1016/j.molcel.2015.08.016.

Herbst, A. *et al.* (2020) 'Mitochondrial DNA deletion mutations increase exponentially with age in human skeletal muscle', *Aging Clinical and Experimental Research* [Preprint]. Available at: https://doi.org/10.1007/s40520-020-01698-7.

Heyn, J., Heuschkel, M.A. and Goettsch, C. (2023) 'Mitochondrial-Derived Vesicles—Link to Extracellular Vesicles and Implications in Cardiovascular Disease', *International*

Journal of Molecular Sciences, 24(3), p. 2637. Available at: https://doi.org/10.3390/ijms24032637.

Hirsch, E.C. *et al.* (1987) 'Neuronal loss in the pedunculopontine tegmental nucleus in Parkinson disease and in progressive supranuclear palsy', *Proceedings of the National Academy of Sciences*, 84(16), pp. 5976–5980. Available at: https://doi.org/10.1073/pnas.84.16.5976.

Hjelm, B.E. *et al.* (2019) 'Splice-Break: exploiting an RNA-seq splice junction algorithm to discover mitochondrial DNA deletion breakpoints and analyses of psychiatric disorders', *Nucleic Acids Research*, 47(10), p. e59. Available at: https://doi.org/10.1093/nar/gkz164.

Hjelm, B.E. *et al.* (2023) 'Large Common Mitochondrial DNA Deletions Are Associated with a Mitochondrial SNP T14798C Near the 3' Breakpoints', *Complex Psychiatry*, 8(3–4), pp. 90–98. Available at: https://doi.org/10.1159/000528051.

Hockenbery, D. *et al.* (1990) 'Bcl-2 is an inner mitochondrial membrane protein that blocks programmed cell death', *Nature*, 348(6299), pp. 334–336. Available at: https://doi.org/10.1038/348334a0.

Hoehn, M.M. and Yahr, M.D. (1998) 'Parkinsonism', *Neurology*, 50(2), pp. 318–318. Available at: https://doi.org/10.1212/WNL.50.2.318.

Höglinger, G.U. *et al.* (2024) 'A biological classification of Parkinson's disease: the SynNeurGe research diagnostic criteria', *The Lancet. Neurology*, 23(2), pp. 191–204. Available at: https://doi.org/10.1016/S1474-4422(23)00404-0.

Holt, I.J., Harding, A.E. and Morgan-Hughes, J.A. (1988) 'Deletions of muscle mitochondrial DNA in patients with mitochondrial myopathies', *Nature*, 331(6158), pp. 717–719. Available at: https://doi.org/10.1038/331717a0.

Holt, I.J., Lorimer, H.E. and Jacobs, H.T. (2000) 'Coupled Leading- and Lagging-Strand Synthesis of Mammalian Mitochondrial DNA', *Cell*, 100(5), pp. 515–524. Available at: https://doi.org/10.1016/S0092-8674(00)80688-1.

Holt, I.J. and Reyes, A. (2012) 'Human Mitochondrial DNA Replication', *Cold Spring Harbor Perspectives in Biology*, 4(12), p. a012971. Available at: https://doi.org/10.1101/cshperspect.a012971.

Honda, T. and Semba, K. (1995) 'An ultrastructural study of cholinergic and non-cholinergic neurons in the laterodorsal and pedunculopontine tegmental nuclei in the rat', *Neuroscience*, 68(3), pp. 837–853. Available at: https://doi.org/10.1016/0306-4522(95)00177-k.

Houten, S.M. *et al.* (2016) 'The Biochemistry and Physiology of Mitochondrial Fatty Acid β-Oxidation and Its Genetic Disorders', *Annual Review of Physiology*, 78(1), pp. 23–44. Available at: https://doi.org/10.1146/annurev-physiol-021115-105045.

Howell, N. *et al.* (2000) 'Transmission of the human mitochondrial genome', *Human Reproduction (Oxford, England)*, 15 Suppl 2, pp. 235–245. Available at: https://doi.org/10.1093/humrep/15.suppl_2.235.

Hsieh, C.-H. *et al.* (2016) 'Functional Impairment in Miro Degradation and Mitophagy Is a Shared Feature in Familial and Sporadic Parkinson's Disease', *Cell Stem Cell*, 19(6), pp. 709–724. Available at: https://doi.org/10.1016/j.stem.2016.08.002.

Hsieh, C.-H. *et al.* (2019) 'Miro1 Marks Parkinson's Disease Subset and Miro1 Reducer Rescues Neuron Loss in Parkinson's Models', *Cell Metabolism*, 30(6), pp. 1131-1140.e7. Available at: https://doi.org/10.1016/j.cmet.2019.08.023.

Hsu, Y.T., Wolter, K.G. and Youle, R.J. (1997) 'Cytosol-to-membrane redistribution of Bax and Bcl-X(L) during apoptosis', *Proceedings of the National Academy of Sciences of the United States of America*, 94(8), pp. 3668–3672. Available at: https://doi.org/10.1073/pnas.94.8.3668.

Hudson, G. *et al.* (2013) 'Two-stage association study and meta-analysis of mitochondrial DNA variants in Parkinson disease', *Neurology*, 80(22), pp. 2042–2048. Available at: https://doi.org/10.1212/WNL.0b013e318294b434.

Hulgan, T. *et al.* (2011) 'European mitochondrial DNA haplogroups and metabolic changes during antiretroviral therapy in AIDS Clinical Trials Group Study A5142', *AIDS (London, England)*, 25(1), pp. 37–47. Available at: https://doi.org/10.1097/QAD.0b013e32833f9d02.

Ibarretxe-Bilbao, N. *et al.* (2010) 'Olfactory impairment in Parkinson's disease and white matter abnormalities in central olfactory areas: A voxel-based diffusion tensor imaging study', *Movement Disorders: Official Journal of the Movement Disorder Society*, 25(12), pp. 1888–1894. Available at: https://doi.org/10.1002/mds.23208.

Ichinohe, N., Teng, B. and Kitai, S.T. (2000) 'Morphological study of the tegmental pedunculopontine nucleus, substantia nigra and subthalamic nucleus, and their interconnections in rat organotypic culture', *Anatomy and Embryology*, 201(6), pp. 435–453. Available at: https://doi.org/10.1007/s004290050331.

Inagaki, Y. *et al.* (1998) 'Directionally evolving genetic code: the UGA codon from stop to tryptophan in mitochondria', *Journal of Molecular Evolution*, 47(4), pp. 378–384. Available at: https://doi.org/10.1007/pl00006395.

Ishihara, N., Eura, Y. and Mihara, K. (2004) 'Mitofusin 1 and 2 play distinct roles in mitochondrial fusion reactions via GTPase activity', *Journal of Cell Science*, 117(Pt 26), pp. 6535–6546. Available at: https://doi.org/10.1242/jcs.01565.

Jankovic, J. (2008) 'Parkinson's disease: clinical features and diagnosis', *Journal of Neurology, Neurosurgery & Psychiatry*, 79(4), pp. 368–376. Available at: https://doi.org/10.1136/jnnp.2007.131045.

Ji, W.-K. *et al.* (2017) 'Receptor-mediated Drp1 oligomerization on endoplasmic reticulum', *The Journal of Cell Biology*, 216(12), pp. 4123–4139. Available at: https://doi.org/10.1083/jcb.201610057.

Jiang, H. *et al.* (2016) 'Adult Conditional Knockout of PGC-1α Leads to Loss of Dopamine Neurons', *eNeuro*, 3(4), p. ENEURO.0183. Available at: https://doi.org/10.1523/ENEURO.0183-16.2016.

Jiao, L. *et al.* (2022) 'Role of Mitophagy in neurodegenerative Diseases and potential tagarts for Therapy', *Molecular Biology Reports*, 49(11), pp. 10749–10760. Available at: https://doi.org/10.1007/s11033-022-07738-x.

Jõers, P. and Jacobs, H.T. (2013) 'Analysis of replication intermediates indicates that Drosophila melanogaster mitochondrial DNA replicates by a strand-coupled theta mechanism', *PloS One*, 8(1), p. e53249. Available at: https://doi.org/10.1371/journal.pone.0053249.

Johnson, K.A. *et al.* (2006) 'The closed structure of presequence protease PreP forms a unique 10,000 Angstroms3 chamber for proteolysis', *The EMBO journal*, 25(9), pp. 1977–1986. Available at: https://doi.org/10.1038/sj.emboj.7601080.

Johnson, M.A., Bindoff, L.A. and Turnbull, D.M. (1993) 'Cytochrome c oxidase activity in single muscle fibers: Assay techniques and diagnostic applications', *Annals of Neurology*, 33(1), pp. 28–35. Available at: https://doi.org/10.1002/ana.410330106.

Jonckheere, A.I., Smeitink, J.A.M. and Rodenburg, R.J.T. (2012) 'Mitochondrial ATP synthase: architecture, function and pathology', *Journal of Inherited Metabolic Disease*, 35(2), pp. 211–225. Available at: https://doi.org/10.1007/s10545-011-9382-9.

Jong, C.J. *et al.* (2019) 'Leptin-induced cardiomyocyte hypertrophy is associated with enhanced mitochondrial fission', *Molecular and Cellular Biochemistry*, 454(1–2), pp. 33–44. Available at: https://doi.org/10.1007/s11010-018-3450-5.

Just, R.S., Irwin, J.A. and Parson, W. (2015) 'Mitochondrial DNA heteroplasmy in the emerging field of massively parallel sequencing', *Forensic Science International. Genetics*, 18, pp. 131–139. Available at: https://doi.org/10.1016/j.fsigen.2015.05.003.

Kadenbach, B. *et al.* (2010) 'New extension of the Mitchell Theory for oxidative phosphorylation in mitochondria of living organisms', *Biochimica Et Biophysica Acta*, 1800(3), pp. 205–212. Available at: https://doi.org/10.1016/j.bbagen.2009.04.019.

Kadenbach, B. (2021) 'Complex IV - The regulatory center of mitochondrial oxidative phosphorylation', *Mitochondrion*, 58, pp. 296–302. Available at: https://doi.org/10.1016/j.mito.2020.10.004.

Kamerkar, S.C. *et al.* (2018) 'Dynamin-related protein 1 has membrane constricting and severing abilities sufficient for mitochondrial and peroxisomal fission', *Nature Communications*, 9(1), p. 5239. Available at: https://doi.org/10.1038/s41467-018-07543-w.

Kang, I., Chu, C.T. and Kaufman, B.A. (2018) 'The mitochondrial transcription factor TFAM in neurodegeneration: Emerging evidence and mechanisms', *FEBS letters*, 592(5), pp. 793–811. Available at: https://doi.org/10.1002/1873-3468.12989.

Kazuno, A. *et al.* (2006) 'Identification of mitochondrial DNA polymorphisms that alter mitochondrial matrix pH and intracellular calcium dynamics', *PLoS genetics*, 2(8), p. e128. Available at: https://doi.org/10.1371/journal.pgen.0020128.

Kenney, M.C. *et al.* (2013) 'Mitochondrial DNA variants mediate energy production and expression levels for CFH, C3 and EFEMP1 genes: implications for age-related macular degeneration', *PloS One*, 8(1), p. e54339. Available at: https://doi.org/10.1371/journal.pone.0054339.

Kerr, J.F., Wyllie, A.H. and Currie, A.R. (1972) 'Apoptosis: a basic biological phenomenon with wide-ranging implications in tissue kinetics', *British Journal of Cancer*, 26(4), pp. 239–257. Available at: https://doi.org/10.1038/bjc.1972.33.

Khawaja, A. *et al.* (2020) 'Distinct pre-initiation steps in human mitochondrial translation', *Nature Communications*, 11(1), p. 2932. Available at: https://doi.org/10.1038/s41467-020-16503-2.

Khrapko, K. (2011) 'The timing of mitochondrial DNA mutations in aging', *Nature Genetics*, 43(8), pp. 726–727. Available at: https://doi.org/10.1038/ng.895.

Khusnutdinova, E. *et al.* (2008) 'A mitochondrial etiology of neurodegenerative diseases: evidence from Parkinson's disease', *Annals of the New York Academy of Sciences*, 1147, pp. 1–20. Available at: https://doi.org/10.1196/annals.1427.001.

Kim, J. *et al.* (2010) 'Mitochondrial loss, dysfunction and altered dynamics in Huntington's disease', *Human Molecular Genetics*, 19(20), pp. 3919–3935. Available at: https://doi.org/10.1093/hmg/ddq306.

Kim, J.J. *et al.* (2024) 'Multi-ancestry genome-wide association meta-analysis of Parkinson's disease', *Nature Genetics*, 56(1), pp. 27–36. Available at: https://doi.org/10.1038/s41588-023-01584-8.

King, G.A. *et al.* (2018) 'Acetylation and phosphorylation of human TFAM regulate TFAM–DNA interactions via contrasting mechanisms', *Nucleic Acids Research*, 46(7), pp. 3633–3642. Available at: https://doi.org/10.1093/nar/gky204.

Kino, K. *et al.* (2017) 'Generation, repair and replication of guanine oxidation products', *Genes and Environment*, 39, p. 21. Available at: https://doi.org/10.1186/s41021-017-0081-0.

Kitada, T. *et al.* (1998) 'Mutations in the parkin gene cause autosomal recessive juvenile parkinsonism', *Nature*, 392(6676), pp. 605–608. Available at: https://doi.org/10.1038/33416.

Knez, J. *et al.* (2016) 'Correlates of Peripheral Blood Mitochondrial DNA Content in a General Population', *American Journal of Epidemiology*, 183(2), pp. 138–146. Available at: https://doi.org/10.1093/aje/kwv175.

König, T. *et al.* (2021) 'MIROs and DRP1 drive mitochondrial-derived vesicle biogenesis and promote quality control', *Nature Cell Biology*, 23(12), pp. 1271–1286. Available at: https://doi.org/10.1038/s41556-021-00798-4.

König, T. and McBride, H.M. (2024) 'Mitochondrial-derived vesicles in metabolism, disease, and aging', *Cell Metabolism*, 36(1), pp. 21–35. Available at: https://doi.org/10.1016/j.cmet.2023.11.014.

Kornblum, C. *et al.* (2013) 'Loss-of-function mutations in MGME1 impair mtDNA replication and cause multi-systemic mitochondrial disease', *Nature genetics*, 45(2), pp. 214–219. Available at: https://doi.org/10.1038/ng.2501.

Kowald, A. and Kirkwood, T.B.L. (2014) 'Transcription could be the key to the selection advantage of mitochondrial deletion mutants in aging', *Proceedings of the National Academy of Sciences*, 111(8), pp. 2972–2977. Available at: https://doi.org/10.1073/pnas.1314970111.

Kramer, M.L. and Schulz-Schaeffer, W.J. (2007) 'Presynaptic alpha-synuclein aggregates, not Lewy bodies, cause neurodegeneration in dementia with Lewy bodies', *The Journal of Neuroscience: The Official Journal of the Society for Neuroscience*, 27(6), pp. 1405–1410. Available at: https://doi.org/10.1523/JNEUROSCI.4564-06.2007.

Krishnan, K.J. *et al.* (2008) 'What causes mitochondrial DNA deletions in human cells?', *Nature Genetics*, 40(3), pp. 275–279. Available at: https://doi.org/10.1038/ng.f.94.

Kujoth, G.C. *et al.* (2005) 'Mitochondrial DNA mutations, oxidative stress, and apoptosis in mammalian aging', *Science (New York, N.Y.)*, 309(5733), pp. 481–484. Available at: https://doi.org/10.1126/science.1112125.

Kunová, N. *et al.* (2022) 'Mitochondrial Processing Peptidases-Structure, Function and the Role in Human Diseases', *International Journal of Molecular Sciences*, 23(3), p. 1297. Available at: https://doi.org/10.3390/ijms23031297.

Kwaśniewski, W. *et al.* (2023) 'Mitochondrial DNA Polymorphism in HV1 and HV2 Regions and 12S rDNA in Perimenopausal Hypertensive Women', *Biomedicines*, 11(3), p. 823. Available at: https://doi.org/10.3390/biomedicines11030823.

Langston, J.W. *et al.* (1983) 'Chronic Parkinsonism in humans due to a product of meperidine-analog synthesis', *Science (New York, N.Y.)*, 219(4587), pp. 979–980. Available at: https://doi.org/10.1126/science.6823561.

Langston, J.W. *et al.* (1984) '1-Methyl-4-phenylpyridinium ion (MPP+): identification of a metabolite of MPTP, a toxin selective to the substantia nigra', *Neuroscience Letters*, 48(1), pp. 87–92. Available at: https://doi.org/10.1016/0304-3940(84)90293-3.

Larsson, N.-G. (2010) 'Somatic mitochondrial DNA mutations in mammalian aging', *Annual Review of Biochemistry*, 79, pp. 683–706. Available at: https://doi.org/10.1146/annurev-biochem-060408-093701.

Lavoie, B. and Parent, A. (1994) 'Pedunculopontine nucleus in the squirrel monkey: distribution of cholinergic and monoaminergic neurons in the mesopontine tegmentum with evidence for the presence of glutamate in cholinergic neurons', *The Journal of Comparative Neurology*, 344(2), pp. 190–209. Available at: https://doi.org/10.1002/cne.903440203.

Lawless, C. *et al.* (2020) 'The rise and rise of mitochondrial DNA mutations', *Open Biology*, 10(5), p. 200061. Available at: https://doi.org/10.1098/rsob.200061.

Lazarou, M. *et al.* (2015) 'The ubiquitin kinase PINK1 recruits autophagy receptors to induce mitophagy', *Nature*, 524(7565), pp. 309–314. Available at: https://doi.org/10.1038/nature14893.

Lee, J.-Y. *et al.* (2010) 'Disease-causing mutations in parkin impair mitochondrial ubiquitination, aggregation, and HDAC6-dependent mitophagy', *The Journal of Cell Biology*, 189(4), pp. 671–679. Available at: https://doi.org/10.1083/jcb.201001039.

Lee, W. *et al.* (2023) 'Molecular basis for maternal inheritance of human mitochondrial DNA', *Nature Genetics*, 55(10), pp. 1632–1639. Available at: https://doi.org/10.1038/s41588-023-01505-9.

van Leeuwen, N. *et al.* (2014) 'Low mitochondrial DNA content associates with familial longevity: the Leiden Longevity Study', *Age (Dordrecht, Netherlands)*, 36(3), p. 9629. Available at: https://doi.org/10.1007/s11357-014-9629-0.

Lewis, S.C., Uchiyama, L.F. and Nunnari, J. (2016) 'ER-mitochondria contacts couple mtDNA synthesis with mitochondrial division in human cells', *Science (New York, N.Y.)*, 353(6296), p. aaf5549. Available at: https://doi.org/10.1126/science.aaf5549.

Li, B. *et al.* (2009) 'Automated inference of molecular mechanisms of disease from amino acid substitutions', *Bioinformatics*, 25(21), pp. 2744–2750. Available at: https://doi.org/10.1093/bioinformatics/btp528.

Li, B. *et al.* (2010) 'Omi/HtrA2 is a positive regulator of autophagy that facilitates the degradation of mutant proteins involved in neurodegenerative diseases', *Cell Death and Differentiation*, 17(11), pp. 1773–1784. Available at: https://doi.org/10.1038/cdd.2010.55.

Liao, C. *et al.* (2017) 'Dysregulated mitophagy and mitochondrial organization in optic atrophy due to OPA1 mutations', *Neurology*, 88(2), pp. 131–142. Available at: https://doi.org/10.1212/WNL.0000000000003491.

Lightowlers, R.N. *et al.* (1997) 'Mammalian mitochondrial genetics: heredity, heteroplasmy and disease', *Trends in Genetics*, 13(11), pp. 450–455. Available at: https://doi.org/10.1016/S0168-9525(97)01266-3.

Lim, J.M., Kim, G. and Levine, R.L. (2019) 'Methionine in Proteins: It's not just for protein initiation anymore', *Neurochemical research*, 44(1), pp. 247–257. Available at: https://doi.org/10.1007/s11064-017-2460-0.

Lin, D.-S. *et al.* (2019) 'Oxidative Insults and Mitochondrial DNA Mutation Promote Enhanced Autophagy and Mitophagy Compromising Cell Viability in Pluripotent Cell Model of Mitochondrial Disease', *Cells*, 8(1), p. 65. Available at: https://doi.org/10.3390/cells8010065.

Lin, J. *et al.* (2004) 'Defects in Adaptive Energy Metabolism with CNS-Linked Hyperactivity in PGC-1α Null Mice', *Cell*, 119(1), pp. 121–135. Available at: https://doi.org/10.1016/j.cell.2004.09.013.

Lin, M.T. *et al.* (2012) 'Somatic mitochondrial DNA mutations in early Parkinson and incidental Lewy body disease', *Annals of Neurology*, 71(6), pp. 850–854. Available at: https://doi.org/10.1002/ana.23568.

Lin, M.-Y. *et al.* (2017) 'Releasing Syntaphilin Removes Stressed Mitochondria from Axons Independent of Mitophagy under Pathophysiological Conditions', *Neuron*, 94(3), pp. 595-610.e6. Available at: https://doi.org/10.1016/j.neuron.2017.04.004.

Linnane, AnthonyW. *et al.* (1989) 'MITOCHONDRIAL DNA MUTATIONS AS AN IMPORTANT CONTRIBUTOR TO AGEING AND DEGENERATIVE DISEASES', *The Lancet*, 333(8639), pp. 642–645. Available at: https://doi.org/10.1016/S0140-6736(89)92145-4.

Liu, W. *et al.* (2011) 'Pink1 regulates the oxidative phosphorylation machinery via mitochondrial fission', *Proceedings of the National Academy of Sciences of the United States of America*, 108(31), pp. 12920–12924. Available at: https://doi.org/10.1073/pnas.1107332108.

Liu, W. *et al.* (2013) 'Mitochondrial fusion and fission proteins expression dynamically change in a murine model of amyotrophic lateral sclerosis', *Current Neurovascular Research*, 10(3), pp. 222–230. Available at: https://doi.org/10.2174/15672026113109990060.

Liu, X. *et al.* (1996) 'Induction of apoptotic program in cell-free extracts: requirement for dATP and cytochrome c', *Cell*, 86(1), pp. 147–157. Available at: https://doi.org/10.1016/s0092-8674(00)80085-9.

Liu, Y. *et al.* (2020) 'Chemical inhibition of FBXO7 reduces inflammation and confers neuroprotection by stabilizing the mitochondrial kinase PINK1', *JCI Insight*, 5(11). Available at: https://doi.org/10.1172/jci.insight.131834.

Lockhart, A. *et al.* (2019) 'RNase H1 and H2 Are Differentially Regulated to Process RNA-DNA Hybrids', *Cell Reports*, 29(9), pp. 2890-2900.e5. Available at: https://doi.org/10.1016/j.celrep.2019.10.108.

Lopez Sanchez, M.I.G. *et al.* (2011) 'RNA processing in human mitochondria', *Cell Cycle*, 10(17), pp. 2904–2916. Available at: https://doi.org/10.4161/cc.10.17.17060.

Lopez Sanchez, M.I.G. *et al.* (2020) 'Methylation of Ribosomal RNA: A Mitochondrial Perspective', *Frontiers in Genetics*, 11, p. 761. Available at: https://doi.org/10.3389/fgene.2020.00761.

Lu, D. *et al.* (2024) 'STAT2/SLC27A3/PINK1-Mediated Mitophagy Remodeling Lipid Metabolism Contributes to Pazopanib Resistance in Clear Cell Renal Cell Carcinoma', *Research (Washington, D.C.)*, 7, p. 0539. Available at: https://doi.org/10.34133/research.0539.

Lu, H., Giordano, F. and Ning, Z. (2016) 'Oxford Nanopore MinION Sequencing and Genome Assembly', *Genomics, Proteomics & Bioinformatics*, 14(5), pp. 265–279. Available at: https://doi.org/10.1016/j.gpb.2016.05.004.

Luo, S. *et al.* (2018) 'Biparental Inheritance of Mitochondrial DNA in Humans', *Proceedings of the National Academy of Sciences*, 115(51), pp. 13039–13044. Available at: https://doi.org/10.1073/pnas.1810946115.

Luo, X. *et al.* (2019) 'Posttranslational regulation of PGC-1α and its implication in cancer metabolism', *International Journal of Cancer*, 145(6), pp. 1475–1483. Available at: https://doi.org/10.1002/ijc.32253.

Lyons, D.M. and Lauring, A.S. (2017) 'Evidence for the Selective Basis of Transition-to-Transversion Substitution Bias in Two RNA Viruses', *Molecular Biology and Evolution*, 34(12), pp. 3205–3215. Available at: https://doi.org/10.1093/molbev/msx251.

Ma, L. *et al.* (2018) 'Breast cancer-associated mitochondrial DNA haplogroup promotes neoplastic growth via ROS-mediated AKT activation', *International Journal of Cancer*, 142(9), pp. 1786–1796. Available at: https://doi.org/10.1002/ijc.31207.

Madsen, C.S., Ghivizzani, S.C. and Hauswirth, W.W. (1993) 'Protein binding to a single termination-associated sequence in the mitochondrial DNA D-loop region.', *Molecular and Cellular Biology*, 13(4), pp. 2162–2171.

Mahlknecht, P., Seppi, K. and Poewe, W. (2015) 'The Concept of Prodromal Parkinson's Disease', *Journal of Parkinson's Disease*, 5(4), pp. 681–697. Available at: https://doi.org/10.3233/JPD-150685.

Maio, N. *et al.* (2016) 'Disease-Causing SDHAF1 Mutations Impair Transfer of Fe-S Clusters to SDHB', *Cell Metabolism*, 23(2), pp. 292–302. Available at: https://doi.org/10.1016/j.cmet.2015.12.005.

Maio, N. and Rouault, T.A. (2020) 'Outlining the Complex Pathway of Mammalian Fe-S Cluster Biogenesis', *Trends in Biochemical Sciences*, 45(5), pp. 411–426. Available at: https://doi.org/10.1016/j.tibs.2020.02.001.

Manaye, K.F. *et al.* (1999) 'Quantification of cholinergic and select non-cholinergic mesopontine neuronal populations in the human brain', *Neuroscience*, 89(3), pp. 759–770. Available at: https://doi.org/10.1016/s0306-4522(98)00380-7.

Manning, G. *et al.* (2002) 'The protein kinase complement of the human genome', *Science (New York, N.Y.)*, 298(5600), pp. 1912–1934. Available at: https://doi.org/10.1126/science.1075762.

Mårtensson, C.U., Doan, K.N. and Becker, T. (2017) 'Effects of lipids on mitochondrial functions', *Biochimica et Biophysica Acta (BBA) - Molecular and Cell Biology of Lipids*, 1862(1), pp. 102–113. Available at: https://doi.org/10.1016/j.bbalip.2016.06.015.

Martin, M. *et al.* (2005) 'Termination factor-mediated DNA loop between termination and initiation sites drives mitochondrial rRNA synthesis', *Cell*, 123(7), pp. 1227–1240. Available at: https://doi.org/10.1016/j.cell.2005.09.040.

Martin, W. and Müller, M. (1998) 'The hydrogen hypothesis for the first eukaryote', *Nature*, 392(6671), pp. 37–41. Available at: https://doi.org/10.1038/32096.

Martínez-Reyes, I. and Chandel, N.S. (2020) 'Mitochondrial TCA cycle metabolites control physiology and disease', *Nature Communications*, 11(1), p. 102. Available at: https://doi.org/10.1038/s41467-019-13668-3.

Matheoud, D. *et al.* (2016) 'Parkinson's Disease-Related Proteins PINK1 and Parkin Repress Mitochondrial Antigen Presentation', *Cell*, 166(2), pp. 314–327. Available at: https://doi.org/10.1016/j.cell.2016.05.039.

Matsuda, S., Kitagishi, Y. and Kobayashi, M. (2013) 'Function and characteristics of PINK1 in mitochondria', *Oxidative Medicine and Cellular Longevity*, 2013, p. 601587. Available at: https://doi.org/10.1155/2013/601587.

Matsuno-Yagi, A. and Hatefi, Y. (2001) 'Ubiquinol:cytochrome c oxidoreductase (complex III). Effect of inhibitors on cytochrome b reduction in submitochondrial particles and the role of ubiquinone in complex III', *The Journal of Biological Chemistry*, 276(22), pp. 19006–19011. Available at: https://doi.org/10.1074/jbc.M101446200.

Matsushima, Y. *et al.* (2021) 'Mitochondrial Lon protease is a gatekeeper for proteins newly imported into the matrix', *Communications Biology*, 4(1), p. 974. Available at: https://doi.org/10.1038/s42003-021-02498-z.

Matsushima, Y. and Kaguni, L.S. (2012) 'Matrix proteases in mitochondrial DNA function', *Biochimica et biophysica acta*, 1819(9–10), pp. 1080–1087. Available at: https://doi.org/10.1016/j.bbagrm.2011.11.008.

Mazzone, P. *et al.* (2005) 'Implantation of human pedunculopontine nucleus: a safe and clinically relevant target in Parkinson's disease', *Neuroreport*, 16(17), pp. 1877–1881. Available at: https://doi.org/10.1097/01.wnr.0000187629.38010.12.

McFadden, C.S. *et al.* (2004) 'Variation in coding (NADH dehydrogenase subunits 2, 3, and 6) and noncoding intergenic spacer regions of the mitochondrial genome in Octocorallia (Cnidaria: Anthozoa)', *Marine Biotechnology (New York, N.Y.)*, 6(6), pp. 516–526. Available at: https://doi.org/10.1007/s10126-002-0102-1.

McLelland, G.-L. *et al.* (2014) 'Parkin and PINK1 function in a vesicular trafficking pathway regulating mitochondrial quality control', *The EMBO journal*, 33(4), pp. 282–295. Available at: https://doi.org/10.1002/embj.201385902.

McQuibban, G.A., Saurya, S. and Freeman, M. (2003) 'Mitochondrial membrane remodelling regulated by a conserved rhomboid protease', *Nature*, 423(6939), pp. 537–541. Available at: https://doi.org/10.1038/nature01633.

Meiser, J., Weindl, D. and Hiller, K. (2013) 'Complexity of dopamine metabolism', *Cell communication and signaling: CCS*, 11(1), p. 34. Available at: https://doi.org/10.1186/1478-811X-11-34.

Menšíková, K. *et al.* (2022) 'Lewy body disease or diseases with Lewy bodies?', *NPJ Parkinson's disease*, 8(1), p. 3. Available at: https://doi.org/10.1038/s41531-021-00273-9.

Mesulam, M.M. *et al.* (1983) 'Central cholinergic pathways in the rat: an overview based on an alternative nomenclature (Ch1-Ch6)', *Neuroscience*, 10(4), pp. 1185–1201. Available at: https://doi.org/10.1016/0306-4522(83)90108-2.

Mesulam, M.-M. *et al.* (1989) 'Human reticular formation: Cholinergic neurons of the pedunculopontine and laterodorsal tegmental nuclei and some cytochemical comparisons to forebrain cholinergic neurons', *Journal of Comparative Neurology*, 283(4), pp. 611–633. Available at: https://doi.org/10.1002/cne.902830414.

Meyer, S., Weiss, G. and von Haeseler, A. (1999) 'Pattern of nucleotide substitution and rate heterogeneity in the hypervariable regions I and II of human mtDNA', *Genetics*, 152(3), pp. 1103–1110. Available at: https://doi.org/10.1093/genetics/152.3.1103.

Miller, K.N., Clark, J.P. and Anderson, R.M. (2019) 'Mitochondrial regulator PGC-1a—Modulating the modulator', *Current opinion in endocrine and metabolic research*, 5, pp. 37–44. Available at: https://doi.org/10.1016/j.coemr.2019.02.002.

Miller, S. and Muqit, M.M.K. (2019) 'Therapeutic approaches to enhance PINK1/Parkin mediated mitophagy for the treatment of Parkinson's disease', *Neuroscience Letters*, 705, pp. 7–13. Available at: https://doi.org/10.1016/j.neulet.2019.04.029.

Mimaki, M. *et al.* (2012) 'Understanding mitochondrial complex I assembly in health and disease', *Biochimica et Biophysica Acta (BBA) - Bioenergetics*, 1817(6), pp. 851–862. Available at: https://doi.org/10.1016/j.bbabio.2011.08.010.

Mogi, M. *et al.* (1996) 'bcl-2 protein is increased in the brain from parkinsonian patients', *Neuroscience Letters*, 215(2), pp. 137–139.

Moisan, F. *et al.* (2016) 'Parkinson disease male-to-female ratios increase with age: French nationwide study and meta-analysis', *Journal of Neurology, Neurosurgery & Psychiatry*, 87(9), pp. 952–957. Available at: https://doi.org/10.1136/jnnp-2015-312283.

Montoya, J. *et al.* (1982) 'Identification of initiation sites for heavy-strand and light-strand transcription in human mitochondrial DNA', *Proceedings of the National Academy of Sciences of the United States of America*, 79(23), pp. 7195–7199. Available at: https://doi.org/10.1073/pnas.79.23.7195.

Montoya, J., Gaines, G.L. and Attardi, G. (1983) 'The pattern of transcription of the human mitochondrial rRNA genes reveals two overlapping transcription units', *Cell*, 34(1), pp. 151–159. Available at: https://doi.org/10.1016/0092-8674(83)90145-9.

Mootha, V.K. *et al.* (2003) 'PGC-1alpha-responsive genes involved in oxidative phosphorylation are coordinately downregulated in human diabetes', *Nature Genetics*, 34(3), pp. 267–273. Available at: https://doi.org/10.1038/ng1180.

Moro, E. *et al.* (2010) 'Unilateral pedunculopontine stimulation improves falls in Parkinson's disease', *Brain: A Journal of Neurology*, 133(Pt 1), pp. 215–224. Available at: https://doi.org/10.1093/brain/awp261.

Morozov, Y.I. *et al.* (2014) 'A novel intermediate in transcription initiation by human mitochondrial RNA polymerase', *Nucleic Acids Research*, 42(6), pp. 3884–3893. Available at: https://doi.org/10.1093/nar/gkt1356.

Morozov, Y.I. *et al.* (2015) 'A model for transcription initiation in human mitochondria', *Nucleic Acids Research*, 43(7), pp. 3726–3735. Available at: https://doi.org/10.1093/nar/gkv235.

Müller, S.K. *et al.* (2013) 'Lewy body pathology is associated with mitochondrial DNA damage in Parkinson's disease', *Neurobiology of Aging*, 34(9), pp. 2231–2233. Available at: https://doi.org/10.1016/j.neurobiolaging.2013.03.016.

Na, J.-H. and Lee, Y.-M. (2022) 'Genotype-phenotype analysis of MT-ATP6-associated Leigh syndrome', *Acta Neurologica Scandinavica*, 145(4), pp. 414–422. Available at: https://doi.org/10.1111/ane.13566.

Naarala, J. *et al.* (1997) 'Cholinergic-induced production of reactive oxygen species in human neuroblastoma cells', *Life Sciences*, 60(21), pp. 1905–1914. Available at: https://doi.org/10.1016/s0024-3205(97)00152-5.

Nair-Roberts, R.G. *et al.* (2008) 'Stereological estimates of dopaminergic, GABAergic and glutamatergic neurons in the ventral tegmental area, substantia nigra and retrorubral field in the rat', *Neuroscience*, 152(4), pp. 1024–1031. Available at: https://doi.org/10.1016/j.neuroscience.2008.01.046.

Nakamura, K. *et al.* (2011) 'Direct membrane association drives mitochondrial fission by the Parkinson disease-associated protein alpha-synuclein', *The Journal of Biological Chemistry*, 286(23), pp. 20710–20726. Available at: https://doi.org/10.1074/jbc.M110.213538.

Nalls, M.A. *et al.* (2019) 'Identification of novel risk loci, causal insights, and heritable risk for Parkinson's disease: a meta-analysis of genome-wide association studies', *The Lancet. Neurology*, 18(12), pp. 1091–1102. Available at: https://doi.org/10.1016/S1474-4422(19)30320-5.

Narendra, D. *et al.* (2008) 'Parkin is recruited selectively to impaired mitochondria and promotes their autophagy', *Journal of Cell Biology*, 183(5), pp. 795–803. Available at: https://doi.org/10.1083/jcb.200809125.

Nashmi, R. *et al.* (2007) 'Chronic nicotine cell specifically upregulates functional alpha 4* nicotinic receptors: basis for both tolerance in midbrain and enhanced long-term potentiation in perforant path', *The Journal of Neuroscience: The Official Journal of the Society for Neuroscience*, 27(31), pp. 8202–8218. Available at: https://doi.org/10.1523/JNEUROSCI.2199-07.2007.

Navarro-Romero, A., Montpeyó, M. and Martinez-Vicente, M. (2020) 'The Emerging Role of the Lysosome in Parkinson's Disease', *Cells*, 9(11), p. 2399. Available at: https://doi.org/10.3390/cells9112399.

Nekhaeva, E. *et al.* (2002) 'Clonally expanded mtDNA point mutations are abundant in individual cells of human tissues', *Proceedings of the National Academy of Sciences of the United States of America*, 99(8), pp. 5521–5526. Available at: https://doi.org/10.1073/pnas.072670199.

Neuspiel, M. *et al.* (2008) 'Cargo-Selected Transport from the Mitochondria to Peroxisomes Is Mediated by Vesicular Carriers', *Current Biology*, 18(2), pp. 102–108. Available at: https://doi.org/10.1016/j.cub.2007.12.038.

Newman, L.E. and Shadel, G.S. (2018) 'Pink1/Parkin link inflammation, mitochondrial stress, and neurodegeneration', *The Journal of Cell Biology*, 217(10), pp. 3327–3329. Available at: https://doi.org/10.1083/jcb.201808118.

Ngo, H.B., Kaiser, J.T. and Chan, D.C. (2011) 'The mitochondrial transcription and packaging factor Tfam imposes a U-turn on mitochondrial DNA', *Nature Structural & Molecular Biology*, 18(11), pp. 1290–1296. Available at: https://doi.org/10.1038/nsmb.2159.

Nicholls, T.J. *et al.* (2018) 'Topoisomerase 3α Is Required for Decatenation and Segregation of Human mtDNA', *Molecular Cell*, 69(1), pp. 9-23.e6. Available at: https://doi.org/10.1016/j.molcel.2017.11.033.

Nido, G.S. *et al.* (2018) 'Ultradeep mapping of neuronal mitochondrial deletions in Parkinson's disease', *Neurobiology of Aging*, 63, pp. 120–127. Available at: https://doi.org/10.1016/j.neurobiolaging.2017.10.024.

Nolfi-Donegan, D., Braganza, A. and Shiva, S. (2020) 'Mitochondrial electron transport chain: Oxidative phosphorylation, oxidant production, and methods of measurement', *Redox Biology*, 37, p. 101674. Available at: https://doi.org/10.1016/j.redox.2020.101674.

Ohkubo, A. *et al.* (2021) 'The FASTK family proteins fine-tune mitochondrial RNA processing', *PLoS Genetics*, 17(11), p. e1009873. Available at: https://doi.org/10.1371/journal.pgen.1009873.

Okatsu, K. *et al.* (2012) 'PINK1 autophosphorylation upon membrane potential dissipation is essential for Parkin recruitment to damaged mitochondria', *Nature Communications*, 3, p. 1016. Available at: https://doi.org/10.1038/ncomms2016.

Olichon, A. *et al.* (2007) 'OPA1 alternate splicing uncouples an evolutionary conserved function in mitochondrial fusion from a vertebrate restricted function in apoptosis', *Cell Death and Differentiation*, 14(4), pp. 682–692. Available at: https://doi.org/10.1038/sj.cdd.4402048.

Ou, Y.-H. *et al.* (2018) 'Aminoglycoside-associated nonsyndromic deafness and speech disorder in mitochondrial A1555G mutation in a family', *Medicine*, 97(42), p. e12878. Available at: https://doi.org/10.1097/MD.0000000000012878.

Ozawa, T. *et al.* (1991) 'Distinct clustering of point mutations in mitochondrial DNA among patients with mitochondrial encephalomyopathies and with Parkinson's disease', *Biochemical and Biophysical Research Communications*, 176(2), pp. 938–946. Available at: https://doi.org/10.1016/s0006-291x(05)80276-1.

Pahapill, P.A. and Lozano, A.M. (2000) 'The pedunculopontine nucleus and Parkinson's disease', *Brain: A Journal of Neurology*, 123 (Pt 9), pp. 1767–1783. Available at: https://doi.org/10.1093/brain/123.9.1767.

Panchal, K. and Tiwari, A.K. (2021) 'Miro (Mitochondrial Rho GTPase), a key player of mitochondrial axonal transport and mitochondrial dynamics in neurodegenerative diseases', *Mitochondrion*, 56, pp. 118–135. Available at: https://doi.org/10.1016/j.mito.2020.10.005.

Park, J. *et al.* (2006) 'Mitochondrial dysfunction in Drosophila PINK1 mutants is complemented by parkin', *Nature*, 441(7097), pp. 1157–1161. Available at: https://doi.org/10.1038/nature04788.

Pauly, M.D., Procario, M.C. and Lauring, A.S. (2017) 'A novel twelve class fluctuation test reveals higher than expected mutation rates for influenza A viruses', *eLife*. Edited by K. Kirkegaard, 6, p. e26437. Available at: https://doi.org/10.7554/eLife.26437.

Pavon, J.M., Whitson, H.E. and Okun, M.S. (2010) 'Parkinson's disease in women: A call for improved clinical studies and for comparative effectiveness research', *Maturitas*, 65(4), pp. 352–358. Available at: https://doi.org/10.1016/j.maturitas.2010.01.001.

Peeva, V. *et al.* (2018) 'Linear mitochondrial DNA is rapidly degraded by components of the replication machinery', *Nature Communications*, 9(1), p. 1727. Available at: https://doi.org/10.1038/s41467-018-04131-w.

Pejaver, V. *et al.* (2020) 'Inferring the molecular and phenotypic impact of amino acid variants with MutPred2', *Nature Communications*, 11(1), p. 5918. Available at: https://doi.org/10.1038/s41467-020-19669-x.

Peña-Blanco, A. and García-Sáez, A.J. (2018) 'Bax, Bak and beyond - mitochondrial performance in apoptosis', *The FEBS journal*, 285(3), pp. 416–431. Available at: https://doi.org/10.1111/febs.14186.

Pérez, M.J. *et al.* (2021) 'Loss of function of the mitochondrial peptidase PITRM1 induces proteotoxic stress and Alzheimer's disease-like pathology in human cerebral organoids', *Molecular Psychiatry*, 26(10), pp. 5733–5750. Available at: https://doi.org/10.1038/s41380-020-0807-4.

Perlmutter, J.D., Braun, A.R. and Sachs, J.N. (2009) 'Curvature Dynamics of α-Synuclein Familial Parkinson Disease Mutants', *The Journal of Biological Chemistry*, 284(11), pp. 7177–7189. Available at: https://doi.org/10.1074/jbc.M808895200.

Persson, Ö. *et al.* (2019) 'Copy-choice recombination during mitochondrial L-strand synthesis causes DNA deletions', *Nature Communications*, 10(1), p. 759. Available at: https://doi.org/10.1038/s41467-019-08673-5.

Petrov, D. *et al.* (2016) 'Evaluation of the Role of JNK1 in the Hippocampus in an Experimental Model of Familial Alzheimer's Disease', *Molecular Neurobiology*, 53(9), pp. 6183–6193. Available at: https://doi.org/10.1007/s12035-015-9522-6.

Picca, A. *et al.* (2023) 'Mitophagy in human health, ageing and disease', *Nature Metabolism*, 5(12), pp. 2047–2061. Available at: https://doi.org/10.1038/s42255-023-00930-8.

Pienaar, I.S. *et al.* (2013) 'Mitochondrial Abnormality Associates with Type-Specific Neuronal Loss and Cell Morphology Changes in the Pedunculopontine Nucleus in Parkinson Disease', *The American Journal of Pathology*, 183(6), pp. 1826–1840. Available at: https://doi.org/10.1016/j.ajpath.2013.09.002.

Piotrowska-Nowak, A. *et al.* (2020) 'Mitochondrial genome variation in male LHON patients with the m.11778G > A mutation', *Metabolic Brain Disease*, 35(8), pp. 1317–1327. Available at: https://doi.org/10.1007/s11011-020-00605-3.

Piro-Megy, C. *et al.* (2020) 'Dominant mutations in mtDNA maintenance gene SSBP1 cause optic atrophy and foveopathy', *Journal of Clinical Investigation*, 130(1), pp. 143–156. Available at: https://doi.org/10.1172/JCI128513.

Plun-Favreau, H. *et al.* (2007) 'The mitochondrial protease HtrA2 is regulated by Parkinson's disease-associated kinase PINK1', *Nature Cell Biology*, 9(11), pp. 1243–1252. Available at: https://doi.org/10.1038/ncb1644.

Poewe, W. *et al.* (2017) 'Parkinson disease', *Nature Reviews. Disease Primers*, 3, p. 17013. Available at: https://doi.org/10.1038/nrdp.2017.13.

Polikanov, Y.S. *et al.* (2015) 'Structural insights into the role of rRNA modifications in protein synthesis and ribosome assembly', *Nature Structural & Molecular Biology*, 22(4), pp. 342–344. Available at: https://doi.org/10.1038/nsmb.2992.

Popov, L. (2022) 'Mitochondrial-derived vesicles: Recent insights', *Journal of Cellular and Molecular Medicine*, 26(12), pp. 3323–3328. Available at: https://doi.org/10.1111/jcmm.17391.

Popow, J. *et al.* (2015) 'FASTKD2 is an RNA-binding protein required for mitochondrial RNA processing and translation', *RNA (New York, N.Y.)*, 21(11), pp. 1873–1884. Available at: https://doi.org/10.1261/rna.052365.115.

Pozo Devoto, V.M. and Falzone, T.L. (2017) 'Mitochondrial dynamics in Parkinson's disease: a role for α-synuclein?', *Disease Models & Mechanisms*, 10(9), pp. 1075–1087. Available at: https://doi.org/10.1242/dmm.026294.

Praefcke, G.J.K. and McMahon, H.T. (2004) 'The dynamin superfamily: universal membrane tubulation and fission molecules?', *Nature Reviews. Molecular Cell Biology*, 5(2), pp. 133–147. Available at: https://doi.org/10.1038/nrm1313.

Prime, M. *et al.* (2020) 'Differentiating Parkinson Disease Subtypes Using Clinical Balance Measures', *Journal of neurologic physical therapy: JNPT*, 44(1), pp. 34–41. Available at: https://doi.org/10.1097/NPT.0000000000000297.

Puigserver, P. *et al.* (1998) 'A cold-inducible coactivator of nuclear receptors linked to adaptive thermogenesis', *Cell*, 92(6), pp. 829–839. Available at: https://doi.org/10.1016/s0092-8674(00)81410-5.

Puspita, L., Chung, S.Y. and Shim, J.-W. (2017) 'Oxidative stress and cellular pathologies in Parkinson's disease', *Molecular Brain*, 10(1), p. 53. Available at: https://doi.org/10.1186/s13041-017-0340-9.

Pyle, A. *et al.* (2005) 'Mitochondrial DNA haplogroup cluster UKJT reduces the risk of PD', *Annals of Neurology*, 57(4), pp. 564–567. Available at: https://doi.org/10.1002/ana.20417.

Pyle, A. *et al.* (2015) 'Extreme-Depth Re-sequencing of Mitochondrial DNA Finds No Evidence of Paternal Transmission in Humans', *PLoS genetics*, 11(5), p. e1005040. Available at: https://doi.org/10.1371/journal.pgen.1005040.

Pyle, A. *et al.* (2016) 'Reduced mitochondrial DNA copy number is a biomarker of Parkinson's disease', *Neurobiology of Aging*, 38, p. 216.e7-216.e10. Available at: https://doi.org/10.1016/j.neurobiolaging.2015.10.033.

Qian, Y. *et al.* (2005) 'Clinical evaluation and mitochondrial DNA sequence analysis in three Chinese families with Leber's hereditary optic neuropathy', *Biochemical and Biophysical Research Communications*, 332(2), pp. 614–621. Available at: https://doi.org/10.1016/j.bbrc.2005.05.003.

Queen, R.A. *et al.* (2017) 'Mitochondrial DNA sequence context in the penetrance of mitochondrial t-RNA mutations: A study across multiple lineages with diagnostic implications', *PloS One*, 12(11), p. e0187862. Available at: https://doi.org/10.1371/journal.pone.0187862.

Quinn, P.M.J. *et al.* (2020) 'PINK1/PARKIN signalling in neurodegeneration and neuroinflammation', *Acta Neuropathologica Communications*, 8(1), p. 189. Available at: https://doi.org/10.1186/s40478-020-01062-w.

Rafiq, H. *et al.* (2022) 'Inhibition of drug induced Parkinsonism by chronic supplementation of quercetin in haloperidol-treated wistars', *Pakistan Journal of Pharmaceutical Sciences*, 35(6), pp. 1655–1662.

Rahman, S. *et al.* (1999) 'A missense mutation of cytochrome oxidase subunit II causes defective assembly and myopathy', *American Journal of Human Genetics*, 65(4), pp. 1030–1039. Available at: https://doi.org/10.1086/302590.

Rahman, S. and Copeland, W.C. (2019) 'POLG-related disorders and their neurological manifestations', *Nature Reviews Neurology*, 15(1), pp. 40–52. Available at: https://doi.org/10.1038/s41582-018-0101-0.

Rappe, A. *et al.* (2024) 'Longitudinal autophagy profiling of the mammalian brain reveals sustained mitophagy throughout healthy aging', *The EMBO journal*, 43(23), pp. 6199–6231. Available at: https://doi.org/10.1038/s44318-024-00241-y.

Read, A.D. *et al.* (2021) 'Mitochondrial iron–sulfur clusters: Structure, function, and an emerging role in vascular biology', *Redox Biology*, 47, p. 102164. Available at: https://doi.org/10.1016/j.redox.2021.102164.

Reardon, S.D. and Mishanina, T.V. (2022) 'Phosphorylation and acetylation of mitochondrial transcription factor A promote transcription processivity without compromising initiation or DNA compaction', *The Journal of Biological Chemistry*, 298(4), p. 101815. Available at: https://doi.org/10.1016/j.jbc.2022.101815.

Reeve, A.K. *et al.* (2008) 'Nature of Mitochondrial DNA Deletions in Substantia Nigra Neurons', *The American Journal of Human Genetics*, 82(1), pp. 228–235. Available at: https://doi.org/10.1016/j.ajhg.2007.09.018.

Reeve, A.K. *et al.* (2009) 'The low abundance of clonally expanded mitochondrial DNA point mutations in aged substantia nigra neurons', *Aging Cell*, 8(4), pp. 496–498. Available at: https://doi.org/10.1111/j.1474-9726.2009.00492.x.

Reznik, E. *et al.* (2016) 'Mitochondrial DNA copy number variation across human cancers', *eLife*, 5, p. e10769. Available at: https://doi.org/10.7554/eLife.10769.

Richter, S. and Lamppa, G.K. (1998) 'A chloroplast processing enzyme functions as the general stromal processing peptidase', *Proceedings of the National Academy of Sciences of the United States of America*, 95(13), pp. 7463–7468. Available at: https://doi.org/10.1073/pnas.95.13.7463.

Riley, B.E. *et al.* (2013) 'Structure and function of Parkin E3 ubiquitin ligase reveals aspects of RING and HECT ligases', *Nature Communications*, 4(1), p. 1982. Available at: https://doi.org/10.1038/ncomms2982.

Rius, R. *et al.* (2019) 'Biparental inheritance of mitochondrial DNA in humans is not a common phenomenon', *Genetics in Medicine*, 21(12), pp. 2823–2826. Available at: https://doi.org/10.1038/s41436-019-0568-0.

Robinson, B.H. (2000) 'Human Cytochrome Oxidase Deficiency', *Pediatric Research*, 48(5), pp. 581–585. Available at: https://doi.org/10.1203/00006450-200011000-00004.

Rodgers, J.T. *et al.* (2005) 'Nutrient control of glucose homeostasis through a complex of PGC-1alpha and SIRT1', *Nature*, 434(7029), pp. 113–118. Available at: https://doi.org/10.1038/nature03354.

Rolheiser, T.M. *et al.* (2011) 'Diffusion tensor imaging and olfactory identification testing in early-stage Parkinson's disease', *Journal of Neurology*, 258(7), pp. 1254–1260. Available at: https://doi.org/10.1007/s00415-011-5915-2.

Rong, Z. *et al.* (2021) 'The Mitochondrial Response to DNA Damage', *Frontiers in Cell and Developmental Biology*, 9. Available at: https://www.frontiersin.org/articles/10.3389/fcell.2021.669379 (Accessed: 10 January 2024).

Roseberry, T.K. *et al.* (2016) 'Cell-Type-Specific Control of Brainstem Locomotor Circuits by Basal Ganglia', *Cell*, 164(3), pp. 526–537. Available at: https://doi.org/10.1016/j.cell.2015.12.037.

Rosenthal, L.P. and Bodley, J.W. (1987) 'Purification and characterization of Saccharomyces cerevisiae mitochondrial elongation factor Tu', *The Journal of Biological Chemistry*, 262(23), pp. 10955–10959.

Ross, O.A. *et al.* (2008) 'Genetic variation of Omi/HtrA2 and Parkinson's disease', *Parkinsonism & Related Disorders*, 14(7), pp. 539–543. Available at: https://doi.org/10.1016/j.parkreldis.2008.08.003.

Rossignol, R. *et al.* (2003) 'Mitochondrial threshold effects.', *Biochemical Journal*, 370(Pt 3), pp. 751–762. Available at: https://doi.org/10.1042/BJ20021594.

Rowe, J.B., Holland, N. and Rittman, T. (2021) 'Progressive supranuclear palsy: diagnosis and management', *Practical Neurology*, 21(5), pp. 376–383. Available at: https://doi.org/10.1136/practneurol-2020-002794.

Russo, M.J. *et al.* (2021) 'High diagnostic performance of independent alpha-synuclein seed amplification assays for detection of early Parkinson's disease', *Acta Neuropathologica Communications*, 9(1), p. 179. Available at: https://doi.org/10.1186/s40478-021-01282-8.

Rutter, J., Winge, D.R. and Schiffman, J.D. (2010) 'Succinate Dehydrogenase—Assembly, Regulation and Role in Human Disease', *Mitochondrion*, 10(4), pp. 393–401. Available at: https://doi.org/10.1016/j.mito.2010.03.001.

Sabouny, R. and Shutt, T.E. (2021) 'The role of mitochondrial dynamics in mtDNA maintenance', *Journal of Cell Science*, 134(24), p. jcs258944. Available at: https://doi.org/10.1242/jcs.258944.

Sagan, L. (1967) 'On the origin of mitosing cells', *Journal of Theoretical Biology*, 14(3), pp. 255–274. Available at: https://doi.org/10.1016/0022-5193(67)90079-3.

Sale, J.E. (2013) 'Translesion DNA synthesis and mutagenesis in eukaryotes', *Cold Spring Harbor Perspectives in Biology*, 5(3), p. a012708. Available at: https://doi.org/10.1101/cshperspect.a012708.

Samuels, D.C., Schon, E.A. and Chinnery, P.F. (2004) 'Two direct repeats cause most human mtDNA deletions', *Trends in Genetics*, 20(9), pp. 393–398. Available at: https://doi.org/10.1016/j.tig.2004.07.003.

Sanchez-Contreras, M. and Kennedy, S.R. (2022) 'The Complicated Nature of Somatic mtDNA Mutations in Aging', *Frontiers in Aging*, 2, p. 805126. Available at: https://doi.org/10.3389/fragi.2021.805126.

Santoro, A. *et al.* (2017) 'DRP1 suppresses leptin and glucose sensing of POMC neurons', *Cell metabolism*, 25(3), pp. 647–660. Available at: https://doi.org/10.1016/j.cmet.2017.01.003.

Sato, M. and Sato, K. (2011) 'Degradation of Paternal Mitochondria by Fertilization-Triggered Autophagy in C. elegans Embryos', *Science*, 334(6059), pp. 1141–1144. Available at: https://doi.org/10.1126/science.1210333.

Sazanov, L.A. *et al.* (2000) 'Resolution of the Membrane Domain of Bovine Complex I into Subcomplexes: Implications for the Structural Organization of the Enzyme', *Biochemistry*, 39(24), pp. 7229–7235. Available at: https://doi.org/10.1021/bi000335t.

Sazanov, L.A. (2015) 'A giant molecular proton pump: structure and mechanism of respiratory complex I', *Nature Reviews Molecular Cell Biology*, 16(6), pp. 375–388. Available at: https://doi.org/10.1038/nrm3997.

Scarpulla, R.C. (2002) 'Nuclear activators and coactivators in mammalian mitochondrial biogenesis', *Biochimica Et Biophysica Acta*, 1576(1–2), pp. 1–14. Available at: https://doi.org/10.1016/s0167-4781(02)00343-3.

Schaefer, P.M. *et al.* (2022) 'Combination of common mtDNA variants results in mitochondrial dysfunction and a connective tissue dysregulation', *Proceedings of the National Academy of Sciences of the United States of America*, 119(45), p. e2212417119. Available at: https://doi.org/10.1073/pnas.2212417119.

Schon, E.A., DiMauro, S. and Hirano, M. (2012) 'Human mitochondrial DNA: roles of inherited and somatic mutations', *Nature Reviews. Genetics*, 13(12), pp. 878–890. Available at: https://doi.org/10.1038/nrg3275.

Schon, K.R. *et al.* (2020) 'Mitochondrial Diseases: A Diagnostic Revolution', *Trends in Genetics*, 36(9), pp. 702–717. Available at: https://doi.org/10.1016/j.tig.2020.06.009.

Schreiber, S.N. *et al.* (2004) 'The estrogen-related receptor alpha (ERRalpha) functions in PPARgamma coactivator 1alpha (PGC-1alpha)-induced mitochondrial biogenesis', *Proceedings of the National Academy of Sciences of the United States of America*, 101(17), pp. 6472–6477. Available at: https://doi.org/10.1073/pnas.0308686101.

Schwartz, M. and Vissing, J. (2002) 'Paternal inheritance of mitochondrial DNA', *The New England Journal of Medicine*, 347(8), pp. 576–580. Available at: https://doi.org/10.1056/NEJMoa020350.

Sengupta, S., Yang, X. and Higgs, P.G. (2007) 'The Mechanisms of Codon Reassignments in Mitochondrial Genetic Codes', *Journal of Molecular Evolution*, 64(6), pp. 662–688. Available at: https://doi.org/10.1007/s00239-006-0284-7.

Shaltouki, A. *et al.* (2018) 'Alpha-synuclein delays mitophagy and targeting Miro rescues neuron loss in Parkinson's models', *Acta Neuropathologica*, 136(4), pp. 607–620. Available at: https://doi.org/10.1007/s00401-018-1873-4.

Sharma, P.K. *et al.* (2025) 'Stereological analysis of cholinergic neurons within bilateral pedunculopontine nuclei in health and when affected by Parkinson's disease', *Brain Pathology (Zurich, Switzerland)*, p. e70011. Available at: https://doi.org/10.1111/bpa.70011.

Sharma, Y. *et al.* (2010) 'Comparative anatomy of the locus coeruleus in humans and nonhuman primates', *The Journal of Comparative Neurology*, 518(7), pp. 963–971. Available at: https://doi.org/10.1002/cne.22249.

Shaw, G.A. (2021) 'Mitochondria as the target for disease related hormonal dysregulation', *Brain, Behavior, & Immunity - Health*, 18, p. 100350. Available at: https://doi.org/10.1016/j.bbih.2021.100350.

Shi, X. *et al.* (2017) 'Intravenous administration of mitochondria for treating experimental Parkinson's disease', *Mitochondrion*, 34, pp. 91–100. Available at: https://doi.org/10.1016/j.mito.2017.02.005.

Shi, Y. *et al.* (2016) 'Mitochondrial transcription termination factor 1 directs polar replication fork pausing', *Nucleic Acids Research*, 44(12), pp. 5732–5742. Available at: https://doi.org/10.1093/nar/gkw302.

Shin, H.-W. and Chung, S.J. (2012) 'Drug-induced parkinsonism', *Journal of Clinical Neurology (Seoul, Korea)*, 8(1), pp. 15–21. Available at: https://doi.org/10.3988/jcn.2012.8.1.15.

Shinotoh, H. *et al.* (1999) 'Positron emission tomographic measurement of acetylcholinesterase activity reveals differential loss of ascending cholinergic systems in Parkinson's disease and progressive supranuclear palsy', *Annals of Neurology*, 46(1), pp. 62–69.

Shoffner, J.M. *et al.* (1989) 'Spontaneous Kearns-Sayre/chronic external ophthalmoplegia plus syndrome associated with a mitochondrial DNA deletion: a slip-replication model and metabolic therapy', *Proceedings of the National Academy of Sciences*, 86(20), pp. 7952–7956. Available at: https://doi.org/10.1073/pnas.86.20.7952.

Shoffner, J.M. *et al.* (1990) 'Myoclonic epilepsy and ragged-red fiber disease (MERRF) is associated with a mitochondrial DNA tRNA(Lys) mutation', *Cell*, 61(6), pp. 931–937. Available at: https://doi.org/10.1016/0092-8674(90)90059-n.

Shokolenko, I. *et al.* (2009) 'Oxidative stress induces degradation of mitochondrial DNA', *Nucleic Acids Research*, 37(8), pp. 2539–2548. Available at: https://doi.org/10.1093/nar/gkp100.

Shutt, T.E., Bestwick, M. and Shadel, G.S. (2011) 'The core human mitochondrial transcription initiation complex', *Transcription*, 2(2), pp. 55–59. Available at: https://doi.org/10.4161/trns.2.2.14296.

Sík, A. *et al.* (2004) 'Self-regulated cleavage of the mitochondrial intramembrane-cleaving protease PARL yields Pbeta, a nuclear-targeted peptide', *The Journal of Biological Chemistry*, 279(15), pp. 15323–15329. Available at: https://doi.org/10.1074/jbc.M313756200.

Simuni, T. *et al.* (2024) 'A biological definition of neuronal α-synuclein disease: towards an integrated staging system for research', *The Lancet. Neurology*, 23(2), pp. 178–190. Available at: https://doi.org/10.1016/S1474-4422(23)00405-2.

Son, J.M. and Lee, C. (2019) 'Mitochondria: multifaceted regulators of aging', *BMB Reports*, 52(1), pp. 13–23. Available at: https://doi.org/10.5483/BMBRep.2019.52.1.300.

Song, M. *et al.* (2017) 'Abrogating Mitochondrial Dynamics in Mouse Hearts Accelerates Mitochondrial Senescence', *Cell Metabolism*, 26(6), pp. 872-883.e5. Available at: https://doi.org/10.1016/j.cmet.2017.09.023.

Soubannier, V. *et al.* (2012) 'Reconstitution of Mitochondria Derived Vesicle Formation Demonstrates Selective Enrichment of Oxidized Cargo', *PLOS ONE*, 7(12), p. e52830. Available at: https://doi.org/10.1371/journal.pone.0052830.

Souder, D.C. *et al.* (2023) 'Mitochondrial regulator PGC-1a in neuronal metabolism and brain aging', *bioRxiv*, p. 2023.09.29.559526. Available at: https://doi.org/10.1101/2023.09.29.559526.

Soyal, S.M. *et al.* (2012) 'A greatly extended PPARGC1A genomic locus encodes several new brain-specific isoforms and influences Huntington disease age of onset†', *Human Molecular Genetics*, 21(15), pp. 3461–3473. Available at: https://doi.org/10.1093/hmg/dds177.

Soyal, S.M. *et al.* (2019) 'The PPARGC1A locus and CNS-specific PGC-1α isoforms are associated with Parkinson's Disease', *Neurobiology of Disease*, 121, pp. 34–46. Available at: https://doi.org/10.1016/j.nbd.2018.09.016.

Spang, A. *et al.* (2015) 'Complex archaea that bridge the gap between prokaryotes and eukaryotes', *Nature*, 521(7551), pp. 173–179. Available at: https://doi.org/10.1038/nature14447.

Spencer, A.C. and Spremulli, L.L. (2004) 'Interaction of mitochondrial initiation factor 2 with mitochondrial fMet-tRNA', *Nucleic Acids Research*, 32(18), pp. 5464–5470. Available at: https://doi.org/10.1093/nar/gkh886.

Spremulli, L.L. *et al.* (2004) 'Initiation and elongation factors in mammalian mitochondrial protein biosynthesis', *Progress in Nucleic Acid Research and Molecular Biology*, 77, pp. 211–261. Available at: https://doi.org/10.1016/S0079-6603(04)77006-3.

Stenqvist, L. *et al.* (2005) 'A juvenile case of MELAS with T3271C mitochondrial DNA mutation', *Pediatric Research*, 58(2), pp. 258–262. Available at: https://doi.org/10.1203/01.PDR.0000169966.82325.1A.

Steriade, M. (2004) 'Acetylcholine systems and rhythmic activities during the waking--sleep cycle', *Progress in Brain Research*, 145, pp. 179–196. Available at: https://doi.org/10.1016/S0079-6123(03)45013-9.

Stewart, J.B. and Chinnery, P.F. (2015) 'The dynamics of mitochondrial DNA heteroplasmy: implications for human health and disease', *Nature Reviews. Genetics*, 16(9), pp. 530–542. Available at: https://doi.org/10.1038/nrg3966.

Stojanovski, D. *et al.* (2004) 'Levels of human Fis1 at the mitochondrial outer membrane regulate mitochondrial morphology', *Journal of Cell Science*, 117(Pt 7), pp. 1201–1210. Available at: https://doi.org/10.1242/jcs.01058.

St-Pierre, J. *et al.* (2003) 'Bioenergetic analysis of peroxisome proliferator-activated receptor gamma coactivators 1alpha and 1beta (PGC-1alpha and PGC-1beta) in muscle cells', *The Journal of Biological Chemistry*, 278(29), pp. 26597–26603. Available at: https://doi.org/10.1074/jbc.M301850200.

Strauss, K.M. *et al.* (2005) 'Loss of function mutations in the gene encoding Omi/HtrA2 in Parkinson's disease', *Human Molecular Genetics*, 14(15), pp. 2099–2111. Available at: https://doi.org/10.1093/hmg/ddi215.

Sundborger, A.C. *et al.* (2014) 'A dynamin mutant defines a super-constricted pre-fission state', *Cell reports*, 8(3), pp. 734–742. Available at: https://doi.org/10.1016/j.celrep.2014.06.054.

Sutovsky, P. *et al.* (2000) 'Ubiquitinated Sperm Mitochondria, Selective Proteolysis, and the Regulation of Mitochondrial Inheritance in Mammalian Embryos1', *Biology of Reproduction*, 63(2), pp. 582–590. Available at: https://doi.org/10.1095/biolreprod63.2.582.

Suzuki, T. and Kamiya, H. (2017) 'Mutations induced by 8-hydroxyguanine (8-oxo-7,8-dihydroguanine), a representative oxidized base, in mammalian cells', *Genes and Environment: The Official Journal of the Japanese Environmental Mutagen Society*, 39, p. 2. Available at: https://doi.org/10.1186/s41021-016-0051-y.

Swenson, S.A. *et al.* (2020) 'From Synthesis to Utilization: The Ins and Outs of Mitochondrial Heme', *Cells*, 9(3), p. 579. Available at: https://doi.org/10.3390/cells9030579.

Tam, Z.Y. *et al.* (2013) 'Mathematical modeling of the role of mitochondrial fusion and fission in mitochondrial DNA maintenance', *PloS One*, 8(10), p. e76230. Available at: https://doi.org/10.1371/journal.pone.0076230.

Tanaka, A. *et al.* (2010) 'Proteasome and p97 mediate mitophagy and degradation of mitofusins induced by Parkin', *The Journal of Cell Biology*, 191(7), pp. 1367–1380. Available at: https://doi.org/10.1083/jcb.201007013.

Taylor, R.W. *et al.* (2003) 'Mitochondrial DNA mutations in human colonic crypt stem cells', *The Journal of Clinical Investigation*, 112(9), pp. 1351–1360. Available at: https://doi.org/10.1172/JCI19435.

Temperley, R. *et al.* (2010) 'Hungry codons promote frameshifting in human mitochondrial ribosomes', *Science (New York, N.Y.)*, 327(5963), p. 301. Available at: https://doi.org/10.1126/science.1180674.

Terrazzino, S. *et al.* (2016) 'Common European Mitochondrial Haplogroups in the Risk for Radiation-induced Subcutaneous Fibrosis in Breast Cancer Patients', *Clinical Oncology (Royal College of Radiologists (Great Britain))*, 28(6), pp. 365–372. Available at: https://doi.org/10.1016/j.clon.2016.02.007.

Terzioglu, M. *et al.* (2013) 'MTERF1 binds mtDNA to prevent transcriptional interference at the light-strand promoter but is dispensable for rRNA gene transcription regulation',

Cell Metabolism, 17(4), pp. 618–626. Available at: https://doi.org/10.1016/j.cmet.2013.03.006.

Thevathasan, W. *et al.* (2011) 'Pedunculopontine nucleus stimulation improves gait freezing in Parkinson disease', *Neurosurgery*, 69(6), pp. 1248–1253; discussion 1254. Available at: https://doi.org/10.1227/NEU.0b013e31822b6f71.

Thivierge, J.-P. (2008) 'Neural diversity creates a rich repertoire of brain activity', *Communicative & Integrative Biology*, 1(2), pp. 188–189. Available at: https://doi.org/10.4161/cib.1.2.7283.

Thusberg, J., Olatubosun, A. and Vihinen, M. (2011) 'Performance of mutation pathogenicity prediction methods on missense variants', *Human Mutation*, 32(4), pp. 358–368. Available at: https://doi.org/10.1002/humu.21445.

Tonazzi, A. *et al.* (2021) 'The Mitochondrial Carnitine Acyl-carnitine Carrier (SLC25A20): Molecular Mechanisms of Transport, Role in Redox Sensing and Interaction with Drugs', *Biomolecules*, 11(4). Available at: https://doi.org/10.3390/biom11040521.

Tong, M., Zablocki, D. and Sadoshima, J. (2020) 'The role of Drp1 in mitophagy and cell death in the heart', *Journal of molecular and cellular cardiology*, 142, pp. 138–145. Available at: https://doi.org/10.1016/j.yjmcc.2020.04.015.

Tresse, E. *et al.* (2023) 'Mitochondrial DNA damage triggers spread of Parkinson's disease-like pathology', *Molecular Psychiatry*, 28(11), pp. 4902–4914. Available at: https://doi.org/10.1038/s41380-023-02251-4.

Trumpower, B.L. (1990) 'The protonmotive Q cycle. Energy transduction by coupling of proton translocation to electron transfer by the cytochrome bc1 complex.', *Journal of Biological Chemistry*, 265(20), pp. 11409–11412. Available at: https://doi.org/10.1016/S0021-9258(19)38410-8.

Trumpower, B.L. (2002) 'A concerted, alternating sites mechanism of ubiquinol oxidation by the dimeric cytochrome bc(1) complex', *Biochimica Et Biophysica Acta*, 1555(1–3), pp. 166–173. Available at: https://doi.org/10.1016/s0005-2728(02)00273-6.

Tseng, L.-M. *et al.* (2009) 'Association between mitochondrial DNA 4,977 bp deletion and NAD(P)H:quinone oxidoreductase 1 C609T polymorphism in human breast tissues', *Oncology Reports*, 21(5), pp. 1169–1174. Available at: https://doi.org/10.3892/or_00000337.

Twig, G. *et al.* (2008) 'Fission and selective fusion govern mitochondrial segregation and elimination by autophagy', *The EMBO Journal*, 27(2), pp. 433–446. Available at: https://doi.org/10.1038/sj.emboj.7601963.

Tzen, C.-Y. *et al.* (2003) 'Melas with point mutations involving tRNALeu (A3243G) and tRNAGlu(A14693g)', *Muscle & Nerve*, 28(5), pp. 575–581. Available at: https://doi.org/10.1002/mus.10473.

Uemura, S. *et al.* (2010) 'Real-time tRNA transit on single translating ribosomes at codon resolution', *Nature*, 464(7291), pp. 1012–1017. Available at: https://doi.org/10.1038/nature08925.

Uhler, J.P. *et al.* (2016) 'MGME1 processes flaps into ligatable nicks in concert with DNA polymerase γ during mtDNA replication', *Nucleic Acids Research*, 44(12), pp. 5861–5871. Available at: https://doi.org/10.1093/nar/gkw468.

Valiente-Pallejà, A. *et al.* (2022) 'Comprehensive summary of mitochondrial DNA alterations in the postmortem human brain: A systematic review', *eBioMedicine*, 76, p. 103815. Available at: https://doi.org/10.1016/j.ebiom.2022.103815.

Vázquez-Coto, D. *et al.* (2022) 'Common mitochondrial haplogroups as modifiers of the onset-age for critical COVID-19', *Mitochondrion*, 67, pp. 1–5. Available at: https://doi.org/10.1016/j.mito.2022.09.001.

Ventura-Clapier, R., Garnier, A. and Veksler, V. (2008) 'Transcriptional control of mitochondrial biogenesis: the central role of PGC-1alpha', *Cardiovascular Research*, 79(2), pp. 208–217. Available at: https://doi.org/10.1093/cvr/cvn098.

Vidyadhara, D.J. *et al.* (2021) 'Differences in Neuronal Numbers, Morphology, and Developmental Apoptosis in Mice Nigra Provide Experimental Evidence of Ontogenic Origin of Vulnerability to Parkinson's Disease', *Neurotoxicity Research*, 39(6), pp. 1892–1907. Available at: https://doi.org/10.1007/s12640-021-00439-6.

Vincent, A.E. *et al.* (2018) 'Subcellular origin of mitochondrial DNA deletions in human skeletal muscle', *Annals of Neurology*, 84(2), pp. 289–301. Available at: https://doi.org/10.1002/ana.25288.

Vincent, S.R. and Kimura, H. (1992) 'Histochemical mapping of nitric oxide synthase in the rat brain', *Neuroscience*, 46(4), pp. 755–784. Available at: https://doi.org/10.1016/0306-4522(92)90184-4.

Virbasius, J.V. and Scarpulla, R.C. (1994) 'Activation of the human mitochondrial transcription factor A gene by nuclear respiratory factors: a potential regulatory link between nuclear and mitochondrial gene expression in organelle biogenesis.', *Proceedings of the National Academy of Sciences of the United States of America*, 91(4), pp. 1309–1313.

Vives-Bauza, C. *et al.* (2002) 'Sequence analysis of the entire mitochondrial genome in Parkinson's disease', *Biochemical and Biophysical Research Communications*, 290(5), pp. 1593–1601. Available at: https://doi.org/10.1006/bbrc.2002.6388.

Vögtle, F.-N. *et al.* (2018) 'Mutations in *PMPCB* Encoding the Catalytic Subunit of the Mitochondrial Presequence Protease Cause Neurodegeneration in Early Childhood', *The American Journal of Human Genetics*, 102(4), pp. 557–573. Available at: https://doi.org/10.1016/j.ajhg.2018.02.014.

Wachsmuth, M. *et al.* (2016) 'Age-Related and Heteroplasmy-Related Variation in Human mtDNA Copy Number', *PLoS genetics*, 12(3), p. e1005939. Available at: https://doi.org/10.1371/journal.pgen.1005939.

Wai, T. and Langer, T. (2016) 'Mitochondrial Dynamics and Metabolic Regulation', *Trends in Endocrinology & Metabolism*, 27(2), pp. 105–117. Available at: https://doi.org/10.1016/j.tem.2015.12.001.

Wallace, D.C. (1986) 'Mitotic segregation of mitochondrial DNAs in human cell hybrids and expression of chloramphenicol resistance', *Somatic Cell and Molecular Genetics*, 12(1), pp. 41–49. Available at: https://doi.org/10.1007/BF01560726.

Wallace, D.C. (1989) 'Mitochondrial DNA mutations and neuromuscular disease', *Trends in Genetics*, 5, pp. 9–13. Available at: https://doi.org/10.1016/0168-9525(89)90005-X.

van der Walt, J.M. *et al.* (2004) 'Analysis of European mitochondrial haplogroups with Alzheimer disease risk', *Neuroscience Letters*, 365(1), pp. 28–32. Available at: https://doi.org/10.1016/j.neulet.2004.04.051.

Wang, D., Kreutzer, D.A. and Essigmann, J.M. (1998) 'Mutagenicity and repair of oxidative DNA damage: insights from studies using defined lesions', *Mutation Research/Fundamental and Molecular Mechanisms of Mutagenesis*, 400(1), pp. 99–115. Available at: https://doi.org/10.1016/S0027-5107(98)00066-9.

Wang, H.-L. *et al.* (2007) 'PINK1 mutants associated with recessive Parkinson's disease are defective in inhibiting mitochondrial release of cytochrome *c*', *Neurobiology of Disease*, 28(2), pp. 216–226. Available at: https://doi.org/10.1016/j.nbd.2007.07.010.

Wang, H.-L. and Morales, M. (2009) 'Pedunculopontine and laterodorsal tegmental nuclei contain distinct populations of cholinergic, glutamatergic and GABAergic neurons in the rat', *The European Journal of Neuroscience*, 29(2), pp. 340–358. Available at: https://doi.org/10.1111/j.1460-9568.2008.06576.x.

Wang, W. *et al.* (2017) 'A conserved retromer sorting motif is essential for mitochondrial DLP1 recycling by VPS35 in Parkinson's disease model', *Human Molecular Genetics*, 26(4), pp. 781–789. Available at: https://doi.org/10.1093/hmg/ddw430.

Wanrooij, P.H. *et al.* (2010) 'G-quadruplex structures in RNA stimulate mitochondrial transcription termination and primer formation', *Proceedings of the National Academy of Sciences of the United States of America*, 107(37), pp. 16072–16077. Available at: https://doi.org/10.1073/pnas.1006026107.

Wanrooij, P.H. *et al.* (2012) 'A hybrid G-quadruplex structure formed between RNA and DNA explains the extraordinary stability of the mitochondrial R-loop', *Nucleic Acids Research*, 40(20), pp. 10334–10344. Available at: https://doi.org/10.1093/nar/gks802.

Wanrooij, S. and Falkenberg, M. (2010) 'The human mitochondrial replication fork in health and disease', *Biochimica Et Biophysica Acta*, 1797(8), pp. 1378–1388. Available at: https://doi.org/10.1016/j.bbabio.2010.04.015.

Wei, W. *et al.* (2017) 'Mitochondrial DNA point mutations and relative copy number in 1363 disease and control human brains', *Acta Neuropathologica Communications*, 5, p. 13. Available at: https://doi.org/10.1186/s40478-016-0404-6.

Weissensteiner, H. *et al.* (2016) 'mtDNA-Server: next-generation sequencing data analysis of human mitochondrial DNA in the cloud', *Nucleic Acids Research*, 44(Web Server issue), pp. W64–W69. Available at: https://doi.org/10.1093/nar/gkw247.

Welter, M.-L. *et al.* (2015) 'PPNa-DBS for gait and balance disorders in Parkinson's disease: a double-blind, randomised study', *Journal of Neurology*, 262(6), pp. 1515–1525. Available at: https://doi.org/10.1007/s00415-015-7744-1.

Wenning, G.K. *et al.* (2022) 'The Movement Disorder Society Criteria for the Diagnosis of Multiple System Atrophy', *Movement Disorders: Official Journal of the Movement Disorder Society*, 37(6), pp. 1131–1148. Available at: https://doi.org/10.1002/mds.29005.

Wheelhouse, N.M. *et al.* (2005) 'Mitochondrial D-loop mutations and deletion profiles of cancerous and noncancerous liver tissue in hepatitis B virus-infected liver', *British Journal of Cancer*, 92(7), pp. 1268–1272. Available at: https://doi.org/10.1038/sj.bjc.6602496.

Whittle, B.J. *et al.* (2024) 'Early-stage idiopathic Parkinson's disease is associated with reduced circular RNA expression', *NPJ Parkinson's disease*, 10(1), p. 25. Available at: https://doi.org/10.1038/s41531-024-00636-y.

Williams, S.L. *et al.* (2013) 'Somatic mtDNA mutation spectra in the aging human putamen', *PLoS genetics*, 9(12), p. e1003990. Available at: https://doi.org/10.1371/journal.pgen.1003990.

Wong, L.-J.C. *et al.* (2002) 'Comprehensive scanning of the entire mitochondrial genome for mutations', *Clinical Chemistry*, 48(11), pp. 1901–1912.

Wu, Z. *et al.* (1999) 'Mechanisms Controlling Mitochondrial Biogenesis and Respiration through the Thermogenic Coactivator PGC-1', *Cell*, 98(1), pp. 115–124. Available at: https://doi.org/10.1016/S0092-8674(00)80611-X.

Xia, D. *et al.* (2013) 'Structural analysis of cytochrome bc1 complexes: Implications to the mechanism of function', *Biochimica et Biophysica Acta (BBA) - Bioenergetics*, 1827(11), pp. 1278–1294. Available at: https://doi.org/10.1016/j.bbabio.2012.11.008.

Xiao, B. *et al.* (2017) 'Reactive oxygen species trigger Parkin/PINK1 pathway-dependent mitophagy by inducing mitochondrial recruitment of Parkin', *The Journal of Biological Chemistry*, 292(40), pp. 16697–16708. Available at: https://doi.org/10.1074/jbc.M117.787739.

Xu, J. *et al.* (2016) 'Autophagy-mediated degradation of IAPs and c-FLIPL potentiates apoptosis induced by combination of TRAIL and Chal-24', *Journal of cellular biochemistry*, 117(5), pp. 1136–1144. Available at: https://doi.org/10.1002/jcb.25397.

Yakubovskaya, E. *et al.* (2014) 'Organization of the human mitochondrial transcription initiation complex', *Nucleic Acids Research*, 42(6), pp. 4100–4112. Available at: https://doi.org/10.1093/nar/gkt1360.

Yamano, K. and Youle, R.J. (2013) 'PINK1 is degraded through the N-end rule pathway', *Autophagy*, 9(11), pp. 1758–1769. Available at: https://doi.org/10.4161/auto.24633.

Yang, L. *et al.* (2014) 'Species identification through mitochondrial rRNA genetic analysis', *Scientific Reports*, 4, p. 4089. Available at: https://doi.org/10.1038/srep04089.

Yang, X.H. and Trumpower, B.L. (1988) 'Protonmotive Q cycle pathway of electron transfer and energy transduction in the three-subunit ubiquinol-cytochrome c oxidoreductase complex of Paracoccus denitrificans.', *Journal of Biological Chemistry*, 263(24), pp. 11962–11970. Available at: https://doi.org/10.1016/S0021-9258(18)37880-3.

Yilmaz, R. *et al.* (2019) 'Biomarkers of Parkinson's disease: 20 years later', *Journal of Neural Transmission (Vienna, Austria: 1996)*, 126(7), pp. 803–813. Available at: https://doi.org/10.1007/s00702-019-02001-3.

Yoneda, M. *et al.* (1992) 'Marked replicative advantage of human mtDNA carrying a point mutation that causes the MELAS encephalomyopathy.', *Proceedings of the National Academy of Sciences of the United States of America*, 89(23), pp. 11164–11168.

Yonova-Doing, E. *et al.* (2021) 'An atlas of mitochondrial DNA genotype-phenotype associations in the UK Biobank', *Nature Genetics*, 53(7), pp. 982–993. Available at: https://doi.org/10.1038/s41588-021-00868-1.

Yoon, Y. *et al.* (2003) 'The mitochondrial protein hFis1 regulates mitochondrial fission in mammalian cells through an interaction with the dynamin-like protein DLP1', *Molecular and Cellular Biology*, 23(15), pp. 5409–5420. Available at: https://doi.org/10.1128/MCB.23.15.5409-5420.2003.

Yoshimi, A. *et al.* (2021) 'Haematological characteristics and spontaneous haematological recovery in Pearson syndrome', *British Journal of Haematology*, 193(6), pp. 1283–1287. Available at: https://doi.org/10.1111/bjh.17434.

Yoshimi, A. *et al.* (2022) 'Pearson syndrome: a multisystem mitochondrial disease with bone marrow failure', *Orphanet Journal of Rare Diseases*, 17(1), p. 379. Available at: https://doi.org/10.1186/s13023-022-02538-9.

Yu, M. *et al.* (2007) 'Reduced mitochondrial DNA copy number is correlated with tumor progression and prognosis in Chinese breast cancer patients', *IUBMB life*, 59(7), pp. 450–457. Available at: https://doi.org/10.1080/15216540701509955.

Yusoff, A.A.M. *et al.* (2019) 'A comprehensive overview of mitochondrial DNA 4977-bp deletion in cancer studies', *Oncology Reviews*, 13(1), p. 409. Available at: https://doi.org/10.4081/oncol.2019.409.

Yu-Wai-Man, P., Griffiths, P.G. and Chinnery, P.F. (2011) 'Mitochondrial optic neuropathies - disease mechanisms and therapeutic strategies', *Progress in Retinal and Eye Research*, 30(2), pp. 81–114. Available at: https://doi.org/10.1016/j.preteyeres.2010.11.002.

Zaepfel, B.L. *et al.* (2021) 'UPF1 reduces *C9orf72* HRE-induced neurotoxicity in the absence of nonsense-mediated decay dysfunction', *Cell Reports*, 34(13), p. 108925. Available at: https://doi.org/10.1016/j.celrep.2021.108925.

Zamzami, N. *et al.* (1996) 'Mitochondrial control of nuclear apoptosis', *The Journal of Experimental Medicine*, 183(4), pp. 1533–1544. Available at: https://doi.org/10.1084/jem.183.4.1533.

Zavialov, A.V., Buckingham, R.H. and Ehrenberg, M. (2001) 'A posttermination ribosomal complex is the guanine nucleotide exchange factor for peptide release factor RF3', *Cell*, 107(1), pp. 115–124. Available at: https://doi.org/10.1016/s0092-8674(01)00508-6.

Zeviani, M. *et al.* (1988) 'Deletions of mitochondrial DNA in Kearns-Sayre syndrome', *Neurology*, 38(9), pp. 1339–1346. Available at: https://doi.org/10.1212/wnl.38.9.1339.

Zhang, H., Burr, S.P. and Chinnery, P.F. (2018) 'The mitochondrial DNA genetic bottleneck: inheritance and beyond', *Essays in Biochemistry*. Edited by C. Garone and M. Minczuk, 62(3), pp. 225–234. Available at: https://doi.org/10.1042/EBC20170096.

Zhang, Z. and Gerstein, M. (2003) 'Patterns of nucleotide substitution, insertion and deletion in the human genome inferred from pseudogenes', *Nucleic Acids Research*, 31(18), pp. 5338–5348. Available at: https://doi.org/10.1093/nar/gkg745.

Zheng, W. *et al.* (2006) 'Origins of human mitochondrial point mutations as DNA polymerase γ-mediated errors', *Mutation Research/Fundamental and Molecular Mechanisms of Mutagenesis*, 599(1), pp. 11–20. Available at: https://doi.org/10.1016/j.mrfmmm.2005.12.012.

Zheng, Y., Luo, A. and Liu, X. (2021) 'The Imbalance of Mitochondrial Fusion/Fission Drives High-Glucose-Induced Vascular Injury', *Biomolecules*, 11(12), p. 1779. Available at: https://doi.org/10.3390/biom11121779.

Zhu, J., Vinothkumar, K.R. and Hirst, J. (2016) 'Structure of mammalian respiratory complex I', *Nature*, 536(7616), pp. 354–358. Available at: https://doi.org/10.1038/nature19095.

Zickermann, V. *et al.* (2003) 'Functional Implications from an Unexpected Position of the 49-kDa Subunit of NADH:Ubiquinone Oxidoreductase*', *Journal of Biological Chemistry*, 278(31), pp. 29072–29078. Available at: https://doi.org/10.1074/jbc.M302713200.

Zimprich, A. *et al.* (2004) 'Mutations in LRRK2 cause autosomal-dominant parkinsonism with pleomorphic pathology', *Neuron*, 44(4), pp. 601–607. Available at: https://doi.org/10.1016/j.neuron.2004.11.005.

Zolkipli-Cunningham, Z. and Falk, M.J. (2017) 'Clinical effects of chemical exposures on mitochondrial function', *Toxicology*, 391, pp. 90–99. Available at: https://doi.org/10.1016/j.tox.2017.07.009.